CYRI-A is recruited to macropinocytic cups and mediates integrin uptake, limiting invasive migration

HOANG ANH, LE

Thesis submitted in fulfilment of the requirements for the Degree of Doctor of Philosophy

October 2020

Cancer Research UK – Beatson Institute
University of Glasgow

Acknowledgement

Firstly, I would like to thank Professor Laura Machesky for so graciously accepting me to her lab. I still remember the first time we talked at the PhD interview. Laura showed me all the cool microscopy videos of melanocytes migrating in the dermis. I remember I was so captivated by this, and the fact that she was the one who discovered the Arp2/3 complex made me knew that her lab was where I wanted to be. Laura has been the most inspiring person to me! I remember every conversation we had, how she told me all about those days when she was still a PhD student, how her experiments went wrong in so many different ways and how happy she was when there were colonies on the agar plates after all those late nights and weekends of nonstop cloning, and her excitement to find out if they had the piece of DNA she was looking for. To me, that is the most relevant thing that I could relate to. She always inspires me to be curious, to be relentless, to be strong but adaptive. She gave me every opportunity to think independently, to make, develop and test my own hypotheses. This is something that I would keep and treasure throughout my scientific career and beyond. I would also like to thank Shehab and Robert for all the discussions we share. Without your expertise and input, many of the work here won't be complete and I am grateful for that! I would also want to thank my advisor Jim Norman for his expert knowledge in integrin trafficking and Leo Carlin for his expert knowledge in imaging.

Throughout these 4 years, it hasn't always been a smooth ride, there are so many ups and downs and, to be honest, it was a rollercoaster to me. The first 2 years were the hardest for me, things didn't go as planned, projects didn't work out as expected, I was struggling with my work-life balance. I would have gone insane if it wasn't for these people that I am so lucky to have in my life. The first person is Clelia. She was a former PhD student with Robert Insall and I am thankful that our labs share space. I remember those days when I just wanted to cry because I didn't think I could do it, and Clelia was always the first person to hear me talk and gave me the most honest advice. In many ways, her journey and mine share many similarities and I think that is what bonds us together. The second

person is my bestie, Farah. She was a former postdoc in Peter Adams's lab and I don't know what bonded us together, but we just clicked. We were both goofy and shared many things in common. I introduced her to the world of bubble tea and all those days sitting in Hi-Tea with Yasmina, chatting away for hours. You're the kindest person I've ever met and will remain my forever bestie. The third person and perhaps the most significant person in my life is my boyfriend Andy. How can I forget all the ranting about my experiments didn't go well and how frustrated I was when things just didn't work out the way I wanted them to be? He's always spent the time to listen to all of my nonsense talks even when he didn't understand all the technical things. Living half the world across from my home country, and dealing with many personal anxiety and difficulties, Andy has always been by my side and support me unconditionally, even when my whole world was on the brink of collapse. There were just so many things happening behind the happy face that I put out, and without these people, I don't think I would be able to get through.

I would like to also thank every single person in Laura's and Robert's lab for accepting me, no matter how exotic and weird I was. They give me the confidence to be true to myself, without worrying about what other people might think of me. Heather, you will always be my TC buddy. We have the best time talking shite together, laugh together, telling silly dad jokes together. Without your positive vibe and your help in teaching me and introducing me to everyone else, I would not be where I am today. I thank Peter for all the knowledgeable and honest advice on the train home. I always look up to you as a role model and your advice is always the most insightful and truthful to me. Doctor Simona, I remember the first time we talked was at the Beatson retreat, and since then, I've been following you everywhere. I even move myself to live near you (unintentionally ;)). You are the sweetest, nicest person I've ever met. I love being around you, and making you laugh, and visiting your flat and playing games on your VR headset and of course, all the parties that the lab just decided to be organised by you in your flat. I want to thank queen Nikki for always sharing your vast knowledge of almost anything I asked, whether it's microscopy, flow cytometry or bioinformatics, as well as your love for Asian cuisine and culture to which I always appreciate. Elaine, you're a newbie but we have formed an instant

connection right the first day we met (maybe it's an Asian thing XD). I enjoyed every conversation we had, even if it's mostly through the phone because of the pandemic. Thank you for always listening to me and I hope you will have the best PhD experience you can get. Of course, to Sophie, for sharing so many memorable moments and photoshoots. We did so many wild things together, for dressing in our pyjamas for the Christmas party and for the nightlong game night. To Vassilis, my bench buddy! We always have this unspoken connection and always seem to understand each other even if it's just eye contact or a smirk. You've been the calmest and most composed person I've ever met, and I think that really does balances out my crazy and wild nature. We really are complementing each other and make the perfect bench mate and deskmate! I would also like to thank Tamas from Shehab's lab. You are one of the nicest people I've met, and I am so lucky that I got the gut to approach you when I initiated the collaboration. You are quiet and shy, and I'm wild and outspoken, we made a great pair working together. I enjoy all of our talks and appreciate all the time you have taken to teach me protein purification, even though I'm still scared of that intimidating machine. You are an excellent scientist, and with a bit more confidence, you can do anything! I would like to thank every other member of the two labs and our neighbour David Bryant's lab for all the help, the chat, the time we spent together. Without all of you, I don't think I could have done it.

I would like to thank my family from Vietnam. Even though we are a world apart, I always know that you always want the best for me and believe in me. I know it is hard to be so far from your son and that you might find it difficult to accept me for who I am, but one thing I can say is to thank you for always trusting in me, and let me fly high and free. I hope as time goes on, you will learn to accept me for who I am, not because to please me, but because it is the right thing to do.

This is the thesis of the pandemic. Never in my life, I could have thought of completing my PhD during a global pandemic. Nothing is more disappointing and scarier than the uncertainty waiting ahead. But will I let that define me? Never! So COVID, you can GO F*CK YOURSELF!

***

If each month of your life is a diamond, then each of us will have roughly 960 diamonds if we live to 80 years old. By the age of 30, you have already lost 1/3 of what was given. So live and treasure every day like it's your last day under the sun. You are unique and special in your own way and never let anyone tell you otherwise.

Anh

***

Author's declaration

I, Hoang Anh Le hereby declare that all of the work in this thesis was performed personally with the following exceptions mentioned below. No part of this thesis has been submitted to other degree or award at this or another university.

Hoang Anh, Le

Chapter 3

- The determination of the crystal structure of CYRI-BΔN and of CYRI-BΔN-RAC1 Q61L (Figure 3.8A, Figure 3.9, Figure 3.11), the structural mapping of the interaction residues (Figure 3.10A, B, C) was done by Dr Tamas Yelland (CRUK Beatson Institute).

Chapter 5

- The *in vivo* tubulation assay was performed by Professor Hongxia Zhao (University of Helsinki) (Figure 5.6).

Chapter 8

- The principle component analysis (PCA) was performed by Dr Robin Shaw (Bioinformatic department-CRUK Beatson Institute) (Figure 8.1).
- The Figure 8.2 and Figure 8.6 was made with the help of Dr Nikki Paul (CRUK Beatson Institute).

Chapter 10

- Figure 10.13 and Figure 10.14 was made by the undergraduate student Julija Povilaikaite under my supervision.

Abbreviations

2D: 2-dimension
3D: 3-dimension

α-MSH: α-Melanocyte-stimulating Hormone

A.
Abi: Abl interactor
Abl: Abelson Tyrosine-Protein Kinase
ADP: Adenosine diphosphate
AP2: Adaptor protein complex 2
aPKC: atypical protein kinase C
APTs: Acyl-protein thioesterases
ARF4: ADP-ribosylation factor 4
Arp: Actin related protein
ArpC: Actin related protein complex
ATP: Adenosine triphosphate
AUC: Analytical ultracentrifugation

B.
bFGF: basic fibroblast growth factor
BTK: Bruton's tyrosine kinase

C.
c-MYC: Cellular myelocytomatosis
cAMP: Cyclic adenosine monophosphate
CAV1: Caveolin-1
CDC42: Cell division control protein 42
CDE: clathrin-dependent endocytosis
CDK5: Cyclin-dependent kinase 5
CDM: Cell derived matrix
cDNA: Complementary DNA
CE: Cytoplasmic extraction
CIE: clathrin-independent endocytosis
CLIC3: Chloride intracellular channel protein
complex
CREB: cAMP-response element binding protein
CRIB motif: Cdc42/Rac interactive binding motif
CRISPR: clustered regularly interspaced short palindromic repeats
CTBP-1: C-terminal-binding protein 1
CTC: circulating tumour cell
CYFIP1: Cytoplasmic FMR1-interacting protein
CYRI: CYFIP-related RAC interactor

D.
DBKD: double knockdown
DBKO: double knockout
DMSO: dimethyl sulfoxide
DOCK: Dedicator of cytokinesis protein
DUF1394: Domain of unknown function 1394

E.

E: Embryonic day
eCFP: enhanced Cyan fluorescent protein
ECM: Extra cellular matrix
EGF: Epidermal growth factor
EGFR: Epidermal growth factor receptor
EHT1864: 5-(5-(7-(Trifluoromethyl)quinolin-4-ylthio)pentyloxy)-2-(morpholinomethyl)-4H-pyran-4-one dihydrochloride
ELMO: Engulfment and cell motility protein
EM: Electron microscopy
EMT: epithelial-to-mesenchymal transition
EPS15: epidermal growth factor receptor substrate 15
EPS8: Epidermal growth factor receptor substrate 8
ERK1/2: Extracellular signal-regulated kinase 1/2
EV: Empty vector

F.

F-actin: Filamentous actin
FA: Focal adhesion
FAC: Fluorescence Activated Cytometry
FAK: Focal adhesion kinase
FAM21: Family with sequence similarity 21
FAM49: Family of unknown function 49
FBS: Fetal bovine serum
FERM: 4.1, ezrin, radixin, moesin
FH: Formin homology
FLPs: filopodium-like protrusions
FMNL2: Formin like protein 2
FRET: Forster resonance energy transfer
FRS2: Fibroblast growth factor receptor substrate 2
FTase: Farnesyltransferase

G.

G-actin: Globular actin
GAB1: GRB2-associated-binding protein 1
GAPs: GTPase-activating proteins
GDP: Guanine diphosphate
GEFs: Guanine nucleotide exchange factors
GFP: Green fluorescent protein
GGTase-1: Geranylgeranyltransferase type I
GPCR: G-protein coupled receptor
GppNHp: 5'-Guanylyl imidodiphosphate
GRB2: Growth factor receptor-bound protein 2
GRP1: general receptor for phosphoinositides 1
GSH: Glutathione
GST: Glutathione S-transferase
GTP: Guanine triphosphate

GWAS: Genome-wide association study

H.

H&E: hematoxylin and eosin
HAX-1: HS1-associated protein X-1
HDAC2: Histonedeacetylase 2
HGFR: Hepatocyte growth factor receptor
HSP90: Heatshock protein 90
HSPC300: Hematopoietic stem/progenitor cell protein 300
HVR: Hypervariable region

I.

i-TASSER: Iterative Threading ASSEmbly Refinement
Icmt: Isoprenylcysteine-O-carboxyl methyltransferase
IPTG: Isopropyl ß- d-1-thiogalactopyranoside
IRsp53: Insulin receptor substrate 53kDa
ITGA5: Integrin alpha 5
ITGB1: Integrin beta 1

K.

KD: knockdown
KIF15: Kinesis-like protein KIF15
KO: knockout

L.

LAP: Latency associated peptide
LB: L-Broth
Lck: lymphocyte-specific protein tyrosine kinase
LIMK: LIM domain kinase
LPAR1: Lysophosphatidic acid receptor 1

M.

M-CSF: Macrophage-colony stimulating factor
MAPK: Mitogen activated protein kinase
MBP: Maltose binding protein
MC1R: melanocortin 1 receptor
ME: Membrane extraction
MEF: Mouse embryonic fibroblast
Mena: Mammalian enable
MES: 2-(N-morpholino)ethanesulfonic acid
metalloproteinase 1
MITF: Melanocyte Inducing Transcription Factor
MLC: Myosin light chain
MLCP: Myosin light chain phosphatase
MMP: Matrix metalloprotease
MOPS: 3-(N-morpholino)
MT1-MMP: Membrane type 1-matrix
mTOR: Mechanistic target of rapamycin
propanesulfonic acid

N.

N-WASP: Neural Wiskott-Aldrich syndrome protein

n.s: non significant
NAP1: Nck-associated protein 1
Ndrg1b: N-myc downstream-regulated 1b
NE: Nucleus extraction
NF: Neurofibromin
NK cells: Natural killer cells
NOX: NADPH oxidase
NPFs: Nucleation Promoting Factors

O.

OHT: hydroxytamoxifen

P.

P-REX: Phosphatidylinositol 3,4,5-trisphosphate-dependent Rac exchanger 1 protein
PAK: p21-activated kinase
Par: Proteinase-activated receptor
PBD: Pak binding domain
PBS: Phosphate buffer solution
PCA: Principle component analysis
PDAC: pancreatic ductal adenocarcinoma
PDGF: Platelet-derived growth factor
PFA: Paraformaldehyde
PH: Pleckstrin homology
Pi: Inorganic phosphate
PI(3,4)P2: Phosphatidylinositol-3,4-bisphosphate
PI(4,5)P2: Phosphatidylinositol-4,5-bisphosphate
PI3K: Phosphoinositide 3 kinase
PIP3: phosphatidylinositol (3,4,5)-trisphosphate
PKB: Protein kinase B
PKC: Protein kinase C
PKD: polycystic kidney disease protein
PLA: Proximity ligation assay
PLK4: Polo Like Kinase 4
PM: Plasma membrane
PMA: phorbol-12-myristate-13-acetate
POPC: 1-Palmitoyl-2-oleoyl-sn-glycero-3-PC
POPE: 1-palmitoyl-2-oleoyl-sn-glycero-3-PE
POPS: 1-palmitoyl-2-oleoyl-sn-glycero-3-phosphatidylserine
PSI: Plexin, semaphorin and integrin
PTB: phosphotyrosine-binding domain
PTEN: Phosphatidylinositol 3,4,5-trisphosphate 3-phosphatase and dual-specificity protein phosphatase
PTP18: Protein tyrosine phosphatase 18

Q.

qRT-PCR: Quantitative reverse transcription polymerase chain reaction

R.

RAB: Ras-related protein Rab
RAC1: Rac-related C3 botulinum toxin substrate 1
RAS: Rat sarcoma protein
RBD: Rac-binding domain
Rce-1: Ras-converting enzyme 1 endoprotease
RCP: Rab-coupling protein
RHOA: Ras homolog family member A
ROCK: Rho-associated protein kinase
ROS: reactive oxygen species
rpm: rotation per minute
rt: room teperature
RTK: Receptor tyrosine kinase

S.

Scar: Suppressor of cAMP receptor
SD: Standard deviation
SEM: Standard error of the mean
SFK: Src family kinase
sgRNA: single guide RNA
SH3: Src-homology domain 3
siRNA: Small interfering RNA
SNX: Sorting nexin
SOS: son of sevenless
SPR: Surface plasmon resonance
SRA1: Specifically RAC1 associated protein 1

T.

TAMs: tumour-associated macrophages
TASP1: Threonine aspartase 1
TBS-T: Tris-buffered saline-Tween
TCC: temporal-colour code
TGF-β: Transforming growth factor beta
Tiam1: T-lymphoma invasion and metastasis-inducing protein 1
TMD: Transmembrane domain
TNC: tenascin-C

U.

uPAR: Urokinase plasminogen activator surface receptor
UVR: UV radiation

V.

v-SNARE: Vesicle-Soluble NSF (N-Ethylmaleimide-Sensitive Factor) Attachment Protein Receptor
VAMP7: Vesicle associated membrane protein 7
VASP: Vasodilator Stimulated Phosphoprotein
VCA: Verprolin, cofilin, acidic
Vps: Vacuolar protein sorting-associated protein

W.

WASH: WASP and Scar homologue
WAVE: WASP-family verprolin homologous protein
WHD: Wiskott-Aldrich homology domain
Wnt: Wingless-related integration site

WRC: WAVE regulatory complex

WT: wild type

WCA: WHD, verprolin, cofilin, acidic

Y.

YAP: Yes-associated protein

Z.

ZFR: Zing finger RNA binding protein

Table of Contents

List of figures

1 Introduction

Migration is one of the most fundamental processes of life. It allows cells to find food, embryos to develop, wounds to heal and even cancer to metastasize. The consensus model for how a cell migrates can usually be divided into 5 steps: (1) leading protrusion by cytoskeletal polymerisation, (2) adhesion formation at the leading edge creating traction forces, (3) rear end contraction through myosin activity, (4) rear adhesion disassembly and (5) adhesion turnover (Sheetz et al., 1999). Each of these processes is regulated through intricate networks of signalling molecules and protein complexes. Even though each step has been studied in detail, the whole picture of how they are coordinated is far from clear. In this first chapter, we will discuss some aspects of cell migration with the focus on the most classic signalling pathways of cell migration starting with the Rho GTPase RAC1. We will focus on topics that will be explored in future chapters: actin dynamic, integrin-dependent cell adhesion, endocytosis and their regulation. An understanding of these key pathways and how they are regulated is necessary to comprehend their role in health, and in diseases such as cancer.

The aim of this study is to elucidate the spatiotemporal localisation of the novel protein CYRI-A by using super-resolution microscopy. We extended our understanding of the functions of the CYRI protein family as a new regulator of macropinocytosis through locally suppressing RAC1-Scar/WAVE signalling. We also show that this function of CYRIs can be utilised to regulate surface integrins in cancer cells, therefore regulating the growth, migration and invasion both in 2D and 3D systems.

1.1 The basis of cell migration and its role in cancer invasion and metastasis

1.1.1 The biochemistry of actin polymerisation in cell migration

Actin is a monomeric protein with an average molecular weight around 42kDa. Genes encoding for actin are some of the most evolutionarily conserved across all kingdoms of life (Gunning et al., 2015). Structurally speaking, monomeric actin (or G-actin) is folded into 4 distinct subdomains 1 to 4 (Figure 1.1) with the two subdomains 1 and 3 shares many structural similarities. The G-actin monomer has an intrinsic asymmetry. The ATP binds to an upper cleft (or the nucleotide-binding cleft) where it makes extensive contacts with the subdomain 3 and 4. The second cleft called the target-binding cleft formed between subdomain 1 and 3 is important for protein interactions (Pollard, 2016). There are several details at the nucleotide-binding pocket that are important for understanding the mechanism of actin polymerisation. The serine 14 residue on subdomain 1 form hydrogen bonds with the γ-phosphate group of a bound ATP molecule. A divalent cation, usually a Mg^{2+} ion, is essential for ATP binding, where it makes ionic bonds with the β- and γ-phosphate. From real crystal structure, this Mg^{2+} ion is chelated by several water molecules (Graceffa and Dominguez, 2003). Serine 14 also forms hydrogen bonds with a histidine 73 located on the sensor loop. The asymmetrical nature of G-actin underlies the polar nature of F-actin with the nucleotide-binding cleft forms the pointed end (minus end) while the target-binding cleft forms the barbed end (plus end). Inside cells, actin polymerisation does not happen spontaneously. The rate-limiting step is the formation of an actin nucleus. Actin dimerization and trimerization are energetically unfavourable, but once the trimer is formed, the addition of the fourth monomer is much more favourable. This step is assisted by the Arp2/3 complex, which we will discuss in later segments. Once the nucleus is formed, ATP-bound actin monomers are added to the barbed end.

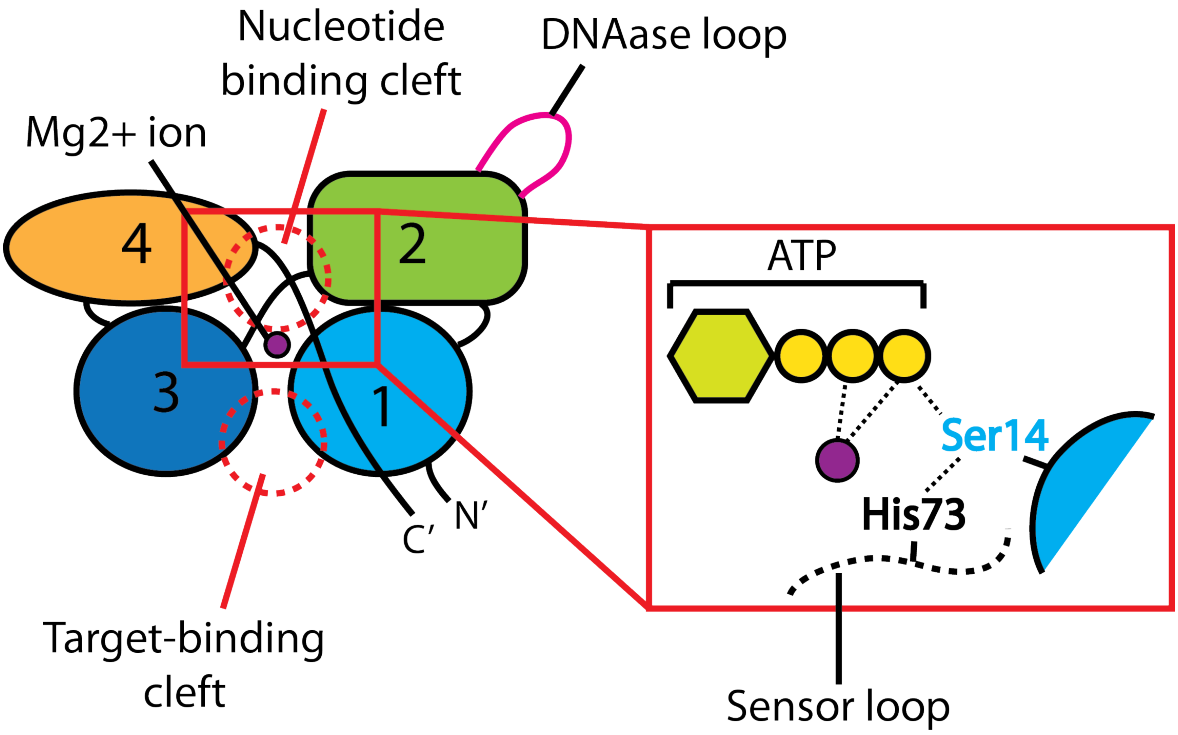

Figure 1.1 Simplistic structural representation of G-actin bound to ATP

G-actin contains 4 subdomains 1-4. Subdomain 1 and 3 share structural similarities. There are two pockets: an upper cleft for ATP and Mg^{2+} ion binding and a lower pocket formed by subdomain 1 and 3 called the target-binding cleft. ATP interacts with subdomain 3 and 4 and residues from subdomain 1 and 2. The DNAase loop (or D-loop) is important for in-filament interactions. Serine 14 forms hydrogen bonds with the gamma phosphate of ATP. The Mg^{2+} ion forms extensive hydrogen bonds with ATP and the water molecule. The loop containing Histidine 73 can sense the presence of ATP hence called the sensor loop.

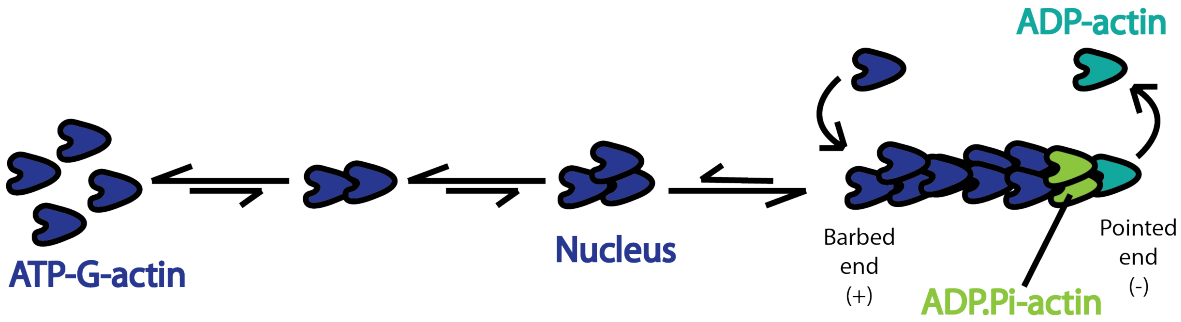

Figure 1.2 A simplistic representation of the actin polymerisation process

The first two steps: actin dimerization and trimerization are the two rate-limiting steps. Once the trimer as formed, the addition of the fourth monomer stabilises the nucleus. In the most simplistic view, ATP-G-actin is added to the barbed while ADP-actin dissociates at the pointed end. ADP.Pi-actin is a stable transient state. The length of the arrow indicates favourable direction.

At the barbed end, both association and dissociation happen more frequently than at the pointed end, hence this end of the actin filament is more dynamic than the other (Figure 1.2). However, the rate of addition of ATP-bound actin is higher than its dissociation at the barbed end, hence the net result is actin addition. In contrast, at the pointed end, the addition of ATP-bound actin is slower than the dissociation of ADP-bound actin, hence the net result is actin disassembly. At steady-state, on average, the addition rate at the barbed end balances out with the dissociation rate at the pointed end, thus keeps the overall length of the actin filament constant, a property called treadmilling. Careful examination by superimposing the crystal structure of ADP- and ATP-bound G-actin revealed a local rearrangement mechanism within the ATP-binding site (Graceffa and Dominguez, 2003, Scipion et al., 2018). Upon binding to the filament, a conformational shift activates the hydrolysis of the bound ATP (Scipion et al., 2018, Merino et al., 2018). When the phosphate group is released, a further conformational change leads to the release the actin monomer from the filament. Using an *in vitro* protein reconstitution assay, the force generated by the addition of monomeric actins into a single filament was calculated to be in the range of 0.25 to 0.56pN (Kovar and Pollard, 2004). This force could be used to push the plasma membrane forward during migration.

1.1.2 The Rho GTPases family

The first Rho GTPase gene was first isolated in the 1980s (Madaule and Axel, 1985) but it was not until 1992, in two landmark papers by Anne Ridley and Alan Hall (Ridley et al., 1992, Ridley and Hall, 1992), that this protein family was put in the spotlight as a major regulator of the actin cytoskeleton. In humans, 20 members of the Rho GTPase family have been discovered. Phylogenetic analysis classified these into 2 groups: the classic and the atypical Rho GTPases. The classic Rho GTPases contains 3 subgroups: the RAC1-related subgroup (RAC1-3, RHOG); the CDC42-like subgroup (CDC42, RHOQ, RHOJ, RHOU, RHOV); and the RHO-A-related subgroup (RHOA, RHOB, RHOC). The atypical Rho GTPases contains the Rnd subgroup (RND1, RND2, RND3), the RHOBTB subgroup (RHOBTB1, RHOBTB2), RHOD, RHOH and RHOF (Wennerberg and Der, 2004, Boureux et al., 2007, Lawson and Ridley, 2018) (Figure 1.3). Rho GTPases are part of the RAS superfamily of 154 proteins that share a similar mechanism of action. They have a molecular weight of around 21kDa and are known to act as molecular switches, active when bound to GTP and inactive when bound to GDP.

1.1.3 RAC1 as an example of a Rho GTPase

Rho GTPase members share many structural similarities with each other. Here we use the structure of RAC1 as an example to describe the mechanistic details of the Rho GTPase activities (Figure 1.4). Structural speaking, there are two parts of a Rho GTPase protein: The G-domain, which is responsible for binding to GTP and the Hypervariable Region (HVR), which is responsible for membrane interaction through lipid modification. The G-domain contains 3 main structures that form the basis for the spring-loaded mechanism: The P-loop (containing the G1 motif), the Switch I loop (containing the G2 motif) and the Switch II loop (containing the G3 motif). In a GTP-binding state, the G1 motif interacts with the β-phosphate group of GTP and catalytic Mg^{2+} ion. This Mg^{2+} ion forms ionic bonds with the negative charges on the β- and γ- phosphate group of GTP as well as the G2 motif. Finally, the G3 motif forms interactions with the γ-phosphate group through a conserved glycine 60 residue. These numerous interactions between GTP and the motifs of the GTPase hold the protein in its active state.

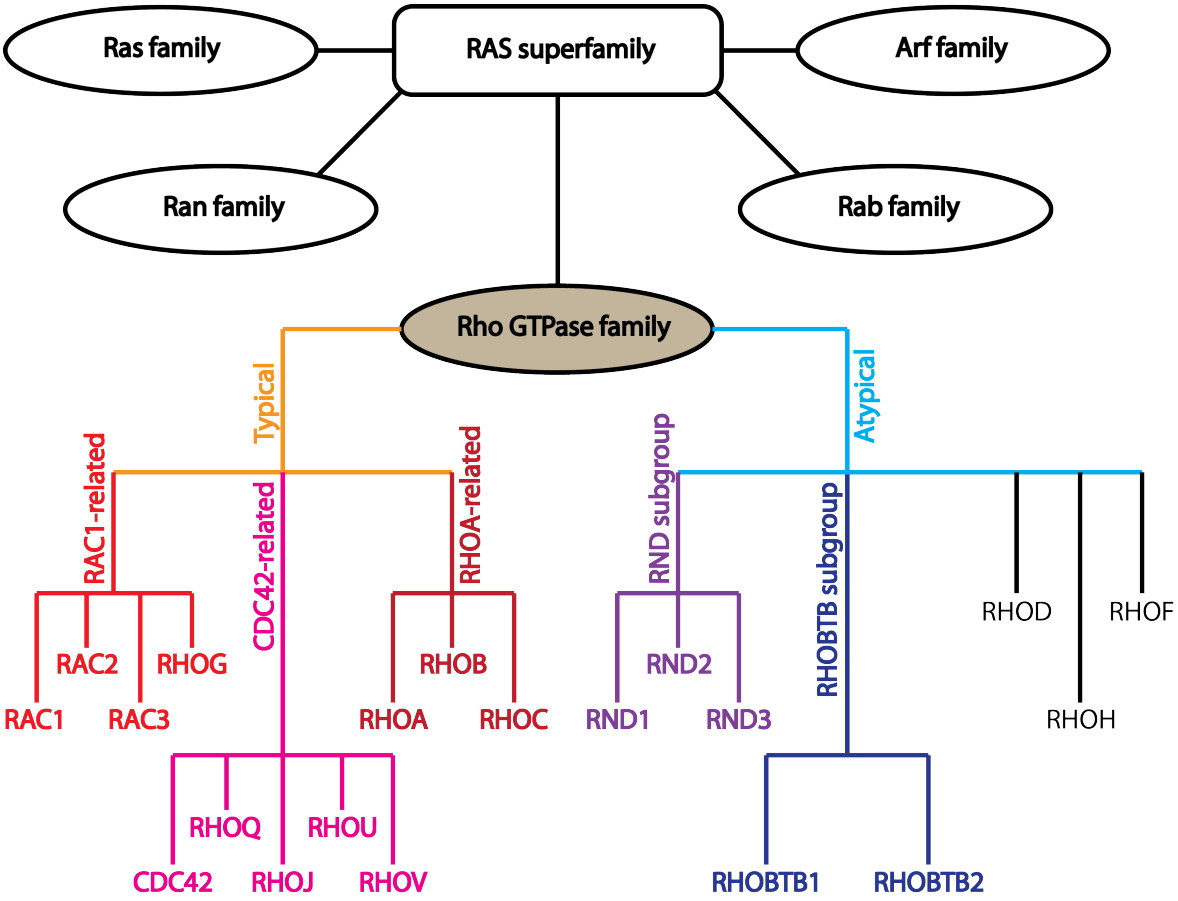

Figure 1.3 The human Rho GTPase family

The Rho GTPase is one of the principal families of the RAS superfamily. The other principles families are the Ras family, the Ran family, the Rab family and the Arf family, all contribute to a total of 154 proteins. Twenty members of the human Rho GTPases family are divided into two groups. The typical group contains the RAC1-, CDC42- and RHOA-related subgroups. The atypical group contains the RND, RHOBTB subgroups along with the lesser-studied RHOD, RHOH and RHOF.

Branches are not to scale and only for illustration purposes only.

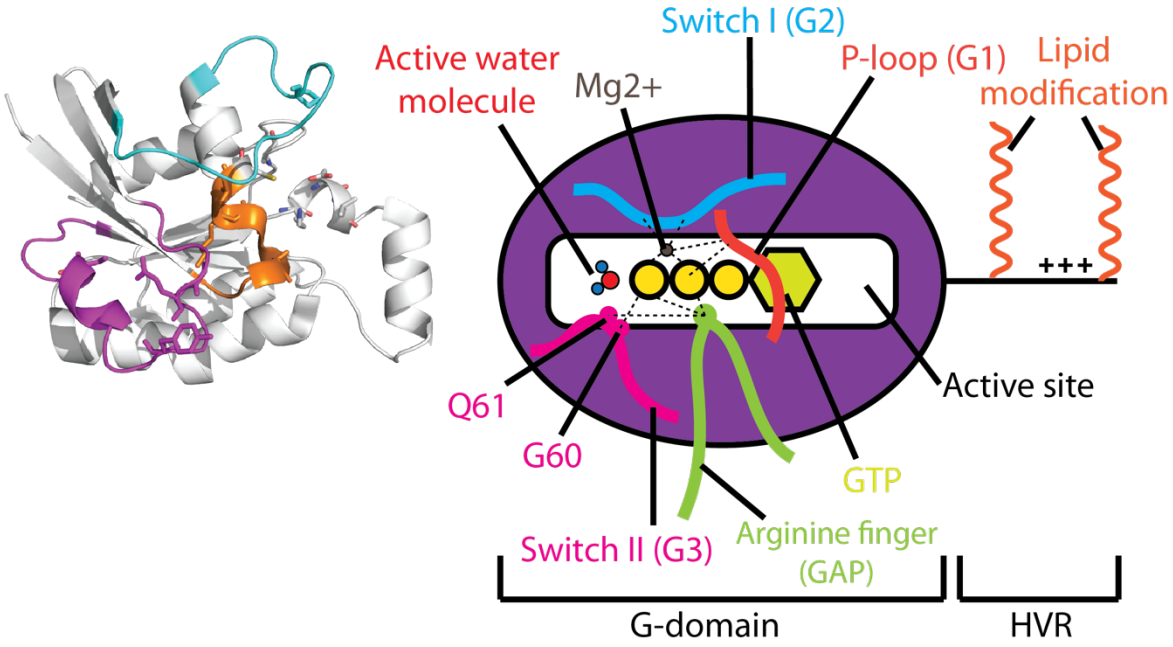

Figure 1.4 Crystal structure of RAC1 (left) (PDB: 3TH5) and its schematic representation (right)

All Rho GTPases are composed of two parts: The G-domain, which is responsible for binding GTP; and the Hypervariable Region (HVR), which is responsible for localising the protein to the correct membrane location and is often not visible in X-ray crystallography due to its high flexibility. The arginine finger belongs to a bound GAP protein. The colour code is kept constant between the crystal structure and the schematic representation. Plus signs represent positive charges. Yellow circles represent phosphate groups of the bound GTP.

When the GTP is released, the straining energy stored in these interactions is converted to the movement of the components back to its original positions, resembling a recoiling spring, hence the name “spring-loaded” mechanism. The HVR is usually composed of around 20 amino acids at the C terminus (Boureux et al., 2007, Etienne-Manneville and Hall, 2002, Haga and Ridley, 2016, Hall, 2000, Hodge and Ridley, 2016). This region, as the name suggests, is the most diverse in the Rho GTPase family and is important for the protein’s correct localisation. It was suggested that the HVR modulates the physical distance between the G-domain and the plasma membrane, which is believed to be important for downstream protein interactions. At the cytoplasmic pH of 7.2, the HVR is positively charged due to the presence of arginine and lysine residues. This forms electrostatic interactions with the negatively charged phospholipids and thus anchor the proteins to the plasma membrane.

However, the major process that directs Rho GTPases to the correct cellular location is lipid modification. The most common signal peptide is the CAAX sequence (C = Cysteine, A = aliphatic, X = any amino acid) at the C-terminus, which is found on 16 out of 20 Rho GTPases (Roberts et al., 2008). The cysteine residue is subjected to a process called prenylation, which is a covalent addition of either a 15-carbon farnesyl or a 20-carbon geranylgeranyl group to the thiol group on cysteine. This double lipidation mechanism also underlies the failure of farnesyltransferase inhibitor for RAS proteins (Sebti and Der, 2003). When Rho GTPases are prenylated, the first reaction is carried out by farnesyltransferase (FTase) and/or geranylgeranyltransferase type I (GGTase-1). Then the AAX motif is cleaved off by a Ras-converting enzyme 1 endoprotease (Rce-1). This allows the access of another enzyme called isoprenylcysteine-O-carboxyl methyltransferase (Icmt) to catalyse the addition of a methyl group to the cysteine. The complete modification increases the hydrophobicity of the C-terminus of Rho GTPases, allowing them to efficiently intercalate their lipid moiety into the lipid bilayer (Peurois et al., 2019, Roberts et al., 2008). For many Rho GTPases, the polybasic positively charged amino acids and the prenylated CAAX motif are the two main drivers for membrane localisation. However, some Rho GTPases, including RAC1, are also subjected to a second lipid modification known as palmitoylation. Despite being less prevalent for Rho GTPases, palmitoylation can contribute significantly to the function of the modified proteins. Mutating the palmitoylation site cysteine 178 significantly reduces RAC1 localisation to lipid rafts on the plasma membrane, affects membrane organisation and the spreading and migration of COS-7 cells (Navarro-Lerida et al., 2012). Palmitoylation requires a prior prenylation to occur and the depalmitoylation reaction is catalysed by acyl-protein thioesterases (APTs).

1.1.4 The GEFs and the GAPs of Rho GTPases

Rho GTPases are evolved in an environment where the concentration of GTP is always exceeding that of GDP by at least 10 times (Bos et al., 2007). This creates a selective pressure for proteins that hydrolyses GTP slowly or exchanges GTP for GDP slowly. The dissociation constant of a bound GDP is extremely small, in a range of 10^{-3} to 10^{-6} per second (Mishra and Lambright, 2016). This coupled with the relatively slow intrinsic GTP hydrolysis makes Rho GTPases biochemically

incompatible to life. This drives the evolution of two sets of enzymes called Guanine nucleotide exchange factors (GEFs) and GTPase-activating proteins (GAPs) that have become essential to Rho GTPases functions. GAPs are a diverse family of proteins with one sole purpose is to help accelerate the hydrolysis process of GTP. Rho GTPases use an active water molecule to act as a nucleophile to attack the γ-phosphate on GTP (Figure 1.5). The water molecule is stabilised and activated by the oxygen atom of the sidechain of the glutamine 61 on the Switch II loop to attack the γ-phosphate of the GTP. However, the glutamine residue is intrinsically flexible, and its alignment is often in the wrong orientation thus making the activation process inefficient. GAPs reduce the flexibility of the glutamine 61 by using a carbonyl oxygen atom of an arginine residue to form a hydrogen bond with the amine group on the glutamine (Figure 1.5). This arginine residue is commonly known as the arginine finger. At the same time, the arginine finger also forms interactions with the β- and γ-phosphate group of the GTP and stabilises their transition phase when the water is attacking. This mechanism of action facilitates the rate of hydrolysis by several orders of magnitude (Bos et al., 2007). Mutations at the glutamine 61 such as the Q61L mutant renders the protein constitutively active. The mutant protein is still able to interact with its GAP but unable to interact with the arginine finger, hence unable to activate the water molecule, leaving the protein in a permanent active conformation. Once the GTP is hydrolysed, in order to reactivate the Rho GTPase again, the protein needs to bind new GTP. As mentioned earlier, the rate of nucleotide exchange in Rho GTPases is extremely slow and their affinity to the bound GDP/GTP is in the range of nano to picomolar. The exchange is significantly enhanced by the activity of GEFs. GEFs utilise a variety of tricks to increase the GDP/GTP rate by disrupting the binding of GDP to the Rho GTPases. The binding of GEF can induce a steric hindrance in the active site of the Rho GTPase, reposition the Switch II loop to an undesired conformation for GTP binding. Some GEFs insert a negatively charged amino acid into the GTP binding pocket to create an electrostatic repulsion on the phosphate group.

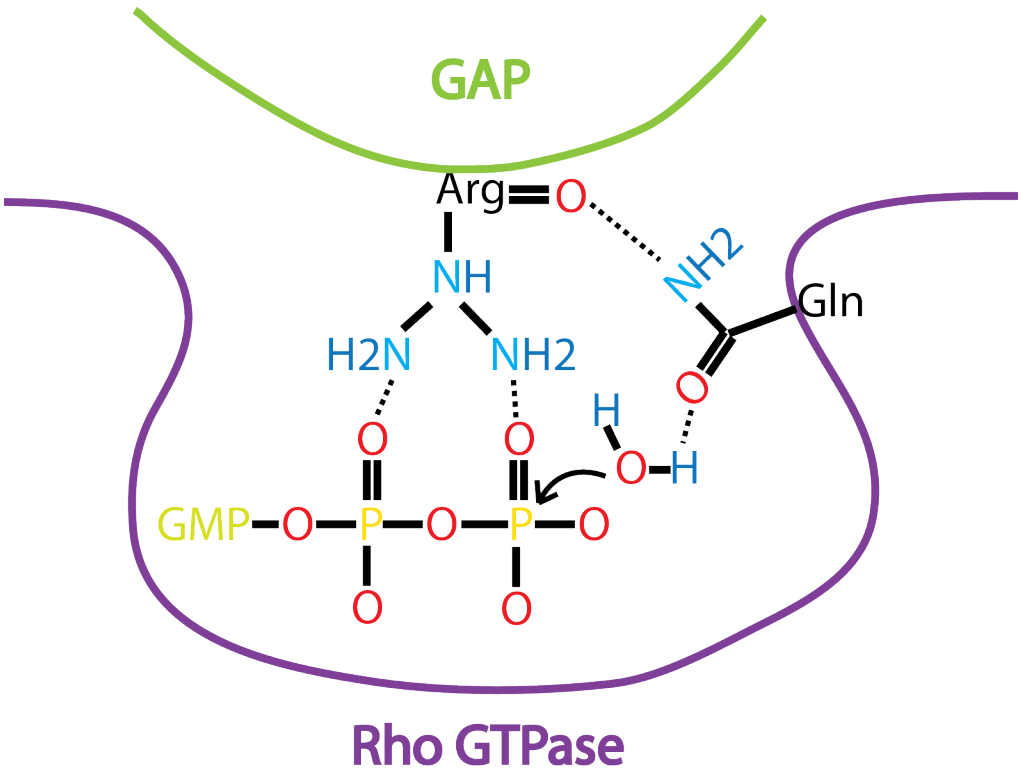

Figure 1.5 Mechanism of GTP hydrolysis in Rho GTPases

The Glutamine 61 on the Rho GTPase forms a hydrogen bond with the active water molecule, stabilises it and acts as a proton acceptor to activate the oxygen atom. The now active oxygen atom in the water molecule can perform a nucleophilic attack on the gamma phosphate group of the GTP. Both the gamma and beta phosphate groups are stabilised by the arginine residue from GAP. This arginine also stabilises the Glutamine 61 to allow it better at stabilising the water molecule. This lowers down the energetic cost and accelerates the hydrolysis reaction.

Other GEFs use a hydrophobic finger to destabilise the bound Mg^{2+} ion (Toma-Fukai and Shimizu, 2019) and lower down the affinity of the bound nucleotide. In a way, GEFs are competing with GDP for the binding of Rho GTPase. Once the GDP is released, another GTP can immediately replace due to its high intracellular concentration. In the next segment, we will explore the cellular role of Rho GTPases, in particular, RAC1 in regulating cell migration.

1.1.5 CDC42 and RHOA with RAC1 – a brief introduction

Cells utilise a variety of different modes of migration and lamellipodial-based migration is perhaps the most well-studied of all. First discovered by Michael Abercrombie in 1970 (Abercrombie et al., 1970) in fibroblasts, lamellipodium is a structure at the front of a migrating cell characterised by its flat fan-shaped morphology. Electron microscopy of lamellipodia revealed an intricate network of microfilaments, now known as the actin network (Abercrombie et al., 1971). With the discovery of the Arp2/3 and the Scar/WAVE complex in actin branching (Machesky and Insall, 1998) along with the earlier reports of the link between RAC1 and the actin cytoskeleton (Ridley et al., 1992, Nobes and Hall, 1995), experiments have confirmed the interconnected relationship of all three components in lamellipodia regulation. The consensus pathway of lamellipodial formation is followed: active RAC1 activates the Scar/WAVE complex, which leads to the release of its autoinhibition; which then binds and activates the Arp2/3 complex to initiate actin branching at a 70° angle from the pre-existing filament; the branched actin network pushes on the plasma membrane leads to the formation of the lamellipodium and cell migration. Even though the overall biochemical pathway is relatively simple, the details of many of the events are still surprisingly elusive.

There are 3 most well-studied Rho GTPases: RAC1, CDC42 and RHOA and their overexpression gives cells characteristic morphologies that have been described many times in the literature (Figure 1.6). CDC42 is known to be important for cell polarity, with its known interactor Par3 and Par6 (Joberty et al., 2000). Yeast genetic experiments have shown that cells lacking CDC42 failed to establish a growth direction, which is usually dictated by the bud scar from the previous division. Instead, these cells grow and form large clumps with no buds (Adams et al., 1990). CDC42, along with N-WASP and IRSp53:Mena are known for their involvement in generating filopodia, a type of cell protrusion composed of parallel actin bundles (Nobes and Hall, 1995, Rohatgi et al., 2000, Carlier et al., 1999), (Krugmann et al., 2001). CDC42 can crosstalk with RAC1 via Par6 and Par3, which leads to Tiam1 – a RAC1 GEF - activation and RAC1 activation in neuroblastoma cells (Nishimura et al., 2005).

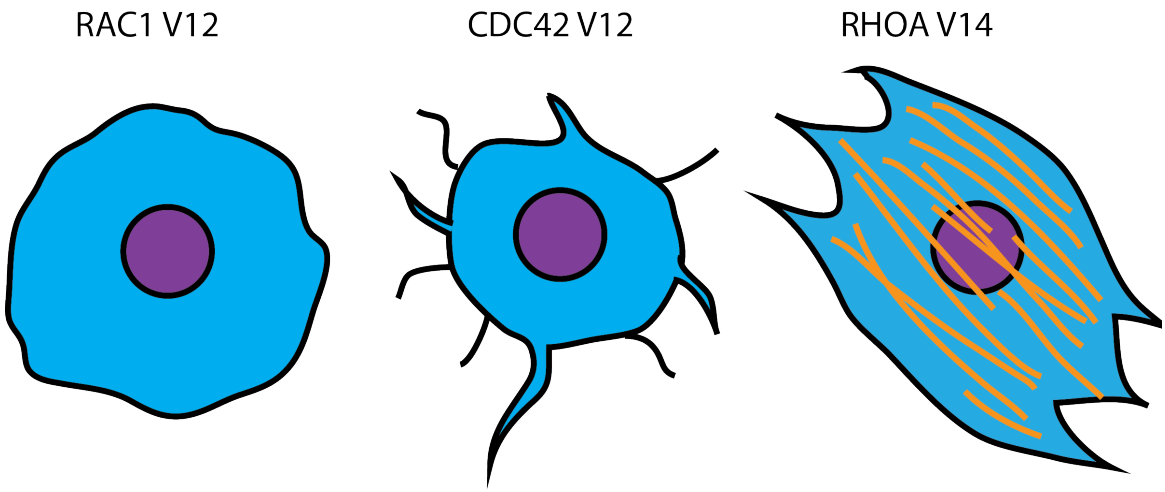

Figure 1.6 The characteristic morphology of cells overexpressing constitutively active RAC1 V12 mutant, CDC42 V12 mutant or RHOA V14 mutant.

RAC1 V12 expressing cells adopt the fried-egg shape with broad, flat and relatively quiet lamellipodia.

CDC42 V12 expressing cells have more filopodia and tend to be smaller.

RHOA V14 expressing cells have more prominent stress fibres running across the cell body on a 2D substrate.

This suggests that lamellipodia and filopodia might not be entirely functionally nor spatially distinct from one another (Beli et al., 2008, Yang et al., 2007, Ridley and Hall, 1992). We will come back to this point in later segments.

RHOA is another major protein that has been associated with cell adhesion and migration. The primary role of RHOA is regulating cell rear contraction and stress fibre formation (Nobes and Hall, 1999, Nobes and Hall, 1995). In cells with RHOA deletion, cell rear is affected while front protrusions remain intact (Allen et al., 1997). A recent study also demonstrated how RHOA can be activated at the rear through the activity of the membrane tension-sensing caveolin and the RhoGEF Ect2 in 3D matrix (Hetmanski et al., 2019). The canonical pathway for RHOA is through the activation of Rho-associated protein kinase (ROCK). ROCK triggers cell contraction by activating Myosin light chain (MLC) while inactivating Myosin light chain phosphatase (MLCP). This underlies the stress fibre-rich morphology in 2D and the blebbing morphology in 3D in cells with elevated RHOA

activity (Ridley, 2001, Amano et al., 2000, Amano et al., 2010, Fackler and Grosse, 2008). A long-standing remark is that RAC1 and RHOA exert an antagonistic bi-stable relationship, where high RAC1 activity coincides with low RHOA activity and vice versa. Active RAC1 activates PAK, which then phosphorylates and inactivates GEF-H1, an RHOA GEF, thus dampens RHOA activity (Byrne et al., 2016). Through the use of FRET biosensors, RHOA signal was found at the very edge of fibroblasts with sporadic patterns at the trailing end (Pertz et al., 2006, Machacek et al., 2009). However, a recent single-molecule microscopy study also done in fibroblasts failed to visualise this edge localisation. However, they found a decrease in the mobilisation of the constitutively active and inactive mutants of RHOA near the lamellipodial tips (Mehidi et al., 2019). This suggests that our understanding of the coordination between the different Rho GTPases during cell migration is still very much incomplete. It is likely that this coordination is highly dynamic and context dependent. In the next segment, we will explore in detail the regulation mechanism between RAC1 and the actin cytoskeleton.

1.1.6 RAC1, Scar/WAVE and the Arp2/3 complex – a complicated picture of cell migration

1.1.6.1 The Scar/WAVE complex

It is widely believed that the direct target of RAC1 in reorganising the actin cytoskeleton is the Scar/WAVE complex, one of the many Nucleation Promoting Factors (NPFs) (Machesky and Insall, 1998, Machesky et al., 1999, Eden et al., 2002). The Scar/WAVE complex is composed 5 subunits: WAVE, Abi, NAP1, SRA1 (or CYFIP1) and HSPC300, with some of these components also exist in multiple isoforms (Nozumi et al., 2003). The two larger subunits SRA1 and NAP1 form a pseudodimer, which acts as a platform for WAVE, Abi and HSPC300 to assemble onto. Normally, the Scar/WAVE complex stays inactive with the WCA domain of the WAVE subunit folded onto itself. The current understanding suggests multiple signals are needed to activate the complex (Figure 1.7). The first major signal is indeed active RAC1. A recent structural analysis has shed some light on the mechanism of this process. By artificially fusing a double mutant active RAC1 (P29S Q61L) to the C-terminus of the WAVE subunit, two distinct binding sites were found on the complex, one near the α4-α6 helices of the WAVE subunit (A-site), and the other on the opposite site (D-site) (Chen et al., 2017). Both the

switch I and switch II region of RAC1 are important for this interaction, perhaps explains why only active RAC1 can interact with the Scar/WAVE complex. The interesting but rather unexpected proposal is the suggestion that it requires two RAC1 molecules for every Scar/WAVE complex to fully activate the complex. Mutations at the A-site completely abolished the complex's function in rescuing lamellipodia formation in SRA1/WAVE mutant B16-F1 and *Dictyostelium* cells (Schaks et al., 2018). On the other hand, Scar/WAVE complex harbouring the D-site mutations still localises to the leading edge of cells albeit with a decreased lifetime and altered lamellipodial morphology. This suggests that the A-site is essential while the D-site is only needed for efficient lamellipodia formation. Furthermore, *in vitro* fluorescent actin polymerisation assay with purified Scar/WAVE complex and prenylated active RAC1 showed no activity, suggesting that active RAC1 alone was not enough to trigger Scar/WAVE activation (Lebensohn and Kirschner, 2009). The addition of liposomes containing phosphatidylinositol (3,4,5)-trisphosphate (PIP3) led to a significant increase in actin polymerisation. Structural analysis shows the existence of a stretch of positively charged amino acids along the back of the Scar/WAVE complex suggests that the electrostatic interactions between the complex and PIP3 on the plasma membrane allows for the correct localisation and optimal activation by active RAC1. This is known as the coincident detection mechanism (Lebensohn and Kirschner, 2009, Koronakis et al., 2011). How exactly binding to the plasma membrane primes the Scar/WAVE complex for activation is not clear. However, the general idea is it brings the complex in close proximity with membrane-bound active RAC1 molecules, and orients it in a way so the released WCA domain can interact with the Arp2/3 complex (Davidson and Insall, 2011). The final regulation imposed on the Scar/WAVE complex is phosphorylation. In the presence of a phosphatase, RAC1 and PIP3 become less efficient in activating the complex and this response is dose-dependent (Lebensohn and Kirschner, 2009).

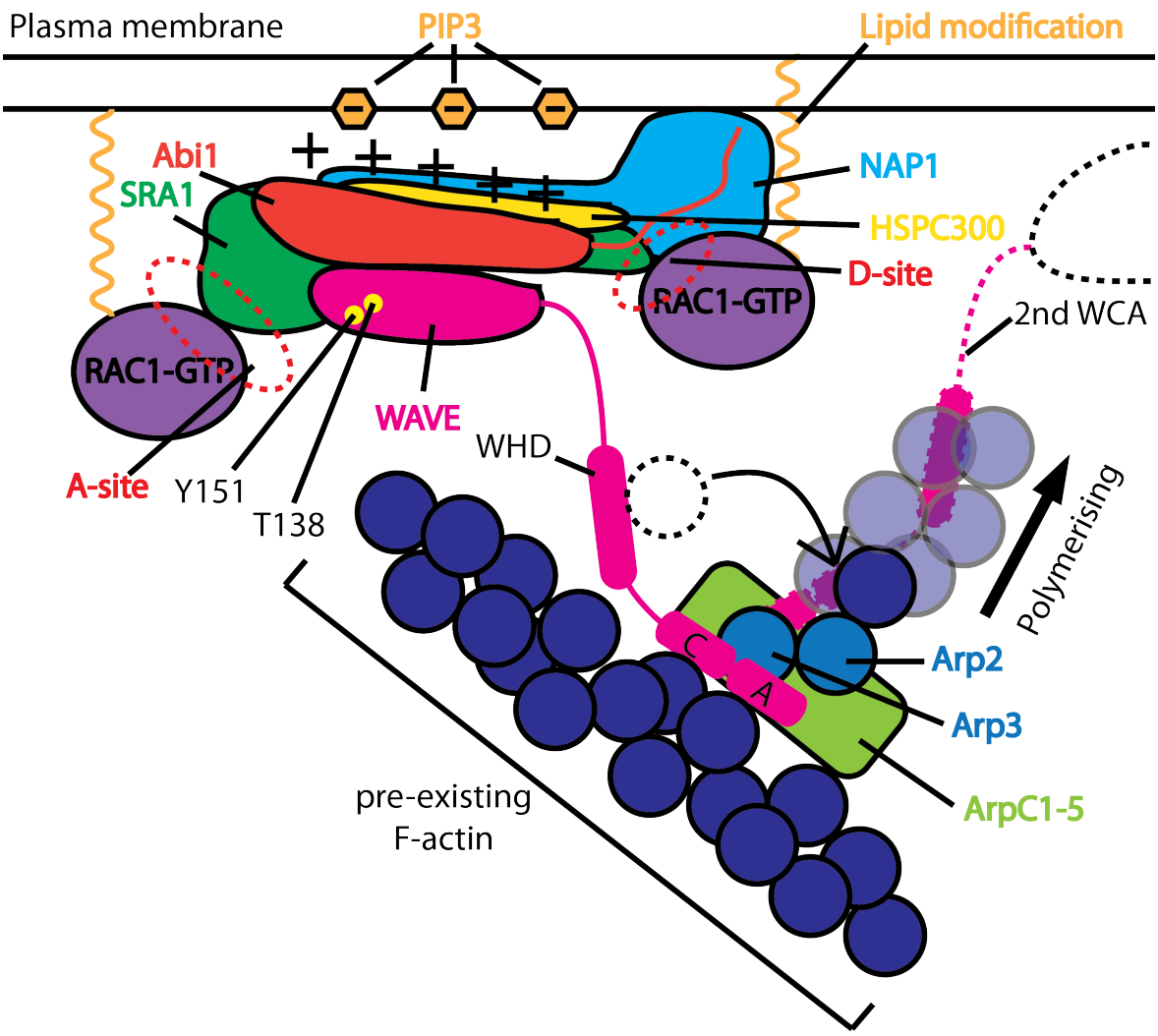

Figure 1.7 A comprehensive schematic representation of how RAC1-Scar/WAVE-Arp2/3 promotes branched actin polymerisation

The Scar/WAVE complex is activated by coincident signals of two lipid-modified active RAC1 at the A- and D-site (red dotted circles), the electrostatic interaction between the positively charged side of the Scar/WAVE complex and the negatively charged PIP3 on the plasma membrane, and the multiple phosphorylations on the WAVE subunit such as Y151 and T138. This leads to the open up of the WCA region of the WAVE subunit. It takes two WCA to effectively activate one Arp2/3 complex. The Arp2/3 complex binds to a pre-existing F-actin using its ArpC1-5 subunits. The Arp2 and Arp3 subunits act as the nucleation centre for actin to polymerise. The WHD binds a monomeric actin which can be transferred to the growing actin filament, allowing the new actin filament to extend at a 70° angle relative to the previous filament.

Several kinases have been associated with the phosphorylation of the Scar/WAVE complex at various sites and subunits. Multiple reports show that the MAPK ERK1/2 can colocalise with the Scar/WAVE complex at the leading edge. Inhibiting ERK with specific inhibitors decreases of phosphorylation signal detected on western blots as well as protrusion dynamic (Mendoza et al., 2011, Danson et al., 2007). Using mass-spectrometry, many phosphorylation sites were identified, including serine 296, 308, 343 and threonine 346 among others (Mendoza et al., 2011, Danson et al., 2007). Apart from ERK, Abl kinase and Src kinase have also been reported to phosphorylate Scar/WAVE complex at other sites such as tyrosine 151 and threonine 138 (Figure 1.7) (Chen et al., 2010, Davidson and Insall, 2011, Lebensohn and Kirschner, 2009). Overall, activation of the Scar/WAVE complex is tightly regulated through multiple layers of signalling.

1.1.6.2 The Arp2/3 complex

The direct downstream effector of the Scar/WAVE complex is the Arp2/3 complex. The WAVE subunit contains the WCA sequence at its C-terminus. The WAVE-homology subdomain (WHD or W) is part of a larger domain known as verprolin (V) and is able to bind monomeric actin and transfer to the bound Arp2/3 complex. The CA domain (which stands for cofilin homology and acidic domains, respectively) is thought to be where the Arp2/3 complex binds and gets activated. Structural studies of the interaction between the WCA domain and the Arp2/3 complex can be challenging owing to the fact that these are all multimeric protein complexes, and results from many of these experiments are sensitive to the experimental conditions. Hence many of the details on the mechanism of action of the Arp2/3 complex came from studying the WCA domain of simpler proteins such as N-WASP, which also belongs to the same family with Scar/WAVE. The Arp2/3 complex is a heptameric complex composed of 7 subunits: ARP2, ARP3, ARPC1 to 5, which was first purified from *Acanthamoeba* (Machesky et al., 1994). Two of the 7 subunits, ARP2 and ARP3 share sequence and structural similarities with monomeric actin, which are believed form a dimer to help with the actin nucleation process. ARP2 and ARP3 also bind ATP, which can trigger a major conformational change to allow the two subunits align in a way that supports actin nucleation (Goley and Welch, 2006).

The ARPC2 and ARPC4 subunit form a dimer to provide the structural foundation for other subunits to build on and is thought to be the contact point with the mother filament. Nevertheless, the exact organisation and function of each of the subunits is still a matter of debate. Initial biochemical analysis using deletion experiment suggested that ARPC3 is needed for interacting with the WCA domain (Machesky and Insall, 1998). However, according to a newer model, the Arp2/3 complex needs two WCA domains to be fully activated (Figure 1.7) (Boczkowska et al., 2014, Ti et al., 2011, Padrick et al., 2011). The first interaction site locates on the ARP2 and ARPC1 subunits and has a high affinity with the WCA domain, and the second site is on the ARP3 subunit and has about 10 times weaker affinity. The WCA domain undergoes a quick on and off rate with the first binding site, and as soon as the WCA detaches, the Arp2/3 complex is transferred to a nearby actin filament. This changes the conformation at the second site and strengthens its affinity to the other WCA domain. The actin monomer bound to the WHD can then be transferred to the ARP2-ARP3 dimer to initiate the polymerisation (Ti et al., 2011). The idea of having two WCA domains to fully activate one Arp2/3 complex is still being viewed cautiously by many in the field. However, considering that the activity of many of these complexes is usually within a localised area on the plasma membrane, it is not surprising if they are indeed involved in co- and cross- interactions. There is some evidence suggesting the Scar/WAVE complexes can assemble into ring-like structures (Pipathsouk et al., 2019) or phase separate on the membrane (Case et al., 2019) to facilitate actin polymerisation. Phosphorylation can also affect the activity of the Arp2/3 complex (Narayanan et al., 2011), along with other factors such as cortactin, which stabilises and activates the Arp2/3 complex (Uruno et al., 2001), or Arpin and coronin, which inhibit the complex (Sokolova et al., 2017). The model of how RAC1 leads to the activation of the Scar/WAVE complex and the Arp2/3 complex has changed and improved significantly over the year. Recent findings also point to a cooperative action between the components of the actin signalling network. It is suggested that at the plasma membrane, the Scar/WAVE complex can act to distribute monomeric actins between nearby filaments (Bieling et al., 2018). Overall, we have explored in-depth the molecular signalling linking the upstream activator RAC1 to the Scar/WAVE complex, the Arp2/3 complex and actin polymerisation. This signalling pathway ultimately leads to the formation of

the branched actin network creating lamellipodia, pushing on the plasma membrane and leading to cell migration.

1.1.7 Lamellipodia, filopodia and invadopodia

There are three main types of actin-based protrusion: lamellipodia, filopodia and invadopodia.

1.1.7.1 Lamellipodia

Lamellipodia are flat, sheet-liked structure characterised by the use of branched actin polymerisation through the RAC1-Scar/WAVE-Arp2/3 signalling axis (Figure 1.7, Figure 1.8). In the absence of the Scar/WAVE complex, other NPFs such as N-WASP is known to effectively replace its function (Veltman et al., 2012). Despite mostly being studied on 2D, lamellipodia have been found *in vivo* in a variety of cell types such as hemocytes in *Drosophila melanogaster* (Evans et al., 2013, Sanchez-Sanchez et al., 2017) or neural crest cells (Li et al., 2019). Lamellipodial extensions are usually accompanied by the formation of adhesion sites to the matrix, linking and transmitting the force generated by the actin cytoskeleton to the substratum. This provides the traction force driving migration (Beningo et al., 2001). There are many regulators of lamellipodia. For example, activated receptor tyrosine kinases recruit and activate RAS, which then activates PI3Ks and subsequently RAC1 GEFs and thus drives lamellipodia formation (Eller-Borges et al., 2015, Yamauchi et al., 2005). The protein lamellipodin binds to the SH3 domain of Abi and is thought to connect active RAC1 molecules to the Scar/WAVE complex. Deleting lamellipodin leads to defects in lamellipodia formation and migration both *in vitro* and *in vivo* (Law et al., 2013). At the level of Arp2/3 complex, we have Arpin. The addition of purified Arpin hampered the branched actin polymerisation in an *in vitro* pyrene-labelled assay (Sokolova et al., 2017). It was suggested that its acidic domain competitively bind the Arp2/3 complex, but does not promote actin polymerisation (Veltman, 2014, Dang et al., 2013). Interestingly, genetic removal of RAC1 in MEFs leads to the loss of lamellipodial localisation of Arpin, suggesting RAC1 is needed for Arpin recruitment.

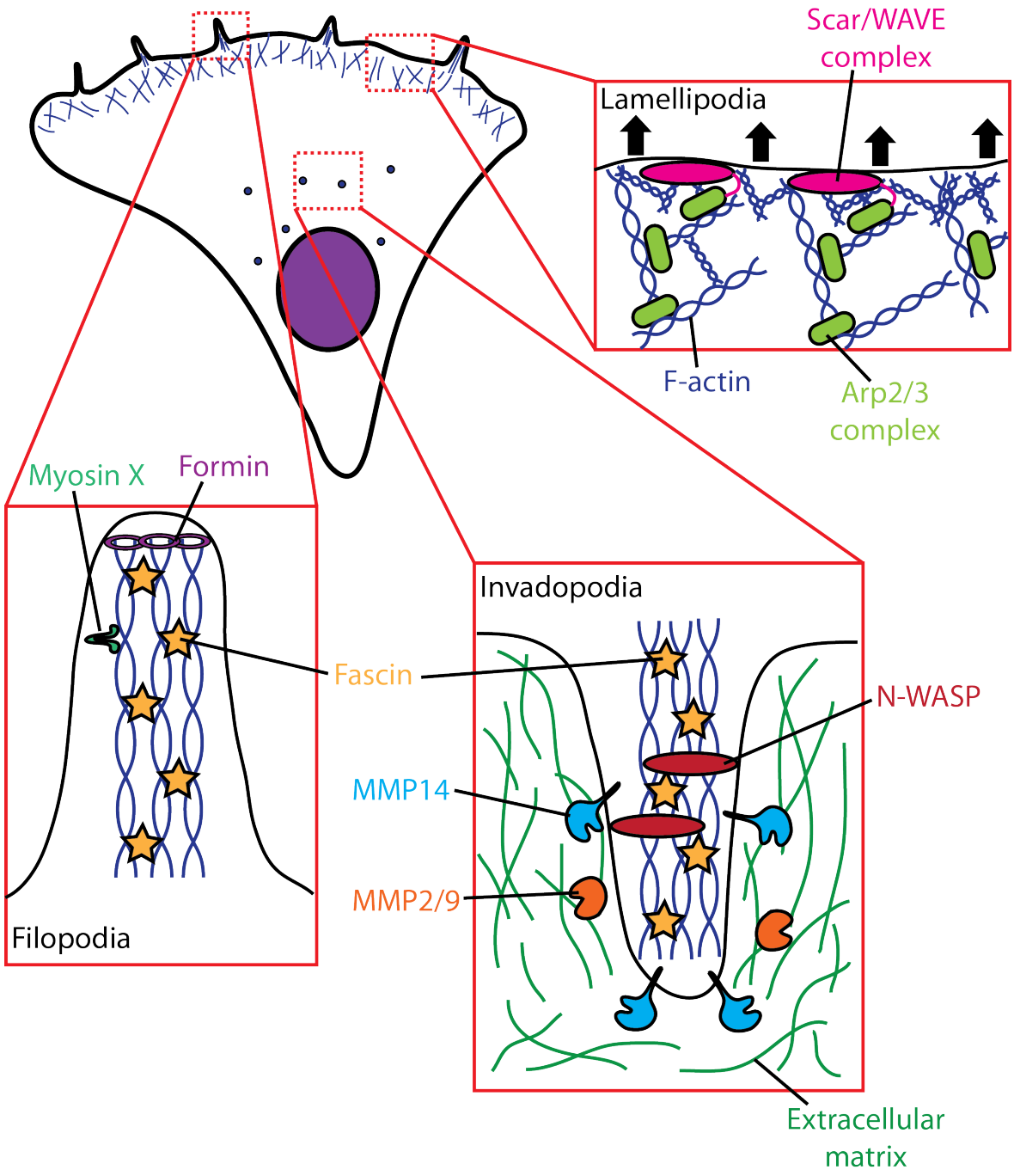

Figure 1.8 Three main types of actin-based protrusion

Lamellipodia are fan-like structures driven by RAC1-Scar/WAVE signalling.

Filopodia are finger-like protrusion driven by Formin/actin-bundling signalling.

Invadopodia are degradative protrusion that is similar to filopodia but with the addition of matrix metalloproteases.

The length of each actin filament is also tightly regulated through actin-binding proteins. Cofilin, for example, has a weak affinity to ADP.Pi-bound actin. The binding of cofilin triggers the release of the hydrolysed phosphate group, which triggers the dissociation of actin from the filament (Blanchoin and Pollard, 1998). This is thought to replenish the monomeric actin pool and provide new materials for new filaments. Capping proteins, on the other hand, are constitutively active heterodimeric protein that binds preferably to the barbed ends of growing actin filaments and prevent the addition of actin monomers. They are important for preventing actin filaments from growing indefinitely. Shorter actin filaments in a branched network have been shown to be more persistent and provide a stronger protrusion force than longer ones (Yang et al., 2005, Bear et al., 2002, Skoble et al., 2001). Both in 2D and 3D, the same machinery is used to regulate lamellipodia. In zebrafish neutrophils, RAC1 is downstream of PI3K and its activation leads to lamellipodia formation (Yoo et al., 2010). During the collective migration of the border cells and nurse cells in the ovary of *Drosophila melanogaster*, E-cadherin of the leader cells forms a positive feedback loop with RAC1 leading to the migration of the cell cluster (Cai et al., 2014). By contrast, during the collective migration of the neural crest cells in *Xenopus*, N-cadherin junctions suppress RAC1 to allow its recycling to the front of the leader cells (Theveneau et al., 2010). Linear elastic extracellular matrix has been shown to induce the sporadic formation of smaller lamellipodia at the leading edge in human foreskin fibroblasts (HFFs) along with the polarisation of RAC1 signalling (Petrie et al., 2012). These observations suggest the molecular mechanism regulating lamellipodia is likely to be conserved in both *in vitro* and *in vivo*.

1.1.7.2 Filopodia

The second form of actin-mediated protrusions is filopodia. Unlike the highly branching actin network in lamellipodia, filopodia are characterised by its straight, parallel bundles of actin filaments (Figure 1.8). With the diameter of around 0.1 to 0.3μm, filopodia feel and probe the surrounding environment of the cell. During the development of *Drosophila melanogaster*, filopodia assist in the closure of the ventral line by interdigitating cells from both sides (Vasioukhin et al., 2000). Filopodia have been shown to act as a guide to direct lamellipodia protrusion and haptotaxis for cell exploration and perhaps neural growth cone

formation (Johnson et al., 2015, Zheng et al., 1996). CDC42 is one of the signalling molecules linked to filopodia formation. Parallel to RAC1, CDC42 activates N-WASP. Through a similar mechanism, N-WASP uses its WCA domain to activate the Arp2/3 complex and drives filopodia formation (Rohatgi et al., 1999). Due to the significantly smaller diameter, the motor protein myosin X is designated to deliver many components to the filopodia formation machinery. Myosin X utilises ATP to walk along the actin filaments and deliver monomeric actin along with adhesion molecules to the tip of filopodia (Kerber and Cheney, 2011, Berg and Cheney, 2002, Berg et al., 2000). Deletion of myosin X in NIH3T3 cells leads to a significant loss of filopodia (Tokuo et al., 2007), while its overexpression induces numerous filopodia formation (Berg and Cheney, 2002). Binding at the tips of filopodia and protecting from capping protein are proteins of the ENA/VASP family (Bear et al., 2002). The polyproline sequence in ENA/VASP can interact with the actin-delivery protein profilin to facilitate actin filament elongation (Winkelman et al., 2014). The formin family protein also plays an important part in generating linear actin filaments. Genetic depletion by siRNA of the formin mDia2 leads to the loss of filopodia, while overexpression of its constitutively active form increased filopodia number in B16F1 cells (Yang et al., 2007). It was shown previously that mDia2 is a direct effector of CDC42. The two proteins interact through a CRIB-like motif on mDia2 and that its filopodia-inducing function is loss when CDC42 is depleted (Peng et al., 2003). Once the filaments are formed, actin-bundling proteins such as fascin hold them together to form bundles (Pollard, 2016). Fascin is recruited from the cytoplasm into the forming filopodia (Vignjevic et al., 2006). Each fascin molecule has a weak affinity to the actin filaments hence many are recruited to bind along the filopodial shaft (Mattila and Lappalainen, 2008, Pollard, 2016). A recent single-molecule analysis confirms this extremely dynamic movement of fascin within the filopodia (Pfisterer et al., 2020).

1.1.7.3 Invadopodia

The third actin-based protrusion we will discuss is invadopodium (Figure 1.8). These 0.5 to 2μm wide structures utilised cancer cells to invade into the surrounding environment. On a 2D substrate, invadopodia are characterised by the puncta or rosette morphology that can be observed on the ventral side of the cells. Immunofluorescent imaging of actin, cortactin, the Arp2/3 complex or N-

WASP can be seen overlapping with the degradation spot on a fluorescent-labelled gelatin matrix (Yamaguchi et al., 2005, Ayala et al., 2006). In a 3D environment, the morphology of invadopodia become less well defined and is often indistinguishable from other actin protrusions. Nevertheless, the molecular makeup of invadopodia is distinct from other structures. Invadopodia formation is usually divided into 3 phases: the initiation, the stabilisation and the maturation phase as outlined in Figure 1.9. During the initiation phase, a cortactin-actin complex recruits N-WASP, Arp2/3 complex and cofilin to form the initiation complex (Helgeson and Nolen, 2013). Cofilin makes direct contacts with the unphosphorylated cortactin and is kept inhibited during the initiation phase (Oser and Condeelis, 2009). The initiation complex has a weak actin polymerisation. A few second after the initiation phase, Tks5 – a scaffolding protein - is recruited (Sharma et al., 2013) to provide structural stabilisation while its PX domain anchors the complex to the PI(3,4)P2-containing plasma membrane. The level of PI(3,4)P2 is quickly ramped up by the additional recruitment of Mena, MenaINV and integrins. Mena interacts with the phosphatase SHIP2 and strengthens the production of PIP3. This stabilizes the core complex. Disruption of this interaction leads to decreased matrix degradation in cancer (Rajadurai et al., 2016, Bear et al., 2002). The splice variant MenaINV and the integrin β1, upon its recruitment, displaces PTP18 and leads to the phosphorylation and activation of cortactin (Weidmann et al., 2016, Mueller and Chen, 1991). The β1 integrin also activates a tyrosine kinase called Arg, which can specifically phosphorylate cortactin (Beaty et al., 2013). Phosphorylated cortactin releases cofilin from its inhibition. This actin severing factor severs and creates more barbed end filamentous actin, which can increase the rate of invadopodia protrusion (Oser and Condeelis, 2009). The free cortactin can also be directed to promote invadopodia membrane recycling, which has been observed in the anchor cell in C.elegans (Hagedorn et al., 2014). Finally, during the maturation phase, once all the components of the original machinery are stabilised, the actin polymerisation is enhanced by the activation effect of CDC42 on N-WASP.

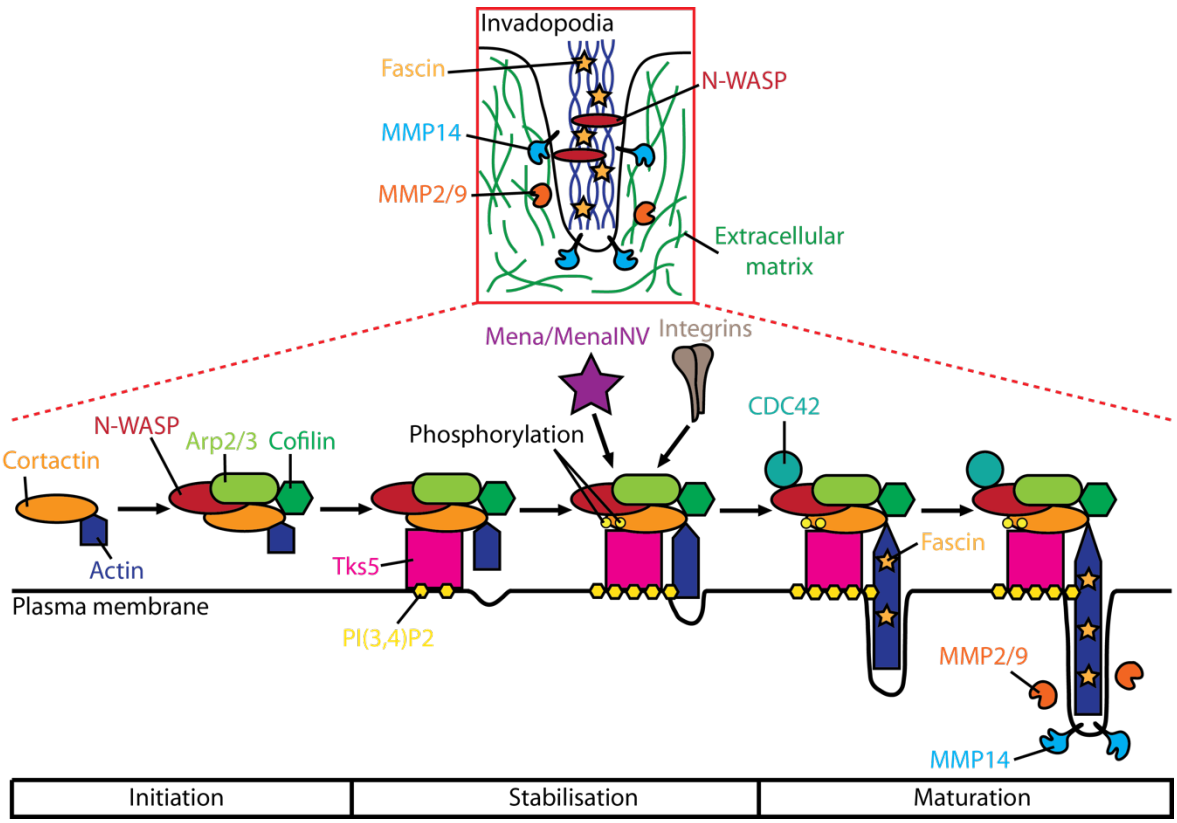

Figure 1.9 The formation process of an invadopodium

The core component of an invadopodium is Cortactin, Arp2/3 complex, N-WASP, Cofilin and actin. They form the initiation complex.

Tks5 stabilises the whole complex and anchor it to a PI(3,4)P2 patch on the plasma membrane via its PX domain. Mena, MenaINV and integrins facilitate actin polymerisation via promoting phosphorylation at tyrosine 421 and 466 on cortactin as well as increase PI(3,4)P2 production to increase complex-membrane anchorage.

CDC42 binds and activate N-WASP to further promoting actin polymerisation. The actin-bundling protein fascin is recruited to stiffening the parallel actin filaments and allow them to push on the plasma membrane, forming a protrusion. MMP14, MMP2/9 are delivered through the endocytic trafficking network to the tip of invadopodia for matrix degradation.

Image adapted and modified from (Eddy et al., 2017)

Similar to filopodia, the parallel actin filaments are bundled up via actin-bundling proteins like fascin. In fact, fascin has been shown to enhance breast and melanoma cancer cell migration in 3D environments. Deletion of fascin leads to the collapse of invadopodia and almost completely ablated matrix degradation (Li et al., 2010). As the invadopodia protrude further, matrix metalloproteases such as MMP14 (or MT1-MMP) and other MMPs are delivered to the tip through the function of N-WASP as well as the exocyst complex and the v-SNARE VAMP7 proteins that regulate endosomal fusion event at the plasma membrane (Yu et al., 2012, Poincloux et al., 2009). External factors can also trigger the formation of invadopodia. Epidermal growth factor (EGF) can activate Src kinase, which can phosphorylate Arg (Mader et al., 2011). Matrix mechanics also contribute an important part where stiff matrices have been shown to promote invadopodia formation (Jerrell and Parekh, 2016, Alexander et al., 2008).

1.1.8 Actin network components in cancer invasion and metastasis

The deadliest aspect of cancer is its ability to invade and metastasise to distant locations. A common estimate suggests that metastasis may contribute up to 90% of cancer-related deaths (Chaffer and Weinberg, 2011). The common consensus pathway of metastasis begins when the cancer cells from the primary tumour gain the ability to migrate (Figure 1.10). This is usually through a process called epithelial-to-mesenchymal transition (EMT). Strictly speaking, EMT only applies to carcinomas since they derive from epithelial cells but can also be loosely defined as the dissociation of cells from the original tumour (Lamouille et al., 2014). Cells undergo EMT are characterised by their loss of cell-cell adhesions such as E-cadherin and the rearrangement of the actin cytoskeleton. This converts cells from a basal-apical polarity into a front-rear polarity, priming them to a mesenchymal, migratory phenotype. These cells invade into the surrounding tissue and are directed towards nearby blood vessels through an EGF-mediated chemotaxis route secreted by tumour-associated macrophages (TAMs) (Linde et al., 2018). The cancer cells and TAMs form a paracrine loop that enhances each other's effects and allows for the intravasation process (Wyckoff et al., 2004, Arwert et al., 2018).

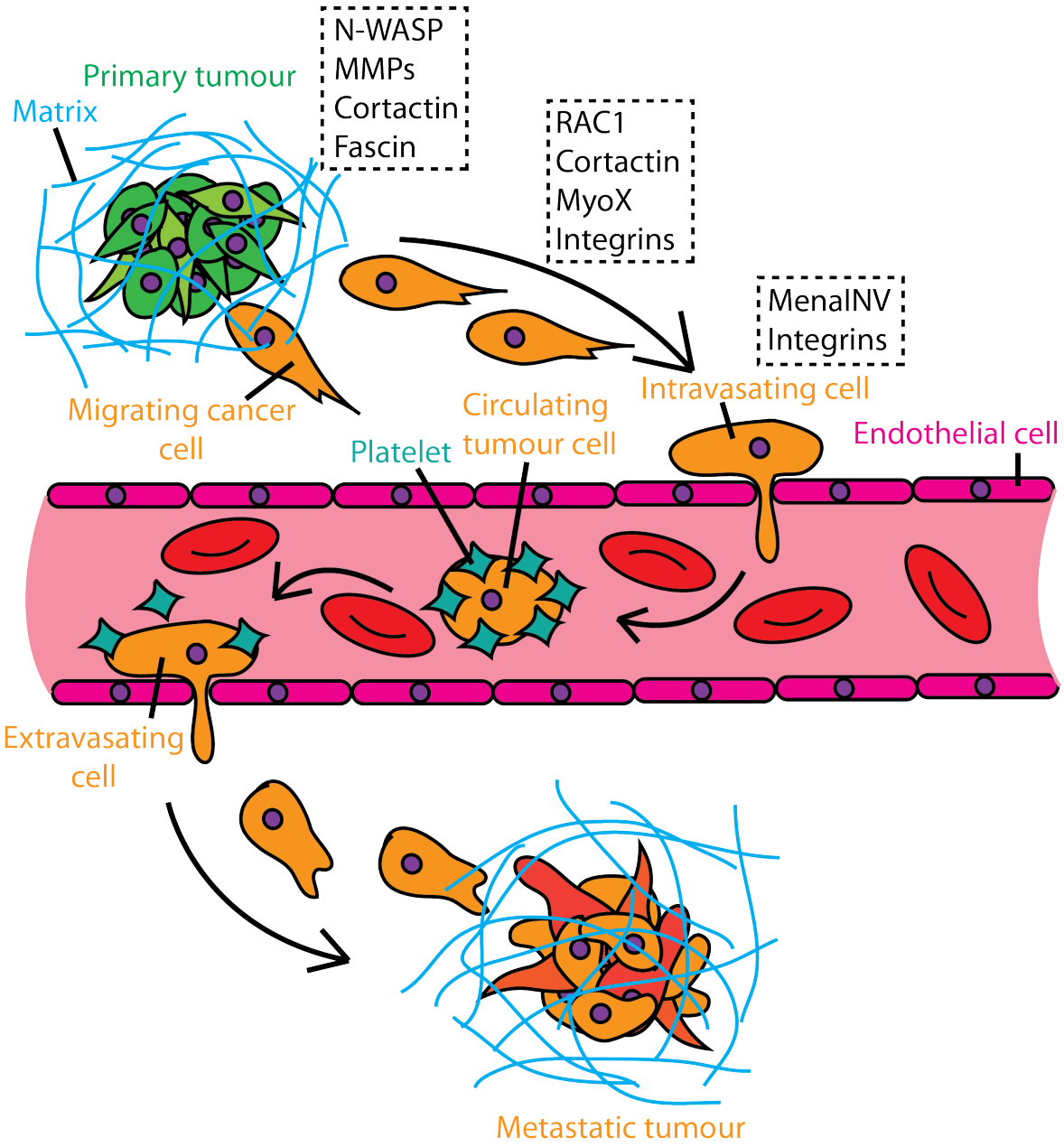

Figure 1.10 The consensus pathway of metastasis

Cancer cells acquire mutations and adaptations to gain the ability to migrate away from the primary tumour and invade into the surrounding tissue. Cancer cells can enter the bloodstream through intravasation and become circulating tumour cells (CTCs). CTCs are protected by platelets before they exit the blood vessel by extravasation at a distant tissue to form the metastatic tumour.

Proteins in dotted boxes are some of the main proteins involved during the invasion and metastasis process.

Once inside the bloodstream, the now circulating tumour cells (CTCs) are surrounded by platelets, which protect them from natural killer cells and other physical forces by generating a layer of fibrinogen (Palumbo et al., 2005). Platelets also exchange chemokines to suppress anoikis by activating YAP-dependent gene expression in the cancer cells (Haemmerle et al., 2017, Heeke et al., 2019). Molecules of selectin on the platelets also facilitate cancer cell anchoring to the blood vessel wall and prime for extravasation (Gay and Felding-Habermann, 2011, Laubli and Borsig, 2010). As the cells exit the blood vessels, they enter the distant tissue and form secondary tumours (Chitty et al., 2018).
Throughout the metastatic cascade, cell migration is unquestionably playing an essential part and each component of this machinery has been found to associate with the different steps during cancer progression.

1.1.8.1 RAC1 in cancer

For the central GTPase RAC1, despite its direct clinical significance with cancer is still poorly understood, the experimental association of RAC1 with cancer progression is evident. In melanoma, increased RAC1 activity leads to increased matrix degradation and aggressiveness in an N-RAS transformed model (Li et al., 2012, Dalton et al., 2013). RAC1 regulated by TIAM2 is also involved in modulating the actin cap protecting the cell nucleus during constricted migration (Woroniuk et al., 2018). The RAC1 specific GEF P-REX1 is needed for melanoblasts and melanoma cell invasion. NRAS Q61K melanoma mice lacking P-REX1 shows increased survival and less invasive melanoma (Lindsay et al., 2011, Welch et al., 2002). Specific deletion of RAC1 in vascular endothelial cells reduces VEGF-induced tumour angiogenesis, which is likely due to defects in endothelial cell migration (Vader et al., 2011). Mutations in RAC1 are surprisingly less common in cancer. There is one recurrent mutation RAC1 P29S, which we will explore in chapter 10, is thought to be the third most common mutation (~9%) in sun-exposed melanoma and has been shown to increase tumour initiation and convey BRAF inhibitor resistance through the sequestration of the tumour suppressor protein NF2 (Lionarons et al., 2019, Mohan et al., 2019). A few other mutations of RAC1 has also been found in other cancer including head and neck, sarcoma and testicular cancer (Cerami et al., 2012). On the other hand, RAC1 amplification is

very common in human cancer and is almost always associated with poorer prognosis (Cerami et al., 2012, Gao et al., 2013, De et al., 2019).

1.1.8.2 The Scar/WAVE complex and cancer

Counterintuitively, Scar/WAVE complex and its component CYFIP have been implicated in suppressing tumour progression in epithelial carcinoma. One study using DNA copy number alteration analysis identified CYFIP1 gene to be one of the hits that are commonly lost during carcinoma development (Silva et al., 2009). It was shown that CYFIP1 loss leads to the loss of E-cadherin adherence junctions – part of the cell-cell adherent network - along with vinculin-mediated cell-matrix interaction. In the presence of a driver mutation of RAS, CYFIP1 knockdown leads to increased cell invasion *in vivo*. In the epidermoid carcinoma A-431 cells, deleting CYFIP1 or Nap1 leads to increased N-WASP and FAK (Focal Adhesion Kinase) activity coupled with increased invasion in a 3D matrix (Tang et al., 2013). Sharing the same counterintuitive function in cancer is the isoform WAVE3. Some studies associate WAVE3 with the increased aggressiveness in breast cancer and its depletion reduces cell migration and invasion (Kulkarni et al., 2012, Sossey-Alaoui et al., 2007). However, other studies could not replicate these findings (Spence et al., 2012). Surprisingly, overexpression of lamellipodin, a Scar/WAVE complex activator described earlier, increases breast cancer invasion in 3D and decreases patient survival (Carmona et al., 2016). This adds to the controversial role of the Scar/WAVE complex being an actin polymerisation driver yet can also be tumour suppressive.

1.1.8.3 The Arp2/3 complex and cancer

The Arp2/3 complex and its subunits are also implicated in different types of cancer. In pancreatic cancer, the ARPC3 and ARPC4 subunit were found to be highly expressed while the ARPC1B and ARPC2 were downregulated. Depleting the Arp2/3 complex leads to significant reduction in pancreatic cancer cell migration and invasion (Rauhala et al., 2013). In the breast cancer cell MDA-MB-231, PLK4 – a serine/threonine kinase - is found to physically interact and perhaps increase the activity of the Arp2/3 complex. Silencing PLK4 through siRNA or flox in MEFs reduces invasion (Kazazian et al., 2017). A direct interaction of the Arp2/3

complex with the p53-induced transcriptional factor WDR63 leads to the inhibition of the Arp2/3 complex and reduction in invasion (Zhao et al., 2020).

1.1.8.4 Other components of the actin network and cancer

Invadopodia and filopodia are wildly believed to be involved in cancer invasion and metastasis. Each of the components described in Figure 1.8 and Figure 1.9 have been associated in cancer. The Table 1.1 summarises some of the descriptions from the literature on the role of these components in cancer invasion and metastasis.

Overall, it is clear that cell migration plays a substantial role in cancer progression. Almost every single component of this complicated pathway is connected one way or another to cancer. The examples provided above are not an exhaustive list and only serve to give the readers some ideas of the complexity of cell migration and how it can be reprogrammed during pathological conditions. In the next segment, we will explore the non-migration roles of actin in a process called macropinocytosis and how this function can cooperate with cell migration.

Table 1.1 The roles of the filopodia and invadopodia components in cancer

Components	Effects	Mechanisms
Fascin	• Filopodia formation • Intercalate cells into the mesothelial layer • Deletion leads to increased survival, less matrix degradation in K-RAS PDAC (Li et al., 2010, Li et al., 2014)	• Stabilise filopodia and invadopodia through actin bundling
β1 integrins	• Increase metastasis in a D2A1 breast cancer model (Shibue et al., 2013)	• Decorating along the shafts • Stabilising filopodium-like protrusion by activating β-parvin, β-PIX, CDC42 and PAK
Myosin X	• Upregulated in invasive breast cancer • Enrichment at the invasive front of tumours • Enhanced and correlated with increased metastasis with p53 mutant background (Arjonen et al., 2014)	• Promoting filopodia formation • Delivering components to filopodia • Recycling of α5β1 integrins to the filopodial tips • Activation of RacGAP1 and RhoA
Rab-coupling protein RCP	• Increased cancer cell invasion (Caswell et al., 2008, Jacquemet et al., 2013)	
N-WASP	• Increased matrix degradation in breast cancer (Yu et al., 2012) • PDAC cancer cells chemotaxis and matrix remodelling • Increased metastasis and reduced survival in PDAC mouse model (Juin et al., 2019)	• Delivery of MMP14 to the filopodial-like protrusions • Intracellular trafficking of the LPAR1 receptor

Cortactin	• Increased migration and invasion in non-metastatic hepatocellular carcinoma cell in an orthotopic model (Chuma et al., 2004) • Increased endothelial transmigration and bone metastasis in MDA-MB-231 nude mice injection (Li et al., 2001) • Head and neck cancer cell invasion (Clark et al., 2007)	• Increased invadopodia formation and matrix degradation • Regulate matrix metalloprotease MMP2/9 and MMP14 secretion
MenaINV	• Increased breast cancer cell migration, haptotaxis towards blood vessels and metastasis (Oudin et al., 2016, Oudin and Gertler, 2017)	• Strong interaction with the integrin $\alpha 5$ • Drives fibronectin-dependent haptotaxis
Matrix metalloproteases	• Collective invasion and leader cells (Chapman et al., 2014, Carey et al., 2013, Mitchell and O'Neill, 2016) • Breach basement membrane (Gligorijevic et al., 2012) • Intravasation (Juncker-Jensen et al., 2013) (Deryugina and Quigley, 2015) • Increased angiogenesis in retinoblastoma (Rojiani et al., 2010, Webb et al., 2017)	• MMP14, MMP1 • MMP2, MMP9

1.2 The machinery of macropinocytosis

In broader terms, actin is responsible for the regulation of the membrane dynamic in cells. Processes like membrane bending and tubulation such as those of endocytosis are largely actin-dependent. Endocytosis is a group of diverse processes including the classic clathrin-mediated endocytosis to the bulky macropinocytosis and phagocytosis. Many of these processes are conserved in a wide range of different species, from yeast to the social amoeba *Dictyostelium* to mammalian cells. In this segment, we will only be focusing on macropinocytosis, a process that was first described almost 90 years ago yet remains the least understood. First described in macrophages and sarcoma cells as large fluid-containing "globules which move centrally and are digested" (Lewis et al., 1931), it was then realised that this intracellular process may act to provide the nutrients needed for cellular growth and metabolism. Over the years, more research has helped us better understand the molecular regulation behind macropinocytosis. The following segment will discuss our current understanding of the process and how actin dynamic is related.

1.2.1 The molecular make-up of macropinocytosis

Macropinosomes are approximately 0.2 to 5μm in size (Egami et al., 2014). From a macroscopic point of view, macropinocytosis is associated with the formation of membrane ruffles. Some of these ruffles fold on to themselves to create endocytic vesicles containing the external materials which are taken up by the cell. A closer look at the molecular make-up reveals many common features with the migration machinery (Figure 1.11). The starting signal of macropinocytosis can derive from the binding of a ligand to a receptor tyrosine kinase (RTK). The now activated RTK undergoes a typical autophosphorylation reaction to recruit the adaptor protein GRB2, which then recruits SOS. SOS is a RAS GEF that activates RAS by recruiting it to the plasma membrane and catalysing the exchange of GTP for GDP (Iversen et al., 2014). The activated RAS directly binds and activates PI3K (Rodriguez-Viciana et al., 1994) and trigger the opening of its substrate-binding domain (Pacold et al., 2000). PI3K phosphorylates and converts PI(4,5)P2 into PIP3. The presence of PIP3 recruits various PH domain-containing proteins, including the RAC GEFs P-REX to activate RAC1 (Welch et al.,

2005, Campa et al., 2015). PI3K itself can also form a complex with Abi1, SOS1 and EPS8, which also possesses RAC GEF activity (Innocenti et al., 2003). Once RAC1 is activated, the classical actin polymerisation route as described in earlier segments is initiated, which leads to the protrusion of the plasma membrane and formation of macropinosomes. This signalling is further assisted by the activation of the kinase PAK downstream of RAC1, which then phosphorylates and activates the LIM kinase (LIMK). LIMK then phosphorylates and inhibits the actin severing protein cofilin thus allows the actin polymerisation to proceed for longer. There are many additional regulation mechanisms exist that influence this process. It is generally accepted that for epithelial cells, growth factors like EGF or PDGF are the main trigger of macropinocytosis, while for macrophages is M-CSF. Quiescent fibroblasts injected with the constitutively active mutant H-RAS form more ruffles and macropinosomes (Bar-Sagi and Feramisco, 1986). Pancreatic cancer cells naturally expressing mutant K-RAS G12C are more macropinocytic than cells expressing wild-type protein (Commisso et al., 2013).

PIP3 is an important component of macropinocytosis yet its exact functions are still rather vague. Inhibiting PI3K or PIP3 production using inhibitors or genetic manipulation significantly suppresses macropinocytosis (Araki et al., 1996, Buczynski et al., 1997). In contrast, deletion of PTEN, the protein responsible for degrading PIP3 into PI(4,5)P2, enhances macropinocytosis (Kim et al., 2018). However, recent discoveries have complicated the picture by proposing the functions of other phosphoinositide moieties (Figure 1.12). One study demonstrated that the sequential degradation from PIP3 -> PI(3,4)P2 -> PI3P -> PI regulates macropinosome formation (Maekawa et al., 2014). The protein SHIP2, which is a phosphatase that converts PIP3 into PI(3,4)P2, when deleted significantly affects dorsal ruffle formation (Hasegawa et al., 2011). PI(3,4)P2 itself strongly binds the PH domain-containing TAPP1. TAPP1 is known to interact with syntrophins and is thought to be important for actin remodelling and membrane ruffle formation in NIH3T3 cells (Hogan et al., 2004). A recent study also found that PI(3,4)P2 is specifically recognised by the PX domain of the sorting nexin 5 (SNX5).

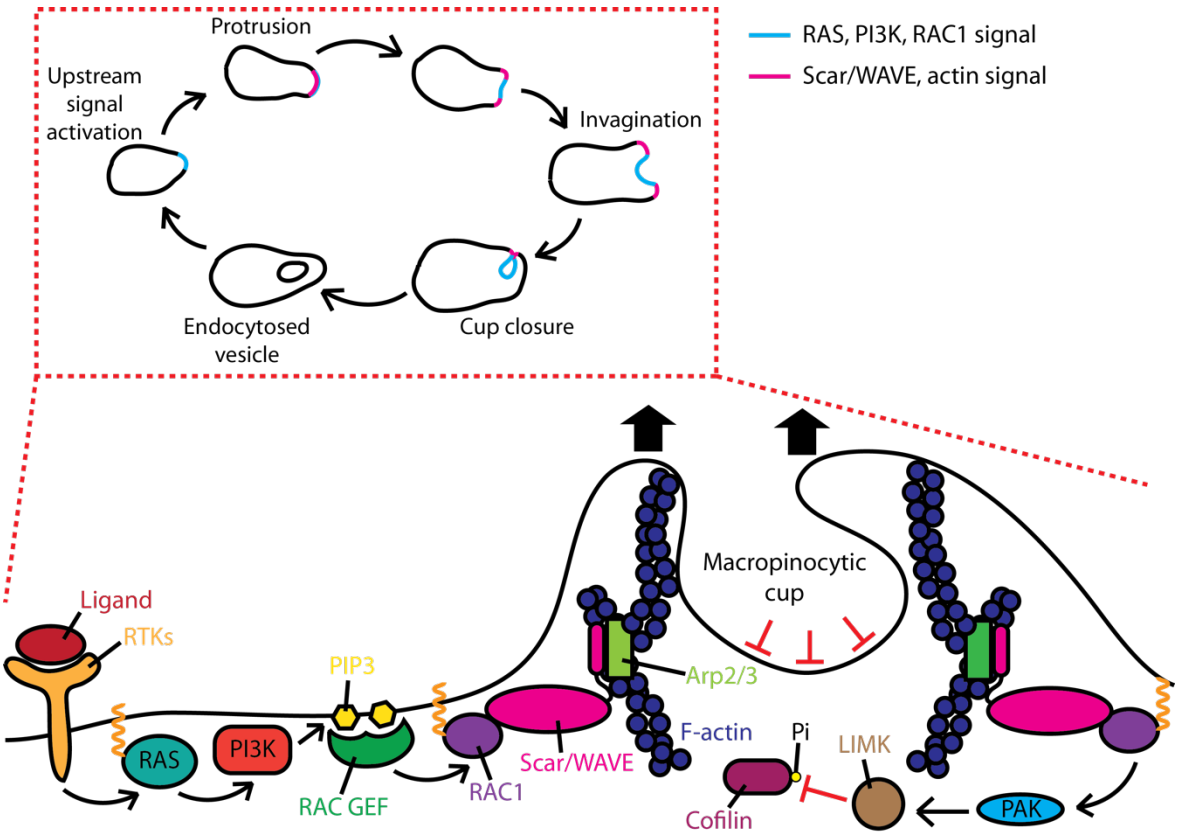

Figure 1.11 The consensus molecular pathway of macropinocytosis

Upper panel: The main events during macropinocytosis. Adapted and modified from (King and Kay, 2019).

Lower panel: Ligand triggers the activation of Receptor Tyrosine Kinase (RTK) leads to the activation of RAS. RAS then activates PI3K leading to the production of PIP3. PIP3 recruits RAC1 GEF, which activates RAC1. Activated RAC1 binds and activates the Scar/WAVE complex, which then activates the Arp2/3 complex and leads to branched actin polymerisation, generating plasma membrane protrusions. Active RAC1 also activates PAK, which then activates LIMK. LIMK phosphorylates and inactivates cofilin, promoting actin polymerisation. The middle of the cup is suppressed (red blunt arrow) leads to the local retraction of the plasm membrane while the sides continue to protrude, forming the cup shape.

SNX5 is a component of the retromer complex (Wassmer et al., 2007), and its deletion leads to a reduction in the number of macropinosomes independent of EGF induction (Lim et al., 2008a, Merino-Trigo et al., 2004). It was hypothesized that SNX5 uses its BAR domain to induce membrane curvature, shifting the balance towards vesicle formation (Hong, 2019). PI(3,4)P2 is then dephosphorylated into PI3P by the phosphatase INPP4B. Deletion of this protein significantly impairs the uptake of dextran in A-431 cells. PI3P recruits the Ca2+-activated K+ channel KCa3.1 which also contributes to macropinocytosis (Maekawa et al., 2014). The precursor of PIP3, PI(4,5)P2 also has a major role in macropinocytosis. Synthesised from PI4P by the enzyme PI4KIIIα (Nakatsu et al., 2012, Balla et al., 2008), PI(4,5)P2 recruits the sorting nexin 9 (SNX9) protein to the membrane. SNX9 oligomerises and directly binds and activates N-WASP to trigger membrane ruffling. Deletion of SNX9 reduced fluid uptake in BSC1 cells (Yarar et al., 2007). N-WASP itself can also be directly stimulated by PI(4,5)P2 through electrostatic interactions with its polybasic domain (Papayannopoulos et al., 2005, Senju et al., 2017). PI(4,5)P2 is also specifically targeted by the enzyme phospholipase C (PLC) and is converted to IP3 and DAG. While IP3 does not have any direct role in macropinocytosis, DAG is a known activator of protein kinase C (PKC), membrane ruffling and cup closure even in the absence of PDGF (Di Sario et al., 2002, Amyere et al., 2000, Yoshida et al., 2018, de Carvalho et al., 2015). One of the potential unique features of macropinocytosis is its susceptibility to pH. The Na+/H+ exchange inhibitor amiloride was found to affect macropinocytosis while leaving other endocytic pathways largely intact. It is believed that this inhibitor decreases the local pH and affects the activity of RAC1 (Koivusalo et al., 2010). It is likely that other signalling pathways also contribute to macropinocytosis. In the next segment, we will discuss how cells spatially organise the molecular machinery of macropinocytosis.

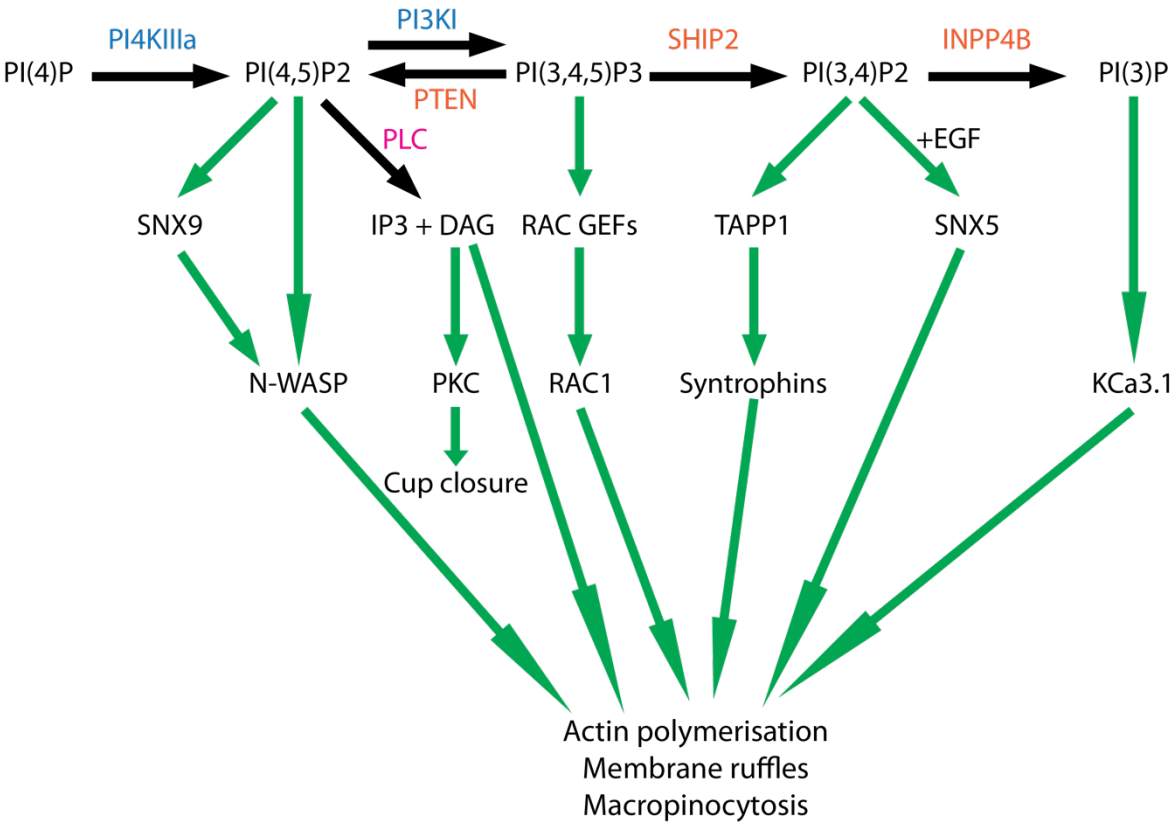

Figure 1.12 A map of the signalling and functions of phosphoinositides in regulating macropinocytosis

Black arrows represent conversion pathways

Green arrows represent activation pathways

Blue highlight represents kinases

Orange highlight represents phosphatases

Pink highlight represents lipases

Affecting any of the components in this pathway will affect the signalling of actin polymerisation and macropinocytosis.

1.2.2 The spatial organisation of macropinocytosis

Macropinocytosis shares many similar components with the migration machinery. However, what differentiates the two processes is the spatial organisation of the different molecules involved. During the formation of macropinosomes, active RAS and PIP3 signals were seen decorating the bottom of the pinocytic cups (Figure 1.13) by using the reporter RAF1-RBD and PH-CRAC in *Dictyostelium*, respectively. Deleting the RAS GAP NF1 leads to significantly larger macropinosomes, suggesting NF1 and RAS regulate the size of these vesicles (Veltman et al., 2016). It is surprising that both PIP3 and RAS are highly localised at specific regions of the plasma membrane despite their intrinsic motile nature. One study using photoactivation has suggested membrane ruffles to act like diffusion barriers (Welliver et al., 2011). However, this model does pose a question of which comes first: an initial ruffle restricting the signal molecules before cup formation or stochastic signals drive membrane ruffles which then further restrict their own diffusion? Some other hypothesis suggests the restriction could be due to the presence of certain tethering molecules. A recent study suggests ForG, a protein found specifically at the base of the pinocytic cups and can interact and be activated by RAS. ForG triggers filamentous actin polymerisation at the base of the cup and its deletion impairs endocytosis (Junemann et al., 2016). It is possible that RAS can be anchored via this way.

In contrast to RAS and PIP3, the Scar/WAVE complex and the Arp2/3 complex are concentrated at the protruding edge, similar to that in lamellipodia. GFP-tagged HSPC300 signal could be seen restricted at the two protruding edges on a 2D surface, but in 3D, it could be seen decorating the rim of the macropinosomes (Veltman et al., 2016). It is believed that this is where branched actin polymerisation is the most active. The localisation of active RAC1 at the macropinosomes is however slightly ambiguous. Visualising RAC1 using GFP-tagged constructs *in vivo* at high spatiotemporal resolution is not frequent due to its homogenous cytoplasmic expression. Studies using FLIM/FRET were unable to overcome this (Yoshida et al., 2009). However, it would make sense if active RAC1 signal overlaps with that of the Scar/WAVE and Arp2/3 complex.

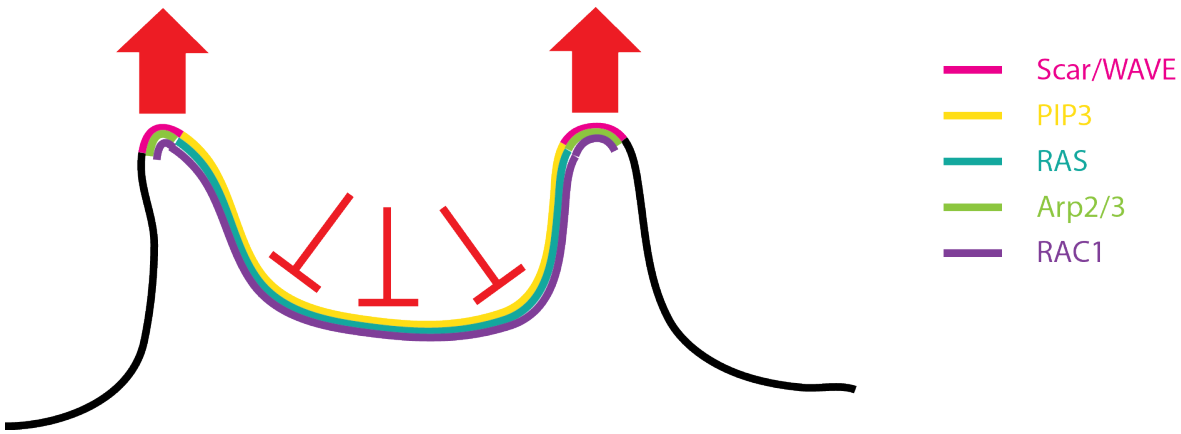

Figure 1.13 The spatial organisation of macropinocytosis

RAS and PIP3 decorate the bottom of the macropinocytic cup while Scar/WAVE complex and Arp2/3 complex are localised to the edge, leading to the differential protrusion of the membrane. Active RAC1 can be visualised throughout the cup.

Red arrows represent the protrusion direction. Red blunt arrows represent the region of suppression of protrusion.

Inspired by (Buckley and King, 2017).

At the same time, active RAC1 present at the centre of the cup can be suppressed by an additional mechanism leading to an invagination driving cup formation. Active RAC1 suppression has been shown to be essential for the completion of macropinocytosis. By using a RAC1 FRET probe in macrophages, active RAC1 signal was seen transiently increased and then disappeared at the macropinosomes (Yoshida et al., 2009). Constitutively inducing RAC1 activity with photoactivation leads to the formation of membrane ruffles but unsuccessful vesicle formation. Only when the activation laser is turned off then the macropinosomes formed and acquired maturation markers (Fujii et al., 2013). An option for active RAC1 suppression could be via suppressing RAS signal and the GAP NF1 has been proposed to be a potential candidate. However, both RAS and RAC1 are multifaceted proteins that are involved in various signalling processes, hence suppressing RAS in order to suppress RAC1 is a rather inefficient mechanism. Surprisingly, however, the literature on how active RAC1 signal was deactivated at the macropinocytic cups is scarce. In macrophages, three RAC GAPs ARHGAP12, ARHGAP25 and SH3BP1 were found to be localised to the base of phagocytic cups (Schlam et al., 2015). However, these proteins were identified to be involved in

phagocytosis rather than macropinocytosis. Despite many similarities between the two processes, certain differences in terms of receptors and the molecules involved still exist. Furthermore, the author specified that only beads of size equal to or greater than 8μm would trigger the recruitment of these RAC GAPs, whereas those smaller are assumed to not require any RAC1-suppressing signal. A recent study has also identified a novel BAR-domain-containing protein called RGBARG in *Dictyostelium*, which can be seen localising to the macropinocytic cups with the strongest signal at the two edges (Buckley et al., 2020). RGBARG contains a RAS GAP and an RHO GEF domain which specifically binds to RACG but not RAC1. It was suggested that RGBARG suppresses RAS at the cup base and activates RAC at the cup edges to help with the formation and completion of macropinosomes. Nevertheless, a general signalling molecule that specifically inhibits RAC1 across the different sizes of macropinosomes still remained undiscovered. Once the invagination is formed, the two edges collapse on to each other and form a complete vesicle. This vesicle buds off from the plasma membrane through an unknown mechanism. CtBP1/BARS protein, which acts during the fission process of Golgi vesicles, was suggested to be involved in the scission process (Haga et al., 2009). Nevertheless, how exactly CtBP1/BARS mediates this process or whether if any other proteins involved remains unclear. Overall, this segment has described a fairly detailed molecular organisation for the formation of macropinosomes. The next segment will discuss the maturation process and the fate of these vesicles.

1.2.3 The fate of macropinosomes and their contents after fission

After the initial internalisation, macropinosomes enter a maturation pathway that shares many similarities with other endocytic processes (Figure 1.14). The vesicles acquire the early endosomal marker RAB5A. However, its exact timing and function during macropinocytosis have been debated since its first description. It was first suggested that RAB5A is needed for the fusion of endosomes together. Depletion of RAB5A leads to a failure in the fusion between bacteria-containing endosomes (Perskvist et al., 2002, Singh et al., 2003). *In vitro* experiments incubating endosomes with the inactive version of RAB5A or with anti-RAB5A blocking antibody results in endosomes unable to fuse (Gorvel et al., 1991).

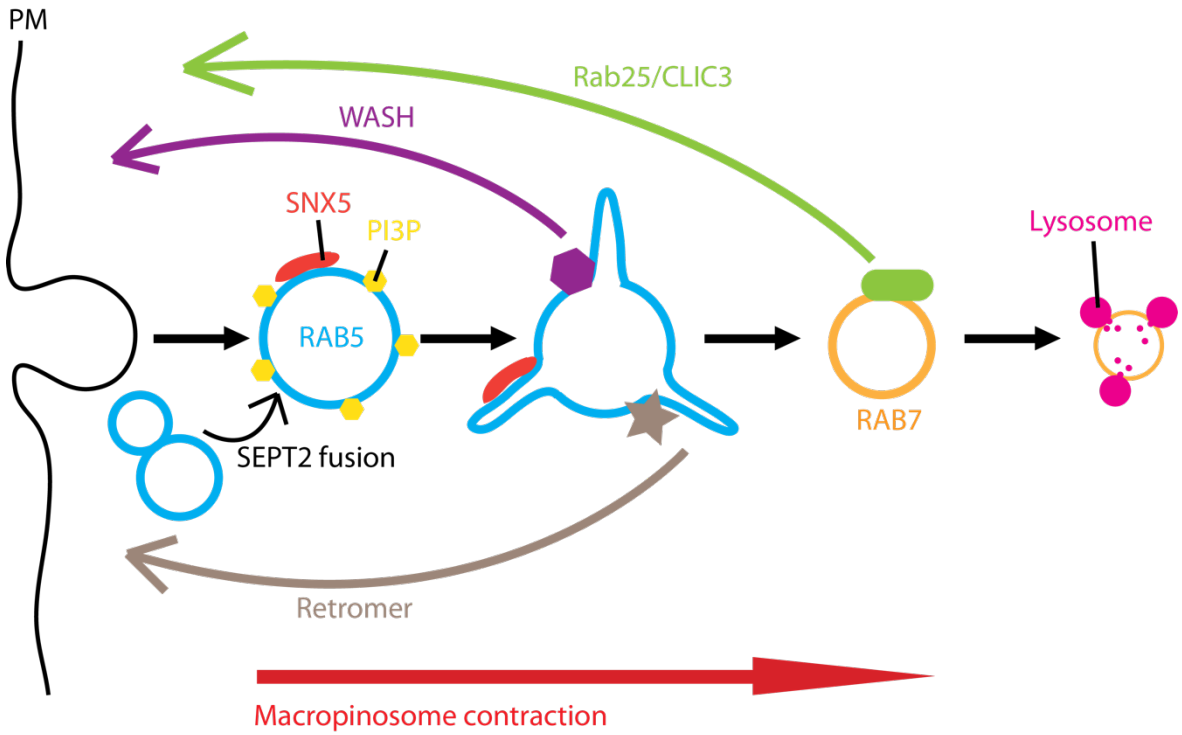

Figure 1.14 The maturation of macropinosomes

After cup closure, the macropinosome proceeds into the cell body and undergo a process called contraction where it reduces in size along with acquiring different molecular markers before fusing with lysosomes for content degradation. Many recycling pathways happen along the way to recycle membrane and proteins back to the plasma membrane.

PM = plasma membrane

Independent of RAB5A, the fusion process can also be supported by the functions of SEPT2. This filamentous GTPase binds specifically to PI(3,5)P2 and localises to the contact sites between endosomes, presumably to bridge and facilitate vesicle fusion (Dolat and Spiliotis, 2016). The role of RAB5A was also extended upstream, to the closing process of macropinosomes. A recent study has discovered a relationship between RAB5A and PI(4,5)P2. Normally, PI(4,5)P2 depletion reduces the thickness of the actin network around the vesicles thus promotes membrane fluidisation and fusion (Levin et al., 2015). The recruitment of RAB5A to the closing macropinosomes leads to the recruitment of two phosphatases OCRL and Inpp5b to dephosphorylate PI(4,5)P2 (Michelle E. Maxson, 2020). Early endosomes also see the recruitment of SNX5 that binds specifically to PI3P and PI(3,4)P2 through its PX domain (Merino-Trigo et al., 2004). Silencing SNX5 leads to a dramatic decrease in the number and size of macropinosomes in bone marrow-

derived macrophages (Lim et al., 2012). As the macropinosome progresses further into the cell, GFP-tagged SNX5, as well as its binding partner SNX1, were detected on tubules projecting out from the vesicles over the course of 5 to 10min (Kerr et al., 2006, Wang et al., 2010). Interestingly, SNX5 is also part of a larger complex known as the retromer complex (Burd and Cullen, 2014) and is involved in the recycling of many receptors and membrane-bound proteins back to the plasma membrane (Wassmer et al., 2007, Kovtun et al., 2018). Another complex that specifically associates with the early endosome is the WASH complex. The WASH complex is also an NPF that can activate the Arp2/3 complex and drive actin polymerisation and the tubulation process. The complex has been shown to be recruited very early on during macropinocytosis as well as at late endosomes to assist with the recycling of various membrane proteins such as integrins (Buckley et al., 2016). The WASH complex is recruited to the retromer complex via a tail domain of its FAM21 subunit. This WASH-retromer complex modulates the polymerisation of actin at the endosome as well as controlling the scission of the tubules (Gomez and Billadeau, 2009, Seaman and Freeman, 2014, Derivery et al., 2009). This recycling pathway has been shown to be important for the retrieval of MMP14 and contribute to the invasiveness of cancer cells in 3D (MacDonald et al., 2018). Membrane tubulation leads to a decrease in the surface area of macropinosomes while retaining most of the intraluminal contents. This contraction process effectively increases the content concentration within the endosomes. The contracting macropinosomes slowly lose their RAB5A marker and are replaced with RAB7 through a process called Rab conversion (Rink et al., 2005). RAB7 marks the identity of late endosomes and has several functions including linking the vesicles to dynein-dynactin complex to be transported to lysosomes (Jordens et al., 2001). RAB7 is also important for controlling the assembly of the V-ATPase complex for proper acidification of the late endosomes (De Luca and Bucci, 2014, Johnson et al., 2016). However, membrane proteins on late endosomes can be rescued one more time through the activity of Rab25 and CLIC3 pathway (Dozynkiewicz et al., 2012). Overall, macropinosome maturation takes a more generic route similar to many other endocytic pathways after scission from the plasma membrane.

1.3 The novel CYRI protein family in actin dynamic regulation

In the previous sections, we have touched on the idea of different regulator proteins exist to regulate the actin cytoskeleton network, particularly negative regulators. We have mentioned in detail how RAC GAPs can accelerate the GTPase activity of RAC1 through the use of its arginine finger (Figure 1.4). We also briefly mentioned Arpin as a negative regulator of the Arp2/3 complex. Within this signalling axis, all but the Scar/WAVE complex itself has their corresponding negative regulators (Figure 1.15). Only until recently that our lab and the Insall lab here at the Beatson Institute have discovered and characterised the first negative regulator of the Scar/WAVE complex that we named CYRI (stands for CYFIP-related RAC interactor). CYRI is encoded by a gene called *Fam49* and was first discovered from using mass spectrometry analysis of a pulldown of potential new interactors of the Scar/WAVE complex in *Dictyostelium* (Fort et al., 2018). In brief, a *nap1* knockout *Dictyostelium* line was expressed with a GFP-tagged NAP1 construct and performed a pulldown mass-spectrometry on. NAP1, as mentioned in earlier segments, is one of the major components of the Scar/WAVE complex. The analysis showed the enrichment of all the other components of the Scar/WAVE complex as expected along with CYRI. In *Dictyostelium*, there is only one version of the gene, however, in mammalians, there are two paralogs *Fam49A* and *Fam49B* (which encodes for CYRI-A and CYRI-B, respectively). Phylogenetic analysis using the PANTHER database from GENEONTOLOGY (http://geneontology.org/) shows that almost all groups of animals within the Eukaryote kingdom contain one single *Fam49* gene except for the clade of Euteleostomi i.e. bony vertebrates, which includes mammals. In this clade, the *Fam49* gene underwent a duplication event that resulted in two paralogs *Fam49A* and *Fam49B*. The following segment will discuss our current understanding of the CYRI protein family and should serve as a foundation for all of the works in the following chapters. From this point onwards, both the genes and the proteins of the *Fam49* family will be referred to as CYRI-A or CYRI-B for consistency.

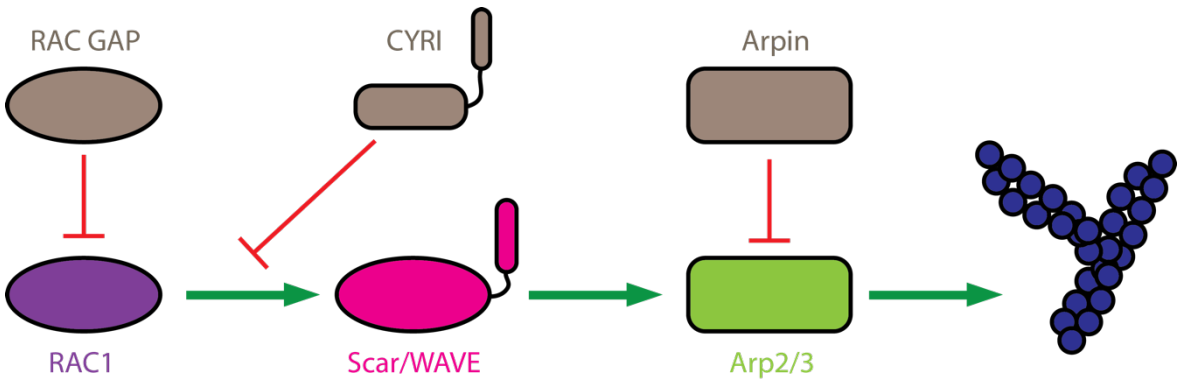

Figure 1.15 The regulators of the RAC1-Scar/WAVE-Arp2/3 signalling axis

RAC1 is suppressed (red blunt arrow) by the activity of RAC GAPs while Arp2/3 complex is suppressed by the competitive inhibitor Arpin. The RAC1 to Scar/WAVE complex signalling axis is inhibited by the novel protein family CYRI.

1.3.1 CYRI-B

1.3.1.1 An introduction to CYRI-B

We start our discussion with CYRI-B since this was recently been characterised (Chattaragada et al., 2018, Fort et al., 2018, Shang et al., 2018, Yuki et al., 2019). An overall analysis using the Human Protein Atlas database shows that in terms of RNA expression level, CYRI-B is most abundant in the brain, bone marrow, lymphoid and blood tissues. In terms of protein level, CYRI-B can be found most concentrated in the brain, kidney and skin tissues, while only moderate in others. CYRI-B was identified in mammalian cells through the use of a genome-wide CRISPR screen. Using a lentiviral sgRNA library in Cas9-expressing Jurkat cells as well as the marker CD69 as a read-out for the activation state of T-cells, CYRI-B was identified to be a negative regulator of T-cell activation (Shang et al., 2018). In fact, according to the Database of Immune Cell EQTL Expression Epigenomics database (https://dice-database.org/), CYRI-B is highly expressed in a wide variety of immune cells, with the highest number of transcripts found in natural killer (NK) cells, classical and non-classical monocytes and CD4, TH1/17 T cells (Figure 1.16). Interestingly, a recent genome-wide study in pregnant women living with or without multiple sclerosis, an autoimmune disease, also showed CYRI-B to be one of the top genes that were altered (Gilli et al., 2010, Gilli et al., 2011).

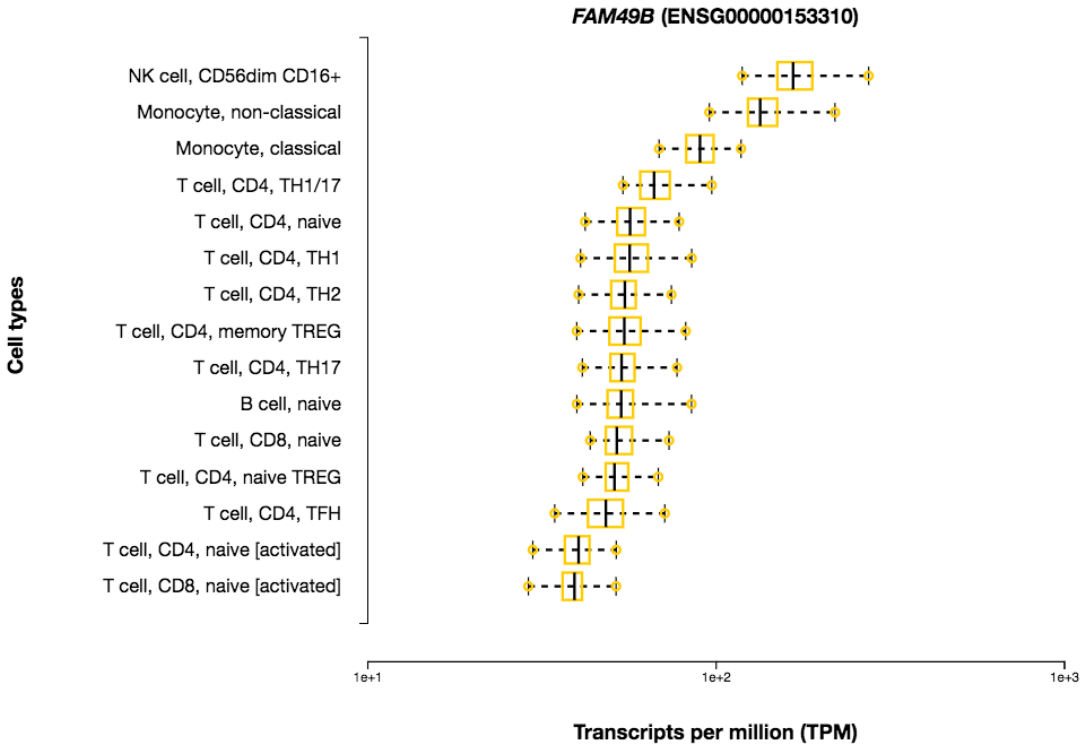

Figure 1.16 The immune expression profile of CYRI-B in transcripts per million (TPM)

CYRI-B is the most highly expressed in NK cell, classical and non-classical monocyte and CD4+ TH1/17 T-cells.

CYRI-B was shown to interact directly with active RAC1 in T-cells and interfere with the RAC1-PAK signalling, which is thought to be important for T-cell activation (Shang et al., 2018). Multiple subsequent studies using *in vitro* GST pulldown assays have confirmed this interaction to be specific to active RAC1 and not the inactive form or the closely related protein CDC42 (Fort et al., 2018, Yuki et al., 2019, Shang et al., 2018). Even though the exact crystal structure of CYRI-B has not been solved, something we will come back to in a later chapter, biochemical and bioinformatic analysis have given us some hints on how CYRI-B behaves (Figure 1.17). InterPro and Pfam analysis predict for the existence of a DUF1394 domain (Domain of Unknown Function 1394) of CYRI-B, which contains an unstructured loop from amino acid 18 to 320 while the first 17 amino acids are predicted to be an α-helix (Fort et al., 2018). This short amino acid stretch may be an autoinhibitory loop, preventing CYRI-B from interacting with active RAC1. This is reminiscent of how the Scar/WAVE complex is activated through active

RAC1 binding, leading to the unfolding of the WCA domain. Multiple sequence alignment identifies the two arginine residues 160 and 161 to be conserved across different species and between the CYRI isoforms and the subunit CYFIP of the Scar/WAVE complex (Fort et al., 2018). Mutating these two residues ablated RAC1 interaction. One hypothesis is that the N-terminal α-helix folds and covers this binding site in an autoinhibitory conformation. The proline 150 is also suggested to be contributing to this interaction (Yuki et al., 2019). However, since proline has a pyrrolidine sidechain, mutating this residue might likely affect the structural integrity of the protein and not necessarily a specific effect on RAC1 binding. Furthermore, the second glycine residue is a consensus myristoylation site (Udenwobele et al., 2017) and indeed it was shown that mutating this glycine to alanine ablated the myristoylation signal in a CLICK chemistry assay (Fort et al., 2018). This myristoylation is believed to be important for the membrane localisation of CYRI-B, however this has not been demonstrated in any of the studies. Thus, one of the big questions that we lack is where does CYRI-B or the CYRI protein family in general localise inside the cell, and we will come back to this point in future chapters.

Taking together, CYRI-B was proposed to be the first negative regulator of the Scar/WAVE complex (Figure 1.18A). The protein acts by directly competing with the Scar/WAVE complex for active RAC1 binding, hence subsequently shutting down actin polymerisation signal. In normal cells, this is thought to enhance the dynamic of the plasma membrane and buffering the activity of the Scar/WAVE complex (Fort et al., 2018). It was reported that the affinity of the Rac-binding domain (RBD) of CYRI-B to active RAC1 is around 22 to 27μM (Fort et al., 2018), while the reported affinity between the Scar/WAVE complex and active RAC1 is ranging from around 0.2μM for the D-site to 11μM for the A-site (Chen et al., 2017). This suggests that for CYRI-B to effectively compete with the Scar/WAVE complex, the number of active CYRI-B molecules needs to be at least 10 times that of the Scar/WAVE complex. This can be achieved by either increasing its local concentration or increasing the total number of molecules inside the cell.

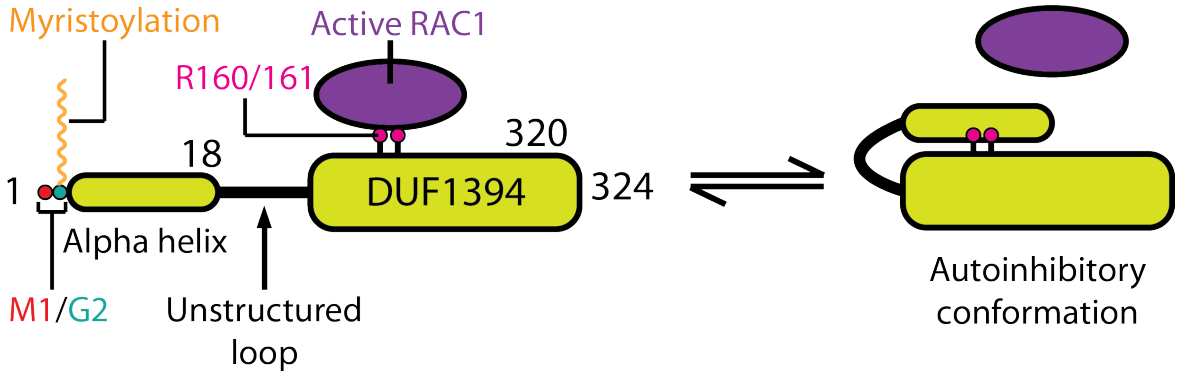

Figure 1.17 The schematic structure of CYRI-B and the putative RAC1 interaction site

Glycine 2 is a myristoylation site. Arginine 160/161 are conserved and crucial for active RAC1 interaction.

In the putative autoinhibitory mode, the alpha helix at the N-terminus folds and blocks the binding site for active RAC1.

A recent quantitative mass-spectrometry study in several cell lines including A-549, HepG2, PG3 and U87 have shown a 5-fold higher in the absolute number of CYRI-B molecules compared to CYFIP1 (Wisniewski et al., 2014), suggesting perhaps other mechanisms rather than just sheer number also play a role. When delete CYRI-B from COS-7 or HeLa cells, the cells adopt a flat and broad lamellipodia (Fort et al., 2018, Yuki et al., 2019) (Figure 1.18B). Measuring the leading edge's dynamic in MEFs upon RAC1 activation by 458nm laser showed CYRI-B KO decrease its membrane dynamic compared to WT cells (Fort et al., 2018). This also affects their migratory behaviour. On a random migration assay, CHL-1 cells lacking CYRI-B tend to migrate faster albeit less directional compared to WT cells. However, in *Dictyostelium*, lacking CYRI-B impaired cell migration towards a source of chemoattractant (Fort et al., 2018). This discrepancy demonstrates that the same protein of the same function can still result in different, sometimes even opposite, effects depending on the system being examined. Directly related to the inhibitory relationship between CYRI-B and the Scar/WAVE complex is the finding that certain bacteria such as *Salmonella* can use a protein called SopE to directly target CYRI-B to the proteasomal system. This is thought to allow for the increased actin polymerisation and membrane invagination to accommodate the bacteria during the infection process (Yuki et al., 2019). *In vitro* cells or bone

marrow-derived macrophages with deleted CYRI-B have an increased bacterial load compared to the WT cells (Yuki et al., 2019).

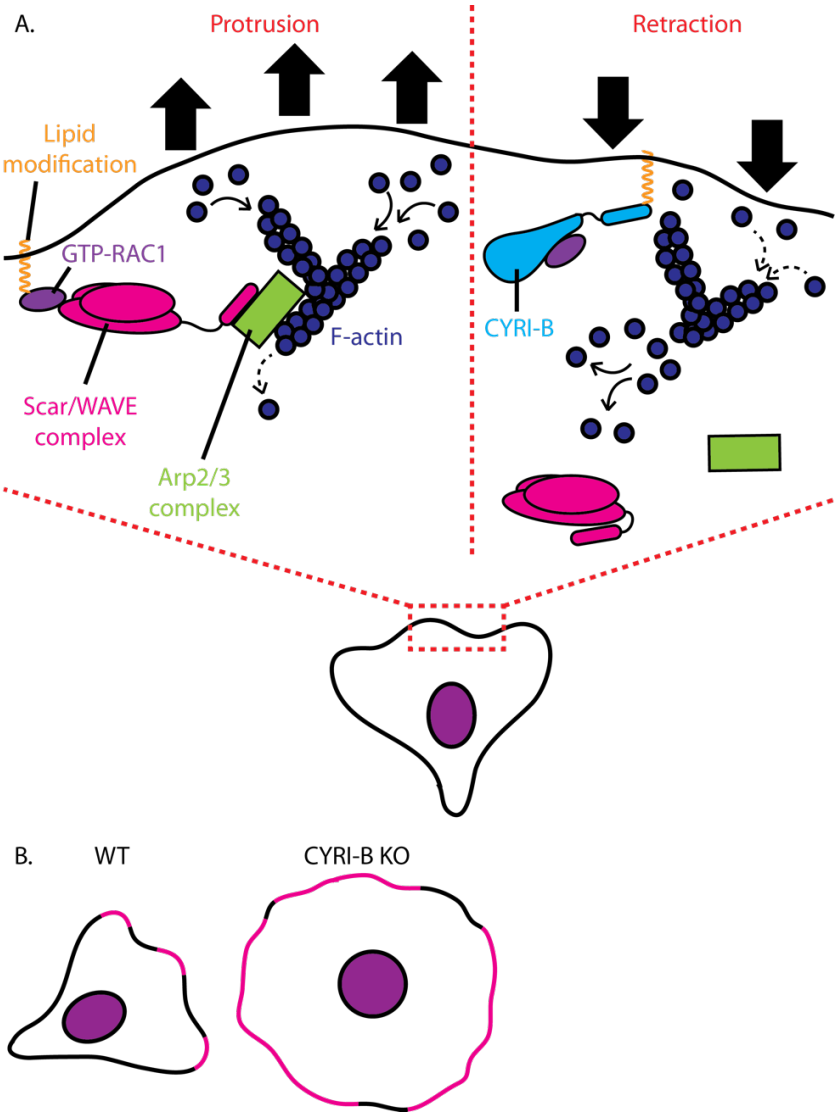

Figure 1.18 The current working model of CYRI-B

A. Actin RAC1 activates the Scar/WAVE complex, leads to the open of the VCA domain, which binds and activates the Arp2/3 complex. The activated Arp2/3 complex binds and promote branched actin polymerisation. The rate of polymerisation is higher than the rate of depolymerisation, hence leading to membrane protrusion. In the presence of CYRI-B, the protein competes with the Scar/WAVE complex for active RAC1 binding, sequester RAC1 and shutdown actin polymerisation signal, leading to membrane retraction.

B. The observed phenotype of wild-type (WT) and CYRI-B knockout (KO) COS-7 with the KO cells adopting a round friend-egg shaped with very little edge dynamic compared to WT cells. Magenta represents the localisation of the Scar/WAVE complex at the cell's leading edge.

1.3.1.2 CYRI-B and cancer

Accumulating evidence is also pointing towards the role of CYRI-B in cancer development. CBioportal analysis shows a startling result with CYRI-B gene being amplified in almost every cancer (Figure 1.19). It is however important to note that the position of the CYRI-B gene on chromosome 8 in human is relatively near the MYC proto-oncogene. The proximity between the two genes might explain for the strong amplification of the CYRI-B gene as a potential passenger amplification along with MYC. Nevertheless, a few recent studies have explored the functional relationship between CYRI-B and cancer. An analysis using the survival data from the Cancer Genome Atlas database shows a complicated relationship between the expression level of CYRI-B and the patient survival (Figure 1.20). In skin cutaneous melanoma, high level of CYRI-B seems to be protective and is associated with a better outcome. On the other hand, in liver hepatocellular carcinoma, high level of CYRI-B is associated with poorer outcome. One study looked at the function of CYRI-B in PDAC development and suggested that CYRI-B loss is correlated with increased lymph node invasion and is promoted by the extracellular matrix at the tumour site (Chattaragada et al., 2018).

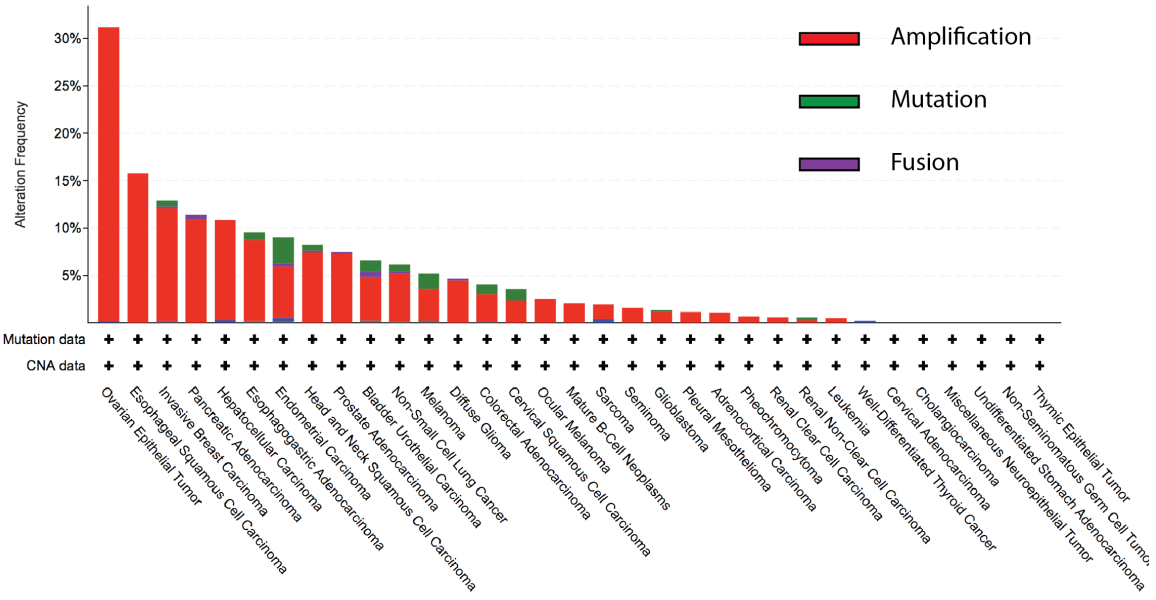

Figure 1.19 CBioportal analysis of showing CYRI-B gene is amplified in a wide range of different cancer

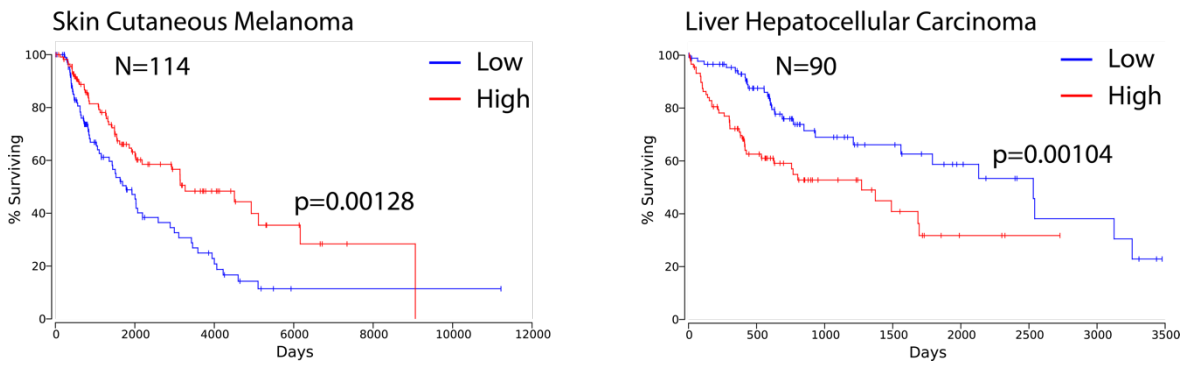

Figure 1.20 Kaplan-Meier survival analysis of CYRI-B in two different types of cancer using the Cancer Genome Atlas database.

In skin cutaneous melanoma, a high level of CYRI-B is associated with a better outcome. In liver hepatocellular carcinoma, high level of CYRI-B is associated with poorer outcome.

Data comparing the first and last 25 percentile of the analysed cohort. N is the number of patients in each category. P value is calculated using log rank test.

The author showed CYRI-B deletion led to fragmented mitochondria, and this was associated with an increased level of the mitochondria fission marker phosphor-DRP1 as well as reactive oxygen species (ROS) production (Fonseca et al., 2019). They showed a startling colocalization of endogenous CYRI-B with the mitochondria using an anti-CYRI-B antibody. However, in our hands, none of the commercial antibodies was able to specifically detect and localise endogenous CYRI-B in immunofluorescent analysis. The antibodies were non-specific enough to give us signal in CYRI-B knockout cells that have been confirmed using western blots. Hence this casts doubt on whether the observed mitochondrial localisation of CYRI-B in this study a product of fluorescent bleed-through or dual excitation from the MitoTracker being used. However, in a constitutively KRAS background, silencing CYRI-B led to an increased invasiveness of HPDE cells, an effect that was consistently observed in many of our cell lines. This suggests that the effect of CYRI-B on the migration of cancer cells is likely to be true and consistent, and that CYRI-B might potentially act as a tumour suppressor (Chattaragada et al., 2018). A similar mode of action was found in liver and colorectal cancer where CYRI-B was found to be a transcriptional target of the Zinc finger RNA binding protein (ZFR). Knocking down ZFR in primary colonic epithelial cells (hCECs) leads to a significant decrease in the RNA level of CYRI-B. Depletion of CYRI-B again led to an increase in cell proliferation in both colorectal and liver cancer cell lines,

adding another layer of support for the tumour suppressive function of the protein. However, in gallbladder carcinoma (GBC), CYRI-B was a downstream effector of the protease TASP1 and was suggested to promote proliferation through activation of the PI3K-Akt pathway (Zhang et al., 2020). In gastric cancer and oral squamous cell carcinoma (OSCC), CYRI-B was also proposed to be a diagnostic marker (Kawahara et al., 2016, Zheng et al., 2019). The discrepancy between these data could be explained by the type of cancer being examined, but we also cannot rule out the effects of the 21 or so (according to the Human Protein Atlas) splice variants of CYRI-B present in the cells. Overall, CYRI-B is a widely expressed protein that acts to interfere with the RAC1-Scar/WAVE signalling axis with a potential role in cancer development.

1.3.2 CYRI-A

1.3.2.1 An introduction to CYRI-A

Out of the two paralogs of the CYRI family, CYRI-A is a much lesser-known member. Comparing the protein sequence between CYRI-A and CYRI-B shows a shared 80% sequence identity. The protein is also predicted to have a similar domain structure to CYRI-B with an N-terminal α-helix connected to the DUF1394 domain through a flexible linker. We will discuss this in more details in chapter 3. According to the Human Protein Atlas, CYRI-A is expressed in various tissues, with the strongest RNA expression in the brain, endocrine and blood tissues and its protein level seems to also be abundant. This, however, should be taken with caution since the protein levels were detected using immunohistology and to our knowledge, the best anti-CYRI-A antibody we have only worked on western blotting. CYRI-A is also expressed in a number of different cells of the immune system. However, unlike the more evenly distributed expression of CYRI-B, CYRI-A expression is more distinctive with the highest level concentrated in the classical and non-classical monocytes, NK cells and naïve B-cells (Figure 1.21). This hints to the potential functions of the CYRI protein family in the immune system and in particular, perhaps a specific requirement of CYRI-A in a subset of immune cells.

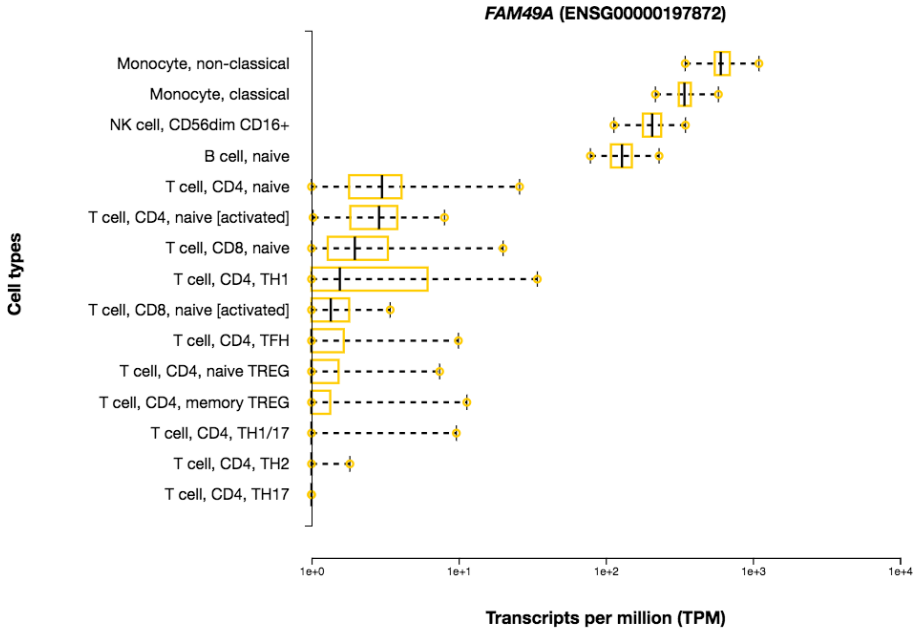

Figure 1.21 The immune expression profile of CYRI-A in transcripts per million (TPM)

CYRI-A is the most highly expressed in the classical and non-classical monocyte, NK cells and naïve B cells.

One report using deep RNA sequencing showed the presence of a long non-coding RNA located between the CYRI-A and MYCN locus and is regulated by the oncogene TAL1 in T-cell acute lymphoblastic leukaemia (Ngoc et al., 2018). It is interesting to note that many of these cells are phagocytic, whose functions are tightly connected to the actin cytoskeleton.

A few recent reports using genome-wide association study (GWAS) have reproducibly associated CYRI-A locus to non-syndromic cleft-lip across people of different ethnicities (Chen et al., 2018, Leslie et al., 2016, Azevedo et al., 2020). Interestingly, another protein RHPN2, an RHOA-binding protein involved in regulating stress fibre organisation, is also found to be significantly associated (Peck et al., 2002). This might suggest a connection between CYRI-A and cell migration. The most detailed study to date on the function of CYRI-A was done in zebrafish (Li et al., 2016b). The authors proposed CYRI-A to be a negative regulator of the tumour suppressor PTEN to regulate T-cell lymphopoiesis. The study established the importance of PTEN in thymus development.

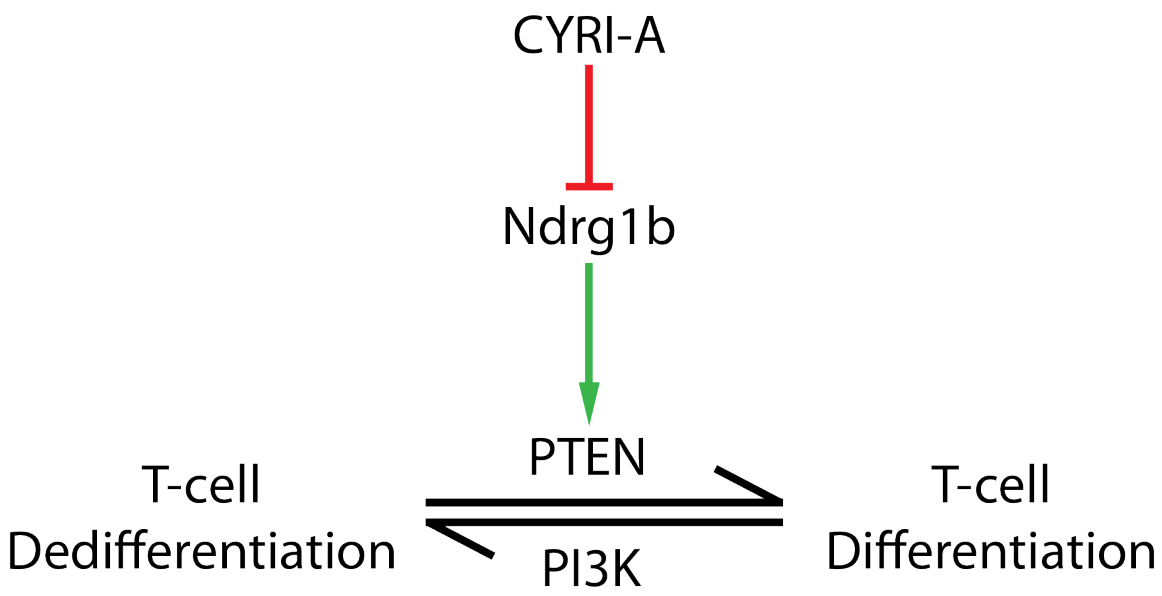

Figure 1.22 The proposed relationship between CYRI-A, Ndrg1b and PTEN in T-cell differentiation regulation

PTEN promotes T-cell differentiation. Ndrg1b activates PTEN while CYRI-A inhibits it potentially via protein-protein interaction.

Deletion of both PTEN a and b genes as well as using PTEN inhibitors SF1670 or VO-OHpic leads to a significant decrease in the size of the thymus. Overexpression of the protein Ndrg1b rescues this phenotype. When overexpressing CYRI-A by microinjection at 1-cell stage embryo, the differentiation of the T-cells was significantly affected and mimicked that of a PTEN loss phenotype. However, this effect of CYRI-A overexpression is reversed by Ndrg1b. The author suggests a potential physical interaction between CYRI-A and Ndrg1b, however, this was not shown (Figure 1.22). It is also worth noting that at the time of this study, the role of CYRI-A on RAC1 was unknown, thus it is entirely possible that the effect on T-cell differentiation could also be via RAC1 modulation.

1.3.2.2 CYRI-A and cancer

The association of CYRI-A with cancer development has not been established. CBioportal analysis shows the CYRI-A gene is mutated in many different cancers, albeit being more diverse compared to CYRI-B. CYRI-A gene alterations can either contain point mutations, gene amplification or deletion.

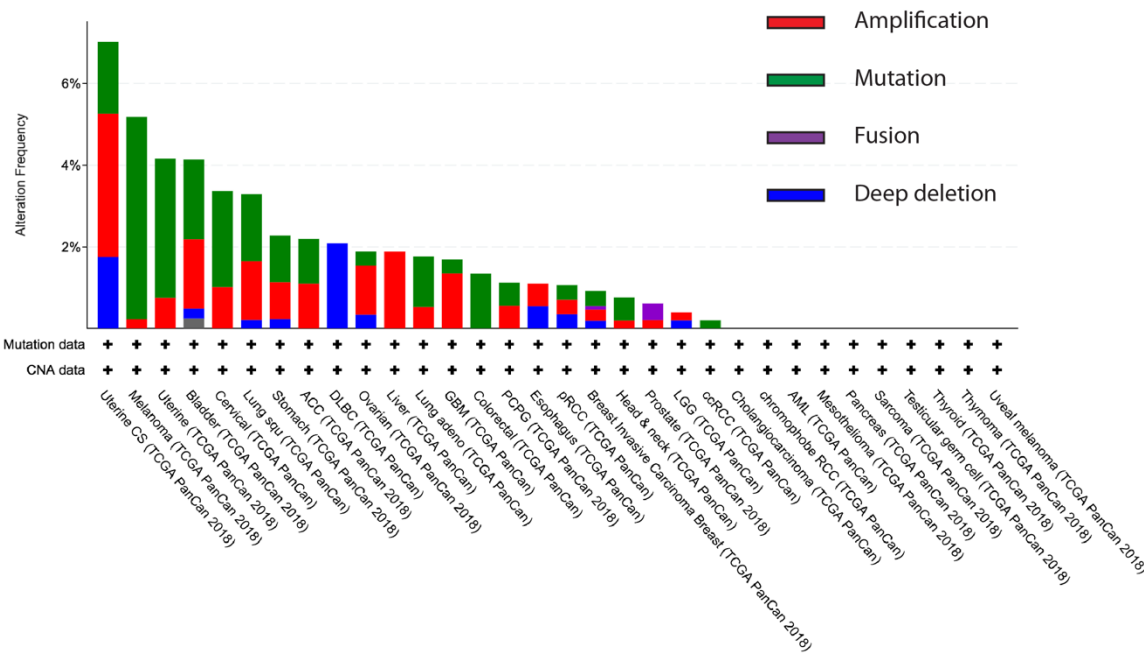

Figure 1.23 The mutation landscape of CYRI-A across multiple cancers

CYRI-A is mutated in a wide range of cancer including point mutations, gene amplification, deep deletion and some fusion.

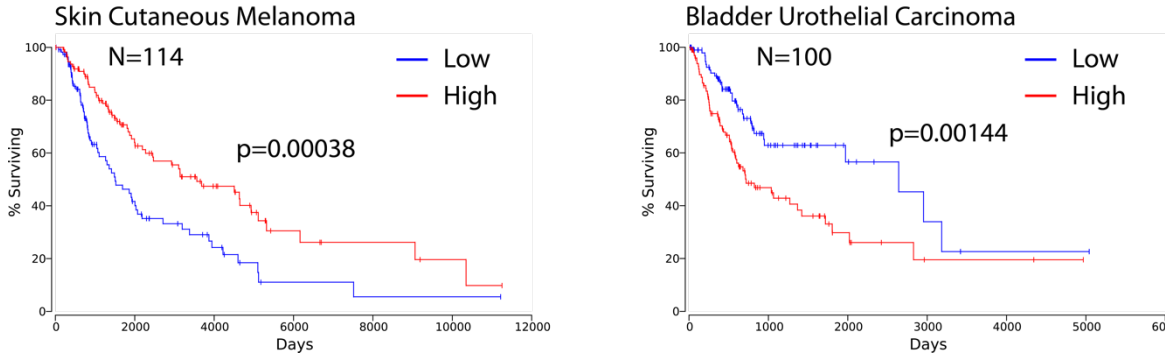

Figure 1.24 Kaplan-Meier survival analysis of CYRI-A in two different types of cancer using the Cancer Genome Atlas database.

High level of CYRI-A correlates with better prognosis in skin cutaneous melanoma while correlates with poorer prognosis in bladder urothelial carcinoma.

Data comparing the first and last 25 percentile of the analysed cohort. N is the number of patients in each category. P value is calculated using log-rank test.

Whether these are passenger or driver mutations is unknown (Figure 1.23). An analysis from the Cancer Genome Atlas database reveals a complicated relationship of CYRI-A with cancer. Similar to CYRI-B, in some cancer such as skin cutaneous melanoma, high level of CYRI-A expression seems to correlate with better prognosis, while in other cancer such as bladder urothelial carcinoma, high CYRI-A correlates with poor prognosis (Figure 1.24). Nevertheless, the very basic biology of CYRI-A has also never been explored. It is unknown whether CYRI-A could interact with active RAC1, whether there are any differences between the two isoforms or what is the relationship between CYRI-A and CYRI-B *in cellulo*. We will come back to some of these questions in more details with in-depth biochemical and cellular analysis in later chapters.

1.4 Integrins

Integrins are some of the most conserved proteins in eukaryotes. They play important functions in various biological processes, from development to pathological conditions such as cancer. As the name suggests, integrins integrate signals from both sides of the membrane. They act as bidirectional transmitters and can be activated by both cytoplasmic signals or "inside-out" signalling and extracellular signals or "outside-in" signalling. The functions of integrins are determined by their structure, their interactions with other effectors and their trafficking inside cells. Due to the vast amount of literature on many aspects of integrin biology, in this segment, we will only focus on describing the general biology of integrins, how they are regulated, how they interact with some common effectors and how their trafficking inside cells affects cancer development.

1.4.1 A general biology of integrins and their signalling

1.4.1.1 Structural overview of integrins

The human integrin proteome contains 18 different α subunits and 8 different β subunits, which through different non-covalent combinations generate a total of 24 heterodimeric pairs of integrins. Integrins belong to the single-span type I transmembrane protein. Their N-terminus (~1000 amino acids) points towards the extracellular space and their C-terminus (~50 amino acids) points to the cytoplasm. A single α-helix passing through the plasma membrane acting as the transmembrane domain (TMD) (Figure 1.25). The extracellular domain or the ectodomain is divided into two regions: the head and the leg region. In a typical α subunit, the head region contains a β propeller and a thigh domain while the leg region contains two Calf domains. Connecting between the Calf 1 and the thigh domain is the knee or the genu, which acts as a door hinge and is flexible enough to allow swinging motion of the integrins. Nine out of 18 α subunits also contain an extra α-I domain which is inserted within the β propeller (not shown). The head region of a β subunit's ectodomain contains a large βA domain (also known as the β-I domain) which is inserted into the hybrid domain and is inserted into the PSI domain. The leg region contains 4 epidermal growth factor (EGF) domain and a β-tail domain. The multidomain structure of the β subunit allows it to be more

flexible than its α counterpart and is important for the function of integrins. In integrins lacking the additional α-I domain, the β propeller domain of the α-subunit and the βA domain of the β subunit come together and form a ligand-binding site. Depending on the different combination of integrin subunits that this binding site can have different specificity for different substrates. The lower part of the β-propeller contains multiple binding sites for Ca2+ ions, which are important for the activity of integrins.

Integrins can change their conformation and this is strongly tied to their functions to transmit signals across the plasma membrane. Even though there are still many debates and more structural studies to be done, for simplicity, we will only discuss the consensus model that is generally believed to explain for integrin activation. The stages of activation of integrins can generally correspond to three states: the bent state, the intermediate state and the fully extended state (Figure 1.26). In the bent conformation, the head region of integrins is thought to interact with the β tail domain and the membrane-proximal region, while the two TMDs of each integrin subunit adopt a coiled-coil conformation (Gottschalk, 2005). In this state, integrins do not have a high affinity for their ligands. However, bent integrins have been observed with ligands before, which suggests that integrins are not necessarily inactive in this state (Takagi et al., 2001). It is thought that in fully inactive integrins, the key factor is the close proximity of the intracellular domains of the two subunits. Disruption of this interaction leads to constitutive activation of the integrins (Han et al., 2006). In the second state, integrins adopt an intermediate conformation with the head region extending away from the tail region. Integrins still remained low affinity to ligands. The fully extended conformation is generally considered to be the active state of integrins. In this state, the ligand-binding site is exposed coupled with the accumulation of focal adhesion complex in the cytoplasmic side. The TMDs are separated by the pulling force exerted by the binding of cytoplasmic proteins to the C-terminus. The movement of the hybrid domain is thought to be essential for forming the ligand-binding site. As the hybrid domain swings out, this creates an internal restructuring within the βA domain and thus forming a ligand-binding site (Xiao et al., 2004).

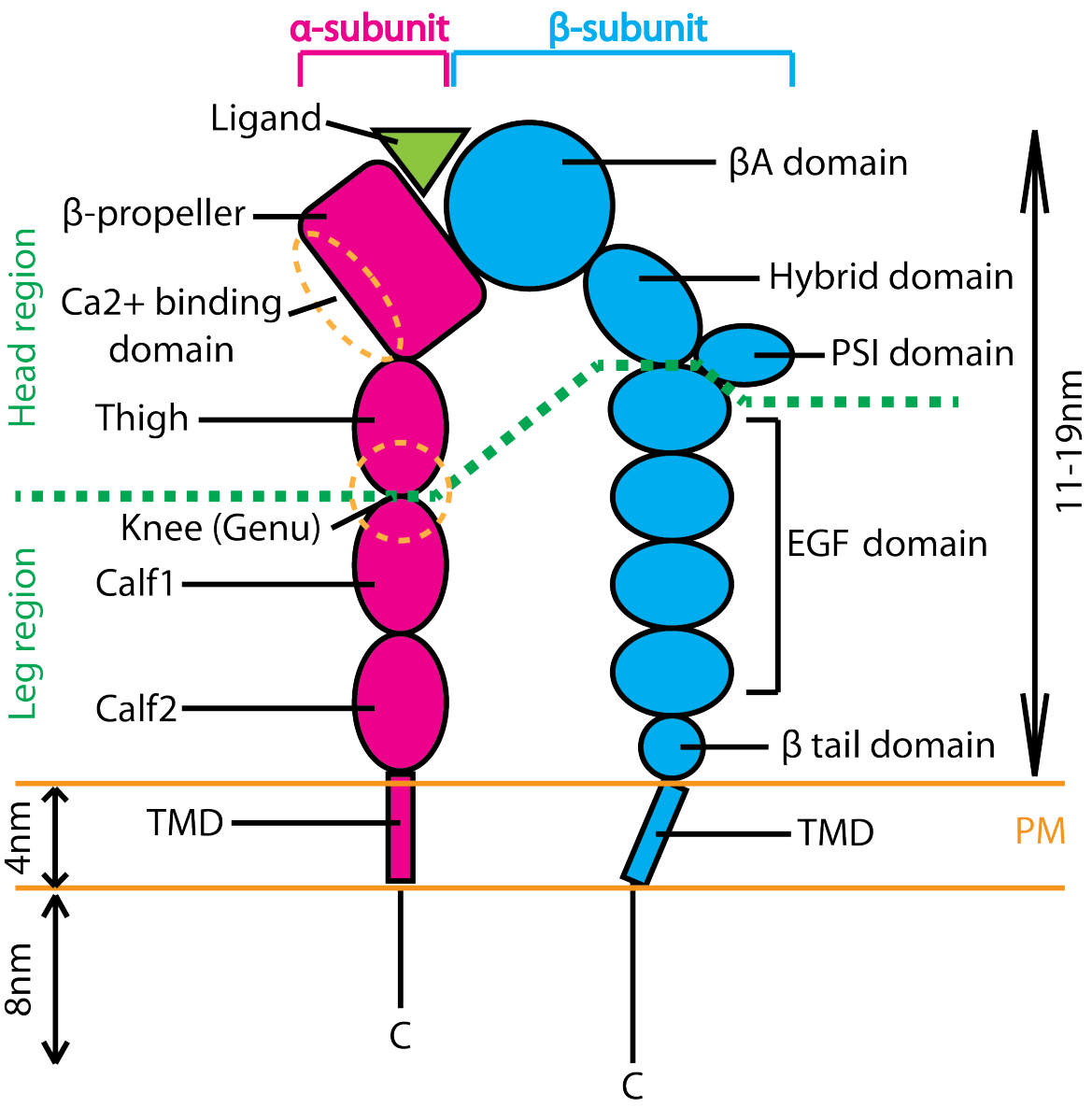

Figure 1.25 The schematic representation of a heterodimeric αβ integrin

A typical structure of an integrin heterodimer. The extracellular part can have a distance to the plasma membrane ranging from 11nm in a bent state to 19nm in an extended state. Some alpha subunit has an extra α-I domain linked to the β-propeller (not shown), which adds an extra 4nm to the total length of the dimer.

TMD = Transmembrane domain

PM = Plasma membrane

PSI domain = Plexin, semaphorin and integrin domain

Adapted and modified from (Askari et al., 2009).

However, the degree of extension of integrins is not necessarily correlated with the degree of activation. In fact, both activation by Mn^{2+} ions or chemokine still produce fully activated integrins despite not fully extended (Askari et al., 2009).

1.4.1.2 The two modes of signal transduction by integrins

As mentioned earlier, integrins transmit "inside-out" and "outside-in" signals. Talin binding to the cytoplasmic tail of the β subunit plays an essential role in the inside-out integrin activation. Talin contains a globular N-terminal FERM domain and a long C terminal domain. In its inactive state, the C terminal domain folds on to the FERM domain, keeping the protein in a closed state (Wegener et al., 2007). PI(4,5)P2 disrupts this interaction through electrostatic interactions thereby activates talin (Saltel et al., 2009, Wang, 2012). The now opened talin competes with the α cytoplasmic tail for the interaction with the membrane-proximal region of the β cytoplasmic tail via the FERM domain (Anthis et al., 2009). Talin and PI(4,5)P2 recruit many other cytoplasmic proteins including kindlin, vinculin, FAK, many of which can directly interact with actin and the actin polymerisation machinery such as Arp2/3 (Gilmore and Burridge, 1996, Bass et al., 1999, Johnson and Craig, 1995). This directly links integrins to the actin cytoskeleton. The retrograde flow of actin polymerisation exerts a pulling force leading to the separation of the TMDs and subsequently integrin activation (Vicente-Manzanares et al., 2009).

The outside-in signalling is best studied in leukocytes and platelets since these cells are often activated upon contact with the blood vessel walls or fibrous proteins in the bloodstream, respectively. It was suggested that the binding of a ligand to integrins triggers a major structural rearrangement of the α-helices within the βA domain which is transmitted into the cytoplasm through the TMD (Gahmberg et al., 2009). The binding to ligands is also regulated by the state of cation binding of the βA domain, with Ca^{2+} ions locks the integrins in the bent state while Mn^{2+} promotes integrin extension (Mehrbod et al., 2013). Ultimately, conformational changes lead to the activation of Src family kinases (SFKs) and FAK, which can activate many downstream effectors (Arias-Salgado et al., 2003). The outside-in pathway can lead to clustering of integrins through binding to multivalent ligands.

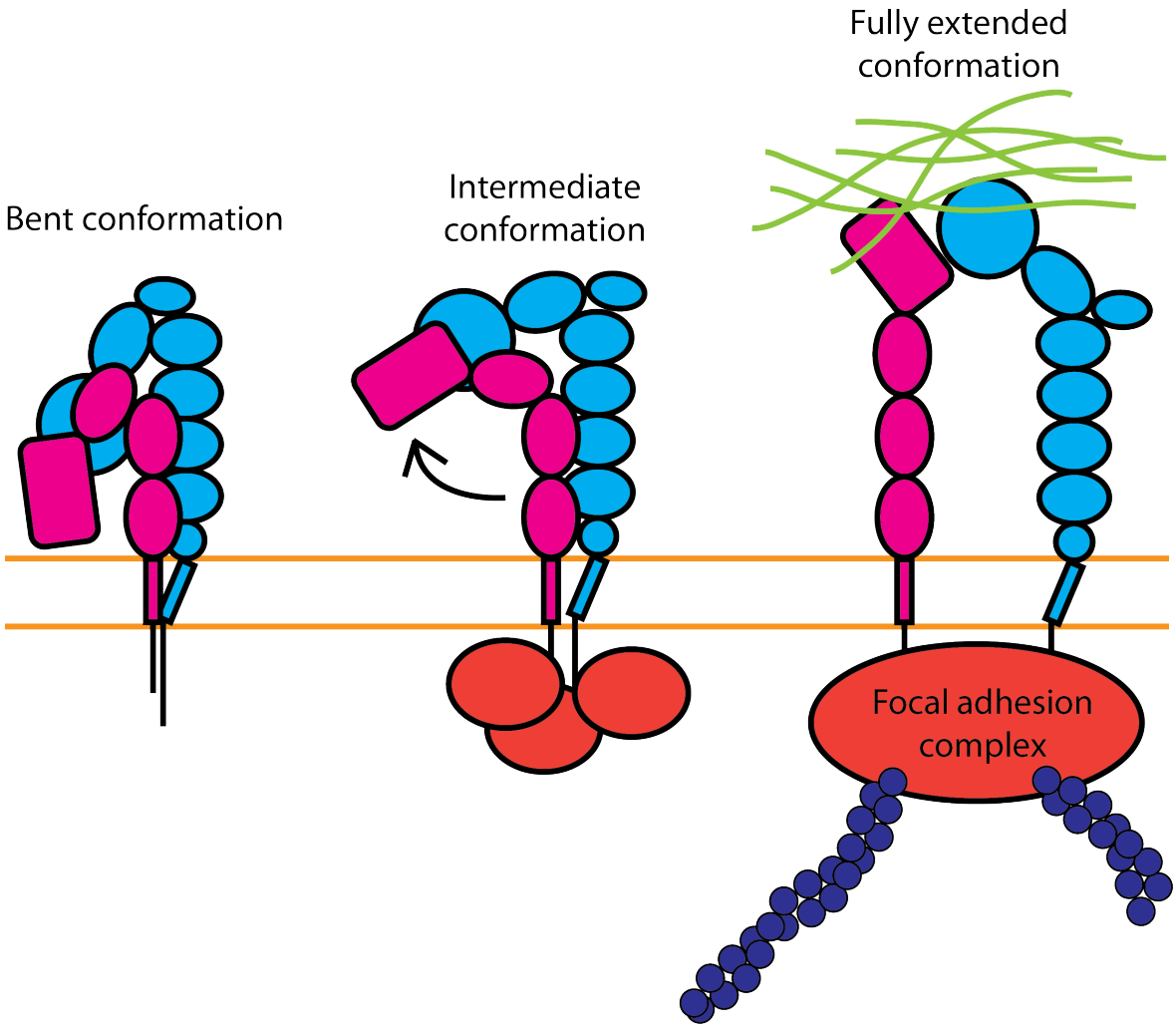

Figure 1.26 The three-conformation model for integrin activation

The bent conformation: The β tail domain makes contacts with the βA and β propeller, keeping the integrin in the folded conformation. The genu region allows for flexibility.

The intermediate conformation: Cytoplasmic proteins are starting to be recruited to the C-terminus of integrins, force the integrins into a slightly open conformation.

The fully extended conformation: The focal complex is fully assembled and forces the integrins into the fully opened state. Ligand binding at the head domain strengthens the open conformation.

This leads to clustering of downstream effectors such as Src kinase, allowing them to autophosphorylate each other and propagate the signal (Arias-Salgado et al., 2003, Law et al., 1999, Miyamoto et al., 1995). The two signalling pathways, even though are conceptually distinct, can influence each other. Binding to ligands can trigger and stabilise the recruitment of intracellular proteins such as Talin, vinculin and kindlin and vice versa, binding of Talin and other intracellular molecules can trigger ligand interaction.

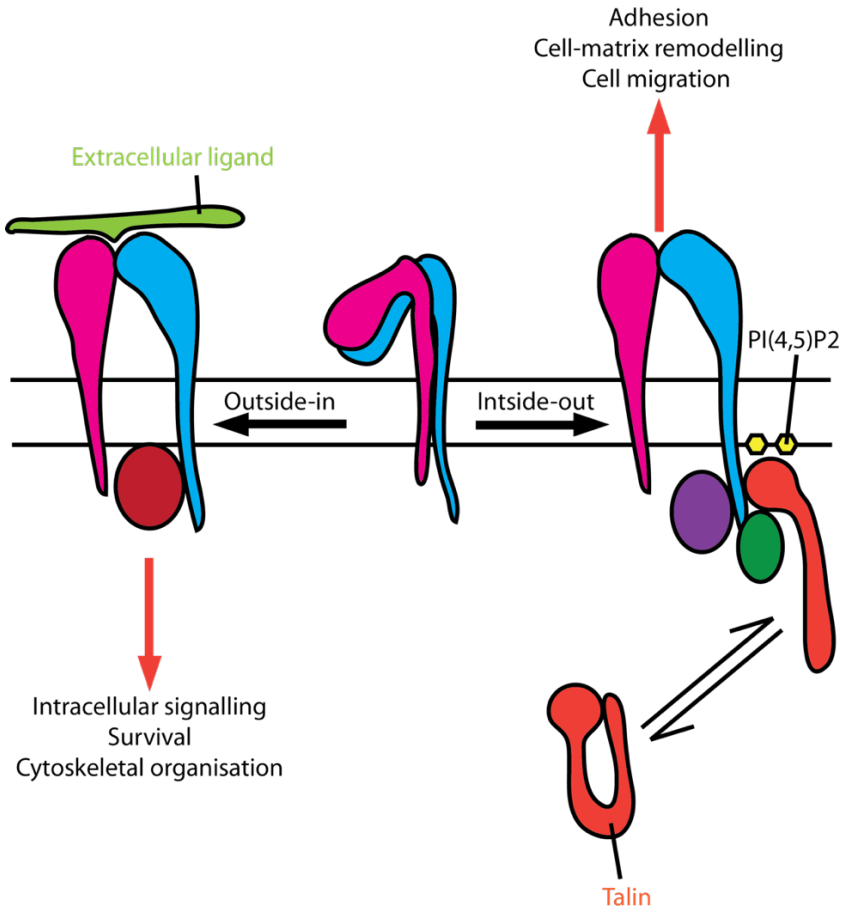

Figure 1.27 Schematic representation of the bidirectional nature of integrins signalling

Inside-out signalling originates from the binding of talin, which is activated by PI(4,5)P2, to the β cytoplasmic tail, which leads to the recruitment of various other focal adhesion associated proteins such as Kindlin, vinculin etc. This focal adhesion complex links integrins to the actin cytoskeleton and integrin activation, which regulates cell migration, adhesion and matrix remodelling.

Outside-in signalling occurs due to the binding of extracellular ligands which triggers conformational changes that propagate into the cytoplasm through the TMD. This recruits various proteins and downstream signalling involved in survival, actin remodelling.

1.4.2 Integrin signalling during cancer migration and progression

Integrins play important functions in regulating cell migration. These bidirectional receptors are part of focal complexes connecting the cytoskeleton to the extracellular matrix. As the actin filaments polymerise, they produce a protruding force pushing the plasma membrane forwards. In the absence of focal adhesions, the tension of the plasma membrane creates an opposing force leading to recoil and retrograde flow of actin. In the presence of focal adhesions, however, this backward flow is reduced, allowing the cell to create traction force pushing forwards (Huttenlocher and Horwitz, 2011). However, integrins are much more than just migration control for the cells. They are involved in various roles and affect a plethora of signalling pathways. Cancer cells have evolved to make use of these pathways to assist their development. The effects of integrins can either derive directly from the integrins themselves or in conjunction with other membrane receptors such as receptor tyrosine kinases (RTKs) or G-protein coupled receptors (GPCRs).

The major downstream effectors of integrins are FAK and SFKs. Ligand binding to integrins trigger the recruitment of FAK molecules leading to the autophosphorylation process at the tyrosine 397. This creates a binding site for the SH3 domain of SFKs such as Src, which in turns maximises the activation of FAK. The Src-FAK complex serves as a central hub for the outside-in signalling cascade and unsurprisingly is utilised by cancer. The Src-FAK complex recruits and phosphorylates p130Cas, which then recruits and activates DOCK180-ELMO complex (Chodniewicz and Klemke, 2004). This complex acts as a RAC1 GEF and promotes cell spreading and migration (Li et al., 2013). The Src-FAK also phosphorylates and activates paxillin, which recruits and activates GIT2 and β-PIX and subsequently RAC1 activation (Lamorte et al., 2003). β-PIX along with its binding partner Scrib are found at the leading edge of migrating breast cancer cells and regulate invadopodia formation (Nola et al., 2008, Md Hashim et al., 2013). Phosphorylated FAK provides docking sites for PI3K to produce PIP3. This activates PKB/ATK and confers apoptosis resistance by promoting 14-3-3-BAD association (Datta et al., 2000). AKT also suppresses the transcriptional activity of many pro-apoptotic proteins of FOXO while increases YAP/TAZ pro-survival activity (Tzivion et al., 2011, Hansen et al., 2015). Internalised integrins activate

FAK in a RAB21-dependent manner and promote anoikis resistant (Alanko et al., 2015).

Overexpression of many integrins also contribute to cancer progression. Increased expression of the activated integrin αvβ3 in MDA-MB-435 human breast cancer leads the concomitant expression of MMP9, which leads to the increased migration towards vitronectin and fibrinogen (Rolli et al., 2003). In prostate cancer, specific upregulation of integrin αvβ6 increased MMP2 expression and bone osteolysis (Dutta et al., 2014). Comparing the surface expression of integrin α5β1 in MDA-MB-231 shows that cells with higher level of this integrin generate seven times stronger contractile force to the surrounding matrix with an increased adhesion and invasion in 3D matrix. This effect is reduced when the α5 subunit was depleted (Mierke et al., 2011). High level of α5 also associates with increased haptotaxis of breast cancer toward fibronectin via the pro-metastatic protein MenaINV (Oudin et al., 2016). Recent advances also show the effects of integrin beyond the cancer cells themselves, with tumour can secrete exosomes containing different types of integrins to assist the formation of the metastatic niche. Integrins can be transferred to normal epithelial cells or cancer-associated fibroblasts to promote their transformation via integrin recycling (Novo et al., 2018, Hoshino et al., 2015, Singh et al., 2016). These pathways are summarised in Figure 1.28.

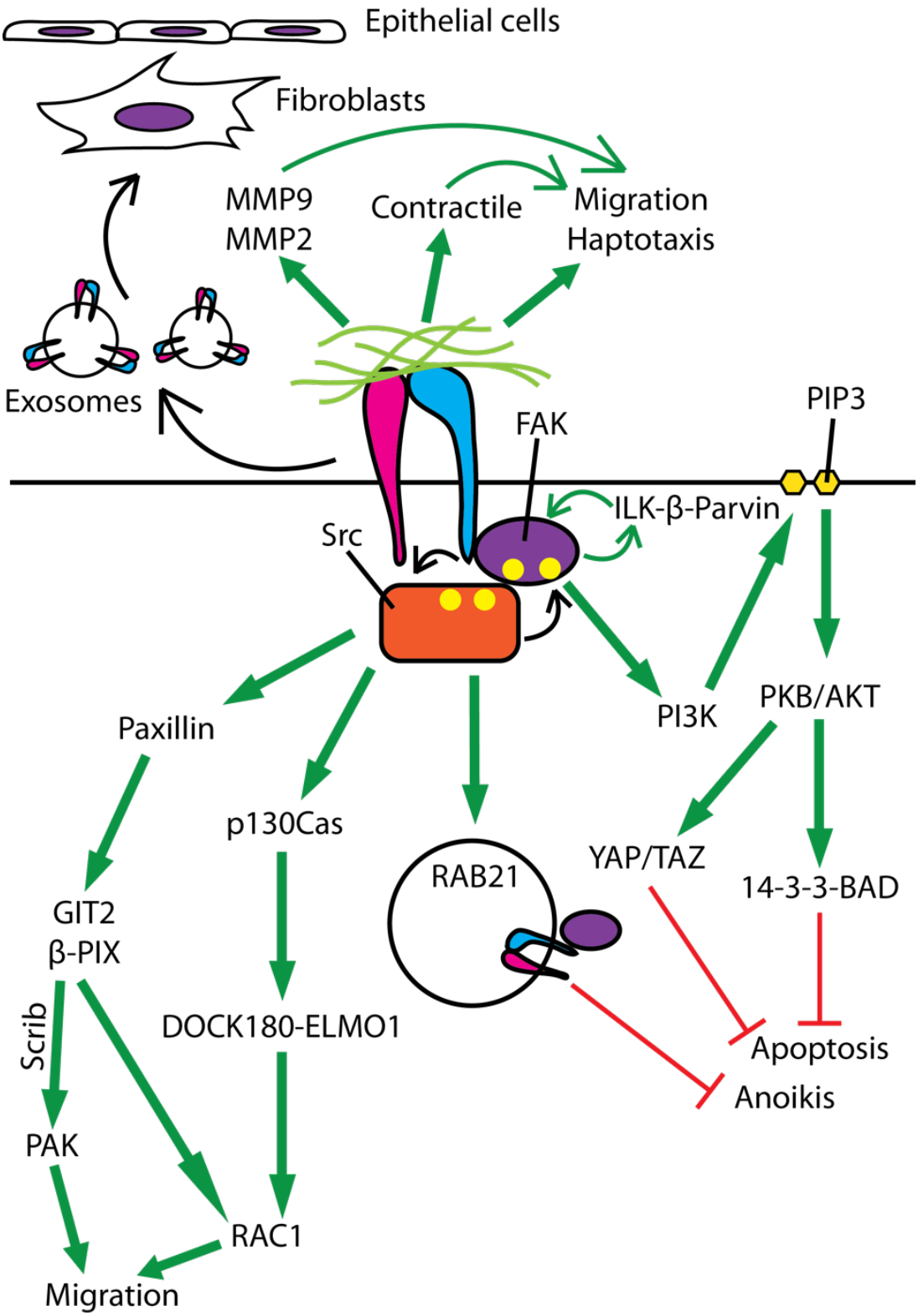

Figure 1.28 The direct involvement of integrin signalling in contributing to cancer progression and survival

Integrins participate in many different pathways that can affect cell migration, cell adhesion, matrix remodelling as well as cell proliferation and survival. Green arrows = activation, red blunt arrows = inhibition.

1.4.3 Integrins coupled with RTKs in cancer migration and progression

Another mode for integrins to exert their effects is to act in conjunction with various membrane receptors such as receptor tyrosine kinases (RTKs). RTKs are transmembrane proteins containing an extracellular ligand binding domain and an intracellular tyrosine kinase domain that can phosphorylate and activate downstream signals. The MAPK pathway sits the centre of cancer signalling by regulating cellular proliferation. Integrins affect this pathway through cooperating with EGF receptor (EGFR). Binding of EGF to EGFR triggers the activity of the kinase domain, which phosphorylates and activates integrin-associated SFKs such as Fyn and YES (Cooper and Giancotti, 2019). SFKs phosphorylate and activate the scaffold protein SHC. This creates binding sites for GRB2 and SOS that together acts as a GEF for RAS (Harmer and DeFranco, 1997, Barberis et al., 2000, Niu et al., 2003). Activated RAS triggers the classical MAPK signalling cascade through a series of phosphorylation of RAF, MEK and ERK1/2. Phosphorylated ERK translocates into the nucleus and activates various transcription factors controlling cell proliferation and survival (Wary et al., 1996, Guo and Giancotti, 2004). A recent discovery shows that the phosphatase protein SHIP2 can be phosphorylated and activated by FGFRs at the focal adhesions. Phosphorylated SHIP2 recruits SFKs to activate FRS2 and GAB1, which lead to the activation of PI3K-AKT signalling and the MAPK cascade (Fafilek et al., 2018, Wang et al., 2015a, Kiyatkin et al., 2006).

Integrins can also directly form complexes with RTKs such as between β1 integrin and c-MET (also known as Hepatocyte Growth Factor Receptor-HGFR). Upon binding to its ligand, c-MET triggers the activation of β1 integrin subunit, leading to the co-internalisation of both proteins into an autophagy-related endomembranes (AREs). Here the two receptors trigger the SHC-ERK1/2 pathway. This has been implicated in mediating anchorage-independent growth of tumour cells both *in vitro* and lung colonisation *in vivo* (Barrow-McGee et al., 2016). Several integrins such as αvβ6 or α8β1 have been shown to also trigger the release of TGF-β from its Latency associated peptide (LAP) (Thomas et al., 2002, Lu et al., 2002). TGF-β acts through its specific TGFβ receptor(s) to promote metastasis (Xie et al., 2018). Many cancers make use of this integrin-dependent TGF-β

activation as an autocrine (Daroqui et al., 2012, Larocca et al., 2013) or paracrine signalling pathway (Li et al., 2008, Scheel et al., 2011).

Joint cross-talks between RTKs and integrins also play important roles in driving EMT in epithelial cells. Activated Src drives the internalisation of the E-cadherin-β-catenin complex via an E3 ubiquitin ligase Hakai (Fujita et al., 2002, Avizienyte et al., 2002). In several cancers, phosphorylated β-catenin translocates into the nucleus and activates the TCF/LEF transcriptional complex, leading to the downregulation of the E-cadherin gene expression. Inhibition of Src using dasatinib restores membrane E-cadherin (Dosch et al., 2019, Owens et al., 2000). Another well-studied example of integrin-receptor crosstalk is the cooperation between integrins and the uPA receptor (uPAR). uPAR does not have a cytoplasmic domain and uses integrins to transmit the signal inside cells. Co-immunoprecipitation experiments show uPAR forms physical interactions with the β1 subunit of integrin heterodimers (Aguirre Ghiso et al., 1999). The binding of uPAR enhances fibronectin and laminin binding to α5β1 or α3β1, respectively, which in turns leads to increased MAPK signalling and cell proliferation (Aguirre Ghiso et al., 1999). This is enhanced in the presence of EGFR. Inhibiting uPAR or EGFR leads to reduced proliferation or a dormant state of carcinoma tumour cells (Wei et al., 2001, Liu et al., 2002). uPAR can act together with the β3 integrin to enhance the downstream signal from DOCK180-ELMO1 complex, leads to increased RAC1-mediated cell migration (Kjoller and Hall, 2001, Lester et al., 2007, Vial et al., 2003, Smith and Marshall, 2010). These interconnected pathways are summarised in Figure 1.29.

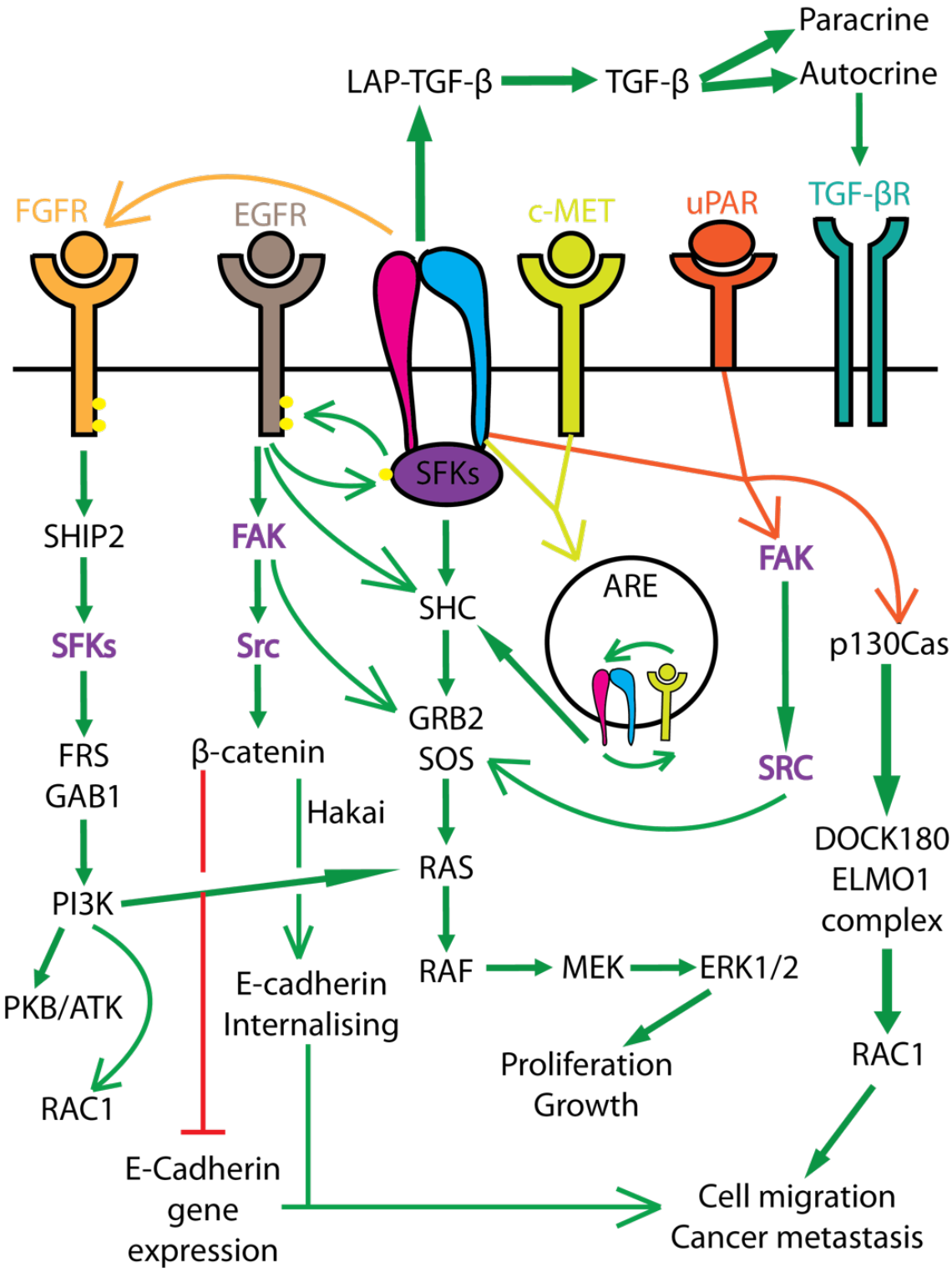

Figure 1.29 Integrin-receptor crosstalk signalling pathways

The interconnected entangled network of signalling between integrins and membrane receptors regulate many aspects of cancer cell biology including cell proliferation, migration and metastasis and dormancy. Green arrows = activation, red blunt arrow = inhibition, yellow circles = phosphorylation.

1.4.4 Integrin trafficking and its effects in cancer

The effects of integrins on cancer progression are not only mediated by the direct intracellular signalling cascades described in the previous sections. A large portion of these effects is attributed through the intracellular trafficking of integrins. The half-life of integrin recycling is less than 15min suggesting that these molecules are constantly trafficked within the cells (Bridgewater et al., 2012). Integrins can be internalised through various different pathways but can be broadly classified into clathrin-dependent and -independent pathways. Once internalised, they can either be directed towards the endolysosomal system for degradation or being recycled back to the plasma membrane through a short-loop RAB4- or long-loop RAB11-dependent recycling pathways.

1.4.4.1 Clathrin-dependent endocytosis of integrins

The most studied pathway for internalising integrins is clathrin-dependent endocytosis (CDE). The core components of this pathway include the BAR domain-containing proteins FCHO-1/2, the adaptor protein complex AP2 responsible for inducing membrane curvature, the scaffold protein such as the epidermal growth factor receptor substrate 15 (EPS15) responsible for stabilising the whole protein complex, and the triskelion clathrin responsible for vesicle formation and maturation. Briefly, the AP-2 complex along with other accessory proteins scan the membrane for PI(4,5)P2 as the starting site for pit formation. Once detected, FCHO-1/2-EPS15 complex is recruited to initiate the membrane bending process while stabilising other protein components. AP2 complex recruits clathrins to assemble into a clathrin cage. Along with the constriction of dynamin at the neck and the pushing force of actin polymerisation, the vesicles are driven inside the cells along with its cargoes (Ritter et al., 2013, Kaksonen and Roux, 2018).

Specific integrins internalised through this process can be regulated by the recruitment of alternative adaptor proteins. An example is the internalisation of the β1 integrin by the scaffolding protein DAB2. In AP2 deficient cells, β1 integrins can still be internalised suggesting the existence of an alternative protein. Deletion of DAB2 specifically affects β1 integrin trafficking but not the transferrin receptor. DAB2 interacts with EPS15 to mediate the internalisation of the β1-containing heterodimeric integrins (Teckchandani et al., 2012).

Another adaptor protein also interacts with the β1 integrins is NUMB, which is implicated in directed cell migration. It was shown that NUMB physically interacts with Par3, which is a partner of the atypical protein kinase C (aPKC). aPKC phosphorylates and prevents NUMB from binding to the cytoplasmic tail of β1 integrin. When the phosphorylation is removed, NUMB can participate in clathrin pit formation and integrin internalisation. Depletion of NUMB impairs this process and affects cell migration (Nishimura and Kaibuchi, 2007).

The α-subunit can also be subjected to specific internalisation signalling. The AP2 adaptor complex can directly interact with the Yxxϕ motif (x is any animo acid and ϕ is bulky hydrophobic amino acid) of a subset of α integrin subunits through its μ2 subunit (De Franceschi et al., 2016). The kinesin motor protein KIF15 is thought to mediate the recruitment of DAB2 to form clathrin pits to specifically internalise the α2 subunit (Eskova et al., 2014). These pathways are summarised in Figure 1.30.

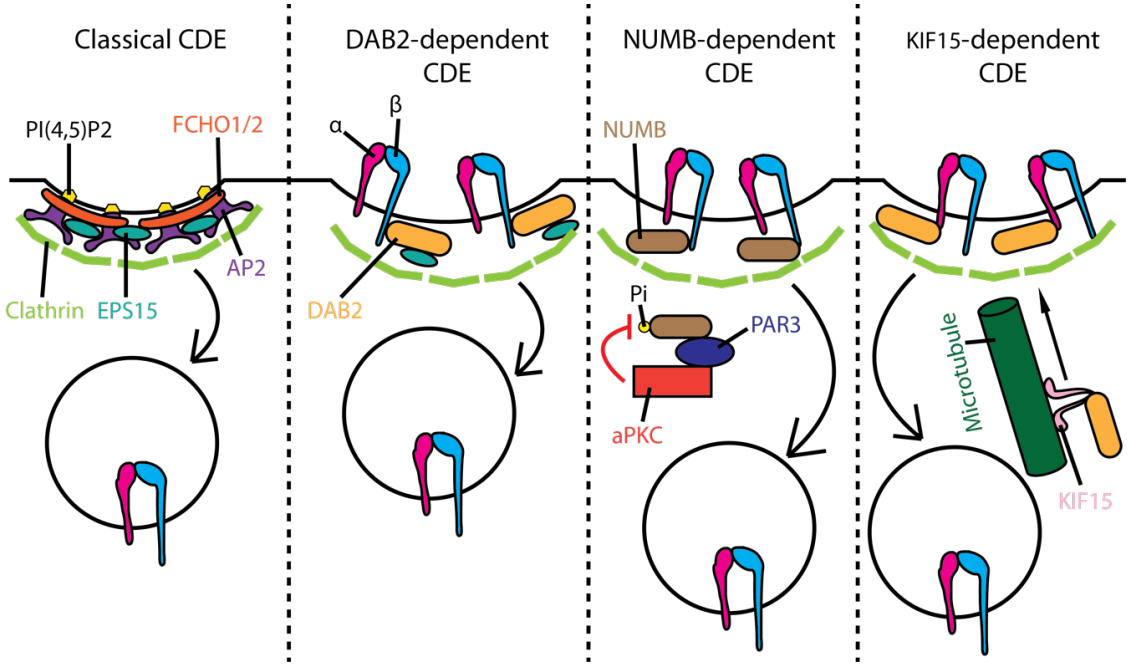

Figure 1.30 Clathrin-dependent endocytosis (CDE) of integrins

These pathways are all derived from the classical CDE with variations in certain specific adaptors to allow integrins to be selectively internalised. Other components are assumed to be present if not shown.

Pi = phosphorylation

1.4.4.2 Clathrin-independent endocytosis of integrins

While the molecular components of CDE are well defined, recent advances are continuously adding more complexity and diversity to clathrin-independent endocytosis (CIE). Because of this, CIE is much less well-defined, and the mechanisms are a lot more varied. Here we defined any mechanism with no obvious involvement of clathrin to be CIE.

RN-Tre is a novel focal adhesion partner, which possesses a GAP activity and promotes GTP hydrolysis in RAB5A. RAB5A is a major endocytic protein, and its overexpression increases the rate of endosome formation and focal adhesion disassembly (Bucci et al., 1995, Mendoza et al., 2013). By suppressing the activity of RAB5A, RN-Tre inhibits the turnover of β1 integrins and increased its surface expression (Palamidessi et al., 2013).

Another type of CIE that has recently been shown to participate in integrin internalisation is caveolae. Characterised by specific subfractions of the plasma membrane containing high levels of specific lipids known as lipid rafts, caveolae formation is mainly driven by the oligomerisation of caveolin proteins, along with pacsins and other actin crosslinking proteins (Echarri and Del Pozo, 2015). The process of formation is regulated by the activity of PKCα (Smart et al., 1995). It was shown that caveolae can internalise integrins through both the α and β subunit. One report found PKCα, which can be activated by syndecan-4, can phosphorylate the formin FMNL2. This in turns interacts with the α integrin subunit to induce actin polymerisation-dependent membrane invagination and endocytosis (Keum et al., 2004, Wang et al., 2015b). On the other hand, caveolin-1 can directly bind to the β subunit and regulate the constitutive internalisation of these integrins (Shi and Sottile, 2008).

The ARF family has also been shown to regulate the flow of integrins in RAB25-expressing cells. Integrin α5β1 was transported from the sides of the cell to the region just underneath the nucleus by tensin. Here, ARF4 mediates the internalisation of these integrins in a Scar/WAVE-actin dependent manner towards the late endosome/lysosome compartment for degradation (Rainero et al., 2015).

However, the exact mechanism of how ARF4 affects the Scar/WAVE complex and RAC1 is not entirely clear.

It is interesting to note that not only receptor-mediated internalisation is involved in integrin endocytosis, bulk uptake such as macropinocytosis also plays a part. In the presence of PDGF, primary mouse fibroblasts form large circular dorsal ruffles enriched with the β3 integrin. These integrins are then endocytosed and follow the classical early to recycling endosome route before being redistributed to new focal adhesions (Gu et al., 2011). Presumably, ligand-bound PDGF receptors activate the PI3K-RAC1 pathway that leads to Scar/WAVE complex-mediated actin polymerisation and membrane ruffling, similar to what we discussed in Figure 1.11. However, there were no obvious specific adaptors present to localise these integrins. In general, the role of macropinocytosis in regulating membrane homeostasis and receptor trafficking is much less well understood. It was also shown before its role in internalising E-cadherin in epithelial cells (Bryant et al., 2007). Recent studies have implicated for the first time the role of macropinocytosis in recycling membrane from the cell rear end to the front to assist neural crest cell migration (Li et al., 2020). Nevertheless, what determines the specificity and how frequent these membrane proteins are internalised by macropinocytosis remains elusive. This sets an example of how cells can utilise virtually any internalisation pathway to monitor integrin and membrane protein trafficking and there are many questions still remain answered. These different pathways are summarised in Figure 1.31 below.

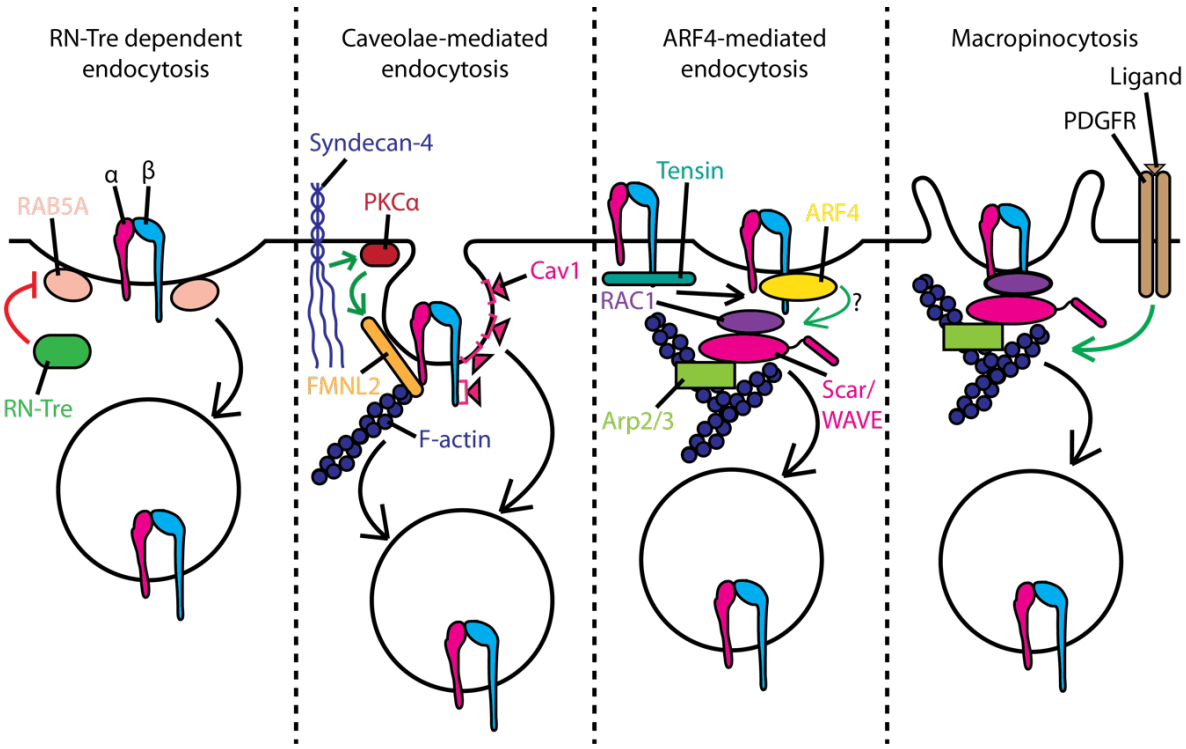

Figure 1.31 Clathrin-independent endocytosis (CIE) of integrins

Different CIE pathways are involved in internalising integrins, with much less defined molecular mechanisms.

Black arrow = proceeding to

Green arrow = activation

Red blunt arrow = inactivation

1.4.4.3 Integrin trafficking and cancer

These internalisation pathways combined with many recycling pathways contribute directly to the migration and invasion behaviour of cancer cells. The very basic functions of integrins to mediate the attachment of cells to the surrounding matrix can have a significant impact just base on where and when these integrins are transported to. In oral squamous cell carcinoma, endocytosis of the αvβ6 integrins is important for the invasion of these cells. The HS1-associated protein X-1 (HAX-1) was identified to be a binding partner of the β6 subunit and its depletion reduces αvβ6 internalisation and migration of these cancer cells (Ramsay et al., 2007). In ovarian cancer cells A-2780, the directed transport of integrin α5β1 from endosomes to the protrusive front by WASH-Arp2/3 complex is important for the invasion process. Depletion of WASH impairs

their invasion in 3D matrices (Zech et al., 2011). In the same cell line, recycling of the integrin α5β1 to the front of filopodial-like protrusions by Rab-coupling protein (RCP) coupled with actin polymerisation triggered through an FHOD3-dependent Arp2/3-independent process drives invasive migration in fibronectin-rich environments both *in vitro* and *in vivo* (Paul et al., 2015). Inhibiting αvβ3 using cRGDfV triggers this RCP-dependent α5β1 recycling pathway and enhances protrusion formation. This redistribution of α5β1 is coupled with the redistribution of EGFRs, which further enhances the actin dynamic and the Akt/PKB survival signalling in p53 mutant-expressing cells (Muller et al., 2009, Caswell et al., 2008). However, in fibroblasts, αvβ3 integrins are part of a short-loop RAB4-dependent recycling pathway that regulates persistent migration. Inhibition of this integrins promotes α5β1 recycling as expected, but this decreases the directionality of the cells by enhancing cofilin activity (White et al., 2007). The choice of which loop of recycling can be dictated by many signals, one of which is PKD. It was shown that PKD can phosphorylate Rabaptin-5, and this is sufficient to drive the short-loop RAB4-dependent recycling of αvβ3 needed for persistent migration and invasion in low fibronectin environment. When Rabaptin-5 is inhibited, cells switch to the long-loop RAB11-dependent recycling of α5β1. This decreases the directionality but increases the cell speed in breast cancer cells, and they also adopt a mesenchymal phenotype to invade in fibronectin rich environment (Christoforides et al., 2012, Paul et al., 2015). These data suggest that the mode and the outcome of integrin recycling are dependent on the different signals at play as well as the cell types being examined.

In melanoma cells, FMNL2 promotes internalisation of the β1-containing heteromeric integrins including α2β1 and α5β1 and this enhances the invasion into fibronectin-containing matrices (Wang et al., 2015b). This perhaps promotes the dynamic of the invasive front and supports the invasion process. In cells expressing high levels of RAB25, integrins recycling from the lysosomes also contribute to the invasion process. In these cells, another highly expressed protein called CLIC3 (Chloride Intracellular Channel Protein 3) mediates the rescue of active α5β1 integrins from the lysosomes and traffics them to the rear of the cells. Here, α5β1 integrins engage with fibronectin substrate and activate Src, which acts to

disassemble adhesions at the rear end of the cells, allowing them to retract and thus moving forwards (Dozynkiewicz et al., 2012, Hamadi et al., 2005, Westhoff et al., 2004). Interestingly, in triple-negative breast cancer cells, CLIC3 also rescues the matrix metalloprotease MMP14 from lysosomes/late endosomes and promotes invasion (Macpherson et al., 2014). A recent report shows that the β1 integrins can induce the phosphorylation of MMP14, which triggers its internalisation and promotes invadopodia formation and cell invasion (Grafinger et al., 2020). This lets us speculate that the trafficking of integrins is likely to also affect other membrane proteins and in many cases promote cancer invasion.

The trafficking of integrins is not only restricted within the boundary of a cancer cell but can also extend to distant locations in the body. Indeed, a recent landmark report showed that exosomes containing specific signature sets of integrins are released into the bloodstream from different types of tumours. The integrins expressed on these exosomes provide the specificity for the anchorage and uptake of these vesicles by different cell types and allow these cells to be reprogrammed ready for the seeding of cancer cells in the future (Hoshino et al., 2015). In p53-mutant containing PDAC, these exosomes also reprogram fibroblasts to remodel the extracellular matrix, making it hospitable for the colonisation of future metastases (Novo et al., 2018). The summary of these pathways is represented in Figure 1.32.

Overall, cumulative evidence has pointed towards the importance and necessity of integrin trafficking in modulating various behaviours of cancer cells. It is certain that not only the signalling coming from the integrins but also the spatiotemporal dynamics of these proteins also plays an essential role. This section is by no mean an exhaustive list, but it should provide the reader with the basic understanding of the signalling of integrins and their connections to the actin cytoskeleton and regulators as this will be important to understand the experiments described in future chapters.

The overall aim of this thesis is to elucidate the cellular functions and localisation of the novel CYRI-A protein. We aim to compare the similarities and differences both biochemically and cellularly between the two paralogous CYRI-A and CYRI-B protein. Finally, we want to understand how CYRIs regulate the actin cytoskeleton dynamics and provide an explanation for their effects on the migration and invasion in cancer.

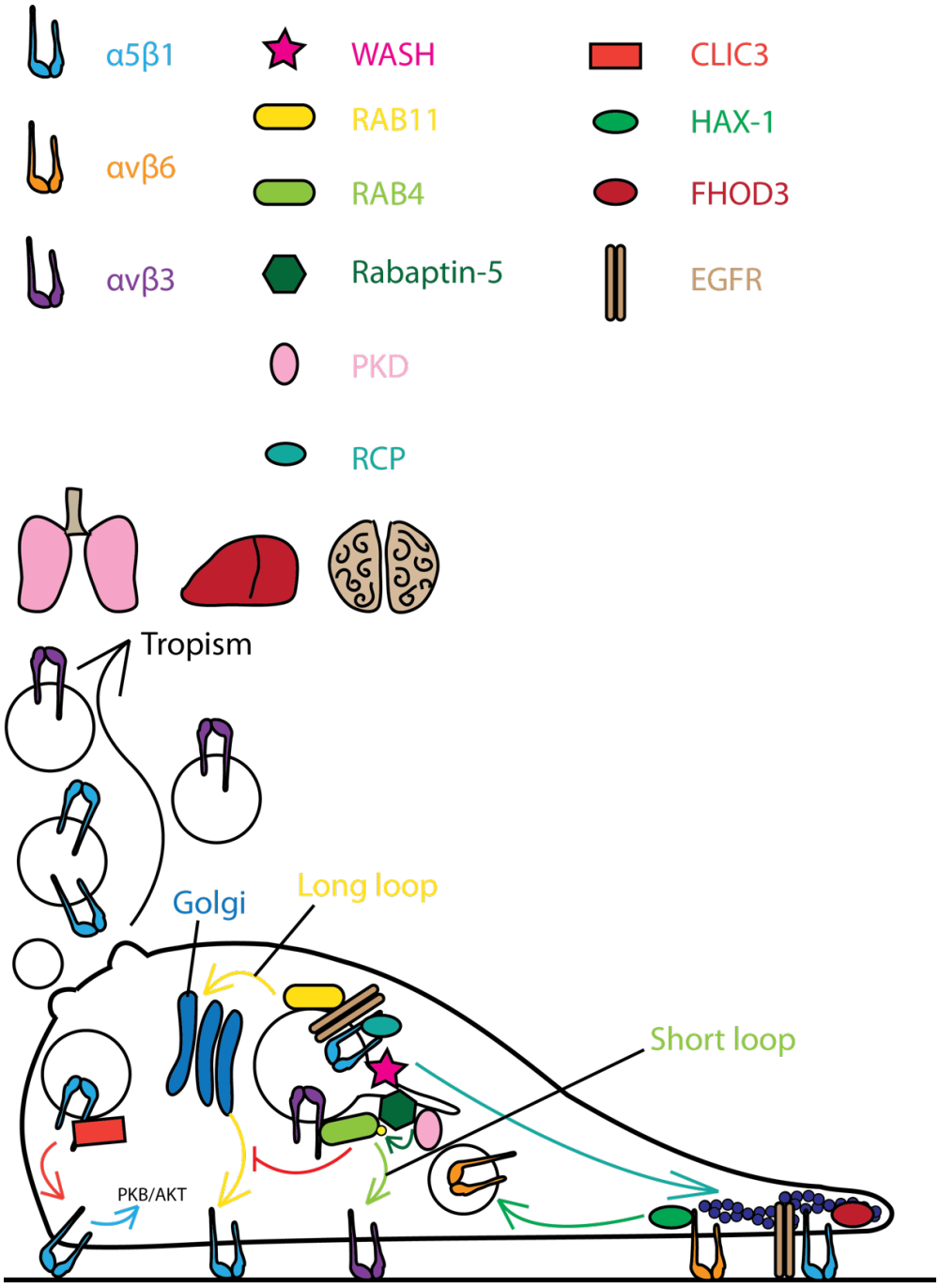

Figure 1.32 Integrin trafficking pathways mediate different modes of cancer cell invasion and metastasis

2 Materials and methods

2.1 Materials and reagents

2.1.1 Cell lines, bacteria strains and culture conditions

Original cell line	Cell type	Source	Original cell line creator	Derived cell lines	Derived cell line creator	Growth media
Mel-10 Mel-11	Transformed mouse melanocyte	1-day old Tyr::NRasQ61K$^{+/o}$ Rac1$^{f/f}$ Ink4a$^{-/-}$ Tyr::CreERT$^{+/o}$ littermate mice	Ang Li	Mel-10/11 overexpressed Rac1^{WT} or mutant Rac1^{P29S} or Rac1^{Q61L}	Self-made	F-12 + 10% FBS + 90μg/ml Primocin + 6μg /ml Blasticidin + 0.135μg/ml PMA
COS-7	Cercopithecus aethiops kidney fibroblast-like cell	ATCC	N/A	CYRI-B knockout ex4.1	Loic Fort & Jamie Whitelaw	DMEM + 10% FBS + 1X Glutamine +1X Pennicilin/Strepmicin
HEK293T	Human Embryonic Kidney cell	Laura Machesky	N/A	N/A	N/A	DMEM + 10% FBS + 1X Glutamine
Phoenix-AMPHO	Derived-HEK293T	B.Ozanne	N/A	N/A	N/A	
CHL-1	Human melanoma cell	ATCC	N/A	N/A	N/A	
A-673	Human Ewing's sarcoma	Sue Burchill	N/A	CYRI-A, CYRI-B single KO CYRI-AB double KO	Self-made	DMEM + 10% FBS + 0.5X Glutamine (+ 1μg/ml Puromicin + 6μg/ml Blasticidin for derived cells)
TIF	Telomerase-immortalised human foreskin fibroblast	Beatson Central Service	N/A	N/A	N/A	DMEM + 10% FBS + 1X Glutamine

Bacterial strains	Source
E.coli DH5α	Peter Thomason
E.coli BL21	

2.1.2 Reagents

Solutions		
Cell culture		
Name		**Source**
DMEM		Gibco #21969-035
MEM		Gibco #11095080
F-12K Nutrient Mixture, Kaighn's Modification		Gibco #21127022
FBS		Gibco #10270-106
L-Glutamine		Gibco #25030-032
2.5% Trypsin, no phenol red (0.25% working conc.)		Gibco #15090046
Penicillin-Streptomycin		LifeTechnologies #15140122
PBS		Beatson Central Service
PE buffer		Beatson Central Service
CASYton buffer		OLS OMNI Life Science #5651808
L-Broth		Beatson Central Service
LB-agar plate		Beatson Central Service
Buffers		
Western blotting		
Name		**Source or Composition**
RIPA buffer		150mM NaCl, 10mM Tris-HCl pH7.5, 1mM EDTA, 1% Triton X-100, 0.1%SDS
MOPS running buffer 20X		Novex #NP0001
Transferring buffer		20% Methanol, 10% Running buffer (Beatson Central Service), dH2O to 2L
Precision Red Advanced Assay solution		Cytroskeleton, Inc. #ADV02
PageRuler pre-stained protein ladder		Thermo Scientific #26616
NuPAGE Protein Sample buffer 4X		Invitrogen #NP0007
NuPAGE Reducing agent 10X		Invitrogen #NP0004
TBS-T		150mM NaCl, 10mM Tris-HCl pH7.4, 2.7mM KCl, 0.1% Tween20 (Beatson Central Service)
Novex Sharp Pre-stained protein standard		Invitrogen #LC5800
Novex Tris-Glycine SDS Sample Buffer (2X)		Invitrogen #LC2676
Novex Tris-Glycine SDS Running Buffer (10X)		Invitrogen #LC2675
Novex Zymogram Renaturing Buffer (10X)		Invitrogen #LC2670
Novex Zymogram Developing Buffer (10X)		Invitrogen #LC2671
Protein work and pulldown assay		
Name		**Source or Composition**
Large-scale protein purification	Bacteria lysis buffer	20mM Tris pH 8.0, 300mM NaCl, 5mM $MgCl_2$ and 2mM beta-mercaptoethanol (BME)
	GST-trap chromatography buffers	Wash buffer: 5mM MgCl2, 150mM NaCl, 20mM Tris pH 7.5, 2mM BME, dH2O. Elution buffer: Wash Buffer + 10mM Glutathione + 10% glycerol
	His-trap chromatography buffers	Buffer A: 300mM NaCl, 25mM Tris pH 7.5, 2mM BME, dH2O Buffer B (Elution buffer): Buffer A + 300mM Imidazole + 2mM BME
	MBP-Trap chromatography buffers	Wash buffer: 150mM NaCl + 20mM Tris pH 7.5 + 2mMl BME + dH2O Elution buffer: Wash Buffer + 10mM Maltose

	Size exclusion buffer	150mM NaCl, 20mM Tris pH 7.5, 2mM DTT; 5mM MgCl2 is added if the protein is a RhoGTPase
Small-scale protein purification and pulldown assay	Bacteria lysis buffer (Buffer A)	50mM Tris 7.5, 50mM NaCl, 5mM MgCl2, 0.25mM DTT
	GST-Trap buffers	Wash buffer 7.5: 100mM NaCl, 25mM Tris pH7.5, 5mM MgCl2 Wash buffer 8: 100mM NaCl, 25mM Tris pH8, 5mM MgCl2 Elution buffer: 100mM NaCl, 25mM Tris pH8, 5mM MgCl2, 10mM Glutathione, 0.1% Triton X100
	GFP- and MBP-Trap bead Wash buffer	100mM NaCl, 10mM Tris pH 7.5, 5mM MgCl2
	GFP-trap Lysis buffer	GFP wash buffer, 0.5% NP-40, protease and phosphatase inhibitors (1X)
	Binding buffer	100mM NaCl, 25mM Tris pH7.5, 5mM MgCl2, 0.1% Triton X100

Integrin kinetic assay	
Name	**Source or Composition**
HBSS buffer	NaCl, 8.0g; KCl, 0.4g; $CaCl_2$, 0.14g; $MgSO_4 \bullet 7H_2O$, 0.1g; $MgCl_2.6H_2O$, 0.1g; $Na_2HPO_4.2H_2O$, 0.06g; KH_2PO_4, 0.06g; glucose, 1.0g; $NaHCO_3$, 0.35g; H_2O, to 1000 ml (http://cshprotocols.cshlp.org/content/2006/1/pdb.rec548.full)
Acid wash buffer	0.2M acetic acid, 0.5M NaCl, pH 2.5
Permeabilisation buffer	20mM Glycine, 0.05%, Triton-X100

Matrix	
Name	**Source or Composition**
Fibronectin, Bovine Plasma	Sigma-Aldrich # F1141
Collagen I, High Concentration, Rat-Tail	Corning #354249
Matrigel Basement Membrane Matrix	Corning #354234
Laminin	Sigma #L2020
Gelatin from pig skin, Oregon-green 488nm	Molecular Probes #G13186
Poly-L-Lysine	Sigma-Aldrich #P4707-50ML
Cell-derived matrix	Beatson Central Service

Chemicals and small molecules	
Name	**Source**
Latrunculin A	Sigma-Aldrich # L5163
Cytochalasin D	Sigma-Aldrich #C2618
LY294002 1.5mg	NEB #9901S
Halt-Proteases Inhibitor Cocktail	Thermo Fisher Scientific #78438
Halt-Phosphatases Inhibitor Cocktail	Thermo Fisher Scientific #78427
4-hydroxytamoxifen (OHT)	Sigma-Aldrich #T176-10MG
Doxycycline	Sigma #D9891
DMSO	Fisher Chemical #D/4121/PB08
Blebbistatin	Sigma-Aldrich #B0560
N-Acetyl-L-cysteine	Sigma-Aldrich #A7250
Lipofectamine 2000	Thermo Fisher Scientific #11668019
Lullaby	OzBiosciences #FLL73000
Puromycin	Invivogen, #ant-pr-1
Blasticidin	Invivogen, # ant-bl-10p
Ampicillin	Sigma #A9518
Kanamycin	Sigma #K4000
IPTG	Sigma #I675

16% paraformaldehyde	Electron Microscopy Sciences #15710
ProLong Diamond antifade mounting media	Invitrogen #P36961
Trametinib	Stratech Scientific Ltd. #S2673
Dasatinib	Stratech Scientific Ltd. #S1021
PF-562271	Stratech Scientific Ltd. #S2890
PF-573228	Stratech Scientific Ltd. #S2013
GM6001	Merck chemicals
Thrombin	Sigma-Aldrich #T4648
Glutathione	Sigma-Aldrich #G6013
D-(+)-Maltose monohydrate	Sigma-Aldrich #M5885-100G
NP-40 Surfact-Amps Detergent Solution	Thermo Scientific #85124
Triton X-100	Sigma-Aldrich #X100-500ML
High molecular biology grade agarose	Melford #MB120
G418	Formedium # G418S
PMA	Sigma-Aldrich #P1585
NaCl	Fisher #S/3160/60
$MgCl_2$	Fisher #M/0600/53
Nuclease-Free H_2O	Ambion #AM9937
Bovine Serum Albumin Fraction V	Sigma-Aldrich #10735108001
N-Acetyl-L-cysteine	Sigma-Aldrich #A7250
tert-Butyl hydroxyperoxide solution 5-6M in decane	Sigma-Aldrich #416665-25mL

Antibodies and dyes

Name	Source	Application	Dilution
Calcein AM	Life Technologies #C1430	Live staining	4μM
Hoechst 33342	Thermo Scientific #62249	IF	1:10,000
Phalloidin 488nm	Molecular Probe #A12379	IF	1:200
Phalloidin 594nm	Molecular Probe #A12382	IF	1:200
Phalloidin 647nm	Molecular Probe #A22287	IF	1:200
Donkey anti Rabbit 680nm	Invitrogen #A21206	WB	1:10,000
Donkey anti Mouse 680nm	Invitrogen #A10038	WB	1:10,000
Donkey anti Rabbit 594nm	Invitrogen #A21207	IF	1:200
Donkey anti Mouse 594nm	Invitrogen #A31203	IF	1:200
Goat anti Mouse 800nm	Thermo Scientific #SA5-35521	WB	1:10,000
Goat anti Rabbit 800nm	Thermo Scientific #SA5-35571	WB	1:10,000
Mouse anti Tubulin (DM1A)	Sigma-Aldrich, #T6199	WB	1:1000
Mouse anti GAPDH	Millipore, #MAB374	WB	1:2000
Rabbit anti Rac1/2/3	Cell Signaling #2465	WB	1:1000
Rabbit anti GST	Cell Signaling #2622	WB	1:1000
Mouse anti GFP (4B10)	Cell Signaling #2955	WB	1:1000
Chicken anti GFP	Abcam #ab13970	IF	1:5000
Monoclonal ANTI-FLAG M2 antibody produced in mouse	Sigma-Aldrich #F3165	WB PLA	1:1600 1:800
HA tag (C29F4) rabbit mAb	Cell Signaling #3724S	PLA	1:800
Anti-MBP Monoclonal Antibody	NEB #8032S	WB SPR	1:10,000 Assay-dependent
Rabbit anti Fam49A	Sigma-Aldrich (discontinued)	WB	1:1000

Rabbit anti Fam49B	Sigma-Aldrich #HPA009076	WB	1:1000
Rabbit anti Integrin beta 1 antibody [12G10]	Abcam #ab30394	WB IF	1:1000 1:200
Recombinant rabbit anti-Integrin alpha 5 antibody [EPR7854]	Abcam #ab150361	WB IF	1:1000 1:200
Anti-Integrin alpha5 (Preservative Free) Antibody, clone SNAKA51	Millipore #MABT201	FACs IF	1:500 1:200
Alexa Fluor 488 anti-human CD29 Antibody TS2/16	BioLegend #303015	FACs	1:500
FITC anti-human CD49e Antibody	BioLegend #328007	FACs	1:500
Alexa Fluor 488 Mouse IgG1, κ Isotype Ctrl (FC) Antibody	BioLegend #400132	FACs	1:500
Rabbit phospho-FAK (Tyr576/577) Antibody	Cell Signaling #3281	WB	1:1000
Rabbit FAK antibody	Cell Signaling #2920S	WB	1:1000
Rabbit phospho-ERK1/2 (Thr202/Tyr204) antibody	Cell Signaling #9101	WB	1:1000
Mouse ERK1/2 antibody	Cell Signaling #9102	WB	1:1000
Rabbit phospho-AKT (S473) (D9E) antibody	Cell Signaling #4060S	WB	1:1000
Mouse (pan) AKT (40D4) antibody	Cell Signaling #2920	WB	1:1000
Mouse anti-MMP-14 Antibody, catalytic domain, clone LEM-2/63.1	Millipore #MAB3329	WB	1:1000
Rabbit Anti MMP9	Abcam #ab38898	WB	1:1000
Rabbit Anti MMP2	Abcam #ab37150	WB	1:1000
Mouse anti Cortactin (4F11)	Millipore #05-180	IF	1:200
Rabbit anti p34-Arc/ARPC2	Millipore #07-227	IF	1:200
Mouse anti Vinculin	Sigma #V9131	IF	1:400
Rabbit anti Phospho-Paxillin (Y118)	Cell Signaling #2541	IF	1:200
Rabbit anti FISH antibody (M-300)	SantaCruz #sc-30122	IF	1:200
Purified mouse anti-human CD49e Clone IIA1	BDBiosciences #555615	Blocking	5μg/ml
Mouse Integrin B1 antibody (P5D2)	SantaCruz #sc-13590	Blocking	5μg/ml
Mouse Integrin alpha 5 antibody (P1D6)	SantaCruz #sc-13547	Blocking	5μg/ml
Rabbit anti HDAC2 antibody	Cell Signaling #2540S	WB	1:1000
Calnexin (C5C9) Rabbit mAb	Cell Signaling #2679S	WB	1:1000
Rabbit HSP90 Antibody	Cell Signaling #4874	WB	1:1000
Rabbit anti Collagen VI [EPR17072]	Abcam #ab182744	WB	1:1000
Rabbit Recombinant Anti-N Cadherin antibody [EPR1791-4]	Abcam #ab76011	WB	1:1000
EGF Receptor (D38B1) XP Rabbit mAb	Cell Signaling #4267	WB	1:1000
InstantBlue, Ultrafast Protein Stain	Scientific Laboratory Supplies #ISB1L-1L	N/A	N/A
Ponceau S	Sigma-Aldrich #P710	N/A	N/A
IncuCyte Nuclight Rapid Red reagent	IncuCyte #4717	Live cell	1:1000
IncuCyte Sytox Green reagent	IncuCyte #4633	Dead cell	1:10,000
Dextran, tetramethylrhodamine, 70,000 MW, lysine fixable (25MG)	ThermoFisher #D1818	Live cell	50μg/ml
Lysotracker Red DND-99 (20x50uL)	Invitrogen #L7528	Live cell	1μM
CellROX Deep Red	Thermo Fisher Scientific #C10422	FACs	1μM
SimpkyBlue SafeStain	Invitrogen #LC6060	Zymography	N/A
Zombie Red fixable viability kit	BioLegend #423110	FACs	1:1000

CellROX Deep Red	Thermo Fisher Scientific #C10422	FACs	1μM

Molecular biology and cloning		
DNA constructs		
Name	**Backbone**	**Source**
GFP-(29-319)-DUF1394-mCYRI-A	pEGFP-C1	Self-made
GFP-(1-319)-DUF1394-mCYRI-A	pEGFP-C1	Self-made
GST-RAC1 WT	pGEX2T	Laura Machesky
GST-RAC1 Q61L	pGEX2T	Laura Machesky
GST-RAC1 P29S Q61L	pGEX2T	Self-made
GST-RAC1 Q61L S41A	pGEX2T	Self-made
GFP-RAC1 WT	pEGFP-C1	Laura Machesky
GFP-RAC1 Q61L	pEGFP-C1	Laura Machesky
GFP-RAC1 T17N	pEGFP-C1	Laura Machesky
GST-mCYRI-B	pGEX2T	Loic Fort
eCFP-PBD-Pak	pECFP-N1	Laura Machesky
MBP-mCYRI-A	pMAL-C5X-MBP	Self-made
MBP-mCYRI-B	pMAL-C5X-MBP	Loic Fort
MBP-mCYRI-B-S157A	pMAL-C5X-MBP	Self-made
MBP-mCYRI-B-S157R	pMAL-C5X-MBP	Self-made
MBP-mCYRI-B-Q153R	pMAL-C5X-MBP	Self-made
MBP-RRDD-mCYRI-A	pMAL-C5X-MBP	Self-made
MBP-His-mCYRI-A	Modified mBP-His-RSF-Duet1 (Shehab Ismail)	Self-made
MBP-His-mCYRI-B	Modified mBP-His-RSF-Duet1 (Shehab Ismail)	Tamas Yelland
MBP-His-mCYRI-B-RAC1 Q61L fusion	Modified mBP-His-RSF-Duet1 (Shehab Ismail)	Tamas Yelland
Untagged CYRI-A	pcDNA3.1	Self-made
CYRI-A-FLAG	pcDNA3.1	Self-made
CYRI-A-FLAG-RRDD	pcDNA3.1	Self-made
GFP-FLAG	pcDNA3.1	Jamie Whitelaw
P17-HA-mCYRI-B	pcDNA3.1	Savvas Nikolaou
P17-GFP-mCYRI-B	pcDNA3.1	Loic Fort
P16-GFP-mCYRI-A	pcDNA3.1(+)	Self-made
P16-mCherry-mCYRI-A	pcDNA3.1(+)	Self-made
P16-mCherry-RRDD-mCYRI-A	pcDNA3.1(+)	Self-made
pLIX401-mVenus-mCYRI-A	pLIX401-mVenus_New MCS (David Bryant)	Self-made
BH-GFP-CYRI-A (CYRI-B helix on DUF1394 of CYRI-A)	pcDNA3.1(+)	Self-made
LifeAct-mTagRFP	LifeAct -mTagRFP-T	Addgene - 54586
mCherry-RAB5A WT	pmCherry-C1	Addgene #55126
mCherry-Clathrin LC-15	pmCherry-C1	Addgene #55019
mApple-Alpha-5-Integrin	pmCherry-C1	Addgene #54864
pcDNA3/hArf1(WT)-mCherry	pcDNA3.1	Addgene #79419
CAV1-mCherry	pmCherry-C1	Addgene #27705
GFP-CYFIP1	pEGFP-C1	Klemens Rottner

PH-GRP1-GFP	pEGFP-C1	David Bryant's lab
PH-BTK-GFP	pEGFP-C1	Addgene #86635
Lck-mScarlet-I	pGEFP-C1	Addgene #98821
GFP-Arp3	pEGFP-C1	Laura Machesky
GFP-Cortactin	pEGFP-C1	Addgene #26722
GFP-hSNX5	pEGFP-C1	Self-made
Pmx-RAC1 WT	Pmx retroviral vector	Heather Spence
Pmx-RAC1 P29S	Pmx retroviral vector	Heather Spence
Pmx-RAC1 Q61L	Pmx retroviral vector	Self-made
pSpCas9(BB)-2A-Puro (PX459) V2.0	Empty backbone	Addgene #62988
pSpCas9(BB)-2A-Blast (PX459) V2.0	Empty backbone	Stephen Tait's lab
pEGFP-C1	Empty backbone	Laura Machesky
psPAX2	empty backbone	Laura Machesky
pCMV-VSV-G	empty backbone	Laura Machesky

siRNA

Target	Sequence (5'-3')	Source
Hs_FAM49A_1 FlexiTube siRNA	CACCTAGACATTGAGAATGAA	Qiagen #SI00384321
Hs_FAM49A_5 FlexiTube siRNA	ATCGATATGAAAGGCTGCATA	Qiagen #SI03150210
Hs_FAM49A_7 FlexiTube siRNA	CTGCAAGACATCCAAGATCGA	Qiagen #SI04266325
Hs_FAM49A_9 FlexiTube siRNA	CAGATTGATGTTAATACTTGT	Qiagen #SI05122656
Hs_FAM49B_6 FlexiTube siRNA	AGGGTAATGGTGGGTGTCATA	Qiagen #SI04278890
Hs_FAM49B_7 FlexiTube siRNA	ATAGAAGAACATTGAGTCGTA	Qiagen #SI04359369
AllStars Negative Control	N/A	Qiagen #SI03650318

CRISPR sgRNA

Target	Sequence (5'-3')	Source
Human CYRI-A	h49A-sgRNA2.1: CACCGCCTGAAGGACGGCGCTGATC h49A-sgRNA2.3: CACCGCTGCAGGCTTACAAAGGCGC	Designed using the Zhang website: https://zlab.bio/guide-design-resources
Human CYRI-B	h49B-sgRNA4.1: CACCGCGAGTATGGCGTACTAGTCA	Designed by Loic Fort

qPCR primers

Target	Source
Hs_ITGA5_1_SG QuantiTect Primer Assay	Qiagen #QT00080871
Hs_ITGB1_1_SG QuantiTect Primer Assay	Qiagen #QT00068124
Hs_MMP14_1_SG QuantiTect Primer Assay	Qiagen #QT00001533
Hs_Fam49B_1_SG QuantiTect Primer Assay	Qiagen #QT00084567
Hs-Fam49A_1_SG QuantiTect Primer Assay	Qiagen #QT00069566
Hs_GAPDH_2_SG Quantitect Primer assay	Qiagen #QT01192646

Sequencing primers

Target	Sequence (5'-3')	Source
EGFP-C1 Fw	GAA GCG CGA TCA CAT GGT C	Beatson Molecular Technology Services
EGFP-C1 Rv	AAC CAT TAT AAG CTG CAA TAA AC	Beatson Molecular Technology Services
EGFP-N1 Fw	GAG GTC TAT ATA AGC AGA GC	Beatson Molecular Technology Services

EGFP-N1 Rv	ACT TGT GGC CGT TTA CGT C	Beatson Molecular Technology Services
pLKO-Fw	CAA GGC TGT TAG AGA GAT AAT	Beatson Molecular Technology Services
Internal GFP Fw	CAT CGA GCT GAA GGG CAT C	Self-made
Internal GFP Rv	CGG TTC ACC AGG GTG TCG	Self-made
Internal mCherry Fw	GTA CCC CGA GGA CGG CGC CC	Self-made
Internal mCherry Rv	TCC GCT CGG AGG AGG CCT C	Self-made
Internal CYRI-A Fw	GAC CAG AGA TCC GAG ATG C	Self-made

Reagents

Name	Source and compositions
2X PrimeStar Master Mix	Takara #R045
50X TAE buffer	2M Tris, 50mM EDTA, 1M Glacial acetic acid, pH~8.3 (Beatson Central Service)
Midori green	Nippon Genetics #MG04
6X DNA loading buffer	12% glycerol, 60mM, Na2EDTA, 0.6% SDS, 0.003% bromphenol blue, 0.003% xylene cyanol, H2O (self-made)
O'GeneRuler 1kb	ThermoScientific #SM1163
SOC medium	2% w/v trypton, 0.5% w/v yeast extract, 10mM NaCl, 2.5mM KCl, 10mM, MgCl2, 20mM glucose (Peter Thomason)
CutSmart	NEB #B7204S

Kits and commercial equipment

Kits

Name	Source
Calcium phosphate transfection kit	Invitrogen #K2780-01
Prescission Red advanced assay	Cytoskeleton Inc. #ADV02
Zymoclean DNA gel recovery kit	ZymoResearch #D4008
DNA clean and concentrator kit-100	ZymoResearch #D4029
Rapid DNA ligation kit	Thermo Scientific #10775841
Q5-site directed mutagenesis kit	NEB BioLabs #E0554
Amaxa Cell Line Nucleofector Kit V	Lonza #VCA-1003
Amaxa Cell Line Nucleofector Kit R	Lonza #VCA-1001
RNeasy Mini kit	Qiagen #74104
DyNAmo HS SYBR Green qPCR kit	ThermoFisher Scientific #F410L
qScript cDNA Synthesis Kit	Quantabio #95047-100
NativePAGE Sample Prep Kit	Invitrogen #BN2008
Thermo Scientific Protein Subcellular Fractionation kit for cultured cells	ThermoFisher Scientific #78840
Duolink In Situ Red Starter Kit Mouse/Rabbit	Sigma-Aldrich #DUO92101
Duolink In Situ PLA Probe Anti-Mouse PLUS	Sigma-Aldrich #DUO92001
Duolink In Situ PLA Probe Anti-Rabbit PLUS	Sigma-Aldrich #DUO92002

Gels and membranes

Name	Source
4-12% NuPAGE Bis-Tris gels	Invitrogen #NP0321
Nitrocellulose blotting membrane	GE Healthcare #10600002
Novex 10% Zymogram Plus (Gelatin) Protein Gels, 1.0 mm, 10-well	Invitrogen #ZY00100BOX

Affinity beads, Columns and SPR	
Name	**Source**
GFP-Trap-A beads	ChromoTek #gta_200
MBP-Trap Agarose	ChromoTek #mbta-20
Glutathione sepharose 4B beads	GE Healthcare #17075601
HiLoad 16/600 Superdrex 75 pg	GE Healtcare #28989333
GSTrap HP column	GE Healthcare #17-5282-01
MBPTrap HP, 1x5ml	GE Healthcare #28918779
Spin Column	Chromotek #sct-10
Series S Sensor Chip CM5, pack of 1	GE Healthcare #29104988
Plasticwares	
Name	**Source**
10cm plastic plate	Corning #430147
6-well plastic plate	Falcon #353046
24-well plastic plate	Falcon #353047
96-well plastic plate	Falcon #353072
MicroAmp Optical96-well reaction plate	Applied Biosystems #8010560
IncuCyte ImageLock Plates - 96-well	Essen Bioscience, Sartorius #4379
35mm glass-bottom dish	MatTek #35G-1.5 20-C
24 well plate; 6.5 mm Transwell with 8.0 µm Pore Polycarbonate Membrane Insert	Corning #3422
E-Plate 16	Acea #05469830001
Cryovials, 1 mL	Greiner bio-one #123263
Precellys CK14 lysing tube	Precellys #03961-1-003
19 mm glass coverslips	VWR #631-0156
Amicon Ultra-4 centrifugal Filter unit	Amicon #UFC801024
Amicon Ultra-15 centrifugal Filter unit	Amicon #UFC901008
Software	
Names	**Version**
Image Studio Lite	LICOR Biosciences Ltd v 5.2.5
NEBaseChanger	NEB v 1.2.6
ApE	M. Wayne Davis v 2.0.47
Fiji	NHI, USA v 2.0.0
Prism	GraphPad v 7.0d
CRISPR Design	Zhang Lab 2015
FlowJo	Becton Dickinson & Company v 10.6.1
Cell Profiler	Carpenter Lab, BROAD Institute v 3.0.0
HALO	Indica Labs v 3.0.311.176
Adobe Illustrator CS5.1	Adobe Systems v 15.1.0
Endnote X8	Clarivate Analytics v 8.2
Incucyte S3	Incucyte Biosciences, Sartorius v 2018 A
Incucyte Zoom	Incucyte Biosciences, Sartorius v 2018 A
Imaris Image Analysis software	Bitplane v 9.2.0
i-TASSER	Zhang lab v 5.1
PyMol	Schrödinger v 2.1
Zeiss software ZEN	Zeiss v 2.1

2.1.3 Units

Abbreviation	Names
°C	degree Celsius
K	Kelvin
M	Molar
μM	micromolar
nM	nanomolar
μm	micrometre
nm	nanometre
g	gram
mg	milligram
μg	microgram
rpm	rotation per minute
sec or s	second
min	minute
h	hour
L	litre
uL	microlitre
Da	Dalton
kDa	kilodalton
V	Volt
mA	milliampere
∑	sum
Kd	dissociation constant
pN	pico Newton

2.2 Cell biology methods

2.2.1 Cell culture maintenance

For maintaining: COS-7, CHL-1 and HEK293T cells are grown in DMEM supplemented with 10% fetal bovine serum and 1X glutamine and 1X Pen/Strep. A-673 cells were grown in the same media but with 0.5X glutamine. Single CRISPR A-673 cells were grown in media containing 1μg/ml Puromycin while double knockout cells were grown in media containing 1μg/ml Puromycin and 6μg/ml Blasticidin.

For passaging: first cells were washed with PBS and 500ul of 0.25% trypsin was added and incubated at 37°C for 2min. Trypsin is blocked by adding 5ml of 10%-serum containing media. Cells were in a 1:10 ratio 2 times a week on Monday and Friday. For experimental testing, cells are grown in selection-free media.

For cryopreservation: from a confluent 15cm plate, cells were detached and collected in a 50ml Falcon tube as described above. The cell suspension was then centrifuged at 1200rpm for 5 mins. The medium was then aspirated, and the cell pellet is washed with 5ml of 1X PBS and recentrifuged. After aspirating out PBS, the cell pellet is suspended in 10ml of cryopreserving media composed of 50% normal growth media, 40% FBS and 10% DMSO. Cell suspension is dispensed into 1ml cryopreservation tube and store at -80^{o}C for at least 24h before transferring to liquid nitrogen.

For recovering from cryopreservation: cryotubes containing cells were drop into a warm water until nearly fully thawed. The cell suspension is then transferred into a 10cm plate containing 10ml of pre-warmed growth medium and allow to attach overnight. The next day, the old medium is removed, and cells are washed with 5ml of 1X PBS before being placed in 10ml of fresh growth medium.

2.2.2 Stable cell line generation

Retroviral transfection:

On day 1, Phoenix-AMPHO cells were plated in 10% serum growth media so that they cover approximately 40% of the area in a 10cm petri dish. Day 2, cells were transfected using Calcium precipitation method. 5μg of DNA plasmid is mixed with 440μl dH2O, 60μl 2M CaCl2 and 500μl 2X HBSS. The solution mixture is incubated at 37^{o}C for 30 min before adding to the cells. The cells are placed at 37^{o}C, 5% CO2 overnight. Day 3, recipient cells were seeded at about 25% confluence. At the same time, the media of the Phoenix-AMPHO cells are changed to 20% serum growth media and placed at 32^{o}C, 5% CO2 overnight. Day 4, recipient cells are infected one in the morning and one in the afternoon. Media from the infected Phoenix-AMPHO cells were placed onto recipient cells after being filtered through a 0.45μm filter. Replace 20% serum growth media back to the Phoenix-AMPHO cells. Recipient cells are incubated at 37^{o}C, 5% CO2 overnight. Polybrene is added in both cases at 10μg/ml to help with the infection process. Day 5 repeat the infection process one more time in the morning. Day 6, recipient cells are split and selected using the appropriate antibiotics. For the generation of Mel-10 and

Mel-11 expressing different versions of the RAC1 protein, 6μg/ml of Blasticidin was used.

Lentiviral transfection:
This protocol is used for both making stable overexpressed cell lines as well as CRISPR/Cas9 knockout cell lines. HEK293T cells were plated at 1.5 x 10^6 cells per 10cm petri dish in DMEM/10%FBS in day 1. The next day, cells were then transfected with the appropriate construct along with packaging vectors as followed: 10μg of the interested construct, 7.5μg of pSPAX2 and 4μg of pVSVG packaging plasmid. DNA constructs were diluted in dH2O to make up 440μl, then 500μl of 2xHBS was added and mixed thoroughly, then 60μl of 2M CaCl2 was added. The mixture is incubated at 37°C for 30min before added to the cells and incubated at 37°C, 5% CO2 overnight. The next day, the medium is changed to 6ml of DMEM/20%FBS, while recipient cells are plated in DMEM/10% FBS at 5x10^5 cells. Day 4, the medium from the transfected HEK293T cells was drawn and filtered through a 0.45μm filter before adding to the recipient cells, along with 2.5μl of polybrene (10mg/ml stock). Repeat the infection process again the next day. Finally, the media containing the appropriate antibiotic(s) are used to select for transfected cells. This protocol was used to create CRISPR/Cas9 single knockout of either CYRI-A, CYRI-B or double knockout of both CYRI-A and B in
A-673. Single knockout cells are resistant to Puromycin (1μg/ml), double knockout cells are resistant to both Puromycin (1μg/ml) and Blasticidin (6μg/ml). For culturing, cells are kept in the appropriate selection media, but for all long-term experiments, the antibiotics are completely removed.

2.2.3 Transient transfection

Lipid-based transfection for DNA construct:
The day before transfection, 3x10^5 cells were seeded per well in a 6-well plate in 2ml of the appropriate growth medium. On the day of transfection, add 2μg of DNA plasmid in the appropriate serum-free medium to make up the total volume of 100μl. Add 5μl of Lipofectamine 2000 to 95μl of serum-free medium. Mix 100μl of the DNA mix with the Lipofectamine mix and leave to incubate at room

temperature for 5 min before adding dropwise to the cell. Cells are incubated overnight at 37°C, 5% CO2.

Lipid-based transfection for siRNA:
$3x10^5$ cells were plated in 2ml of media. The next day, the medium is changed into 1.8ml. For one well in a 6-well plate, to prepare the siRNA reaction mix, 20nM of siRNA was added to the appropriate volume of serum-free medium to makeup a total of 100μl. At the same time, 7μl of Lullaby is added to 93μl of serum-free medium. Then 100μl of the siRNA-medium mix is added to 100μl of Lullaby-medium mix and leave for incubation at room temperature for 20 minutes before adding to the cells. Cells were incubated with the siRNA for 48h, before being treated again with the second round of siRNA for 24h. If after 48h, the cells are too confluent, they will be passaged (as described) with a ratio of 2:3 and leave for 4h to reattach before treating with siRNA. Cells usually retain their knockdown within 5 days after the second round of treatment.

Amaxa electroporation:
Cells were trypsinised and resuspended in 5ml of growth medium as described above. Cells were then counted using the CASY cell counter system. $1.5x10^6$ cells were taken out and centrifuged at 1200 rpm for 5 min. Cells were washed with 1X PBS and pelleted by centrifugation as before. At the same time, to make the DNA solution, mix 82ul of the appropriate Nucleofactor solution with 12μl of solution Supplement 1, then add 2μg of DNA plasmid. Aspirate out the PBS once cells have centrifuged and mix the cell pellet with the DNA solution by gently pipetting up and down. The cell suspension is then transferred to an electroporation vial and electroporate using the appropriate programme from the Amaxa electroporator.

2.2.4 Immunofluorescence

Coverslips curation: Glass coverslips are submerged in concentrated nitric acid for 30min. The acid is then washed away with a constant flow of water for 15min.

Immunofluorescence: Glass coverslips are coated with the appropriate matrix for 1 to 2h before washed 3X with PBS. $2x10^5$ cells are seeded and left for 4h in the incubator to fully adhere. Cells are then fixed with 4% PFA in PBS for 10-15min,

then washed 3X with PBS. Permeabilisation is done in 5min then washed with PBS again. Primary antibody mixed with 5% BSA in PBS is incubated with the cells for 1h. Secondary antibody, phalloidin and DAPI are mixed in 5% BSA in PBS and incubated with the cells for 1h. Cells are mounted onto glass slide using Prolong Diamond mounting media. Images are taken using the Zeiss710 or Zeiss880 confocal system.

2.2.5 Invadopodia assay

Coverslips are coated with Poly-L-Lysine (0.005%) in PBS for 20min, then coated with AlexaFluor 488 gelatin (1mg/ml) for 20min before being fixed with 8% glutaldehyde. Cells are seeded on to coverslips and can include 5uM GM6001 overnight to block any premature matrix degradation. After the overnight incubation, the cells have properly adhered to the substratum, the GM6001 can be washed away and cells are allowed to degrade the matrix for at least 4h before being fixed according to a normal immunofluorescence protocol as described above. Images are taken using the Zeiss710 or Zeiss880 confocal system.
Degradation index = degraded matrix area / area covered by cells

2.2.6 Image-based internalisation assay

$5x10^5$ of A-673 cells are seeded on to fibronectin-coated glass coverslips overnight in a 12-well plate. The next day, the plate is placed on ice and cells are washed with ice-cold PBS before being incubated with the SNAKA51 antibody mixed with HBSS buffer for 1h. Cells are induced to internalise the integrins by adding 1ml of 37°C growth media and are immediately transferred to an incubator for 30min. After the incubation, the uninternalized integrins are removed by using an acid wash buffer (pH 2.5) for 1.5min. Cells are then fixed as a typical immunofluorescence. Cells are imaged using the Zeiss880 super-resolution microscope with Plan-Apochromat 63x/1.4 oil DIC M27 lens. Only healthy cells, which can be identified by the morphology of the nucleus, are randomly selected for analysis.
Internalisation index = total area of internalised signal / cell area

2.2.7 Proximity ligation assay (PLA)

The assay is performed according to the manufacturer protocol. In brief, COS-7 cells are co-transfected with CYRI-A-FLAG tag and P17-HA-CYRI-B. Cells are blotted with mouse anti-FLAG and rabbit anti-HA to detect the interaction between CYRI-A and CYRI-B *in cellulo*. Images are taken using the Zeiss710 confocal microscope 20x dry lens.

The degree of interaction = the area of the PLA signal / cell area

2.2.8 Western blotting

Cells are grown to 80% confluence on a 6-well plate. 100μl of RIPA buffer is added to lyse the cells. Cell lysate is collected and centrifuged at 15,000rpm for 10min. The protein concentration is measured using the PrecisionRed solution at OD600 before equal amount mixed with 1X Reducing Agent and 1X Sampling buffer is boiled for 5min at 100°C and then loaded onto a 4-12% Bis-Tris NuPAGE gel in 1X NuPAGE MOPs buffer. The gel is run at 180V until the dye reaches the bottom of the gel. The gel is transferred onto a Nitrocellulose membrane (0.45μm pore) assembled into a cassette. The transferring process is done in transferring buffer for 90min at 240mA. Once finished, the membrane is blocked in 5% BSA in TBST-T for 30min before incubated with the primary antibody overnight at 4°C. The next day, the membrane is washed 3X in TBS-T before incubated with the corresponding secondary antibody at room temperature (rt) for 1h. The membrane is washed 3X with TBS-T and viewed with the LiCor system.

If the samples are tissues, they are mixed with RIPA buffer supplemented with protease and phosphatase inhibitors and put in CK14 lysing tube. The lysing process is carried out in a pre-chilled Precellys homogenizer (3 blasts of 30sec with 90sec gap between each blast). Once finished, tubes are gently centrifuged at 500rpm to deplete the foam. The lysate is transferred into a new Eppendorf tube and proceed to a normal western blot.

2.2.9 Focal Adhesion Kinase (FAK) activation assay

$1.5x10^6$ A-673 cells are suspended in 1ml of serum-free media and rotate at rt for 1h to deplete outside-in integrin signal. Then, cells are seeded on fibronectin-coated 6-well plate for different amount of time before being lysed and subjected to the typical western blot.

2.2.10 Integrin degradation assay

$5x10^5$ cells were seeded onto a fibronectin-coated 6-well plate and allowed to adhere overnight. The next day, cells are treated with 10nM Cycloheximide for 0, 30, 60, 120 or 180 minutes and lysed using the typical western blot as described above.

2.2.11 Subcellular fractionation

The procedure is performed according to the manufacturer protocol by ThermoFisher. $1.5x10^6$ cells were used to extract the different fractions and subject to a typical western blot as described. Calnexin is used as a marker for the membrane fraction, HDAC2 is used as a marker for the nucleus and Hsp90 is a marker for the cytoplasmic fraction.

2.2.12 Detecting secreted proteins and Zymography

$1x10^6$ cells were seeded onto a 6-well plate in full growth media overnight. The next day, the cells were washed 3X with PBS and the media was replaced with 2ml of serum free media and grow for 24h in the incubator. The next day, the conditioned media is collected and centrifuged at 2000rpm for 5min to get rid of cell debris. Transfer 1.5ml of the media into a 15ml 10kDa concentration tube and centrifuged at 3800g for 10min to concentrate the volume to 500μl. The concentrated media can be subjected to a typical western blot for protein level detection. Otherwise, the conditioned media can be subjected to a zymography protocol. In brief, the samples are run in Novex Tris-Glycine SDS running buffer. The gel is then incubated in 100ml of Renaturing buffer for 30min under gentle agitation at rt. The Renaturing buffer is then replaced with 100ml of Developing buffer and incubate for another 30min under gentle agitation at rt. The Developing buffer is replaced with a fresh 100ml of Developing buffer and the zymogram gel is incubated at 37°C overnight. The next day, the gel is washed 3X with deionised

water for 10min each before being stained in 40ml of SimplyBlue SafeStain undergentle agitation at rt. The gel can be viewed using the myECL Imager and analysed using ImageJ. This protocol is optimised from the one described here: http://protocol-place.com/assays/gelatin-zymography/gelatin-zymography-protocol/.

2.2.13 Fluorescent live-cell imaging of vesicle dynamics

Cells expressing fluorescently labelled proteins are plated on fibronectin-coated 35mm glass-bottom dish for 4h to fully adhere. Cells are imaged in an enclosed chamber supplied with 5% CO2 at 37°C and are typically imaged every 9s. Any additional treatment during the imaging process is added half-way through the imaging process. Images are acquired with the AiryScan Zeiss880 Super-resolution system with Plan-Apochromat 63x/1.4 oil DIC M27 lens coupled with digital deconvolution.

2.2.14 Long-term time-lapse imaging

$2x10^5$ cells are seeded on either fibronectin coated 6-well plate or CDM-coated 6-well plate for 4h to fully adhere. Cells are then imaged using the Nikon TE2000 microscope equipped with a PlanFluor 10x/0.30 objective every 15min for 20h. Individual cells are manual tracked using the MTrack ImageJ plug-in. The average velocity and spider plot of each cell are calculated using Chemotaxis tool ImageJ plug-in. Cells can also be stained with Calcein AM and images can be acquired for cell shape analysis.

2.2.15 Proliferation assay and wound-healing assay with the IncuCyte system

Both assays are done on fibronectin-coated 96-well plate.

Proliferation assay: $1x10^4$ cells are seeded into each well and stained with Nuclight rapid red reagent for the total number of cells and Sytox green reagent for dead cells. Images are acquired every hour for 48h and are analysed using the Zoom software (IncuCyte Biosciences, Sartorius).

#living cells(t_n) = #Nuclight-positive cells(t_n) – #Sytox green-positive cells(t_n)

The rate of proliferation = #Living cells(t_n) / #Living cells(t_0)

= number of

Wound-healing assay: $7x10^4$ cells are seeded into each well to form a cell monolayer. The wound is made using the IncuCyte wound maker. Images are taken every 1h for until the wound is fully closed. Analysis is done using the Zoom software.

Wound closing rate = $\sum$(Wound area(t_n) – Wound area(t_{n-1})) / t (um/h)

Wound confluence(t_n) = Area covered by cells(t_n) * 100 / Total area (%)

Rate of confluence = Wound confluence(t_n) / Wound confluence(t_0)

2.2.16 Inverted invasion assay

The plugs are made by mixing rat-tail collagen I, Matrigel and fibronectin (CFM plugs) in ice-cold PBS to the final concentration of 4, 4, 1 mg/ml respectively. 100ul of the mixture is pipetted into each of the transwells (8um pore) and let to solidify at 37°C. Once solidified, 100μl of cell suspension containing $5x10^4$ cells is pipetted at the bottom side of the transwell. The cells are left to settle and adhere for 4h in the incubator before the transwells are transferred to a new well containing 500μl of serum-free media. 100μl of full serum containing media is added on top of the CFM plug to act as a chemoattractant for the cells to migrate to. Inhibitors can also be included. Cells are left to invade for 5 days before being stained with 500μl of Calcein AM. The plugs are imaged in z-stack with 10μm distant using the Olympus FV1000 confocal microscope at UplanSApo 20x/0.74 objective.

Invasion index = ($\sum$Area of cells beyong 10um / $\sum$Area of cells in all slices) * 100%

2.2.17 Organotypic assay

The assay is done according to the published protocol by Paul Timpson "Organotypic Collagen I Assay: A Malleable Platform to Assess Cell Behaviour in a 3-Dimensional Context". In brief, collagen I is extracted from frozen rat tail using acetic acid. Collagen plugs are made by mixing collagen with TIF cells in a slightly alkaline pH adjusted by NaOH. The plugs are allowed to contract for 8 days until they can fit into a 24-well plate. $5x10^4$ cells are then seeded on top of the plugs and left to grow in full media for 5 days. The plugs are then transferred to a metal mesh placed inside a 6cm dish. Full media are added until touching the bottom of the metal mesh, creating a liquid-air interface. This interface acts as a chemoattractant to allow cells to invade into the plugs. Media are changed every

2 days for 2 weeks before the plugs are cut in half and fixed in 4% PFA and proceeded to H&E histology staining. The histology is analysed using HALO software.

Invasion index = (∑area of invading cells / ∑area of the tissue) * 100%

2.2.18 Agarose low attachment growth assay

Autoclaved 4% agarose in PBS solution is mixed with full growth media to the final concentration of 0.7%. 1.5ml of this is pipetted into a 6-well plate to form the bottom layer. 3x104 cells are mixed with the agarose and media to the final concentration of 0.35% agarose and 1.5ml of this solution is quickly pipetted to for the top layer. Finally, 2.5ml of either full growth or serum-free media are added on top. Any inhibitor is mixed with the top layer as well as the layer of the media on top to the desired concentrations. Cells are grown for 10 days before images are taken with a typical tissue culture bright-field microscope. Media are changed every 2 days. For each condition, 5 random images at x10 lens are taken and the size of the spheroids are manually measured using the Freehand selection tool in ImageJ.

2.2.19 Fluorescent Activated Cell Sorting (FACs) of surface proteins and ROS

Surface proteins:

$10x10^6$ cells are plated on 15cm dish overnight. The next day, cells are trypsinised and filtered through 0.45um filter to obtain a single cell solution. Cells are centrifuged at 1200rpm for 5min before being stained with Zombie Red reagent and fixed in 4% PFA for 15min. Cells are centrifuged and washed 1X with PBS before being blocked with ice-cold 10% serum-containing PBS for 30min. Cells are then centrifuged again and incubated with the corresponding primary antibodies for 15min without permeabilisation, washed with PBS and incubated with the secondary antibody for 15min if the primary antibodies are not fluorescently conjugated. Cells are washed again and kept in PBS to be analysed using the Attune NxT system. IgG is used for negative control. All samples are processed using the FlowJo sorfware (Becton Dickinson & Company, v. 10.6.1).

ROS production:

$3x10^5$ cells are seeded into 6-well plate, either scramble or CYRI-B KD. Cells can then be treated with either 20mM NAC for 60min, 100uM tert-Butyl hydroxyperoxide solution (H2O2) for 30min or both in the same order. Cells are then stained with CellROX Deep Red dye and DAPI before being trypisinised, wash with 1X PBS and then analysed using the Attune NxT system.

2.2.20 xCELLigence cell spreading assay

E-Plate 16 is coated with fibronectin for 2h prior to cell seeding. Single cell suspension of $1x10^5$ cells are seeded to each well in full growth media and immediately transferred to an Acea RTCADP xCELLigence device. Based on the degree of electrical impedance created by cell spreading, the cell index is calculated:

Cell $index_t = (Rce_t - R_b)/15$

Rce_t = cell-electrode impedance at time t

R_b = background impedance

15 is a constant value for the device

2.2.21 Cell derived matrix (CDM) with TIF cells

Plates are first coated with 0.2% gelatin (Sigma G1393 100mls, 2%) crosslinked by 1% glutaldehyde (Sigma G6257-mls, 25%) at rt for 30min. The plate is washed 2X with PBS and quenched with 1M glycine for 20min. TIF cells are seeded onto the gelatin coated plate in TIF media. Cells are fed with freshly made TIF media + ascorbic acid (1:1000 dilution) + Pen Strep solution (1:100 dilution) every 2 days. On the extraction day, cells are washed once with PBS at rt before lysed with extraction buffer (20mM NH4OH, 0.5% Triton X-100 in PBS with Ca^{2+} and Mg^{2+}) for 2min. Extraction buffer is aspirated, and DNase solution is added and incubated for 30min. The solution is aspirated, and the plate is washed twice with PBS. CDM plates are stored in PBS + Pen Strep (1:100 dilution) + Fungizone (1:100 dilution) at 4°C.

2.3 Protein biochemistry methods

2.3.1 Small scale GST-tagged protein purification

A colony of BL21 E.Coli containing the expression construct of a GST-tagged RAC1 is pre-inoculated in 200ml of LB in the presence of the appropriate antibiotic(s) at 37°C under constant shaking at 200rpm. The next day, 10ml of this preculture is added to 1L of LB with antibiotics and grow in the same condition. OD600 is checked until it reaches 0.4 then induced with 200μM of IPTG. Cells are left induced overnight at 18°C under constant rotation. The next day, cell pellet is collected by centrifugation at 2000rpm for 15min. The supernatant is discarded, and the pellet is suspended in 3ml of lysis buffer (containing DTT). The suspension is then lysed using sonication for 10sec for a total of 8 times, with 10sec break interval. The lysate is then centrifuged at 20,000rpm, 20min at 4°C using a Beckman Coulter Ultracentrifuge. The supernatant is aliquoted 1ml into 1.5ml Eppendorf tubes and stored at -80°C for preservation. At the same time, for each condition tested, pipette out 25μl of Glutathione sepharose bead suspension into a 1.5ml Eppendorf tube. The beads are washed 3 times with 500μl of ice-cold wash buffer and pelleted by centrifuging at 3000rpm, 2min at 4°C. The beads are then incubated with 1ml of bacterial lysate for 1h rotating at 4°C. Then, the beads are centrifuged at 3000rpm, 2min at 4°C and are washed 3X with wash buffer pH 7.5 and 1X with wash buffer pH 8. To elude the GST-tagged proteins from the beads, the beads are incubated in elution buffer (which contains 10mM Glutathione) overnight rotating at 4°C. It is crucial that the pH of the elution buffer is correctly adjusted back to 8 as Glutathione is slightly acidic and will decrease the pH when added. The next day, the beads are pelleted by centrifuging at 9000rpm at 4°C. The supernatant is now pipetted onto a Chromotek spin column and centrifuged at 3000rpm, 4°C for 3min to filter out any residual beads. The flow-through now contains the purified GST-tagged protein and can be aliquoted and stored at -80°C for future use.

2.3.2 In vitro pulldown assays

GST-Trap pulldown from cell lysate:

GST-tagged proteins are conjugated to Glutathione sepharose beads as described in 2.3.1 from bacterial lysate. The level of conjugation is estimated by staining InStant Blue and the amount of conjugated proteins are used between conditions. COS-7 cells are transfected with GFP-tagged constructs and lysed using GFP lysis buffer (containing 0.5% NP-40). The lysate is cleared by centrifuging at 15,000rpm for 10min. Protein level is estimated using PrecisionRed solution and 1.5mg of protein is used per condition. GST-conjugated beads are incubated with the cell lysate for 1.5h at 4^{o}C in rotating. The beads are then pelleted and washed 3X with wash buffer and then subjected to a standard western blot as described in 2.2.8. The pulldown signal is normalised to the GST signal detected from the beads.

MBP-Trap pulldown with recombinant proteins:

MBP-Trap beads are conjugated to MBP-tagged proteins the same way as for GST-tagged proteins described in 2.3.1 with the MBP beads are washed with the appropriate MBP wash buffer. Equal amount of conjugation is also tested. For each binding reaction, 30μl of MBP-conjugated beads (~6ug of protein) is mixed with 30μg of GST-tagged protein in binding buffer to the total volume of 500μl. The reaction is incubated at 4^{o}C with rotation for 1.5h before pelleting by centrifugation and washed 3X with the binding buffer and subjected to a standard western blot as described earlier. The membrane before being blotted with the primary antibody is incubated with PonceuS to reveal the loading amount for quantification later.

For competition assay, 30μg of GST-CYRI-B and increasing concentrations of untagged RAC1 are mixed with the MBP-CYRI-A beads and processed similarly.

2.3.3 Large-scale protein purification

The construct includes MBP-CYRI-A, MBP-CYRI-B, MBP-His-CYRI-A or MBP-His-CYRI-B. This is used for surface plasmon resonance (SPR) experiments and crystallography.

BL21 pLysS (Promega) cells expressing protein of interest is grown, induced and centrifuged in the same condition as described in 2.3.1. Into each bottle now left with bacterial cell pellet, add roughly 3ml of lysis buffer (containing BME).

Resuspend the bacterial pellet by vortexing. The bacterial cell suspension is then passage through a Microfluidizer at 20,000kPa twice to lyse. The lysate is collected and centrifuged for 45min, 20,000rpm at 4°C and filtered through 0.45μm filter. The filtered lysate is then loaded onto a corresponding affinity column eg. GST-Trap, MBP-Trap, His-Trap. The column is then washed with 50ml of lysis buffer before being cleaved overnight with thrombin if the desired protein is untagged. The next day, the flow through is loaded onto a 75 pg size exclusion gel filtration column that has been calibrated with the appropriate size exclusion buffer. The different fractions are collected, run and examined for the correct molecular size on a 4-12% NuPAGE SDS gel using Instant Blue staining. The fractions containing the most amount of protein are pooled together and concentrated using the concentration column (10kDa size cut-off, Amicon, #UFC801024) and aliquoted and stored at -80°C.

2.3.4 Determining the crystal structure of CYRI-BΔN and CYRI-BΔN-RAC1 Q61L fusion

This protocol is performed by Dr. Tamas Yelland, a post-doc from Dr. Shehab Ismail's lab in collaboration with us.

Purification of seleno-methionine substituted MBP-His-CYRI-BΔN:

B834(DE3) expressing the protein construct was grown overnight before 10ml of the preculture is transferred to 1L of unlabelled medium (Molecular Dimensions) and grow until OD600 reaches 0.5. Cells were pelleted by centrifugation and washed 3X in PBS before incubating in seleno-methionine containing medium for 40min at 20°C. Cells are then induced with 0.4mM IPTG for 16h. The next day, cells are lysed using the microfluidizer 20,000 psi in a buffer containing 50mM Tris pH 8.0, 300mM NaCl, and 5mM BME. The lysate is loaded onto a His-Trap column before washing with 20mM Imidazole and then eluded using an imidazole gradient from 0-300mM. Fractions were pooled and dialysed overnight at 4°C in the presence of TEV in a buffer containing 20mM Tris pH 8.0, 150mM NaCl, 5mM imidazole, and 2mM BME. The next day, the protein is passed through a His-Trap column and the flow through is collected, pooled and concentrated before loaded onto a 200 pg insert "Superdex" before 75 pg and 200 pg size exclusion column equilibrated in 10mM Tris pH7.5, 50mM NaCl and 2mM DTT.

Purification of seleno-methionine substituted MBP-His-CYRI-BΔN-RAC1 Q61L fusion protein:

The procedure is the same as for MBP-His-CYRI-BΔN. After the second His-Trap purification, the flow throughs are pooled and concentrated to 1ml. Nucleotide exchange is performed by adding 50mM EDTA, then add GppNHp at a 10:1 molar ratio (1 molecule of RAC1 Q61L is exposed to 10 molecules of GppNHp) and incubate for 2h. Once finished, the mixture is loaded onto a 200 pg insert "Superdex" before 200 pg size exclusion column that has been equilibrated with a buffer containing 10mM Tris pH 8.0, 50mM NaCl, 4mM MgCl2 and 5mM DTT.

Crystallisation of seleno-methionine labelled CYRI-BΔN with native RAC1 Q61L:

Initial rectangular crystals of CYRI-BΔN were obtained in Morpheus G8 at 291K at 8mg/ml following a larger crystal screen. These will then be selected and optimised using reagents containing 0.1M carboxylic acid, 8% MPD_P1K_P33 and 0.1M MOPS/HEPES-Na pH 8.0 (Molecular Dimensions). Crystals were cryo-protected in the same condition with 20% MPD_P1K_P33 and flash frozen in liquid nitrogen.

Crystals of CYRI-BΔN-Rac1Q61L were obtained in PolyEthylene Glycols II (PEGsII) C6 at 11mg/ml and were optimised to contain 8% v/v PEG4,000, 0.1M Tris pH 8.5 and 0.2M sodium acetate at 279K. Crystals preserved in liquid nitrogen in a cryoprotectant containing the reservoir solution and 25% v/v glycerol. Data were collected at Beamlines I03 and I04 at the Diamond Light Source. Details can be found in (Yelland et al., 2020).

2.3.5 Surface Plasmon Resonance (SPR)

Purified proteins from large-scale purification is used for SPR due to its high purity. Anti-MBP antibody is added to size-exclusion buffer and then immobilised onto CM5 gold Sensor chip. MBP, MBP-CYRI-A or MBP-CYRI-B is then flown through to immobilise on the chip to reach approximately 10,000 units. Then purified untagged RAC1 Q61L are flown into each of the channel with increasing concentrations from 0 to 80μM. From here, a kinetic graph is generated using the Biacore T200 software and fitted to estimate the Kd of the interaction between active RAC1 and CYRIs.

2.3.6 In vitro tubulation assay with liposomes

This experiment is performed in collaboration with Professor Hongxia Zhao at the University of Helsinki. We provided the purified proteins while the assay is performed by people from Professor Hongxia Zhao's lab.

Materials

1-Palmitoyl-2-oleoyl-*sn*-glycero-3-PC (POPC), 1-palmitoyl-2-oleoyl-*sn*-glycero-3-PE (POPE), 1-palmitoyl-2-oleoyl-*sn*-glycero-3-phosphatidylserine (POPS) were purchased from Avanti Polar Lipids.

Preparation of Unilamella Vesicles

Lipids were mixed and dried under a stream of nitrogen, and further maintained under vacuum for at least 2h to remove the remaining organic solvent. The dry lipids were hydrated in 20 mM HEPES, pH 7.4, and 150 mM NaCl for 1h at room temperature and unilamellar vesicles were obtained by extrusion though a polycarbonate filter (400-nm pore size) using a mini extruder (Avanti Polar Lipids).

Electron microscopy

The negative-staining samples were prepared by mixing 0.8μM protein with 250μM unilamellar vesicles (with a diameter of 400 nm) in 20 mM Hepes buffer, pH 7.5, and 150 mM NaCl at rt. The mixture was applied to the glow-discharged Pioloform (Agar Scientific)- and carbon-coated copper grids and stained with 3% uranyl acetate. At each step, excess solution was removed by filter paper. The membrane morphologies were examined with JEM-1400 (Jeol) with a Orius SC 1000B bottom-mounted charge-coupled device camera (Gatan). The lipid composition was POPC:POPE:POPS= 65:15:20. Untagged CYRI-A can must be used at the first thaw and cannot be refrozen.

2.4 Molecular biology methods

2.4.1 PCR and DNA electrophoresis

For a typical PCR reaction, 10ng of DNA is mixed with 100ng of each forward and reverse primers in 10μL of 2X PrimeStar Max Premix to the total volume of 20μl. The reaction was carried out in a BioRad Thermocycler as followed:

1) 5min at 98°C
2) 10sec at 98°C
3) 15sec at Tm (specific for each primer set)
4) 1min/kb at 72°C
5) Repeat steps 2-4 for 20 cycles
6) 15min at 72°C
7) Keep at 4°C until used

The product is mixed with 1X loading sample buffer and run in a 1% agarose gel supplemented with 0.001% Midori green for 35min at 100V and viewed under a long wavelength UV light. The product is excised out by scalpel and recovered using the Zymoclean DNA gel recovery kit exactly according to the manufacturer's protocol.

2.4.2 Restriction digest

All digestion is performed with restriction enzymes and buffers purchased from NEB. A typical reaction contains 10μl of DNA sample, 1μl of each restriction enzymes, 1X buffers and dH2O to 20ul total. Restriction digest is typically allowed for 1h at 37°C but can also be digested overnight. DNA plasmid is also dephosphorylated using CIP phosphatase to increase efficiency. The mixture is then purified using the Zymogen DNA purify and concentrator kit.

2.4.3 Ligation

Ligation reaction is performed using the Rapid DNA ligation kit. A typical ligation reaction contains an insert to vector ratio of 1 in 5, 1μl of the ligase and 2μl of ligation buffer, dH2O to 20μl final volume. The reaction mix is incubated for 5-15min at rt before transformation.

2.4.4 Transformation of competent cells and colony selection

50μl of DH5α or 100ul of BL21 (for protein production) is added to a 6ml plastic tube on ice. No more than 100ng of DNA is added to the bacteria and gently flicked to mix and incubated on ice for 15min. The bacteria are heatshocked at 42°C for 50s before resting again on ice for 2min. Then 3.5ml of SOC media is added and incubated at 37°C with constant agitation at 200rpm for 1h before 100μl of the cell suspension is spread on agar plate containing the suitable antibiotics. The next day, at least 8 colonies are selected, grow in 3.5ml of LB overnight before the cells are pelleted and sent to the central service for sequencing.

2.4.5 Q5-site directed mutagenesis

The primers are designed using the NEBaseChanger website (https://nebasechanger.neb.com/). The reaction is performed according to the guideline by NEB. Briefly, 10ng of parental backbone is mixed with 0.5μM of each primer and 1X of Q5 Hot start high-fidelity master mix to the final volume of 20μl. The PCR is as followed:

1) 30sec at 98°C
2) 10sec at 98°C
3) 15sec at Tm (specific for each primer set)
4) 30sec/kb at 72°C
5) Repeat steps 2-4 for 25 cycles
6) 2min at 72°C
7) Keep at 4°C until use

1μl of the mixture after PCR is then used for ligation and the parental DNA is digested using KLD mix. It is then transformed into competent DH5α cells as described in 2.4.4.

2.4.6 Quantitative RT-PCR (qRT-PCR)

RNA extraction from cell is performed according to the protocol using the RNeasy mini kit. The purity of the RNA sample is checked using the Nanodrop. RNA is then converted into cDNA using the qScript cDNA Synthesis Kit. 1μg of RNA is mixed with 1X qScript mix to the final volume of 20μl as followed:

1) 5min at 25°C

2) 30min at 42°C

3) 5min at 85°C

4) Keep at 4°C

A master mix containing Primer Master Mix, nuclease-free H_2O and 2x DyNAmo HS SYBR Green qPCR mix in the ratio of 1.5 : 2.5 : 5 respectively is made. Primers for genes of interest is purchased from Qiagen. For each qPCR reaction, 10μM of each primer is mixed with 9μl of the Primer Master Mix and 1μl of the cDNA mix in each well of the MicroAmp Optical 96-well reaction plate. The qPCR reaction is done using the QuantStudio Real-Time PCR system as followed:

1) 3min at 95°C

2) 20sec at 95°C

3) 30sec at 57°C

4) 30sec at 72°C

5) 40 cycles of steps 2-4

6) 5min at 72°C

Each condition contains 3 technical replicates as well as a negative control containing dH2O and ACTB and GAPDH as housekeeping control gene. The fold change is calculated using the $\Delta\Delta C_t$ method:

$\Delta C_t = C_t$(gene of interest) – C_t(housekeeping gene)

$\Delta\Delta C_t = \Delta C_t$(treated condition) - ΔC_t(untreated condition)

Relative fold difference = $2^{-\Delta\Delta Ct}$

C_t = the cycle threshold of the sample, Δ = the difference between two conditions.

2.4.7 RNA sequencing

$5x10^6$ cells of the control pLKO, DBKO1 or DBKO2 were seeded one day prior to RNA extraction. After 24h, RNA was extracted using Qiagen RNeasy mini kit according to the manufacturer protocol. One microgram of RNA per sample in a total of 4 biological replicates was sent for sequencing using an Illumina NextSeq 500 sequencer.

2.5 Subcutaneous injection model

This work is done with the help of a former postdoc Karthic Swaminathan.
Mel-11 transformed melanocytes are grown to 80% confluence before trypsinised and resuspended in full growth media as described in 2.2.1. Trypsin is washed away and replaced with fresh media. $1x10^6$ cells are counted and suspended in 100ul of media and is then injected subcutaneously to the right flank of C57BL/6 mice. For each cell line, 8 mice were used. Cells are left to grow for 1 week before the first check and after this, mice are checked every 2-3 days and tumour is measured. Mice are sacrificed when the tumour reached the 12mm in size or show sign of bleeding. Tumour, skin, liver, lungs and lymph nodes are collected for histology staining for H&E and Ki67.

2.6 Statistical analysis

All experiments are performed at least 3 times independently, unless stated otherwise. Unpaired t-test and paired t-test are used for to compare the mean between 2 samples, while ANOVA with multiple comparison is used for 3 or more samples. For all experiments, each data point is a cell and all data from each independent replicate is pooled except for Figure 3.16 where data are plotted in a superplot (Lord et al., 2020) format to illustrate a different way of analysing the data. Both ways of representing data can have pros and cons. Pooling all data point from each biological replicate risks of the type 1 error or false positive due to high number data points. While superplot reduces this to the number of biological replicates (typically N=3), which reduces the power of the test and risks of type 2 error or false negative at $p<0.05$, which can potentially lead to loss of data with interesting biological significance. We chose the first way of representing the data but carefully evaluate the exact value of the p value of each dataset to make sure the statistical analyses represent what was being observed. Graphs represent mean value with error bars are S.E.M unless stated otherwise. All statistical analyses are done using Graphpad Prism software.

3 Biochemical characterisation of the CYRI protein family: CYRI-A and CYRI-B

3.1 Introduction

At the time when this project was first initiated, nothing was known about the function of CYRI-A. Much effort was directed towards deciphering the roles of its cousin protein CYRI-B, both by our lab and also others. All of these studies while utilising multiple different systems ranging from epithelial cells (Fort et al., 2018), T-cells (Shang et al., 2018) to mouse model (Yuki et al., 2019) agreed on one major molecular event: CYRI-B interacts specifically to active RAC1. Since CYRI-A and CYRI-B share at least 80% sequence identity with very similar predicted crystal structures, we decided to query whether CYRI-A could do the same. In this chapter, by utilising *in vitro* pulldown assays and surface plasmon resonance (SPR), we set out to answer the questions of whether CYRI-A would be able to interact with active RAC1 and at what affinity. Furthermore, based on previous proteomic analysis, we revealed a potential homo- and hetero-dimerization between CYRI-A and CYRI-B. We compared our proteomic data with public databases and confirmed using *in vitro* pulldown assays and *in vivo* proximity ligation assays.

3.2 Results

3.2.1 Sequence and structural comparison between CYRI-A and CYRI-B

CYRI-A and CYRI-B are both derived from the same ancestral gene about 800 million years ago and through the process of gene duplication, the two paralogous isoforms were created. By definition, paralogues are genes that were diverged from one common gene but reside in different locations in the same genome. Paralogues can harbour enough random mutations to start having divergence in their functions. The CYRI-A protein has 323 amino acids while CYRI-B has 324. Comparing their sequences shows that the vast majority (80%) of the amino acid sequence is similar (Figure 3.1A). CLICK chemistry experiments done on CYRI-B has shown that the 2nd glycine residue is a site for myristoylation, which

is thought to be important for the function of CYRI-B at the membrane to sequester active RAC1 (Fort et al., 2018). This site is conserved between CYRI-A and CYRI-B. The two arginine residues of CYRI-B (160/161), which are important for active RAC1 binding, are also present in CYRI-A (159/160). The one major difference between the two proteins at the amino acid sequence is the presence of the 10th cysteine residue in CYRI-B but is missing in CYRI-A. This cysteine is predicted to be important for palmitoylation-a reversible post-translational modification thought to be important for membrane localisation. The importance of this difference remains unknown. Since no crystal structure for CYRI-A is available, we made use of an online structure predicting software, I-TASSER (https://zhanglab.ccmb.med.umich.edu/I-TASSER/). Interestingly, I-TASSER makes use of the existing crystal structure of CYFIP, which shares about 18% sequence identity with CYRI-A to help with the prediction. The predicted structure of CYRI-A shows an L-shape protein with its first α helix (amino acid 1 to 18) connected to a compact domain composed of 12 α helices (α2 to 13) (known as the Domain of Unknown Function 1394 or DUF1394) via a flexible linker of 11 amino acids (Figure 3.1B, i). Overlaying the two predicted structures of CYRI-A and CYRI-B shows a remarkably similar 3D organisation (Figure 3.1B, ii). However, when we classify the surface amino acid side chains according to their polarity properties (Figure 3.1C), we found that the N-terminal helix of CYRI-A is decorated with a continuous stretch of hydrophobic residues on one side (black dotted line) and a continuous stretch of hydrophilic residues on the other (red dotted line). On the contrary, CYRI-B's helix lacks this polarity with the inner side is patched with alternate hydrophilic (red dotted lines) and hydrophobic regions. In another word, CYRI-A is predicted to contain an amphipathic N-terminal helix. An amphipathic helix is a common mechanism for many proteins such as the small GTPases ARF used to anchor itself to the plasma membrane (Gimenez-Andres et al., 2018, Lundmark et al., 2008). We hypothesised that this helix may also serve the same function for CYRI-A, allows the protein to bind to the membrane, perhaps in compensation for the lack of a potential palmitoylation site at 10th cysteine residue. This could potentially allow for differences in membrane binding kinetics between the two isoforms.

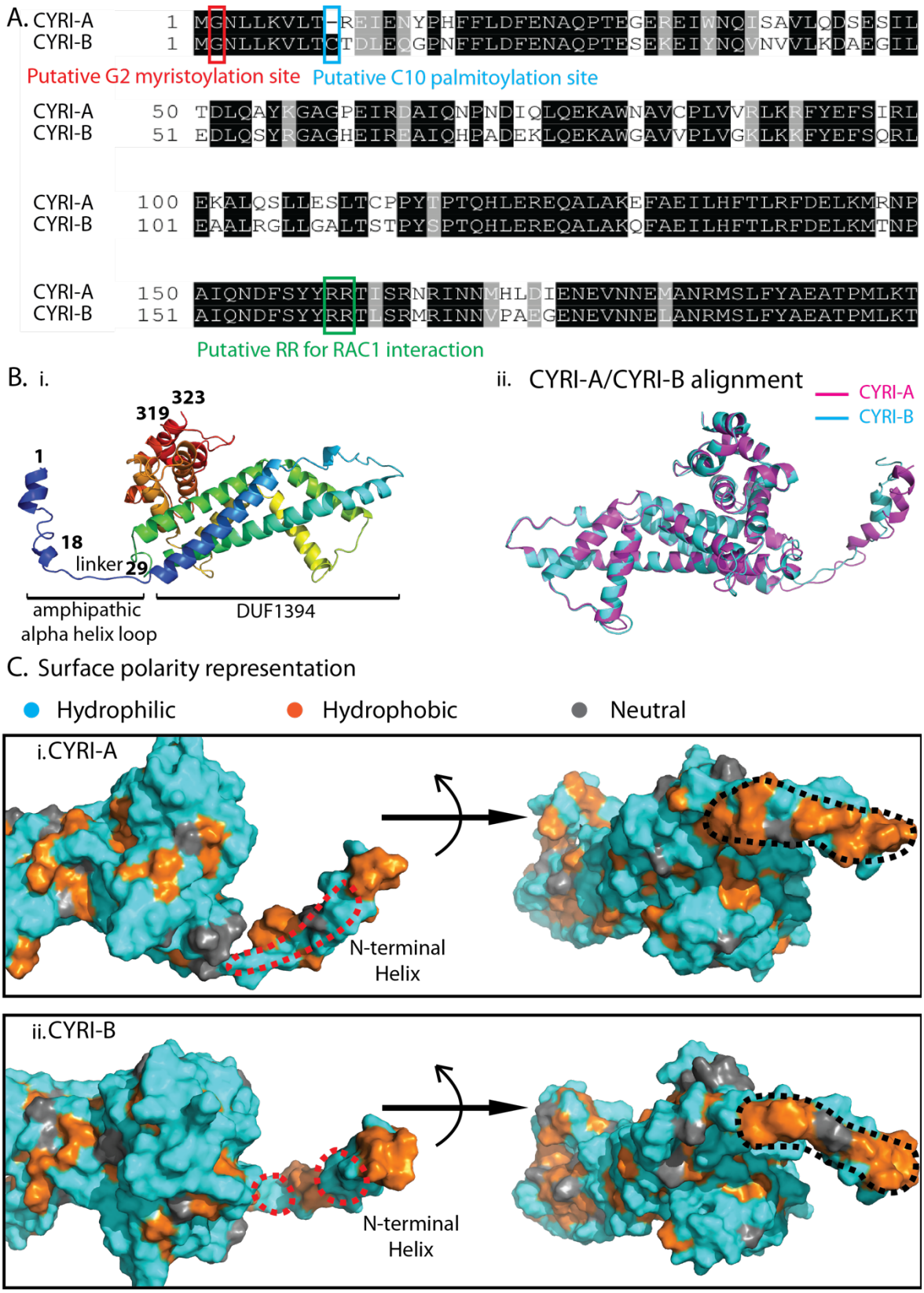

Figure 3.1 Protein sequence and structural analysis comparison of the CYRI protein family

A. Protein sequence comparison between mouse CYRI-A and CYRI-B shows an 80% sequence identity shared between the two. Both contain the conserved 2nd Glycine residues (red box) for myristoylation and the two Arginine residues (159/160 for CYRI-A and 160/161 for CYRI-B) (green box) for RAC1 interaction. CYRI-A lacks the 10th cysteine residue (cyan box) that is thought to be important for palmitoylation.

B. i) Domain structures of the predicted crystal structure of CYRI-A. ii) Structural alignment of the predicted crystal structures of CYRI-A (magenta) and CYRI-B (cyan).

C. Surface polarity comparison between CYRI-A and CYRI-B. Orange represents hydrophobic residues, cyan represents hydrophilic residues and grey represents neutral residues. Red dotted line highlights hydrophilic regions, black dotted line highlights hydrophobic regions.

3.2.2 CYRI-A binds active RAC1 and is autoinhibited by its N-terminal α-helix

CYRI-B binds active RAC1 and is regulated by its N-terminal helix *in vitro*. Previous reports proposed the N-terminal helix (amino acid 1 to 29) as an autoinhibitory loop for the protein (Fort et al., 2018). In the presence of this loop, the RAC-Binding Domain (RBD) of CYRI-B (amino acid 30-236), which belongs to the DUF1394 domain was unable to interact with the active RAC1 from cell lysates in pulldown experiments (Fort et al., 2018). We decided to generate similar protein constructs for CYRI-A to test out this hypothesis. The DUF1394 domain of CYRI-A is predicted to be from the amino acid 29 to 319, so to specifically test for the binding capacity of this domain, we decided to retain its whole sequence integrity. The N-terminal helix of the protein is either retained or deleted (amino acid 1 to 28). Both of these constructs were then conjugated to a GFP protein and transfected into COS-7 cells. Recombinant GST-tagged proteins were generated through using an *in vitro* E.Coli bacterial system and immobilised onto glutathione beads. The CRIB domain of PAK was used as our positive control and GFP as our negative control for active RAC1 binding (here used RAC1 Q61L - a constitutively active mutant). Cell lysates were incubated with beads containing the GST-tagged protein for 1h (Figure 3.2A). As expected (Figure 3.2B), GFP only resulted in no detectable binding to any of our GST constructs, reassuring that any detectable binding was not due to non-specific interactions with the fluorescent protein. The positive control CRIB domain strongly interacted with the GST-RAC1 Q61L suggests that our experimental conditions were suitable for the interaction to occur.

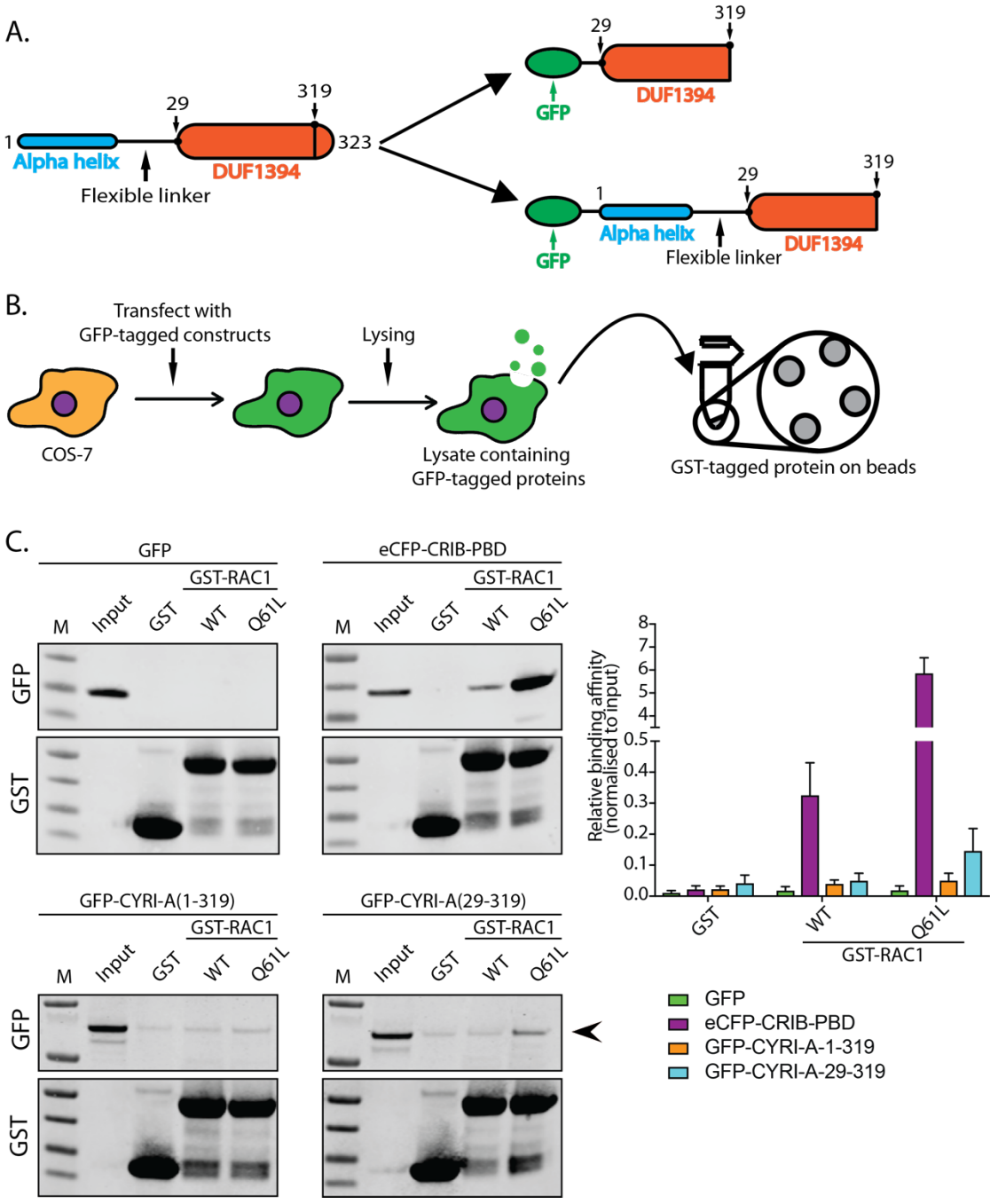

Figure 3.2 CYRI-A interacts with active RAC1 in vitro

A. The schematic representation of the two constructs of GFP-tagged DUF1394 of CYRI-A

B. The schematic representation of the *in vitro* pulldown used to detect CYRI-A and RAC1 interaction.

C. Representative western blot of the *in vitro* GST pulldown assay. 4 conditions: GFP, eCFP-CRIB-PBD, GFP-CYRI-A(1-319) and GFP-CYRI-A(29-319) are being tested against GST, GST-RAC1 WT and GST-RAC1 Q61L. The arrow shows that only when the N-terminal helix is removed then the DUF1394 domain of CYRI-A can bind active RAC1. Graph (right) shows the quantification from at least 3 independent experiment. Mean ± SEM.

GST-RAC1 WT also had a weak interaction with the CRIB domain, possibly due to the residual amount of bound GTP present in the protein from the bacteria. However, this interaction is considerably weaker compared to the Q61L mutant. Consistent with our prediction, the DUF1394 domain of CYRI-A was able to interact with active RAC1 (black arrow), despite being relatively weaker compared to the CRIB domain. Furthermore, this binding under these particular experimental conditions was only possible when the N-terminal helix was removed, evident by the fact that the construct containing the N-terminal helix produced no detectable signal with the active RAC1. This is similar to what was found with CYRI-B and was proposed that the N-terminal helix acts as a negative regulatory loop that inhibits CYRI's active RAC1-binding function. RAC1 WT, on the other hand, did not show any significant signal with CYRI-A. These data confirmed that CYRI-A can specifically bind active RAC1 through an autoinhibitory regulation mechanism similar to CYRI-B.

3.2.3 Surface Plasmon Resonance (SPR) confirms the direct interaction between CYRI-A and active RAC1 with a stronger affinity than CYRI-B

The interaction affinity, which can be interpreted as the dissociation constant Kd between the RBD of CYRI-B and active RAC1 was reported to be around 20μM (Fort et al., 2018). This is a weak interaction and was suggested to be compensated by the natural abundance of CYRI-B in the cell. However, CYRI-A, based on our experience, is much less abundant compared to CYRI-B in various cell types that we tested. So, for the protein to be able to bind active RAC1 inside cells, we hypothesised that perhaps CYRI-A needs to possess a higher affinity to active RAC1 to compensate for its lower abundance. To address this question, we turned to a quantitative method known as Surface Plasmon Resonance (SPR) (Figure 3.3A). Since the GST-tagged CYRI-A was completely insoluble in solution and could not be purified, we turned to MBP-tagged of the full-length version of both CYRI-A and CYRI-B to be immobilised bait proteins. For the prey protein, we used full-length RAC1 Q61L produced from digesting GST-tagged of the protein with thrombin. SPR is sensitive to protein concentrations. Once we have saturated the chip platform with MBP-CYRIs, to capture the kinetics of the interaction binding, RAC1 Q61L had to be used at a wider serial dilution, which we chose to range from 0 to 80μM. This ensured that any biologically interesting interaction

with a dissociation constant larger than 20μM could still be captured. Figure 3.3B, C show the calculated binding kinetic for both CYRI-A and CYRI-B to active RAC1. The Kd value of CYRI-B was within the range of the previously reported value (~18.3μM) suggesting that our experimental conditions faithfully recapitulated previous reports. Interestingly, the binding of CYRI-A to RAC1 reaches saturation at 20μM, much earlier than our maximum value at 80μM. This converts into a Kd of 2.47μM, suggesting that the binding affinity of CYRI-A is about 10 times (1 order of magnitude) stronger than that of CYRI-B. Figure 3.3D, E show the raw response curve. Each peak represents the strength of the signal at different concentrations. The drop in the signal represents the wash phase in between injections. As can be seen, for CYRI-B, the protein was soluble, each wash completely restored the baseline signal. However, for CYRI-A, since the protein was more insoluble, the recovery phase was not as efficient, with each wash led to a slight accumulation of unfolded proteins. The response signals between the two proteins were also different, 0 to 150 for CYRI-A compared to 0 to 500 in CYRI-B. This might potentially be due to the differences in the purity of each protein, which leads to the difference in the number of active molecules (aka response signals) between CYRI-A and CYRI-B even though the total protein concentration loaded are the same. However, it is important to note that these values did not affect the calculated Kd, but rather suggested the relative proportion of active molecules present within the population. This means that for CYRI-A, even with a smaller percentage of active molecules, its lower Kd value reassures our observation that CYRI-A still retains a higher affinity to active RAC1 than CYRI-B. All of these details were taken into account when the Kd values were calculated.

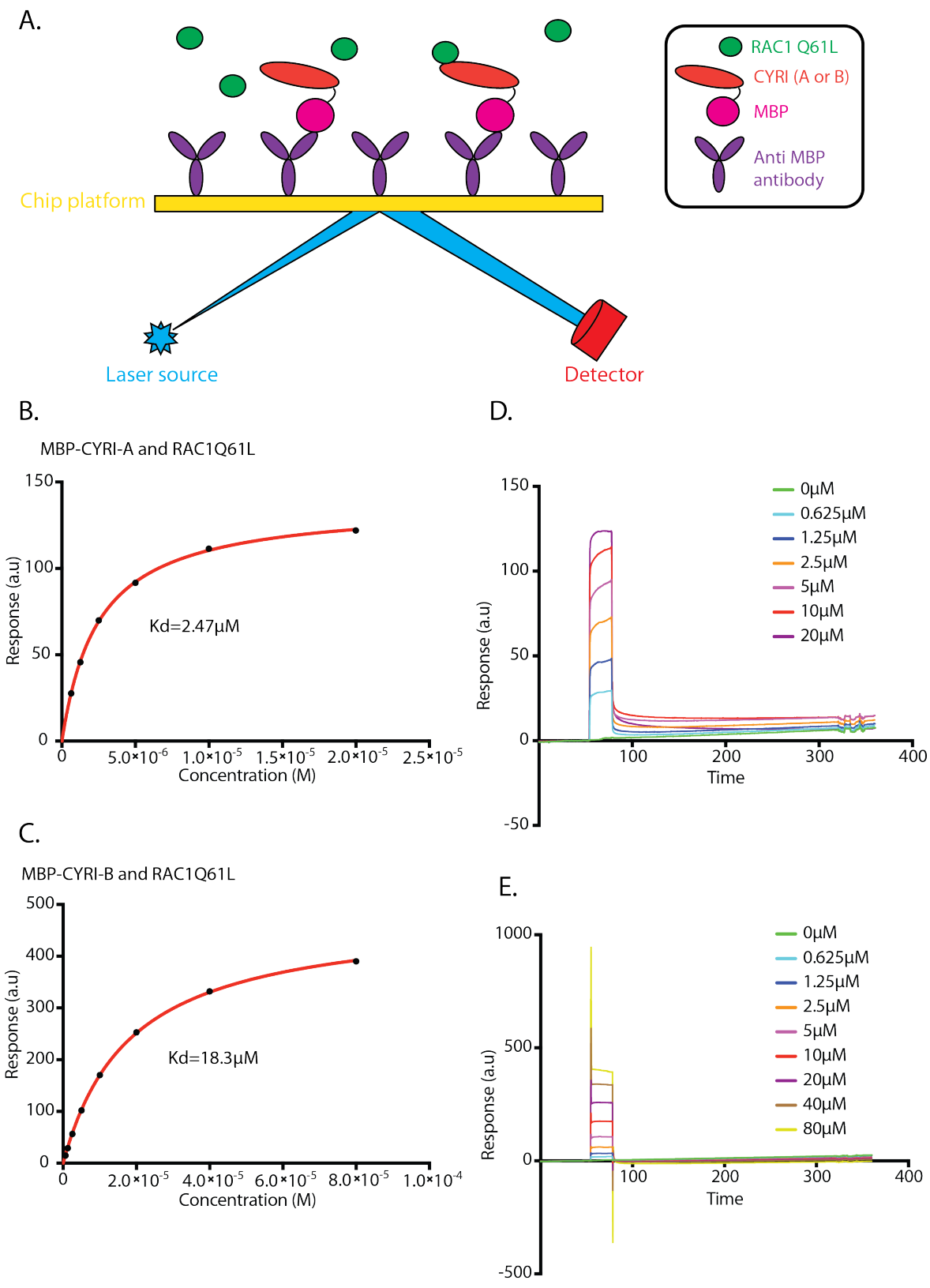

Figure 3.3 Surface Plasmon Resonance (SPR) comparing the active RAC1 binding affinity between CYRI-A and CYRI-B

A. Schematic representation of how SPR works. In brief, anti-MBP antibodies are adsorbed on the chip platform (usually made from metal, here is gold). MBP or MBP-tagged of full-length either

CYRI-A or CYRI-B is then captured by the antibodies. Then untagged full-length active RAC1 Q61L molecules are injected into each channel at various concentration. If a binding event happens, this will change the absorption profile of the incident light and can be converted into measurable signal and thus the dissociation constant Kd of that interaction event.

B, C. The calculated binding curves for both proteins based on the raw profiling curves on the right-hand side. The measured Kd for CYRI-B is around 18.3μM, which is approximately equal to what has been reported (Fort et al., 2018). The Kd for CYRI-A is about 1 order of magnitude higher at about 2.47μM.

D, E. The raw binding response curve for both CYRI-A and CYRI-B at different RAC1 concentrations.

3.2.4 CYRIs form homo- and heterodimeric complexes

Previous proteomic analysis of GFP trap for CYRI-B in COS-7 cells (Loic Fort thesis) revealed CYRI-A to be a significant protein interactor with CYRI-B. This was interesting because it hinted us to a novel mechanism of oligomerisation between CYRI molecules that potentially is biologically significant. We first used bioinformatic analysis of public proteomic databases to search for whether this potential interaction had been documented. We used 3 independent curated interactome databases: STRING (https://string-db.org/) (Szklarczyk et al., 2019), BioGRID (https://thebiogrid.org/) (Oughtred et al., 2019) and IntAct-EMBL (https://www.ebi.ac.uk/intact/?conversationContext=3) (Orchard et al., 2014). These databases import protein-protein interactions that have been detected experimentally, through direct deposition or literature curation with manual or automatic correction. STRING and BioGRID databases also specify the type of interaction between the queried proteins, either physical or genetic interactions. From all three databases, CYRI-A and CYRI-B were both predicted to be physically interacting with each other (Figure 3.4).

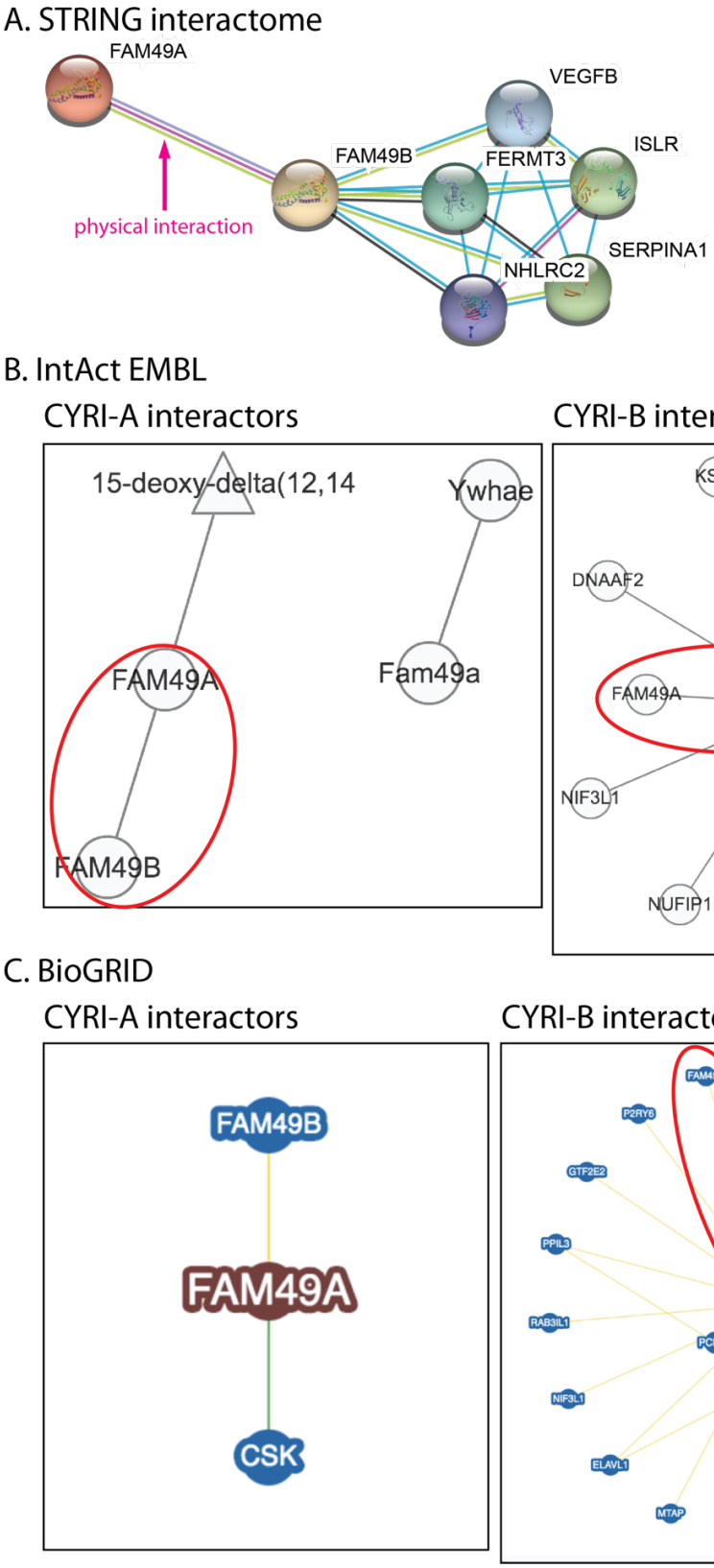

Figure 3.4 Interactome analysis of CYRI-A (Fam49A) and CYRI-B (Fam49B)

A) STRING, B) IntAct-EMBL and C) BioGRID database suggest a physical interaction between CYRI-A and CYRI-B exists (red circles). Data are curated and/or imported from the literature automatically or manually.

To confirm these predictions, we performed MBP-trap pulldown experiments using recombinant CYRIs as baits similar to what used for the SPR experiment. MBP-tagged CYRI-A was immobilised onto MBP-trap beads and incubated with 30μg of either purified GST-tagged RAC1 WT as the negative control, GST-tagged RAC1 P29SQ61L mutant as the positive control (Fort et al., 2018,Chen, 2017 #142) or GST-tagged CYRI-B

Figure 3.5A). Binding was detected using an anti-GST antibody. RAC1 WT did not show any detectable interaction as predicted, while the double mutant RAC1 P29SQ61L showed a striking interaction band. Interestingly, we also detected a weak but consistent signal between CYRI-A and CYRI-B (

Figure 3.5A, arrow). Coomassie gel showed an equal loading of GST-tagged proteins, ruling out any artefact due to unequal protein amount. Quantification showed the CYRI-B signal was significantly stronger compared to RAC1 WT signal. The existence of the heterodimeric interaction leads us to wonder whether a homotypic interaction was also possible. We performed pulldown experiments with both the MBP-tagged and GST-tagged CYRI-B (

Figure 3.5B). Using the same set up as before, we observed a detectable signal between CYRI-B molecules. These data provided the evidence for the existence of a direct homo- and heterotypic interaction between CYRI molecules *in vitro*.

To test whether CYRI oligomerisation also happened *in cellulo*, we utilised a technique called proximity ligation assay (PLA) (Figure 3.6A). The general principle of the technique relies on the fact that for the two proteins to interact with each other, they need to be in proximity to each other. We first use primary antibodies of two different species i.e. rabbit and mouse to specifically recognise each protein. We then applied the corresponding oligonucleotide-conjugated secondary antibody on the sample. If the two proteins are in proximity from each other (where their epitopes are no more than 40nm apart), upon adding specific DNA primers, the two oligonucleotides on the secondary antibodies will be able to form a circularised oligonucleotide. By adding a mixture containing a polymerase and fluorescently labelled nucleotides, the amplified signal from the polymerisation reaction can be detected as fluorescent dots using any standard

confocal microscope. We co-transfected COS-7 cells with a FLAG-tagged CYRI-A and an internal HA-tagged CYRI-B construct (P17-HA-CYRI-B).

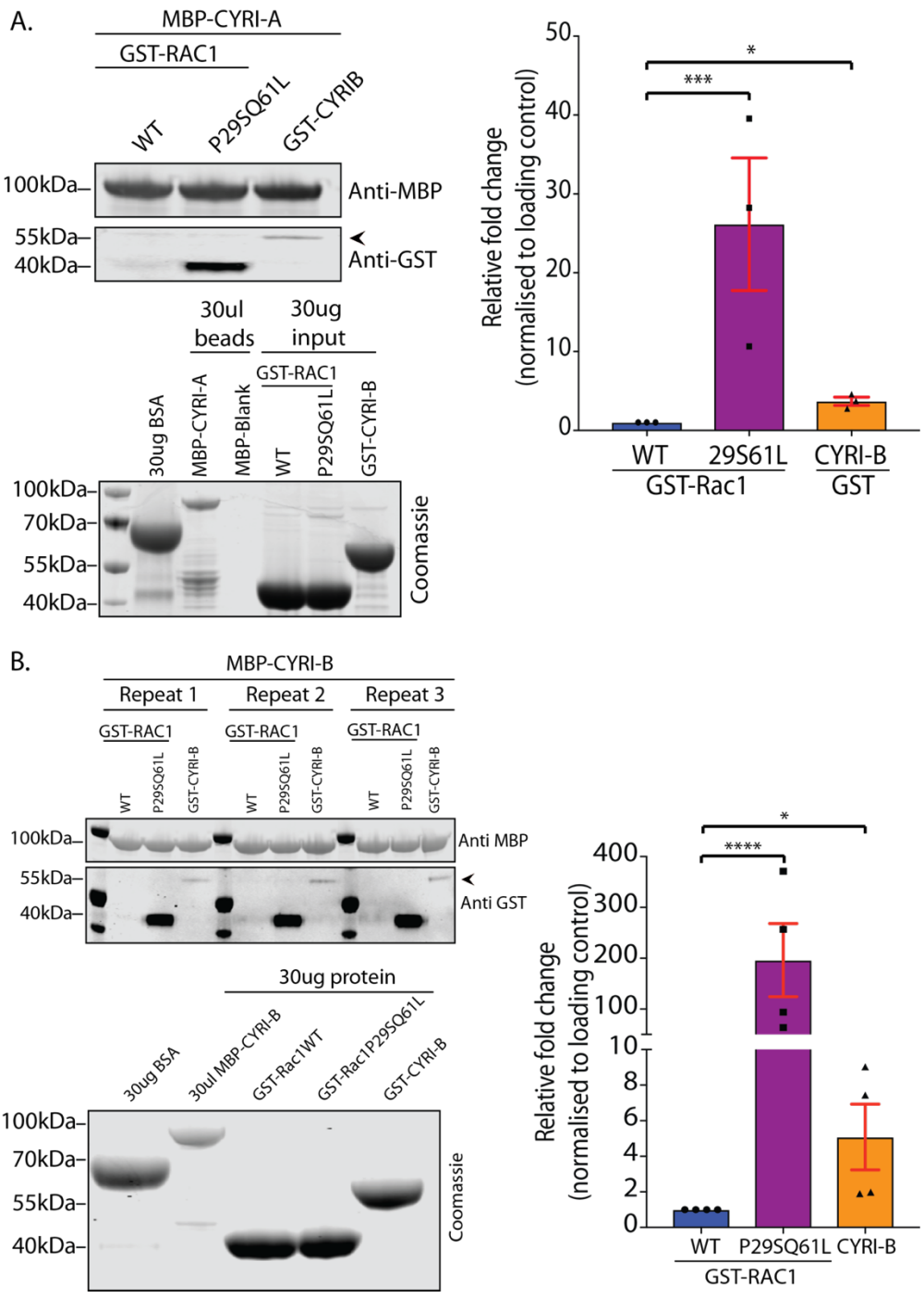

Figure 3.5 CYRI proteins could form hetero- and homotypically complexes

A. MBP-tagged CYRI-A interacts with GST-tagged CYRI-B. The right graph shows the quantification from 3 independent experiments. Signals were normalised to MBP loading.

B. MBP-tagged CYRI-B interacts with GST-tagged CYRI-B. The right graph shows the quantification from 4 independent experiments. Signals were normalised to MBP loading.

Statistical analysis uses ANOVA with multiple comparisons of log base 10 transformed data points. Mean ± SEM. *p<0.05, ***p<0.001, ****p<0.0001.

We checked for the functionality of the CYRI-B construct and indeed the HA tagged protein was able to rescue CYRI-B KO COS-7 cells (Figure 3.7). The FLAG-tagged CYRI-A construct is also functional and will be revisited in chapter 4. The strategy and the purposes of making internally tagged CYRI constructs will be discussed in detail in Chapter 5. Figure 3.6B shows that only COS-7 cells containing both constructs with both the anti-FLAG and the anti-HA antibody showed detectable PLA signals. Quantification showed the significantly higher signal detected in the "FLAG+HA" condition compared to conditions with no antibodies or only one antibody. These data provide the evidence for the existence of a heteromeric complex between CYRI molecules *in cellulo*.

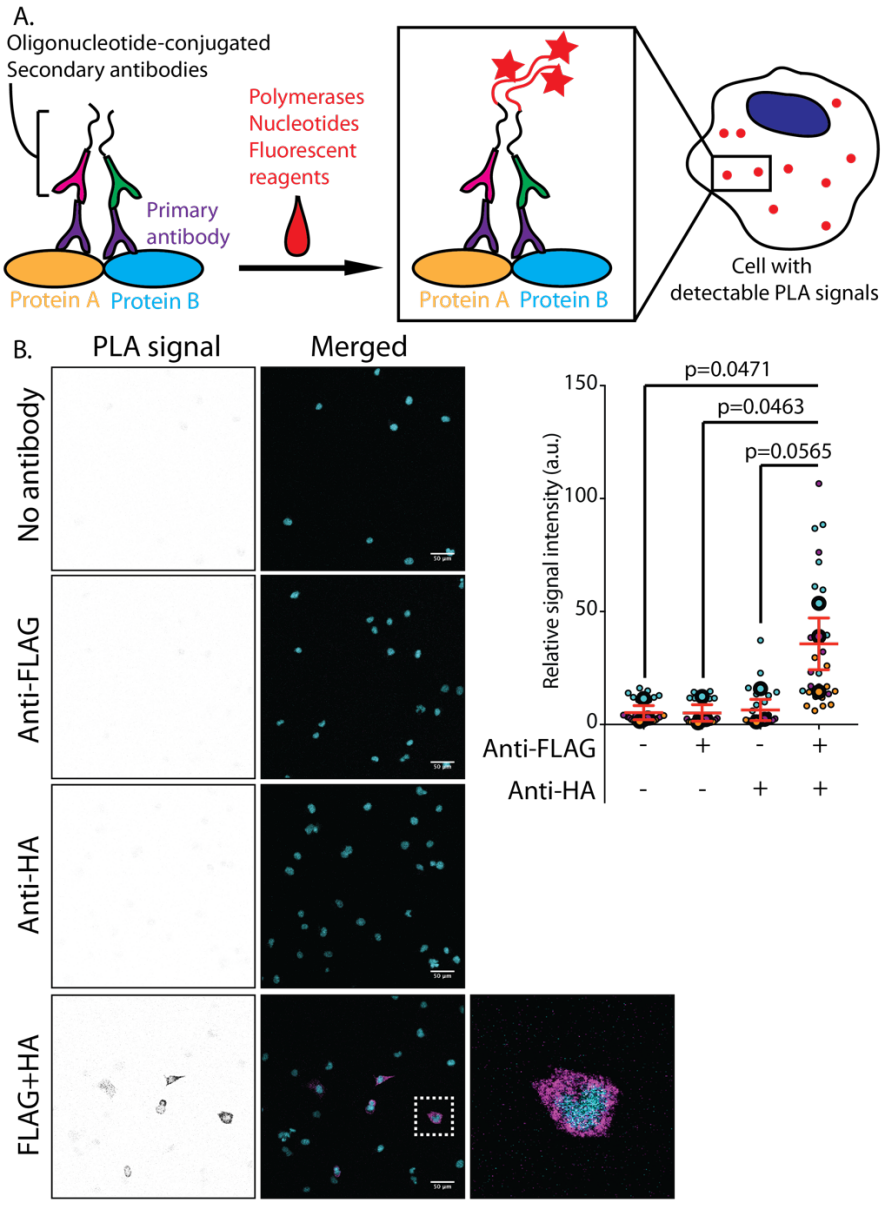

Figure 3.6 Proximity Ligation Assay (PLA) showing CYRI-A and CYRI-B forming heterooligomer complexes *in cellulo*

A. Schematic representation of the PLA assay. If the two proteins interact or within 40nm proximity to each other, the antibodies specifically recognising each protein and their respective secondary antibodies would also be placed within their vicinities. This allows the conjugated oligonucleotides to be polymerised by the added polymerase mix. The polymerisation reaction gives off the signal as fluorescence and can be detected with a standard confocal microscope.

B. COS-7 cells transfected with CYRI-A-FLAG and P17-HA-CYRI-B showed PLA signal only when both anti-FLAG and anti-HA antibody were used. Large dots are average from independent experiment. Small dots are individual cells. Mean ± SEM. ANOVA with multiple comparisons. Scale bar = 50μm.

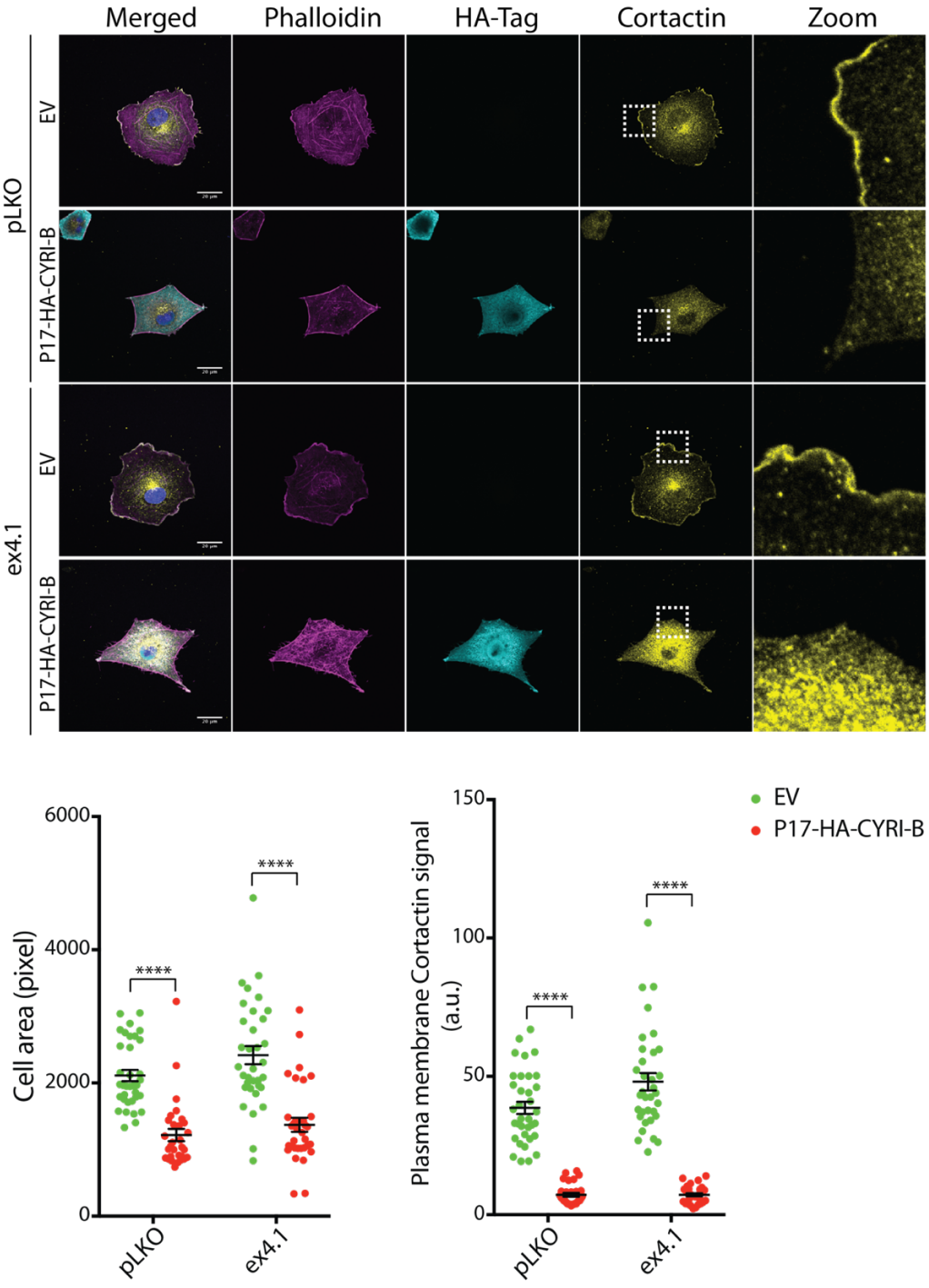

Figure 3.7 P17-HA-CYRI-B rescued phenotypes of CYRI-B KO COS-7 cells

COS-7 cells of either control pLKO or CYRI-B KO were transfected with P17-HA-CYRI-B construct. Cortactin was used as the marker for the leading edge of lamellipodia and the proxy for the Arp2/3 complex. Both the cell area and the leading-edge signal of Cortactin were significantly dropped upon re-expression of the construct. Data from 3 independent experiments. Mean ± SEM. Unpaired t-test. ****$p<0.0001$. Scale bar = 20μm

3.2.5 The structural studies of CYRI-B and RAC1

To fully understand the dimeric complex of CYRIs as well as how CYRIs interact with RAC1, knowledge of their structures is essential. We established a collaboration with the group of Dr Shehab Ismail and set out to determine the crystal structure of CYRI-B alone and in complex with active RAC1. This project was a joined effort between me and Shehab's senior postdoc Dr Tamas Yelland. We planned to solve the structure of the DUF1394 domain of CYRI-B, which we termed CYRI-BΔN before attempting to obtain a co-crystal structure of RAC1 Q61L-CYRI-BΔN complex.

Initial attempts to solve the structure of the full-length CYRI-B failed due to the natural flexibility of its N-terminal helix. We next truncated the entire helix from amino acid 1 to 25 to assist with the X-ray diffraction process and termed this construct CYRI-BΔN (Figure 3.8A). Comparison between the structure of CYRI-BΔN and the structure of the full-length CYRI-B predicted by I-TASSER showed a striking resemblance. Apart from the missing N-terminal helix, all 12 other α-helical bundles were organised in similar positions and orientations (Figure 3.8B). This validated our previous prediction of the structure and placed the predicted structure of CYRI-A to likely be correct and reliable for future experiments. Having obtained the structure of CYRI-BΔN, we then attempted to determine its structure in complex with active RAC1. Initial trials by mixing purified CYRI-BΔN and RAC1 failed because RAC1 tended to crystallise separately. To optimise, we first loaded RAC1 Q61L with the non-hydrolysable GTP-analogue GppNHp. We introduced a 10 amino acid linker (GSAGSAGSAG) to connect the RAC1 molecule to the C-terminus of CYRI-BΔN in a 1 to 1 ratio to increase their chance of interacting. The co-crystal structure showed the active RAC1 binds to the N-terminal subdomain of CYRI-BΔN (Figure 3.9A). A closer inspection of the interaction surface revealed the Switch I loop of RAC1 was responsible for the majority of the interaction with the total interaction surface of around 1097Å (Figure 3.9B). Mapping the interaction surface showed 12 pairs of interacting residues between RAC1 and CYRI-BΔN (

Figure 3.10A).

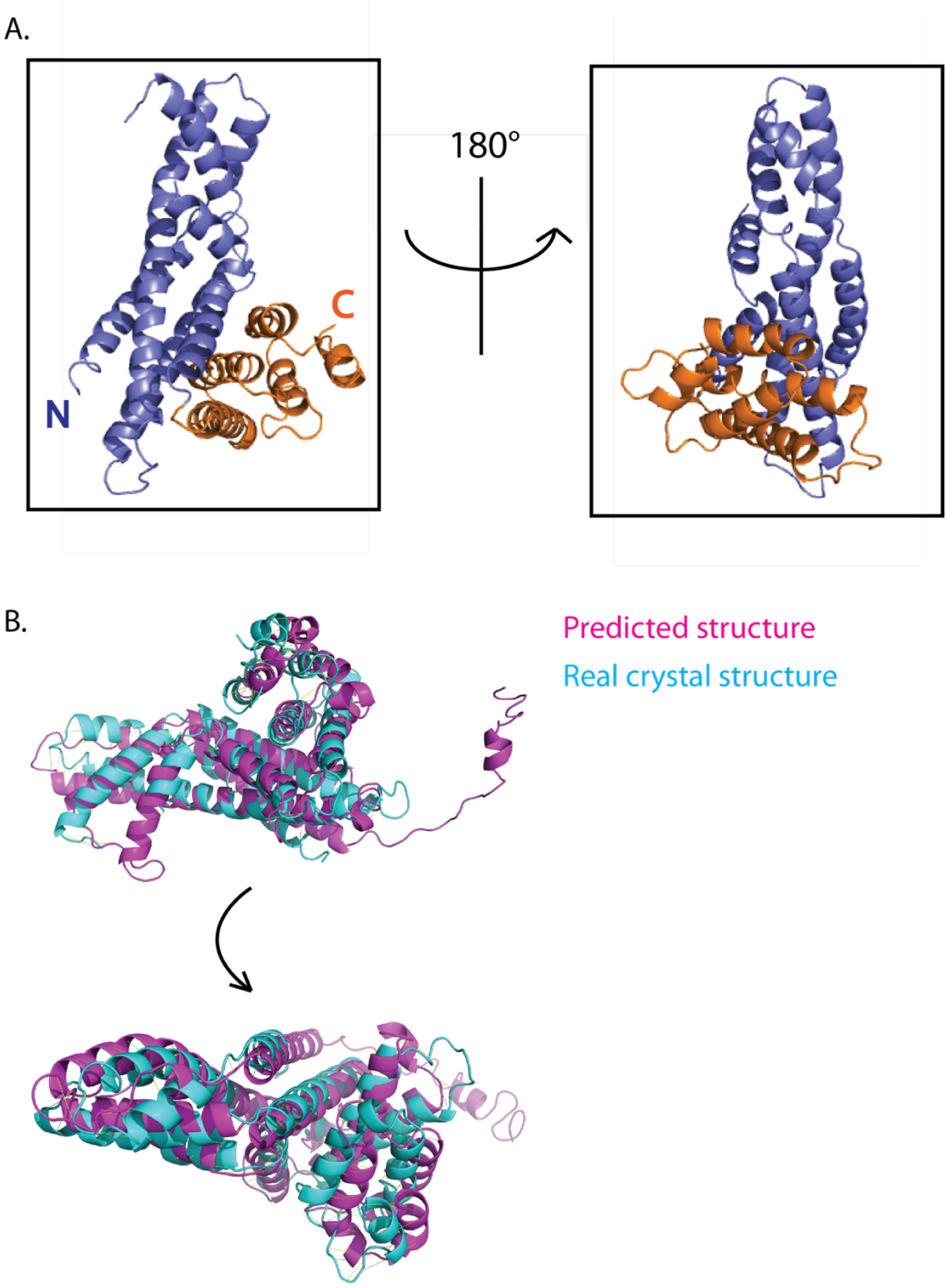

Figure 3.8 Comparison between the predicted structure and the real crystal structure of CYRI-B

A. The real crystal structure of CYRI-BΔN.

B. Alignment of the predicted structure of CYRI-B (magenta) with the crystal structure of CYRI-BΔN (cyan) shows a striking resemblance.

We observed the previously characterised residue arginine 160 on CYRI-BΔN (R160) (Fort et al., 2018) formed ionic bonds with an oxygen atom of the peptide bond of the 37th phenylalanine residue (F37) and an oxygen atom of the sidechain carboxyl group of the 38th aspartic acid (D38) residue on RAC1 (
Figure 3.10B). The proline 150 on CYRI-BΔN was also previously suggested to be involved in the interaction with RAC1 (Yuki et al., 2019). Even though we did not observe any residues from RAC1 that could directly interact with this proline, based on the biochemical nature of this amino acid, we believe P150 was likely to contribute to the architecture and structural framework of CYRI-B. Mutating this would likely affect the overall structure of CYRI-B and hence its ability to interact with other effectors (
Figure 3.10B). These observations of the crystal structure agreed with our current understanding of how active RAC1 would interact with CYRI-B. To further validate our structure, we decided to mutate the glutamine 153 (Q153) and serine 157 (S157) on CYRI-B as well as the serine 41 (S41) on RAC1 Q61L, which were also parts of the predicted interaction surface. We performed pulldown assays to test whether these mutations would disrupt CYRI-B:RAC1 interaction. Indeed, mutating any of the residues on CYRI-B dramatically reduced the detected signal. A similar observation is made with the S41A mutation on RAC1 Q61L, even though the effect is much less dramatic. This could perhaps due to the presence of the constitutively active Q61L mutation (
Figure 3.10D, E).

Closer inspection of the crystal structure revealed an unexpected detail. The C-terminal subdomain (to which we termed the Rachet subdomain) of CYRI-BΔN appeared to adopt an open conformation upon contacting with active RAC1. In its closed conformation, its 305th tyrosine residue (Y305) would induce a steric clash with the 2nd glutamine residue (Q2) on RAC1 (Figure 3.11A). From the crystal structure, we would predict a domain swapping mechanism between 2 CYRI monomers (Figure 3.11B). The swapped Rachet subdomain occupied a similar position in the neighbouring CYRI-B molecule but with a shift of 5Å (Figure 3.11C, red arrow). This shift was enough to prevent any further steric clash between this domain and the second RAC1 molecule based on the obtained crystal structure.

From this particular observation, it was suggested that perhaps the binding of active RAC1 could lead to the dimerization of CYRIs.

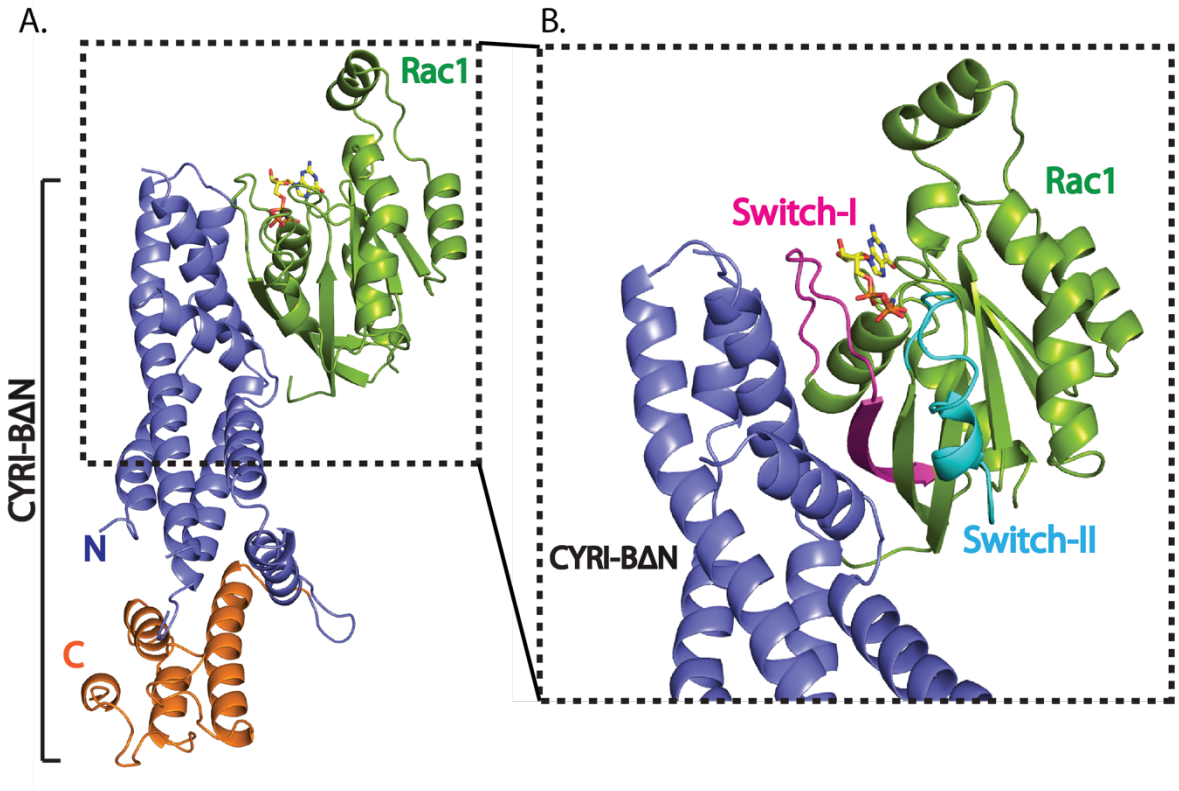

Figure 3.9 Co-crystal structure of CYRI-BΔN and RAC1 Q61L

A. The whole crystal structure showing active RAC1 (green) interacts with the N-terminal subdomain of CYRI-BΔN. GppNHp is in stick representation.

B. Zoom in to the interaction surface showing the Switch I (magenta), but not Switch II (cyan) loop of RAC1 that is responsible for the interaction.

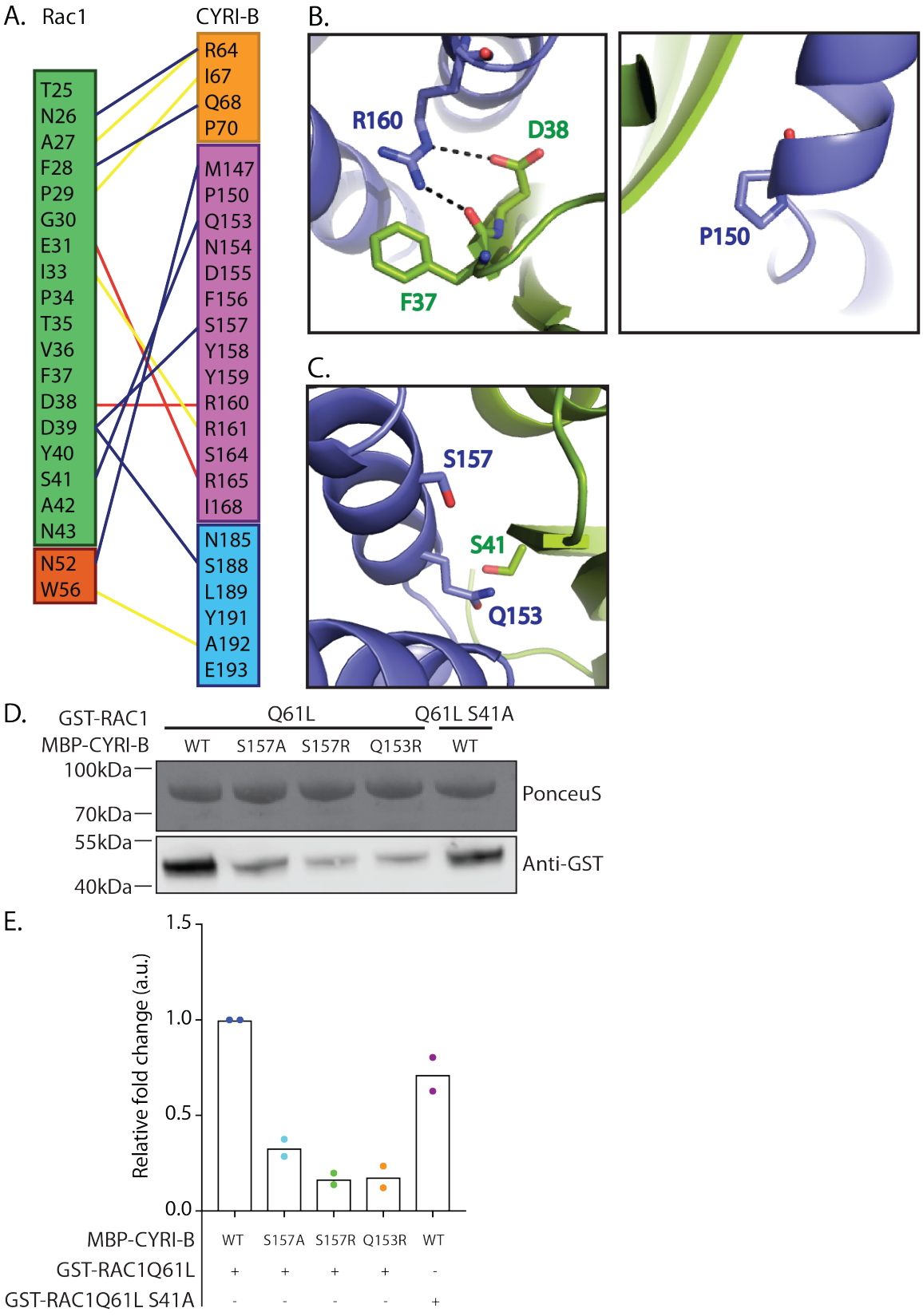

Figure 3.10 Validating RAC1 Q61L- CYRI-BΔN interaction surface

A. Interacting residue map between RAC1 Q61L and CYRI-BΔN. Lines represent the interaction. Black line: hydrogen bond, red line: salt bridge, yellow line: hydrophobic interaction.

B. Residues that were identified previously through biochemical analysis involved in active RAC1 interaction (CYRI-BΔN in blue, RAC1 Q61L in green) appears in our co-crystal structure.

C. Residues thought to be important for active RAC1 interaction identified through analysing the crystal structure.

D. Mutagenesis of newly identified residues reduces the interaction affinity between active RAC1 and CYRI-B in an MBP pulldown assay, thus reconfirming the validity of the observed interaction surface.

E. Quantification of the MBP pulldown assay shows the drastic decrease in the binding affinity of RAC1 Q61L with mutant CYRI-B and vice versa. Data from 2 independent experiment. Normalised to signal detected between CYRI-B WT and RAC1 Q61L.

On the other hand, another dimeric crystal is observed from the crystal structure of CRYI-BΔN alone (Figure 3.12). In this dimer structure, the two CYRI-B monomers could be seen facing each other which resembles two hands cupping, hence the name “hand-cupped model”. Interestingly, from this model, we predict that the arginine 160 of one monomer could form a salt bridge with the alanine 192 of the other monomer. This arginine 160 and 161 are crucial for the binding of active RAC1 to CYRI-B (Fort et al., 2018), while the arginines 159/160 are important for CYRI-A based on the sequence conservation. If this model is correct, then dimerization of CYRIs should oppose active RAC1 binding, or in other words, RAC1 competes for the same binding site with the dimer. To test which dimer complex is likely to be correct, we mutated the two arginines 159/160 into aspartic acids (RRDD mutant) in CYRI-A to test whether the previously detected interaction is disrupted. Indeed, the mutations completely ablated CYRI-A’s ability to bind active RAC1 and significantly reduced the dimerization signal in both *in vitro* pulldown (Figure 3.13) and *in cellulo* PLA assay (Figure 3.14). It is important to note that neither the Rachet domain nor the N-terminal helix is important for the dimerization to occur.

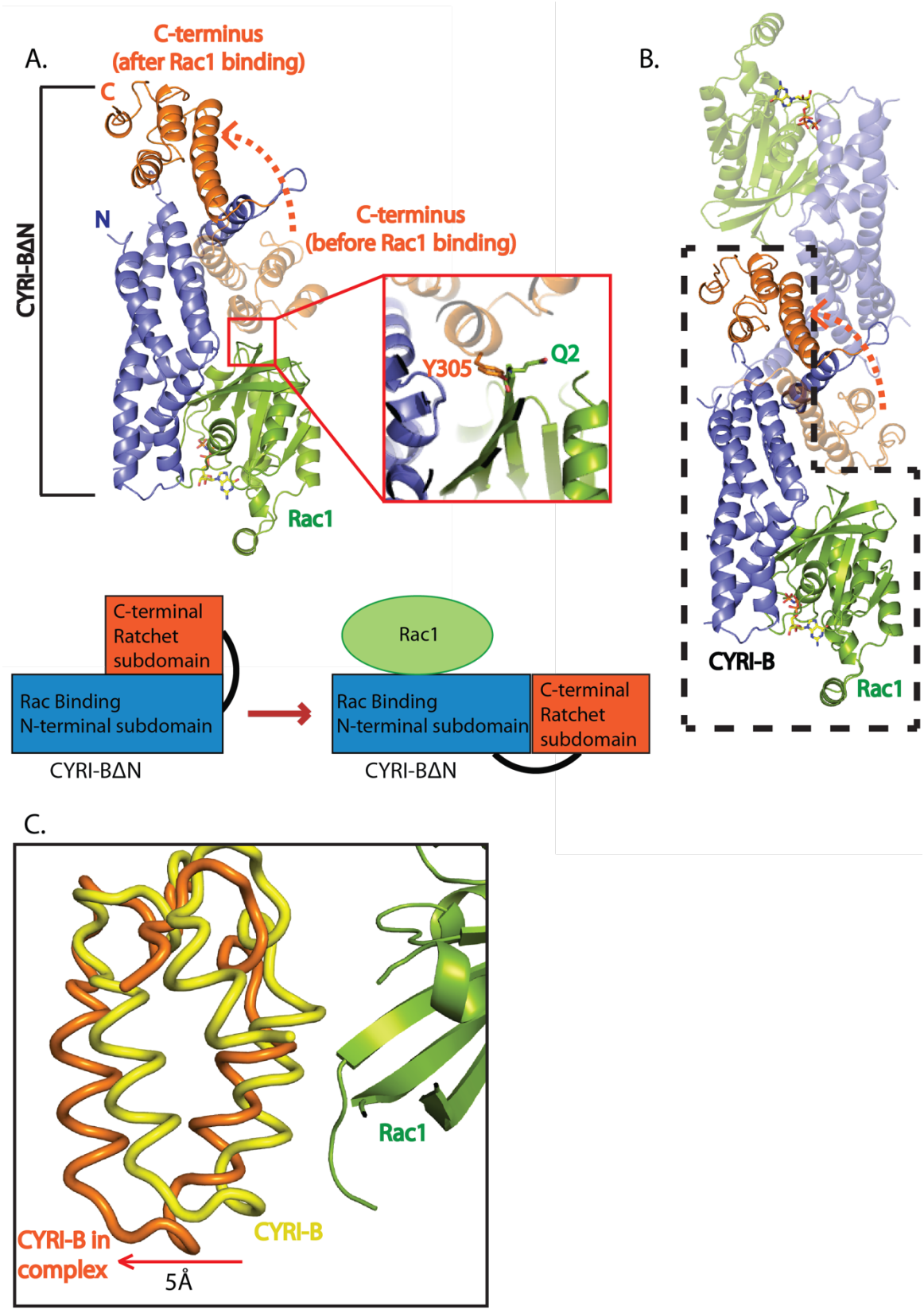

Figure 3.11 Co-crystal structure of RAC1 Q61L-CYRI-BΔN reveals a domain swapping mechanism between CYRI molecules

A. The steric clash between the 305th tyrosine (Y305) residue of CYRI-BΔN and the 2nd glutamine (Q2) residue of RAC1 Q61L induces the Rachet subdomain (C-terminus, orange) of CYRI-BΔN to open up (dashed arrow). Cartoon representation of the opening mechanism.

B. Dimerization between CYRI-BΔN molecules potentially through an active RAC1-induced domain swapping mechanism. One monomer is in solid colour, the other is in 50% transparency.

C. The Rachet subdomain of one monomer occupies at a similar position as the Rachet subdomain of the second monomer but with a 5Å shift. This hence makes it possible for the second RAC1 molecule to bind without introducing any secondary steric clash.

The CYRI-B's Rac-binding domain (RBD) composed of amino acid 30 to 236, which lacks the Rachet domain is still able to interact with MBP-CYRI-A, suggesting that this domain is not needed for the CYRI dimerization (Figure 3.15). When deleting the first 16 or 30 amino acids from the N-terminus of CYRI-A and performing a pulldown assay with GST-RAC1 or full-length CYRI-B, signals were still detected between these truncated versions of CYRI-A and the active RAC1 or the full-length CYRI-B. This strongly suggests that CYRI dimerization is mediated only by a small portion of the DUF1394 domain which contains the two conserved arginine residues. We then performed a competition pulldown assay where MBP-CYRI-A or CYRI-B was allowed to interact with GST-CYRI-B in the presence of increasing active RAC1 (RAC1 Q61L) concentrations (Figure 3.16). If active RAC1 promotes CYRI dimerization, then in the presence of the protein, we should see an increase in the dimer signal. In contrast, if active RAC1 molecules were to compete for the same binding site as CYRI monomers, we should observe a decrease in the dimeric signal. Indeed, in the presence of an increasing RAC1 level, the dimer signal could be seen gradually decreased. At 30μg of RAC1, the dimer signal reduced by 50% in both hetero- and homodimeric complex. These data confirmed that active RAC1 was indeed competing for the same binding site as CYRI monomers. The existence of CYRI dimers is perhaps acting as an autoinhibition mechanism, adding an extra layer of regulation to the CYRI signalling. This also ruled out the domain swapping mechanism that we described earlier on. We still believe that the Rachet domain is a feature of CYRI as its electron density was visible in the crystal structure, however, the clash between RAC1 and the tyrosine 305 residue was likely to be a crystal-packing artefact.

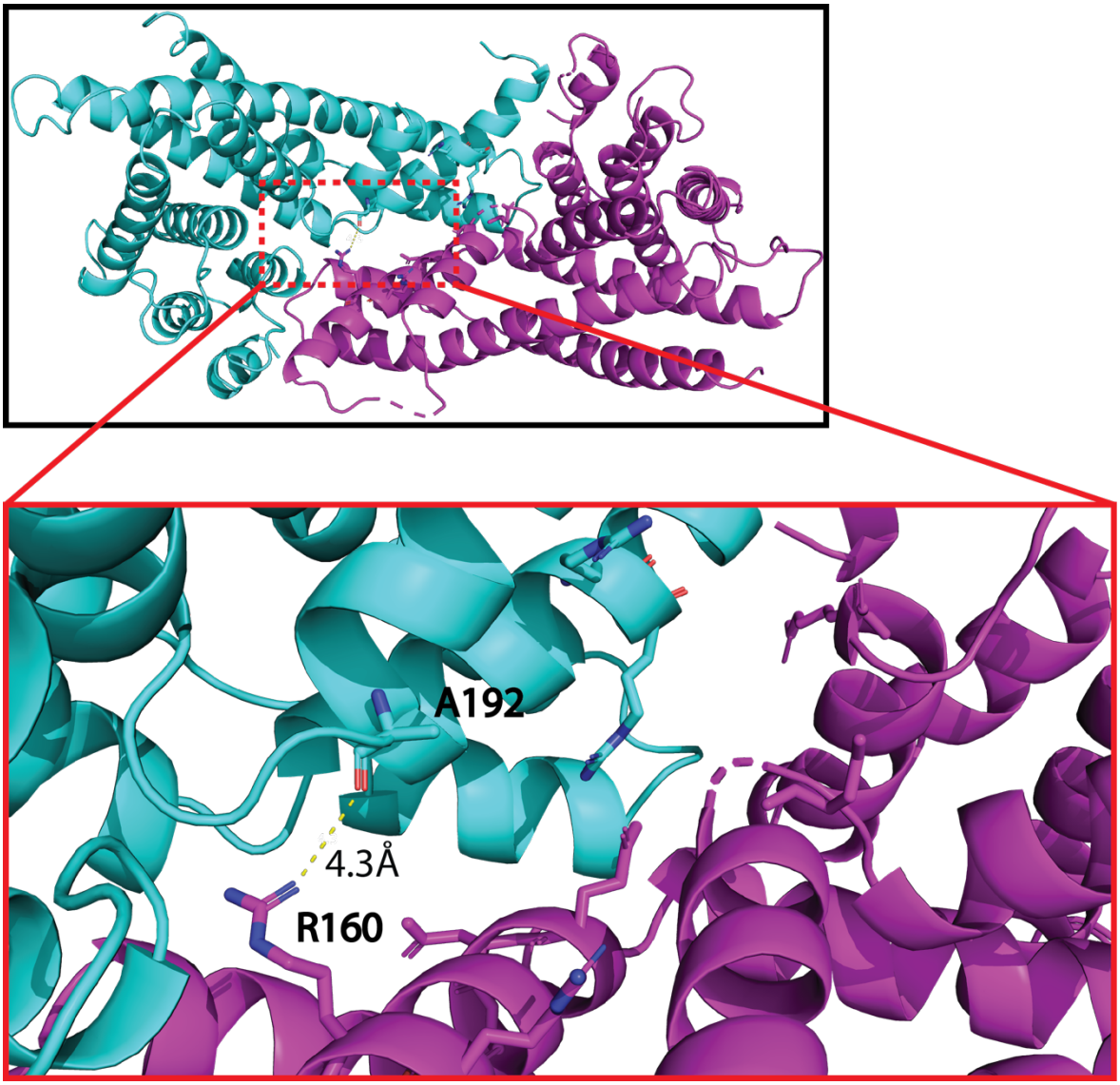

Figure 3.12 CYRI-B forms dimeric complex in a hand-cupped model

Two monomers of CYRI-B molecule come together in a hand-cupped model. A few amino acids were thought to be involved at the interface, in particular, the nitrogen atom of the amine group of the arginine 160 of one monomer could be seen forming a salt bridge (4.3Å) with the oxygen atom from the carboxyl group of an alanine 192 of the other monomer. Interestingly, this arginine together with the arginine 161 are known to be important for active RAC1 interaction.

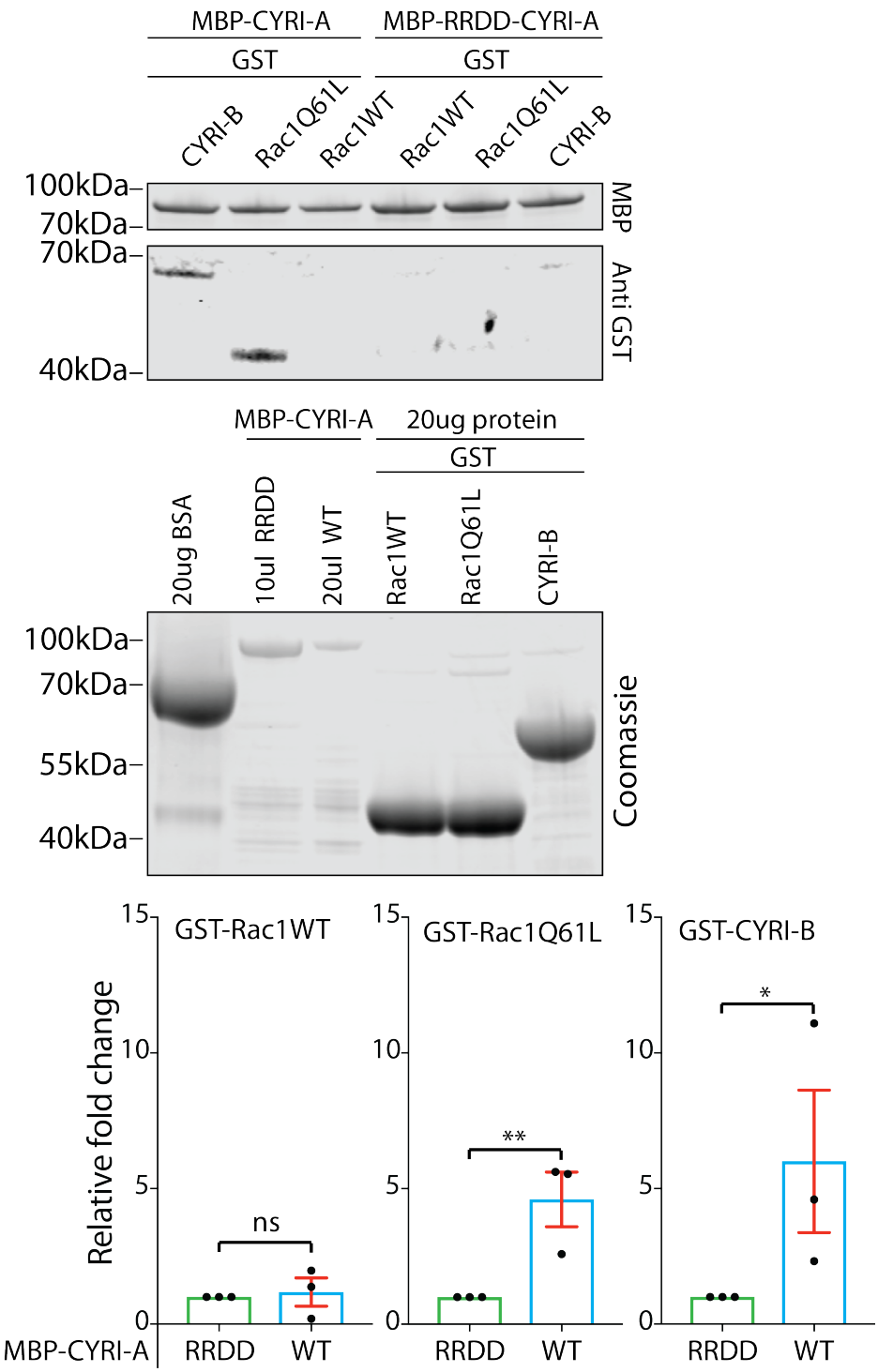

Figure 3.13 Mutating the two arginines 159/160 into aspartic acids (RRDD mutant) in CYRI-A disrupt hetero-dimerization *in vitro*

Western blot shows the disappearance of both active RAC1 and CYRI-B signal when incubated with CYRI-A-RRDD mutant. Quantification shows the significantly lower signal of CYRI-A-RRDD compared to CYRI-A WT with CYRI-B. Data from 3 independent experiments. Mean ± SEM. Unpaired t-test of normalised log base 10 data points. *p<0.05, **p<0.01.

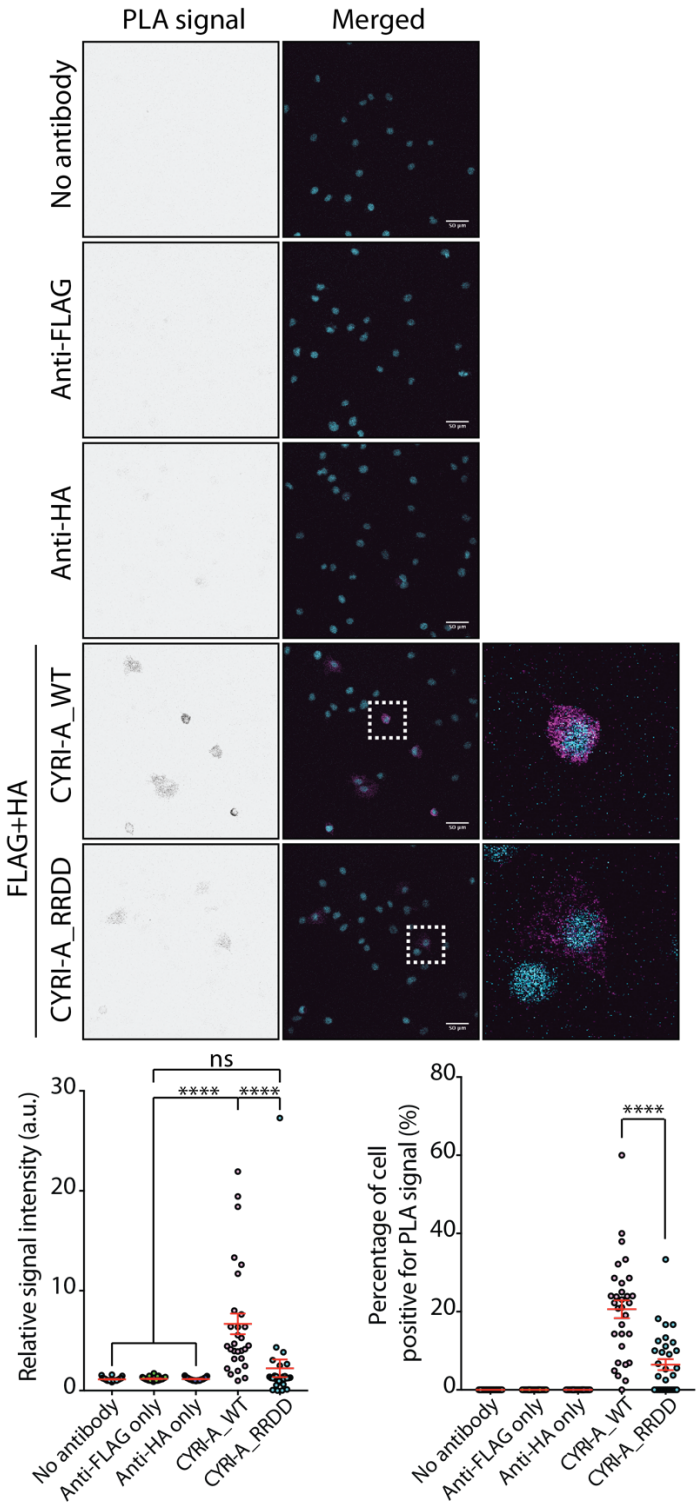

Figure 3.14 Mutating the arginine 159/160 of CYRI-A into aspartic acid (RRDD) disrupted hetero-dimerization with CYRI-B *in vivo*

PLA signal detected in CYRI-A WT condition while significantly decreased in the CYRI-A-RRDD condition. Scatter plot represents mean value ± SEM from 3 independent experiments. Statistical analysis includes ANOVA with multiple comparisons (left graph) and unpaired t-test (right graph). ****p<0.0001. Scale bar = 50μm

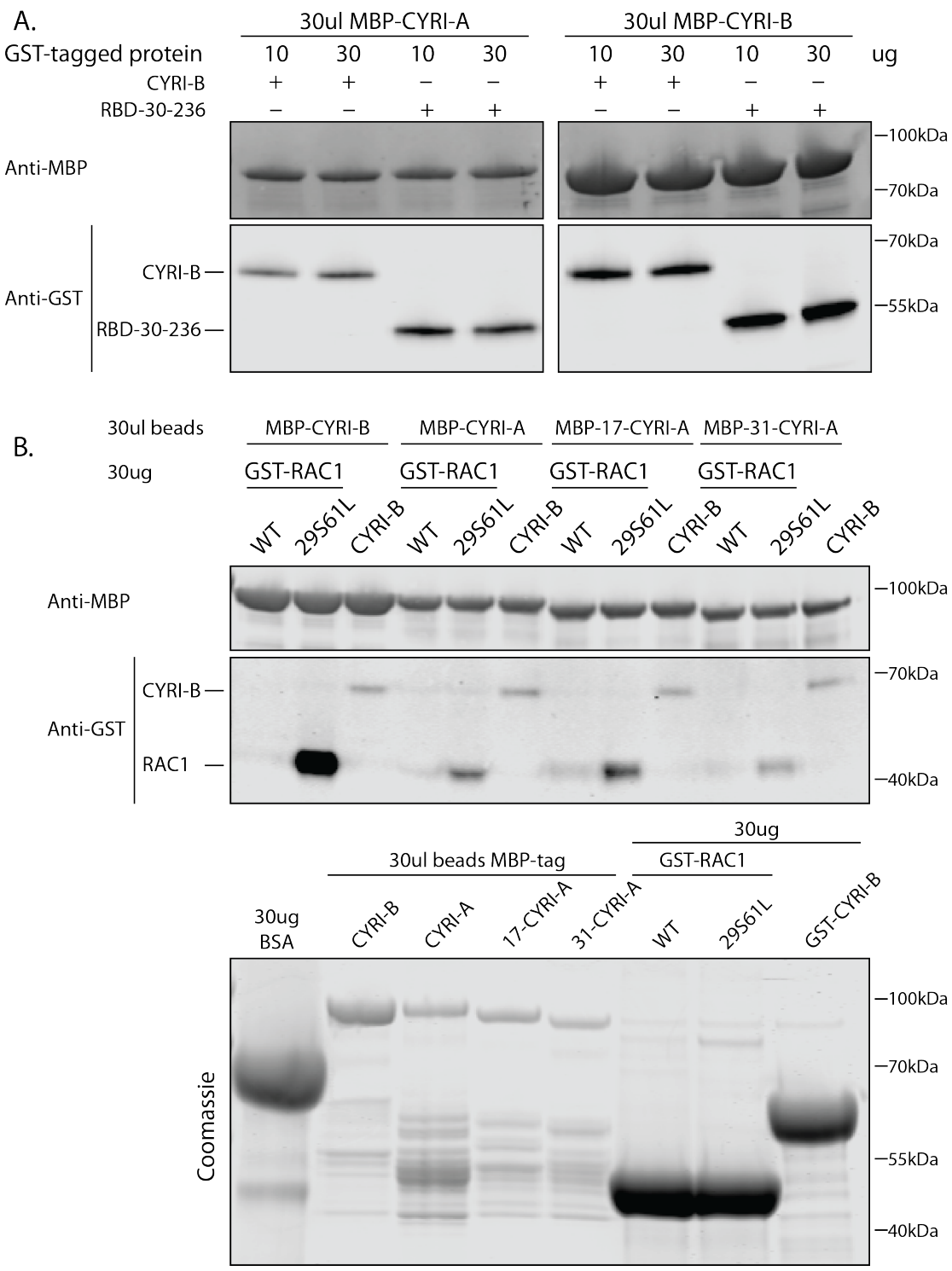

Figure 3.15 The Rachet domain and the N-terminal alpha helix of CYRI are not essential for the dimerization to occur

A. MBP-CYRI-A or B pulldowns GST-CYRI-B or GST-RBD-30-236 (which lacks the Rachet domain) shows that this domain is not needed for the dimerization to occur.

B. MBP pulldown of full-length CYRI-B, CYRI-A or CYRI-A lacking the first 16 or 30 amino acids with GST-RAC1WT, P29SQ61L or full-length CYRI-B. This shows that the N-terminal helix is also not important for CYRI dimerization.

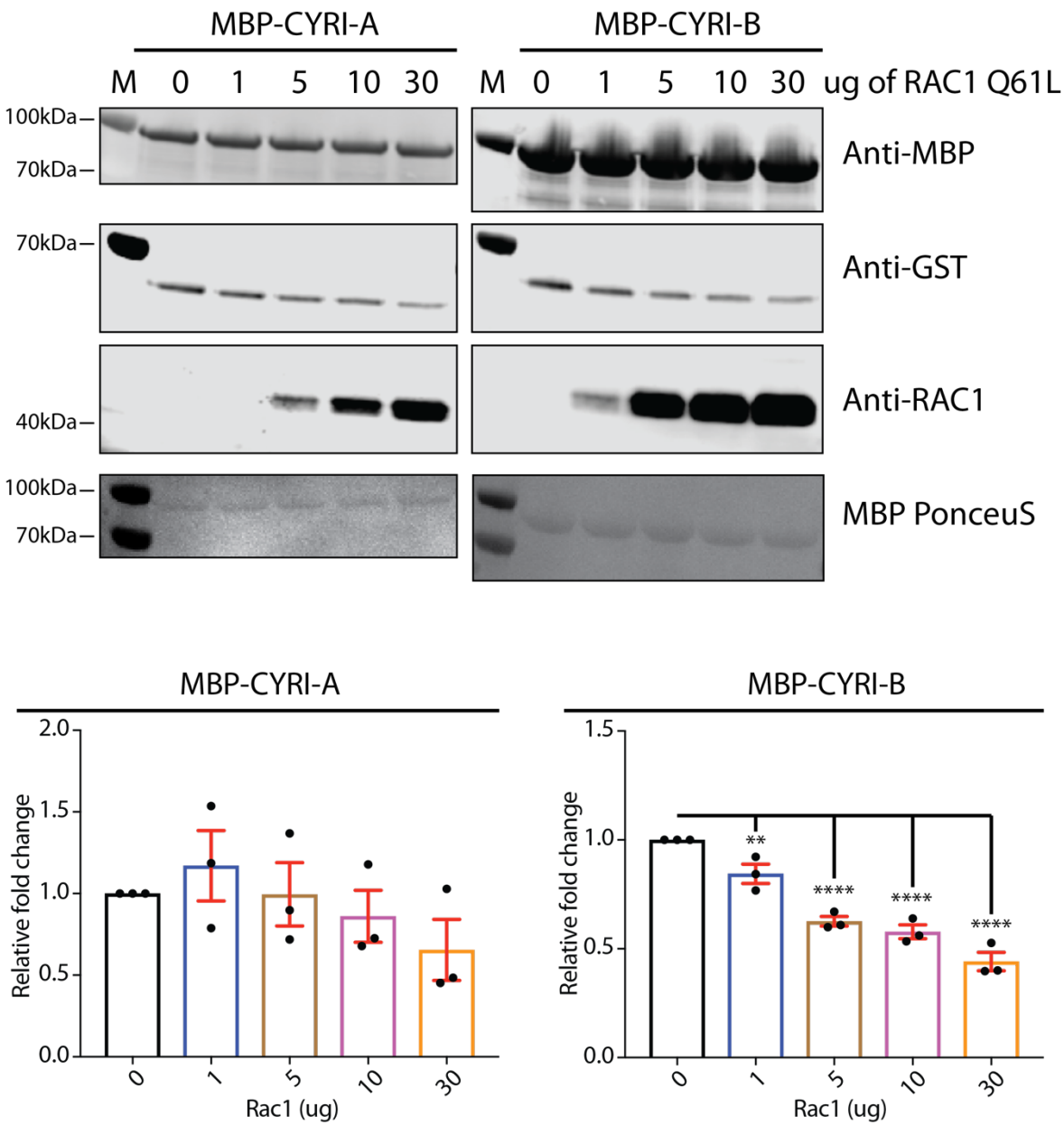

Figure 3.16 Active RAC1 competes for monomeric CYRI and disrupt the CYRI dimeric complex

MBP-CYRI-A or CYRI-B pulldowns with GST-CYRI-B in the presence of increased active RAC1 (RAC1 Q61L) concentration. The more active RAC1 is present, the less of the dimeric complex signal. The signal is normalised to PonceuS MBP loading control. Data from 3 independent experiments. Mean ± SEM. ANOVA with multiple comparisons. **p<0.01, ****p<0.0001.

3.3 Discussion

In general, the CYRI protein family is highly conserved, both in terms of their amino acid sequences and perhaps also 3D structure. Despite this, certain differences may hint about the functional distinctions between the two isoforms. The lack of a palmitoylatable cysteine residue at the 10th position and the presence of an amphipathic helix in CYRI-A suggests a potential different membrane dynamic for this protein compared to CYRI-B. It is also plausible that the presence of this amphipathic helix on CYRI-A might be responsible for the difficulty in purifying the protein *in vitro* as these could allow proteins to clump together more readily. CYRI-A did seem to behave similarly to CYRI-B in terms of its ability to bind active RAC1. However, surprisingly CYRI-A/RAC1 interaction is much tighter than that of CYRI-B. It is also important to note that this was the first time that this interaction was detected between RAC1 and a full-length CYRI. Needless to say, this raises a question on the differences between our SPR experiment and the pulldown assay, where the N-terminal helix seemed to be playing an inhibitory role. This can potentially be explained by several reasons. First, our pulldown assay was done with cell lysates containing overexpressed CYRI constructs. Being in mammalian cells perhaps allow the protein to be post-translationally modified differently from that in bacteria, and this could have resulted in the differences in protein behaviours. Secondly, in an *in vitro* saturated environment of an SPR experiment, molecules of CYRI could be forced into an active conformation due to the close distance with others on the same chip. This perhaps allows the protein to adopt an open conformation and thus is more readily to bind active RAC1. Thirdly, there are potentially many unknown CYRIs interactors that have yet to be discovered. Perhaps, inside cells, these regulators can interact with the N-terminal helix and keep CYRIs in their closed, inactive conformation. Removing the helix also removes the binding site for these regulators, hence allow for the active RAC1 to bind. These regulators are not present in our *in vitro* SPR, thus allow CYRIs to spontaneously adopt their active form. Nevertheless, these data are the first to confirm the differences between CYRI-A and CYRI-B in terms of their affinity with active RAC1, but more experiments are needed to test whether this is biologically significant.

Together with Tamas Yelland from the Ismail lab, we determined for the first time the crystal structure of CYRI-BΔN alone and in complex with active RAC1. Our crystal structure strongly agreed with the current understanding of how RAC1 interacts with CYRIs. Furthermore, we uncovered a novel dimeric complex of CYRIs where monomeric CYRIs interact with each other through a hand-cupped mechanism, sharing the same interaction interface with RAC1 binding. We believe this might act as an autoinhibitory mechanism, adding an extra layer of buffering for CYRI activity. It would be interesting to investigate further whether this dimerization is happening in solution or on the plasma membrane. We hypothesize that perhaps there is an equilibrium between monomeric CYRIs, which reside in the cytoplasm and dimeric CYRIs, which are present on the membrane. Based on the relative signal intensity on western blots, the affinity between monomeric CYRIs appears to be weaker than that between CYRI and active RAC1. This prompted us to believe that dimeric CYRI might act as a gatekeeper, and only be activated once the level of active RAC1 crossed a certain threshold. Many components of the actin network regulators have been shown to function in cluster or multimeric complexes. The Scar/WAVE complex, for example, has been shown to form ring-like structures in cells upon latrunculin treatment (Pipathsouk et al., 2019). N-WASP is thought to also phase separate near the plasma membrane (Case et al., 2019). Hence it might not be so surprising if CYRIs could also do the same. However, more experiments will need to be done in order to confirm this hypothesis. One way we could potentially probe for the functionality of the dimerization in cells is to use an inducible dimerization system such as the rapamycin FKBP-FBP system. Addition of rapamycin can result in the clumping of CYRI molecules, which can increase its local concentration and thus dimerization. If CYRI dimerization interferes with RAC1 binding, then the addition of rapamycin should lead to increased cell spreading due to more active RAC1 being liberated.

On another note, the co-crystal structure could provide us with a better insight into how active RAC1 interacts with the Scar/WAVE complex. CYRIs share about 18% sequence identity with CYFIP, one of the five subunits of the Scar/WAVE complex. In fact, the predicted structure of CYRIs by I-TASSER was based on the crystal structure of CYFIP. This suggests that perhaps the binding of RAC1 to CYRIs is homologous to how RAC1 would interact with CYFIP. For over 20 years since the

discovery of the Scar/WAVE complex, we still do not understand exactly how active RAC1 activates this complex. Since CYRIs is thought to be the direct competitor of the Scar/WAVE complex for active RAC1, it is likely that the two would share similar features. Indeed, when overlaying the structure of CYRI to CYFIP, we saw a striking similarity (data not shown). By further understanding how RAC1 interacts with CYRIs, we could potentially unravel the mystery of how this same molecule activates the Scar/WAVE complex.

The surprisingly large Kd value between CYRI-B and active RAC1 also puts the direct competition hypothesis in question. Even when taking into account the relatively large abundance of CYRI-B in the cells compared to the Scar/WAVE complex, a Kd of almost 20μM would still be considered high. The measured Kd for the A-site to active RAC1 is 0.27uM (Chen et al., 2017). So, in order for CYRI-B to bind half of the active RAC1, its concentration will need to be at least 74 times higher than that of the Scar/WAVE complex, and this is about 9 times for CYRI-A. What made CYRI a good competitor is still a question remains to be answered? One experiment we can do to test whether CYRIs are indeed directly competing with the Scar/WAVE complex for active RAC1 binding is to transfect cells with the CYRI-RAC1 Q61L fusion construct. If CYRI and the Scar/WAVE complex are not direct competitors and if it is the binding of CYRI to RAC1 that triggers a secondary signal to compete with the Scar/WAVE complex, then the presence of a fusion CYRI-RAC1 complex would result in a phenotype similar to Scar/WAVE inhibition. This would definitely be an interesting experiment to try out. In the future chapters, we will focus on the biological behaviours of CYRIs and how do they control the phenotypes of the cells.

4 CYRI-A and CYRI-B functionally compensate each other

4.1 Introduction

Having established the similarity between CYRI-A and CYRI-B biochemically, the next question we asked is how CYRI-A behaves inside cells? Many cell lines express CYRI-B endogenously, but only a few numbers of them express both isoforms. In this chapter, through rescuing and knockout experiments, we will probe for the functional relationship between CYRI-A and CYRI-B. Previous reports have provided us with phenotypic data of cells lacking CYRI-B (Fort et al., 2018, Shang et al., 2018, Yuki et al., 2019). Because of the increase in the level of non-sequestering active RAC1, COS-7 cells lacking CYRI-B adopt the round or C- shape with broad, WAVE2-enriched lamellipodia. Since the antibody for WAVE2 was discontinued, we replaced this with an Arp2/3 complex antibody, which should have a similar localisation to the Scar/WAVE complex at the lamellipodia and acts as a suitable alternative marker. We made use of this characteristic phenotype and how it is altered as the readout for the effect of CYRIs. Finally, we generated the first CYRI double knockout (DBKO) cell lines using CRISPR-Cas9 technology to study the effects of cells lacking both isoforms.

4.2 Results

4.2.1 CYRI-A rescues the effects of CYRI-B deletion in COS-7 cells

Previous works have shown COS-7 cells lacking CYRI-B seeded on top of laminin-coated coverslips adopt the “fried-egg” and C-shape with a prominent enrichment of WAVE2 at their leading edges. This was explained due to the elevated number of active RAC1 molecules that were no longer being sequestered. Active RAC1, as mentioned in chapter 1, can now bind and activate the Scar/WAVE complex, leading to the activation of the Arp2/3 complex and branched actin polymerisation. It was also reported for the use of WAVE2 and cortactin antibodies to label lamellipodia-liked structures (Fort et al., 2018).

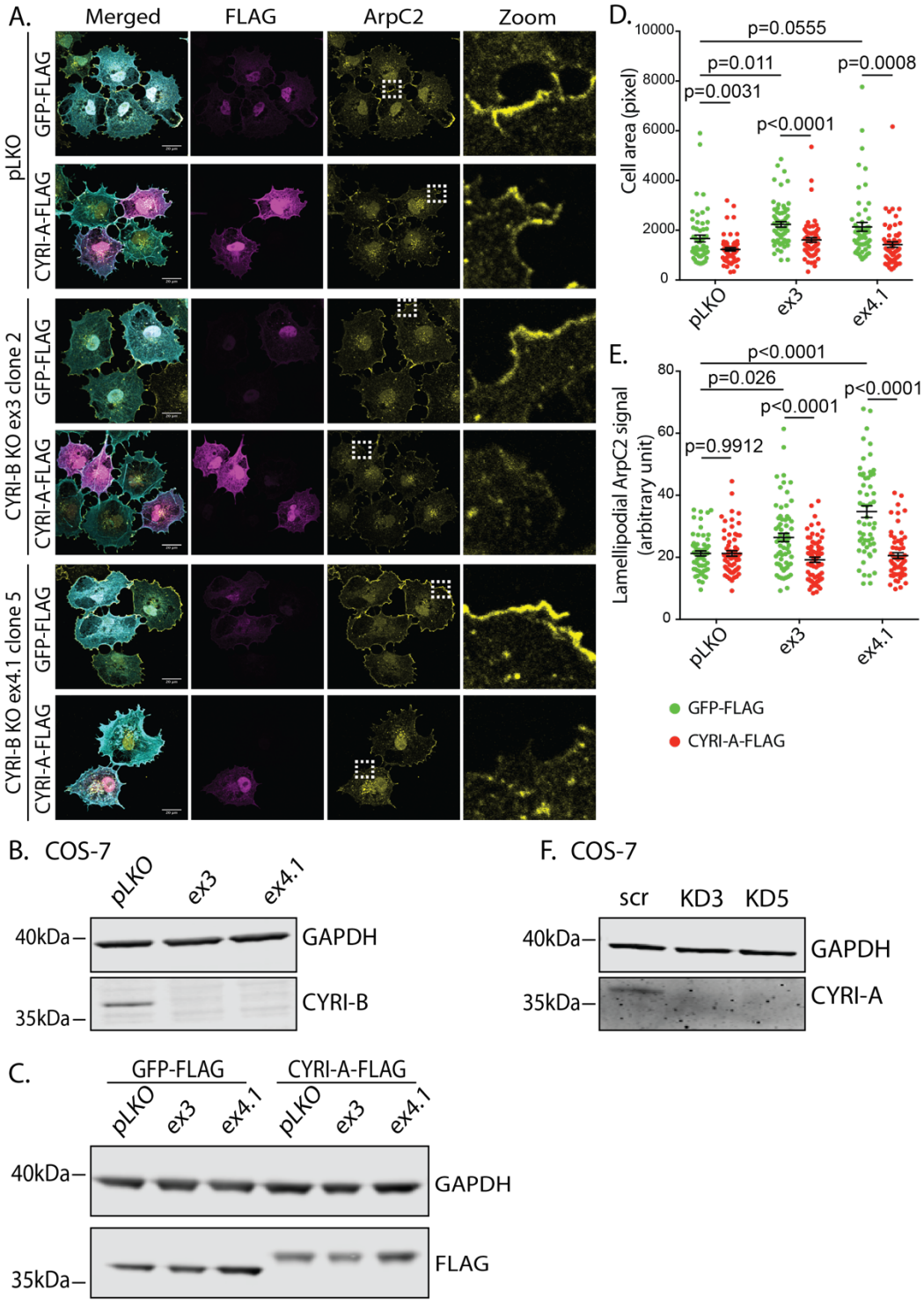

Figure 4.1 CYRI-A-FLAG rescues the effects of CYRI-B knockout

A. COS-7 cells either the control pLKO or CYRI-B KO (ex3 clone 2 and ex4.1 clone 5) were transfected with either GFP-FLAG or CYRI-A-FLAG. Transfected cells were seeded on fibronectin-coated coverslips for 4h before being fixed and stained for Phalloidin, anti-FLAG and anti-ArpC2 antibody. CYRI-A leads to a decrease in the cell spreading area and Arp2/3 localisation at the leading edge compared to cells transfected with the GFP control. Scale bar = 20μm.

B. Western blot shows the relative overexpression level of the constructs between the three cell lines.

C. Western blot confirms the knockout efficiency of CYRI-B by CRISPR-Cas9.

D, E. Quantification of cell area and Arp2/3 signal intensity at the leading edge of A) show the significant decreases in both aspects of cells overexpressing CYRI-A. Scatter plot of 3 independent experiments. Mean ±SEM. Unpaired t-test.

F. Western blot showing the endogenous expression of CYRI-A in COS-7 with siRNA knockdown to confirm antibody specificity. Scr = scramble siRNA, KD3 and KD5 = 2 siRNA.

We reintroduced either a CYRI-A-FLAG construct (Figure 4.1) or a bicistronic CYRI-A-mVenus vector (Figure 4.2) into these COS-7 cells to ask whether CYRI-A can reverse the effects of CYRI-B-loss. Fibronectin is used to coat the coverslips to keep it consistent with future experiments in later chapters. In both cases, CYRI-A on its own can indeed rescue the phenotypes of CYRI-B deletion, both in cell spreading area and the enrichment of the Arp2/3 complex at the leading edge, which was measured by using a 1-pixel-thick manual tracing tool (Figure 4.1D, E, Figure 4.2C, D). The relatively similar (Figure 4.1B) or higher (Figure 4.2B) overexpression level of cells expressing the control construct compared to CYRI-A suggest that the phenotypes we observe are not a side effect of protein overexpression. As can be seen in the zoomed images, comparing between the control pLKO and the two CYRI-B knockout lines, we observed a nice continuous enrichment of the Arp2/3 complex around the leading edge of the knockout cells, while this is patchier and more cytosolic in the pLKO. This agrees with previous observations made with the WAVE2 antibody. For the control pLKO cells, only the spreading area is affected by CYRI-A overexpression but not the Arp2/3 signal (Figure 4.1E, Figure 4.2D). This suggests that cell spreading area and the Arp2/3 localisation are two separate phenotypes potentially regulated by two different mechanisms but are both related to CYRIs. We also noticed that naturally, the COS-7 cells do express a very low level of CYRI-A endogenously compared to CYRI-B (Figure 4.1F). It is likely that at this level, CYRI-A might not be enough to compensate for the effects of CYRI-B loss. Hence, in COS-7, CYRI-B seems to contribute more to the regulation of RAC1 and the Scar/WAVE complex than CYRI-A.

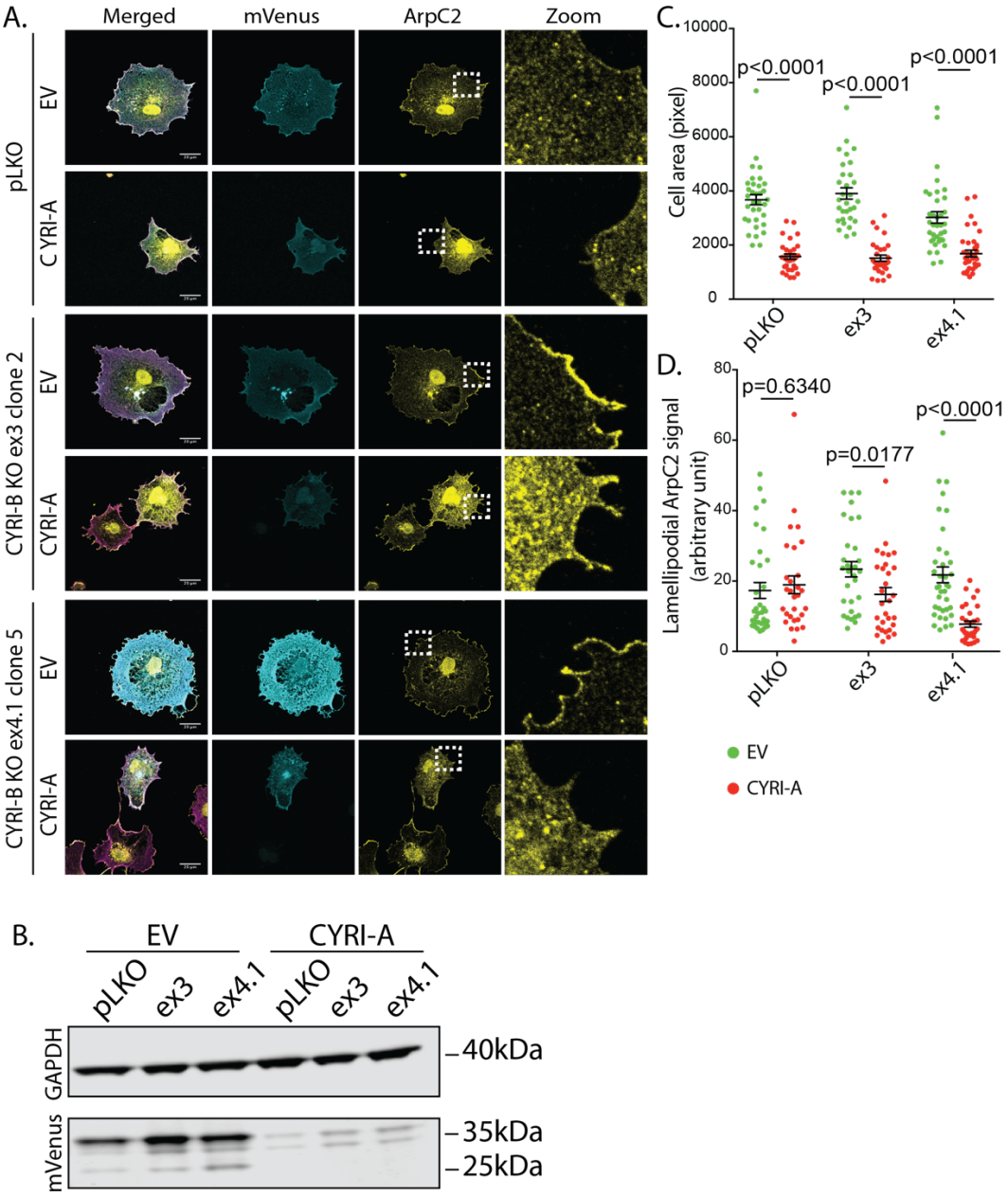

Figure 4.2 Full-length CYRI-A in a bicistronic vector rescues the phenotypes of CYRI-B knockout

A. COS-7 cells either control pLKO or CYRI-B knockout (ex3 clone 2 and ex4.1 clone 5) were transfected with either an empty vector (EV) or a CYRI-A-mVenus bicistronic vector. The cells were then induced with 1nM Doxycycline for 48h before being seeded on Fibronectin-coated coverslips for 4h and fixed and stained for GFP (for mVenus), Phalloidin and Arp2/3 complex. Scale bar = 20um. B. Western blot shows the relative expression of mVenus (1:1 ratio with CYRI-A) (blotted with anti-GFP antibody) between cell lines. Scale bar = 20μm

C, D. Quantification shows the decrease in both the cell spreading area and the Arp2/3 localisation at the leading edges of cells expressing CYRI-A compared to its corresponding control. Scatter plot of 3 independent experiments. Mean ±SEM. Unpaired t-test.

4.2.2 CYRI-A and CYRI-B cooperatively regulate cell shape and migration behaviour

Having established the function of CYRI-A through an overexpression system, we next verify this in an endogenous system. Unlike CYRI-B which can be found in almost every cell line, CYRI-A has a much more restricted expression pattern. In order to determine the cell lines expressing both CYRI-A and CYRI-B at a comparable level, we searched the public database Expression Atlas (https://www.ebi.ac.uk/gxa/home), with a focus on cancer cells. The dataset is derived from more than 100,000 different curated RNA sequencing experiments across 63 different species from multiple different cell lines. Searching through the different types of human cancer favours our prediction that CYRI-B seems to be much more widely expressed in cancer compared to CYRI-A (Figure 4.3), despite the normal tissue expression data suggest CYRI-A and CYRI-B are equally abundant (Chapter 1). As can be seen in Figure 4.3, most of the cell types in melanoma and pancreatic ductal adenocarcinoma (PDAC) only express CYRI-B. However, we noticed that many sarcoma lines express both proteins at a comparable level. We thus obtained the A-673 cell line from Professor Sue Burchill (from the Leeds Institute of Cancer and Pathology) for further studying.

We first utilised small-interfering RNA (siRNA) technology to knockdown CYRIs in the A-673 cells. Depleting just CYRI-B leads to a 20% increase in the number of C-shaped cells and it is 30-40% in the case of CYRI-A depending on the siRNA used (Figure 4.4A). However, a more robust and dramatic C-shape phenotype was observed when both isoforms were depleted (from now on referred to as Double Knockdown or DBKD), with 50 to 55% of the cells adopting the C-shape (Figure 4.4B). Many cells showed a front-rear polarised shape with a convex leading edge and a concave backside. Western blots and quantitative PCR confirmed the efficiency and specificity (Figure 4.4C-E) of our siRNA. Together, this suggests that CYRI-A and CYRI-B are at least partially functionally compensating each other. However, we did not detect any significant change in the mRNA level of one isoform when the other is depleted (Figure 4.4D, E), even though there obviously seems to be a trend. These data suggest a compensatory relationship between CYRI-A and CYRI-B at the protein level and perhaps might also be at the gene expression level.

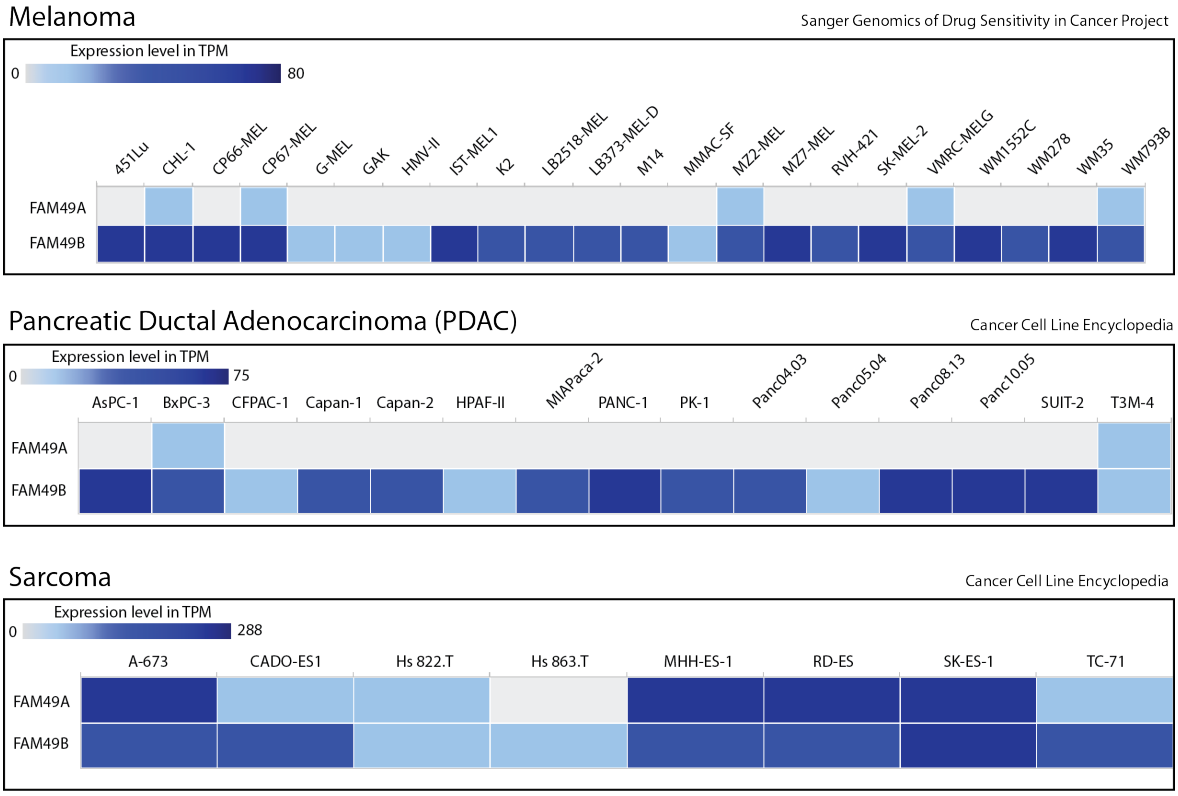

Figure 4.3 Expression atlas of CYRI-A and CYRI-B in several different types of cancers

Gene expression of CYRI-A and CYRI-B from multiple different cell lines of melanoma, Pancreatic Ductal Adenocarcinoma and Sarcoma origin represented in Transcript Per Kilobase Million (TPM).

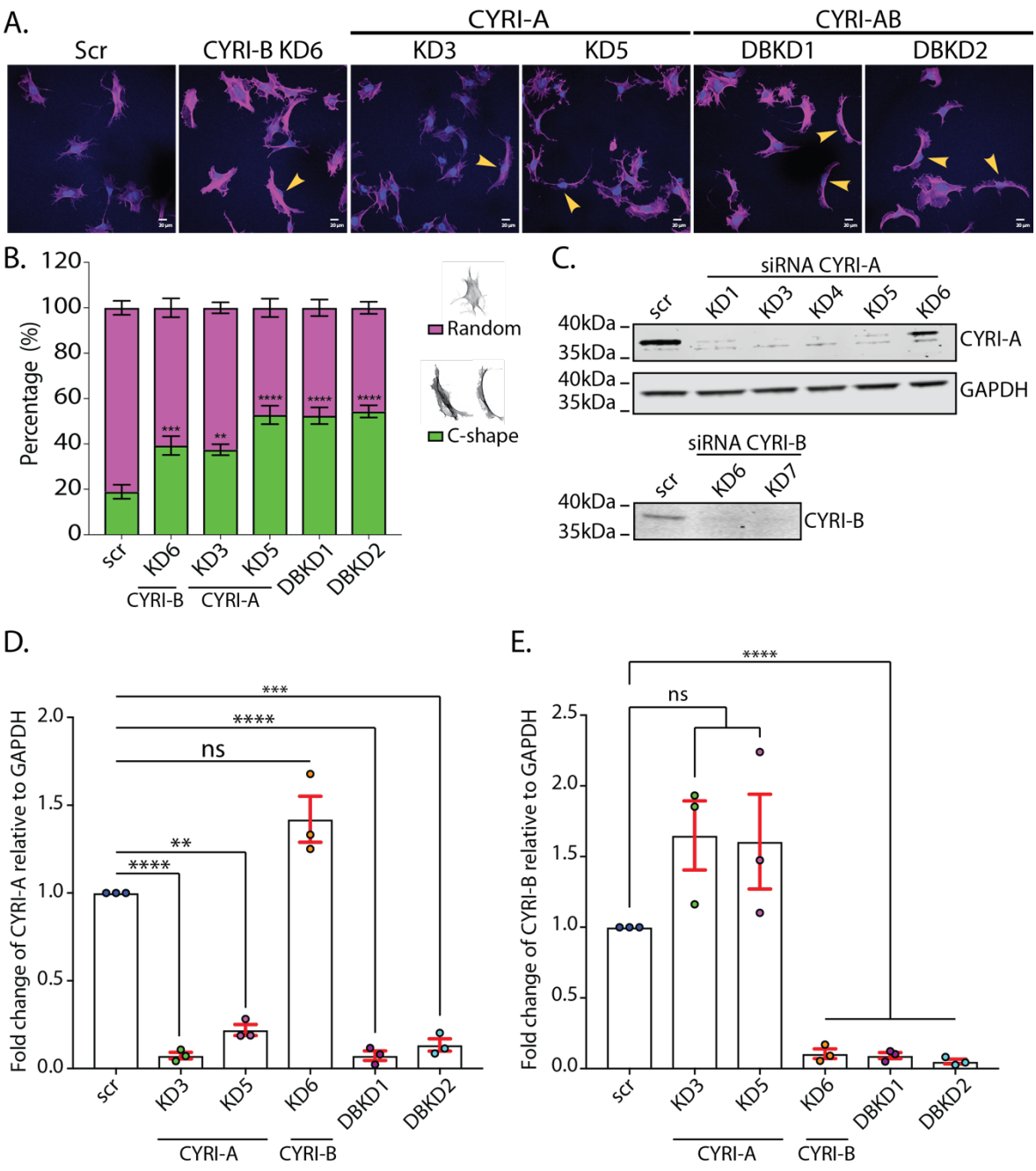

Figure 4.4 Knocking down CYRIs affect cell spreading morphology and migration

A. Depletion of CYRI affects A-673 spreading morphology. Scale bar = 20μm

B. Quantification of the percentage of cells adopting either the random or the C-shape. Knocking down CYRI increases the percentage of cells adopting the C-shape (CYRI-B KD6, CYRI-A KD3 and KD5), with the strongest effect when both CYRI isoforms were depleted (DBKD1 and DBKD2) (~50% cells with C-shape comparing to ~20% in the control pLKO).

C. Western blots show the knockdown efficiency of 4 independent siRNA targeting CYRI-A and two independent siRNA targeting CYRI-B. For convenient purposes, 2 siRNA for CYRI-A KD3 and KD5 and 1 siRNA for CYRI-B KD6 were chosen for further experiments.

D, E. RT-qPCR confirming the efficiency and specificity of the siRNA. Statistical analysis done on log-transformed values.

ANOVA with multiple comparisons, mean ± SEM of 3 independent experiments. *p<0.05, **p<0.01, ***p<0.001, ****p<0.0001.

Because of the dramatic change in the spreading morphology of the DBKD cells, we were wondering whether this could translate into differences in their ability to migrate. We imaged our knockdown cells migrating using a long-term time-lapse system every 15min for 20h. On a 2D fibronectin-coated substrate where cells are free to migrate in any direction, we observed a gradual increase in the mean velocity between conditions, from ~0.3μm/min in the scramble-treated cells to around ~0.45μm/min for the two DBKD cells (Figure 4.5A). To test the migration of these cells in a more physiological condition, we turned to cell-derived matrices (CDM). CDM is made by fibroblasts and forms a thin layer of a 3D meshwork of fibres, which contains collagen, fibronectin and other glycosylated signalling molecules. It has been shown that the CDM can recapitulate the stiffness and post-translational modifications of many proteins in many *in vivo* tissues (Kaukonen et al., 2017). Upon seeding these cells on CDM, we observed the same trend of increasing of the mean velocity in siRNA-treated cells. However, the difference between the scramble (scr) and the two DBKD cells are much more profound under this condition, with an almost 2-fold increase in their mean velocity (~0.2-0.25μm/min) compared to the scramble cells (0.1μm/min) (Figure 4.5B).

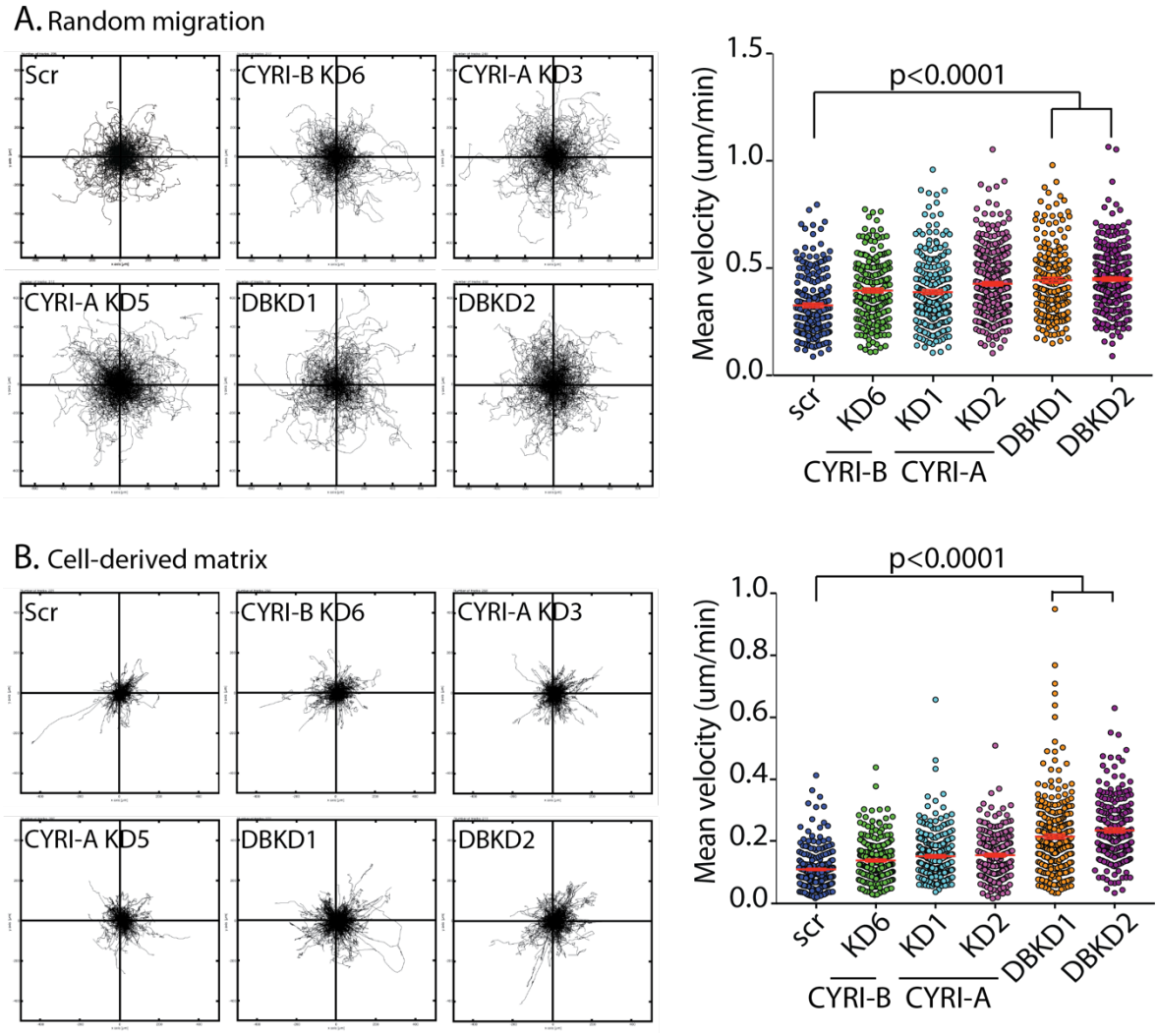

Figure 4.5 CYRI-knockdown cells have migration advantage on both 2D and 3D cell-derived matrix (CDM)

Spider plots of cells migrating on a 2D Fibronectin-coated matrix (A) and in a 3D CDM (B) show a gradual increase in the mean velocity of the knockdown cells. In both cases, the DBKD cells have the highest mean velocity in both setups (0.5μm/min on 2D, 0.2μm/min in CDM) and are significantly higher than the control scramble. Scatter plots of 3 independent experiments. Mean ±SEM. ANOVA with multiple comparisons. scr = scramble, KD = siRNA, DBKD = double knockdown.

The dramatic phenotypes of the DBKD cells prompted us to study them further. However, the transient nature of siRNAs is not ideal for long term experimentation as their effects will start to wear off after a few days, so we decided to generate stable knockout cell lines using the genome editing technology CRISPR-Cas9. Initial attempts were to use a GFP-tagged CRISPR-Cas9 construct to transiently introduce the Cas9-sgRNA into the cells, then using Fluorescence Activated Cytometry (FAC) to sort out the transfected cells. However, this strategy proved to be difficult as the sorted single cells were not able to adhere to and survive long enough on 96-well tissue culture dishes. For these reasons, we utilised the lentiviral transfection and select for transfected cells using puromycin and blasticidin. To verify our previous observations with the knockdown cell lines, we performed immunofluorescence and migration assays. We observe up to 70% of the population with the C-shape in the DBKO cells comparing to just 10-15% of the control pLKO (Figure 4.6A-C). We also measured the spreading area of these cells using an optimised pipeline of CellProfiler. We found that the DBKO cells were about 30% larger on a 2D substrate compared to the control or the single knockout cells (Figure 4.6D). 2D random migration analysis also agreed with our knockdown migration data (Figure 4.6E). Reintroducing untagged CYRI-A back into the DBKO cells by overexpression was sufficient to restore their original mean velocity and brought it back down to the baseline level (~0.25μm/min) (Figure 4.6F). The superior migration ability of the DBKO cells also seems to be independent of external activation such as serum, as these cells migrated just as good with or without 10% serum activation (Figure 4.6G). Finally, we confirmed that our DBKO cell lines also migrated faster than the control or the single knockout in CDM (Figure 4.6H). We also assessed the collective migration ability of our CRISPR cells using wound healing assays with the Incucyte system. Confluent monolayers of either control pLKO, single knockout or DBKO cells were plated on a fibronectin-coated 96-well plate and imaged over 2 days. In agreement with our random migration assays, DBKO cells closed the wound at a rate of about 25% faster than the other cell lines after only 28h (Figure 4.7A-C).

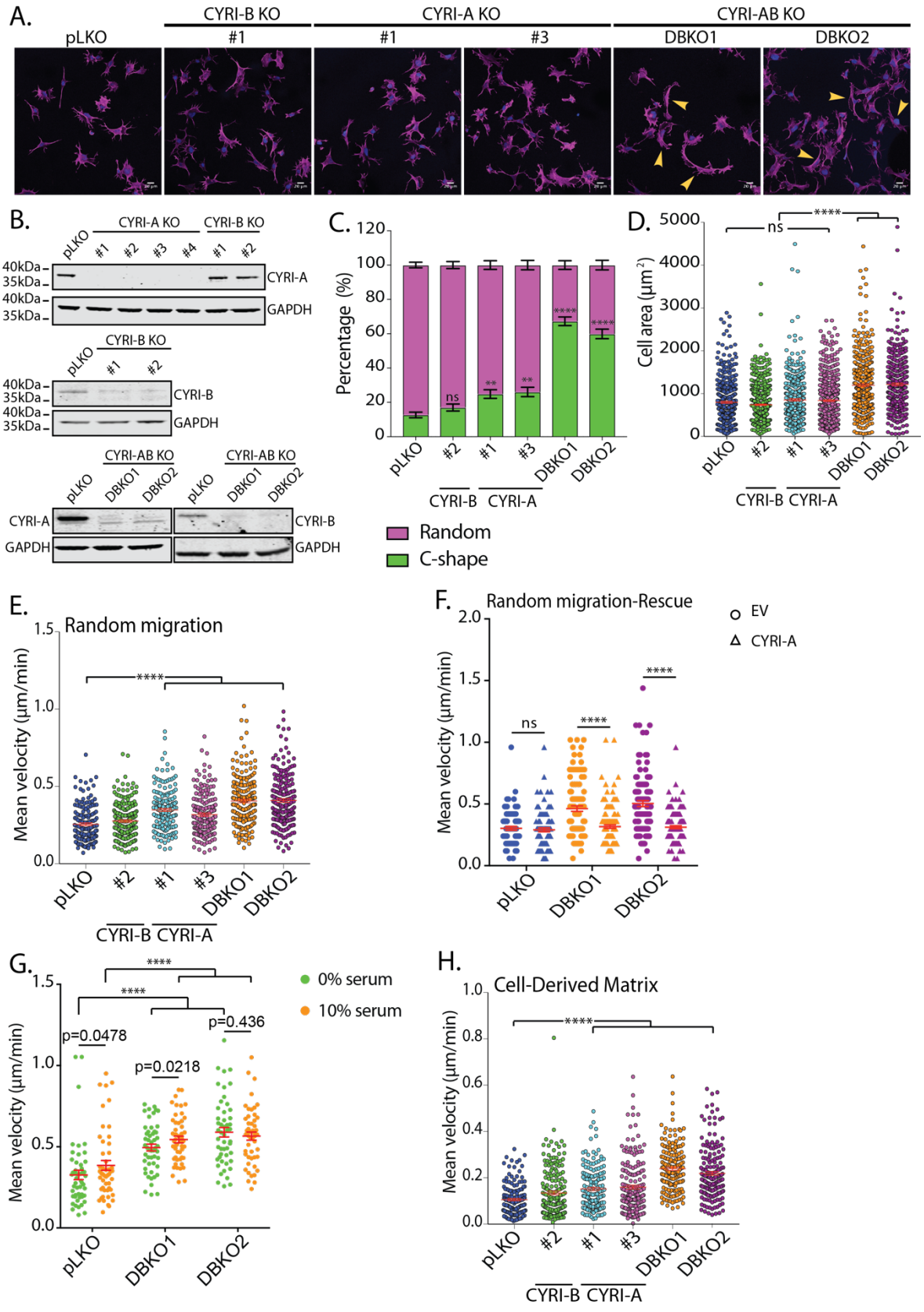

Figure 4.6 CRISPR CYRI cells replicate the observation with the siRNA-treated cells

A. Immunofluorescent images of CRISPR CYRI A-673 shows the dramatic morphological changes in cells without both CYRI-A and CYRI-B. Scale bar = 20μm.

B. Western blot shows the efficiency and specificity of the knockout. CRISPR KO #2 for CYRI-B, CRISPR KO #1 and #3 for CYRI-A and two double knockout (DBKO) 1 and 2 were selected for further experimentation.

C, D. Shape analysis and cell spreading area quantification show a significant increase in the percentage of cells adopting the C-shape in the two DBKOs (~70 %) and a ~30% increase in their spreading area on fibronectin-coated coverslips. Statistical analysis from 3 independent experiments. Mean ± SEM. ANOVA with multiple comparisons.

E. Random migration shows the gradual increase in the mean velocity of the KO cells compared to the control (pLKO) with the strongest difference between the two DBKO (~0.45μm/min) compared to 0.25μm/min of the control. Statistical analysis from 3 independent experiments. Mean ± SEM. ANOVA with multiple comparisons.

F. Reintroducing untagged CYRI-A into the DBKO cells reduced their speed back to the baseline level. Statistical analysis from 3 independent experiments. Mean ± SEM. Unpaired t-test.

G. Random migration before and after 10% serum induction between the control pLKO and two DBKO cell lines. Statistical analysis from 2 independent experiments. Mean ± SEM. ANOVA with multiple comparisons and unpaired t-test.

H. Cell-derived matrix migration analysis shows the same increase in the mean velocity of the DBKO cells (~0.25μm/min) compared to the control pLKO (~0.1μm/min). Statistical analysis from 3 independent experiments. Mean ± SEM. ANOVA with multiple comparisons.

*p<0.05, **p<0.01, ***p<0.001, ****p<0.0001.

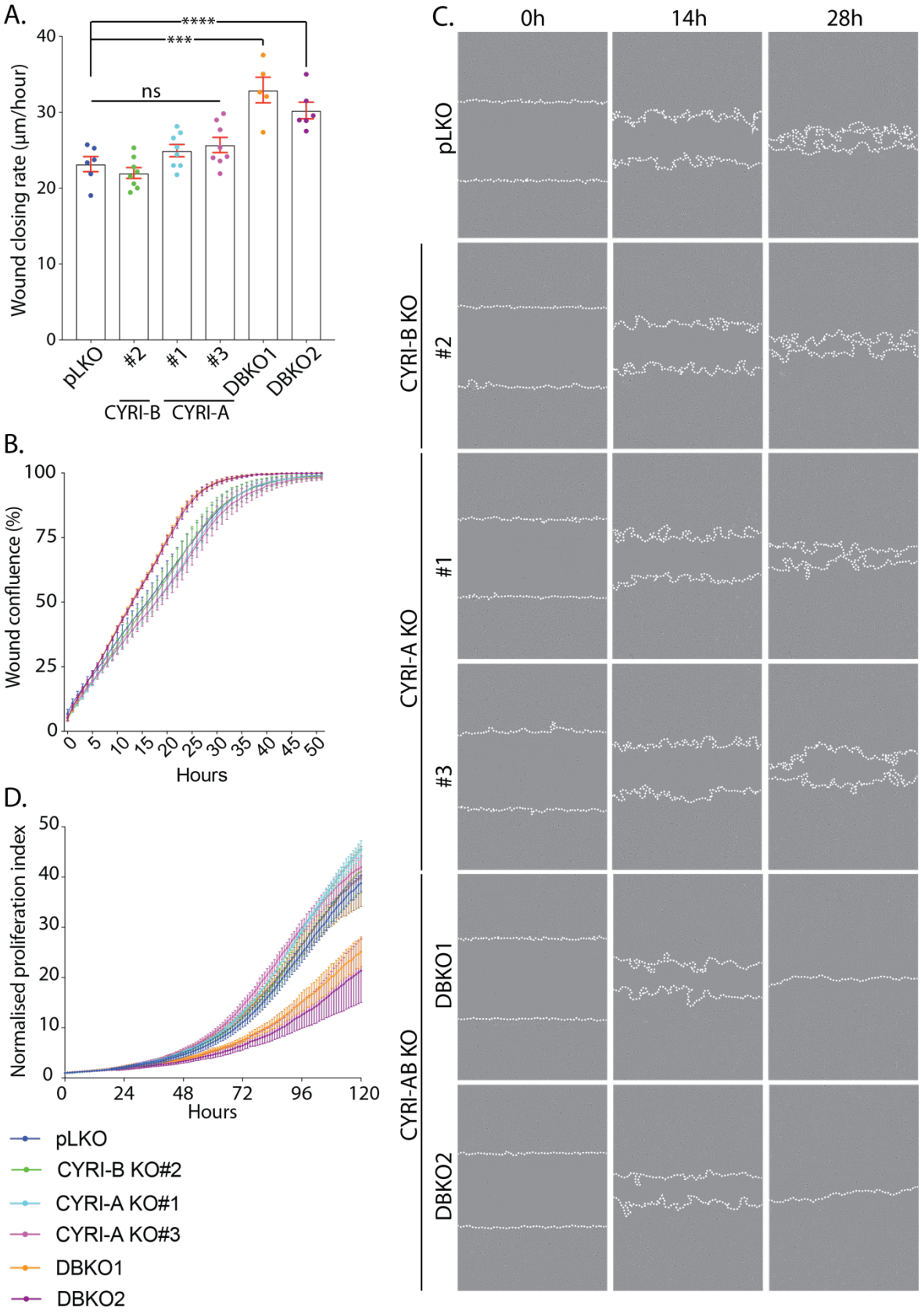

Figure 4.7 CYRIs affect the collective migration and proliferation of A-673 cells

A, B. Wound healing assay of CYRI-CRISPR A-673 cells. Both DBKO cell lines close and cover the wound faster than the control pLKO or the single knockout cell lines. Mean ± SEM. ANOVA with multiple comparisons. *p<0.05, **p<0.01, ***p<0.001, ****p<0.0001.

C. The panel shows the wound closing process over 28h duration. Scatter plots of at least 3 independent experiments.

D. Proliferation assay shows the normalised proliferating rate of the two DBKO cell lines (slope = 0.11) is smaller than the control pLKO or the single knockout (slope = 0.15). Data from 3 independent experiments. Slope is calculated at the inflection point of the sigmoidal curve.

This is, however, not due to a faster proliferation rate by the DBKO cells. In fact, the DBKO cells have a slower proliferation rate compared to the control and the single knockouts when the cell numbers were normalised to the number of dead cells and the number of cells at time 0 (Figure 4.7D). The calculated slope of the growth curve for the two DBKO cell lines is around 0.11, which is shallower than 0.15 of the others. Overall, the data suggest that both CYRI-A and CYRI-B are involved in regulating cell spreading morphology and migration both in 2D and 3D.

4.2.3 CYRIs potentially regulate reactive oxygen species (ROS) level in cells

One of the emerging functions of RAC1 is the regulation of ROS production. It was suggested that upon activation, active RAC1 translocate to the membrane where it interacts with the protein NADPH oxidase (NOX), which is in complex with the p67-p47phox protein complex. This activates NOX, leads to the reduction of a molecule of O2, forming the superoxide (Bokoch and Diebold, 2002, Raz et al., 2010). ROS exert many different biological functions including inflammation (Mittal et al., 2014), cell division and apoptosis (Elumalai et al., 2017), or even driving cancer initiation through Wnt signalling (Myant et al., 2013). Given the role of CYRIs in regulating RAC1 activity, it is possible that this can have a consequence on ROS homeostasis. To address this question, we turned to FACs analysis to probe for any change in the level of ROS in cells lacking CYRIs. Due to the circumstances, the data presented here are only preliminary and we only managed to compare between the control and CYRI-B knockdown A-673 but not CYRI-A or double knockdown.

We knockdown CYRI-B from A-673 then treat both the control and KD cells with either 20mM of NAC (a ROS scavenger molecule) for 60min, 100μM of H2O2 in the form of Tert-Butyl hydroperoxide for 30min or both in that order. We then stained the cells with 1μM of a ROS dye called CellROX Deep Red reagent and DAPI before analysing with the flow cytometer (Figure 4.8A). Cells treated with H2O2 expectedly resulted in an excessive amount of ROS as detected in both the signal intensity and the number of positive signals (Figure 4.8B). In contrast, cells treated with NAC have the amount of ROS reduced by at least 30% in both the scramble and KD condition. NAC also able to marginally counteract the effect of H2O2 addition. Comparing the relative values between the scramble and the KD6 condition, we can see a consistent increase of 20% of ROS production in cells lacking CYRI-B in both tested parameters. It would be interesting to see whether CYRI-A single knockdown could also affect this and whether depletion of both would result in a stronger phenotype. More experiments will definitely be required to understand this effect better.

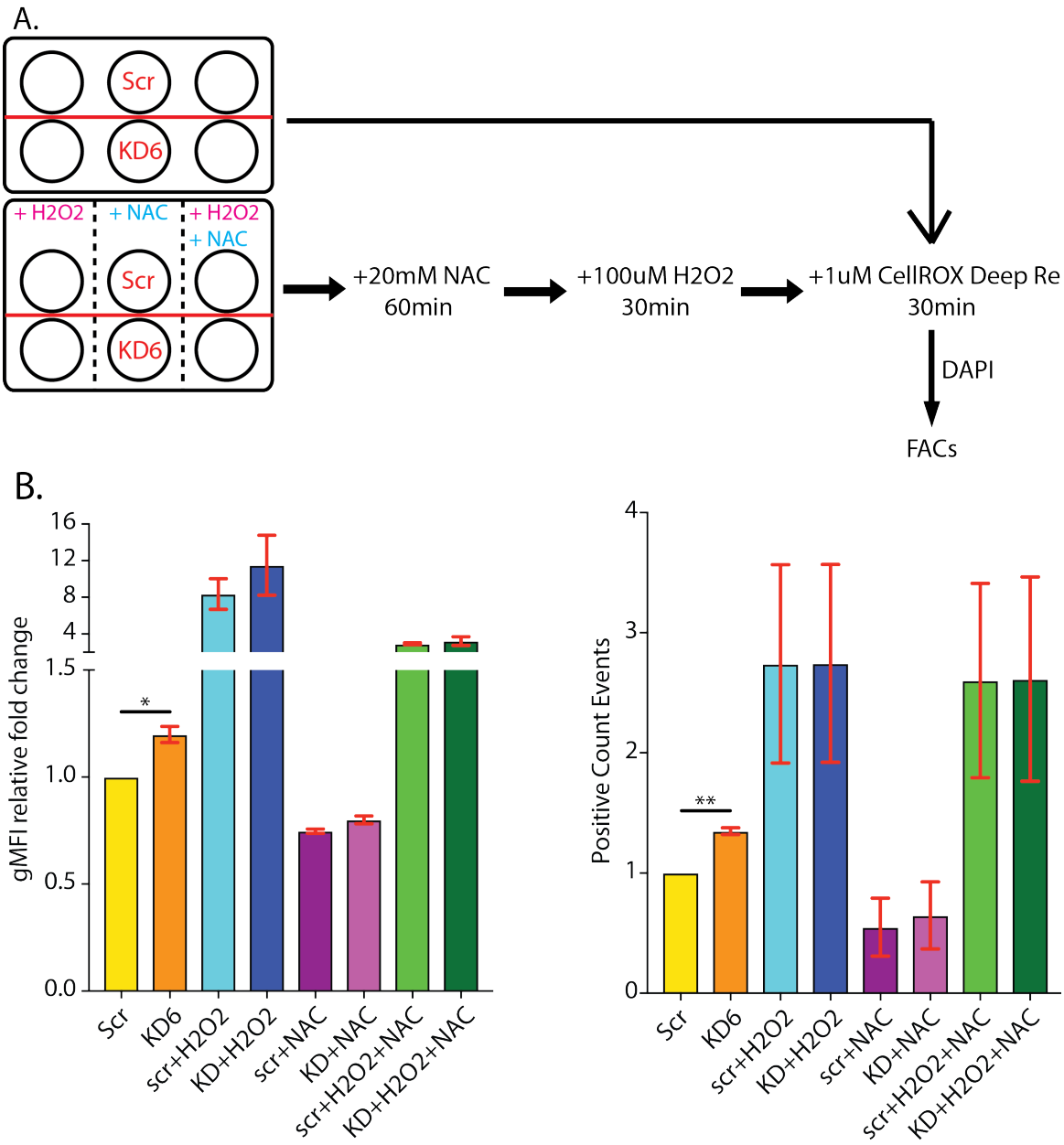

Figure 4.8 CYRI-B potentially regulates ROS production in A-673 cells

A. The schematic representation of the ROS assay. Cells treated with H2O2, NAC or both act as positive controls for the assay.

B. Flow cytometry shows that depletion of CYRI-B leads to a 20% increase in ROS production in these cells, quantified by both the geometric mean fluorescent intensity (gMFI) and the number of positive signal events. Data from 2 independent experiments. Statistical analysis using unpaired t-test. *p<0.05, **p<0.01

4.3 Discussion

The data here suggest that both CYRI-A and CYRI-B share a similar mode of activity in modulating the activity of RAC1 inside cells. This is evident by the fact that COS-7 cells overexpressing with CYRI-A lost their lamellipodia and the characteristic localisation of the Arp2/3 complex at the leading edge. It is, however, possible that CYRIs may regulate this through additional mechanisms due to the observation that the control pLKO COS-7 overexpressed with CYRI-A had only reduced spreading area but no change in the signal of Arp2/3 complex at the lamellipodial edge.

We also established the A-673 cell line as a model system to study the relationship between CYRI-A and CYRI-B *in cellulo*. A-673 is a well-characterised Ewing's sarcoma cell line with the specific chromosomal translocation between chromosome 11 and 22 resulting in a fusion between the gene EWSR1 (a transcriptional regulator) and FLI1 (a DNA-binding protein) (Martinez-Ramirez et al., 2003). This leads to the production of the fusion protein EWS/FLI1 and modulates the activity of multiple genes such as suppressing p53 and upregulating the proto-oncogene c-Myc (Cantile et al., 2013). Multiple reports have also suggested the involvement of RAC1 signalling in Ewing's sarcoma invasion and metastasis. Basic fibroblast growth factor (bFGF) signalling in the bone microenvironment has been shown to trigger the activation of Phosphoinositide-3 Kinase (PI3K) and subsequently RAC1, which enhances cell migration and invasion (Kamura et al., 2010). Stress signals from within a tumour can also trigger the upregulation of a membrane receptor CXCR4 (Krook et al., 2014) to allow cells to respond to an SDF-1α gradient. This activates downstream effectors including RAC1 and CDC42 to allow cells to start migrating. Since we have established the functional importance of CYRIs in modulating RAC1 signalling, this makes studying CYRIs relevant in this context.

In all cases, removing both CYRI isoforms from A-673 cells produced the most dramatic phenotypes. This could be explained because both CYRIs are believed to have the ability to sequester active RAC1. When both are removed, the sudden increase in the level of active RAC1 would result in the dramatic phenotypes

observed. RAC1 activates actin polymerisation, thus having a higher level of the active form of the protein leads to drastic cytoskeletal reorganisation. This is reflected on the bigger lamellipodia and the faster migration speed, particularly in cells lacking both CYRI isoforms. Furthermore, double deletion of CYRIs also seems to affect cell division. This was an interesting observation, but we, unfortunately, did not explore further. However, one possible explanation was the involvement of RAC1 during G2/M progression. Constitutively active RAC1 is shown to accumulate in the cytoplasm to inhibit cell division (Michaelson et al., 2008). In CYRI deleted cells, perhaps this led to a global increase in RAC1 activity, thus led to the incoordination of the cell cycle machinery resulting in a decrease in cell proliferation. It is also interesting to point out the uncoupling relationship between migration and proliferation. Numerous studies have provided evidence that cancer cells that are undergoing migration tend not to proliferate and vice versa. In prostate and bladder cancer, for example, the tumour-initiating cells were enriched with epithelial gene profiles while the migratory mesenchymal cells were lacking any tumour initiation ability (Celia-Terrassa et al., 2012). In carcinoma, epithelial-mesenchymal transitioned (EMT) cells were shown to be invasive and motile. These cells helped pave the way for non-EMT cells to metastasise and form distant colonies (Tsuji et al., 2008). This is reminiscent of the phenotypes we observed in our case. The migratory CYRI DBKO cells proliferate slower while the less migratory control pLKO cells proliferate at a higher rate.

It is also important to note that even though the phenotypes we described were the most prominent when both CYRI isoforms were deleted, single depletion or deletion of each isoform still results in some minor phenotypes. For example, we proposed the link between CYRIs and ROS production where depletion of CYRI-B could lead to a moderate 20% increase in ROS. This was also recently shown in pancreatic cancer cells lacking CYRI-B, where the increased mitochondrial fission leads to increased ROS production and cell migration and invasion (Chattaragada et al., 2018). It is unknown whether deletion of CYRI-A would result in the same phenotype. This suggests that the two isoforms are only partially functionally compensating each other and that they can potentially be regulated differently.

In the next chapter, we will explore the potential localisation and dynamics of CYRIs inside cells, and explore the differences between CYRI-A and CYRI-B.

5 Localising CYRI-A inside cells and fitting into the consensus pathway of macropinocytosis

5.1 Introduction

One of the most challenging aspects of studying an unknown protein like CYRI-A is the lack of tools. There is currently no commercially available antibody that is specific enough to directly visualise CYRI-A with immunofluorescence. We therefore relied on fluorescent tagging of CYRI-A to localise it. In this chapter, we will discuss our strategy of labelling and imaging CYRIs. This has revealed us the unexpected involvement of CYRI-A as well as its kinetics in the process of endocytosis, in particular macropinocytosis. We also reveal a close relationship between PI3K-RAC1-actin-CYRI-A and other effectors including the Arp2/3 complex and cortactin through the use of live-cell imaging in conjunction with specific inhibitors. This makes CYRIs, particularly CYRI-A to be a novel player of macropinocytosis. It is important to note that the majority of this report will be focusing on CYRI-A with occasional touches on CYRI-B for comparison purposes. To avoid any conflict of interest, we will not go into too much detail about CYRI-B.

5.2 Results

5.2.1 Tagging strategy for CYRIs

To date we have little information of CYRI localisation or dynamics in cells. Tagging CYRIs for immunofluorescent visualisation has been proved to be troublesome. Labelling the proteins with any fluorescent protein such as GFP or mCherry at either N- or C-terminus resulted in no specific localisation *in cellulo*. These tagged proteins also seemed to lose their functions as no rescued phenotype was detected when performing rescue experiments possibly due to the tag interfering with the myristoylation and thus plasma membrane localisation.

In a general biochemical pathway of myristoylation, the N-terminal methionine residue must first be removed by an enzyme called methionine aminopeptidase 2. This exposes the 2nd glycine that can be myristoylated by an

enzyme called N-Myristoyl transferase 1/2 (Udenwobele et al., 2017). The myristoyl tail inserts into the lipid bilayer and allows the protein to function (Figure 5.1A). Adding a fluorescent protein at the N-terminus is likely to interfere with this process and thus render the tagged protein inactive (Figure 5.1B, i). When the tag is at the C-terminus, it could also prevent CYRIs from binding to active RAC1 or downstream effectors (Figure 5.1B, ii). However, based on the predicted structures of CYRIs, the N-terminal helix is connected to the DUF1394 domain via a flexible linker that opens when CYRIs are active, we thus decided to insert the fluorescent protein at this linker (Figure 5.1B, iii). Loic Fort, our former PhD student was responsible for the cloning of CYRI-B, while I applied this to the cloning of CYRI-A. First, an extra two restriction sites were introduced into the DNA plasmid sequence of CYRI, just after the codon coding for the 16th proline residue (CYRI-A) or 17th proline residue (CYRI-B) using mutagenesis. This insertion will be just after the predicted N-terminal helix of CYRI. The identity of the restriction sites depends on the sequence of the protein and the vector to ensure that they are not overlapping and easy to manipulate in later cloning stages. In this case, HindIII and BamHI were chosen for CYRI-A while XHoI and NheI were chosen for CYRI-B. Once the new restriction sites were introduced, a PCR product of a fluorescent molecule with matching restriction sites can be inserted. From this point onwards, these constructs are generally referred as P16-[Tag]-CYRI-A and P17-[Tag]-CYRI-B with [Tag] being the appropriate fluorescent proteins GFP, mCherry or smaller tags such as HA-tag.

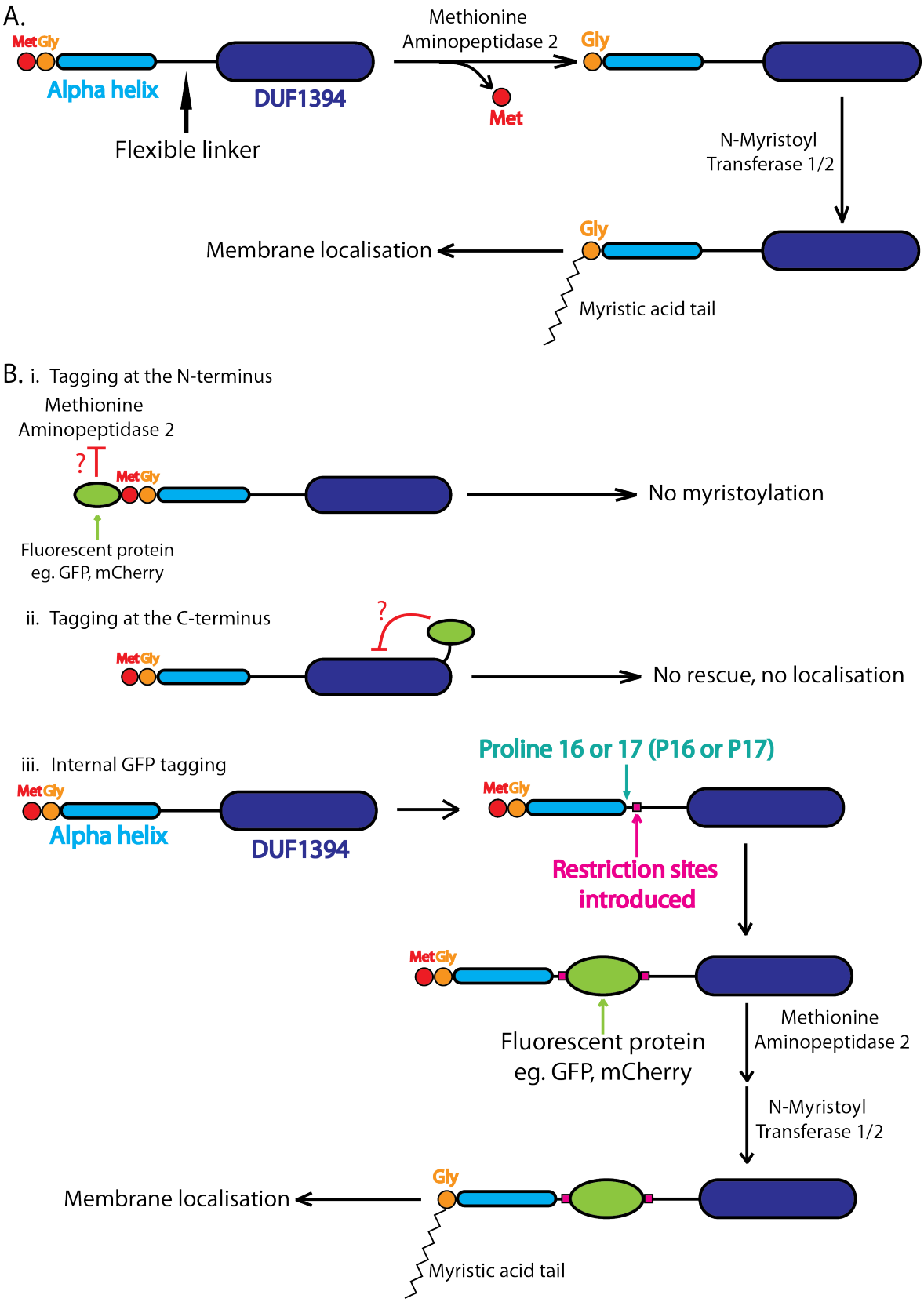

Figure 5.1 Schematic representation of A) the hypothetical myristoylation process and B) the tagging strategy for CYRIs.

Met = Methionine, Gly = Glycine. Red blunt arrow = inhibition.

To assess the functionality of these new constructs, we first reintroduced them back into the COS-7 CYRI-B KO system that we described in chapter 3 to see whether they can rescue the CYRI-B knockout phenotypes. Indeed, overexpressing either P16-GFP-CYRI-A or P17-GFP-CYRI-B was able to decrease the spreading area and the leading edge Arp2/3 signal of these cells (Figure 5.2A). It is interesting to point out that the Arp2/3 signal at the leading edge was also decreased in the control pLKO cells, unlike when rescuing with the CYRI-A-FLAG or bicistronic CYRI-A construct (Figure 5.2B). We reasoned that the internal GFP constructs were perhaps more active due to the inserted fluorescent protein forcing CYRIs into an open state. Nevertheless, this is the first confirmation that the fluorescently labelled CYRI constructs remain active *in cellulo*.

We next performed a cellular fractionation assay to explore the fraction of CYRI proteins in the cytoplasm, membrane or nuclear fractions. First, we checked for the localisation of native, endogenous CYRIs using A-673 cells. Each fraction was probed with the appropriate marker proteins, calnexin for the membrane, Hsp90 for the cytosol and HDAC2 for the nucleus. As can be seen, the native endogenous CYRI-A and CYRI-B are enriched in the cytosolic and membrane fraction but not the nucleus (Figure 5.3A). Thus, CYRIs likely have a dynamic localisation between the plasma membrane and the cytoplasm. We also cannot rule out other sources of membranes in the membrane fraction such as the endoplasmic reticulum or the Golgi apparatus. We are also aware of a fraction of Hsp90 present in the membrane extraction which might be coming from the cytoplasmic fraction despite our best effort. However, this fraction is relatively minor comparing to its main cytoplasmic pool, suggesting that the CYRI signal in our membrane fraction was likely to originate mostly from the membrane network itself (Figure 5.3A).

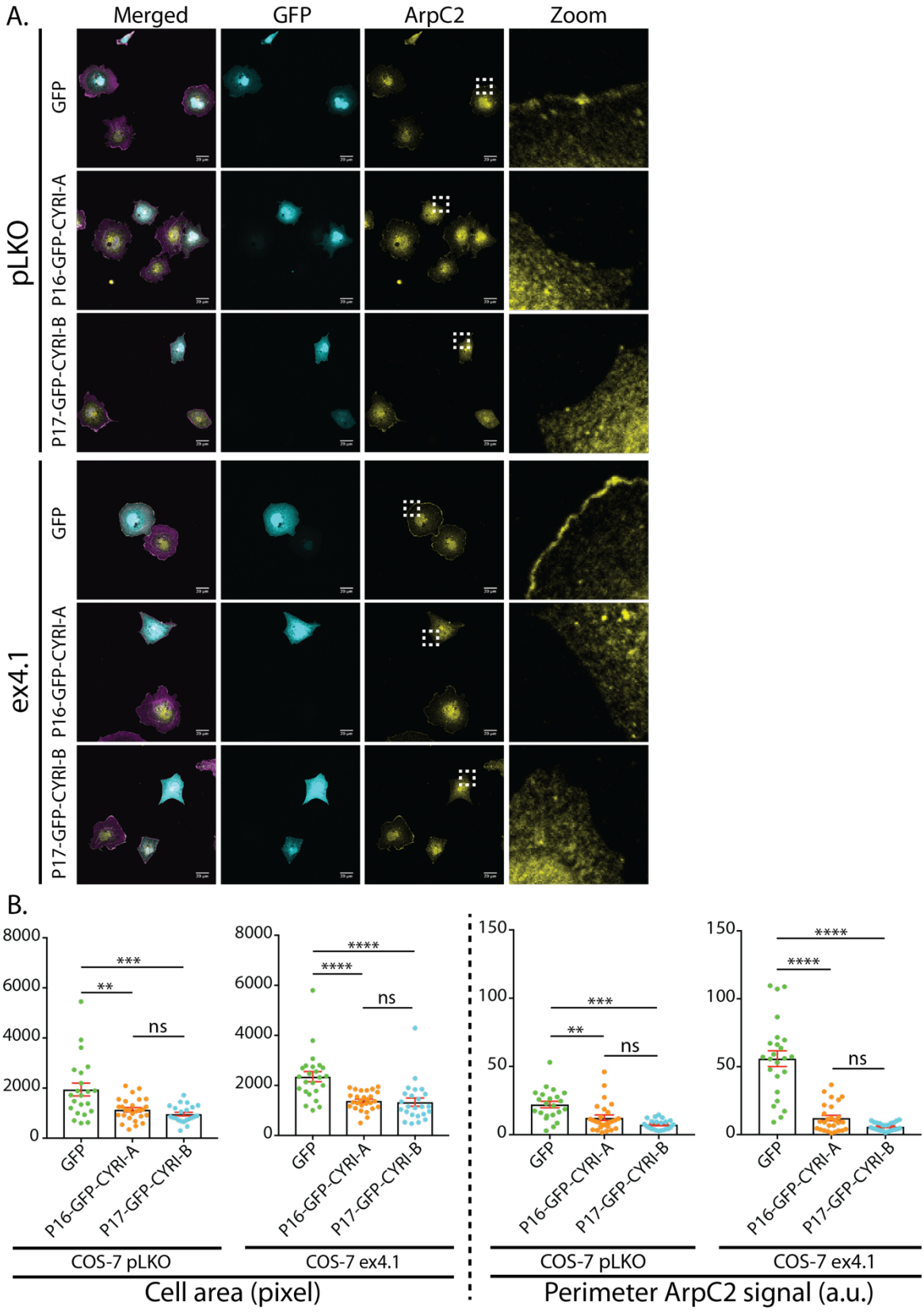

Figure 5.2 Internal GFP CYRI-A and CYRI-B rescued CYRI-B KO phenotypes in COS-7

A. Immunofluorescent imaging of COS-7 control pLKO or CYRI-B KO clone ex4.1 expressing either GFP or the internal GFP CYRI-A or CYRI-B constructs. Zoom show the signal intensity of the Arp2/3 complex at the edge of the lamellipodia. Scale bar = 20μm

B. Quantification of the cell area and the Arp2/3 signal at the leading edge in cells expressing GFP alone or the internal GFP CYRI-A or CYRI-B. In both the pLKO and the ex4.1 cell and in both parameters, there is a significant decrease in the cell area as well as Arp2/3 signal. Statistical analysis of 3 independent experiments. Mean ± SEM. ANOVA with multiple comparisons. *p<0.05, **p<0.01, ***p<0.001, ****p<0.0001.

We consider these results as a reference frame to compare to the localisation of our internal GFP tagged proteins (Figure 5.3B). We overexpressed either GFP or the two internal GFP tagged CYRI constructs in HEK293T cells and performed the same cellular fractionation. For GFP, we observed no specific accumulation in any of the fraction. We believe this is because GFP is a small protein (28.3kDa) and has been shown to diffuse into the nucleus through the nuclear pores (Seibel et al., 2007) and the high number due to the overexpression can lead to non-specific interactions with many membrane compartments. In contrast, our internal GFP-tagged CYRI proteins show accumulation in the cytosolic and the membrane fraction, with only a relatively minor nuclear accumulation for CYRI-B, which could be due to its strong production in HEK293T cells. We do notice a slightly higher accumulation of calnexin and Hsp90 in the nucleus in this blot than expected. However, this does not result in higher nucleus signals for the GFP-tagged proteins suggesting that this spillover does not contribute to the overall localisation of the GFP-tagged CYRIs. Overall, our data suggest for the function and localisation of GFP-tagged CYRI constructs. We will next utilise these two constructs, with a strong focus on CYRI-A in particular, to resolve their spatiotemporal localisation and kinetics in a cellular context.

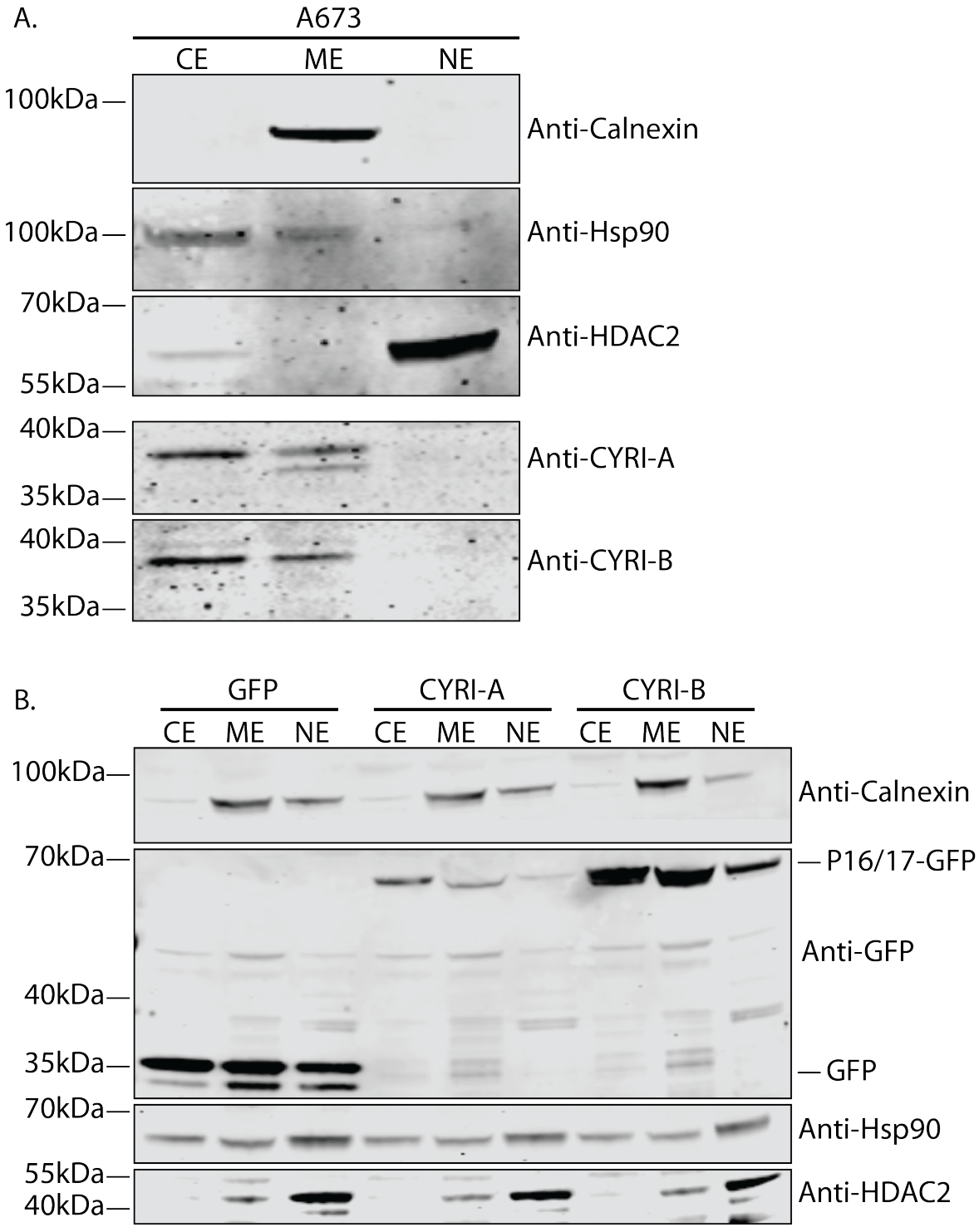

Figure 5.3 Cellular fractionation experiment

A) Endogenous CYRI-A and CYRI-B from A-673 and B) P16-GFP-CYRI-A and P17-GFP-CYRI-B overexpressed in HEK293T cells. CE = cytoplasmic extraction, ME = membrane extraction, NE = nuclear extraction.

5.2.2 CYRI proteins localise to endocytic vesicles but with different membrane-interacting behaviours

Having constructed and established functional GFP tagged CYRI constructs, the next steps aim at visualising the proteins inside cells. We first introduced the P16-GFP-CYRI-A construct into HEK293T and CHL-1. Surprisingly, CYRI-A signal was seen very prominently enriched around many vesicular structures with the occasional tubules or projections (Figure 5.4A,D). The vesicles on average have a diameter of around 2μm, while the tubules can be as long as 7μm (Figure 5.4B,C,E,F). However, the size and the frequency of these structures can vary depending on the cell types. In this case, HEK293T cells tend to form more prominent and bigger vesicular structures than in CHL-1. We noticed that CYRI-A vesicles are in the range of macropinosomes (0.2-5μm in diameter) (Canton, 2018). However, vesicles with smaller diameters are sometimes present, suggesting that CYRI-A might also be involved in other endosomal structures. One of the most interesting features of CYRI-A signal is its dynamic nature. CYRI-A has a very transient localisation on the vesicles. The average lifetime of this localisation usually ranges from ~30s in CHL-1 to ~50s in HEK293T, but some can be longer or shorter (Figure 5.4C,F). CYRI-A positive vesicles also tend to be found at parts of the cell where ruffling occurs, such as at the leading edge, which is reminiscent to that of macropinosomes. When we expressed the internal GFP CYRI-A construct in COS-7 cells, we often observe an amorphous region of CYRI-A near the cell protrusions (Figure 5.4G). This region can be as wide as 15μm (orange double arrow) or as slim as a few microns. CYRI-A resided in this cytosolic portion and could be seen recruited to the plasma membrane (arrows) and then ultimately on vesicular structures. Furthermore, on some occasions, we also observed COS-7 cells performed large engulfment, which in some way reminiscent of phagocytosis with CYRI-A decorating the ruffles and the endocytosed vesicles. It is therefore tempting to speculate the potential function of the protein in phagocytic cells such as macrophages and dendritic cells.

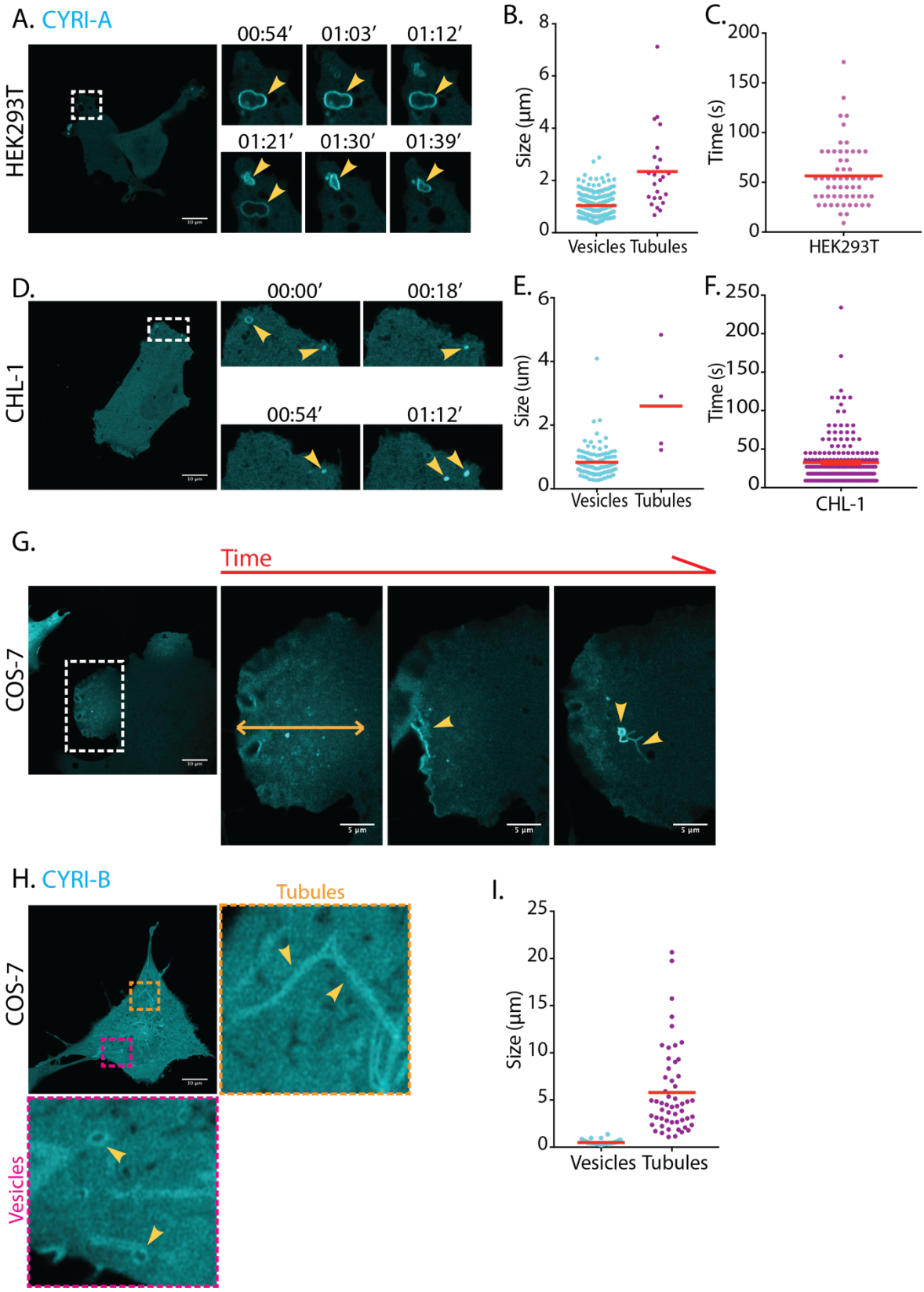

Figure 5.4 CYRI-A and CYRI-B localise to vesicular and tubular structures

A-F. HEK293T and CHL-1 cells expressing P16-GFP-CYRI-A construct. CYRI-A decorates many vesicular structures with occasionally forming tubules with sizes ranging from 0.4 to 4µm or longer for tubules. HEK293T: N=204 events in 18 cells for vesicles and N=24 events in 10 cells for tubules;

CHL-1: N=96 events in 11 cells for vesicles, N=4 events in 3 cells for tubules. Average lifetimes: 50s in HEK293T (N=58 events in 5 cells) and 30s in CHL-1 (N=200 events in 11 cells). Scale bar = 10μm.

G. CYRI-A signal can also be found as an amorphous area (orange double arrow) near cell protrusions that can be recruited to vesicles when needed. Scale bar = 10μm and 5μm.

H, I. CYRI-B forms tubular structures much more frequently than vesicles. Tubules: 1 to 21μm (N=16 events in 3 cells); vesicles: on average 0.5μm (N=22 events in 4 cells). Scale bar = 10μm

Cells are imaged every 9s. Red lines represent the mean value.

Transfection of HEK293T with the P17-GFP-CYRI-B construct caused aberrant cell rounding, so we transfected the CYRI-B construct into COS-7 cells instead. Cells expressing CYRI-B formed copious numbers of tubular structures, which occasionally broke into smaller vesicles (Figure 5.4H). CYRI-B tubules can be much longer than CYRI-A's and can reach up to over 20μm in length. CYRI-B vesicles, on the other hand, are usually much smaller than vesicles decorated with CYRI-A. They could be as small as 0.5μm and were usually derived from pre-existing tubules. CYRI-B signal, unlike CYRI-A, did not seem to show strong accumulation around these structures. In addition, it also persisted on the vesicles and tubules for the whole imaging duration, which was completely different from the behaviour we observed for CYRI-A. Previous reports hypothesized that CYRI-B acts locally (Fort et al., 2018) at the plasma membrane to sequester active RAC1. Here we confirm a proportion of CYRI-A do indeed localise to the plasma membrane, the protrusions in particular, but only when it is recruited by an unknown signal. The other proportion exists in a cytosolic pool and seems to be enriched near the location where it will be needed. However, for CYRI-B, we could not observe any obvious plasma membrane localisation but only on the tubules.

One of the questions that arise from these observations is the striking differences in terms of the morphology and the signal intensity of CYRIs at the vesicles. Looking at the amino acid sequence of the two proteins as well as their predicted crystal structures, there were certain differences that have been discussed in Chapter 3, one of which is the N-terminal helix. We hypothesize that

this helix is important for the localisation and binding kinetics of the proteins to the membrane. CYRI-A harbours an amphipathic helix while CYRI-B does not. Along with this, CYRI-A also lacks one of the cysteine residues at position 10, which is predicted to be important for palmitoylation. This perhaps could give CYRI-A its transient membrane binding nature and CYRI-B persistent binding. To explore further the function of the N-terminal helix, we swap the N-terminal helix of CYRI-B to CYRI-A (which we denoted as BH-GFP-CYRI-A) and vice versa (AH-GFP-CYRI-B). Unfortunately, due to some timing problem, the AH-GFP-CYRI-B was not imaged. Nevertheless, we were able to image the BH-GFP-CYRI-A construct (Figure 5.5). The P16-GFP-CYRI-A and the P17-GFP-CYRI-B localised as expected (Figure 5.5A, B). Intriguingly, our fusion construct BH-GFP-CYRI-A showed striking features that resemble the phenotypes of both CYRI-A and CYRI-B (Figure 5.5C). The fusion protein was highly enriched around endocytic structures resembling that of CYRI-A. However, these structures are long tubules and more importantly, the transient nature of CYRI-A was completely gone. Measuring the signal intensity around these structures and normalised it to the surrounding background revealed that indeed the BH-GFP-CYRI-A signal was comparable to P16-GFP-CYRI-A and was significantly higher than that of P17-GFP-CYRI-B (Figure 5.5D). This result suggests that whether it is the intrinsic biochemical property or the post-translational lipid modifications, the N-terminal helices of CYRIs do indeed play an important role in regulating the localisation of the proteins on the plasma membrane. However, the fact that CYRI-A with CYRI-B's N-terminal helix still retains some of its properties suggests that the DUF1394 also contributes to the localisation, possibly via differential post-translational modifications. A quick search through the curated phosphorylation database PhosphoSitePlus (https://www.phosphosite.org/homeAction) revealed the amino acid tyrosine 116 (Y116) of CYRI-B and lysine 316 (K316) of CYRI-A are potential sites for phosphorylation and ubiquitination, respectively. This could be followed up to further explore the regulation of CYRI dynamic localisation.

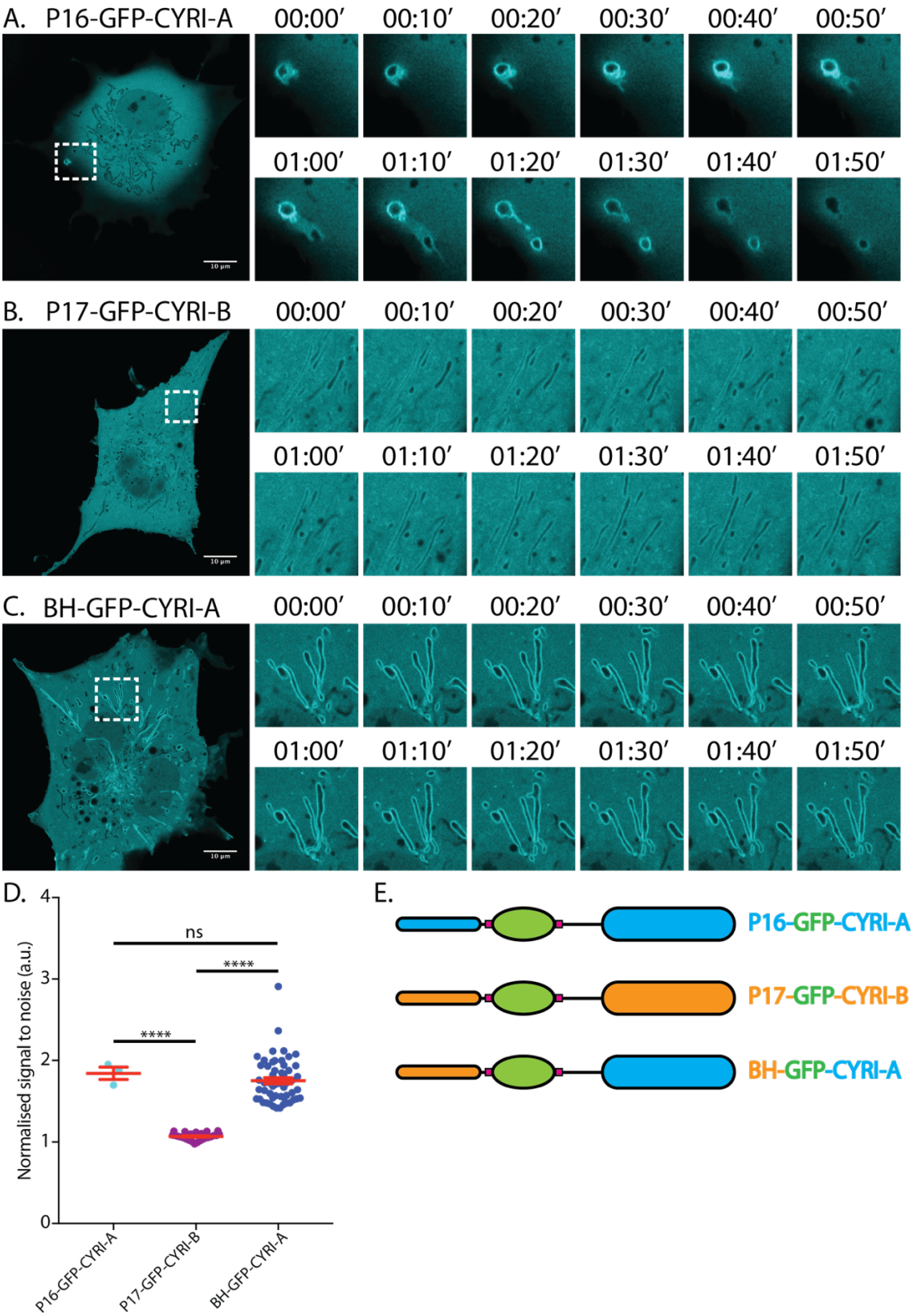

Figure 5.5 Both the helix and the DUF1394 domain affect the behaviour of CYRI proteins on the endocytic membrane

COS-7 cells expressed either A) P16-GFP-CYRI-A, B) P17-GFP-CYRI-B or C) BH-GFP-CYRI-A construct. As can be seen, BH-GFP-CYRI-A construct has both the properties of CYRI-A and CYRI-B. Scale bar = 10μm.

D) Quantification of the CYRI signal around the vesicles in the first frame relative to the background of P16-GFP-CYRI-A (N=3 events in 2 cells), P17-GFP-CYRI-B (N=25 events in 2 cells) and BH-GFP-CYRI-A (N=54 events in 2 cells). Mean ± SEM. ANOVA with multiple comparisons. ****p<0.0001.

E) Cartoon representation of the wild-type P16-GFP-CYRI-A, P17-GFP-CYRI-B and the hybrid BH-GFP-CYRI-A construct.

Since many of the tubules we observed inside cells were decorated with CYRIs, and that many of these structures seemed to derive from pre-existing vesicles, one of the questions we have was could CYRIs contribute to membrane tubulation? To address this question, we collaborated with Professor Hongxia Zhao from the University of Helsinki and utilised an *in vitro* membrane tubulation assay with recombinant CYRI-A and CYRI-B. Liposomes were made from a mixture of POPC, POPE and POPS and then subjected to electron microscopy protocol. Liposomes that did not have any protein were uniform and round (Figure 5.6). However, and perhaps surprisingly, liposomes containing recombinant CYRI-B at various concentrations did not result in any membrane tubulation. In contrast, liposomes mixed with recombinant CYRI-A formed extensive membrane tubulation even at a concentration as low as 0.4μM (Figure 5.6). More interestingly, at higher concentration of 4μM, small and fragmented vesicles were observed. We hypothesized that perhaps at high concentrations, the tubulation effect of CYRI-A was strong enough to drive the budding-off process of many smaller vesicles. This observation would be in line with our observation *in cellulo* where membrane tubules could be seen protruding out from CYRI-A positive vesicles and suggested that CYRI-A could actively be involved in driving membrane tubulation and facilitating endosome formation. Surprisingly, we did not observe any tubulation in any concentration with CYRI-B.

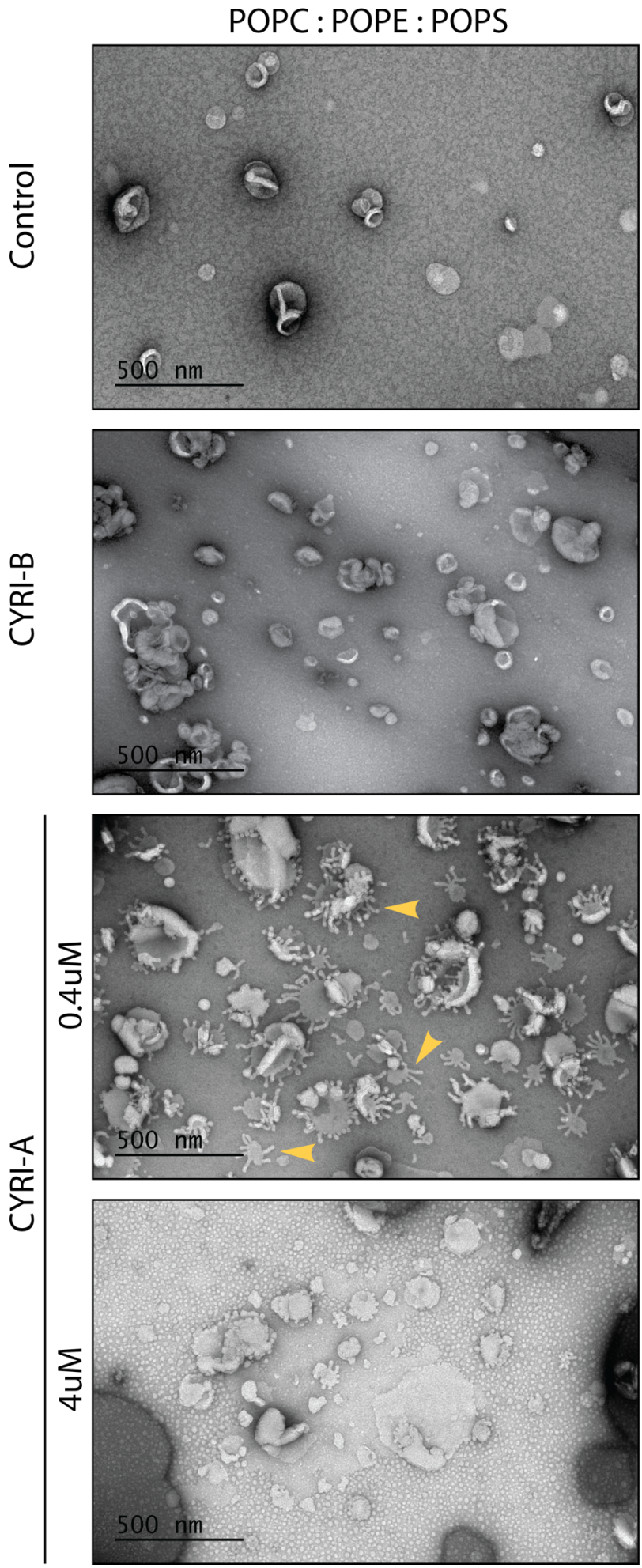
POPC : POPE : POPS
Control
500 nm
CYRI-B
500 nm
CYRI-A
0.4uM
500 nm
4uM
500 nm

Figure 5.6 CYRI-A but not CYRI-B induces membrane tubulation and budding *in vitro*

POPC:POPE:POPS liposomes were mixed with purified full-length recombinant CYRI-A or CYRI-B at various concentrations and observed with electron microscopy. Both the control liposomes without any protein and liposomes with CYRI-B show no visible tubulation. Liposomes mixed with CYRI-A form extensive tubulation at 0.4μM. At 4μM, the extensive tubulation leads to the formation of many smaller liposomes, presumably through budding off from the larger ones. Scale bar = 500nm.

Credit: Professor Hongxia Zhao, University of Helsinki. We provided the proteins while the experiments were carried out in Professor Zhao's lab.

5.2.3 CYRI vesicles are part of the RAB5A endocytic network

The observation of endosomal vesicles positive for CYRIs leads us to wonder about their identity. We query the relationship between CYRIs and a well-known marker for the endocytic network RAB5A (Bucci et al., 1994, Chen et al., 2009, de Hoop et al., 1994). COS-7 cells were co-transfected with either GFP as the negative control or the internal GFP-tagged CYRI-A or B along with a mCherry-tagged RAB5A construct. RAB5A localised to many endocytic vesicles of different sizes and can be seen moving from the cell periphery to the perinuclear region. GFP alone was homogenously cytoplasmic and did not co-localise on vesicles with mCherry-RAB5A (Figure 5.7A, B). However, CYRI-A shows a more dynamic and specific localisation (Figure 5.7C-E). At first, we observed brief colocalization events between CYRI-A and RAB5A signal in many vesicles. We noticed that these brief colocalization events are in fact sequential events between CYRI-A and RAB5A signals. As the endosome progressed into the cell, CYRI-A signal got brighter before quickly declined. At the same time, as CYRI-A signal went down, RAB5A signal started to increase (Figure 5.7D). We also observe similar behaviour between CYRI-A and RAB5A in HEK293T cells (Figure 5.7F-H) suggesting that these events are likely to be conserved between different cell lines. Measuring the duration of CYRI-A on these vesicles before the appearance of RAB5A gives us an estimate of the resident time to be around 50s in both cell lines (Figure 5.7E, H).

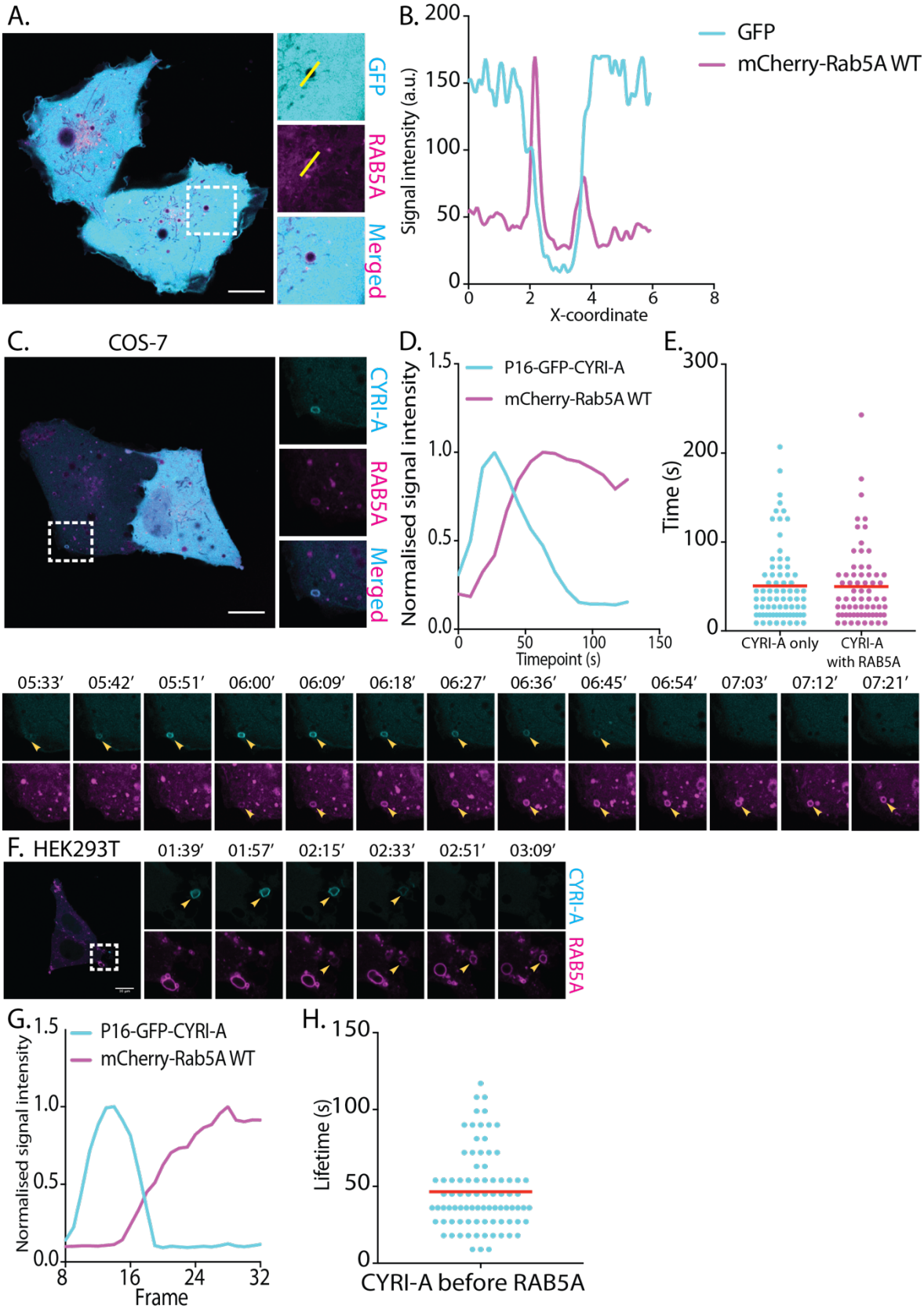

Figure 5.7 CYRI-A vesicles are linked to RAB5A endocytic network

A, B. GFP (cyan) and mCherry-RAB5A (magenta) show no specific localisation between the two signals. Line graph of a representative vesicle shows no colocalization between the GFP signal and the mCherry signal.

C-H. CYRI-A (cyan) signal preceded RAB5A signal in both COS-7 (C-E) and HEK293T cell (F-H). Following the spike up of CYRI-A signal is the RAB5A signal (line graphs). CYRI-A alone signal lasts ~50s before RAB5A arrives (N=75 events in 8 cells for COS-7, N=84 events in 7 cells for HEK293T). CYRI-A and RAB5A colocalise in COS-7 for about ~50s before CYRI-A signal completely disappears (N=68 events in 8 cells). Yellow arrows indicate vesicles.

Cells are imaged every 9s. Red lines represent the mean value. Scale bar = 10μm.

In COS-7, CYRI-A would slowly fade away as RAB5A appeared, and this would take another 50s (Figure 5.7E). Overall, these observations placed CYRI-A upstream of RAB5A in the endosomal pathway. In comparison, CYRI-B and RAB5A show a much more persistent and long-lasting colocalization (Figure 5.8). CYRI-B decorated many of the intracellular tubular structures that often branched off along with RAB5A. However, we did not observe any dynamics between the two proteins.

5.2.4 CYRI-A vesicles are macropinosomes by nature

CYRI-A vesicles usually have an average size of around 1 to 2μm and often were found near membrane ruffles. The relatively large diameter and the leading-edge localisation led us to hypothesize these vesicles could be of macropinosome origin. In *Dictyostelium*, CYRI protein had been found to associate with macropinosomes in an unbiased proteomic screen but this was not followed up to our knowledge (Journet et al., 2012). To test our hypothesis, we label the fluid phase outside the cells using Dextran 70kDa. If CYRI-A positive vesicles are macropinosomes, we would expect to observe the fluorescence of the Dextran within these structures. Indeed, this is the case as shown in Figure 5.9. We tested on three different cell types, COS-7, HEK293T and CHL-1 and in all cases, CYRI-A positive vesicles were seen frequently taking up Dextran. Up to 75% of CYRI-A positive vesicles in COS-7, 88% in HEK293T and almost 100% in CHL-1 cells contain Dextran suggesting that the majority if not all of CYRI-A vesicles are macropinosomes by nature.

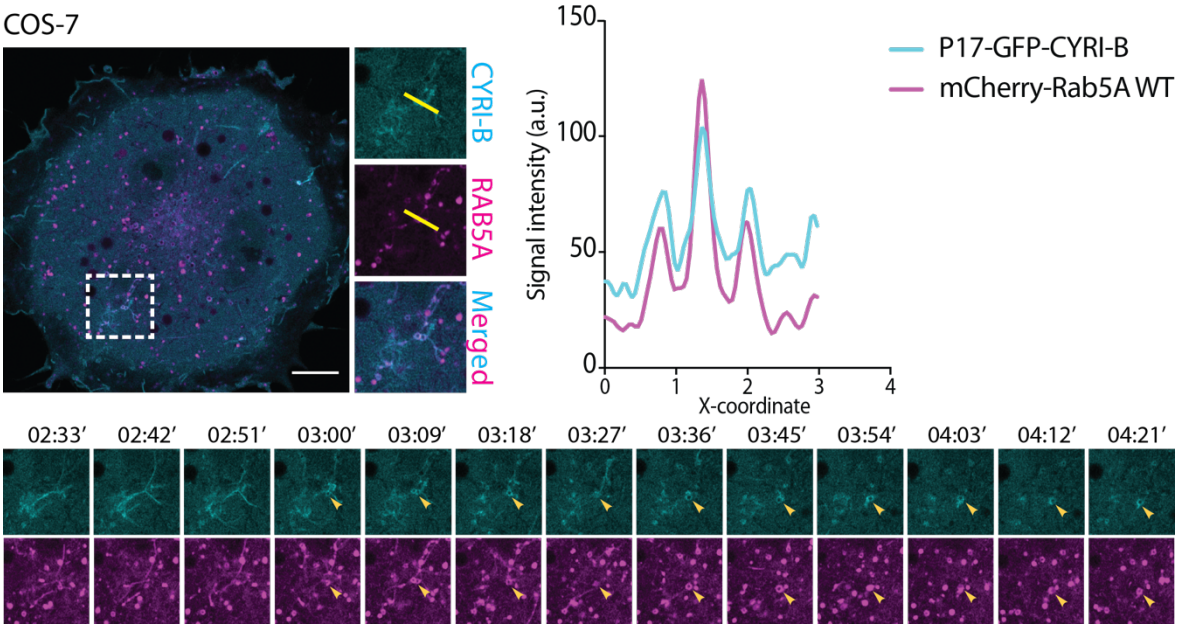

Figure 5.8 CYRI-B shows a persistent colocalization with RAB5A

COS-7 cells were co-transfected with P17-GFP-CYRI-B (cyan) and mCherry-RAB5A (magenta). The line graph shows a strong colocalization between the two proteins of one timepoint (yellow line in the zoom image). Still images show the persistent localisation of the two markers throughout the imaging duration. Cells are imaged every 9s. Scale bar = 10μm.

Measuring the diameter of these Dextran-positive, CYRI-A positive vesicles, we confirmed that they were within the range of macropinosomes (1 to 1.5μm on average in diameter) and 5μm on average in length for tubules. We also have evidence that CYRI-B positive tubules also contain Dextran (data not shown). To exclude other common endocytic pathways, we co-expressed CYRI constructs with either CLC15 (for Clathrin endocytosis), CAV1 (for Caveolin dependent endocytosis) or ARF1 (for ARF1-dependent endocytosis) in COS-7 cells. In all cases, we observed no obvious colocalization between CYRI signal and any of the listed markers (Figure 5.10). Most of the vesicles derived from these markers are much smaller than CYRI-positive vesicles. Indeed, when we measure the apparent size of Clathrin coated vesicles, they were usually around 0.2 to 0.4μm in diameter, which are significantly smaller than CYRI-positive vesicles (typically around 0.5-1μm). It should be noted that the apparent size of CLC15-positive vesicles measured here appears to be larger than the expected size of clathrin-coated vesicles, which should be around (0.04-0.2μm) (Kirchhausen et al., 2014).

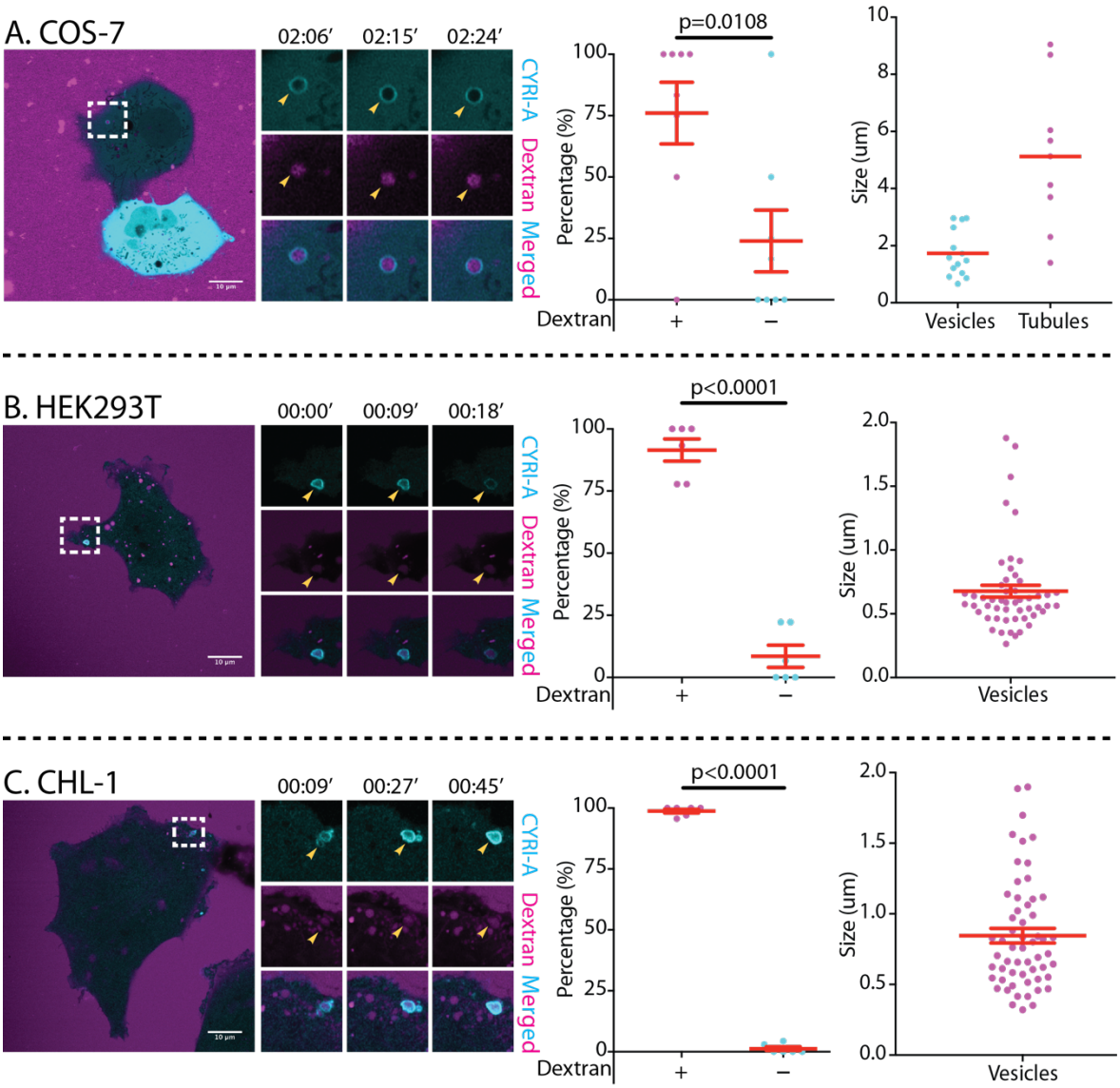

Figure 5.9 CYRI-A vesicles are macropinosomes

(A) COS-7, (B) HEK293T and (C) CHL-1 cells expressing P16-GFP-CYRI-A construct in the presence of 500ug/ml of Dextran70. CYRI-A positive vesicles contain Dextran70 (arrows). Quantification showing most of the CYRI-A positive vesicles contain Dextran (75% in COS-7 (N=9 cells), 88% in HEK293T (N=6 cells), ~100% in CHL-1 (N=6 cells)) (left graphs). The size of vesicles is around 1-2um (N=15 events in 7 cells in COS-7, N=53 events in 6 cells in HEK293T, N=57 events in 6 cells in CHL-1) and tubules are around 5um (N=10 events in 7 cells in COS-7). Statistical analysis using unpaired 2-tail t-test. Mean ± SEM. Scale bar = 10μm.

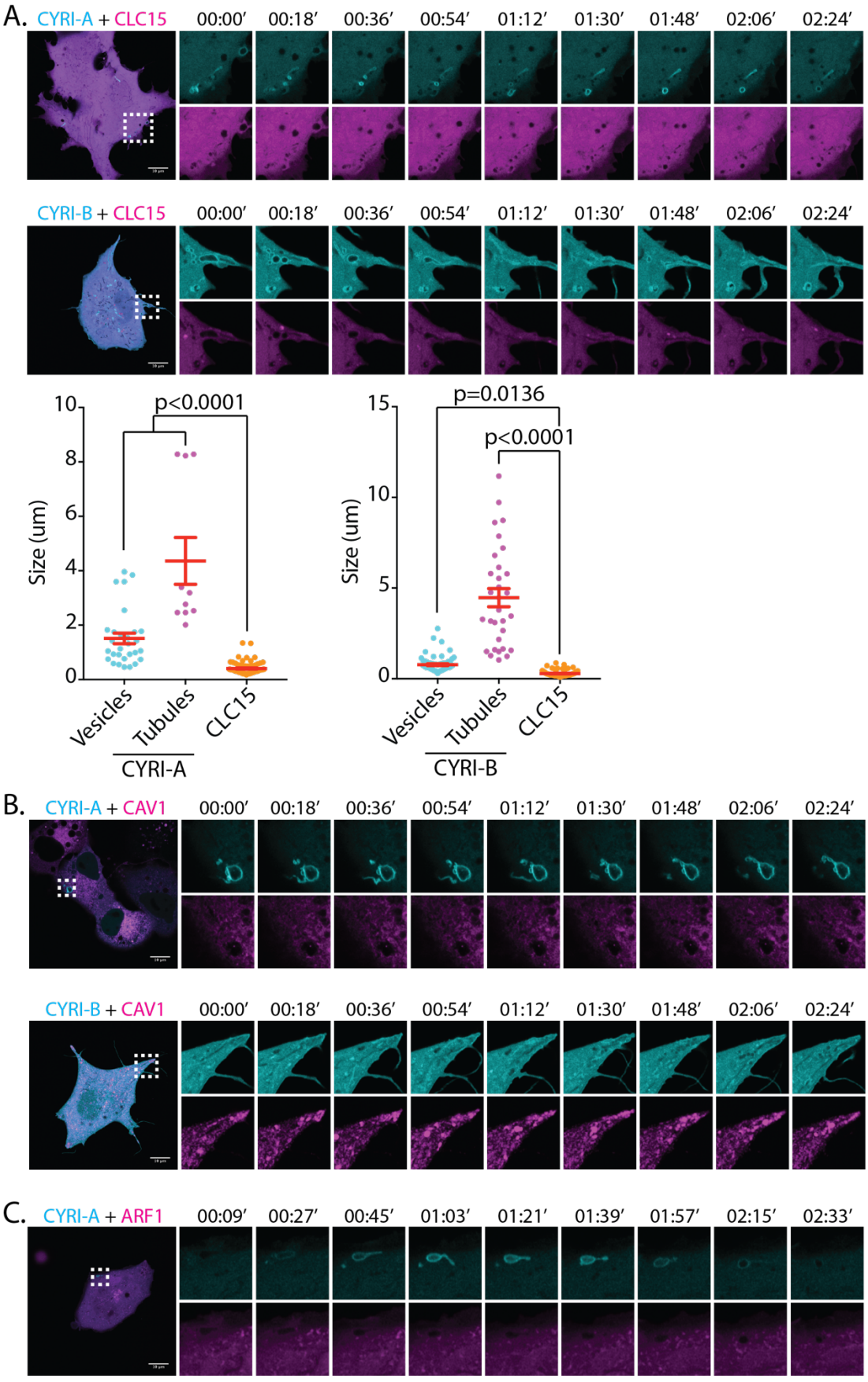

Figure 5.10 CYRI-A and CYRI-B are not co-localising with Clathrin, Caveolin or ARF1

COS-7 cells were co-transfected with either P16-GFP-CYRI-A or P17-GFP-CYRI-B and either A) mCherry-tagged CLC15 (for Clathrin Light Chain 15), B) CAV1 (for Caveolin) and C) ARF1. No colocalization between CYRIs and any of the other markers for other endocytic pathways. Scatter plot shows the CYRI-positive vesicle and tubule size compared to Clathrin vesicles (0.2-0.4μm). CYRI-A vesicles are from N=25 events in 6 cells, CYRI-A tubules are from N=8 events in 4 cells, CYRI-B vesicles are from N=85 events in 5 cells, CYRI-B tubules are from N=31 events in 5 cells. Clathrin for CYRI-A is from N=87 events in 6 cells, Clathrin for CYRI-B is from N=93 events in 5 cells. Statistical analysis is done using ANOVA with multiple comparisons. Mean ± SEM. Scale bar = 10μm.

This could be due to the diffraction limit of the microscope to small structures which limits the precise measurement of these structures. Nevertheless, these data strongly suggest that CYRIs are involved in macropinocytosis and are distinctive from other endocytic pathways.

5.2.4 CYRI-A forms a regulatory loop with actin at the macropinosomes

In mammalian cells, actin has been implicated in driving many of the endocytic processes, including clathrin-dependent and clathrin-independent processes. Actin polymerisation exerts forces on the vesicles to facilitate the inwards movement of endocytic cups into the cell. The hydrostatic force of the cytosol tends to push the plasma membrane outwards, thus suppressing any invagination which is the first step of many endocytic processes. Actin polymerisation counteracts this tension. In macrophages, filamentous actin (F-actin) was shown to extend and push on the plasma membrane creating “tent pole” structures that can then be formed into large macropinosomes (Condon et al., 2018). Knowing the important functions of actin in macropinosome formation and that CYRIs are likely to be involved in this process, we asked whether we could localise actin to CYRI vesicles. We co-transfected COS-7 with either GFP, P16-GFP-CYRI-A or P17-GFP-CYRI-B and LifeAct-RFP (Figure 5.11). GFP shows no specific localisation with LifeAct-RFP as expected, however, both CYRI-A and CYRI-B shows a strong colocalization with the actin signal around endosomes (Figure 5.11A). In COS-7 cells, many of the endosomes appear to have an oscillating signal between actin and CYRI-A, but all follow a similar manner: the actin signal spiked up then being followed by the CYRI-A signal, then both decreases. Tracking these signals over time clearly demonstrates this behaviour (Figure 5.11B, i). However, we

found it difficult to decipher the temporal relationship between actin and CYRI-A in COS-7 due to the cortical LifeAct signal was not always clear. We turned to HEK293T cells, which naturally form more ruffles, to try to answer this question (Figure 5.11B, ii). Agreeing with the data in COS-7, tracking the signal between actin and CYRI-A on endosomes showed the same dynamic relationship between the two proteins. Furthermore, we were able to measure the duration that actin spent at the endosomes before CYRI-A arrived to be around 36s. Actin spent another 54s colocalising with CYRI-A before both signals disappeared (Figure 5.11B, ii, right graph). Due to the relatively large endosomes along with the more dynamic actin network, we also noticed an interesting behaviour of actin. As the endosomes entering the cell and CYRI-A signal disappearing, the actin also changed from surrounding the vesicles into being polarised to one side and pushed the vesicles forwards. We believed that this phenomenon is known as actin comet tail. What exactly is the link between CYRI-A and the actin comet tail remain to be elucidated.

On the other hand, CYRI-B maintains a steady and static colocalization with actin throughout the imaging duration. However, interestingly, in many occasions, we did observe CYRI-B tubules seemed to align with the actin fibres (Figure 5.11C). It has been shown that actin polymerisation is needed to stabilise the tubulation process of endosomes (MacDonald et al., 2018, Puthenveedu, 2010 #98), hence it is tempting to speculate that this could be the case.

The dynamic relationship observed between actin and CYRI-A is likely to suggest a suppressive relationship between the two signals. Active RAC1 sits at the centre of the actin cytoskeleton organisation by activating the Scar/WAVE complex. By binding and sequestering RAC1, CYRI can indirectly affect this process and thus acts like a fine tuner to modulate the function of actin at endosomes. We would also argue the same mechanism applied to CYRI-B. The persistent binding kinetic of CYRI-B on the vesicular membrane is perhaps what kept the actin signal from spiking up and prevented it from oscillating.

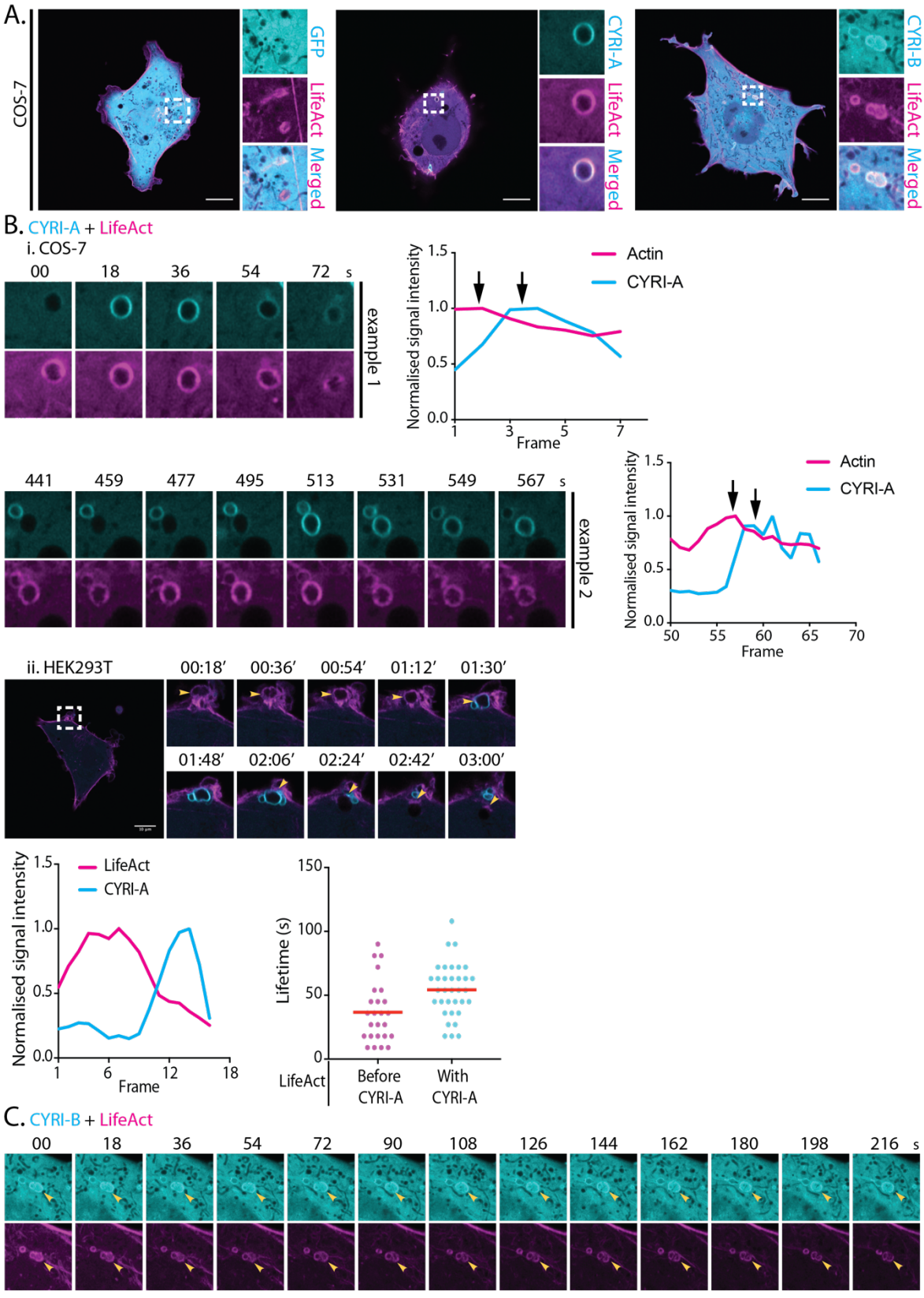

Figure 5.11 CYRI-A and CYRI-B colocalise with actin and CYRI-A suppresses actin polymerisation

A. CYRI-A and CYRI-B but not GFP colocalise with LifeAct in COS-7 cells.

B. Actin signal is followed by CYRI-A signal in i) COS-7 (black arrows shows the peak of the signals) and ii) HEK293T cells. Line graphs show the signal intensity of CYRI-A and actin over time. Scatter plot quantify the lifetime of the LifeAct signal before the arrival of CYRI-A (~36s) (N=25 events in 10 cells) and also during CYRI-A (~54s) (N=34 events in 10 cells). Red lines represent the mean value.

C. CYRI-B and actin show a persistent colocalization throughout the imaging duration.

Cells are imaged every 9s. Scale bar = 10μm.

Since actin helped with the formation of macropinosomes, we were wondering how disrupting actin polymerisation would affect CYRI-A behaviours? We transfected COS-7 or HEK293T with the internal GFP-tagged CYRI-A and LifeAct-RFP, and imaged cells before and after the addition of 1μM latrunculin, which binds to monomeric actin and prevents it from polymerizing (Figure 5.12). Before the addition of latrunculin A, we observed CYRI-A localising to large vesicles, which usually lasted for around 100s in COS-7 or around 50s in HEK293T cells. These vesicles formed and then slowly disappeared through multiple imaging frames. However, as soon as latrunculin A was added, the cells immediately responded. Large actin cables stretching across the cells quickly disappeared, along with the cortical actin meshwork. This resulted in a dramatic collapse of the cell along with the formation of actin focal point structures that are called actin asters (Figure 5.12A, B, yellow arrows). CYRI vesicles quickly deformed and started to protrude multiple tubules. These structures were unstable, active and short-lived. Along with it, multiple CYRI-A vesicles quickly formed and disappeared within one frame of imaging. Quantifying these vesicles showed a significant decrease in their lifetimes in the presence of latrunculin A (Figure 5.12C) (100s to 40s in COS-7, 50s to 20s in HEK293T). Many vesicular structures seemed to form in the vicinity of the actin asters, suggesting either the remnant of actin polymerisation in these asters could still support vesicle formation or the actin asters themselves could somehow act as the seed for membrane curvature and tubulation. More interestingly, many of the vesicles also seemed to form in area where there was no actin either (Figure 5.12A, B, arrows). However, latrunculin A has been shown to activate the Scar/WAVE complex through an unknown mechanism (Millius et al., 2009).

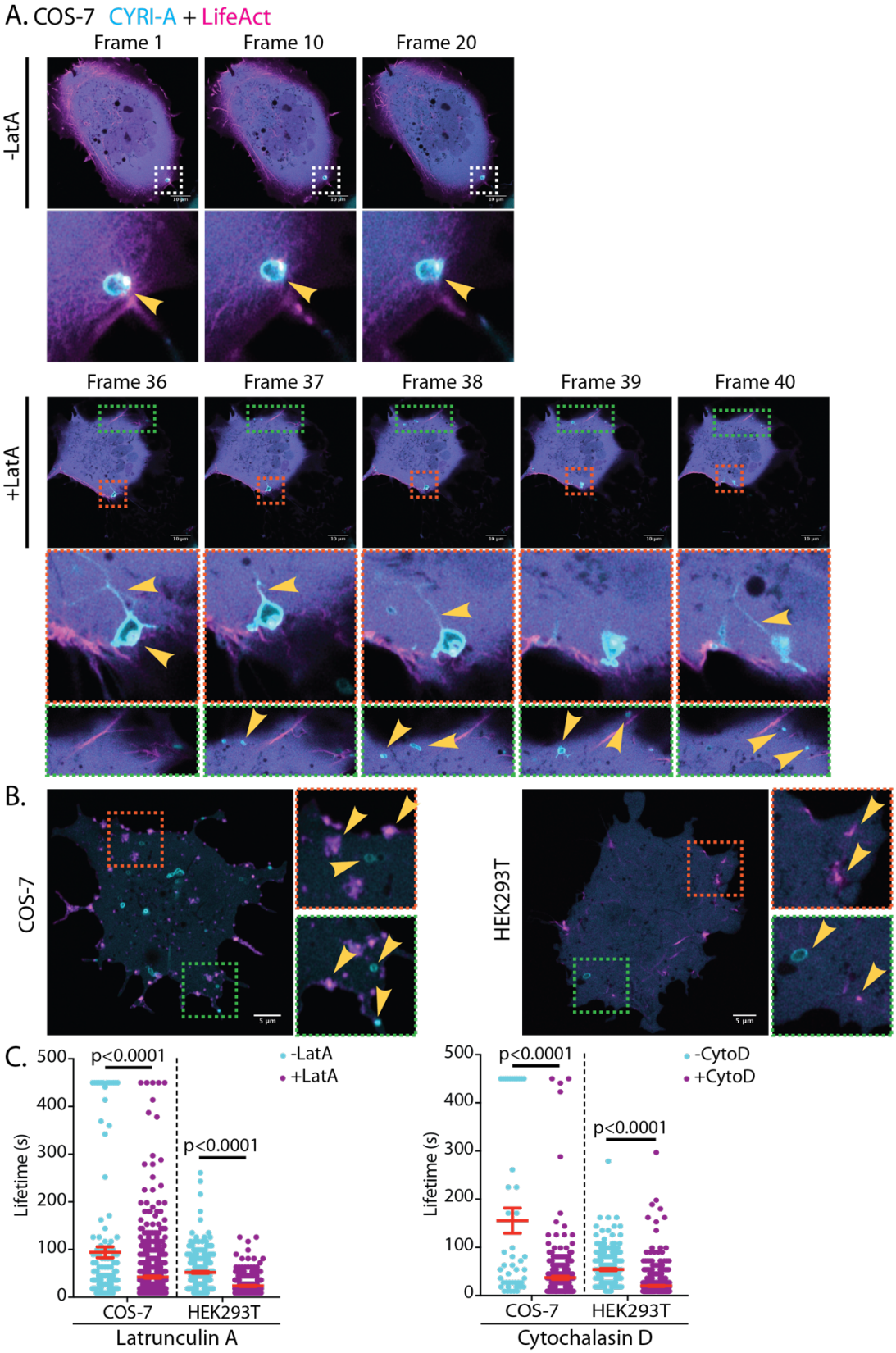

Figure 5.12 Actin polymerisation affects the morphology and lifetime of CYRI-A vesicles

A. COS-7 cells transfected with P16-GFP-CYRI-A and LifeAct-RFP. Frame 1 to 20: Before 1uM latrunculin A (-LatA); Frame 21 to 40: After 1uM latrunculin A (+LatA). Arrows show CYRI-A positive vesicles. Cells are imaged every 30s. Scale bar = 10μm.

B. Actin and vesicles morphology in COS-7 and HEK293T cells after latrunculin treatment. Actin asters in magenta. Scale bar = 10μm.

C. Quantification of the lifetime (s) of CYRI-A positive vesicles with and without 1μM LatA or 1μM cytochalasin D (CytoD) in COS-7 and HEK293T cells. Data from 3 independent experiments. Mean ± SEM. Statistical analysis using 2-tail unpaired t-test.

To rule out this potential side effect on CYRI-A's dynamic, we repeated the experiment using another actin inhibitor, cytochalasin D, which binds and caps the barbed end of actin filaments. Indeed, the same effects were also observed in cells treated with cytochalasin D. This confirmed that the effects we have seen were not due to the off-target effects of the inhibitors. These results suggested a feedback effect that actin has on CYRI vesicle formation. In addition to the suppressing effect that CYRI exerts on actin polymerisation, actin polymerisation in turn seems to also be able to regulate the morphology, frequency and the lifetime of CYRI vesicles. Hence, CYRIs, particularly CYRI-A can form a regulatory feedback loop with actin, allowing the two signals to modulate each other. The observation of CYRI-A vesicles forming even in the absence of actin polymerisation suggested again CYRI-A might be able to directly induce vesicle formation. Overall, the data suggest that CYRI-A and actin form a regulatory loop that modulates the formation of endocytic vesicles.

5.2.5 CYRI-A is recruited to active RAC1 on the vesicular membrane

Macropinosome formation is strictly dependent on actin polymerisation and is thought to be initiated by active RAC1. We also established that CYRI-A could directly bind active RAC1 in chapter 3. Thus, it could be possible for us to visualise the interaction between CYRI-A and RAC1 in real-time. The initial idea was to use the constitutively active RAC1 Q61L as the reporter for RAC1 localisation and compare this to the dominant-negative RAC1 T17N (Figure 5.13). However, it turned out that this idea was not as successful as anticipated. HEK293T cells transfected with the active RAC1 adopt the expected round shape with broad lamellipodia. We also observed the accumulation of RAC1 Q61L as the lamellipodia

protruded forward (yellow dotted line) and its disappearance as the cell retracted (cyan triangle arrows), suggesting a correct behaviour for the protein. However, despite some degrees of colocalization between CYRI-A and RAC1 Q61L (Figure 5.13A, arrows), the signals were weak, and the vesicles were much smaller and not having the characteristics we observed previously. It had been shown that having an excessive level of RAC1 activity could suppress the formation of endosomes (Fujii et al., 2013,Schlam, 2015 #103), as well as decreasing the dynamic of the leading edge. Cells transfected with the dominant-negative RAC1 T17N, on the other hand, showed no membrane ruffling. Instead, they presented with many blebbing structures (Li et al., 2016a,Sarner, 2000 #104). Interestingly, the RAC1 T17N also seemed to be found specifically at the plasma membrane and the nuclear envelope with no obvious localisation to any vesicular structures (Figure 5.13B). We found no specific CYRI-A signal with RAC1 T17N. For those reasons, we decided to use the GFP-tagged RAC1 WT instead (Figure 5.14A). We reasoned that this would give the cell more flexibility in adjusting and modulating the activity of RAC1. HEK293T cells expressing RAC1 WT had a slight increase in size but still formed membrane ruffles. RAC1 WT could be seen decorating both the plasma membrane and the cytosol. When the macropinosome cup started forming, we observed RAC1 signal at the very beginning decorating the base of the cup (Bohdanowicz and Grinstein, 2013,Schlam, 2015 #103,Hinze, 2018 #106). When it was approximately 45s to 50s into the process, RAC1 signal spiked up, while CYRI-A signal started to appear (Figure 5.14A, graphs). This faint signal was sharply surging up right after the RAC1 signal. On average, CYRI-A and RAC1 signal lasted for around 50s before both went away. It is important to note that, as discussed in Figure 5.11B.ii, the time frame of the actin signal on the vesicles before CYRI-A arrived is closely similar to that of the RAC1 signal, both around 45 to 50s. Both actin and RAC1 spent the next 50s with CYRI-A before they dispersed. Knowing that RAC1 signal is upstream of actin, this is strongly suggesting that CYRI-A controls actin signal through modulating RAC1 activity. It is worth mentioning that we believe RAC1 triggers actin polymerisation throughout the formation process of vesicles and not just when the signal surged up. The surge in RAC1 was more likely as an indication of an overactivation or over-recruitment and CYRI-A acted as a brake to dampen this down. To visualise if it was active RAC1 at the vesicles, we utilised the PAK-binding domain (PBD) that has been used

as an active RAC1 reporter for live-imaging (Amato et al., 2019). We tested in three different cell lines HEK293T, COS-7 and CHL-1 and in all three, we saw both a strong colocalization between the CYRI-A and the PBD signal and the same sequential relationship between PBD and CYRI-A (Figure 5.14B). The total duration of the event is depending on the cell type, but it is usually shorter in CHL-1 and longer in HEK293T, but the relative timing between the signals is conserved.

We have shown that CYRIs bound active RAC1 through its DUF1394 domain and previous reports had identified the two arginines 160 and 161 on CYRI-B as important binding sites (Fort et al., 2018). Mutating the corresponding arginine residues 159 and 160 in CYRI-A also completely abrogated its active RAC1 interaction (Figure 3.13). To visualise whether the mutant CYRI-A could be localised to endosomes, we co-transfected COS-7, HEK293T and CHL-1 the wild-type P16-mCherry-CYRI-A and either the wild-type P16-GFP-CYRI-A or the double arginine mutant that we refer to as P16-GFP-CYRI-A-RRDD. Cells expressing both wild-type constructs of CYRI-A are visibly less dynamic, perhaps due to the overly high level of CYRI that suppressing most of the active RAC1. However, we still detected both the GFP and the mCherry signal in nearly every endocytic event (Figure 5.15A). In contrast, in cells expressing both the wild-type and the mutant construct, only the wild-type signal could be seen whereas the signal of the mutant is absent in all of the examined events (Figure 5.15B). This strongly suggests that the ability to bind active RAC1 of CYRI-A is crucial for its recruitment to macropinosomes. Putting all together, these data suggest that CYRI-A regulates macropinocytosis through fine-tuning actin polymerisation via suppressing specifically overactive RAC1 at the base of macropinocytic cups.

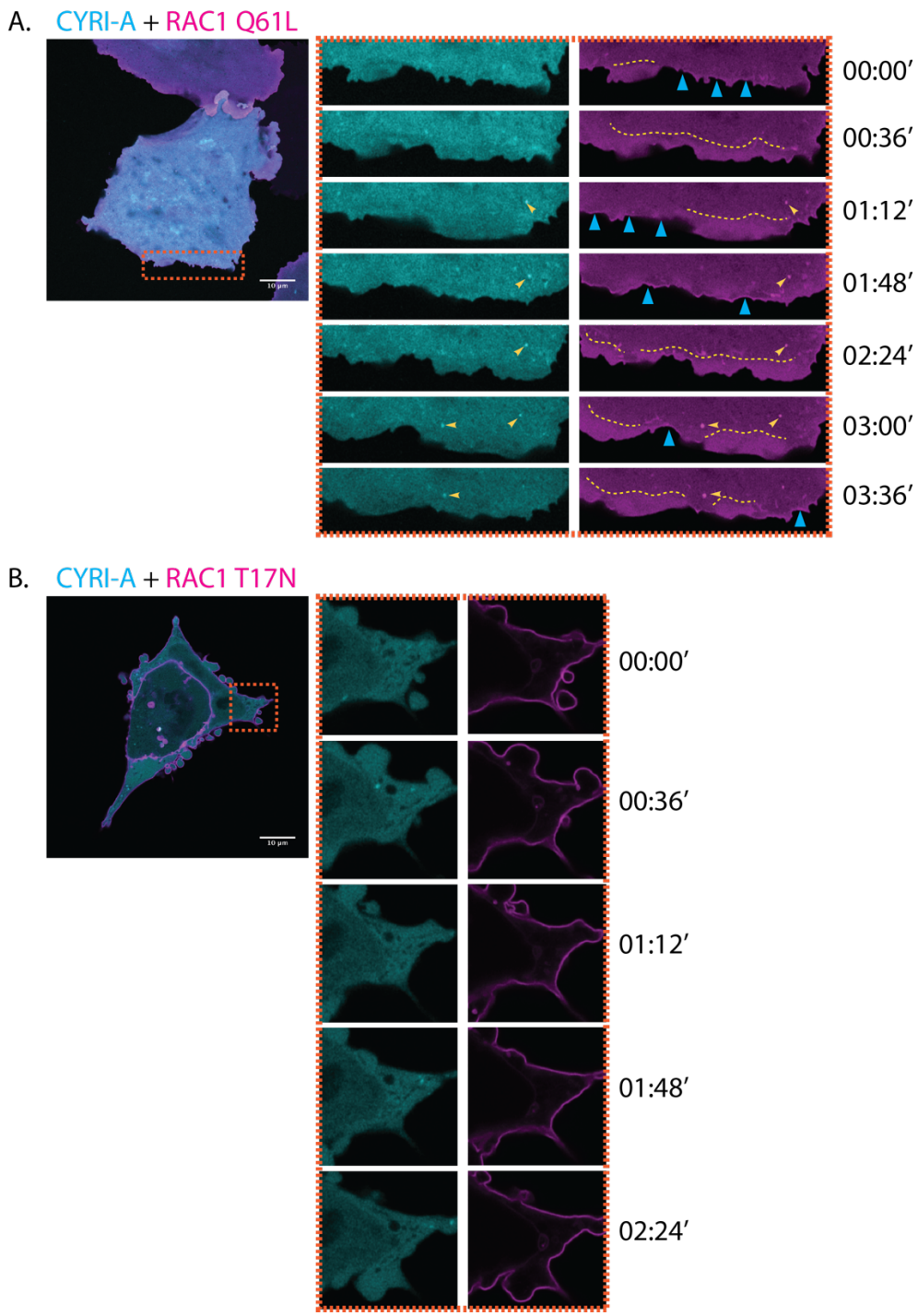

Figure 5.13 GFP-tagged RAC1 Q61L and T17N are not suitable for localising with CYRI-A construct in HEK293T cells

A. RAC1 Q61L causes broad and flat lamellipodia and show limited colocalization with CYRI-A. Yellow dotted lines show the accumulation of RAC1 Q61L at the protruding edges, while cyan arrows show the retraction edge with no RAC1 accumulation. Scale bar = 10μm.

B. RAC1 T17N causes blebbing phenotype and lamellipodial collapse and show no colocalization with CYRI-A. Scale bar = 10μm.

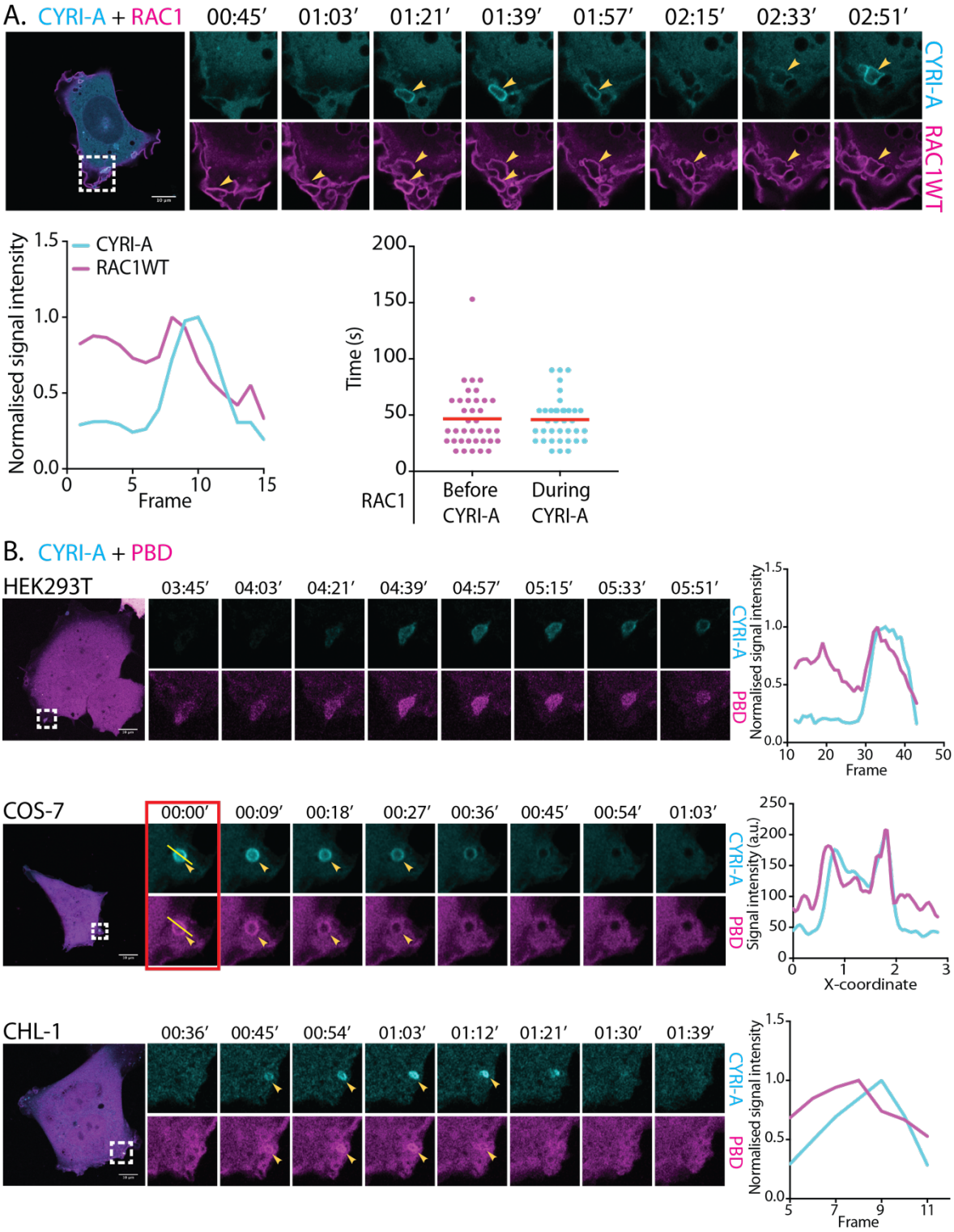

Figure 5.14 CYRI-A colocalises with active RAC1 at the endocytic vesicles

A. HEK293T cells co-expressing P16-mCherry-CYRI-A and GFP-RAC1 WT. RAC1 signal spike is followed by CYRI-A signal (upper panel, left graph). RAC1 localises to the vesicles for about 50s before CYRI-A is recruited. The signals stay together for about another 50s before both disappear (right graph, N=37 events in 4 cells). Cells are imaged every 9s. Red lines represent the mean value.

B. Active RAC1, labelled by PAK-binding domain (PBD) strongly colocalises with CYRI-A. CYRI-A signal surges up right after PBD signal in HEK293T, COS-7 and CHL-1. Apart from the right-hand side graph of COS-7 showing the strong colocalization between CYRI-A and PBD, the other graphs of tracking over time show the CYRI-A signal hit the peak just after PBD signal.

The red box indicates the frame where line graph is plotted. Scale bar = 10μm.

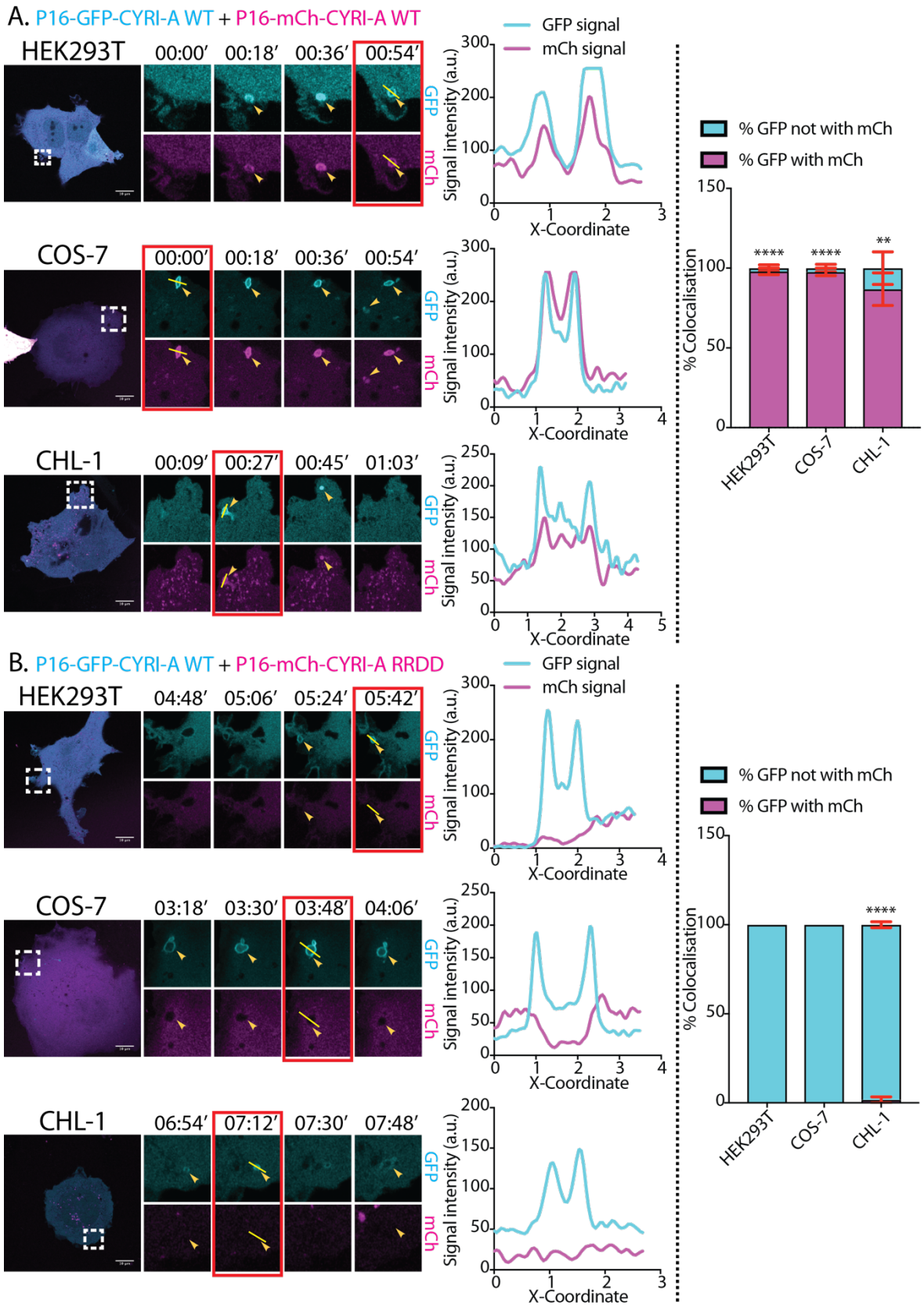

Figure 5.15 Mutating Arginine 159/160 into Aspartic acid (RRDD mutant) in CYRI-A abrogates CYRI-A's ability to be recruited to macropinosomes

A. Co-localising between P16-GFP-CYRI-A WT and P16-mCh-CYRI-A WT. In all 3 cell lines, HEK293T, COS-7 and CHL-1, the two markers are colocalising with each other at the macropinosomes (line graphs). Quantification of the percentage of GFP signal colocalise with the mCherry signal shows the two signals are almost always found at the same location (N=7 cells for HEK293T, N=6 cells for COS-7, N=3 cells for CHL-1).

B. P16-mCh-CYRI-A RRDD is not recruited to macropinosomes and is absent from P16-GFP-CYRI-A signal. Line graphs show no colocalization between the two signals. Quantification shows close to 100% of the time that the GFP signal is found without the mCherry signal at macropinosomes (N=5 cells for HEK293T, N=5 cells for COS-7, N=3 cells for CHL-1).

Statistical analysis used unpaired t-test. **p<0.01, ****p<0.0001. Mean ± SEM. Red boxes indicate the frame where a line graph is plotted. Cells are imaged every 9s. Scale bar = 10μm.

5.2.6 Scar/WAVE complex localised to the edge of membrane ruffles that eventually formed CYRI-A positive vesicles

Active RAC1 drives actin polymerisation by activating the Scar/WAVE complex. Having shown that active RAC1 colocalised with CYRI-A, as well as actin, we next queried whether CYRI-A co-localised with the Scar/WAVE complex. Imaging the Scar/WAVE complex was more challenging than many other reporters described earlier. Overexpressing the fluorescently tagged version of any subunit of the Scar/WAVE complex usually lead to no specific localisation as cells naturally prefer native protein complex. To overcome this, we made use of a B16F1 cell line that had got their Scar/WAVE complex knockout by deleting the CYFIP1 and 2 isoforms using CRISPR/Cas9 which was generated in the lab of Professor Klemens Rottner (referred to as CYFIP1/2KO). Naturally, the B16F1 cells form uniform and smooth lamellipodia when plated on laminin-coated coverslips. However, CYFIP1/2KO cells completely lose these structures and instead form spiky protrusions and adopt a more spindle morphology. By re-introducing the GFP-tagged CYFIP1 construct, we could rescue this phenotype (Schaks et al., 2018) and at the same time be able to visualise the localisation of the Scar/WAVE complex. We co-expressed both the GFP-CYFIP1 and P16-mCherry-CYRI-A in this cell line and the first thing we noticed was the reformation of lamellipodia with an enrichment of the Scar/WAVE complex signal at their leading edges (Figure 5.16). At the same time, we also noticed the formation of multiple fast CYRI-A positive vesicles, thus confirmed our previous data and re-established the behaviour of

CYRI-A in endocytic trafficking as a common behaviour in multiple different cell lines. Tracking both CYFIP1 and CYRI-A signal over time revealed that indeed the Scar/WAVE complex is present at the beginning of the vesicle formation as described in the literature (Ferreira and Boucrot, 2018,Bloomfield, 2016 #137). The signal was usually derived from a pre-existing membrane ruffle nearby, thus reconfirmed the mechanism of macropinosome formation. CYRI-A was recruited as soon as the vesicles were drawn into the cell from the ruffle and its signal quickly peaked out right after CYFIP1 (Figure 5.16, graph). This behaviour matched exactly the active RAC1 signal described in Figure 5.14, reassuring both the consensus model of Scar/WAVE activation and our model of CYRI-A activity at the site of endocytosis.

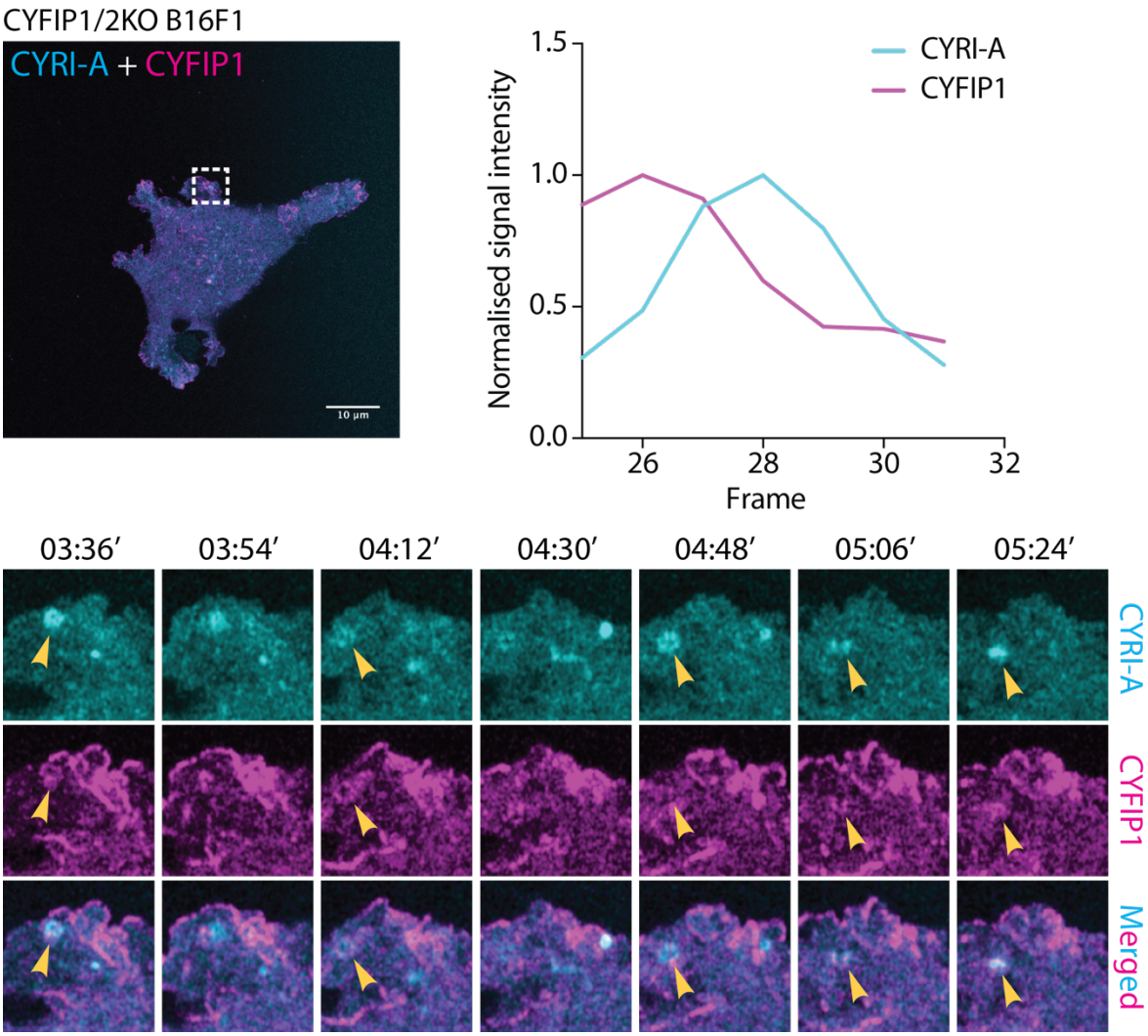

Figure 5.16 Scar/WAVE complex signal appears at the site of CYRI-A vesicles in B16F1 cells

CYFIP1/2KO B16F1 cells were co-transfected with P16-mCherry-CYRI-A and GFP-CYFIP1 as the marker for the Scar/WAVE complex. The CYFIP1 signal appeared and peaked just before CYRI-A also reached its maximum signal intensity. CYFIP1 and CYRI-A shared a short colocalization. Cells are imaged every 9s. Scale bar = 10μm.

5.2.7 CYRI-A recruitment to macropinosomes is PhosphoInositide-3 Kinase (PI3K) dependent

It has been long known that phosphoinositides are crucial to the formation of macropinosomes. The sequential breakdown of many phospholipid entities has been associated with the progression and maturation of macropinosomes (Maekawa et al., 2014). Phosphatidylinositol-3,4,5-trisphosphate or PIP3 is one of the major contributors to this process. The lipid can directly recruit many PH domain-containing adaptors like Akt/PKB to which genetic ablation strongly suppressed macropinocytosis. The degradation of PIP3 into subsequent lipid products like PI(3,4)P2 or PI(4,5)P2 or other signalling molecules like IP3 and DAG can directly affect the actin cytoskeleton (Rupper et al., 2001,Bohdanowicz, 2013 #107). Thus, it is important to visualise the spatiotemporal resolution between CYRI and PIP3. To visualise PIP3, we utilise a GFP-tagged PIP3 specific reporter PH-Grp1 (Halet, 2005,Lai, 2013 #111) (Figure 5.17). We co-expressed the PH-Grp1 construct along with P16-mCherry-CYRI-A in HEK293T, COS-7 and CHL-1. In all cases, we observed the PH-Grp1 signal at the very beginning of the macropinosome formation process, restricting to the base of the endocytic cup when the membrane was invaginating. This agreed with previous observations on the functions of PIP3 during macropinosome initiation (Araki et al., 2007, Araki et al., 1996). The PIP3 signal increased until it hit the peak as the vesicles closed up and started to be delivered into the cytoplasm. Unlike actin or RAC1 signal where there was usually a 50s overlap with the CYRI-A signal, PIP3 signal usually appeared for about 38 to 44s before disappearing entirely before CYRI-A appeared (Figure 5.17, line graphs). This fits with the reported lifetime of PIP3 to be less than 60s (Rupper et al., 2001) from the beginning of the formation process. The appearance of CYRI-A and PIP3 signal is likely to be mutually exclusive. We used a second PIP3 reporter PH-Btk to confirm our observation (Figure 5.18) and again, we observed the peak of Btk well before CYRI-A hit its peak. There is however a slight prolong in the time the PH-Btk construct spent on the vesicles before CYRI-A got recruited. Even though it has been shown that the affinity of PH-Grp1 and PH-Btk to PIP3 is similar with the Kd around 27nM (Kavran et al., 1998), the two PH domains could interact with different effectors within the cells (Varnai et al., 2005), thus slightly affect their membrane-binding lifetimes.

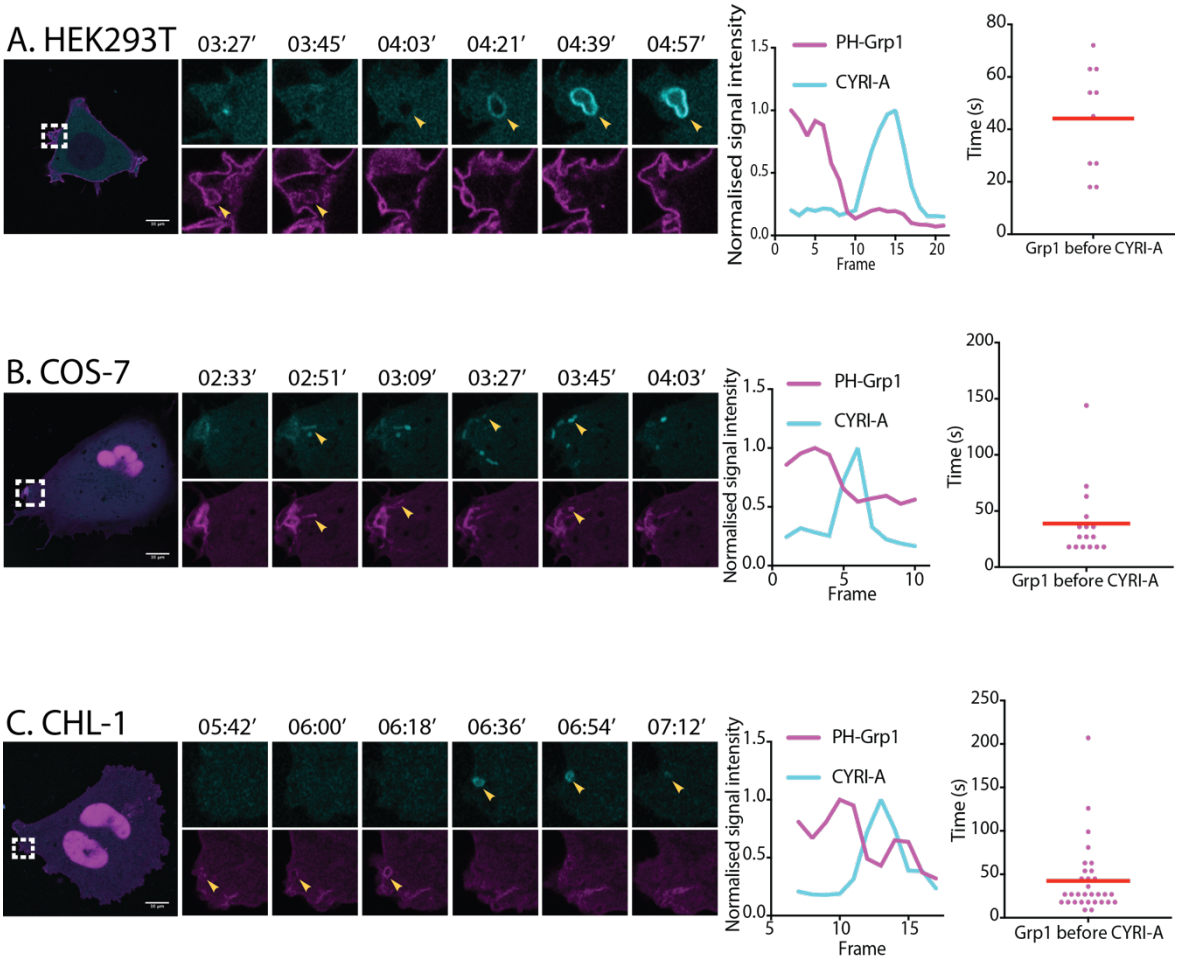

Figure 5.17 CYRI-A is recruited to the macropinosomes just after PIP3 signal

HEK293T, COS-7 or CHL-1 cells were co-transfected with the GFP-tagged PH-Grp1 (specific PIP3 reporter) and P16-mCherry-CYRI-A. In all cases, PIP3 signal was seen at the beginning of the process for ~38-44s, CYRI-A signal appears once PIP3 signal was gone (N=9 events in 3 cells for HEK293T, N=31 events in 3 cells for COS-7 and N=16 events in 3 cells for CHL-1). Cells are imaged every 9s. Red lines represent the mean value. Scale bar = 10μm.

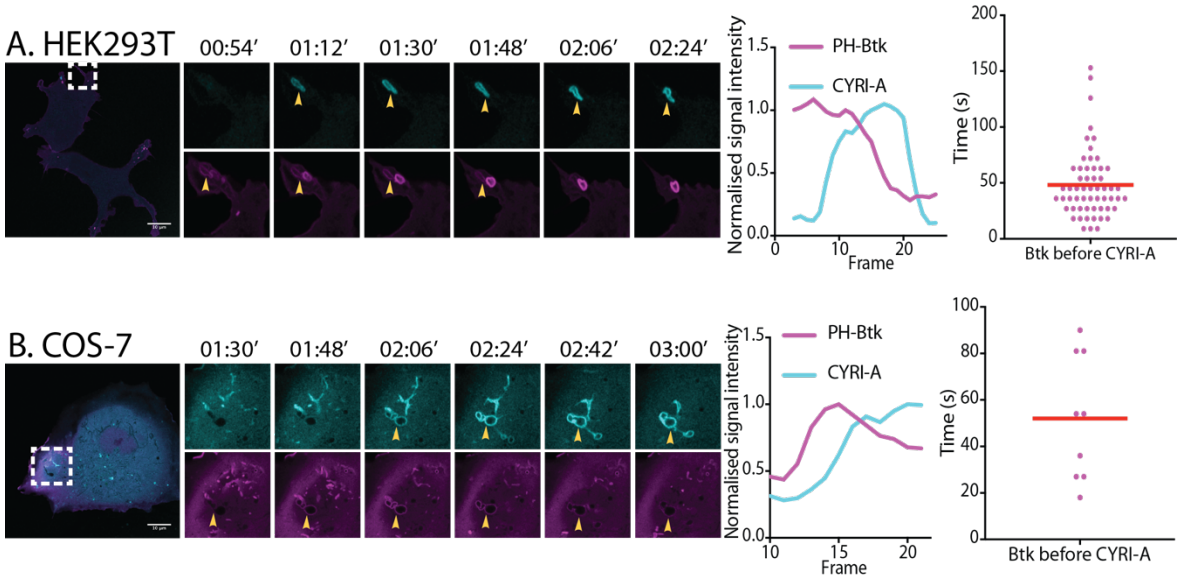

Figure 5.18 PIP3 reporter PH-Btk also behaves similarly to PH-Grp1 in A) HEK293T and B) COS-7.

HEK293T and COS-7 are transfected with GFP-PH-Btk and P16-mCherry-CYRI-A. Line graphs show the normalised signal intensity of Btk and CYRI-A over time. Scattered plots show the average time of Btk signal before CYRI-A arrives. N=57 events in 6 cells forHEK293T, N=9 events in 1 cell for COS-7. Cells are imaged every 9s. Red lines represent the mean value. Scale bar = 10μm.

Because of the importance of PIP3 in macropinosomes and also PIP3 is upstream of CYRI-A, we wondered if inhibiting PIP3 would affect CYRI-A localisation. Before treatment, multiple CYRI-A vesicles formed continuously at the leading edge of the cell (Figure 5.19, example 1). We also observed again the formation of the cytosolic pool of CYRI-A that resided close to the protrusion front of the cell (Figure 5.19, example 2, double arrow). However, within 30s of adding 20μM of LY294002, the vesicles and the cytosolic pool completely disappeared (Figure 5.19, graph). We observed reduced membrane ruffling in the presence of the inhibitor, just as being reported before (Araki et al., 1996), suggesting that CYRI-A recruitment was largely not directly due to membrane ruffles but rather the signalling localised there. These data fit with the current understanding of macropinocytosis. Overall, the recruitment of CYRI-A to endocytic vesicles is strongly dependent on the activity of PI3K.

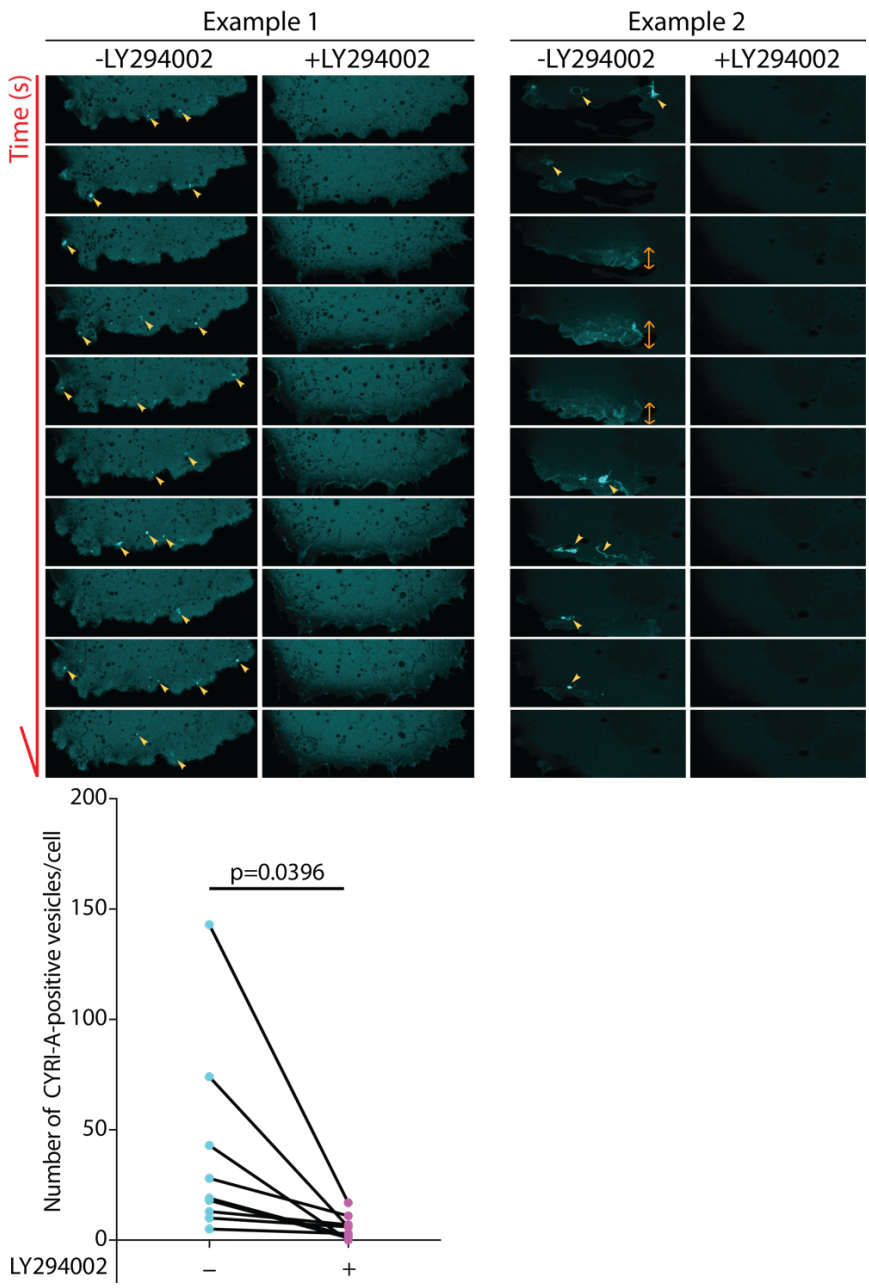

Figure 5.19 CYRI-A vesicle formation is PI3K-dependent

COS-7 cells expressing the P16-GFP-CYRI-A construct were imaged every 30s before and after 20μM LY294002. Each example is of the same cell. Both vesicles and the cytosolic pool of CYRI-A close to the leading edge were abolished upon the addition of the inhibitor. The bottom graph shows the quantification of the number of vesicles before and after treatment. Data from 9 different cells. Statistical analysis using paired t-test.

5.2.8 Membrane curvature preceded CYRI-A recruitment

One of the questions that we had when we first observed the localisation of CYRI-A onto the endocytic vesicles was whether the protein was recruited before, during or after the invagination of the plasma membrane? Even though the late recruitment of the protein relative to the PIP3 signal already hinted us the answer, we would still like to reconfirm this with a membrane marker. In order to visualise just the plasma membrane, we utilised the mScarlet-tagged N-terminal sequence of Lck protein. Lck is a member of the Src family of tyrosine kinase that is commonly found in T cells and is involved in membrane trafficking. The N-terminal region of the protein is palmitoylated and myristoylated to localise to the plasma membrane (Chertkova et al., 2020). By co-expressing the Lck and CYRI-A construct in HEK293T cells (Figure 5.20), we observed the initial invagination process of the plasma membrane was about 40s before CYRI-A was recruited, suggesting that it was unlikely that CYRI-A initiated the formation of macropinocytic cups. However, the vesicles when CYRI-A was recruited were usually still attached to the plasma membrane and not fully matured into endocytic structures. This suggests that CYRI-A might play a role in driving the budding process of macropinosomes. Nevertheless, this hypothesis will need to be further validated.

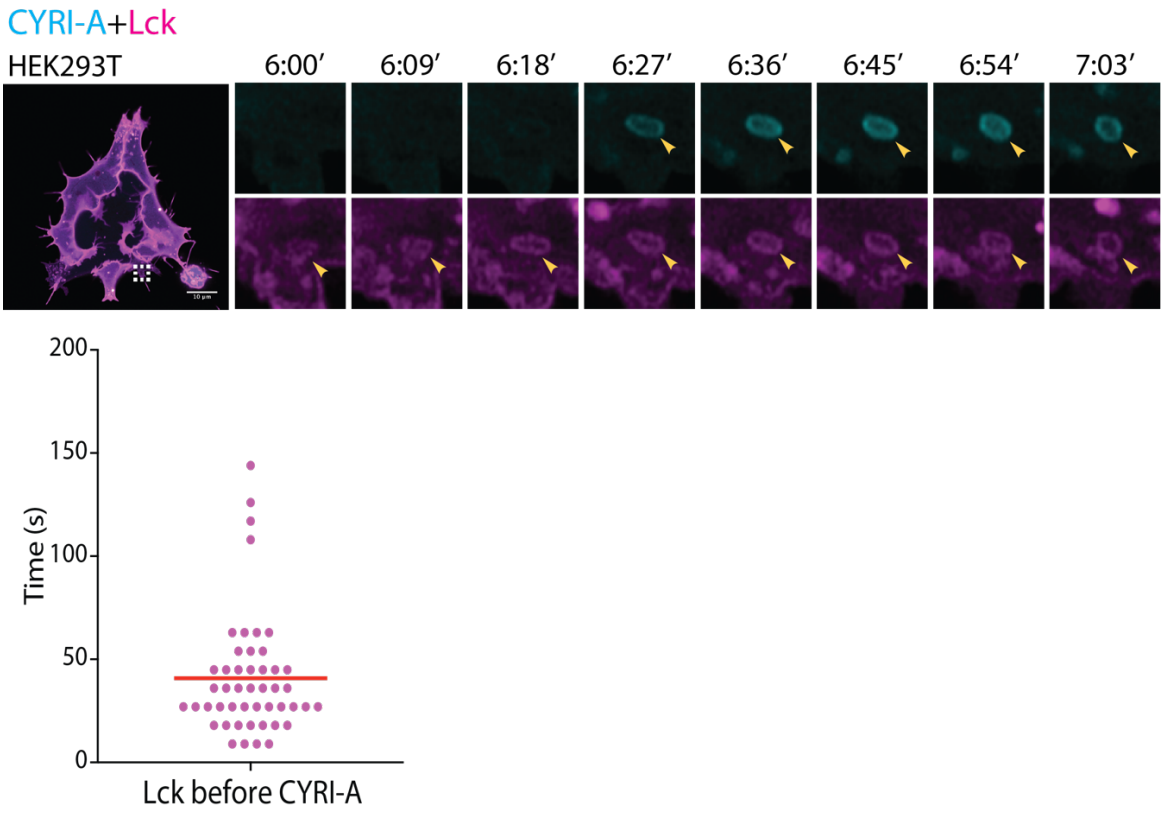

Figure 5.20 Membrane invagination preceded CYRI-A recruitment

HEK293T cells co-expressed P16-GFP-CYRI-A and mScarlet-Lck. The membrane invagination process happened ~40s before CYRI-A was recruited (scattered plot). N=48 events in 10 cells. Red line represents the mean value. Scale bar = 10μm.

5.2.9 Localising the Arp2/3 complex and cortactin on CYRI-A macropinosomes

The branched actin network created by the Arp2/3 complex is thought to play an important role in driving membrane ruffles and macropinosome formation (Swaney and Li, 2016,Rotty, 2017 #133). Furthermore, it has been reported that macropinosomes could also result from circular dorsal ruffles, which has also been observed in our system (Mettlen et al., 2006). Cortactin, another actin regulator protein, played a role in this process. Cortactin binds to and stabilises the branched actin network created by the Arp2/3 complex (Weaver et al., 2001), thus promote actin polymerisation. It is thus of our interest to understand where do the Arp2/3 complex and cortactin fit into the picture with CYRI-A.

We co-expressed GFP-tagged Arp3 and P16-mCherry-CYRI-A in either HEK293T or COS-7 and imaged the cells over time every 9s. In both cell types, the Arp2/3 signal appeared strongly as puncta after CYRI-A signal had disappeared

(Figure 5.21). We managed to capture the Arp2/3 complex at the edge of a closing macropinosome (Figure 5.22, lower panel, arrow). This signal disappeared as CYRI-A was recruited, and then reappeared again as puncta at much stronger intensity. The line graph shows where the double peaks of the Arp3 signal are marked with black arrows, and the orange arrow shows the drop of the signal (Figure 5.22). The Arp2/3 puncta first appeared to move randomly on the outside of the internalised vesicles. However, within 18 to 27s, they started to polarise and accumulated to one side of the vesicles. This was quickly followed by a sudden acceleration of the vesicles into the cell accompanied by a tail of Arp2/3. This tail structure is commonly known as an actin comet tail, and Arp2/3 complex is one of the main drivers involved in this phenomenon (Welch and Way, 2013,Lambrechts, 2008 #136,Fehrenbacher, 2003 #135). The Arp2/3 complex was also described to be involved in membrane tubulation through the WASH complex to recycle many membrane proteins back to the plasma membrane. However, we could not observe any specific localisation of the complex to any tubule structure.

To observe cortactin, we also co-transfected HEK293T and COS-7 with P16-mCherry-CYRI-A and GFP-Cortactin and imaged over time (Figure 5.23). We also observed that cortactin patrolled the outside of CYRI-A vesicles in puncta quite early on during the forming process similar to the Arp2/3 complex (Figure 5.23B). Cortactin was quickly to accumulate to one side of the vesicles and pushed the vesicles into the cytoplasm. We could not observe any obvious localisation of cortactin to membrane tubules either. It is very likely that both Arp2/3 complex and cortactin shares similar functions in this context or perhaps work together. Overall, we believe that the Arp2/3 complex and cortactin are parts of CYRI-A vesicles, perhaps to drive membrane ruffles and closure. More prominently is their repolarisation on vesicles and their role in driving the formation of actin comet tails to help to transport the vesicles into the cell.

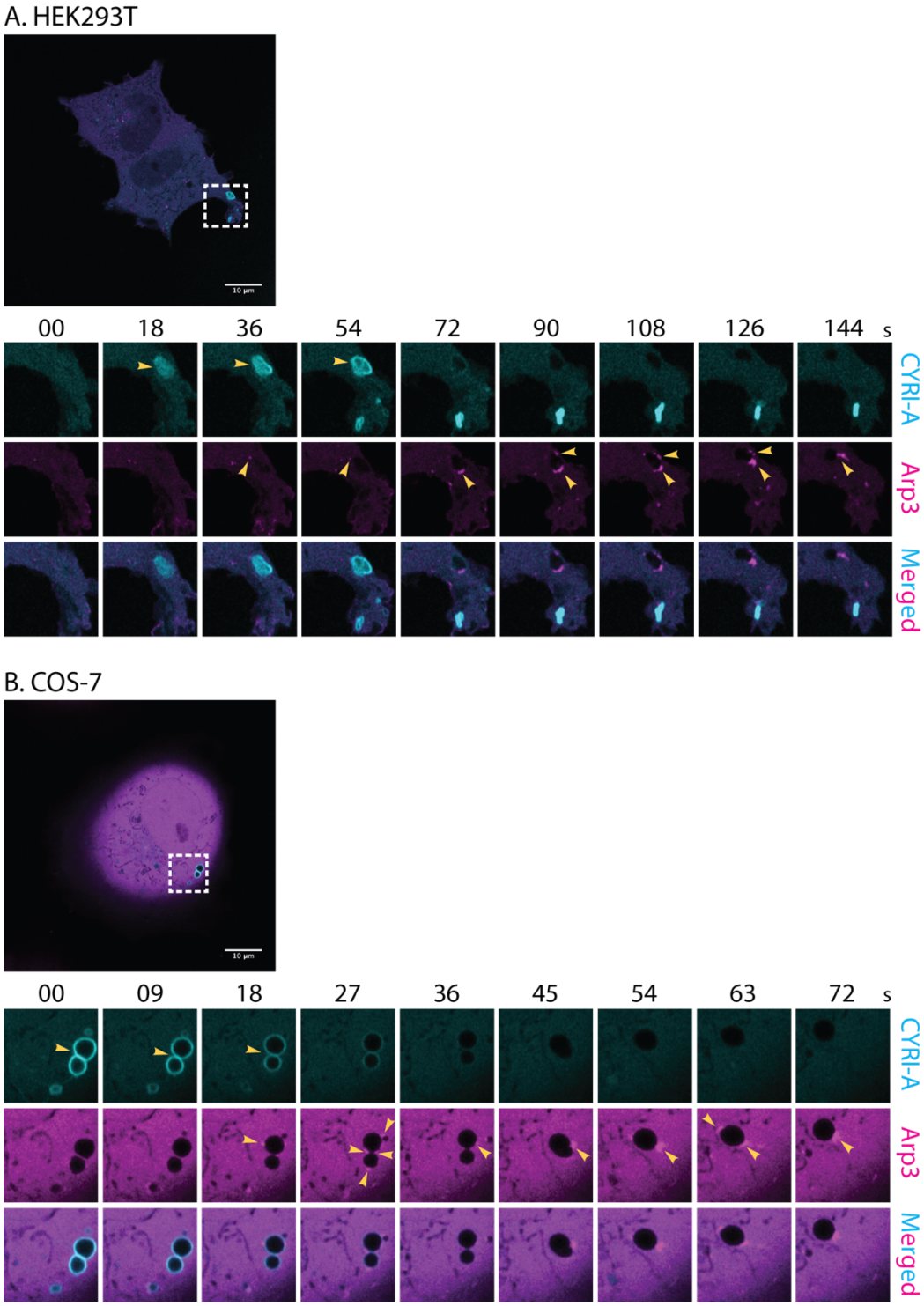

Figure 5.21 Arp2/3 complex is only visible as puncta structures on CYRI-A vesicles after CYRI-A disappeared

A) HEK293T and B) COS7 co-expressed P16-mCherry-CYRI-A and GFP-Arp3. Arp2/3 complex appears as puncta outside the vesicles initially before accumulating to one side of the vesicles and push them forward (arrows). Cells are imaged every 9s. Scale bar = 10μm.

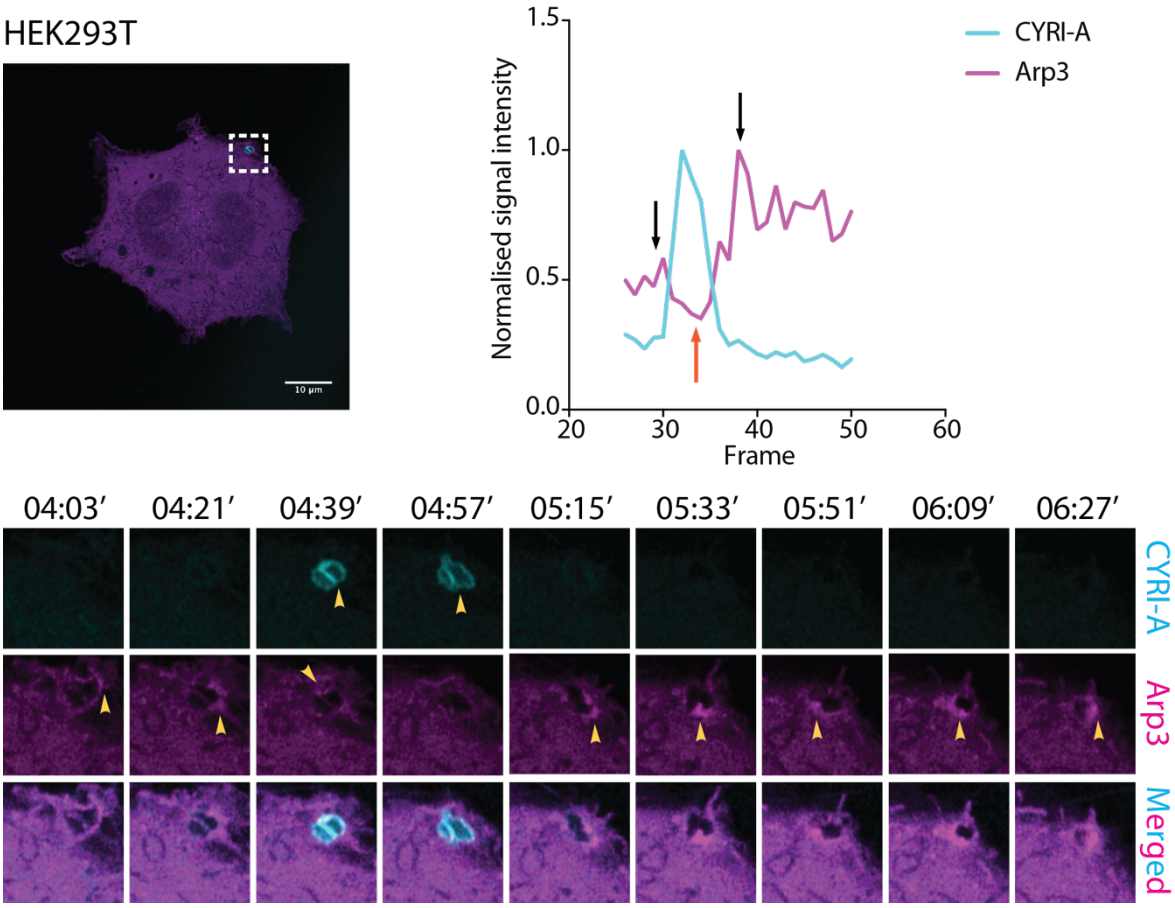

Figure 5.22 Arp2/3 complex is detected at the closing edge of macropinosome

HEK293T cells co-expressed P16-mCherry-CYRI-A and GFP-Arp3 and imaged over time. Arp2/3 complex signal could be seen focused at the closing edge of a macropinosome (arrow) before disappeared as CYRI-A was recruited, and then reappeared again after CYRI-A signal was gone. The line graph shows the double peaks of the Arp3 signal (black arrows) and the drop as CYRI-A signal peaked (orange arrow). Scale bar = 10µm.

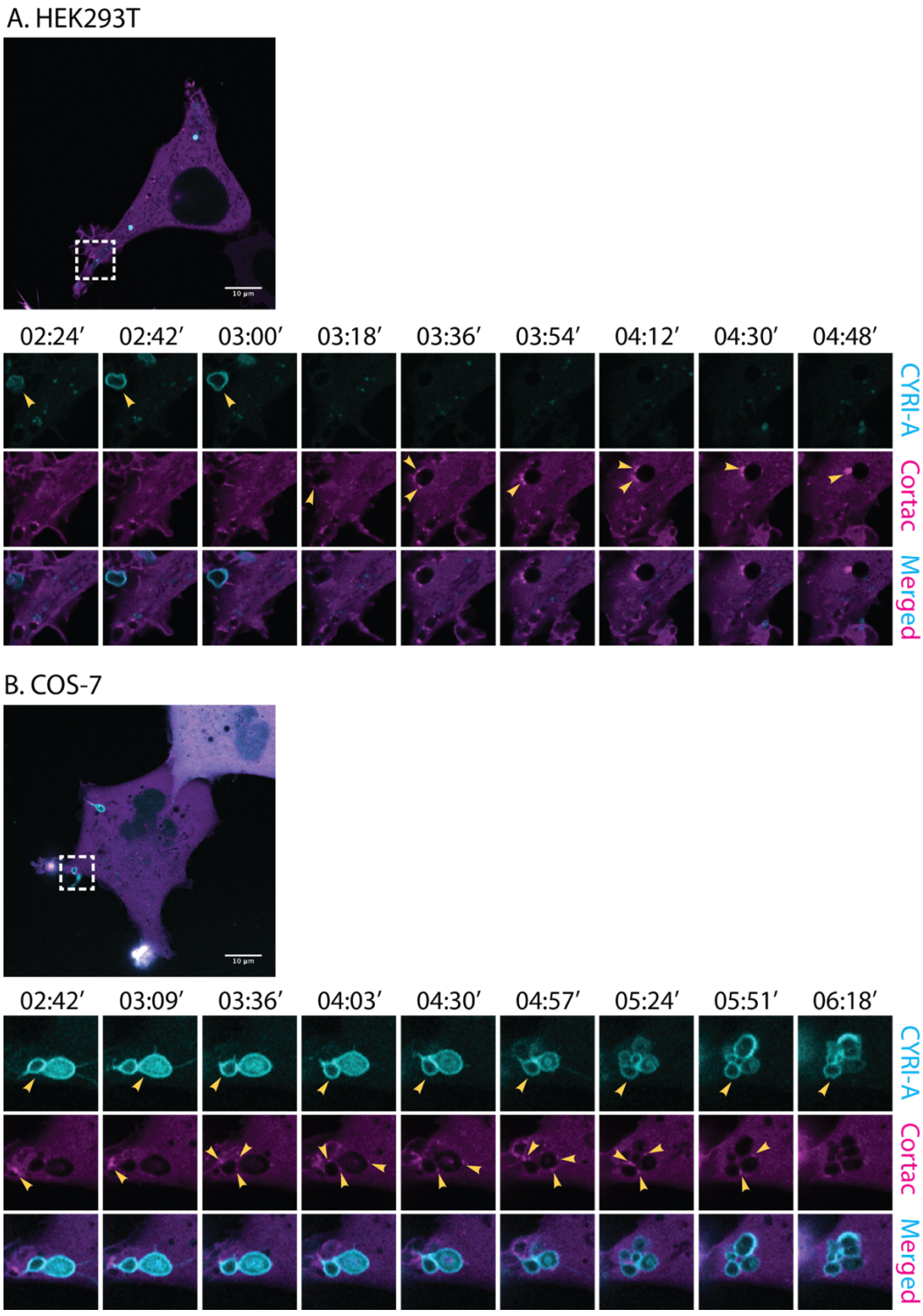

Figure 5.23 Cortactin decorated CYRI-A positive vesicles and formed comet tails similar to Arp2/3 complex.

A) HEK293T and B) COS7 co-expressed P16-mCherry-CYRI-A and GFP-Cortactin. Cortactin (Cortac) appears as localised puncta and to some extent, a diffused signal outside the vesicles initially before accumulating to one side of the vesicles and pushing them forward (arrows). Cells are imaged every 9s. Scale bar = 10µm.

5.2.10 CYRI-A vesicles are targeted to lysosomal degradation

Since we have shown the pathway of CYRI-A vesicles, from forming at the cell leading edge to converting into early endosomes by Rab5A recruitment, we next investigated the later destination of these vesicles and their cargoes. To visualise the late endosomes and lysosomes, we stained cells with LysoTracker, a commercially available dye that fluoresced at low pH such as in acidified endosomes. We expressed the internal GFP-tagged CYRI-A and imaged over time (Figure 5.24). In general, the acidification event of CYRI-A vesicles happened the latest compared to other signalling events described earlier, typically around 4 minutes or longer. For small vesicles (Figure 5.24, example 1), the acidification started within 3 to 4 minutes since CYRI-A disappeared. The process happened quick and usually required only 1 fusion event with a lysosome. However, for larger vesicles (Figure 5.24, example 2) such as those formed by phagocytosis-liked processes, the time frame could be as long as 10 to 15 minutes before acidification happened. On these vesicles, after CYRI-A signal faded, multiple lysosomes started to make contacts. They usually took multiple attempts before one could be seen stably adhere to the endosomes. Then as time progressed, more lysosomes were recruited, and the acidification started.

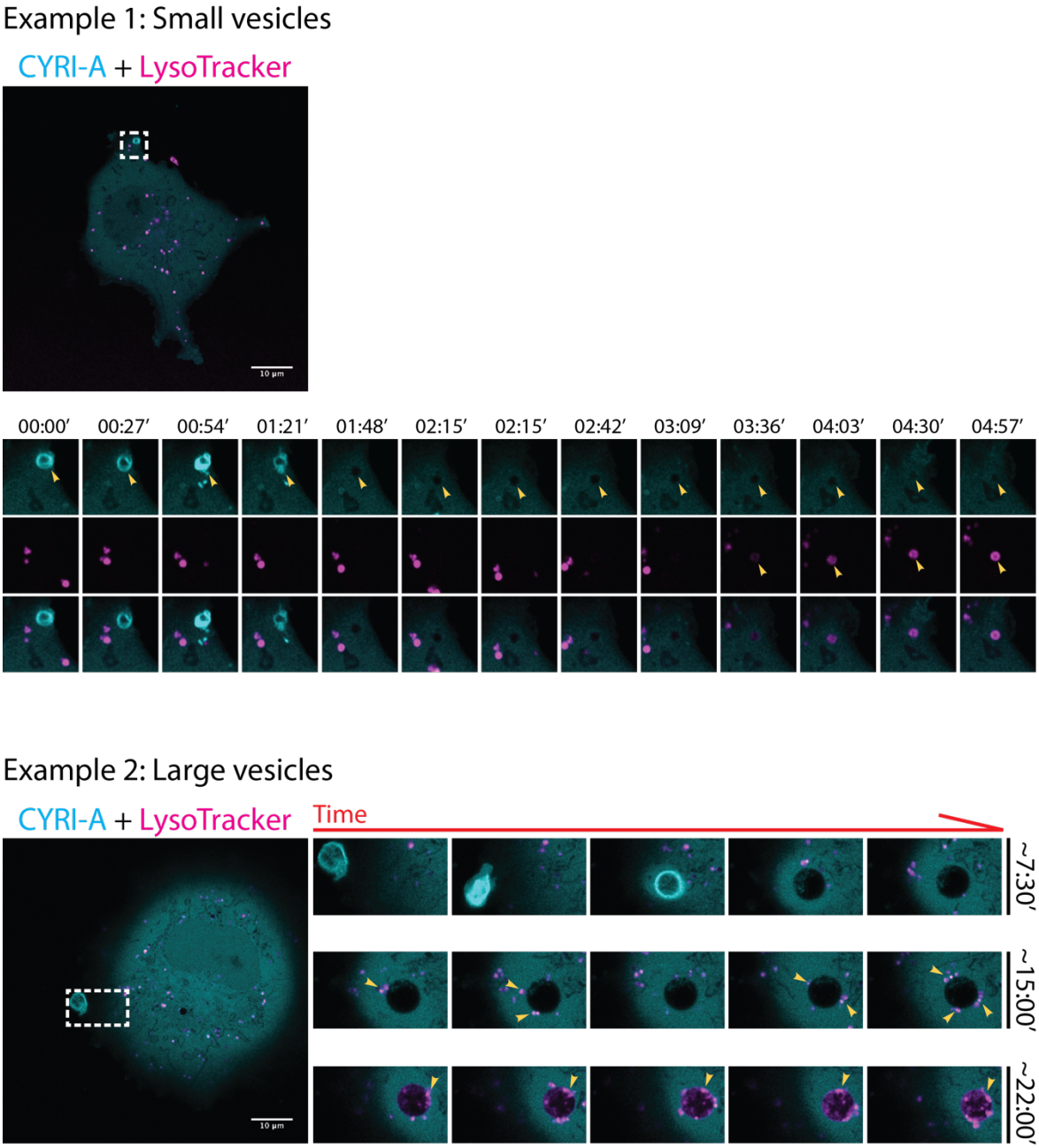

Figure 5.24 CYRI-A vesicles are eventually fused with lysosomes to form endolysosomes

COS-7 were expressing P16-GFP-CYRI-A and stained with LysoTracker Red and imaged for every 9s. Small vesicles (example 1) tended to quickly acidify after CYRI-A disappear within less than 5 minutes. Large vesicles (example 2) took much longer and require multiple lysosome binding and fusion events before eventually acidifying. Scale bar = 10μm.

5.3 Discussion

CYRI proteins were first highlighted as regulators of cell migration since it was first discovered and characterised (Fort et al., 2018). Their localisation within the cells has been assumed to be mostly at the plasma membrane, particularly at the membrane protrusion through myristoylation and palmitoylation. Here we established for the first time the novel function of CYRIs, particularly CYRI-A, in the process of macropinocytosis. We have successfully created a novel construct of CYRIs, an internal fluorescent tagging construct between the N-terminal helix and the DUF1394 domain, to allow visualisation of the localisation and kinetics of the proteins *in cellulo*. Using these constructs, we were able to reveal the differences between CYRI-A and CYRI-B, especially in terms of their membrane-binding kinetics. CYRI-B showed a surprisingly static and stable localisation on tubular structures inside cells, while in contrast, CYRI-A showed a significantly more dynamic behaviour. Swapping the N-terminal helix of CYRI-B onto CYRI-A led to the loss of CYRI-A's natural dynamics but its strong enrichment on the membrane remained. This suggests that the N-terminal helix, the DUF1394 domain and possibly any post-translational modification such as myristoylation and phosphorylation, all play a part in determining CYRI's behaviours inside cells.

Localising CYRI-A with other markers of different stages of the endocytic process revealed the novel involvement of CYRI-A in macropinocytosis and placed the protein at the early formation point in the process. PIP3 drives the activation of RAC1 through presumably recruiting many of its RAC1 GEFs (Welch et al., 2002,Campa, 2015 #119). RAC1 then activates the Scar/WAVE complex, which then activates the Arp2/3 complex to drive actin polymerisation at the leading edge, forming membrane ruffles and invagination. As the vesicles form and just before they are pinched off from the plasma membrane, CYRI-A is recruited from the nearby cytoplasmic pool to suppress active RAC1 and dampen down actin polymerisation. This recruitment is strongly dependent on its ability to bind active RAC1 since mutating the conserved arginine 159/160 residues completely abolished its recruitment. Suppressing RAC1 signalling is important because it has been shown by other groups that constitutive activation of RAC1 renders macropinosomes unable to complete. By using photoactivatable RAC1, it was

shown that when RAC1 was continuously activated, macropinosomes never pinched off from the plasma membrane and failed to acquire maturing markers (Fujii et al., 2013,Yoshida, 2009 #138). The process only completed once the activation was switched off. These data argued that RAC1 inactivation is also important for macropinocytosis. A report has found ARHGAP12, ARHGAP25 and SH3BP1 to be the three RAC1 GAPs responsible for the inactivation (Schlam et al., 2015). However, the process being investigated in this report was phagocytosis. And even though phagocytosis and macropinocytosis share many common molecular mechanisms, many other molecular events are different between the two. In addition, the author mentioned that the recruitment of these RAC1 GAPs was only observed when the cells were challenged with large particles, around 8μm, while smaller particles did not require these proteins. Whereas in our case, CYRIs were observed to localise to vesicles ranging from as small as 0.4μm to as large as 7μm. Unlike a GAP which actively promoting GTPases activity in RAC1, CYRIs inhibit RAC1 signalling by sequestering the protein. This suggests that CYRIs are perhaps the more general and immediate response at the site of macropinocytosis. The transient spatiotemporal dynamic of CYRI-A, as well as the correlation between CYRI-A signal and RAC1, Scar/WAVE and actin signal, suggests that CYRI-A could act as a gate controller, maintaining the appropriate amount of driver signals before they go overboard. It is worth noting that not all dextran-positive vesicles are CYRI-A positive, which begs a question of whether CYRI-A macropinosomes are distinct from other macropinosomes? This is a question that will need to be addressed in future studies. One of the mysteries of macropinocytosis is how cells achieve a well-defined spatial position of the different signals at the cup. The cells could maintain actin protrusions on the two sides of the macropinosomes while suppressing it in the middle of the cup. How the cells achieve this is still largely unknown. We propose that CYRIs could be the factor that contributes to this spatial organisation through directly modulating RAC1 signalling. We also found the dependence of CYRI-A vesicles to PI3K signalling upon treating cells with LY294002. Treated cells are still able to form membrane ruffle may suggest the recruitment of CYRI-A to macropinocytic cups is dependent on PI3K signalling. However, to conclusively rule out other mechanism such as the reduced membrane ruffling affects CYRI-A recruitment,

more experiments such as artificially inducing membrane ruffles independently of PI3K will be needed.

More interestingly is the fact that inhibiting actin polymerisation itself could in turns affect CYRI-A and vesicle dynamics. In the presence of latrunculin A or cytochalasin D, CYRI-A vesicles could still form but with a much shorter lifetime compared to the control. This effectively hints to a regulatory loop imposed between CYRIs and actin where one regulates the other's activity. This fits in nicely with the idea of CYRIs being able to sense the actin polymerisation threshold and modulate it. Furthermore, CYRI-A vesicles were still able to form even in places where the actin signal was not detected. We believe that in the presence of actin depolymerising agents, the cell cortex could no longer maintain its membrane tension (Chalut and Paluch, 2016, Chugh and Paluch, 2018), and this perhaps led to the formation of membrane curving pits that could then be further driven into vesicles by CYRI-A. Our *in vitro* tubulation assay also suggested that at least CYRI-A does have the intrinsic ability to drive membrane tubulation. This in turns agreed with the *in cellulo* data where we observed tubules of CYRI-A protruding out from internalised vesicles. This could be the result of its amphipathic helix allowing the protein to intercalate into the lipid bilayer, thus inducing membrane curvature and priming the tubulation process. However, this will need to be further tested by reperforming the assay with a helix-truncated CYRI-A. However, at high concentration of CYRI-A, we also saw the formation of lipid droplets suggesting that the excessive tubulation process could result in these vesicles. This could be an additional function of CYRI-A in macropinocytosis since the protein was usually recruited just before the scission event happened. We were surprised, nevertheless, to observe no tubulation with CYRI-B, which seems counterintuitive with the *in cellulo* data. However, we need to take into account the fact that the *in vitro* experiment has excluded post-translational modifications like myristoylation and palmitoylation. This in turns could significantly affect the ability of CYRI-B to bind to a membrane. Furthermore, CYRI-B lacks an amphipathic helix, unlike CYRI-A. This suggests perhaps CYRI-B would need further post-translational modifications to be able to perform the same task as CYRI-A. Further experiments examining these potential post-translational modifications can give us more important information on the mechanism of how CYRIs are functioning, and how CYRI-A and CYRI-B are

differentially regulated. Once the CYRI vesicles formed, Arp2/3 complex and cortactin will polarise to one side and form an actin comet tail, deliver the vesicles further into the cells. The vesicles quickly take on their maturing markers such as RAB5A, before being fused with lysosomes and getting their cargoes degraded.
It is important to note that, however, overexpression of proteins in cells can potentially affect their physiology. One way to overcome this is to tag the endogenous protein using the CRISPR system, which is currently a working progress in the lab. Furthermore, inserting a fluorescent molecule internally to a protein might also result in its aberrant regulation such as certain residues might now be subjected to modifications. Future experiments should focus on establishing a post-translational modification profile for both native and tagged proteins. This should hopefully give us a better understanding of what are the differences and similarities between these different versions of CYRIs and hopefully gives us more confidence in the cellular behaviours we observed.

Overall, we have identified a perhaps unexpected role of CYRIs in the endocytic trafficking network, in particular macropinocytosis (Figure 5.25). The model supports the idea that CYRI-A (and perhaps also CYRI-B) could act as a local inhibitor of the Scar/WAVE complex through sequestering active RAC1 at the site of macropinosomes. We propose that the novel CYRI protein family be the new players in endocytosis by acting as a quick responder to fine-tuning and guarding the signal of active RAC1 and actin.

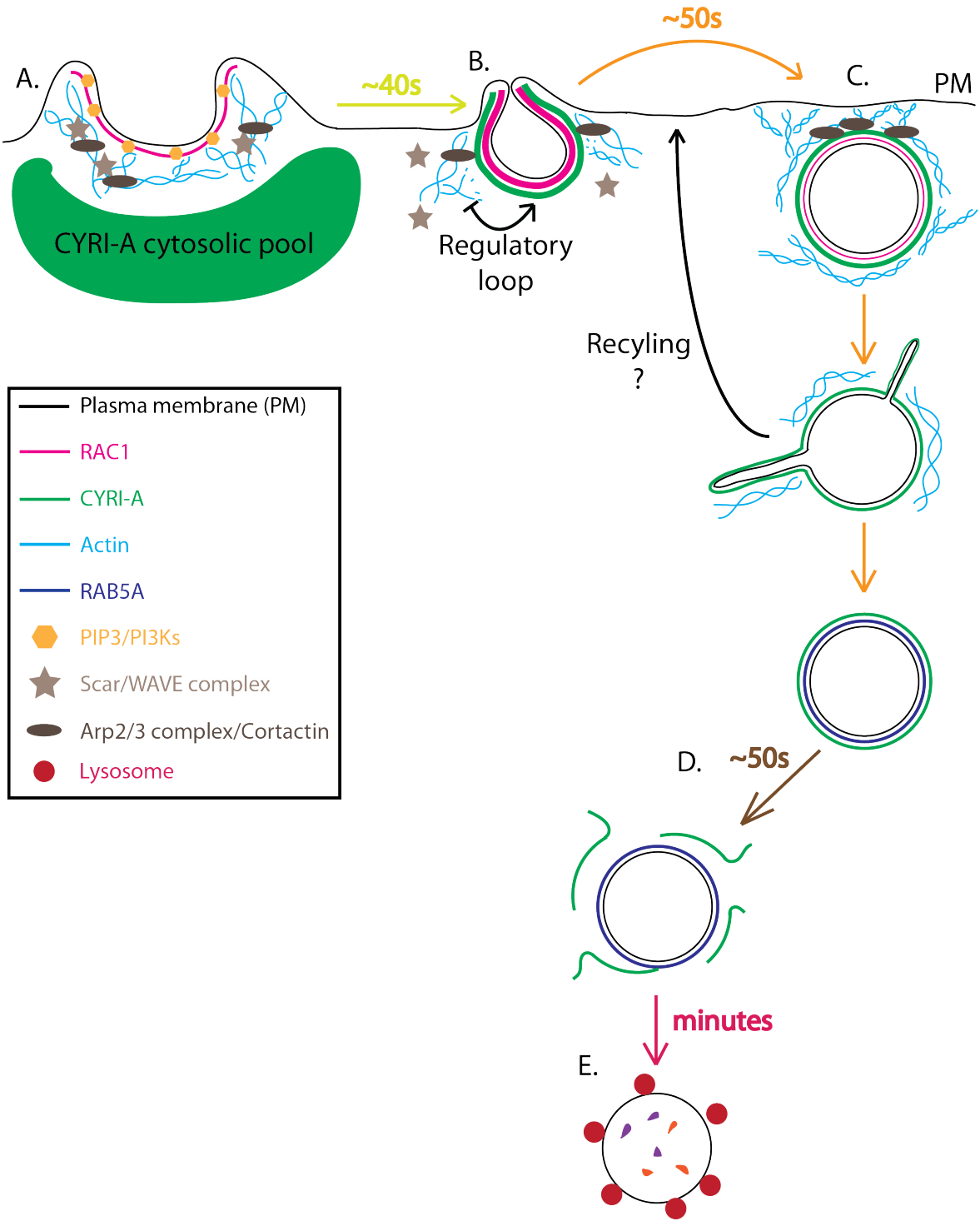

Figure 5.25 The working model of macropinocytosis for CYRIs

A. PI3K and PIP3 signalling activates RAC1, which in turns activate the Scar/WAVE complex and drives actin polymerisation and membrane ruffling. The cytosolic pool of CYRI-A is usually found near the cell leading edge and membrane ruffles.

B. After around 40s, RAC1 signalling starts to peak out (represented by the thicker magenta line). CYRI-A signal also starts to increase, meanwhile RAC1 and actin signal starts to dive down. Actin and CYRI-A have a regulatory relationship, represented here as the double-headed arrow.

C. After around 50s from B, the macropinosome formed and bud off from the plasma membrane. CYRI-A signal starts to decline, and at the same time Arp2/3 complex and cortactin start forming puncta structures. These puncta polarise to one side of the vesicles and accelerate them into the cell. CYRI positive membrane tubulation has also been observed during the process, and presumably for recycling of certain integral proteins.

D. CYRI-A signal completely disappeared and is replaced by endosomal markers such as RAB5A, which marks the early endosome. This process could take around 50s.

E. Finally, as the endosomes progress, they gain different markers and eventually are fused with lysosomes, leading to protein degradation. This transition could take up to 10-15min.

The thickness of different lines represents their relative signal intensity.

6 CYRIs regulate Integrin trafficking

6.1 Introduction

So far, we have mostly discussed the intracellular behaviour and localisation of CYRIs. However, it has been shown repeatedly that one of the most prominent phenotypes of CYRI knockout cells is the significant increase in lamellipodia spreading. In chapter 4, we have shown the functionally compensatory relationship between CYRI-A and CYRI-B. We described cells lacking both CYRI-A and B adopting the characteristic C-shape morphology with an overall increase in the cell area. These cells were observed with long extended arms with a defined prominent leading edge. The change in shape was shown to affect the migration speed in both 2D and 3D context. It is also widely accepted that integrin signalling could both directly contribute to cell attachment and spreading (Cavalcanti-Adam et al., 2007,Tawil, 1993 #158) as well as activate RAC1 through the Src-kinase/RAC-GEFs pathway (Huveneers and Danen, 2009). In this chapter, by using imaging and flow cytometry techniques, we explore further the mechanism of CYRIs and provide an additional explanation that relates integrin trafficking to the observed phenotypic changes.

6.2 Results

6.2.1 CYRI-double knockout (CYRI DBKO) cells have an increased substrate attachment

The shape of a cell maintains an intimate relationship with its migration and adhesion ability. It was reported that the amount of focal adhesion protein is positively correlated with the ability of a cell to attach to the substratum (Chen et al., 2003,Carthew, 2005 #152). Based on the fact that CYRI DBKO cells adopt the spreading phenotype, we asked whether this would convey a change in substrate adhesion. To answer this question, we utilised an *in vitro* spreading assay called the XCelligence impedance assay (Figure 6.1). The assay is based on the principle of electrical current impedance with the higher impedance positively correlates with the number and the degree of spreading of the cells.

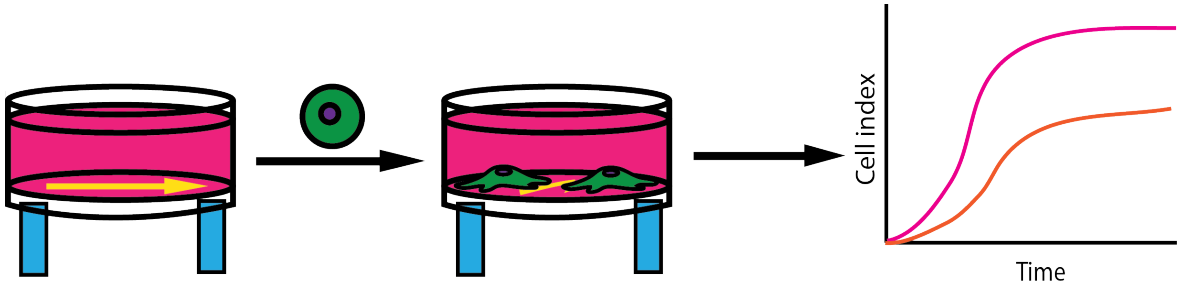

Figure 6.1 Schematic representation of the working principle of the XCelligence impedance system

A small electrical current (with the voltage of 22mV) is running across the plate (yellow arrow) from one electrode to the other (cyan rectangular plates). Cell attachment (green) impedes the current and this is detected as the read out "Cell index" as a function of time.

XCelligence plates were coated with fibronectin and A-673 cells of different genotypes were plated. Upon seeding, DBKO cells quickly settled and spread on the 2D substrate with an almost doubled kinetic compared to the control pLKO and the single knockouts after 100 minutes (Figure 6.2A). It is important to note that the same number of cells between conditions was used, and the total experiment lasted 8 hours. This ruled out the contribution of any differences in the initial cell count or cell division from the final readouts. We also reconfirmed with immunofluorescence (Figure 6.2B). After only 30 minutes of seeding, the DBKO cells had already well attached and adopted a circular spreading shape. In contrast, the control pLKO and single KO cells were struggling to form adhesions with many appearing small or rounded-up with spikey protrusions. Even after 2 hours, the cells still looked irregular with many long and thin pseudopods, whereas the DBKO had already adopted its characteristic C-shape. This was shown in the quantification of the spreading area (Figure 6.2B, right graph). These data show that DBKO cells attached much more efficiently to the matrix, suggesting an additional involvement of the adhesion machinery such as integrins. Thus, we set out to identify a potential Integrin-dependent pathway that could contribute to the observed phenotypes of CYRIs DBKO cells.

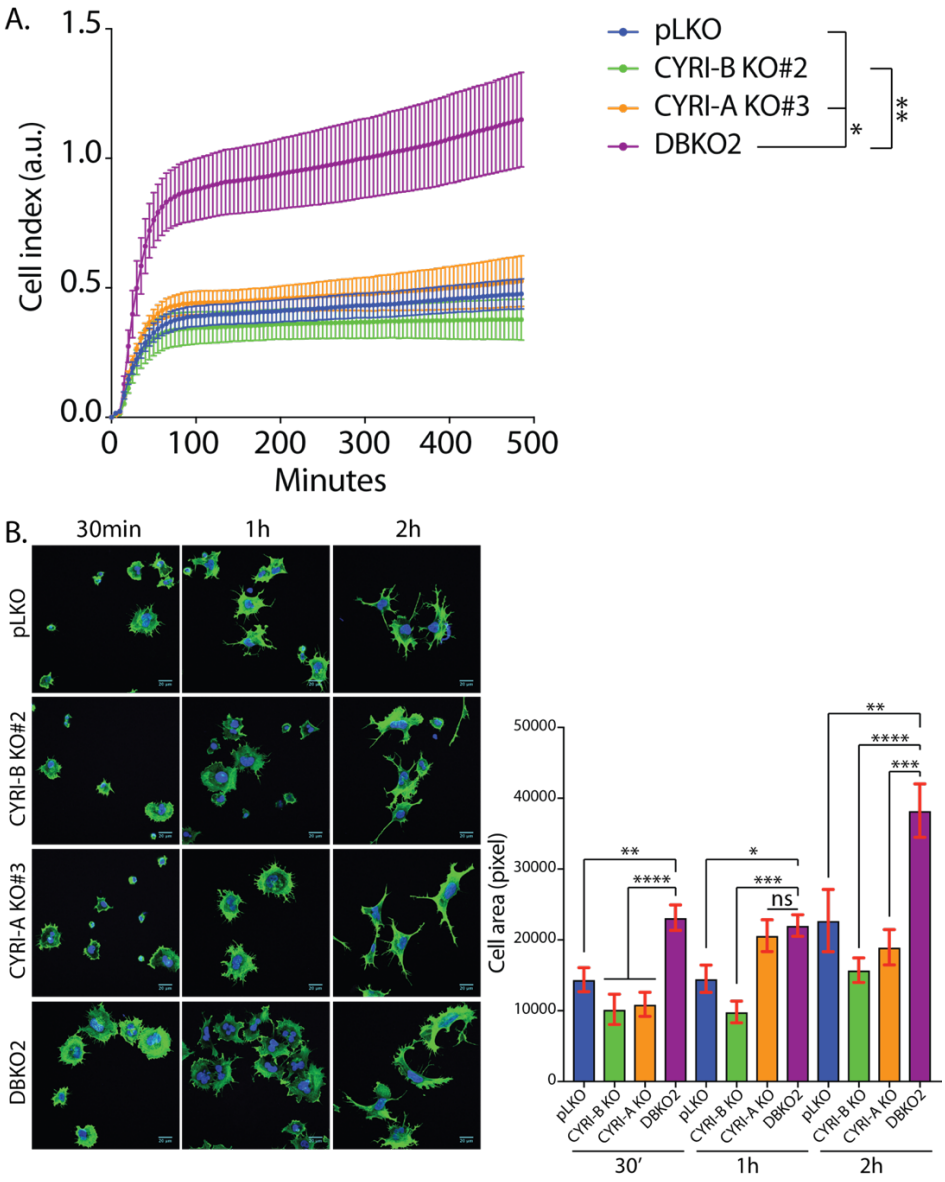

Figure 6.2 CYRI DBKO A-673 cells exhibit a superior ability to attach and spread on 2D fibronectin matrix

A. Xcelligence assay between the control (pLKO), single CYRI-B (CYRI-B KO#2), single CYRI-A (CYRI-A KO#3) and CYRI-DBKO (DBKO2) cells. The DBKO cells exhibit an almost doubled matrix adhesion ability compared to the other three cell lines. Single KO cells did not show any increased adhesion activity compared to the control. Statistical analysis from 3 independent experiments with ANOVA and multiple comparisons. Mean ± SD. *p<0.05, **p<0.01.

B. Representative immunofluorescent images of A-673 cells plated on fibronectin substrate and fixed at various time points. At the 30min time point, the DBKO cells have already attached and spread more efficiently compared to the control pLKO or the single knockout. Quantification shows the significantly larger spreading area of the DBKO cells compared to other types. Statistical analysis from 1 experiment. Mean ± SEM. ANOVA with multiple comparisons. Scale bar = 20μm.

6.2.2 CYRI DBKO A-673 cells have an increased surface expression of Integrins

Knowing that integrins play a central role in cell-matrix interaction, we thus asked whether we could detect any change of their surface expression in DBKO cells. To address this question, we performed Fluorescence-activated Cell Sorting (FACs) experiment. We tested for multiple different integrins including integrin αV, α5, α6, β1 (TS2/16) and β3 without the use of permeabilization buffer to specifically detect their surface expression (Figure 6.3A). We observed a significant right shift in the signal of integrin α5 and β1 but not α6 nor β3, suggesting an increase in their surface expression. We also observed a minor increase in αV (data not shown). These data are consistent with our observation of the spreading phenotype since integrin α5β1 as well as αVβ1 are known interactors with the RGD motif on fibronectin (Wu et al., 1993, Zhang et al., 1995). Quantification of the area under the curve shows a roughly 50% increase in the fluorescent signal from the two DBKO cell lines (Figure 6.3B). Interestingly we also observed an approximately 30% increase in the size of the DBKO cells in suspension compared to the control (Figure 6.3C). We went one step further to ask if we could detect the state of the integrins on the surface. To do this, we utilised a specific anti active integrin α5 called SNAKA51 (Clark et al., 2005) which detects the open conformation of this integrin. As can be seen in Figure 6.4A and B, CYRI DBKO cells showed a higher surface level of the active integrin conformation. Next, we asked whether this change was also affecting other membrane proteins such as MT1MMP. However, FACs analysis revealed no change to the surface presentation of this matrix metalloprotease (Figure 6.4A, B). This suggested that there is a certain degree of specificity in terms of the surface expression of integrins. Furthermore, the increase in the surface integrins was unlikely due to the increase in the cell size shown in Figure 6.3C. Western blotting showed a slight increase but consistent in the protein level of both integrin α5 and β1 in the DBKO cells (Figure 6.5A). However, quantitative reverse transcription PCR (qRT-PCR) analysis showed no change in the gene expression level of the two integrin genes compared to the control pLKO (Figure 6.5B). This suggested that the difference in the surface expression of these integrins were not due to the change in gene expression but rather at the protein level.

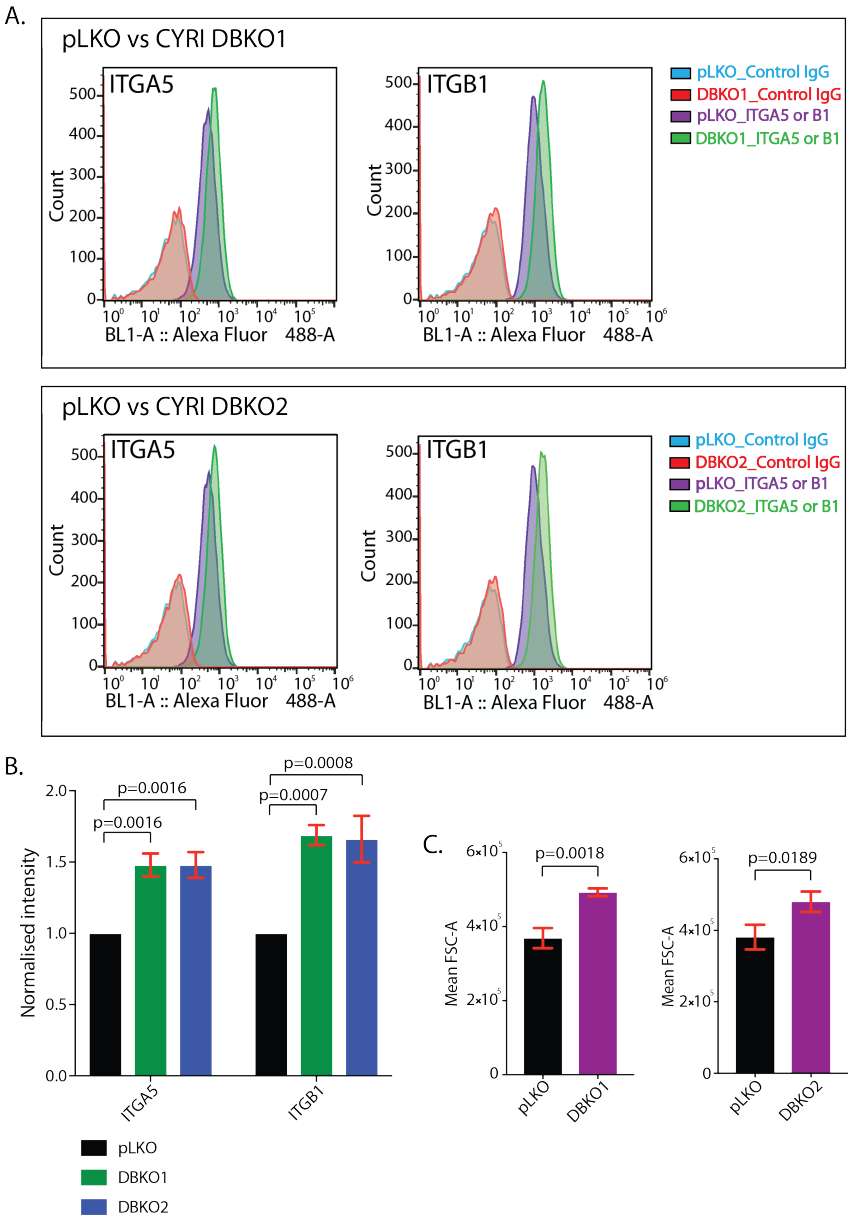

Figure 6.3 CYRI DBKO A-673 cells have an increased expression of Integrins on the surface compared to control pLKO cells

A. Flow cytometry analysis of surface expression of Integrin $\alpha5\beta1$ in the control pLKO and CYRI DBKO cells. Two independent CYRI DBKO cell lines were tested and both showed increases in the surface expression of total Integrin $\alpha5$ or Integrin $\beta1$.

B. Quantification of the relative signal intensity showing a 50% increase in Integrin signal in the DBKO cells compared to the control pLKO.

C. FSC-A signal also revealed a slight increase in the size of the DBKO cell compared to the control.

Statistical analysis from 3 independent experiments. ANOVA with multiple comparisons. Mean ± SEM.

The increase in the detected protein level without changing gene expression level also suggested these integrins must somehow be protected from degradation. We first estimated the rate of degradation of these integrins using the protein translation inhibitor cycloheximide. Inhibiting newly synthesized proteins will allow us to measure the rate of degradation of the existing proteins. The degradation of integrin β1 was shown, however, the antibody we used did not work well as expected for all experiments, so all quantification was done on integrin α5 only (Figure 6.5C). Surprisingly, the degradation rate of the integrin α5 in the DBKO1 cells was slightly higher compared to the control pLKO. This was represented by a steeper slope coefficient in the linear regression of the log base 10 transformed data (-0.0036 for DBKO1 versus -0.0025 for pLKO) (Figure 6.5D). However, reinvestigating the western blots showed that even though the rate of degrading integrin is higher in the knockout cells, the absolute amount of integrin α5 at each time point was always higher in these cells compared to the control (Figure 6.5E). This suggests there must be an additional mechanism protecting these integrins in CYRI DBKO cells. This led us to hypothesize that CYRI DBKO cells might have a defect in the trafficking that led to an apparent longer retention of integrins on the plasma membrane. This could be due to a reduced internalisation rate and/or an increased rate of rescuing and recycling back to the plasma membrane.

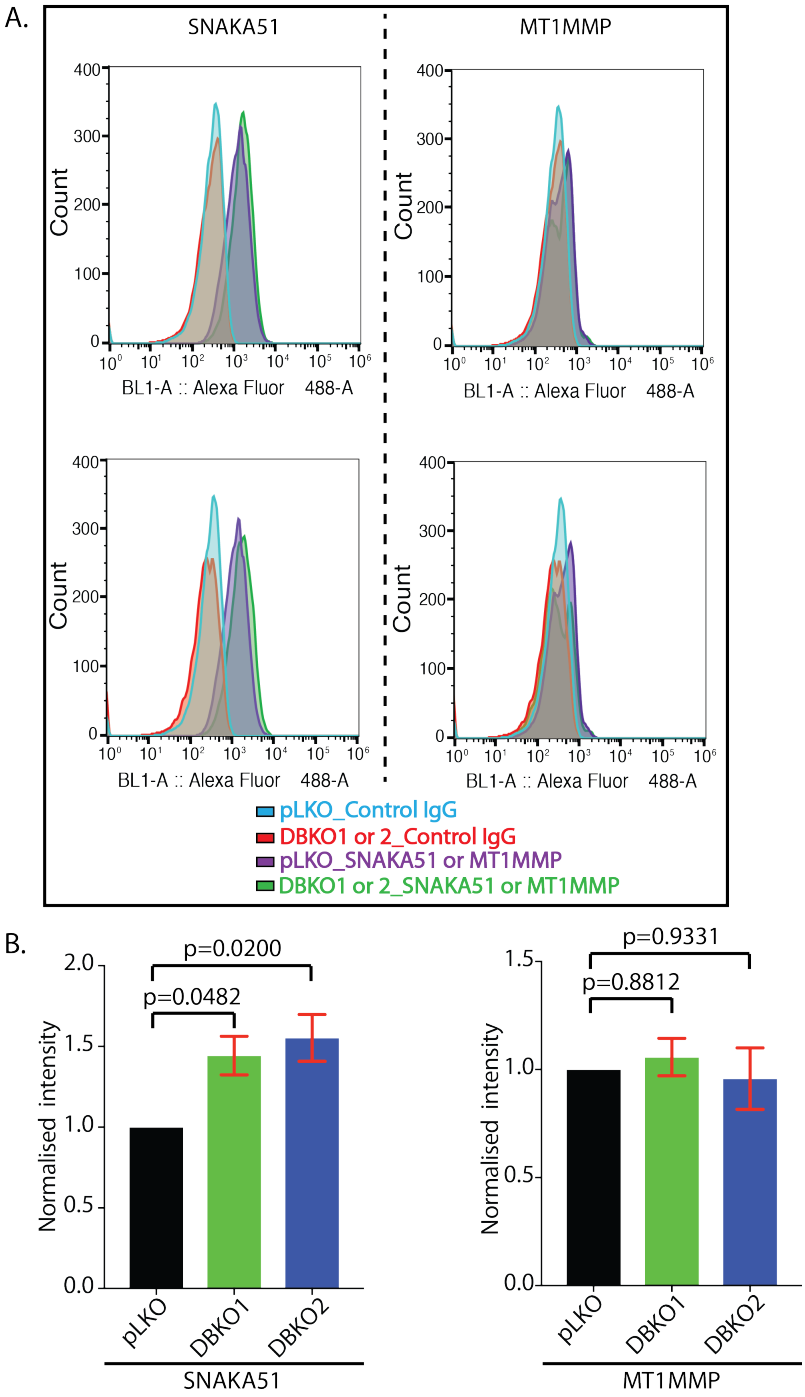

Figure 6.4 Active integrin α5 (SNAKA51) is more enriched on the surface but not MT1MMP in CYRI DBKO A-673 cells

A. Flow cytometry analysis showing the shift of SNAKA51 signal (active integrin α5) on the surface of CYRI DBKO cells but not MT1MMP.

B. Quantification shows the DBKO cells have a 40 to 50% higher level of active surface integrin α5 compared to the control pLKO. There are no detectable differences in terms of the surface level of MT1MMP between cell lines. Statistical analysis from 3 independent experiments. ANOVA with multiple comparisons. Mean ± SEM.

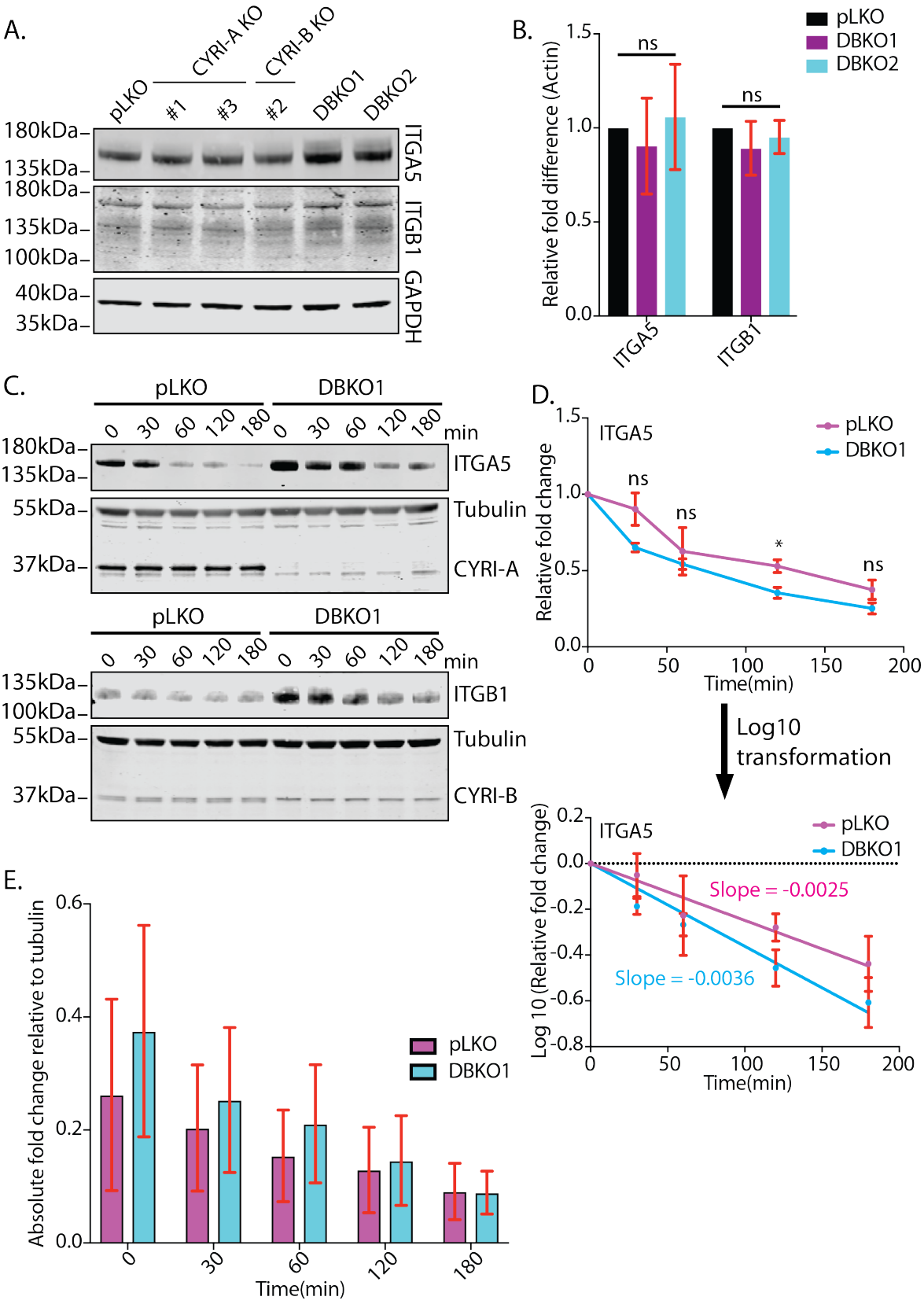

Figure 6.5 CYRI DBKO A-673 cells express more Integrins but not due to gene expression

A. Western blot showing a slight increase in the protein level of integrin $\alpha 5\beta 1$.

B. qRT-PCR (right graph) shows no change in gene expression of α5 and β1 between the DBKO cells and the control pLKO. Statistical analysis of 3 independent experiments. Mean ± SEM. ANOVA with multiple comparisons. ns = p>0.05.

C. Integrin degradation assay showing the degradation kinetics of integrin α5 and β1 upon treatment with 20ug/ml of Cycloheximide over different time points.

D. Quantification of the degradation kinetics of Integrin α5 (left, top graph) showing no significant difference between the control pLKO and DBKO1 cells. Linear regression analysis (bottom, left graph) of log base 10 transformation from the left graph, however, shows a slightly steeper slope in DBKO1 (-0.0036) compared to the pLKO (-0.0025) suggesting a slightly higher degradation rate observed in the DBKO1 cells. Unpaired t-test. ns = p>0.05, *p<0.05.

E. The absolute protein level (normalised to the corresponding tubulin level) showing the higher protein level of integrin α5 in DBKO cells compared to pLKO cells at every time point except for 180min. Mean ± SEM.

Since we have shown the increased surface expression of integrins α5 and β1 using flow cytometry, we moved on to verify this using immunofluorescent imaging. Staining with total integrin α5 and β1 as well as active integrin α5 SNAKA51 antibodies revealed striking numbers of integrin adhesion sites on the basal surface of the DBKO cells (Figure 6.6). Quantifying the area and the number of adhesion sites per cell showed that in both cases, DBKO cells were higher in both parameters relative to control cells (Figure 6.6D, E). This is in agreement with our flow cytometry data. Reintroduction of CYRI-A-FLAG into DBKO1 cells rescued their phenotypes and reduced integrin patches size and the number of adhesions per cell to the level indistinguishable from the control pLKO (Figure 6.7). This suggested that overexpression of CYRI-A was enough to reverse the phenotypes and was in strong agreement with the complementary relationship between CYRI-A and CYRI-B we have established in earlier chapters. Overall, evidence suggests that CYRI deletion leads to a gene expression-independent trafficking-dependent plasma membrane retention of integrins and thus an increased expression on the cell surface. In the next segment, we will discuss the possible mechanisms that contribute to this phenotype.

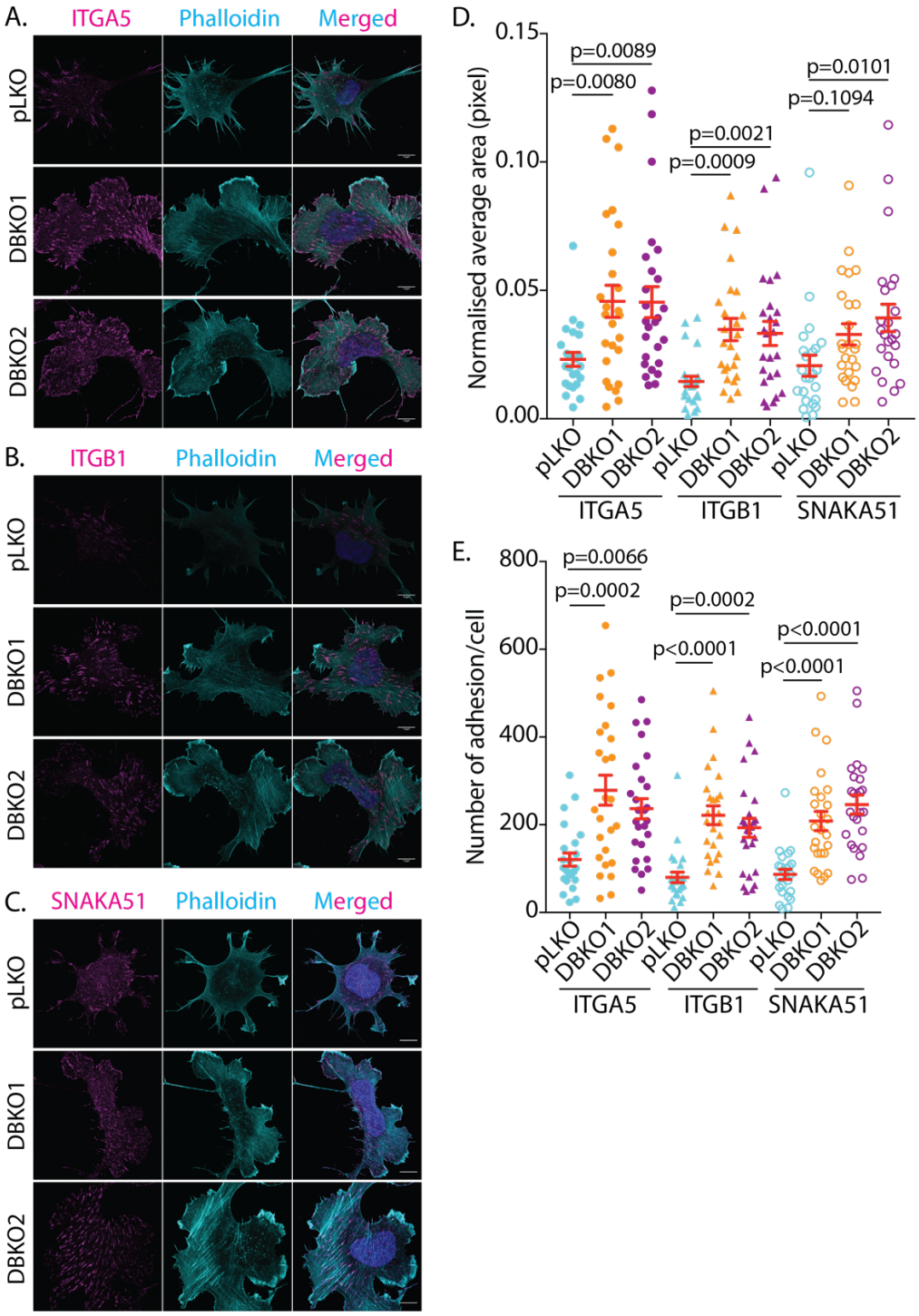

Figure 6.6 Integrin adhesion sites are larger and more numerous in CYRI DBKO A-673 cells compared to the control pLKO

A-C. Immunofluorescent images of the control pLKO and two DBKO cells stained for total integrin α5 and β1 and active α5 (SNAKA51). Scale bar = 10μm.

D, E. Quantification of the area and the absolute number of adhesions showing DBKO cells are consistently higher than control pLKO cells. Statistical analysis from 3 independent experiments. Mean ± SEM. ANOVA with multiple comparisons. Scale bar = 10μm.

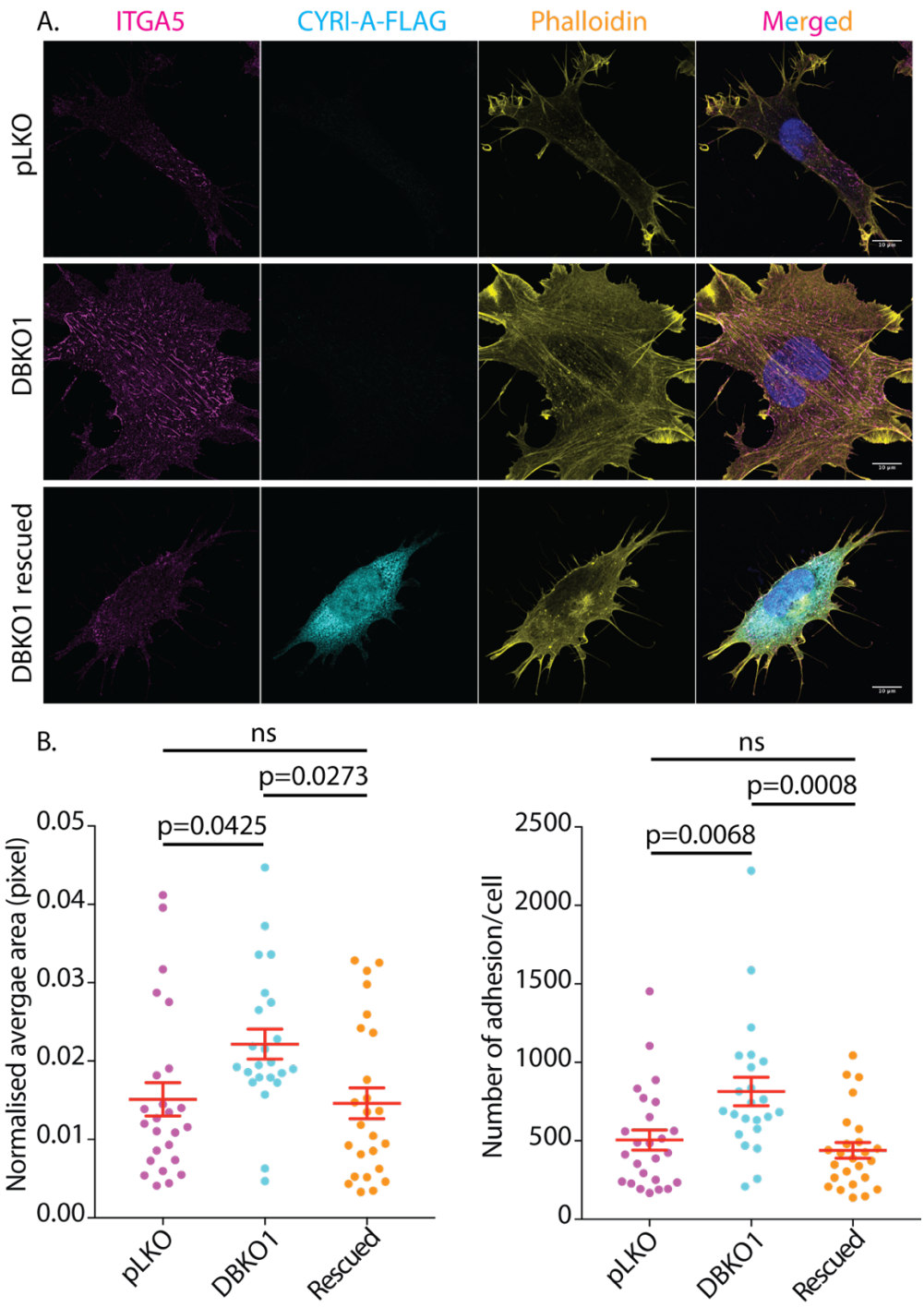

Figure 6.7 Reintroduction of CYRI-A rescues CYRI KO phenotypes in A-673 cells

A. Immunofluorescent images of the untransfected control pLKO and DBKO1 or CYRI-A-FLAG-transfected DBKO1 cell. Integrin α5 patches could be seen more numerous on the DBKO1 cells than in the pLKO or the rescued cells. Scale bar = 10μm.

B. Quantification showed a significant drop in both integrin size and number in cells transfected with CYRI-A-FLAG construct. Statistical analysis of 3 independent experiments. Mean ± SEM. ANOVA with multiple comparisons.

6.2.3 Integrin α5β1 can be internalised through CYRI-positive vesicles

The combined evidence of the effects of CYRIs deletion on the surface expression of integrins and the role of CYRIs in endocytic trafficking in chapter 5 prompted us to test whether integrins could be one of the cargoes of CYRI vesicles. We turned to live-cell imaging using COS-7 and HEK293T cells that had proved to be an easy system for imaging to address this question. We first co-transfected COS-7 or HEK293T with the internal GFP-tagged CYRI-A and mApple-tagged integrin α5 (mApple-ITGA5) and plated the cells on fibronectin-coated glass-bottomed dishes. CYRI-A, as expected, accumulated on large endocytic vesicles. We observed numerous vesicles containing the integrin α5 trafficking back and forth within the cell (Figure 6.8A). Apart from those moving outwards, many vesicles were actively moving inwards and tended to derive from the tip of protrusions or membrane ruffles. Interestingly, we could detect integrin signal concentrated on CYRI-A-positive vesicles. As these vesicles moving inwards along with the disappearing of the CYRI-A signal, the integrin signal is still seen persisting on these structures. We tested the same hypothesis for CYRI-B in COS-7 cells as CYRI-B-transfected HEK293T cells were not healthy. Integrins could be seen as a bright spot at the tip of filopodia (Figure 6.8B). CYRI-B, as expected, formed predominantly tubular vesicles and could be seen to actively draw integrins inwards, ultimately lead to the disassembly of these focal adhesion structures. Unlike its counterpart CYRI-A, CYRI-B persisted on the vesicles with the integrin signal. It was challenging to visualise where did these vesicles go as the CYRI-B signal was less prominent and the vesicles tended to be smaller. Nevertheless, these data provided the first direct evidence for the involvement of CYRIs in integrin trafficking.

However, the system above relies on overexpression of integrins, which could potentially lead to artefacts. Hence, we decided to examine if endogenous integrins could also be found on CYRI vesicles by using immunofluorescent imaging. We first tested our hypothesis in COS-7 cells. Integrin α5 could be localised to both CYRI-A and CYRI-B vesicles with a strong colocalization signal shown in the intensity plot (Figure 6.9A). We managed to visualise integrin β1 on CYRI-A vesicles but failed to detect any obvious colocalization on CYRI-B (Figure 6.9B).

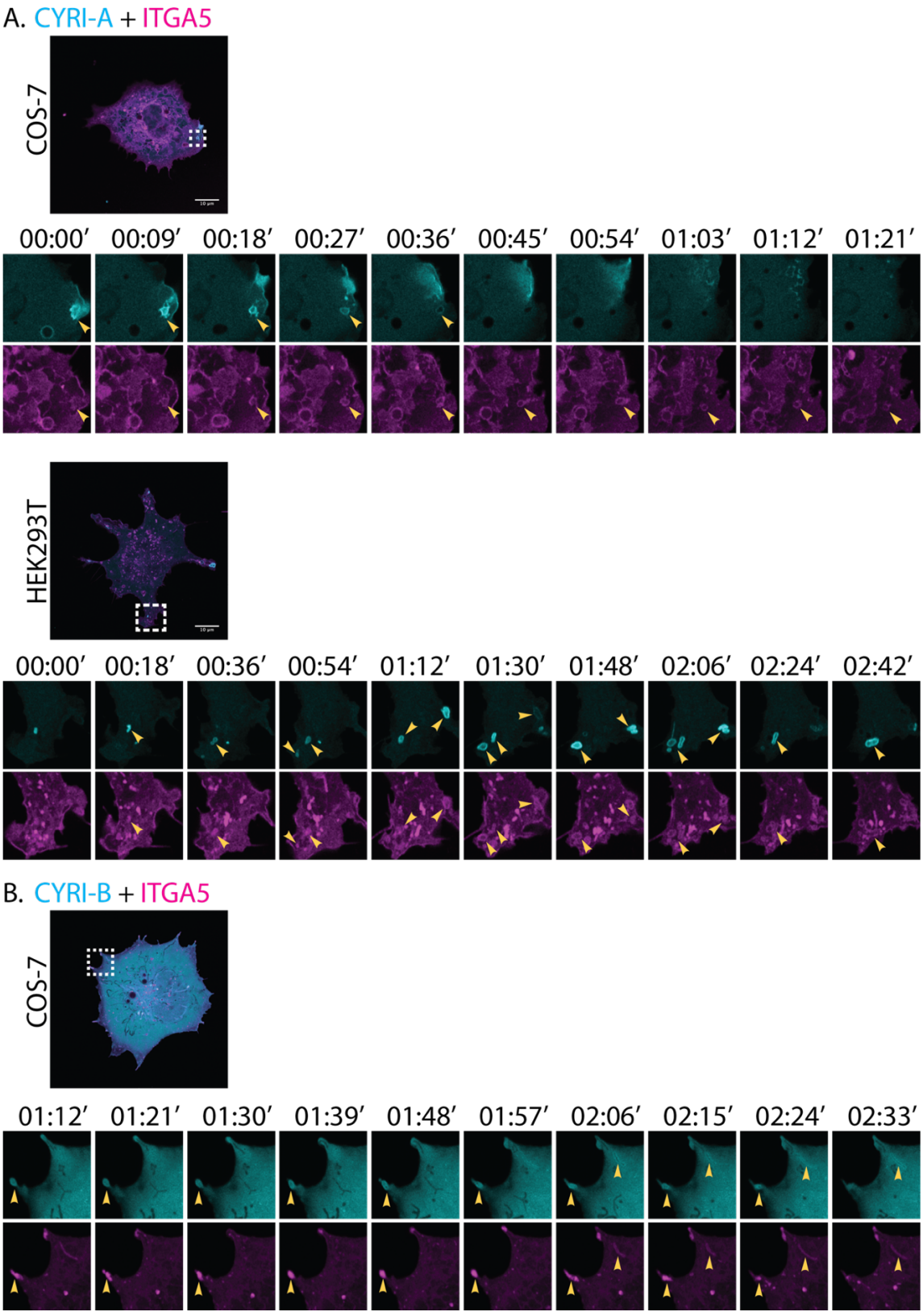

Figure 6.8 Integrin α5 localised to CYRI-positive vesicles

A. COS-7 or HEK293T co-expressed both GFP-tagged CYRI-A and mApple-tagged ITGA5. Integrin α5 could be seen localised to the CYRI-A positive endocytic vesicles in both cell types.

B. COS-7 cells co-expressed GFP-tagged CYRI-B and mApple-tagged ITGA5. CYRI-B could be seen formed its distinctive tubular structures at the foal adhesion site where ITGA5 located. These tubules were then drawn into the cell leading to the dissociation of the focal adhesion site.

Scale bar = 10μm

To make the spatial visualisation clearer, we reconstructed the 3D structure of the vesicles and rotated them along the x-axis (Figure 6.10). As can be seen, CYRI-A forms a dome-shaped structure pointing toward the inside of the cell with integrins and phalloidin signal were also seen on the vesicles (Figure 6.10A, B). Visualising CYRI-B was more challenging as its vesicles tended to be smaller and flatter, and the signal was usually weak. Nevertheless, we managed to capture a vesicle that was forming at the edge of the cell. Again, integrins and actin signal could be seen at the same location (Figure 6.10C). In general, it was more difficult to visualise the β1 subunit on CYRI vesicles. We believed this reflected the more versatile nature of this subunit. Integrin β1 could partner with a wide range of other α subunits and thus was subjected to many other trafficking signals all at once. Whereas integrin α5 could only be found with the β1 subunit, hence could be more restrictive in terms of its internalising dynamic. Nevertheless, this provided evidence that CYRI vesicles do contain endogenous integrins. Since we have validated many observations in COS-7 cells, we would like to also validate our observations in the A-673 cell line. The reason that we could not do as many visualisation experiments with this cell line as we would have wanted was due to their inherently difficult nature to image. The cells were not ideal for expressing proteins and for some unknown reasons were more prone to bleed-through and dual-excitation artefact while live-imaging. Nonetheless, we first asked whether our internal GFP-tagged CYRI-A and CYRI-B could be observed in the A-673 cells, and above all would they behave similarly to what has previously been described? We co-expressed P16-GFP-CYRI-A or P17-GFP-CYRI-B along with the mCherry-tagged RAB5A in the DBKO1 A-673. We found that the double knockout cells are significantly better at expressing proteins compared to the wild type pLKO. Cells transfected with RAB5A formed numerous vesicles. However, as noticed in Figure 6.11, the signal from the mApple channel (magenta) could also be seen in the GFP (cyan) channel.

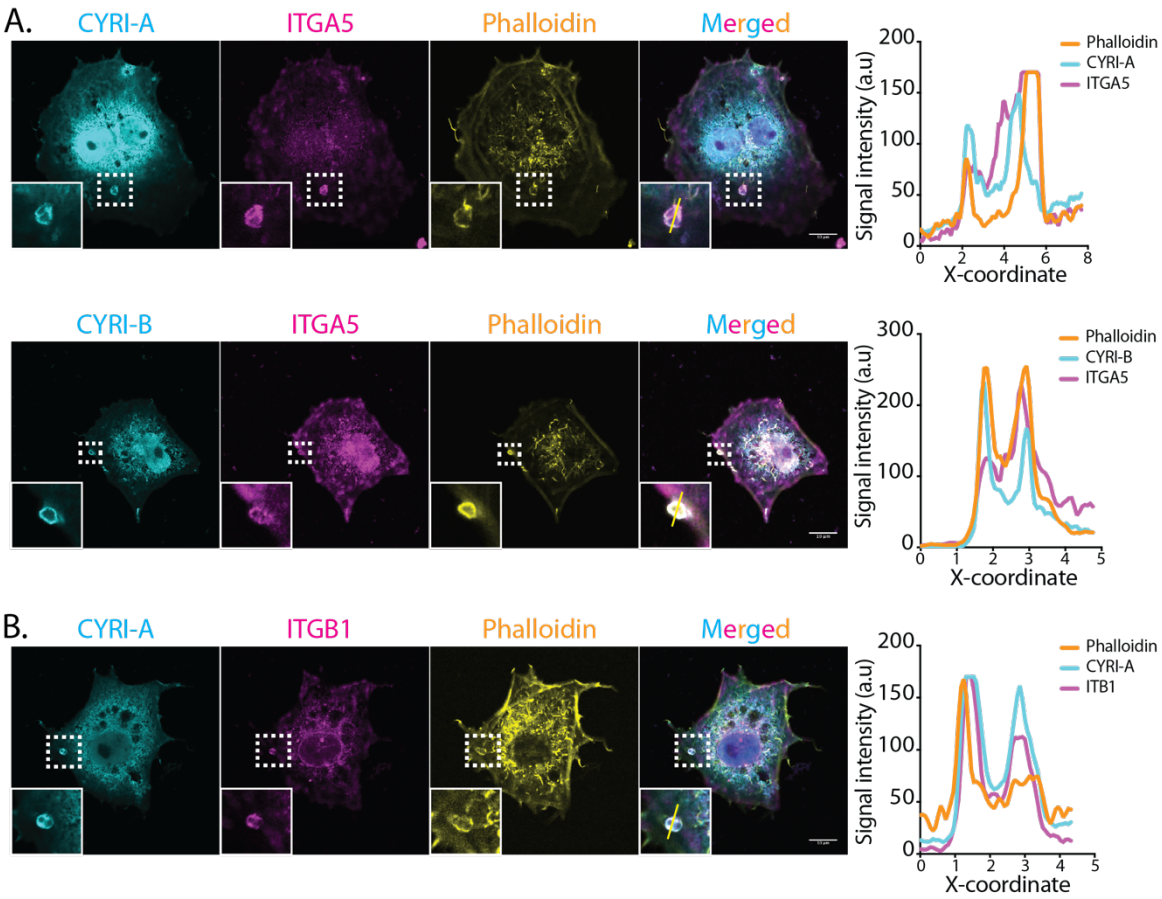

Figure 6.9 Endogenous integrin α5β1 localised to CYRI-positive vesicles in COS-7 cells

A. Integrin α5 localised with CYRI-A and CYRI-B signal on vesicles. Intensity plot (right side) showed a strong co-localisation signal between CYRI, ITGA5 and phalloidin.

B. Integrin β1 can also be found on CYRI-A vesicles as can be seen on the intensity plot on the right-hand side.

Scale bar = 10μm.

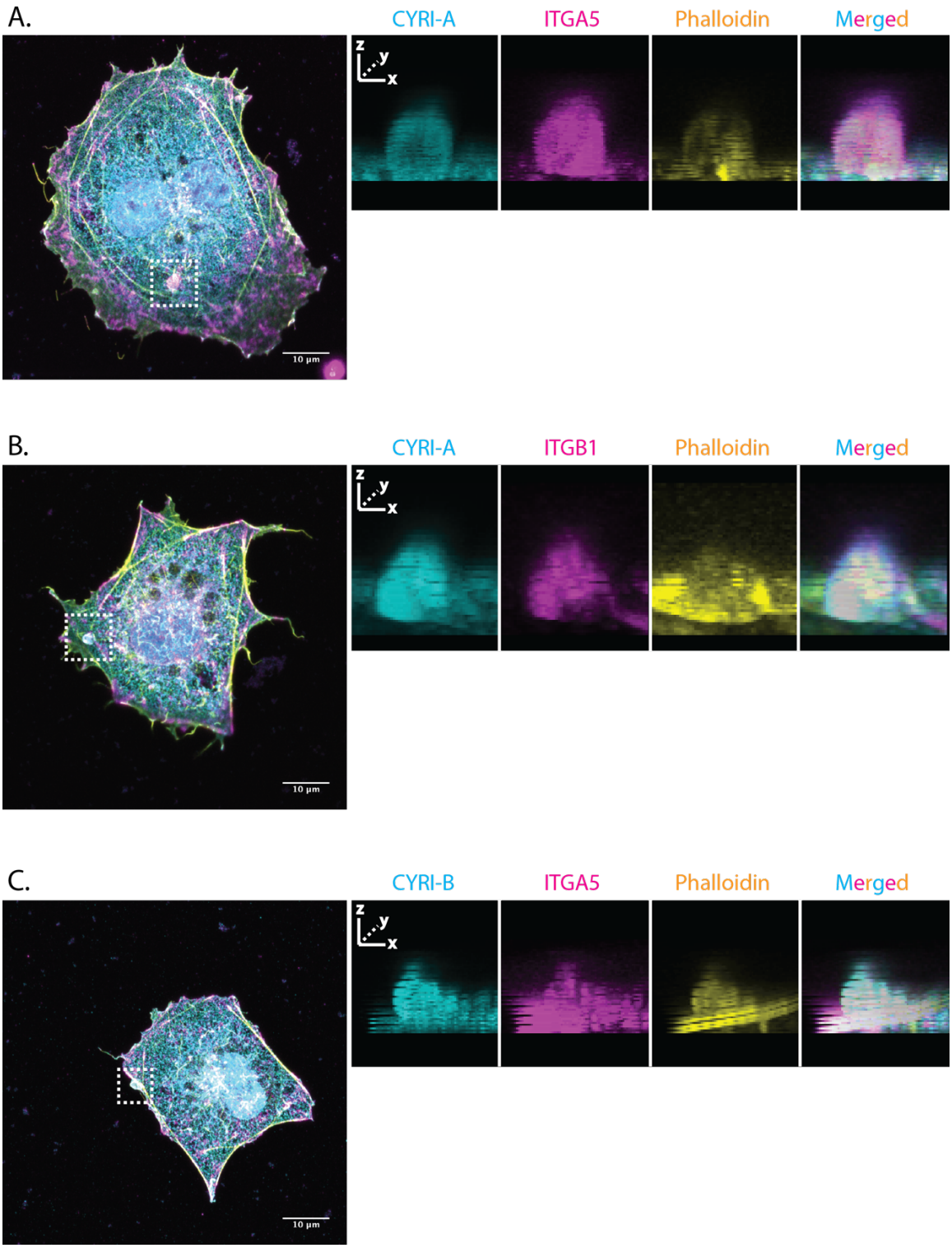

Figure 6.10 3D projection of CYRI vesicles containing integrin α5β1 in COS-7 cells

In all cases, integrins and actin (phalloidin) signal could be seen at the same location as the CYRI signal. The dome-shaped negative curvature vesicles could be seen grabbing up the integrins into the cell. z-stack projection of slices every 0.18μm. Scale bar = 10μm.

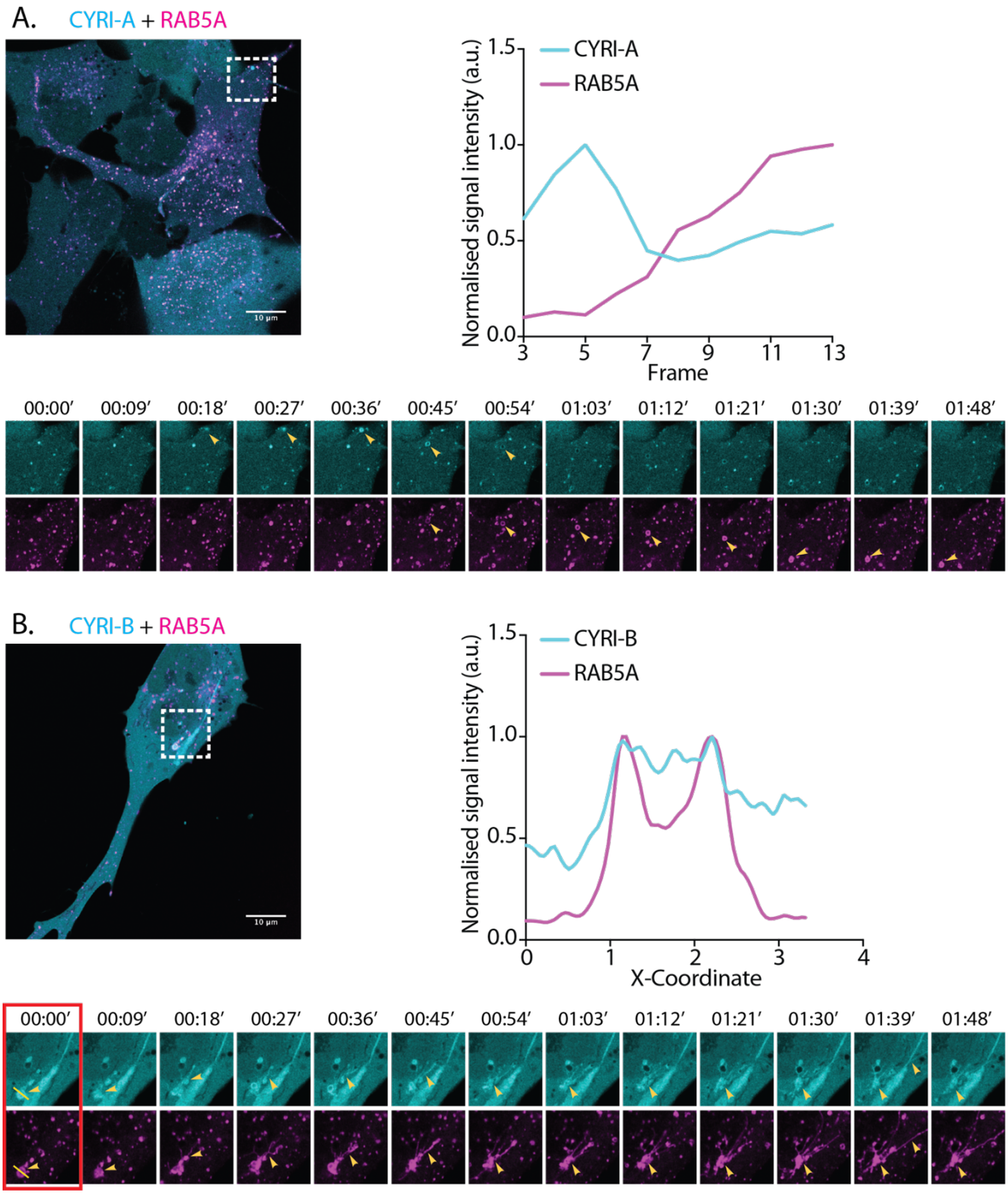

Figure 6.11 The internal GFP-tagged CYRI-A and CYRI-B also localise to endocytic vesicles in CYRI DBKO1 A-673

A. CYRI-A localises to the endosome upstream of RAB5A.

B. CYRI-B showed a persistent localisation with RAB5A throughout the imaging process.

Scale bar = 10µm.

We have set up the microscope so that bleed through would be minimised through a series of filters, thus this indicated that dual excitation was in effect, which happen when the shorter wavelength excites the fluorophore of the longer wavelength. Dual excitation leads to the bright spots of the mApple signal, which tends to have higher local concentrations of the protein, got excited by the 488nm laser coming from the GFP channel. We could see this as the almost perfect colocalization of the GFP spots with the mApple spots, hence one must be careful when interpreting this data. Nevertheless, we could identify the real signal by looking at what is present in the GFP channel and is absent in the mApple channel. We observed CYRI-A-positive vesicles quickly formed at the leading edge of the cell then moved inwards and switched to RAB5A signal (Figure 6.11A). For CYRI-B, the protein was regularly seen persisting on thin tubules zipping through the cytoplasm as described in other cell lines (Figure 6.11B). These observations strongly suggested the behaviours of CYRI-A and CYRI-B constructs were conserved across many cell types, including the A-673 cells. We then asked whether we could also localise integrins on these endocytic vesicles. Indeed, immunofluorescent imaging showed endogenous integrin α5 and β1 present on these CYRI-positive vesicles (Figure 6.12). They were also frequently colocalising with the actin marker phalloidin. Overall, we showed that in A-673 cells, integrins could be found concentrated on CYRI positive vesicles.

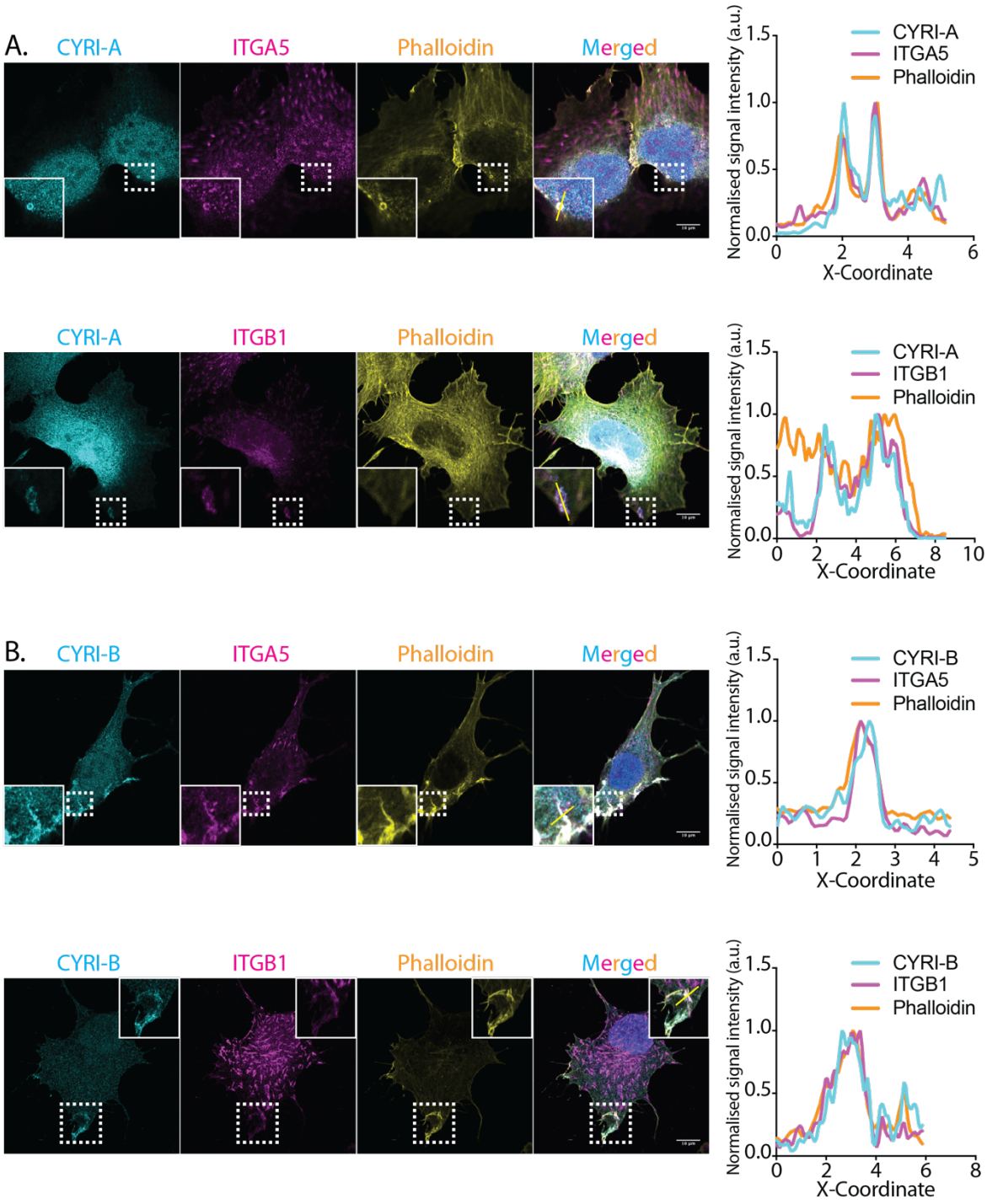

Figure 6.12 Integrin α5β1 localise CYRI-positive vesicles in DBKO1 A-673 cells

CYRI-A vesicles A) and CYRI-B tubules B) contain endogenous integrin α5 and β1. Right graphs show strong colocalization of the integrin signals with the vesicles. Scale bar = 10μm.

To test whether integrin internalisation requires CYRI proteins, we performed an image-based internalisation assay described in Figure 6.13 (Pietila et al., 2019,Arjonen, 2012 #163). Both cell types at 0min of internalisation showed no obvious integrin signal inside or outside as expected (Figure 6.14). At the 30min timepoint, however, we discovered that while the control pLKO cells had a strong accumulation of the integrin signal residing at the perinuclear region, the DBKO1 cells did not. Quantification showed that the internalisation capacity of the control pLKO was about 2 times higher than the DBKO1 cells. Overall, the data suggest the involvement of CYRIs in the internalisation of integrin $\alpha5\beta1$ in A-673 cells.

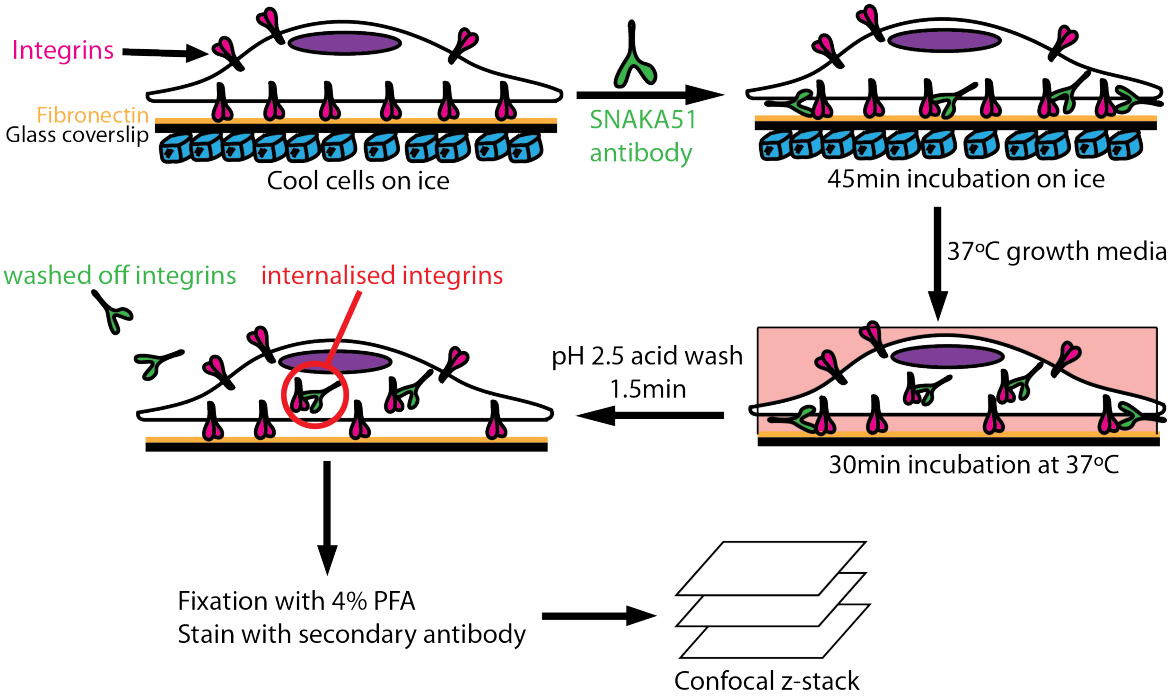

Figure 6.13 Image based internalisation assay schematic representation

Cells were plated on fibronectin-coated coverslips and left on ice to stop any endocytic trafficking. Cells were then incubated with anti-active integrin $\alpha5$ SNAKA51 in HBSS buffer on ice for 45min. Internalisation was triggered by adding 1ml of 37°C growth media and incubated for 30min in a cell incubator. After incubating, cells were washed with 500µl of pH2.5 acetic buffer for 1.5min to remove any residual surface-bound SNAKA51 antibody, while leaving the internalised integrins and antibody unaffected. Cells were then fixed with 4% PFA and stain for secondary antibody DAPI. Cells were imaged using z-stack imaging with a confocal microscope.

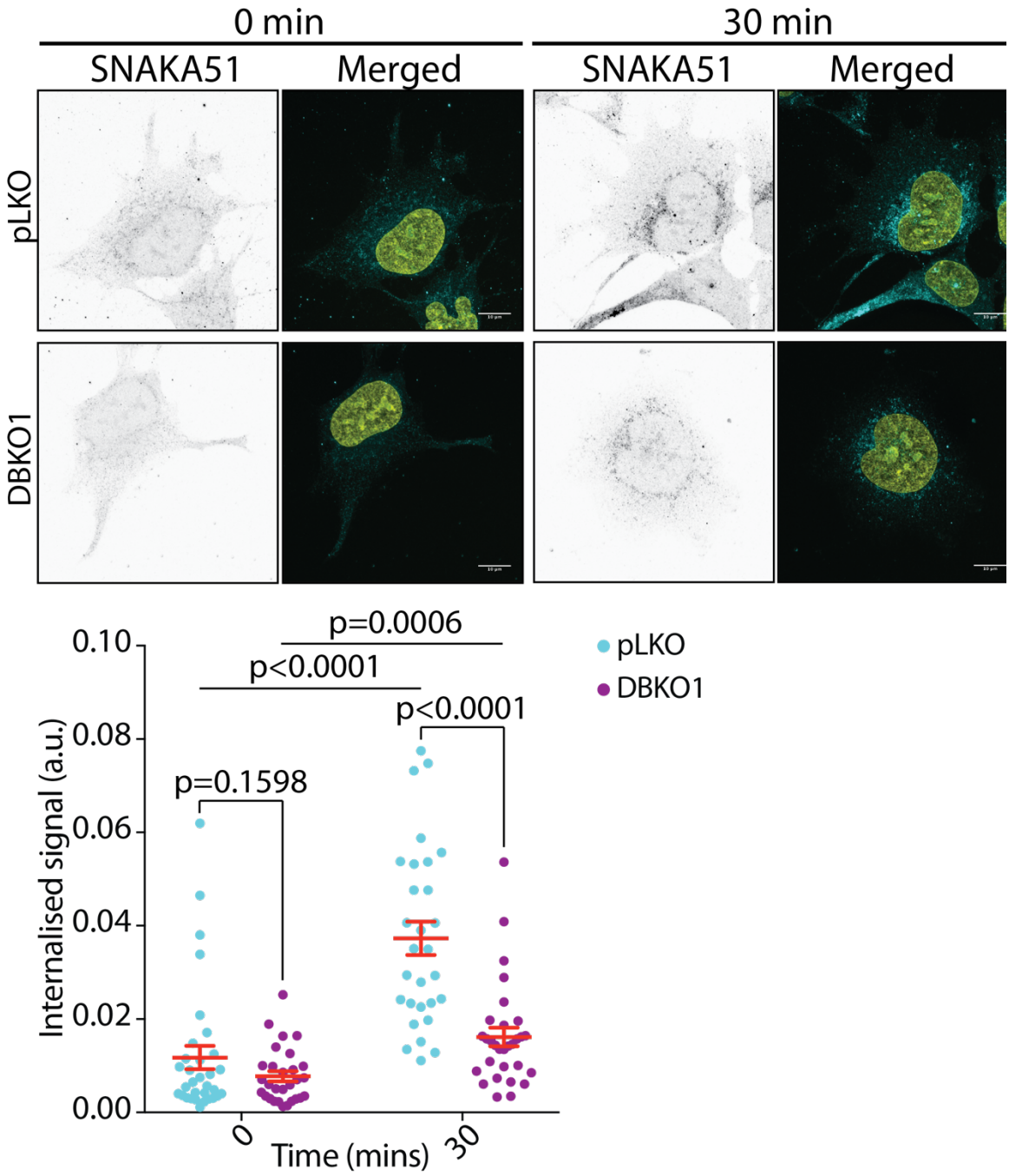

Figure 6.14 CYRI DBKO A-673 cells have a reduced apparent integrin internalisation capacity compared to control pLKO cells

Image-based internalisation assay of active integrin α5 SNAKA51 between the control pLKO and the DBKO1 cells at 0 and 30min incubation. The control pLKO showed an increased intracellular signal of SNAKA51 compared to the DBKO1 cells at the 30min timepoint. Quantification from 3 independent experiments. Mean ± SEM. Unpaired 2-tail t-test. Scale bar = 10μm.

6.3 Discussion

In this chapter, we have provided evidence for a novel function of CYRI proteins in mediating integrin trafficking, thus controlling cell-matrix adhesions. We showed that deletion of CYRIs in A-673 cells increased surface expression of integrin $\alpha5\beta1$, thus enhanced their ability to attach and adhere to the fibronectin matrix. Western blots show the amount of integrin $\alpha5\beta1$ was slightly higher in the CYRI DBKO cells compared to the control or single knockouts, but qPCR shows no change in terms of gene expression. Counterintuitively, the rate of degradation of integrins upon cycloheximide treatment in the DBKO cells was slightly higher than other cell lines. This suggests that the protective mechanism for integrins in the DBKO cells has to be robust enough to counteract the effect of the increased degradation. We hypothesised that one of these mechanisms is membrane retention. We reconfirmed the behaviour of CYRI-A and B in A-673 as consistent with other cell lines, suggesting that the effects and phenotypes we observed are conserved across different cell types. We provided direct evidence showing CYRI vesicles indeed contained integrins as their cargoes, and these vesicles formed negative curvature into the cell. Internalisation assay clearly showed the apparent increase of almost 2 times of internalised integrin signals of the control pLKO cells after 30min of temperature induction compared to CYRI DBKO cells, which might also perhaps explain the 1.5 times higher of surface integrins on the DBKO cells compared to the control. Since cells lacking only 1 isoform of CYRI behave similarly to the control cells as shown in previous chapters, we conclude that CYRI-A and CYRI-B could functionally compensate each other in regulating integrin trafficking. In cells lacking both CYRIs, this leads to a longer retention of active integrins on the surface, thus allow them to adhere to the surrounding matrix and migrate more efficiently. It is also important to note that the rate of degradation and the rate of internalisation are not necessarily dependent on each other. On one hand, cells can internalise their cargoes with a fast rate and degrade them with an equally fast rate. On the other hand, it is equally likely to internalise cargoes at a fast rate but degrade them at a slower rate and vice versa. The apparent increased internalisation signal in the pLKO cells compared to the DBKO1 might not only be contributed by the lower in the internalisation rate but also increase in the recycling rate back to the cell surface. The possible interaction

between CYRI-mediated internalisation versus other pathways remains to be answered. We believe CYRIs could interfere with RAC1 signalling at a much more localised manner at the endocytic vesicles. CYRIs regulate integrin internalisation through mediating the formation of macropinosomes, and in addition to regulate cell spreading through RAC1-Scar/WAVE-Arp2/3-actin signalling axis, CYRIs could also influence how cells spread by using integrin signalling. It has indeed been previously shown that integrin β3 can be taken into the cells via macropinosomes in fibroblasts (Gu et al., 2011). Thus, we offered a simple novel mechanism to explain how CYRIs might regulate cell shape and adhesion through mediating integrin uptake via macropinocytosis. Furthermore, since we have also shown that the majority of CYRI-positive vesicles were macropinosomes, which are important for taking up nutrients, it would be interesting to study the effect of CYRIs on the cellular metabolic landscape. The relationship between migration and macropinocytosis has been suggested to be incompatible with each other (Veltman et al., 2014). From chapter 3, we have briefly shown that CYRI DBKO cells had a slower proliferation rate compared to the control or single knockout. This might suggest that deleting CYRIs could switch the cells from a proliferative state into a migratory state, which also agreed with our migration data. The traffic of integrins in a cell is inherently affecting how the cell interacts with its surrounding environment. In the context of cancer, this can affect the invasion and metastasis process (Seguin et al., 2015, Caswell et al., 2009, Rainero et al., 2015, Dozynkiewicz et al., 2012). In the next chapter, we will further explore the consequences of these phenotypes in cancer cells in 3D settings.

7 The effects of integrin signalling on CYRI-knockout cancer cells

7.1 Introduction

In previous chapters, we have discussed the effects of CYRI deletion on the morphology and migration behaviour of cancer cells both on 2D fibronectin substratum and in 3D cell-derived matrix. We have established that CYRI proteins are involved in integrin trafficking from the plasma membrane into the cell and lacking CYRIs lead to an increase in the apparent retention of active integrin $\alpha5\beta1$ on the cell surface, which can affect cell adhesion and migration. Integrin $\alpha5\beta1$ has long been implicated in supporting cancer cell survival and migration. In breast cancer, hypoxia can upregulate integrin $\alpha5\beta1$ to induce 3D invasion in tumour spheroids and haptotaxis (Ju et al., 2017, Oudin et al., 2016). MDA-MB-231 cells expressing higher levels of integrin $\alpha5\beta1$ are associated with a higher degree of acto-myosin contractility in 3D collagen, which is thought to promote invasion (Mierke et al., 2011). In Ewing's sarcoma, tenascin-C (TNC) is associated with the increased proliferation, invasion and angiogenesis and integrin $\alpha5\beta1$ signalling is thought to trigger TNC expression via YAP nuclear translocation (He et al., 2019). Furthermore, depletion of CYRIs has been shown to lead to a global increase in RAC1 activity (Fort et al., 2018). RAC1-Scar/WAVE signalling network has been implicated in cancer metastasis and is a known downstream effector of integrins (Kjoller and Hall, 2001, Lester et al., 2007, Vial et al., 2003, Smith and Marshall, 2010). This leads us to wonder whether the increased surface expression of $\alpha5\beta1$ integrins would have an impact on the behaviour of CYRI DBKO cells. In this chapter, we will explore the physiological consequences of CYRI deletion as well as provide an explanation for these phenotypes using various model systems, ranging from 2D to 3D model.

7.2 Results

7.2.1 CYRI DBKO cells are more invasive

Our migration data in CDM in chapter 4 showing an almost double in the speed of CYRI DBKO cells compared to the control and single knockout cells. To observe the morphology of these cells in more details, we turned to live-cell imaging of GFP-tagged LifeAct transfected cells in CDM (Figure 7.1). The first thing we noticed was that CYRI DBKO cells form numerous dynamic filopodium-like protrusions (FLPs). These structures could be seen constantly moving, pulling on and feeling the surrounding matrix. Compared to these cells, the control was much less dynamic. Occasionally cells did form FLPs, however, these events were sparser and less frequently. To quantify these dynamics, we generated the temporal-colour code (TCC) images of these cells, with each colour represented the state of the cells at a particular time point. Visually, we could see the DBKO cells were much more active with many FLPs spreading in all directions compared to the pLKO cells (Figure 7.1B). To quantify this, we calculated the area of difference between the cell at frame 1 and the TCC image as the proxy for the dynamic under the assumption that the more dynamic and numerous the FLPs were, the larger the area covered in the TCC image (Figure 7.1A). We made use of the automated thresholding algorithms in ImageJ to generate a pipeline. As can be seen in the graph in Figure 7.1B, the difference in area is larger in DBKO cells (~464um^2) compared to the control cells (~301um^2). FLPs and filopodia have been frequently associated with cancer progression. It is believed that these protrusive structures allow the cancer cells to probe the surrounding environment as well as forming points of contacts with the matrix (Jacquemet et al., 2017,Shibue, 2013 #172). They lead the migrating front where integrins are recycled back to assist the invasion process (Paul et al., 2015) and can also act as matrix-degrading structures through N-WASP-mediated MMP14 delivery (Yu et al., 2012). The actin-bundling protein fascin, for example, localises to and stabilises invadopodia and FLPs to assist invasion in melanoma and pancreatic cancer cells (Li et al., 2010, Li et al., 2014).

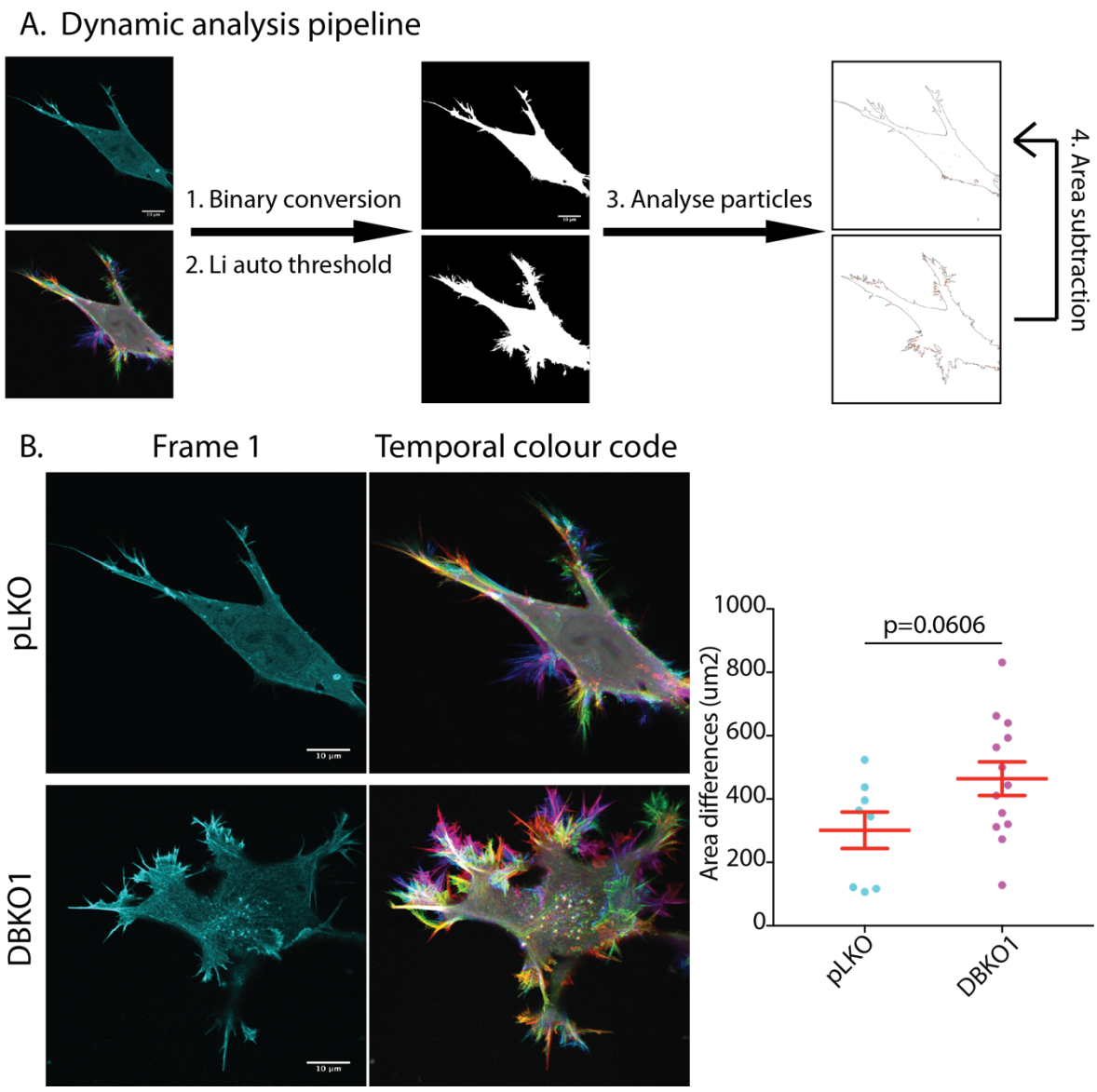

Figure 7.1 CYRI DBKO A-673 are more dynamic in CDM than the control pLKO

A. Dynamic analysis pipeline: live images are converted to temporal-colour code image (TCC) (rainbow image). Frame 1 and the TCC image are then 1. binary converted and 2. an auto threshold using Li algorithm is applied. The resulting images are thresholded and analysed by using 3. analyse particle function. The area of the TCC image is subtracted by the area of the frame 1 image and the difference is used as a proxy for how dynamic one cell is.

B. Representative images of the control pLKO versus the CYRI DBKO in CDM. Quantification shows CYRI DBKO cells (~464um^2) are more dynamic than control pLKO (~301um^2) in 3D. Mean ± SEM. Unpaired 2-tail t-test. Scale bar = 10µm.

Because we see an increase in protrusions, we hypothesized that this would allow the DBKO cells to invade more effectively. We, therefore, performed an inverted invasion assay. Figure 7.2A shows the schematic representation of the assay. To mimic the complex matrix environment inside the body, Matrigel is supplemented with collagen and fibronectin at 4 and 1 mg/ml, respectively. The assay revealed a startling difference in the invasive capacity between the control and the DBKO cells (Figure 7.2B). The majority of the control cells did not migrate beyond 20μm. We also noticed that most of the cells were adopting a spherical shape. On the other hand, two lines of CYRI DBKO cells were aggressively invading into the plug beyond 90μm and up to 200μm. These cells also adopted a more spread and spindle shape, suggesting that they were forming adhesions to the surrounding matrix. The invasion index was calculated by measuring the total area of invading cells beyond 10μm and divided by the total area of cell starting from 0. On average, 25% of DBKO cells invade into the matrix plug beyond 10μm compared to just 5% for the pLKO cells.

To reconfirm our observation in a more physiologically relevant condition, we turned to the organotypic assay (Timpson et al., 2011) (Figure 7.3A). As expected, H&E staining showed a striking difference between the control pLKO and two DBKO lines (Figure 7.3B). The invasion index was quantified by measuring the area of invasion and normalised to the total area of the plug. This showed that both DBKO lines showed a stronger degree of invasion with numerous cells could be seen burrowing into the collagen plug compared to the control. This was in line with the data from the inverted invasion assay. Overall, deletion of CYRIs leads to a significant increase in the invasive capacity of cancer cells in 3D culture.

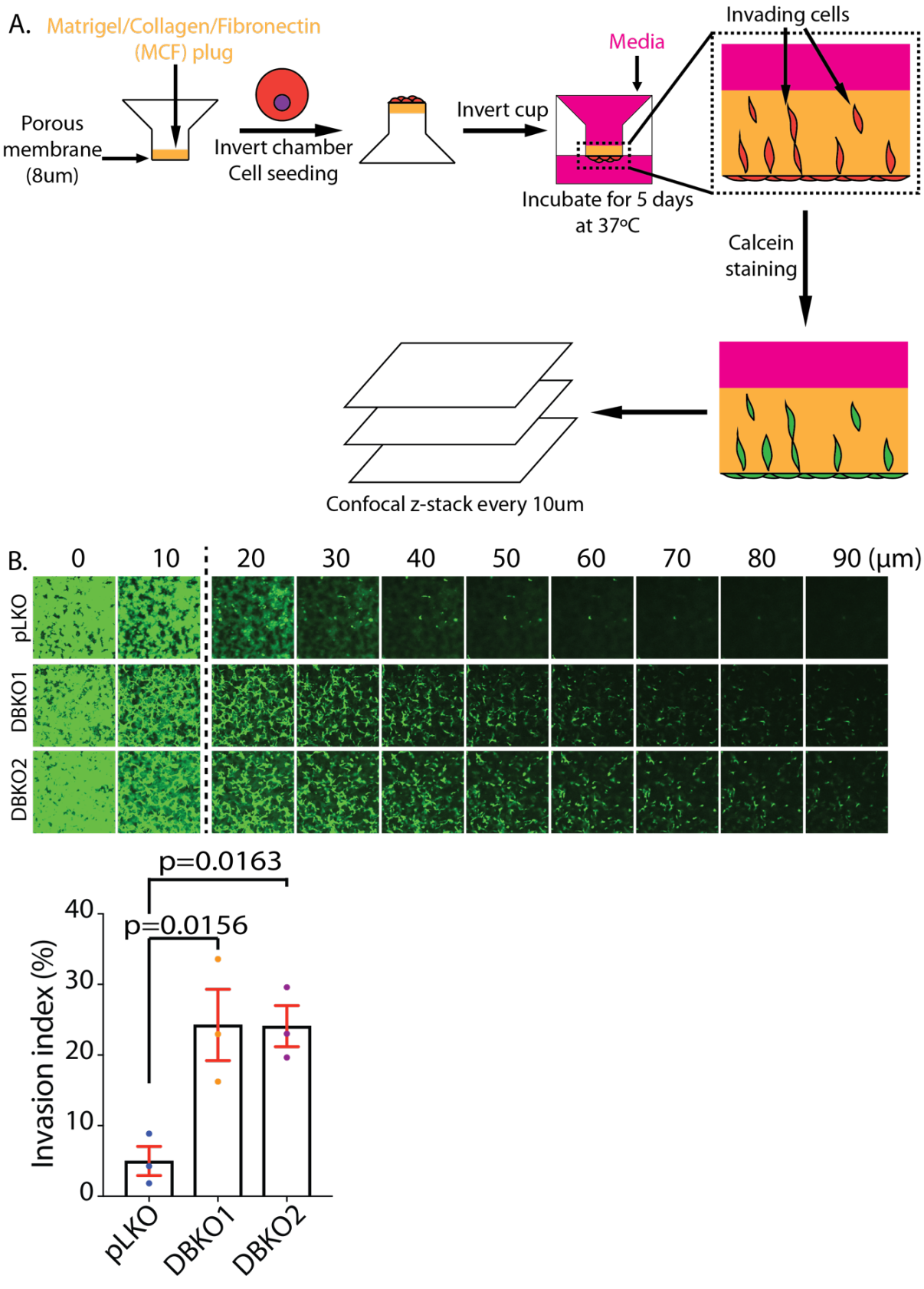

Figure 7.2 CYRI DBKO A-673 cells are significantly more invasive in an inverted invasion assay

A. Schematic representation of an inverted invasion assay. Matrigel, Collagen I and Fibronectin (MCF) were mixed to the final concentration of 4,4,1mg/ml respectively and pipetted into the well of the inverted chamber. The cells were then seeded on top of the membrane (8μm pore size) on the other side and let to settle. Full growth media were added at the bottom and the top chamber. If any treatment was used, the reagent was added to the top chamber. Cells were left in the incubator at 37°C for 5 days before stained with 1mg/ml Calcein AM. Confocal microscope with z-stack every 10μm was used to image the cells.

B. Inverted invasion assay shows the two independent CYRI DBKO cells 1 and 2 invaded deep into the MCF plug while the control pLKO did not. Quantification from 3 independent experiments. Mean ± SEM. ANOVA with multiple comparisons.

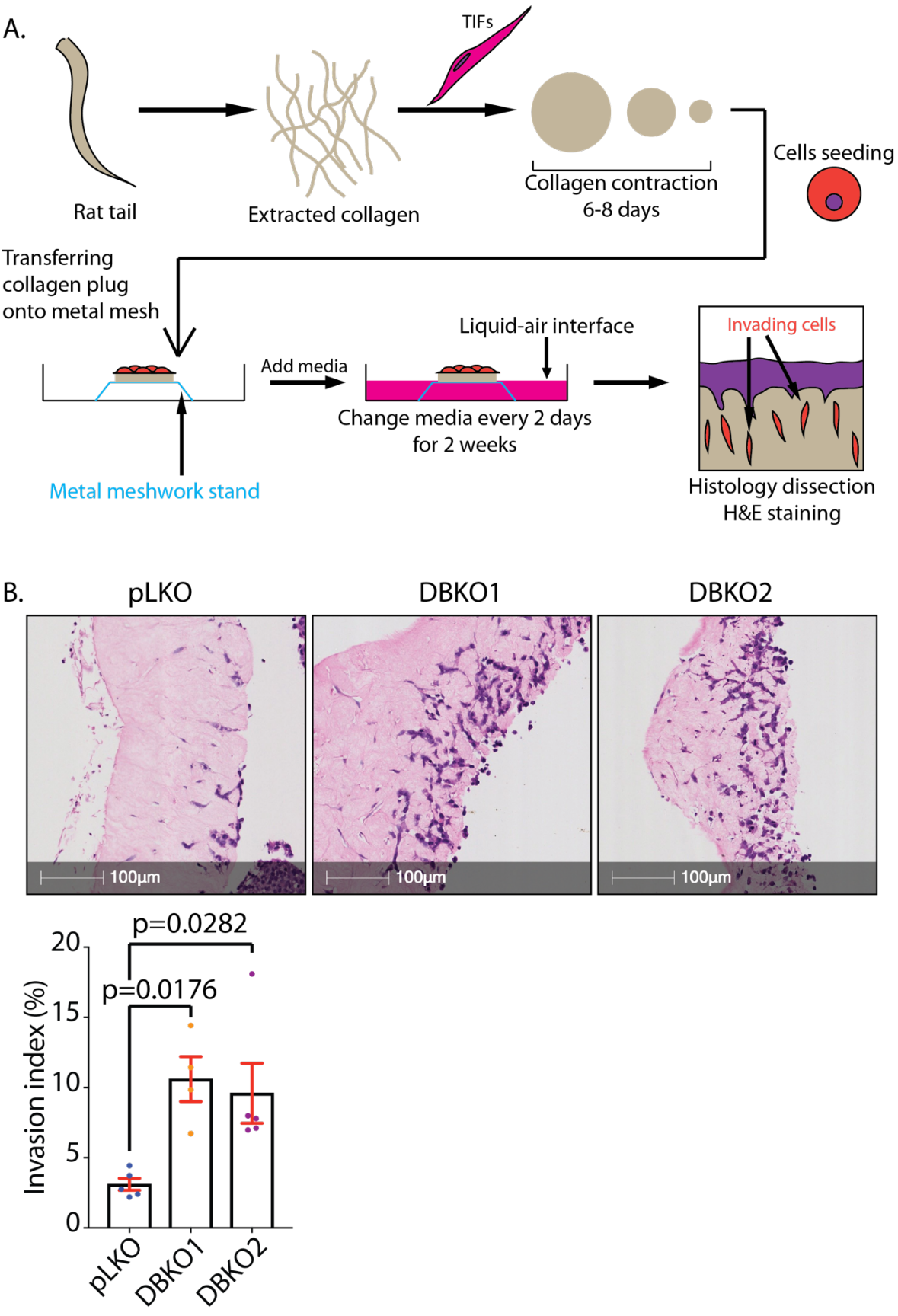

Figure 7.3 CYRI DBKO A-673 cells are invading significantly more than the control pLKO cells in an organotypic assay

A. Schematic representation of an organotypic assay. Collagen I was extracted from rat tails. Collagen plug was made by mixing telomerase-immortalised fibroblasts (TIFs) and allowed to contract under a slightly alkaline pH for 6 to 8 days until the plug was small enough to fit in a well of a 24-well plate. Cells were then seeded on top of the collagen plug and transferred to a metal mesh in a 6cm dish. Media was added and changed every 2 days so as to only touch the bottom of the collagen plug, forming a liquid-air interface. Cells were incubated at 37°C for 2 weeks before being collected for histology processing.

B. H&E staining of an organotypic assay showing the extensive invasion of 2 independent CYRI DBKO cell lines compared to the control pLKO. The invasion direction is from right to left. Quantification from 3 independent experiments. Mean ± SEM. ANOVA with multiple comparisons.

7.2.2 Integrin functions were important for cell migration and invasion in CYRI KO cells

CYRI deletion led to the upregulation of surface integrins as well as an increase in protrusion dynamics and invasion in 3D. We hypothesised that integrin signalling also played a part in contributing to the invasive phenotypes we observed. We first tested whether inhibiting integrin $\alpha5\beta1$ could affect the adhesion and spreading of the A-673 cells by using a specific blocking antibody IIA1. IIA1 has been shown to specifically bind and inhibit the heterodimeric $\alpha5\beta1$ integrins. Studies have shown IIA1 to be able to reduce cell adhesion in breast cancer cells *in vitro* (Nam et al., 2010) as well as reduce the number of metastasis and tumour volume in ovarian xenograft *in vivo* (Sawada et al., 2008,Schaffner, 2013 #184). We incubated 5μg/ml of either IgG or IIA1 antibody with the control pLKO cells or two CYRI DBKO cell lines in serum-free media on rotation at room temperature for 1h to allow efficient binding. Cells were then seeded on fibronectin-coated coverslips and allowed to spread for 4h before being fixed in 4% PFA. As visible in Figure 7.4A, while the control pLKO were largely polygonal with local membrane ruffles, the majority of the DBKO cells were seen adopting the C-shape with broad leading edge lamellipodia when treated with IgG. However, when being treated with the IIA1 antibody, all three cell lines dramatically decreased their spreading area by at least 2 times and their eccentricity by 20%. Control cells show severely impaired adhesions with most of the cells rounded in shape.

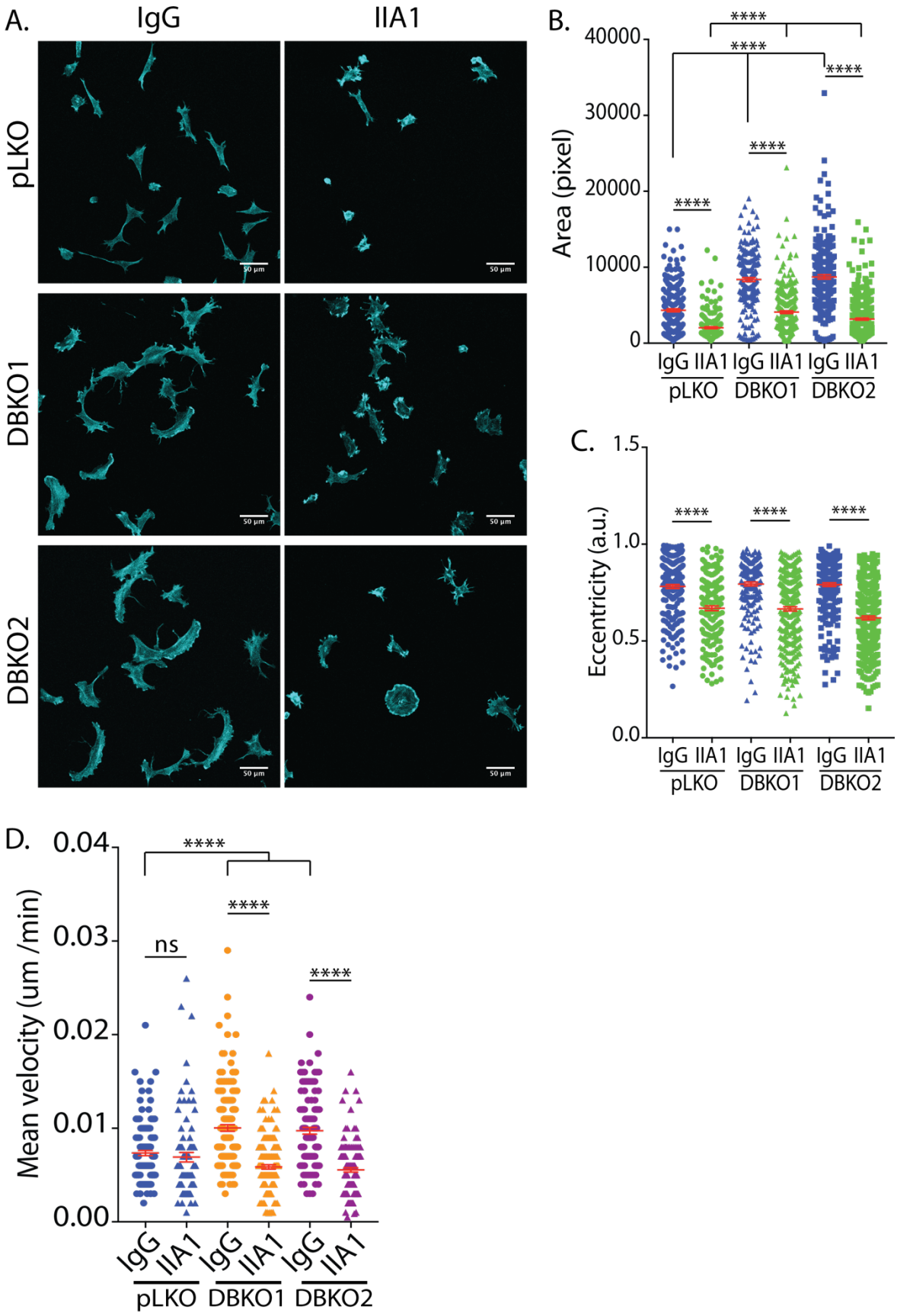

Figure 7.4 Integrin α5β1 is important for cell adhesion, spreading and migration

A. Blocking Integrin $\alpha5\beta1$ with blocking antibody IIA1 reduced cell adhesion and spreading on fibronectin matrix in both control and CYRI DBKO cells. Scale bar = 50μm

B, C. Graphs showed the dramatic drop in both the area (2-time drop) and eccentricity (20% drop) of the IIA1-treated cells. ANOVA with multiple comparisons.

D. Blocking Integrin $\alpha5\beta1$ with blocking antibody IIA1 reduced random migration of just CYRI DBKO cells but not the control pLKO. Unpaired 2-tailed t-test and ANOVA with multiple comparisons.

Data from 3 independent experiments. Mean ± SEM. ****p<0.0001, ns = p>0.05

The two DBKO cells were also struggling to spread but were still slightly larger than the treated pLKO. We then functionally validated the impact of $\alpha5\beta1$ inhibition on cell migration behaviour using a random migration assay. As before, cells were pre-treated with IgG or IIA1 for 1h before seeding on fibronectin-coated plate and image over time. As expected, the migration speed of both the DBKO cells was significantly halted to basal level (from 0.01μm/min to just 0.005μm/min after treatment), indistinguishable from the control pLKO. Interestingly, however, the IIA1-treated pLKO cells were not affected by this treatment suggesting that at the basal level, certain integrins were no longer the dominant factor in regulating cell migration. Overall, these data showed that integrin signalling was essential for cell adhesion and played an important role in the increased migration in CYRI DBKO cells. Inhibiting this signalling was enough to abrogate the enhanced phenotypes in DBKO cells.

Since $\alpha5\beta1$ inhibition affected CYRI-mediated adhesion and migration on 2D, we asked whether inhibiting the same signalling would affect its invasion in 3D. We performed again the inverted invasion assay, however, this time we included the blocking antibody in the media (Figure 7.5). The control pLKO cells showed no difference in terms of their invasion between the IgG and the IIA1 treatment. This was in line with our migration data (Figure 7.4B) showing inhibition of $\alpha5\beta1$ did not affect their migration. However, as expected, the invasion of both DBKO cells was dramatically inhibited by approximately 50%. Cells treated with IIA1 were noticeably round in shape suggesting their inability to successfully spread and adhere to matrix fibres. Expectedly, inhibiting just one integrin $\alpha5$ or $\beta1$ using specific inhibiting antibody P1D6 and P5D2, respectively

also affected the invasion of the DBKO cells (Figure 7.6). It is interesting to note that inhibition of β1 integrins seems to be more potent than α5 (60% reduction compared to 30 to 40% reduction, respectively), which could possibly be due to the β1 integrin being a part of a wider range of heterodimeric integrin complexes. None of these inhibition strategies further reduced the already poorly invasive control pLKO cells. Overall, we conclude that integrin α5β1 signalling is important for CYRI DBKO cells to adhere to the surrounding matrix, allowing them to become more invasive. Inhibition of single integrin α5 or β1 or specifically targeting the heterodimeric α5β1 was enough to ablate this phenotype.

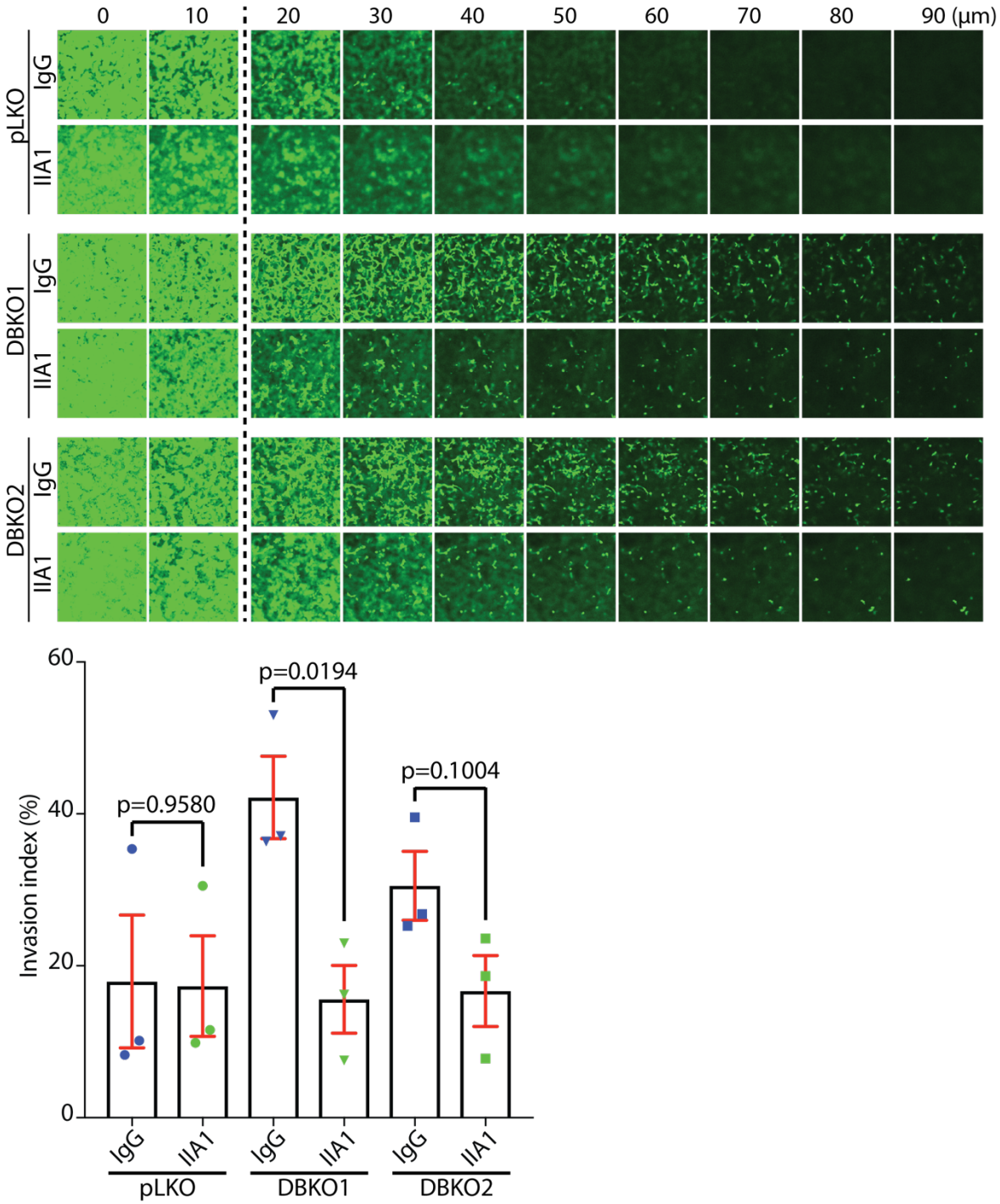

Figure 7.5 Blocking integrin α5β1 reduces 3D invasion of CYRI DBKO cells

The control pLKO and CYRI DBKO cells (DBKO1 and DBKO2) were seeded onto the MCF plug in the presence of either 5μg/ml IgG or IIA1 mixed in the growth media. Invasion index showed no difference between the IgG-treated vs the IIA1-treated group in the control pLKO cells, while there was a dramatic decrease (~50% to 60% reduction) in the invasion capacity of the DBKO cells. Data from 3 independent experiment. Mean ± SEM. Unpaired 2-tailed t-test.

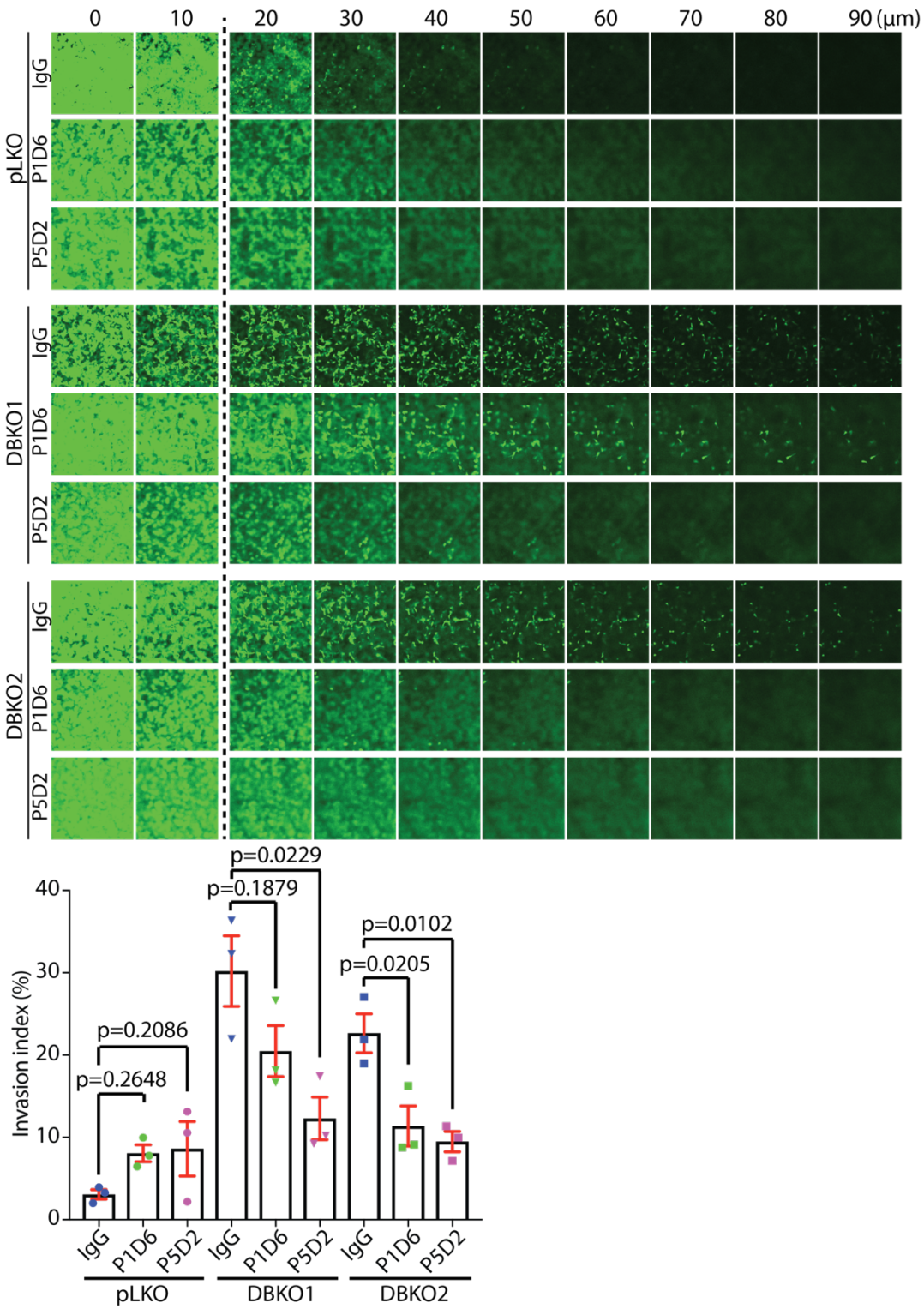

Figure 7.6 Individually inhibit integrin α5 or β1 also inhibits CYRI DBKO cell invasion

Individually inhibition of integrin α5 or β1 using specific inhibiting antibody P1D6 (30% to 40% reduction) and P5D2 (50% to 60% reduction), respectively reduced the invasion capacity of DBKO cells but not the control pLKO. Data from 3 independent experiment. Mean ± SEM. ANOVA with multiple comparisons.

7.2.3 Integrin signalling promotes growth under low-attachment conditions

Apart from mediating cell adhesion and invasion in cancer, evidence also suggested the involvement of integrin signalling in helping cancer cells resisting to anoikis – a type of programmed cell death occurred when adhesive cells are detached from the surrounding matrix (Guadamillas et al., 2011). It was proposed that the small GTPase protein RAB21 was involved in mediating the internalisation of the β1 integrin (Pellinen et al., 2006). These integrin-containing endosomes were found to have active FAK localisation (Alanko et al., 2015), which was thought to contribute to the anoikis resistant phenotype in MDA-MB-231 cells. Since CYRI DBKO cells have increased surface expression of integrin α5β1, we first questioned their behaviour under a low-attachment condition using an agarose low attachment assay. Agarose prevents cells from making adhesions due to the lack of appropriate substrate. The schematic representation of the workflow of the assay is shown in Figure 7.7A. It is important to note that due to the 3D nature of the assay, cell colonies were distributed both above and below the focal plane so only those that were in the same focal plane were included in final the analysis. As can be seen in Figure 7.7B, CYRI DBKO cells form significantly larger colonies (about 2 times) compared to the control pLKO. This effect, however, was abolished when cells were grown in serum-free media, suggesting that serum and other essential nutrients were needed. We hypothesised that due to the inability to form proper adhesion contacts with the agarose, cells were forced to internalise their integrins through various mechanisms. These internalised integrins could then activate focal adhesion kinase (FAK) on the endosomes, thus conveyed the anoikis resistance. CYRI DBKO cells with higher levels of integrin α5β1 thus became more resistant to anoikis. Nevertheless, direct visualisation of endosomal FAK is still needed to confirm the hypothesis.

To probe for the downstream effector activation of integrins, we performed an integrin activation assay. Control pLKO or two DBKO cell lines were incubated in serum-free media in suspension for 1h to shut down all integrin signalling. The cells were then either lysed immediately or being seeded on a fibronectin-coated 6-well plate for 30 or 60 min to activate integrins before being subjected to immunoblotting.

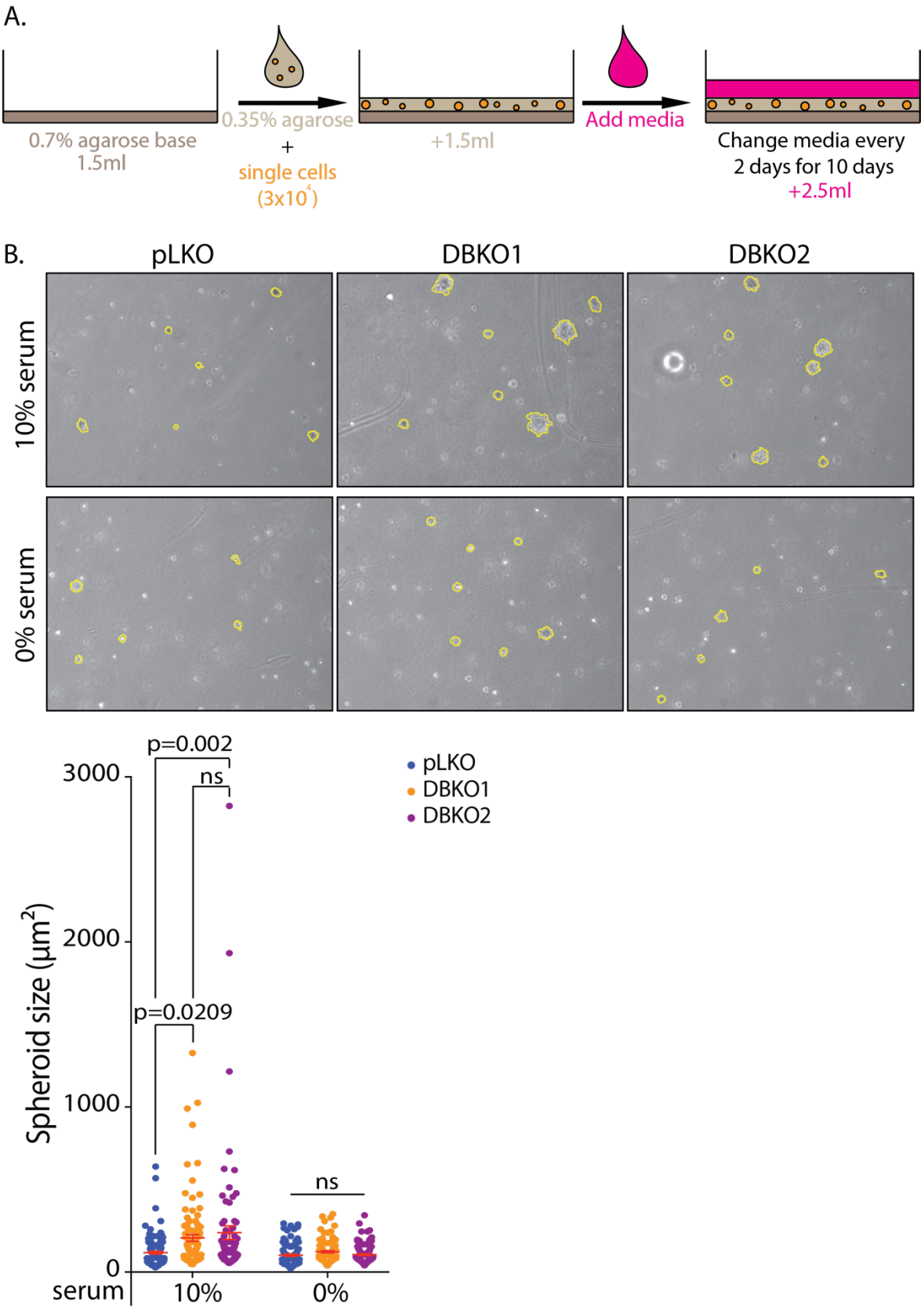

Figure 7.7 CYRI DBKO cells have a growth advantage in a low-attachment condition

A. Schematic representation of the agarose low-attachment assay. First, 1.5ml of the base is made using 0.7% agarose mixed with full serum media. Single-cell suspensions of $3x10^4$ cells were mixed with agarose to the final volume of 1.5ml at 0.35% and layered on top of the base. Once solidified, 2.5ml of full media were placed on top of the layers. The media are changed every 2 days for 10 days before images can be taken using a standard brightfield microscope.

B. CYRI DBKO cells form almost double-sized colonies than the control pLKO cells in the presence of 10% serum. However, this effect is gone when the serum is removed. Quantification from 3 independent experiments. Mean ± SEM. ANOVA with multiple comparisons. ns = $p>0.05$.

A typical signalling pathway from integrins is the recruitment and activation of FAK, which leads to the activation of PI3K and GRB2. PI3K phosphorylates and produces PIP3, which is then bound by Akt/PKB and subsequently activated by other proteins such as mTORC2. GRB2 on the other hand activates the RAS-RAF-MEK pathway, which ultimately leads to the activation of ERK1/2 (Shishido et al., 2014). When we performed our integrin activation assay comparing the control and the DBKO cells, all 3 cell lines were deprived of phosphor-FAK (pFAK) at 0 min time point. After 30 and 60 min of plating, however, we saw a small but consistent increase in the pFAK levels in both the DBKO cell lines compared to the control (about 20% increase) (Figure 7.8, top graph). Unfortunately, due to the fact that both the antibodies for phosphorylated and total FAK were from the same species, we had to blot these on two separate membranes, thus inherently introduced more variability into the quantification. Nevertheless, the effect was consistent between repeats. For phosphor-Akt (pAkt), no phosphorylation signal was detected at 0 min timepoint. However, no obvious differences were seen at the 30 and 60 min timepoint between the cell lines, suggesting that this signalling route was not altered upon CYRI deletion in A-673 cells (Figure 7.8, middle graph). Perhaps the most surprising observation came with ERK1/2. Even after 1h of incubation in suspension, phosphor-ERK1/2 (pERK1/2) was still present in all 3 cell lines suggesting a slower dephosphorylation rate in these cells. After 30 and 60 min of plating, there was a decrease in the level of pERK1/2 in the DBKO cells compared to the control pLKO, with the most significant in the latter timepoint (~30% decrease) (Figure 7.8, bottom graph).

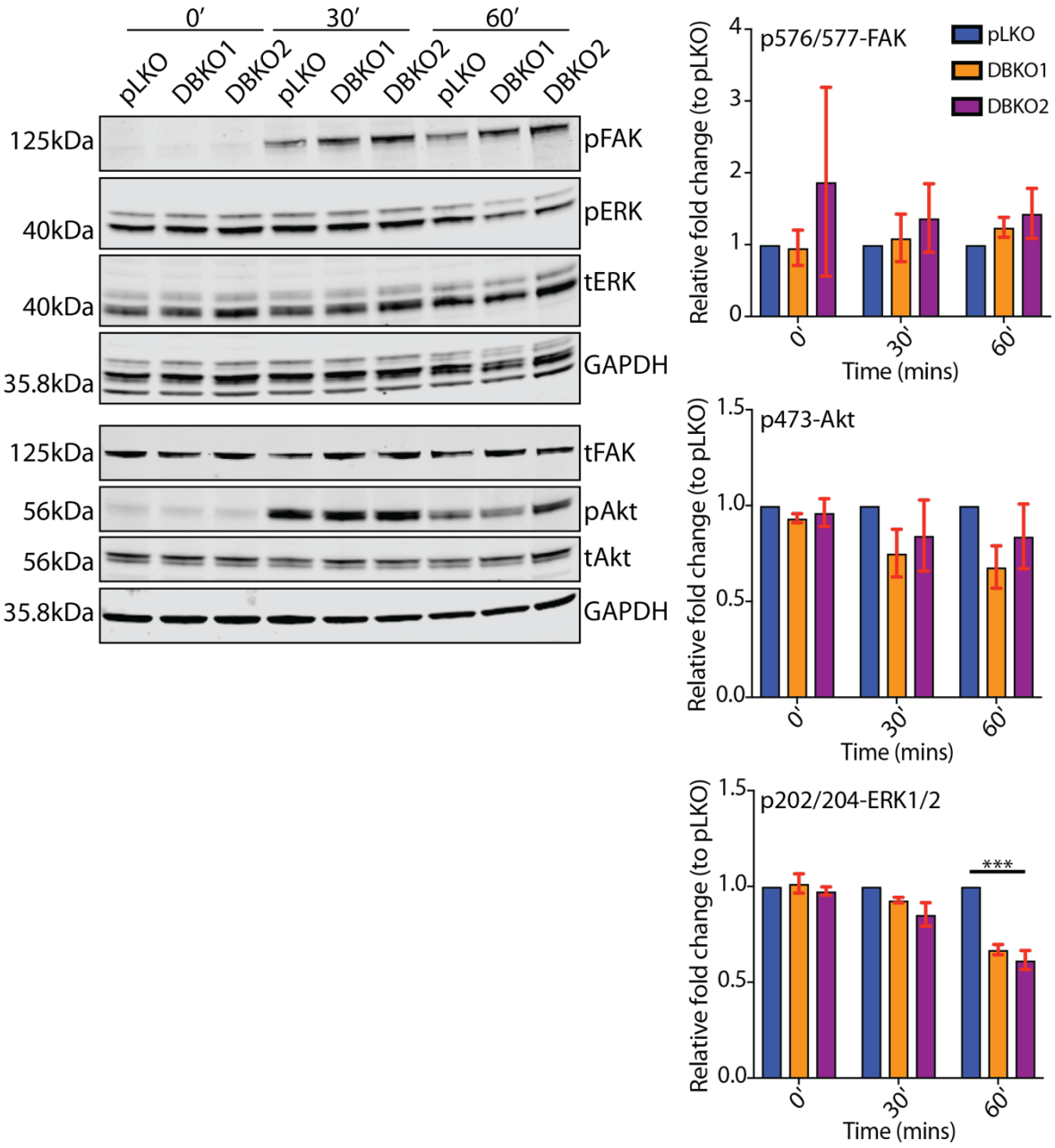

Figure 7.8 Integrin activation increases pFAK while decreases pERK1/2 level in CYRI DBKO cells

A representative western blot of pLKO, DBKO1, DBKO2 cells after 0, 30 and 60 min activation by fibronectin coating. The level of phosphorylated FAK (Tyr576/577) is slightly but consistently increased after 30 and 60 mins of plating. No apparent change in phosphorylated Akt (Ser473) but surprisingly a significant decrease in phosphorylated ERK1/2 (T202/Y204) after 60min of plating. p = phosphorylated, t = total.

Graphs plotted from 3 independent experiments with the band intensity normalised to that of the pLKO cells within each time point to show the relative difference between the pLKO and the DBKO cells. ANOVA with multiple comparisons. ***p<0.001

If FAK was indeed involved in promoting anoikis resistant phenotype in CYRI DBKO cells, then inhibiting it or its partner effector Src kinase should reduce the colony size (Beausejour et al., 2012, da Costa et al., 2018, Loza-Coll et al., 2005). We utilised the same set up as previously shown but adding either DMSO or 1μM FAK inhibitors (PF-562271 or PF-573228) or 200nM Dasatinib to the growth media every 2 days for 10 days. These pFAK inhibitors had been used to inhibit the signalling from the β1 integrin during stromal hyper-activation upon developing BRAF inhibitor resistance in melanoma (Hirata et al., 2015). In both cell lines, the addition of 1μM PF-inhibitors or 200nM Dasatinib significantly reduced the size of the colonies. However, we did notice that PF-inhibitors seemed to be less potent than Dasatinib, evident by PF-563228 failed to reduce the size of pLKO cells. Dasatinib, on the other hand, potently suppressed colony formation of both the control and the DBKO cell line, with a 50% decrease in DBKO1 cells to the same level as treated pLKO. This was perhaps because Dasatinib could inhibit both FAK and Src kinase (Caccia et al., 2010). These data strongly suggest the role of the Integrin-FAK-Src axis in promoting anoikis resistance in CYRI DBKO cells.

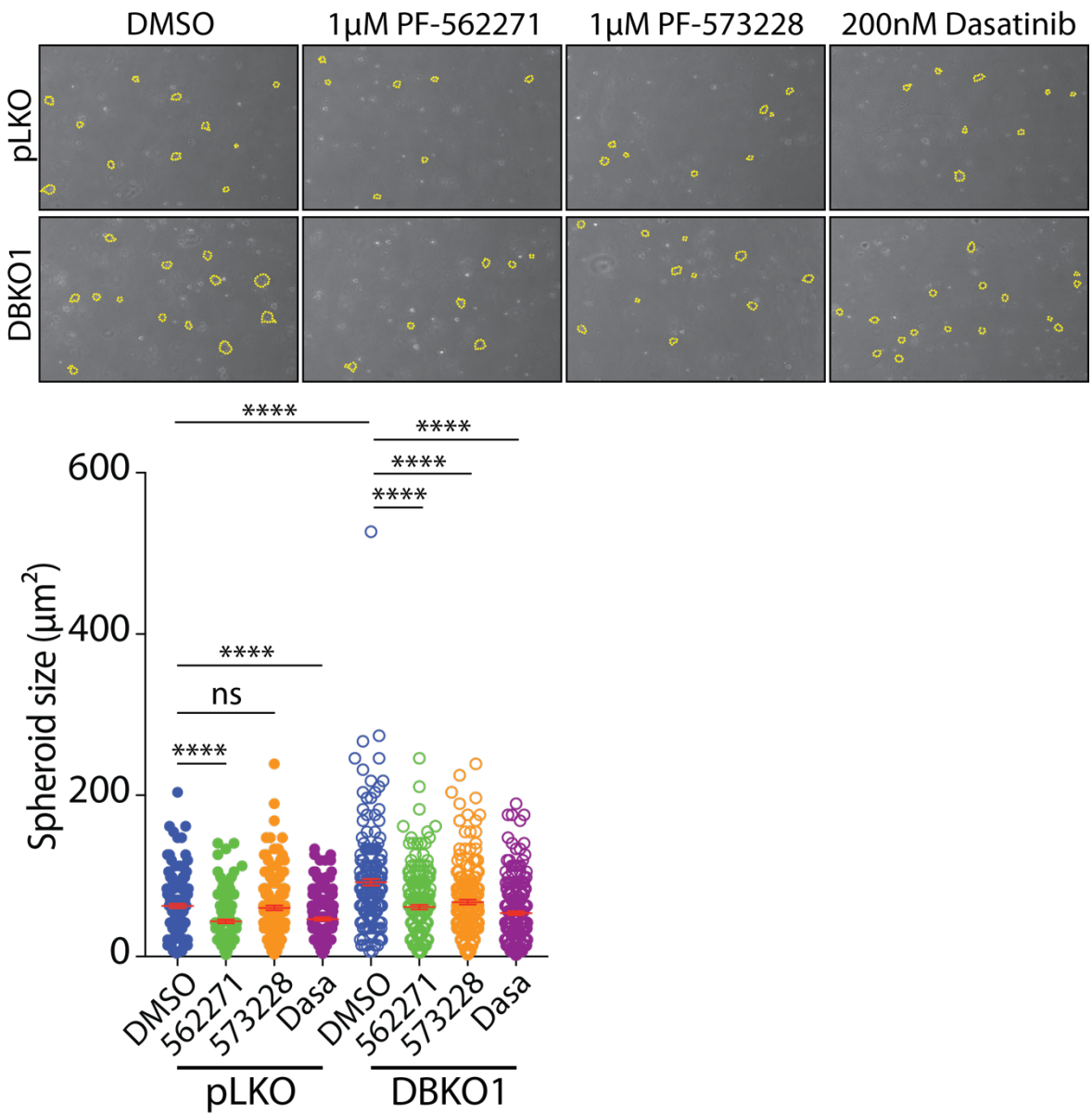

Figure 7.9 Inhibiting FAK-Src kinase signalling suppresses colony formation in agarose

Agarose low-attachment assay of the control pLKO and CYRI DBKO1 cells in the presence of FAK inhibitors (PF-562271 and PF-573228) and Src inhibitor (Dasatinib or Dasa). DBKO1 formed larger colonies than pLKO. FAK and Src inhibitors successfully reduced the colony size of DBKO1 cells to basal level (40% decrease). The scattered plot represents data from 3 independent experiments. Mean ± SEM. ANOVA with multiple comparisons was used between each group. Unpaired 2-tailed t-test was used to compare between DMSO pLKO and DMSO DBKO1. ns = $p>0.05$, ****$p<0.0001$.

7.3 Discussion

Overall, through the use of several physiologically relevant 3D invasion models, we show that CYRI DBKO cells are indeed more invasive than the control pLKO. Upon deletion of CYRIs, cells become more active in 3D with the formation of many FLPs, which have been repeatedly shown to be important for the invasive migratory behaviour of cancer cells. Through the use of the inverted invasion assay as well as organotypic assay, we clearly demonstrated the highly invasive nature of CYRI DBKO cells compared to the control. The role of CYRIs in cancer has not been explored due to the novel nature of these proteins. However, both CYRI-A and CYRI-B are altered in a plethora of different cancers (Chapter 1). A recent study looking at pancreatic cancer suggests the role of CYRI-B in regulating mitochondrial dynamic and ROS production (Chattaragada et al., 2018). Depletion of CYRI-B in PDAC cells leads to the fission of mitochondria and increased cell migration and invasion. This suggests that CYRIs might potentially have a role in tumour progression.

Here we provided an additional mechanism explaining for the invasive phenotype by exploring the new function of CYRIs in the endocytic trafficking. We proposed that CYRIs regulate the internalisation of integrins, here as $\alpha5\beta1$ in A-673 cells. Upon deletion of CYRIs, more active integrins were retained on the surface and this allowed the cells to adhere better to the surrounding matrix, remodel it and promote its own invasion. Inhibiting these surface integrins using blocking antibodies significantly suppressed the spreading and invasion. This raised an interesting point about the connection between RAC1 and integrins signalling. In the DBKO cells, the level of active RAC1 was presumably increased leading to an increase in the spreading area. However, inhibiting integrins function almost completely abrogated this phenotype suggesting that this signalling played a significant role and upstream of RAC1. Without this signalling input, CYRI deleted cells, despite their higher RAC1 level, were not able to obtain the characteristic C-shape phenotypes described in previous reports (Fort et al., 2018). Nevertheless, the relationship between integrins and RAC1 is complicated and it is possible that the two acts independently from one another. A way to examine this would be to treat cells with either a RAC1 inhibitor, an integrin

inhibitor or both. If the inhibition effect is non-additive, it would suggest that both signals belong to the same pathway and vice versa. It would also be interesting to probe deeper into how these cells modulate their surrounding matrix. Second-harmonic generation microscopy would allow us to see the changes in the matrix. Atomic force microscopy could be used to probe the physical force exerted by the cells onto their surroundings. We could also utilise an assay called Matrigel-on-top (Lee et al., 2007) to have a closer look at the cellular morphology and distribution of integrins in 3D and how they interact with the surrounding fibres.

These extra integrins also provided the necessary activation to FAK and Src to prevent cells from undergoing anoikis. Inhibiting these upstream signals strongly reduced the growth of colonies under low attachment conditions. It was indeed a surprise that both Akt and ERK1/2 pathway was not reacting the way we would anticipate. We would predict that a sustained or elevated ERK1/2 signalling might have been responsible for the higher ability to proliferate in the agarose assay in the DBKO cells. However, a recent publication using gliotoxin, a molecule extracted from the fungus *Aspergillus fumigatus* showed that cells treated with this toxin undergo anoikis (Haun et al., 2018). Gliotoxin targeted integrins, which inhibited FAK activation and subsequently the phosphorylation of p190RhoGAP. This allowed RHOA to be activated and led to the phosphorylation and activation of the pro-apoptotic protein Bim, which initiated anoikis. This process is independent of the classical Akt and ERK1/2 pathway and thus leads us to hypothesise that perhaps our CYRI DBKO cells have downregulated this Bim-dependent anoikis pathway to form larger colonies. If this pathway was indeed responsible, then a simple western blot should show a decrease in the phosphorylated level of Bim in the DBKO cells. Alternatively, inhibiting Bim phosphorylation in the pLKO cells should increase their capacity to form colonies. Unfortunately, due to the circumstance, we were not able to test this hypothesis and so it is left open for now. In the next chapter, we will briefly explore an emergent property of CYRI DBKO cells to secrete matrix proteins and metalloproteases and how this could also assist the invasive capacity of these cells.

8 RNA sequencing analysis reveals changes in CYRI deleted cells that can contribute to cancer invasion

8.1 Introduction

So far, we have provided the evidence for the important functions of CYRIs in regulating many cellular activities including cell spreading, cell migration, integrin trafficking and cancer invasion. Since RAC1 being a direct target of CYRIs, and its function can affect many processes inside cells including gene expression, we suspect that deletion of CYRIs would have a broad impact on the cells. To gain better insights into the effects of CYRI deletion, we thus performed an RNA sequencing analysis comparing the gene expression profile between the control pLKO and two independent CYRI DBKO cell lines DBKO1 and DBKO2. We validated several hits using western blotting, invadopodia assay and zymography and revealed that CYRI DBKO cells have an altered secretome with secreted proteins that can promote invasive phenotypes in a 3D inverted invasion assay.

8.2 Results

8.2.1 RNA sequencing reveals substantial gene expression alterations between the control and CYRI DBKO cells

RAC1 plays an essential role in regulating many cellular processes, from actin cytoskeleton reorganisation to the expression of many genes (Westwick et al., 1997, Shi et al., 2016). We decided to sequence the RNA of our CRISPR A-673 cells to gain insights into what pathways might have been altered upon CYRI deletion. To check for the reproducibility between replicates based on the raw gene expression files, we performed the Principal Component Analysis (PCA) (Figure 8.1). The first two principal components (PCs) explained the majority of the variation within the dataset (94%), with PC1 took up 91% and PC2 took up 3%. This means the control pLKO and the DBKO groups are very distinct from each other, and this explains 91% of the variation in the system. While the difference between each replicate for each cell type is only minor and made up of 3% of the variation. This suggested that our CRISPR-Cas9 systems, in particular, our single-

guide RNAs used to generate these two cell lines were specifically targeting the CYRI genes thus their changes were consistent with one another.

8.2.1.1 The upregulated genes upon CYRI deletion

Analysing the data revealed 3586 genes that were significantly changed between pLKO and DBKO1 and 3888 genes that were significantly changed between pLKO and DBKO2 (the p-value cut off is 0.05). Gene ontology enrichment analysis was used to group the different genes into categories of up- and down-regulated pathways upon CYRIs deletion. Interestingly, among the pathways that upregulated were those involved in adhesion, matrix remodelling and GTPase regulation (Figure 8.2). Among the cell adhesion category, many integrins were significantly upregulated at least 2 folds compared to the control. Among these were integrin α3, which involved in laminin binding and had been suggested to be a marker for EMT in breast cancer (Shirakihara et al., 2013) and β5, which involved in binding to osteopontin or vitronectin and was important for the tumorigenicity in breast cancer (Bianchi-Smiraglia et al., 2013). Importantly, the mRNA level of integrin α5 and β1 were not observed to be changed between the control pLKO and the DBKO cells, reconfirming our qPCR data (Figure 6.5B) and our hypothesis on the alteration of trafficking of these integrins rather than changing in their gene expression level.

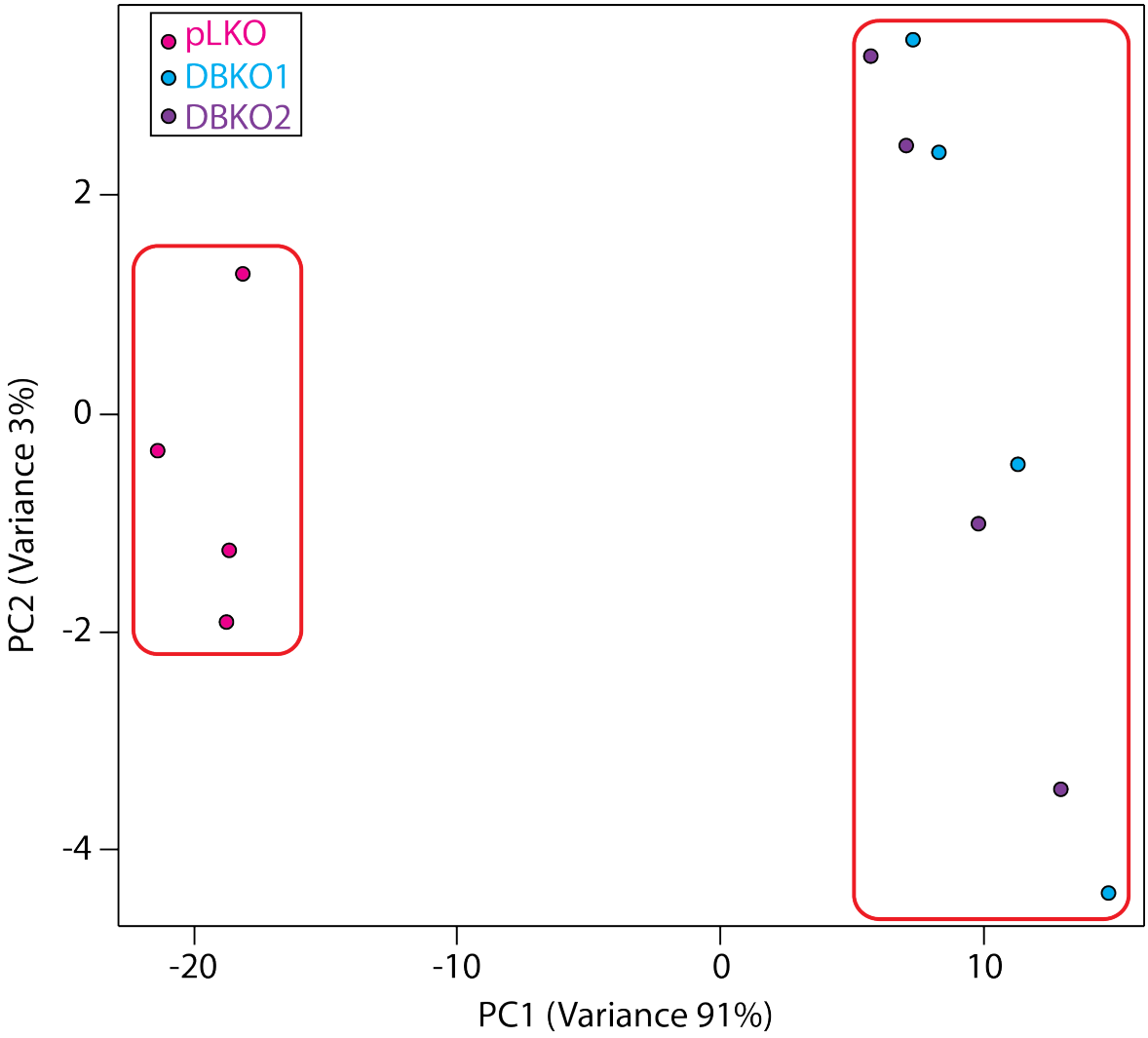

Figure 8.1 Principal Component Analysis (PCA) plot of three tested cell lines with 4 biological replicates each

The 4 replicates of the control pLKO cell line (magenta) are clustered together (red boxes) and separated from the replicates of the DBKO cell lines. 4 replicates of DBKO1 (cyan) are in the same cluster with 4 replicates of DBKO2 (purple) suggesting these two cell lines are indeed similarly comparable to one another. PC1 is responsible for 91% of the variation while PC2 is only responsible for 3%. Together, PC1 and PC2 can explain for 94% of the total variation in the dataset.

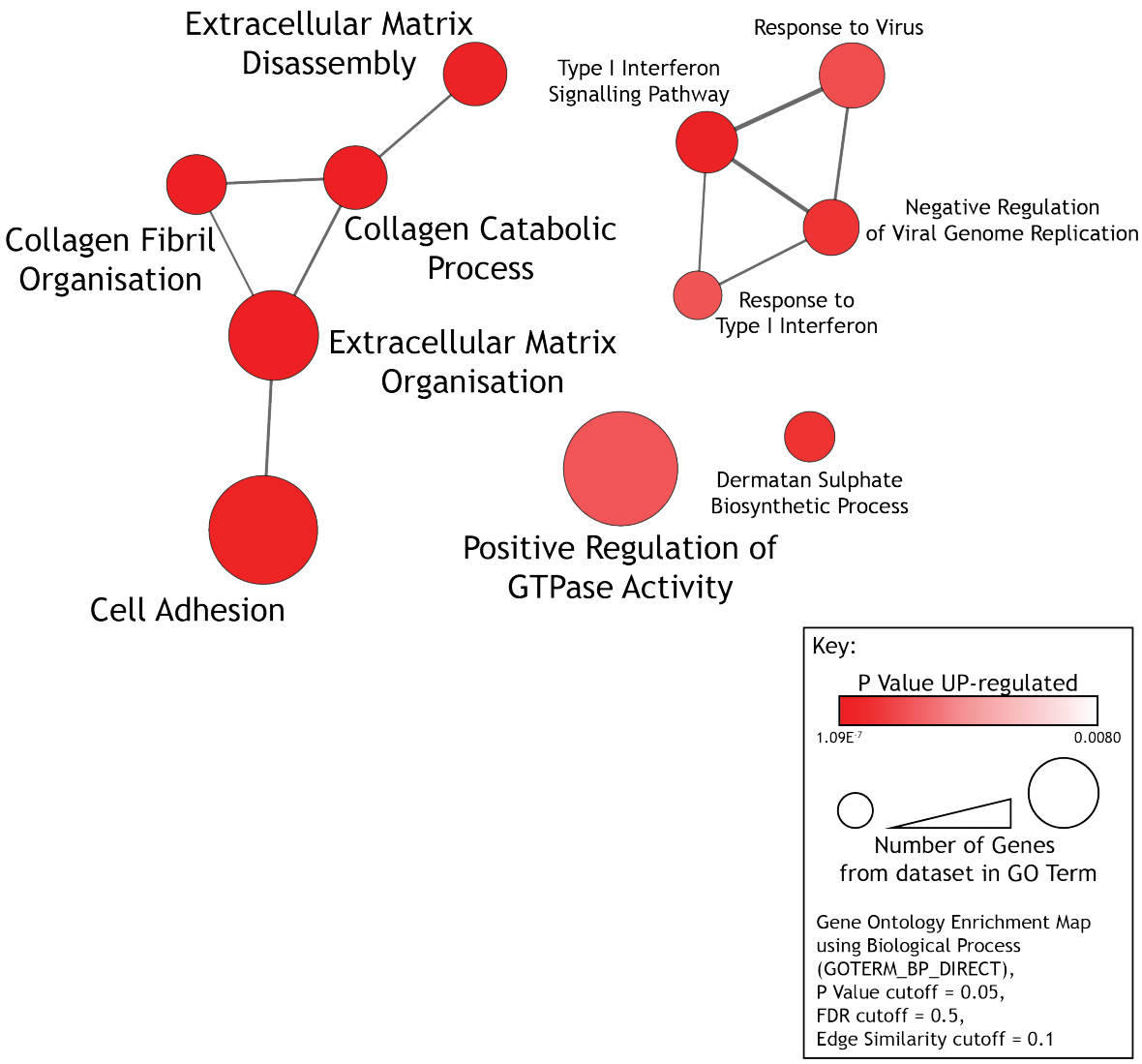

Figure 8.2 Gene ontology enrichment analysis of up-regulated pathways

The most significantly upregulated groups are those involved in cell adhesion, extracellular matrix remodelling, GTPase regulation and viral-related processes. Black lines represent the functional connection between groups.

Another interesting group of upregulated genes were those involved in extracellular matrix remodelling such as collagen and matrix metalloproteases. One of the top upregulated collagen genes in both DBKO cell lines was collagen VI. Numerous recent evidence has been pointing towards the pro-tumorigenic function of this special type of collagen (Chen et al., 2013). COL6A1 was suggested to correlate with poor prognosis in pancreatic (Owusu-Ansah et al., 2019), renal cell carcinoma (Wan et al., 2015) and cervical cancer (Hou et al., 2016). Secreted collagen VI from adipocytes could enhance cancer cell survival and growth through interacting with NG2/chondroitin sulfate proteoglycan receptor expressed on the surface of cancer cells (Iyengar et al., 2005). Recent evidence also showed a direct effect of collagen VI on increasing cancer cell migration and invasion in breast cancer (Wishart et al., 2020). We validated the elevated Col6a1 in our cells at the protein level using western blotting. Cells were grown overnight at the same density in serum-free media to allow for the detection of any secreted protein. The conditioned media were collected and concentrated down to 500μl. At the same time, cells were lysed for detection of intracellular collagen. As can be seen (Figure 8.3), both DBKO lines contained and secreted an almost double the amount of collagen VI compared to the control pLKO. Despite the evidence for the pro-tumorigenicity of this type of collagen in many different cancers, the direct functions of collagen VI in CYRI DBKO cells are still to be elucidated.

Matrix metalloproteases were also among the most upregulated genes in CYRI DBKO cells. Perhaps it came to no surprise that these proteases are highly upregulated in many cancers due to its involvement in invasion and metastasis. These proteases could be secreted (MMP2, MMP9) or directly delivered to the invasive front (MMP14) to allow the cancer cells move through the dense matrix fibres (Yu et al., 2012, Xu et al., 2005). MMP14 was also recently shown to mechanically direct the formation of invadopodia independently of its protease activity to help breast cancer cells invade (Ferrari et al., 2019). Along with this, N-cadherin and EGFR, which are markers for EMT (Mrozik et al., 2018, Hazan et al., 2000) were also strongly increased. We again validated these using western blotting (Figure 8.4).

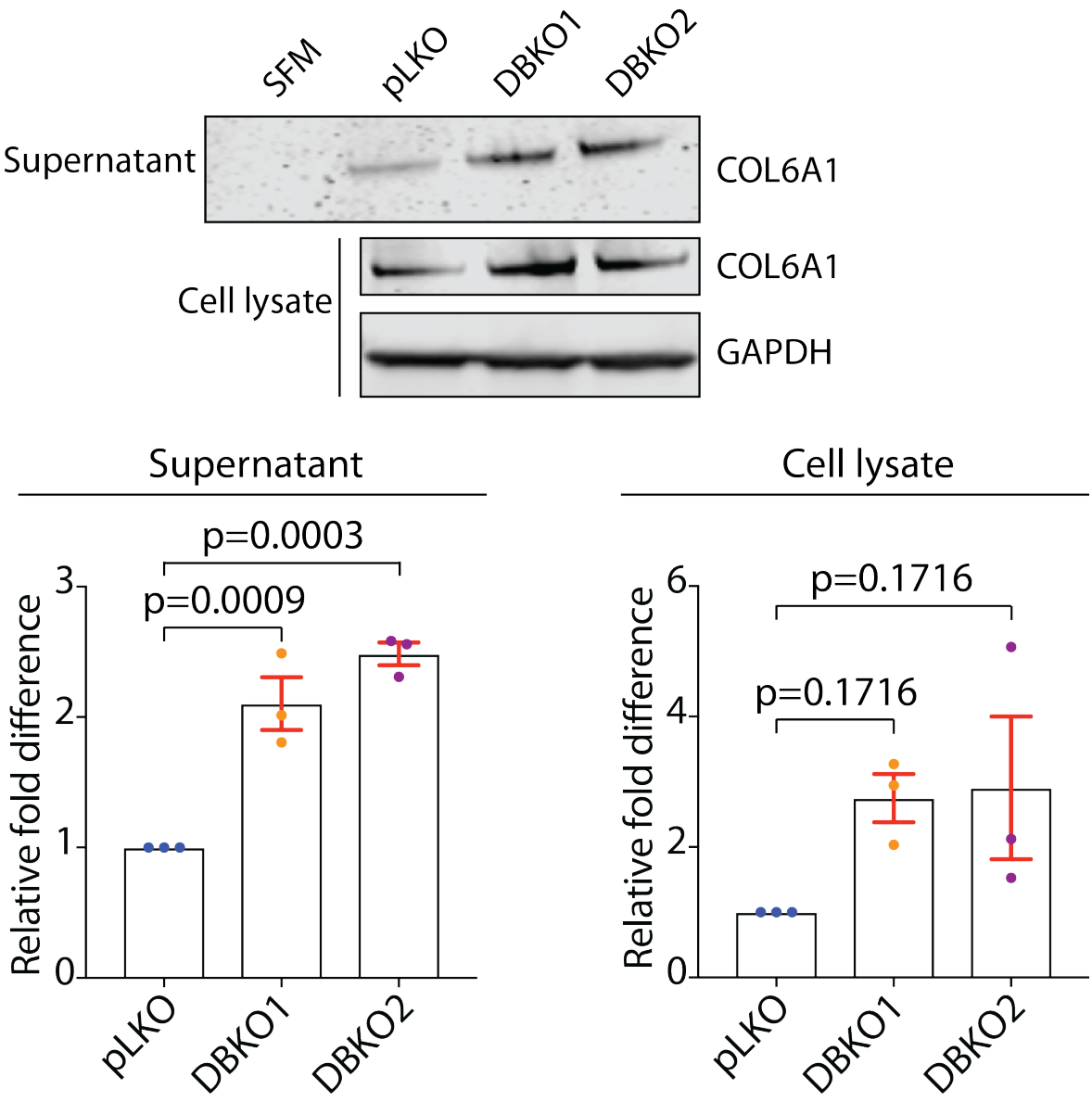

Figure 8.3 CYRI DBKO cells express and secrete higher level of Collagen VI compared to control pLKO

Conditioned media were collected and concentrated and subjected to western blotting for COL6A1. The same cells were lysed to blot for intracellular COL6A1. In both cases, CYRI DBKO cells produced at least 2x more collagen VI compared to the control pLKO. Data from 3 independent experiments. Mean ± SEM. ANOVA with multiple comparisons. SFM = serum-free media.

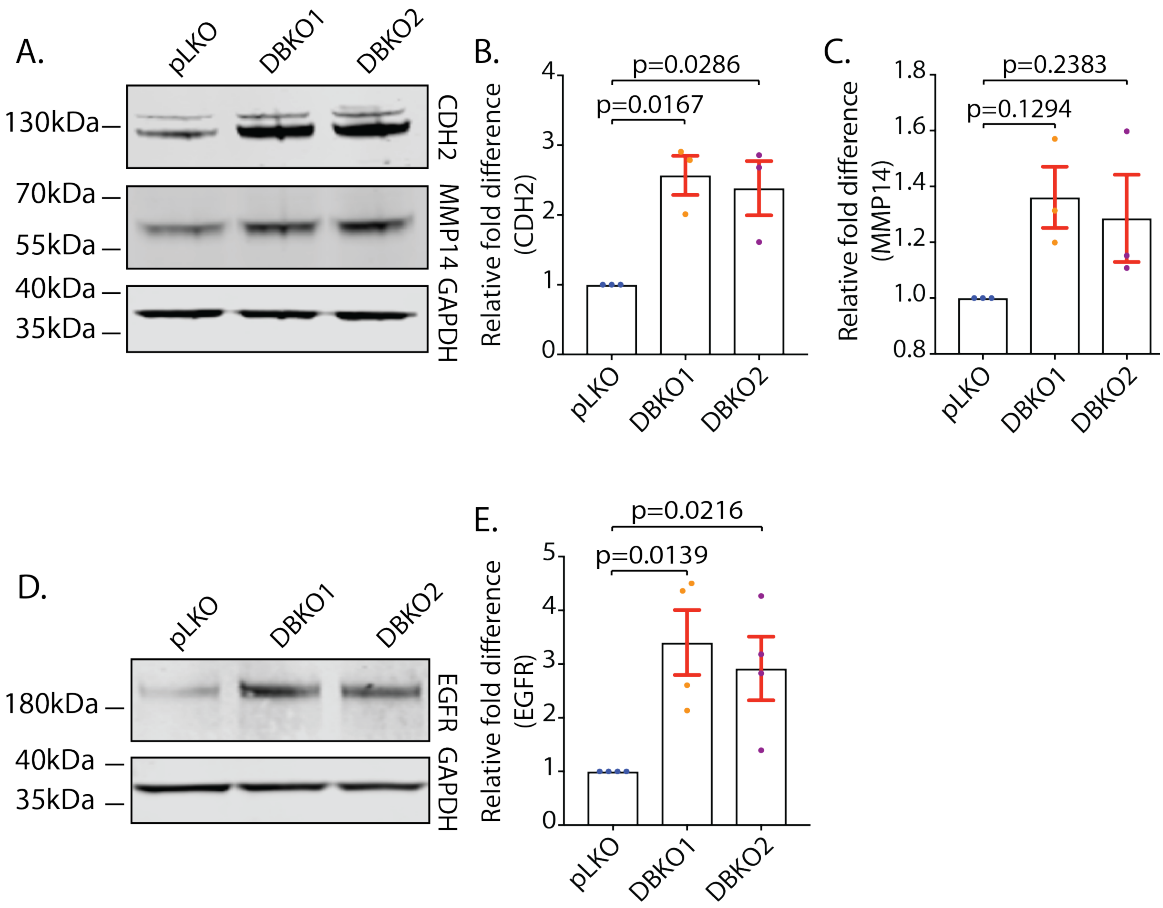

Figure 8.4 N-Cadherin, MMP14 and EGFR are also among the upregulated genes in CYRI DBKO cells

Western blot showing the increased levels of A-C) N-Cadherin, MMP14 and D, E) EGFR. Quantification from at least 3 independent experiments. Mean ± SEM. ANOVA with multiple comparisons.

For the secreted protease MMP2, we performed zymography along with western blotting to detect whether CYRI DBKO cells also expressed and secreted these proteins as predicted (Figure 8.5). Indeed, both the secretion level as well as the degradative activity of MMP2 were significantly higher in CYRI DBKO cells compared to the control pLKO.

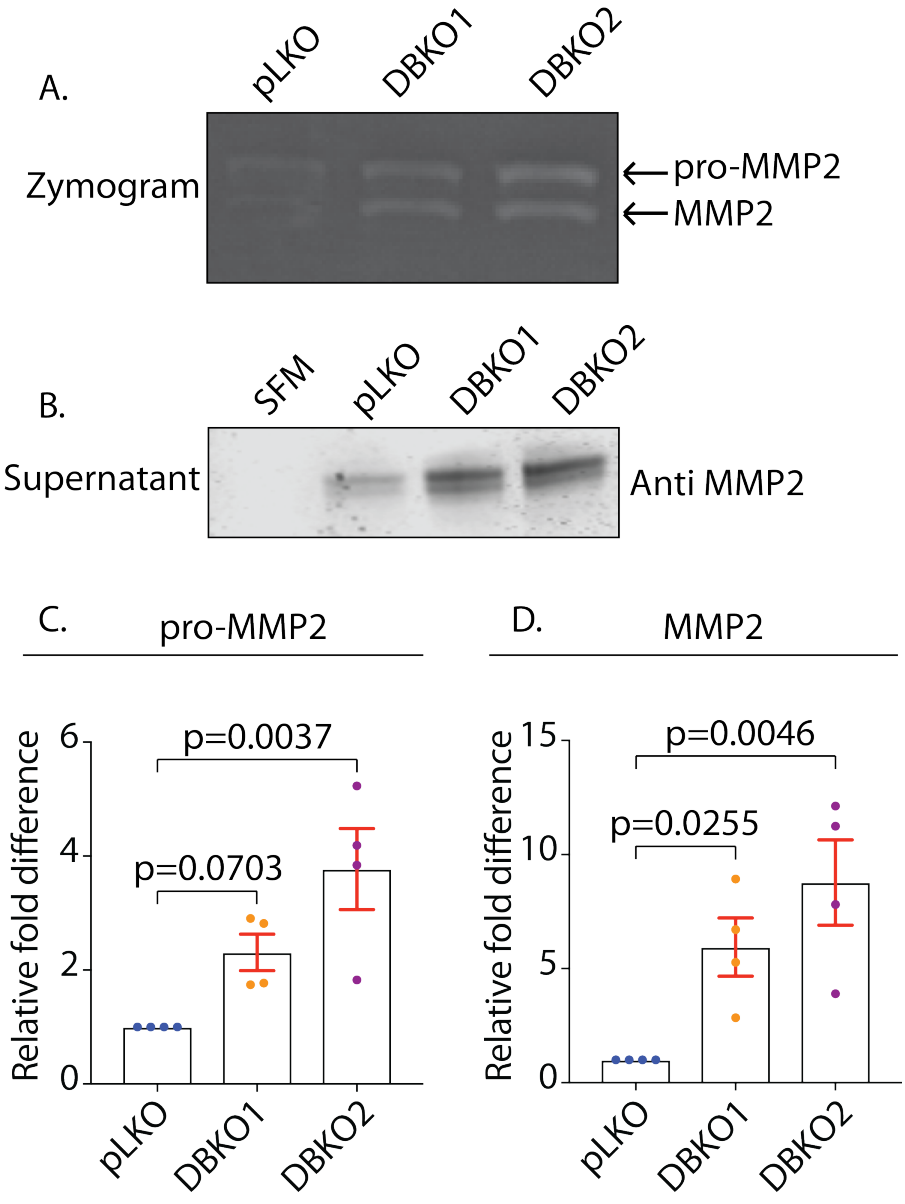

Figure 8.5 Zymography and western blotting show the increased secretion and expression of MMP2 in DBKO cells compared to the control pLKO

Part of the conditioned media was subjected to concentration and A) zymography to detect protease activity, and the other part is subjected to B) western blotting to detect the level of secretion. In both cases, more MMP2 was secreted from the DBKO cells and these ultimately degraded more. C, D) Quantification of zymography showed the consistent increase of the degradation level exerted by both pro- and matured MMP2 on the gel. Data from 4 independent experiments. Mean ± SEM. ANOVA with multiple comparisons. SFM = serum-free media.

Overall, many of these upregulated genes have been extensively documented in the metastatic cascade of cancer, from being parts of the EMT process to directly contributing to remodelling the surrounding environment. These observations strongly support the invasive phenotypes of CYRI DBKO cells we have described in earlier chapters. Whether any of these changes could contribute to the invasion of CYRI DBKO cells will be addressed in the next section.

8.2.1.2 The down-regulated genes upon CYRI deletion

Along with many upregulated genes, RNA sequencing also revealed many genes that were downregulated upon CYRIs deletion. Many of these downregulated pathways include transcription regulation, cellular proliferation and apoptotic processes (Figure 8.6). Many of the common proliferation markers such as BUB1, PLK1, CCNB1 or MKI67 (Whitfield et al., 2006) were dramatically downregulated upon CYRI deletion. This was interesting because it again agrees with our previous observation that DBKO cells proliferate slower than control pLKO cells on 2D fibronectin-coated surface (Chapter 4). Due to the interest of time, we did not validate any of the gene candidates yet, but they are potentially interesting to explore in future experiments. Overall, on one hand, the RNA sequencing data were strongly in support of many of our previous experimental observations. On the other hand, it has opened up many more interesting questions and potentially also provided many explanations to the phenotypes we observed. In the next section, we will explore an additional mechanism that assists in the invasion of the CYRI DBKO cells.

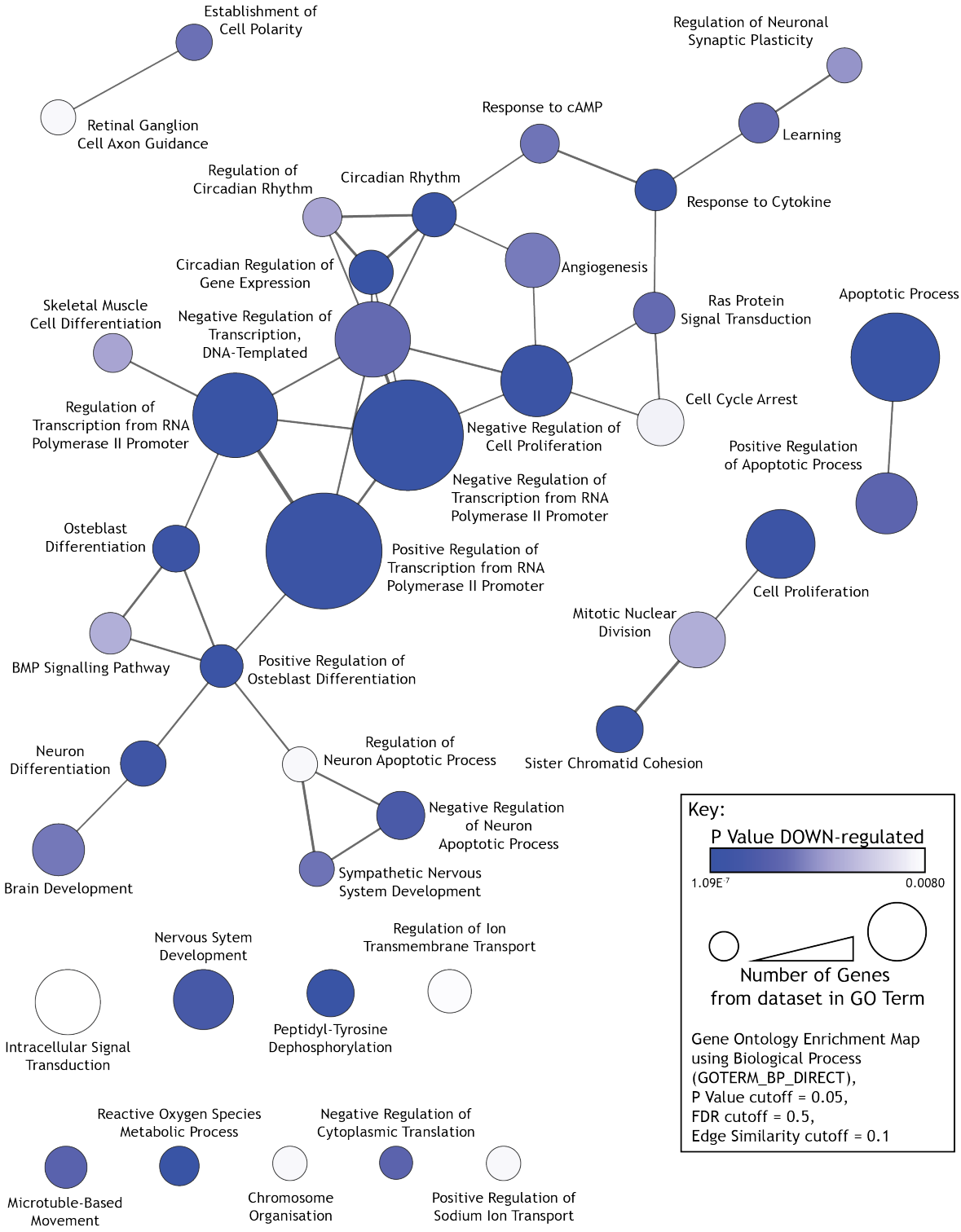

Figure 8.6 Gene ontology enrichment analysis of down-regulated pathways

Many different pathways were down-regulated upon CYRIs deletion. Among these are pathways involved in transcription regulation, cell proliferation, cell polarity, neuron-related pathways and apoptosis. Black lines represent the functional connection between groups.

8.2.2 CYRI DBKO cells invasion is dependent on matrix metalloproteases

RNA sequencing data along with western blotting and zymography all pointed towards the increased expression and secretion of matrix metalloproteases in CYRI DBKO cells. This prompted us to test for the direct connection between this phenotype and the invasive capacity of the DBKO cells. We first asked whether the increased expression of MMPs would affect the matrix degradation ability of these cells by using an invadopodia assay (Figure 8.7). We pre-treated the cells with the pan-MMP inhibitor GM6001 because CYRI DBKO cells adhere much quicker to the matrix than the control pLKO as shown in chapter 6 and therefore blocking their initial MMP activity to synchronise the cells would make it more valid to compare the true degradation capacity between these cell lines. While CYRI DBKO cells form numerous successful degradative invadopodia marked by phalloidin with more degradative spots, the control pLKO cells had fewer of these structures (Figure 8.8, upper panel). Normalising the area of degradation to the number of cells visible within each field of view clearly showed that the DBKO cells could degrade the matrix at least 3 times more effective than the control pLKO (Figure 8.8, graph).

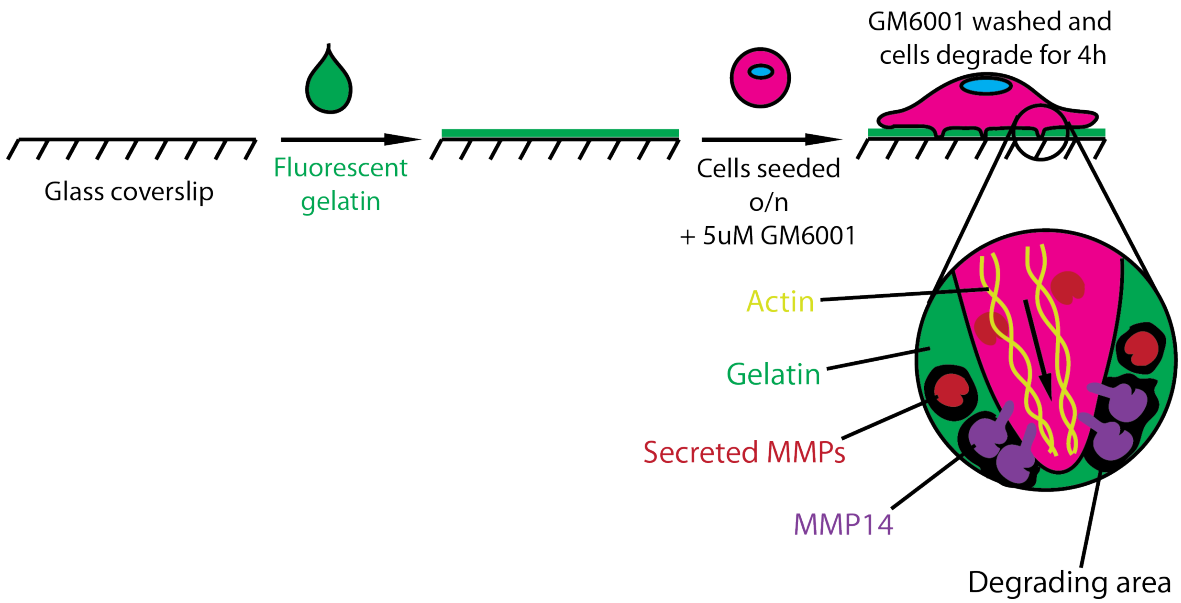

Figure 8.7 Schematic representation of the invadopodia assay

Acid-treated glass coverslips were coated with 1mg/ml fluorescently labelled gelatin. Cells were seeded on top of the coverslips along with 5μM GM6001 overnight. The next day, GM6001 was washed away with PBS and cells were allowed to degrade for 4h before fixing with 4% PFA. The degradative capacity is contributed largely by the cell's membrane-bound and secreted MMPs that were delivered to the invadopodia.

Since matrix degradation is strongly associated with cancer cell invasion, and that CYRI DBKO cells were shown repeatedly to be much more invasive, we wondered whether inhibiting matrix degradation by GM6001 would be enough to inhibit their invasion. We utilised our inverted invasion assay and treated the DBKO cells either with DMSO or GM6001 (Figure 8.9). Blocking the degradative ability of MMPs did indeed significantly reduce the invasion ability of these cells. Quantifying the invasion index showing a 2x reduction in the number of cells invaded beyond 10μm (from 40% to 20%) in the treated conditions in both DBKO cell lines. This indeed strongly suggested that matrix degradation by MMPs, presumably the secreted MMP2 and the membrane-bound MMP14, was important for CYRI DBKO cell matrix invasion. Overall, apart from matrix adhesion that we discussed in previous chapters, matrix degradation also played a significant role in regulating CYRI DBKO invasion and potentially metastasis.

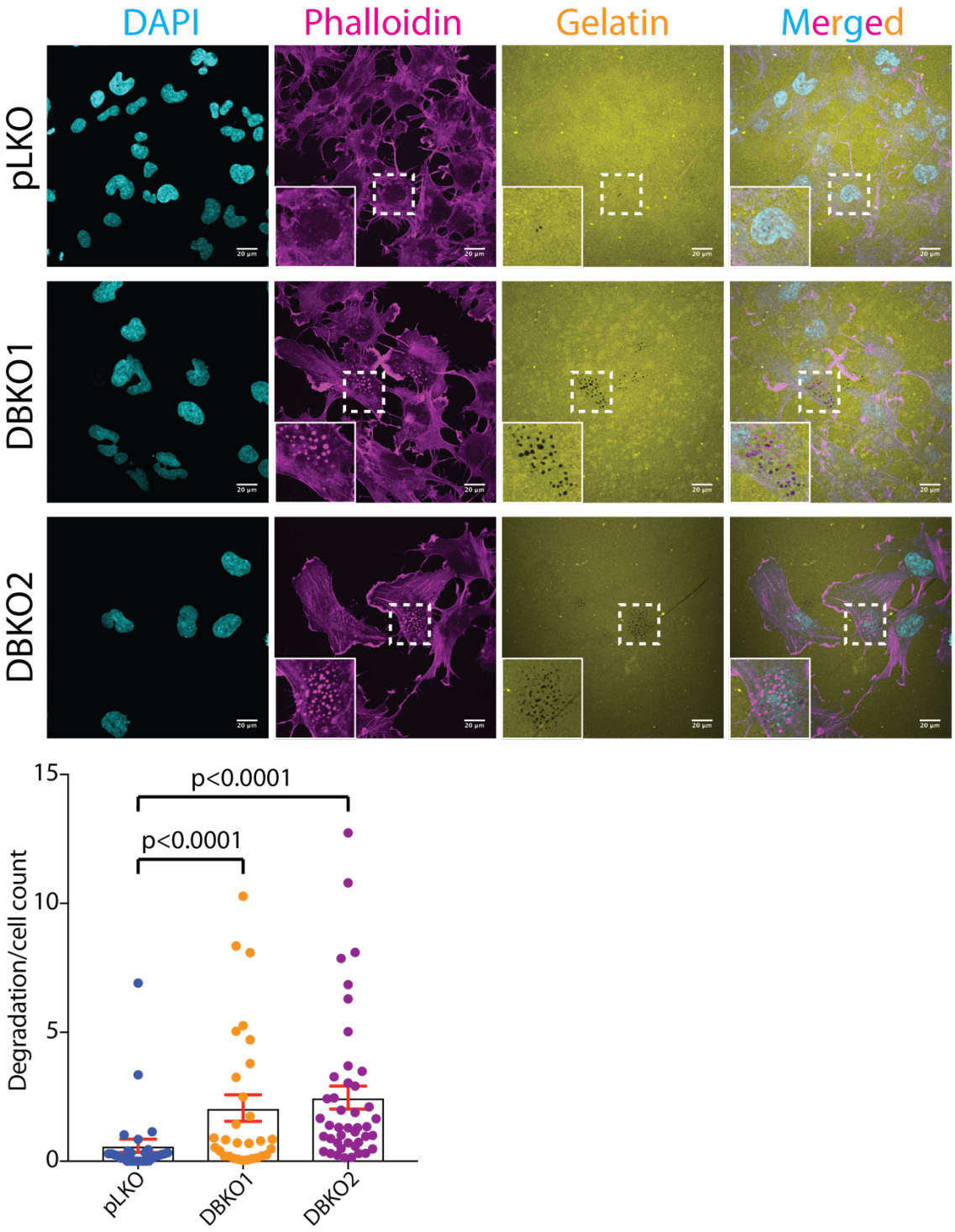

Figure 8.8 CYRI DBKO cells have higher matrix degradation capacity compared to the control pLKO

Invadopodia assay shows both CYRI DBKO cell lines are better (3x higher) at degrading the gelatin matrix (black spots) compared to the control. Quantification from 3 independent experiments. Mean ± SEM. ANOVA with multiple comparisons. Scale bar = 20µm.

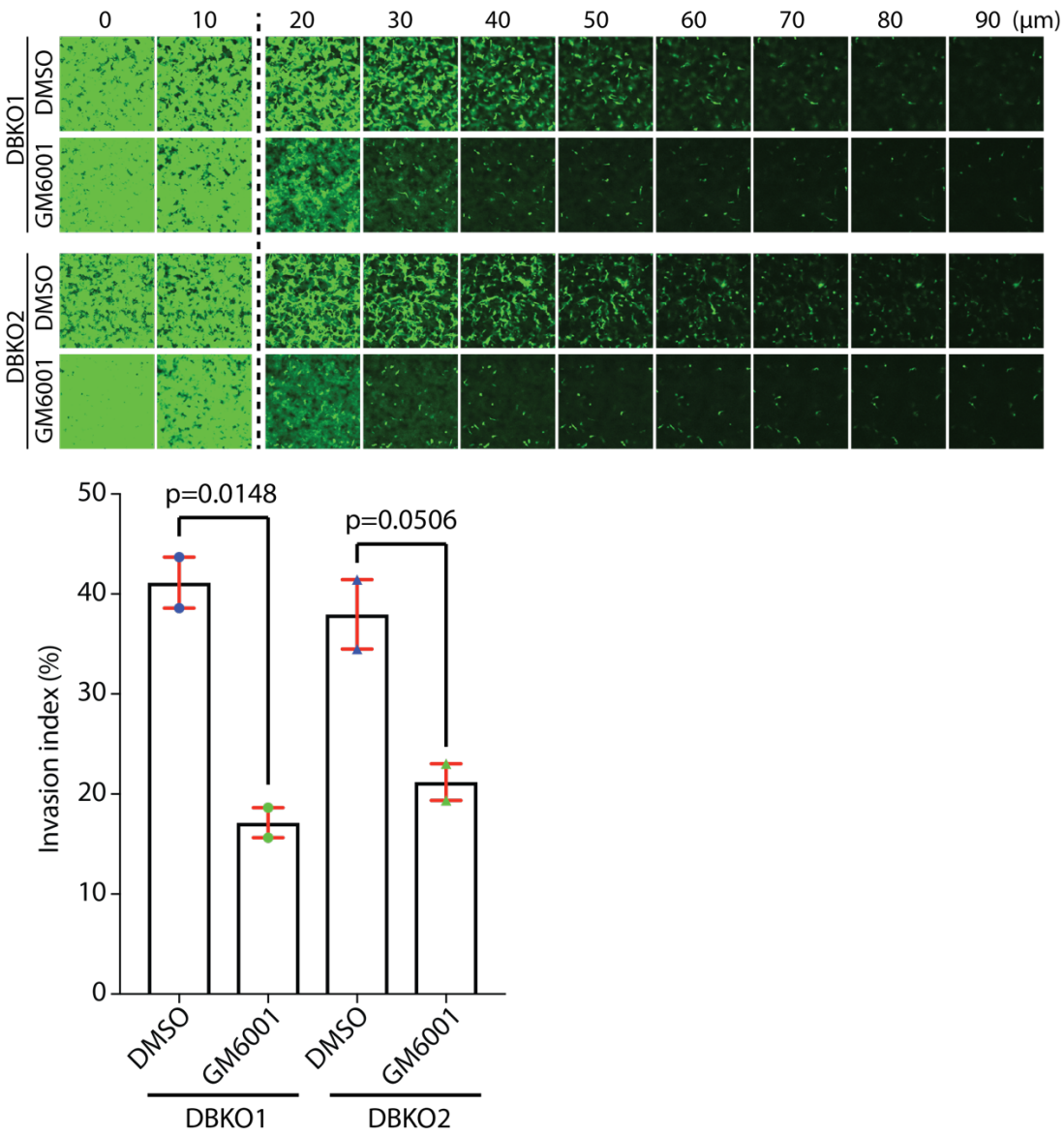

Figure 8.9 CYRI DBKO cells invasion is MMP-dependent

CYRI DBKO cells were subjected to an inverted invasion assay in Matrigel supplemented with fibronectin and collagen in the presence of DMSO or 5µM GM6001 for 5 days. The invasion index beyond 10µm of the treated cells (approximately 20%) is dramatically less than the control condition (approximately 40%). Data from 2 independent experiments. Mean ± SEM. Unpaired 2-tailed t-test.

8.3 Discussion

In this chapter, by utilising RNA sequencing, we have both confirmed many of the previous observations including cell proliferation and integrin surface expression as well as opening up many more questions on the effects that CYRIs could have on different cellular processes. Principle component analysis (PCA) showed a strong reproducibility between two independent CYRI CRISPR cell lines, suggesting that the effects we observed were very unlikely due to any confounding factor introduced by the CRISPR process or RNA sequencing. We discovered that upon CYRI deletion, many genes involved in cell-matrix interaction and matrix remodelling were upregulated, these include many integrins, collagens and matrix metalloproteases. Along with this are many genes involved in cell division and apoptosis that were downregulated. Even though we have not tested the down-regulated genes, considering the strong statistical power of RNA sequencing along with many of the cellular behaviours we observed experimentally, we believe these genes could potentially be interesting to explore in future experiments. The relationship between cell migration and cell proliferation is a topic that worth exploring further as this lies at the heart of cancer dormancy and metastatic seeding cascade. Even though CYRI DBKO cells proliferate slower on a 2D substrate, they clearly proliferated much more successfully under stressful conditions like those in the agarose low-attachment assay. It would be interesting to study how these cells could regulate their own plasticity to switch between migration and proliferation.

How CYRI deletion affects these genes transcriptionally is also another intriguing question. Previous works have linked the adhesions to fibronectin to the gene expression regulation through the Hippo pathway (Kim and Gumbiner, 2015). It was shown that fibronectin specifically triggers the activity of the FAK-Src-PI3K pathway, which leads to the translocation of YAP to the nucleus. It is tempting to speculate that our DBKO cells with an increased amount of surface integrin $\alpha5\beta1$ might utilise this pathway to regulate the expression of many genes. Another study even showed a direct function of FAK in the nucleus to suppress p53 activation by enhancing MDM2-mediated p53 degradation, which affects cell proliferation and

apoptosis (Lim et al., 2008b). Whether CYRIs could affect any of these processes will need future experiments to address.

We also discovered that many of the secreted proteins were also enhanced, including collagen VI and MMP2, both of which have been implicated in cancer invasion and metastasis (Owusu-Ansah et al., 2019, Chen et al., 2013, Xu et al., 2005, Wan et al., 2015). It would be interesting to examine closer how do CYRI deletion affect this secretion process, what drives the enhanced expression and secretion of these proteins. Recently, there have been some suggestions on the role of RAB6 as a master regulator of exocytosis. A recently published paper showed that RAB6 utilised the microtubule tracks to deliver cargo proteins to the proximal regions of focal adhesions for secretion (Fourriere et al., 2019). This is relevant since our CYRI DBKO cells have an increased level of surface integrins and ultimately enhanced level of adhesions. This might act as the depositing sites for the secreted proteins and could potentially explain for the phenotypes we observed. Nevertheless, the exact mechanism remains to be elucidated.

We also found that apart from the ability to adhere to the surrounding matrix, the ability to degrade it with metalloproteases also contributed significantly to the invasion ability of the CYRI DBKO cells. We believed that the increased secretion of MMP2 that we detected in the supernatant as well as the increased expression of MMP14 may well be playing a part in this. This was supported when the pan-MMP inhibitor GM6001 could significantly reduce the invasion of the DBKO cells. It is unclear whether deleting CYRIs could also affect the trafficking of these proteases to specific structures in the cells like invadopodia or FLPs. Furthermore, how deletion of CYRIs affect invadopodia formation and dynamics and whether it is a RAC1-dependent process or not is also unclear. While the role of MMPs in cancer invasion might be more obvious, the role of the secreted collagens such as collagen VI in this process were still elusive. It would be interesting to see whether knocking down some of these collagen genes or blocking the machinery responsible for their secretion would affect how the cells behave.

9 Discussion, conclusions and working model

In this report, we characterised and proposed the function of the novel protein CYRI-A to be a new player in macropinocytosis and integrin trafficking.

9.1 CYRIs fit in the consensus model of macropinocytosis

The consensus model of macropinocytosis begins with the activation of PI3K, which leads to the production of the phosphoinositide PIP3. PIP3 recruits many PH domain-containing proteins including RAC1 GEFs, which leads to the activation of RAC1. Activated RAC1 triggers the Scar/WAVE-Arp2/3-actin cascade, which ultimately leads to membrane ruffles and formation of macropinosomes (King and Kay, 2019). Even though the role of RAC1 activation in this process is well-known, recent evidence also points out the equally important role of RAC1 inactivation (Fujii et al., 2013). In the closely related pathway of phagocytosis, several RAC1 GAPs have been identified to be responsible for shutting down RAC1 signalling to assist for the completion of phagosomes (Schlam et al., 2015). However, to our knowledge, no such equivalent molecule has been described for macropinocytosis. Here, we propose CYRIs, or CYRI-A in particular, to act as a RAC1 signalling suppressor at the macropinocytic cups by binding and sequestering active RAC1 (Figure 9.1). By internally tagging CYRI-A with fluorescent proteins and utilising super-resolution live-cell imaging technique, we placed CYRI-A downstream of activated RAC1 and upstream of RAB5A recruitment during the formation of macropinosomes. Whether sequestering active RAC1 the only mechanism of action of CYRIs is still a matter of debate. There has been some speculation on whether CYRIs possess RAC1 GAP activity. This speculation arose from the observation that CYRIs bind specifically to active RAC1 (Bos et al., 2007) and the CYRI-BΔN-RAC1 complex crystal structure contains arginine residues involved in active RAC1 interaction, which are reminiscent of the arginine finger involved in GTP hydrolysis from a GAP protein (Bos et al., 2007, Haga and Ridley, 2016). Since the affinity of CYRIs to active RAC1 ranging from 2μM for CYRI-A to 20μM for CYRI-B, to directly compete with the Scar/WAVE complex, the number of molecules of CYRI must be at least 9 times higher than that of the Scar/WAVE

complex. However, if CYRIs can trigger GTPase activity in RAC1, their absolute number of molecules inside cells will no longer need to be as high. This is an interesting idea and initial experiments are being conducted to address some of these hypotheses.

Another interesting hypothesis for the function of CYRIs is to regulate membrane homeostasis. Macropinocytosis takes up a large area of the plasma membrane and if they are not being recycled back, the cells will run out of membrane to internalise (Bloomfield and Kay, 2016). Since CYRIs suppress RAC1 signalling, it is possible that the resulting macropinosomes are smaller and thus allow for the recycling of the membrane from other compartments before the next macropinosomes can be formed. To address this hypothesis can be difficult, however. We would need a reversible photoconvertible membrane marker that would change its colour upon internalisation. This would allow us to calculate the rate of membrane internalisation between the control and CYRI knockout cells.

Interestingly, CYRIs are highly expressed in many immune cells. Considering the similarities between macropinocytosis and phagocytosis, one could speculate the involvement of CYRIs in the latter process. Furthermore, membrane ruffles are not only present during phagocytosis but also processes such as cytotoxic T-cells making contacts with cancer cells (Ritter et al., 2015). During the release of granzymes into the cancer cells, the actin network at the immunological synapse needs to be depleted. Could CYRIs be involved in this process is a fascinating question that would be fantastic to follow up.

9.2 CYRIs and membrane tubulation

In addition to the idea of suppressing RAC1 signalling at the macropinosomes, preliminary data also point out the role of CYRI-A in driving membrane tubulation *in vitro* and *in cellulo*. On endosomes, the role of membrane tubulation is the most well-studied in the case of the WASH complex. Similar to the Scar/WAVE complex, the WASH complex can induce actin polymerisation but through interacting with the retromer complex, which drives membrane tubulation (Cullen and Steinberg, 2018). We frequently observe CYRI-A decorates

these protrusions coming out from endosomes, thus tempting us to speculate its role in membrane tubulation. The exact mechanism of how CYRI-A, or in a broader sense CYRIs, does this is still a mystery. One hypothesis based on the predicted crystal structure of CYRI-A suggests the potential involvement of the amphipathic N-terminal helix. This helix could potentially allow CYRI-A to intercalate into the membrane and induce curvature to drive tubulation (Chabanon et al., 2017, McMahon and Boucrot, 2015). But one can also theorise that CYRI-A modulates the WASH complex activity directly through a yet to be discovered mechanism. On the other hand, the helix in CYRI-B is not amphipathic, thus potentially explain to why it did not induce tubulation in liposomes. *In cellulo* however, CYRI-B is frequently found on long tubules deriving from the plasma membrane. We theorise that post-translational modifications such as myristoylation or palmitoylation could play a role. However, it is important to note that our constructs are unusual in a way which the fluorescent molecule is inserted within the protein. Even though this approach has been successfully done before (Sheridan et al., 2002, Hughes et al., 2001), it is without its own compromise. In the case of CYRIs, inserting a fluorescent molecule in between the N-terminal helix and the DUF1394 domain could force the protein in an open conformation. However, this could also subject the proteins to unanticipated modifications inside cells. Preliminary data of palmitoylation using CLICK chemistry shows the P17-GFP-CYRI-B protein is highly lipidated (data not shown). This could potentially affect the kinetics of the protein in the cells.

From our biochemical and structural data, we also predicted the existence of the homo- and heterodimeric complex of CYRIs. The interface between two monomers shares similar residues with the RAC1 binding site, suggesting a novel autoinhibitory mechanism for CYRIs. We speculate that this dimerization can act as a reservoir of CYRIs at the plasma membrane, and this can be released when RAC1 activity surpasses certain thresholds (Figure 9.2). When we titrated with increased concentration of active RAC1, we indeed observed a corresponding decrease in CYRI dimerization. However, the exact affinity between CYRI molecules in a dimer is unclear. It is indeed difficult to measure such affinity with techniques like SPR since dimerization might also happen in solution. We speculate, however, that this dimerization probably occurs on the plasma

membrane. This is because the relatively large interaction surface between the two monomers might interfere with the binding of the N-terminal helix and this can perhaps allow the helix to anchor to the plasma membrane. We did attempt to detect this dimerization in suspension using analytical ultracentrifugation but failed to observe any dimer. This perhaps suggests an anchoring platform such as a lipid bilayer is needed for the dimerization to occur. Nevertheless, a direct visualisation technique is needed to confirm this hypothesis. Furthermore, the consequences of CYRI dimerization might go beyond RAC1 regulation. BAR domain proteins induce curvature through dimerization on the surface of a lipid membrane (Simunovic et al., 2015), could CYRI dimers do the same? We also observed CYRI-A being recruited to macropinocytic cup just moments before the budding off happens, could this process be assisted or accelerated by CYRIs? It would definitely be interesting to visualise CYRIs on a lipid membrane perhaps by using electron microscopy. Single-molecule microscopy has also been used to study the membrane dynamics of RHO GTPases and discovered their nanoclusters at the plasma membrane (Remorino et al., 2017, Mehidi et al., 2019). Perhaps, in future studies, we could utilise this technique to gain better insights into the molecular dynamics of CYRIs at the nanoscale.

9.3 CYRIs internalise integrins through macropinocytosis

We linked the role of CYRIs at the macropinosomes to the internalisation of integrins, which has consequences on cell migration and cancer invasion. We found that certain integrins such as $\alpha5\beta1$ can be concentrated at CYRI-positive vesicles and delivered inside the cells. Macropinocytosis can be thought of as an unconventional way to traffic integrins but indeed it has been described in fibroblasts upon PDGF induction previously (Gu et al., 2011). CYRIs help to resolve the macropinosomes by suppressing overactive RAC1 and thus allow for the internalisation of integrins (Figure 9.1). In cells lacking CYRIs, integrins are retained for longer on the plasma membrane, thus contributing to the migration and invasion effects of cancer cells. There are several unanswered questions. What concentrates these integrins at these CYRI-positive vesicles? Proteomic analyses did not detect integrins as binding partners of CYRIs, so an additional protein must exist to perform this task. We speculate that, however, in cells

lacking CYRIs, macropinocytosis could still occur due to the existence of other compensatory pathways such as RAC1 GAPs (Schlam et al., 2015). It would be useful to compare the kinetics of macropinocytosis between control and CYRI knockout cells and whether cells lacking CYRIs would result in a slower rate of formation but with larger macropinosomes? CYRIs finetune and coordinate the activity of the actin cytoskeleton for an efficient macropinosome formation. Too much or too little of CYRIs would negatively impact this process, and the same logic is applied to RAC1 (Fujii et al., 2013, Ikeda et al., 2017). There has been one report where the authors showed that *Salmonella* bacteria actively target CYRI-B to the ubiquitination pathway to allow for an enhanced RAC1 activation and increase in the infection rate (Yuki et al., 2019). This could perhaps create some confusion on the requirement of CYRIs in macropinocytosis that we proposed compared to what has been reported. However, it is important to differentiate bacterial invasion from physiological macropinocytosis. On one hand, bacterial invasion requires a pliable actin network that can be easily controlled by the bacteria. Salmonella bacteria tend to actively induce membrane ruffles locally at the site of infection through using a set of various proteins (Ly and Casanova, 2007). On the other hand, macropinocytosis requires the cell's internal machinery to actively grabbing external substances, which certainly would require the membrane and the protein components of the actin network to be more dynamic and fine-tuned. Indeed, when CYRI-B is deleted from fibroblasts, their lamellipodial dynamics is significantly decreased compared to the control cells (Fort et al., 2018). The two processes are fundamentally different from one another.

Furthermore, we have not addressed the effects of deleting CYRIs on other endocytic pathways in this report. Pathways such as CDE, CIE and other recycling pathways that we described in the introduction are more traditionally involved in integrin trafficking. Could the deletion of CYRIs perturb these other pathways and ultimately leads to changes in membrane receptors is another important question that needs to be studied further.

Having shown CYRI DBKO cancer cells with enhanced surface integrin $\alpha5\beta1$ to be much more invasive through a series of *in vitro* and *in vivo*-mimicking assays, we

would also like to test whether this would correlate with higher metastasis in an *in vivo* model. It is unclear to why Ewing's sarcoma cells such as our A-673 cell line expressing both CYRI-A and CYRI-B and what is the significance of these two proteins in the cells. However, through our experiments, it is clear to us that the deletion of both CYRIs in A-673 cells makes them much more invasive through the use of their surface integrins and their enhanced matrix metalloprotease secretion. Ewing's sarcoma is highly metastatic and tends to originate from the bone. Hence an orthotopic xenograft model where cells are injected into or near the bones and both local invasion and distant metastasis at the lungs can be examined makes a simple and quick method to confirm our observations *in vivo* (Jacques et al., 2018, Vormoor et al., 2014). We could also combine with the use of second-harmonic generation microscopy to probe for the effects of the CYRI DBKO cells on the surrounding matrix.

Overall, this report has described the previously unknown spatiotemporal localisation and functions of the CYRI protein family in macropinocytosis and integrin trafficking. We provide an additional explanation to the previously observed phenotypes in CYRI knockout cells. These details are summarised in the two figures below.

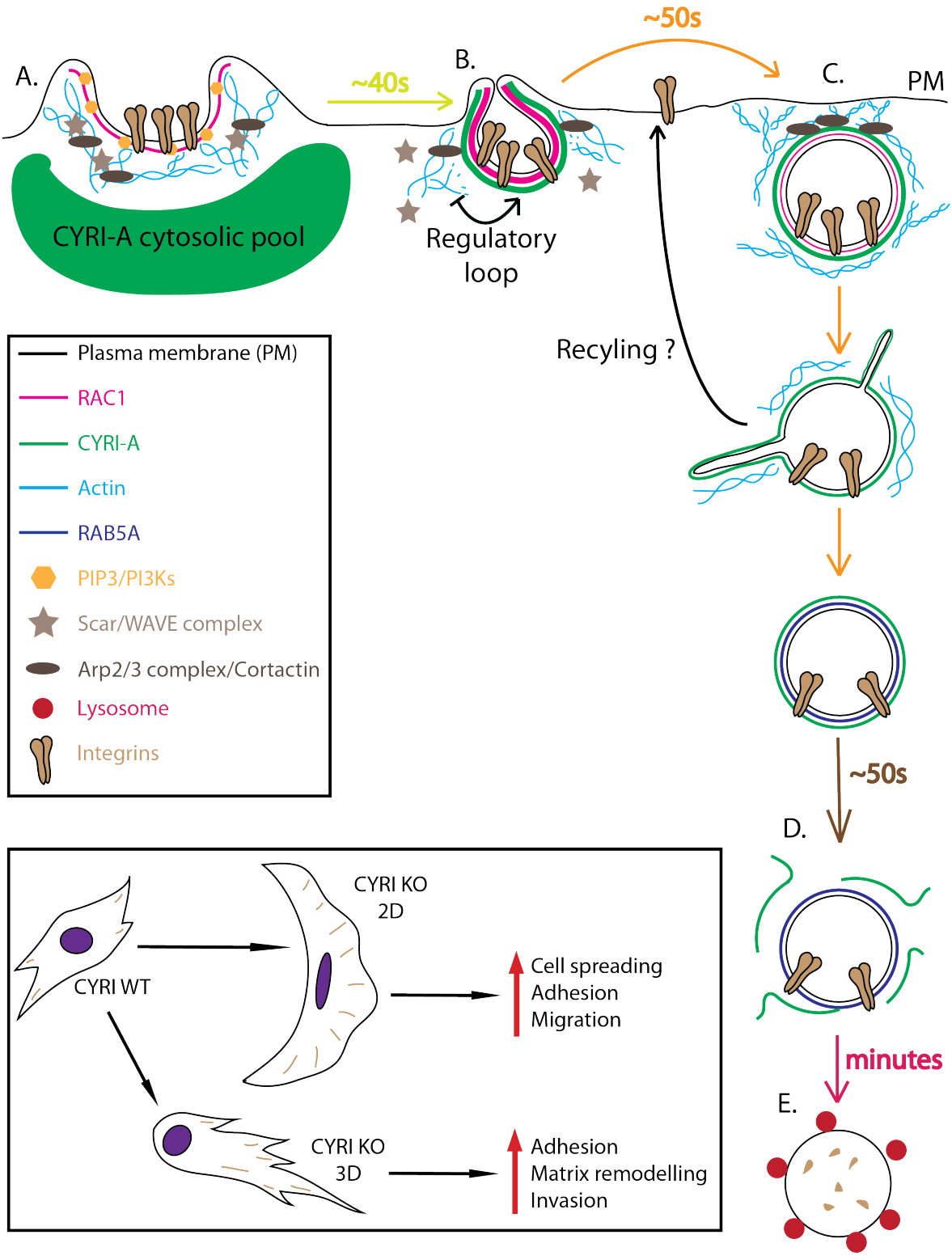

Figure 9.1 The overall spatiotemporal localisation of CYRI-A in macropinocytosis and the effects of CYRI deletion in cancer cells through integrin trafficking

This figure is an extension of Figure 5.25 with the inclusion of integrin trafficking. For detailed legend, refer back to this figure in chapter 5.

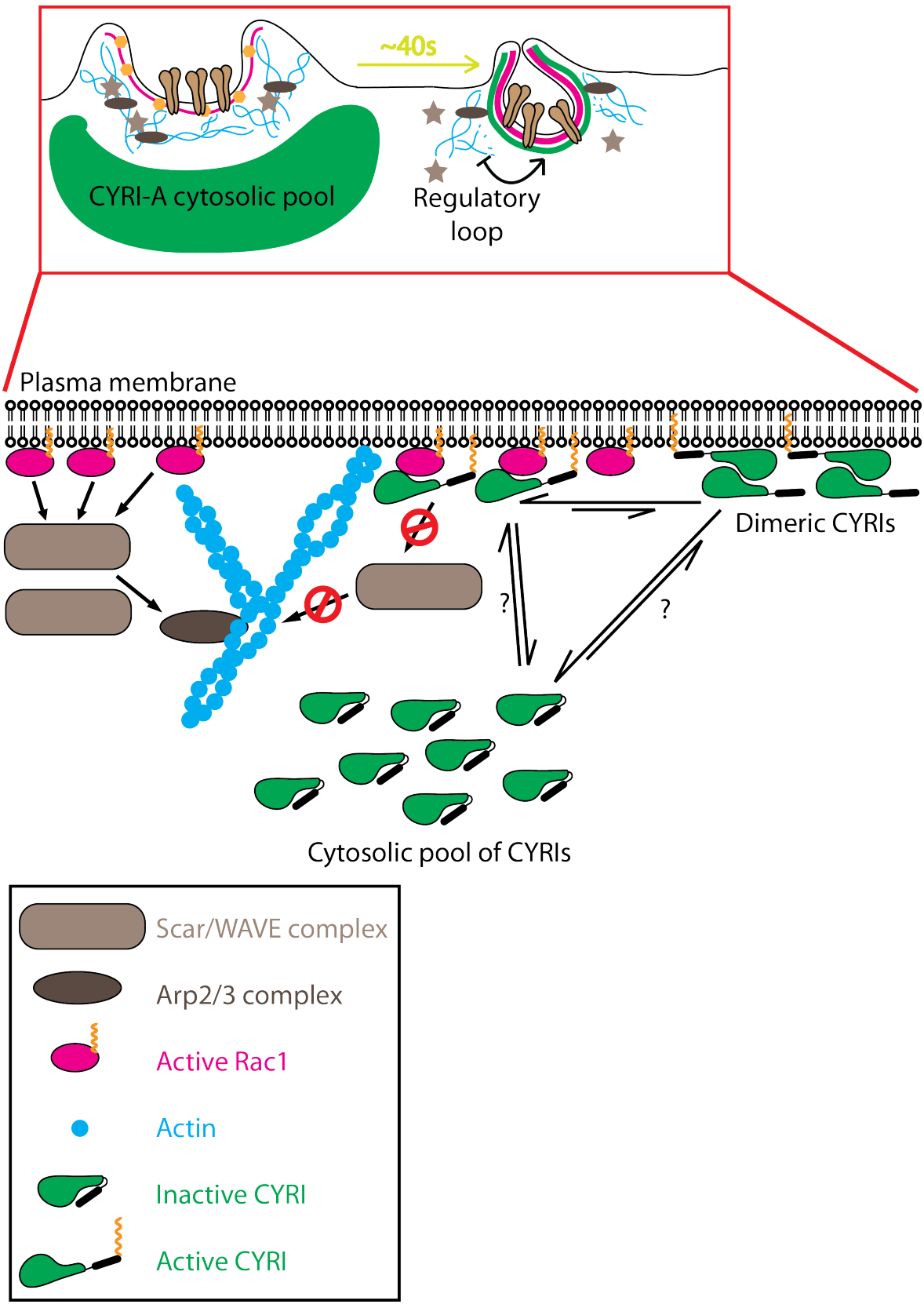

Figure 9.2 A close up model of what we propose to how CYRIs work

Active RAC1 molecules are myristoylated and localised to the macropinocytic cups or at the leading edge of a cell. They activate the Scar/WAVE complex and subsequently the Arp2/3 complex, leading to branched actin polymerisation. CYRIs exist in a cytosolic pool near where active RAC1s

reside, presumably in a monomeric state. They might be in equilibrium with an autoinhibited myristoylated dimeric CYRIs which resides on the membrane. When the activity of active RAC1 crossed a certain threshold value, this shifts the autoinhibited dimeric CYRI into the active RAC1 binding form. This ultimately shuts down the signalling towards actin polymerisation. Active RAC1 binding might also occur from the direct recruitment of monomeric CYRIs from the cytoplasmic pool.

10 Investigating the role of the recurrent RAC1 P29S mutant in melanoma

10.1 Introduction

Skin cancer is one of the most common types of cancer. There are many subtypes, but the most aggressive form is melanoma. In the UK, around 16,000 people are diagnosed with melanoma alone and around 2,300 people die of this disease every year. Melanoma is characterised by the uncontrollable cell proliferation of the pigment-producing cells called melanocytes. There are many different types of melanoma such as uveal melanoma, but the most common and prominent type is cutaneous (skin) melanoma.

Melanocytes are derived from melanoblasts which are in turn derived from the neural crest stem cells. During the development of vertebrates, the neural plate folds to separate the neural tube and the epidermis (Figure 10.1). The inward movement leads to the merging of the two border cell populations, forming the roof plate. Neural crest cells in the roof plate then enter epithelial to mesenchymal transition (EMT) in a process called delamination. These cells enter a transition zone called the migration staging area (MSA) where they split into two populations. One population differentiates into melanoblasts and migrate dorsolaterally, while the second form neurogenic cells which are restricted to migrate ventrally (Figure 10.2). New evidence suggests that this neurogenic population can also contribute as a source of melanoblasts, however, the dorsolateral population is still accepted to be the major source (Petit and Larue, 2016, Vandamme and Berx, 2019). At E10 to E11.5, melanoblasts start expressing one of the earliest markers for melanocyte differentiation called Melanocyte Inducing Transcription Factor (MITF). At E11.5 onward, melanoblasts start invading into the epidermis where the microenvironmental conditions support quick and productive cell proliferation. A part of the melanoblast population resides in the dermis, where they potentially undergo asymmetric cell division where the daughter cells continue to migrate upwards to the epidermis (Petit and Larue, 2016), while the mother cells reside in the same location.

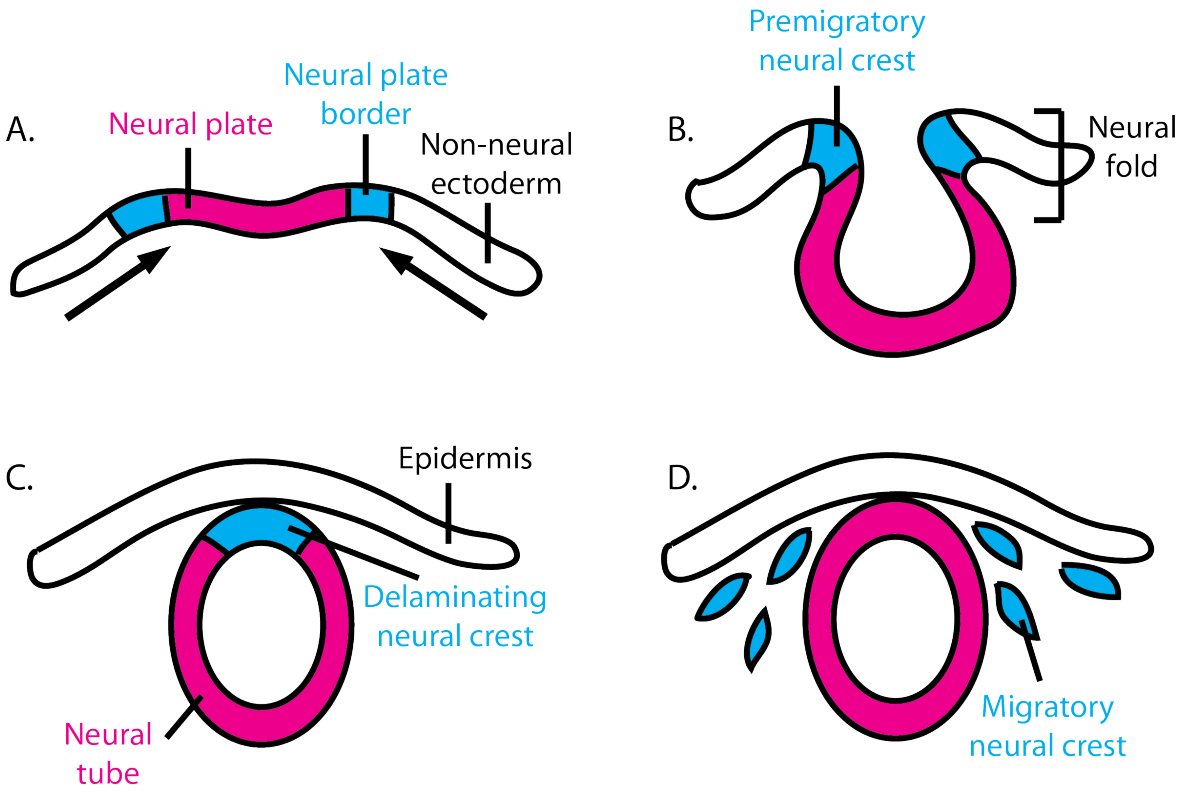

Figure 10.1 The origin of neural crest cells

A-B. During the development in vertebrates, as the neural plate fold, it brings the two neural plate borders close together. Black arrows indicate the direction of movement.

C. The neural plate forms the neural tube. The neural plate borders now form the roof plate containing delaminating neural crest cells.

D. Neural crest cells migrate ventrally and dorsal laterally, differentiate into many different types of cells during this process, including melanoblasts and subsequently melanocytes.

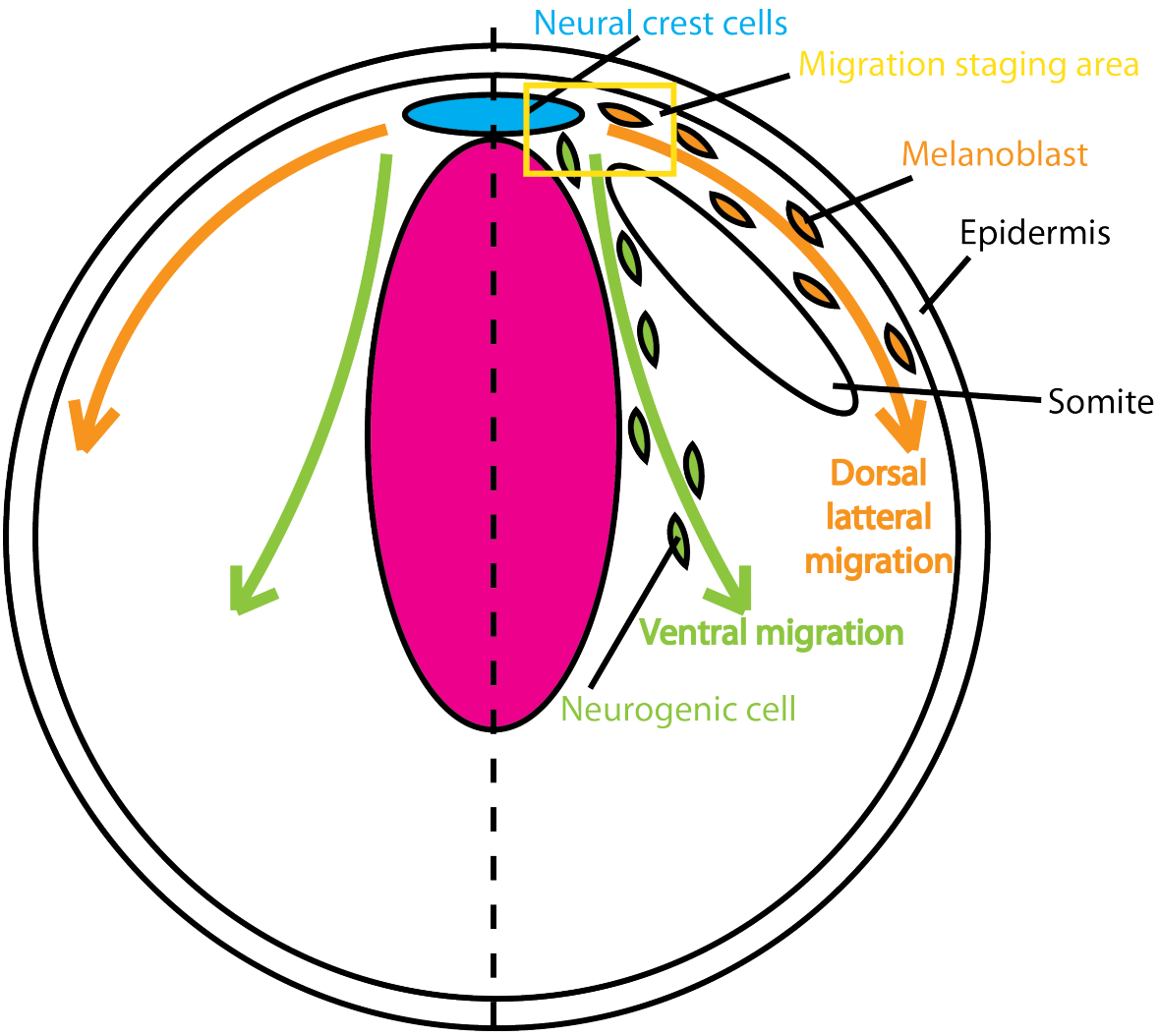

Figure 10.2 The migration routes of neural crest cells

Neural crest cells (cyan) migrate from the roof plate of the neural tube (magenta) into a migration staging area (MSA) where they split into two populations. One population migrate along the dorsal lateral surface and differentiate into melanoblasts-precursors for melanocytes. The other population migrate along the ventral side to form other neuro-related cell types such as glial cells, etc.

Figure adapted and modified from (Vandamme and Berx, 2019).

Epidermal melanoblasts distribute throughout the skin and in humans, they split into at least three subpopulations. One resides in the hair follicles and differentiates into matured melanocytes that contribute to hair colour. The second subpopulation resides in the hair follicle bulge and become melanocyte stem cells and acts as a reservoir for follicular melanocytes. The third population scattered on the skin to contribute to skin tone and colour. Melanocytes are thought to be part of a defence mechanism of the skin. When UV radiation (UVR) from sunlight damaged keratinocytes in the skin, this causes them to release a hormone called α-Melanocyte-stimulating Hormone (α-MSH). α-MSH binds to a G-protein coupled receptor (GPCR) called MC1R on the surface of melanocytes and triggers the RAS, RAF, MEK and ERK, alongside with cAMP-PKA-CREB pathway. This leads to the phosphorylation and activation of MITF. The phosphorylated MITF translocates into the nucleus and switches on genes involved in melanogenesis to produce melanin. Melanin is then transferred to the keratinocytes to surround their nucleus and protect them from further UV damage. Melanocytes rarely divide but regain this capacity during the development of melanoma.

There are three most common mutations in melanoma. The first and most common mutation in melanoma is BRAF(V600E) and is found in up to 60% of the patients (Davies et al., 2002, Zaman et al., 2019). However, we will not go into detail since our work will not be focusing on it.

The second most common mutation in melanoma occurs on one of the isoforms of the RAS family protein, NRAS substituting the amino acid glutamine 61 to leucine (Q61L). NRAS Q61L, even though, is upstream of RAF, only occurs in about 15-20% of all melanoma. Other mutations are also found on other isoforms, however, NRAS Q61L seems to be the most prominent (>80%) (Munoz-Couselo et al., 2017). Patients with NRAS mutant present with aggressive histopathological phenotypes, including thicker primary tumours, higher proliferative index and more metastatic compared to BRAF mutant (Devitt et al., 2011). Currently, there is no specific inhibitor for NRAS mutant patients, which contributes to its worse prognosis. Biochemically speaking, NRAS is a small GTPase that binds GTP in its active form and GDP in its inactive form. In the active state, the switch I and switch II loop of the proteins are both involved in coordinating the phosphate

groups of GTP (Figure 10.3). The switch I uses a magnesium ion (Mg^{2+}) to form a salt bridge interaction with the β- and γ-phosphate while the switch II uses its glycine 60. This keeps the protein locked in its active state. When the GTP is hydrolysed, the two switches recoil back to their original locations, in a "loaded-spring" mechanism. The localisation of RAS is also important for its activity. Its C-terminus with positively charged lysine residues along with cysteines that can be palmitoylated allows the protein to interact with the negatively charged lipid bilayer. RAS, on its own, is slow at hydrolysing its GTP (Hunter et al., 2015) and needs the assistance of another protein family called GTPase activating proteins or GAPs. The mechanism of action of GAPs has been described in chapter 1. The NRAS Q61L mutant has the hydrophobic leucine in the place of glutamine, which is not able to make hydrogen interactions with the arginine finger from the GAPs and thus render the protein unable to hydrolyse its GTP (Prior et al., 2012,Simanshu, 2017 #247).

The third most common mutation, which will be the focus of our discussion in this chapter, is a newly discovered missense mutation on the gene RAC1, replacing proline 29 with a serine residue (P29S). Defined as a recurrent mutation meaning it is frequently mutated and unlikely to happen by chance, RAC1 P29S is estimated to occur in up to 9% of sun-exposed melanoma and is caused by a specific UVB-damage C>T transition (Krauthammer et al., 2012, Halaban, 2015). Surprisingly, mutations in the Rho GTPase family have not been previously associated much to cancer, despite their important roles in regulating many essential cellular processes such as cell migration, cell proliferation and growth. In both studies, the authors used exome sequencing to mine for new mutations in melanoma and RAC1 P29S was identified (Krauthammer et al., 2012, Halaban, 2015). COS-7 cells expressing this mutant adopt broader lamellipodia compared to wild-type cells (Krauthammer et al., 2012, Davis et al., 2013). Pulldown shows RAC1 P29S interacts stronger with many of its downstream effectors than the wild-type RAC1, including the serine/threonine kinase PAK1 (Krauthammer et al., 2012, Davis et al., 2013). Wild-type RAC1 belongs to the same superfamily as RAS, and more specifically the Rho GTPase family. The mechanism of activation of RAC1 follows the same loaded-spring mechanism as for RAS (Figure 10.3) (Schaefer et al., 2014). The P29S mutation of RAC1 occurs on its switch I region.

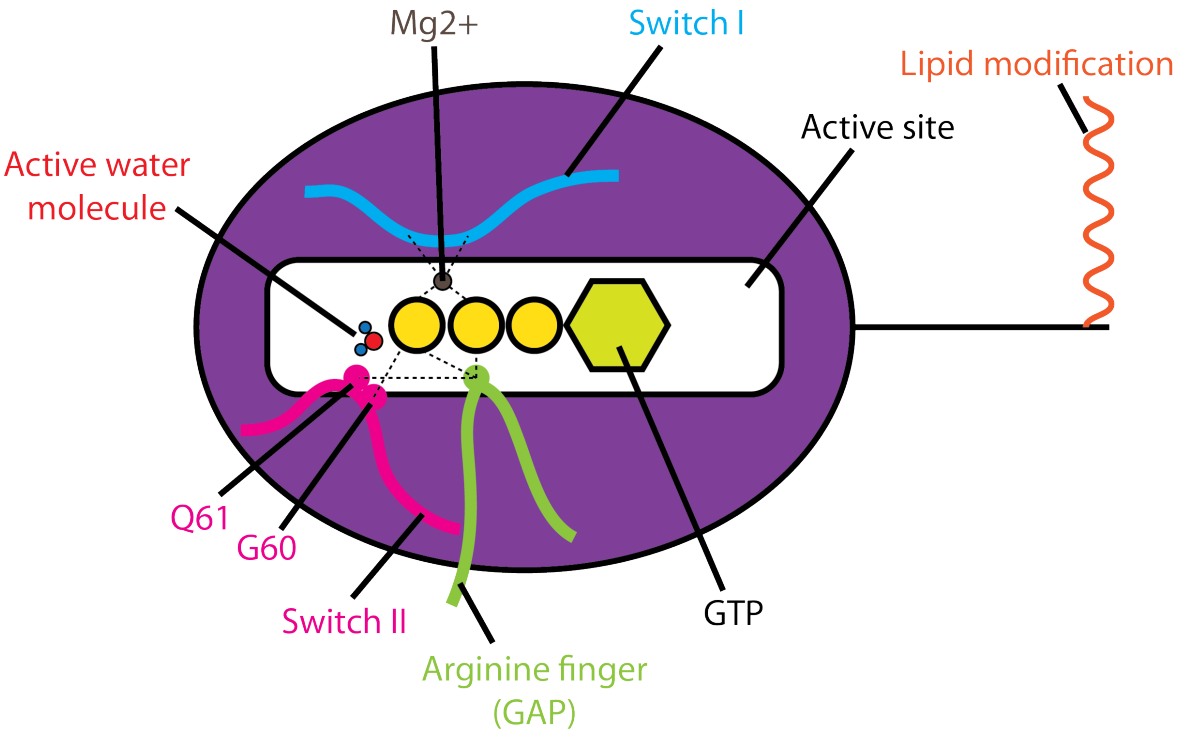

Figure 10.3 The structural and mechanistic representation of the RAS small GTPase

When GTP bound, the switch I loop coordinates a magnesium ion (Mg^{2+}) that stabilises the beta- and gamma-phosphate of the GTP. The switch II loop uses its Glycine 60 to form a hydrogen bond with the gamma phosphate. This holds the protein in its active GTP-bound conformation.

During GTP hydrolysis, a GTPase-activating protein (GAP) inserts its arginine finger into the active site, position its arginine to form an interaction with the β- and γ-phosphate as well as the Glutamine 61 of the switch II loop. This stabilises the switch II loop and allows it to interact and activate a water molecule that will be involved in the hydrolysis reaction of GTP.

RAS is bound to the membrane through lipid modification at its C-terminus.

Since proline induces strain into the peptide bond, substituting with a serine increases the flexibility of this region. It was shown that the serine could make direct hydrogen bonds to the guanosine group of the GTP, which is more similar to a RAS GTPase than to Rho GTPases (Krauthammer et al., 2012). The consequence of this interaction is currently unclear, however, biochemical assays showed that while RAC1 P29S retains its normal GTPase function, it can exchange GDP for GTP three times faster than its wild-type counterpart (Davis et al., 2013). This leads to the association of the term "fast cycler" to RAC1 P29S. The first report suggested that RAC1 P29S tended to occur independently of the other NRAS and BRAF mutations in melanoma and that it is found quite earlier on during melanoma development. However, a recent study found a slight increase in the rate of co-occurrence between RAC and NRAS mutation but not with BRAF (Vu et al., 2015). This makes the conclusion of whether RAC1 P29S is a driver mutation or an associated mutation more complicated to assess. However, since cells expressing RAC1 P29S produce phenotypes, this suggests RAC1 P29S is a gain-of-function mutation. A few studies using cell lines with a BRAF mutant background show that expressing RAC1 P29S increases their resistance to RAF and MEK inhibitors both *in vitro* and *in vivo* (Watson et al., 2014). However, other studies using other cell lines show mixed results, where some show a modest resistance while others are highly sensitive to MEK inhibition and RAF inhibition (Halaban, 2015, Vu et al., 2015), putting the conclusion about drug resistance in question. Even though drug resistance might not be present in every cell line, more studies however are still exploring the molecular mechanism behind those that do resist. A recent paper proposes a mechanism where RAC1 P29S acts independently from the classical MAPK pathway. Using melanoma cell lines with a BRAF V600 background, they showed that these cells resist and form broader lamellipodia upon treatment with BRAF inhibitors. This pathway was shown to be also independent of focal adhesions. The authors proposed that in the presence of BRAF inhibitors, RAC1 P29S leads to the increased PAK activity, which leads to increased phosphorylation of the tumour suppressor protein NF2. Phosphorylated NF2 is then trapped at the lamellipodia, preventing it from translocating into the nucleus to induce a growth arrest signal (Mohan et al., 2019). In a recent *in vivo* study (Lionarons et al., 2019), the authors described that mice harbouring just the RAC1 P29S mutant specifically in melanocytes did not develop melanoma, while

whole-body expression of this mutant leads to lymphoma. Only when RAC1 P29S was combined with the BRAF V600E mutation in melanocytes did these mice developed a significantly higher number of melanoma tumours compared to just the BRAF mutation alone. This argues against the role of RAC1 P29S as the main initiator, but rather an accelerator in melanomagenesis. It was also shown that cells expressing RAC1 P29S can switch its transcriptional programme to mesenchymal through the use of the WAVE-Arp2/3-Serum Response Factor (SRF) axis. These cells are shown to be more resistant to BRAF inhibitors and apoptosis. It is interesting to note that the constitutively active mutant RAC1 Q61L has rarely been found in human cancer, despite its presumably higher activity than RAC1 P29S. It is possible that an overactive RAC1 can negatively affect the cell cycle and other cellular processes that require a more dynamic RAC1 signalling. At the same time, many of these studies seem only to focus on combining the mutant RAC1 with a BRAF mutant background, but none has assessed the behaviour of RAC1 in an NRAS mutant. We utilised our previously established NRAS ^{Q61K} INK4A$^{-/-}$ RAC1$^{f/f}$ transformed melanocyte model and introduced RAC1 P29S exogenously to study its effects. We also compared the effect of P29S mutant with the constitutively active Q61L. Using the combination of cell biology and *in vivo* subcutaneous injection model, we showed that despite its *in vitro* increase in matrix degradation, RAC1 P29S in an NRAS background did not affect the metastasis *in vivo*.

10.2 Results

10.2.1 RAC1 P29S increases cell spreading area of NRAS transformed melanocytes

RAC1 is a master regulator of the actin cytoskeleton. Numerous studies have implicated the function of RAC1 with actin dynamics (Fort et al., 2018, Li et al., 2016a, Eden et al., 2002). Previous reports show that COS-7 cells expressing the RAC1 P29S mutant form more membrane ruffles compared to just RAC1 WT (Davis et al., 2013, Krauthammer et al., 2012). However, these studies have not addressed whether this mutation would also affect the melanocytes, which is ultimately where melanoma would derive from. We first generated our melanocytes expressing the mutant RAC1 P29S using retroviral gene delivery. The Mel-11 line melanocyte (Li et al., 2012) was infected with retrovirus containing the gene encoding for the mutant RAC1. To first reconfirmed the activity of RAC1 P29S in these cells, we analysed their morphology by staining them with Calcein AM and plated on fibronectin-coated dishes. Random images were taken and analysed using CellProfiler (Figure 10.4). Cells expressing either the empty vector (EV) or WT RAC1 adopt a more spiky and polygonal morphology. On the other hand, cells expressing either the P29S or the constitutively active Q61L, in general, adopt more well-spread phenotypes with many cells displaying broad lamellipodia, which is expected of cells expressing an activated RAC1 (Nobes and Hall, 1999, Nobes and Hall, 1995). Melanocytes containing the mutant RAC1 on average are 30% larger in spreading area compared to both the control EV and WT RAC1. The roundness index, however, is only minorly increased in these mutant cells, perhaps due to the fact that the control EV and WT RAC1 can form protrusion around the cells that may have masked away its spikey appearance.

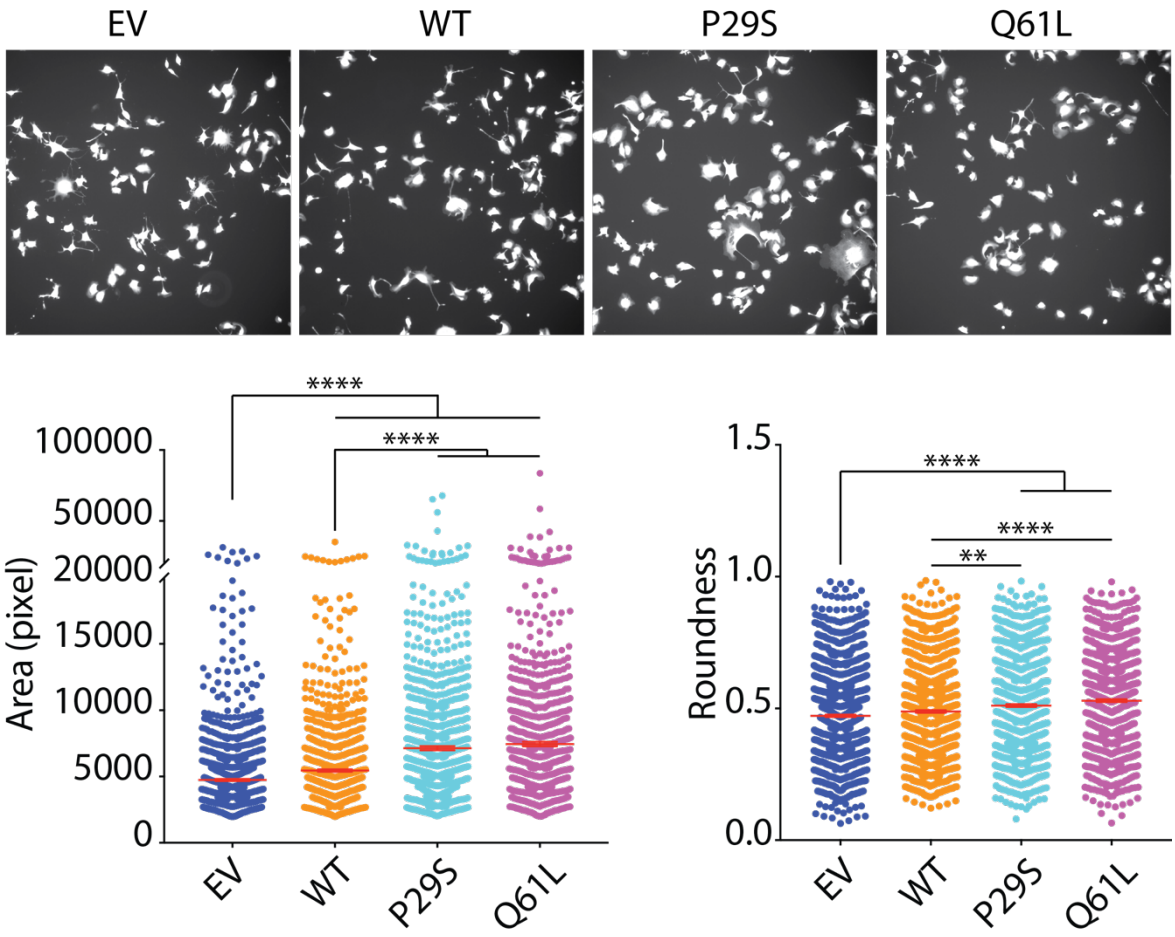

Figure 10.4 Analysis of the morphology of melanocytes containing RAC1 WT or mutants on fibronectin substrate

Mel-11 melanocytes expressing either an empty vector (EV), WT RAC1, RAC1 P29S or the constitutively active RAC1 Q61L were plated on fibronectin-coated plates. Cells were stained with Calcein AM and imaged at random locations. Cell area and roundness were analysed using Cellprofiler. Statistical analysis of 3 independent experiments. Mean ± SEM. ANOVA with multiple comparisons. **p<0.01, ****p<0.0001.

In normal cells, RAC1 has been suggested to act as a cytokinesis inhibitor. The protein signal is lost at the cleavage furrow while RhoA signal is concentrated to regulate the constriction ring (Jordan and Canman, 2012). It was also suggested that inhibition of RAC1 is necessary for the inhibition of cell adhesion, which allows the cell body to contract and prepare for the division process. However, RAC1 can also play a positive role in cell cycle progression (M F Olson, 1995). There have been reports on the role of RAC1 being important to meiosis in oocytes (Halet and Carroll, 2007) as well as the proliferation and development of progenitor cells in the brain (Leone et al., 2010). In cancer, deletion of the RAC1 GEF protein Tiam1 impedes RAS-dependent tumour proliferation (Malliri et al., 2002). Furthermore, mice harbouring RAC1 P29S mutant develop multiple tumours and cells expressing the mutant can proliferate more under BRAF inhibition (Lionarons et al., 2019, Mohan et al., 2019). We hence tested the proliferation capability of our melanocytes using the Incucyte system (Figure 10.5). Interestingly, all three melanocyte lines expressing either RAC1 WT or mutant RAC1 proliferated faster (slope ~0.019) compared to cells containing the empty vector (slope ~0.016). At the same time, the percentage of dead cells, labelled by Sytox green is also higher in the EV cells. Interestingly, the cells with the lowest level of dead cells are those containing WT RAC1 and RAC1 P29S, while cells with the Q61L mutant are somewhere in between. This suggests that perhaps RAC1 P29S is capable of driving melanocyte proliferation similar to a WT RAC1 while avoiding the negative effects of a constitutively active mutant Q61L. Overall, the data suggest that active mutants of RAC1 promote lamellipodial spreading and cell proliferation in melanocytes.

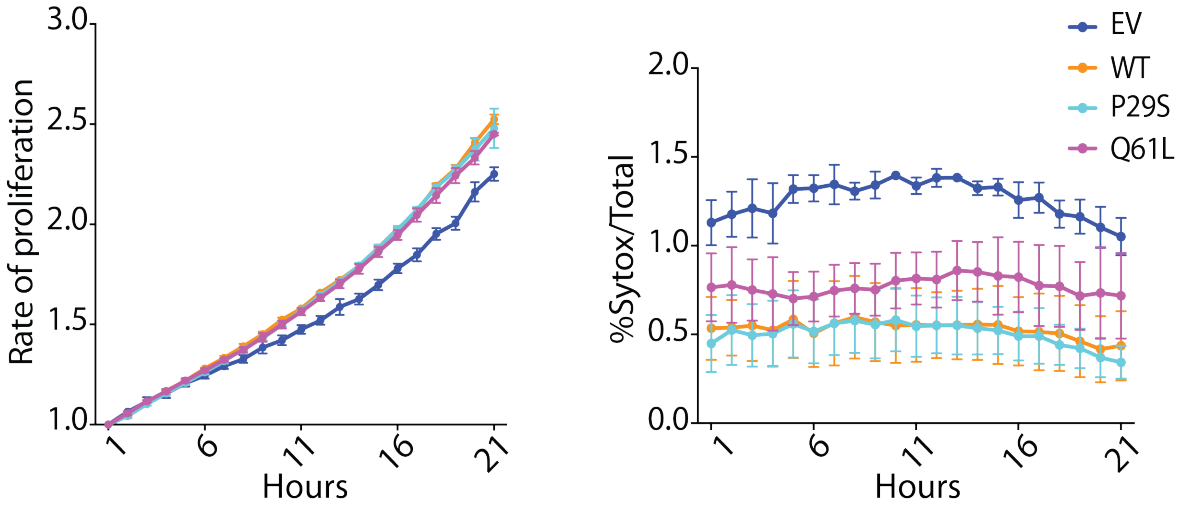

Figure 10.5 Additional expression of RAC1 leads to increased cell proliferation and lower cell death in melanocytes

Melanocytes are plated on fibronectin-coated 96-well plates and image every hour using the Incucyte system. Cells are stained with Nuclight Red for total cell count and Sytox green for dead cells. Melanocytes expressing RAC1 are proliferating faster than EV cells (slope ~ 0.019 vs ~0.016) while their percentage of dead cells is lower than EV cells. The rate of proliferation is calculated by normalising the number of living cells from each time point to the first time point. Data from 3 independent experiments. Mean ± SEM. Slope was calculated by log base 10 transformation and fit to a linear regression model.

10.2.2 Active RAC1 increases matrix degradation in NRAS transformed melanocytes

Previous reports showed that the invasion of NRAS mutant melanocytes is dependent on RAC1 (Li et al., 2012). RAC1 deleted cells adopt a stubby morphology in the 3D environment of the skin and are unable to degrade the matrix as well as invade into collagen plugs. We hence performed invadopodia assay similar to what to we described in chapter 8 to test whether RAC1 P29S would affect matrix degradation. On fixed gelatin matrix, melanocytes expressing the mutant RAC1 P29S formed large lamellipodia compared to cells only expressing WT RAC1 (Figure 10.6). These cells also seem to have denser actin cables with numerous actin dots present at the centre of the cells. Most of these dots are also colocalised with the cortactin signal, which we used as a marker for invadopodia (Li et al., 2010, Weaver et al., 2001, Clark et al., 2007). Comparing the degradation between the two cell lines, we could clearly see the significantly higher amount of matrix degradation per cell area in the mutant line compared

to the WT. These cells also form more invadopodia compared to the control (~20 per cell for WT and ~50 per cell for P29S). However, when we compared between melanocytes expressing the P29S mutant with the constitutively active Q61L, we did not observe any significant differences (Figure 10.7). This suggests that *in cellulo*, the two RAC1 mutants behave similarly to each other. We verified this observation again with a second melanocyte line Mel-10 (Li et al., 2012) (Figure 10.8), and indeed cells expressing the fast-cycler mutant P29S or the constitutively active mutant Q61L degrade the matrix more and form more numerous invadopodia compared to cells expressing WT RAC1. No differences between the two mutant lines were also detected. Overall, these data provide the evidence for the role of RAC1 P29S in promoting matrix degradation and invadopodia formation in NRAS transformed melanocytes.

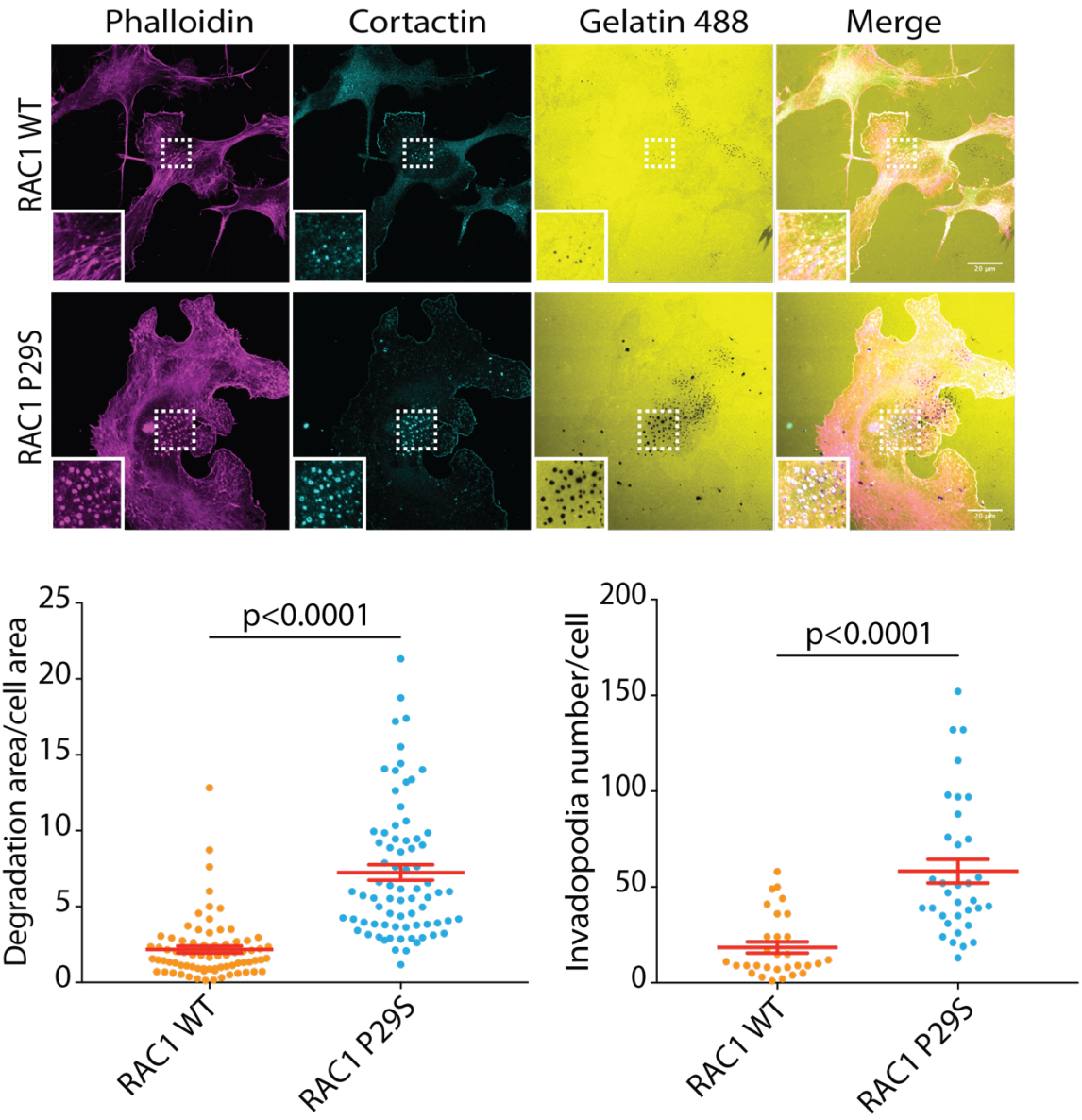

Figure 10.6 Mel-11 melanocytes expressing RAC1 P29S form more invadopodia and degrade matrix more compared to WT cells

Melanocytes expressing either WT RAC1 or RAC1 P29S were plated on fluorescently labelled gelatin. Mutant cells can be seen degrade significantly more (black dots) as well as form more invadopodia spots than WT cells. Statistical analysis from 3 independent experiments. Mean ± SEM. Unpaired two-tailed t-test. Scale bar = 20μm.

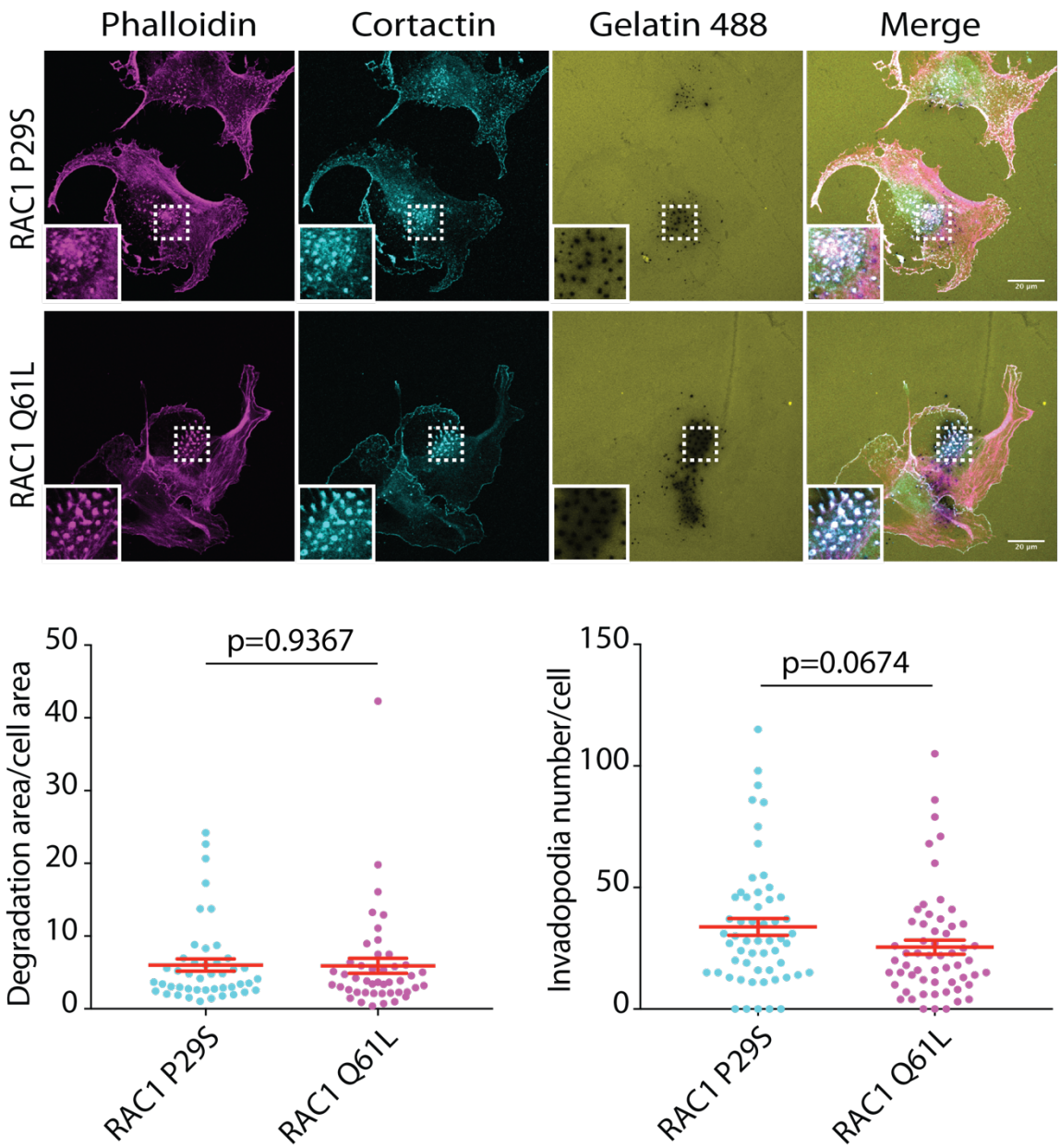

Figure 10.7 RAC1 P29S and Q61L cause a similar degree of matrix degradation in NRAS transformed Mel-11 melanocytes

Both RAC1 P29S and Q61L mutant cause the same degree of matrix degradation and filopodia number formation in melanocytes. Data from 3 independent experiments. Mean ± SEM. Unpaired two-tailed t-test. Scale bar = 20μm.

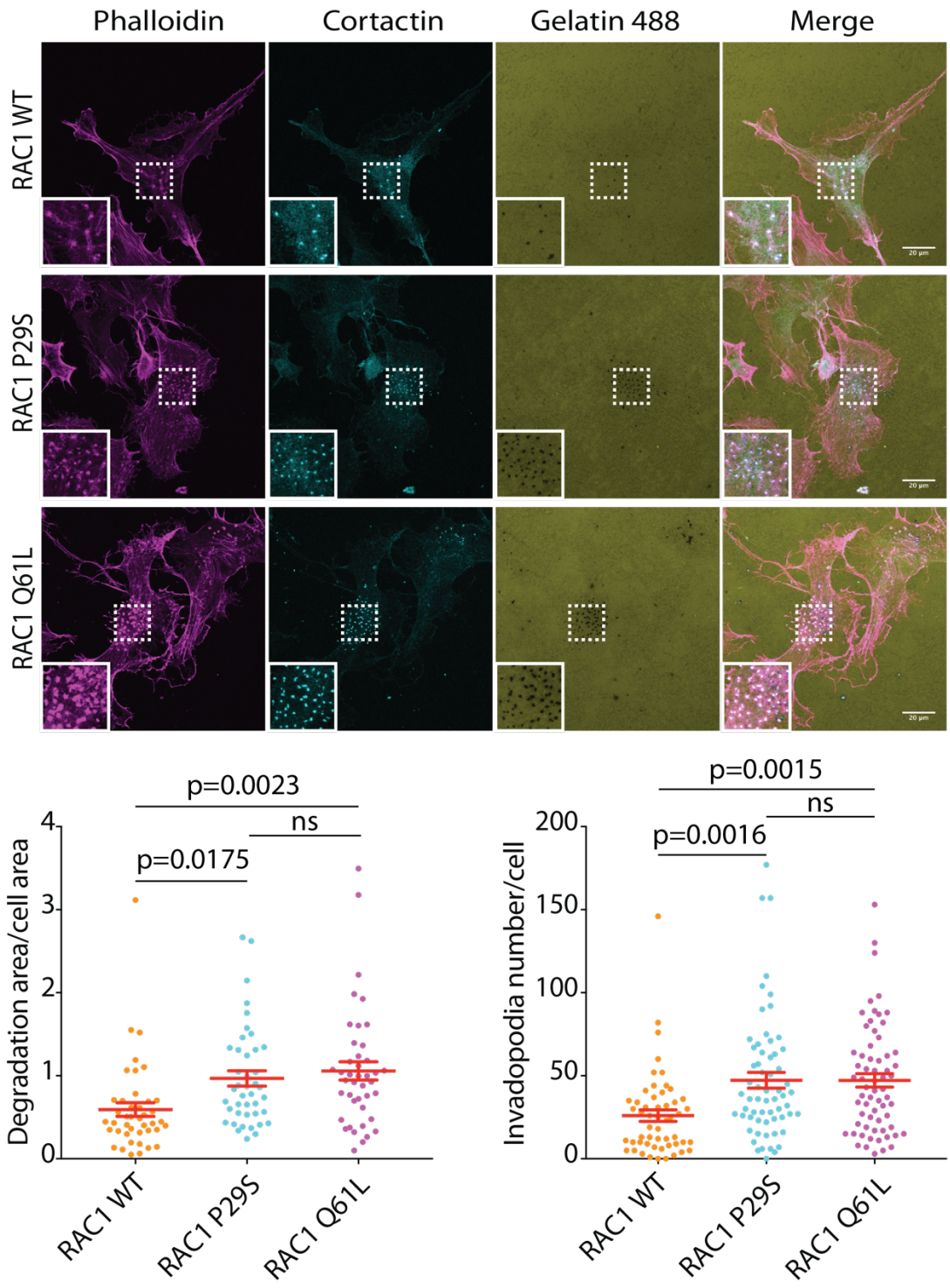

Figure 10.8 The effect of mutant RAC1 is conserved in a second line of melanocyte (Mel-10)

Mel-10 cells were transfected with the same constructs as previously. Cells expressing the mutant RAC1 P29S and Q61L degrade the matrix more and form more numerous invadopodia compared to cells expressing RAC1 WT. Data from 3 independent experiments. Mean ± SEM. ANOVA with multiple comparisons. Scale bar = 20μm. ns = p>0.05.

10.2.3 Active RAC1 mutant increases focal adhesion formation and migration ability of melanocytes

Active RAC1 expression leads to the formation of broader lamellipodia and rounder cells, and RAC1 is involved in nascent focal adhesion formation (Guo et al., 2006). To query a role for Rac1 in focal adhesion formation, we plated the melanocytes on fibronectin-coated coverslips and stained for vinculin and paxillin (Chen et al., 2003, Caccia et al., 2010, Nobes and Hall, 1995). Indeed, melanocytes expressing the active mutant forms of RAC1 form more focal adhesions and at higher density compared to cells expressing WT RAC1 (~70 focal adhesion per cell in the two mutant RAC1 compared to just ~30 in WT RAC1) (Figure 10.9). Again, no differences were observed between the P29S and Q61L expressing cells suggesting their similar activity *in cellulo*.

10.2.4 Active RAC1 affects the migration and potentially the drug response in melanocytes

RAC1 is a master regulator of the actin cytoskeleton. We first decided to test the effect of mutant RAC1 on the migratory behaviour of melanocytes using a random migration assay. Interestingly, all 4 cell lines are extremely dynamic on the 2D fibronectin substrate. Tracking the cells over time reveals the two cell lines expressing the mutant RAC1 are only marginally faster than cells expressing the EV or WT RAC1 (Figure 10.10, upper panel). Interestingly, we notice P29S and Q61L cells also migrate in a less directional manner and are often rotating around itself, while EW and WT cells usually extend longer protrusions and often move in a straight line for longer period of time (Figure 10.10, bottom panel). This perhaps suggests that active RAC1 is important for the rate of lamellipodial protrusion hence affecting the speed, but the enhanced broad lamellipodial spreading might also make the cells more likely to spin around itself. We tested the migration of these cells in a 3D cell-derived matrix (CDM) environment (Figure 10.11). To our surprise, EV cells were much more migratory in this environment compared to WT, P29S and Q61L cells. EV cells usually form 1 single protrusion while the other cell lines form multiple protrusions in all directions. No detected difference in the directionality between cell lines was perhaps the result of the anisotropic nature of the CDM we used, which were highly parallel.

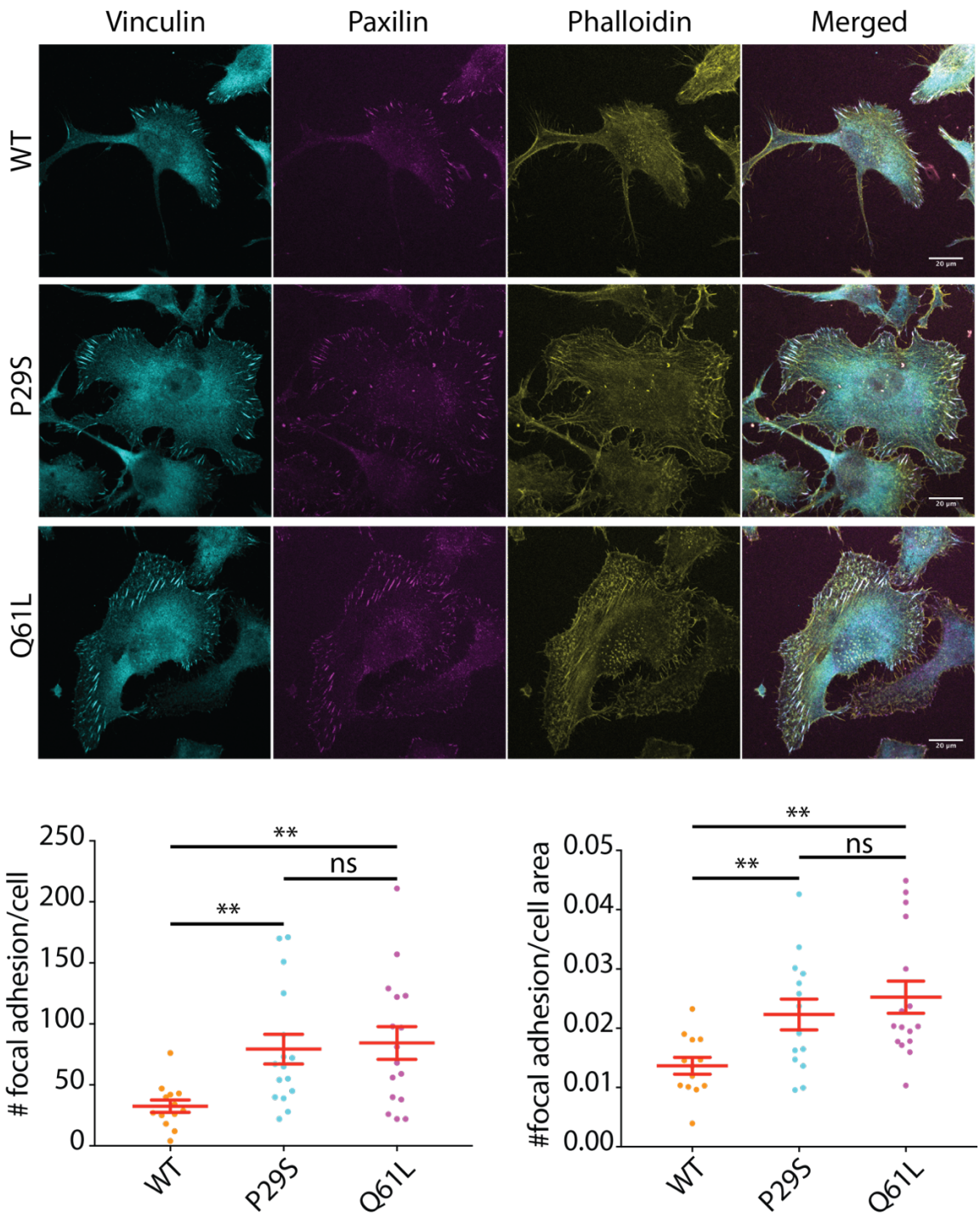

Figure 10.9 Active RAC1 increases focal adhesion formation in melanocytes

Cells expressing either RAC1 P29S or RAC1 Q61L form more focal adhesion per cell (~70 focal adhesions per cell) and at higher density (focal adhesion per cell area) than cells expressing WT RAC1 (~30 focal adhesions per cell). Data from 3 independent experiments. Mean ± SEM. ANOVA with multiple comparisons. ns = $p>0.05$, **$p<0.01$. Scale bar = 20μm.

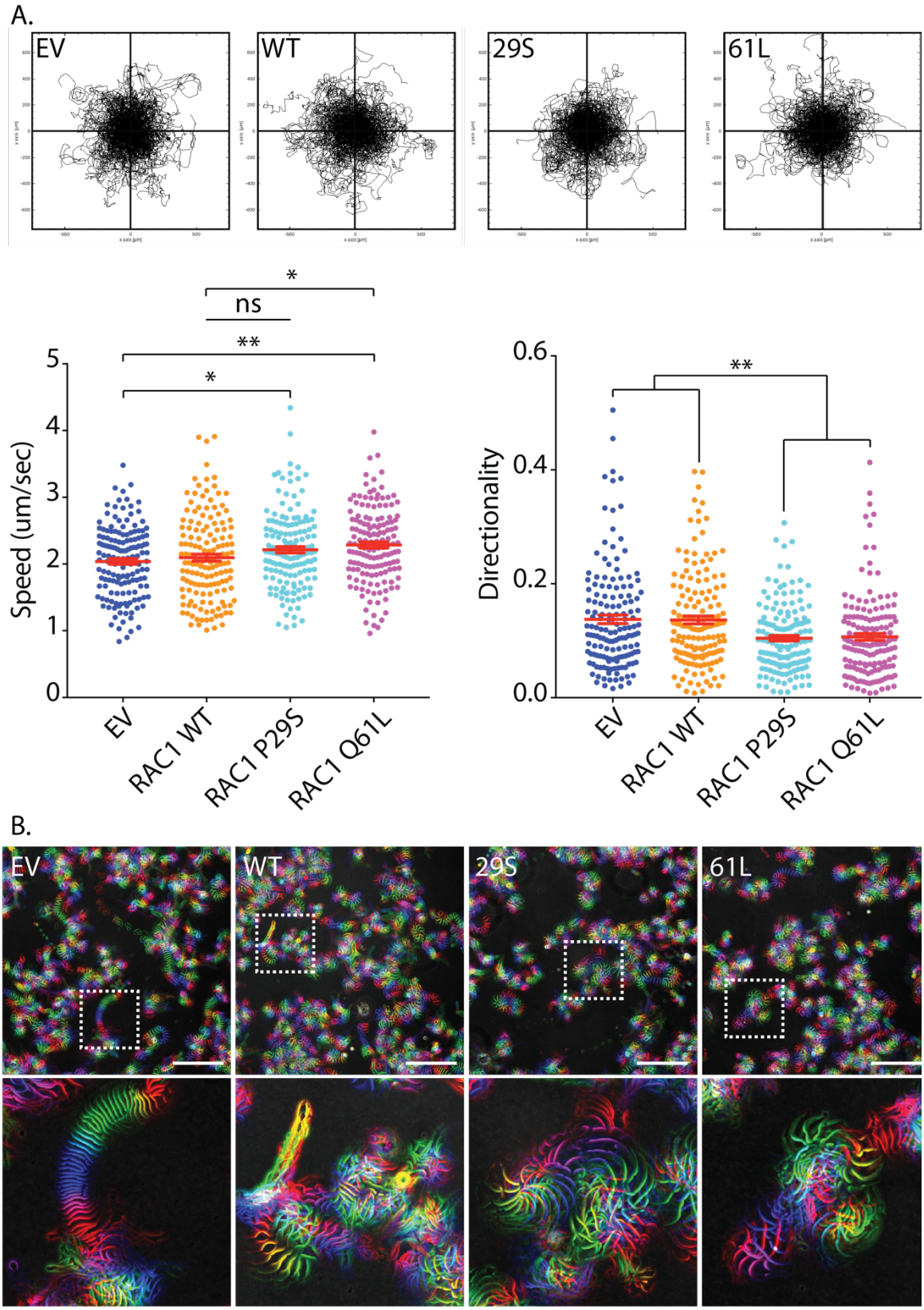

Figure 10.10 Melanocytes expressing active RAC1 are only marginally migrating faster on 2D matrix but with less directionality

A) Spider plots showing migration trajectories of each melanocyte migrating on a 2D fibronectin substratum.

Quantification shows melanocytes expressing RAC1 P29S and Q61L are marginally faster but less directional than the melanocytes expressing EV and perhaps RAC1 WT construct.

B) Temporal-colour coded images of the random migration assay with each shade of colour represents a position in time of each of the cells. EV and WT have more cells with a straight trajectory, while 29S and 61L have more cells engaged in circular motions.

Data from 3 independent experiments. Mean ± SEM. ANOVA with multiple comparisons. ns = $p>0.05$, *$p<0.05$, **$p<0.01$. Scale bar = 200μm.

Closer examination of the morphology of these cells shows us that overexpression of RAC1, whether WT or mutants, resulted in an increase in the number of primary protrusions, which we defined as protrusions directly connected to the cell body, compared to the EV cells (Figure 10.12). These protrusions were often observed distributing around the cells and on average are 150μm in length. In the case of EV cells, there was usually one main but shorter protrusion (100μm on average). This perhaps explains the difference in the migration velocity between these cell lines.

It was reported that BRAF V600/RAC1 P29S mutant-containing melanoma cells are more resistant to BRAF inhibitors (Lionarons et al., 2019, Watson et al., 2014), we tested the effect of Trametinib on our melanocytes. We treated each cell line with either DMSO or 100nM Trametinib and image over 48h using the Incucyte system (Figure 10.13A). Taken into account the number of dead cells, all four cell types grow exponentially over time with the three RAC1-overexpressing cell lines are slightly faster than the EV as expected, in the presence of DMSO. When we treated these cells with 100nM Trametinib, we observed a drastic decline in the proliferation rate of all cell lines, especially the empty vector. Melanocytes containing the two mutant RAC1 seem to be more resistant to the effect of the drug and are slightly better than WT RAC1 cells.

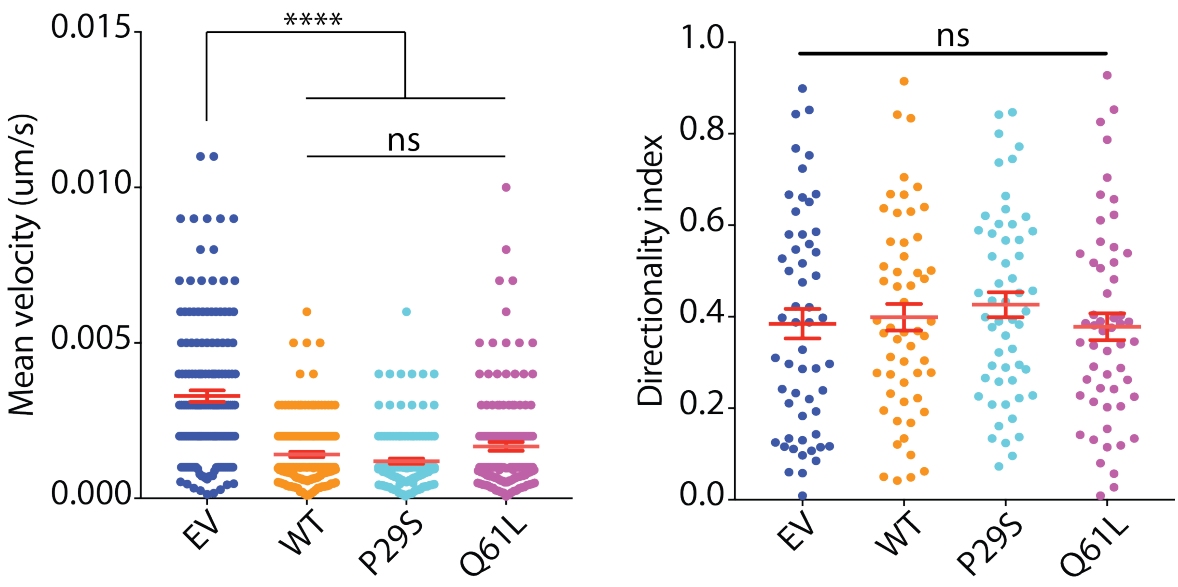

Figure 10.11 Melanocyte migration analysis in 3D cell-derived matrix (CDM)

Cells expressing WT or mutant RAC1 are significantly less motile (~3 times less) in CDM compared to cells expressing an empty vector but with no significant difference in their directionality. Data are from 3 independent experiments. Statistical analysis using ANOVA with multiple comparisons. Mean ± SEM. ns = p>0.05, ****p<0.0001.

Since these cells also expressing endogenous RAC1 alleles that could potentially contribute to the observed phenotypes, we decided to induce the deletion of the endogenous RAC1 alleles using OHT (Figure 10.13B) (Li et al., 2012). Again, in the absence of Trametinib, all four cell lines were growing as expected. The two cell lines expressing WT and P29S RAC1 were more proliferative compared to the EV cells now containing no or minimum amount of endogenous RAC1. Melanocytes expressing Q61L RAC1 proliferating faster than the EV at the beginning but quickly plateaued. This could perhaps due to the constitutively active RAC1 being inhibitory to cell division (Haga and Ridley, 2016, Jordan and Canman, 2012). In the presence of Trametinib, we observe more or less an exact same inhibition effect as before. The EV cells are more strongly inhibited compared to WT, P29S and Q61L cells. One interesting phenotype we observed is the increase in cell spreading after long term exposure to Trametinib. In all four cell types, after 48h, they adopt a flat, fried-egg morphology with broader lamellipodia (Figure 10.14). We observe the same behaviour in melanocytes having their endogenous RAC1 removed (OHT treated cells) (Figure 10.15), nevertheless, cells lacking all RAC1 seem to be the least responsive.

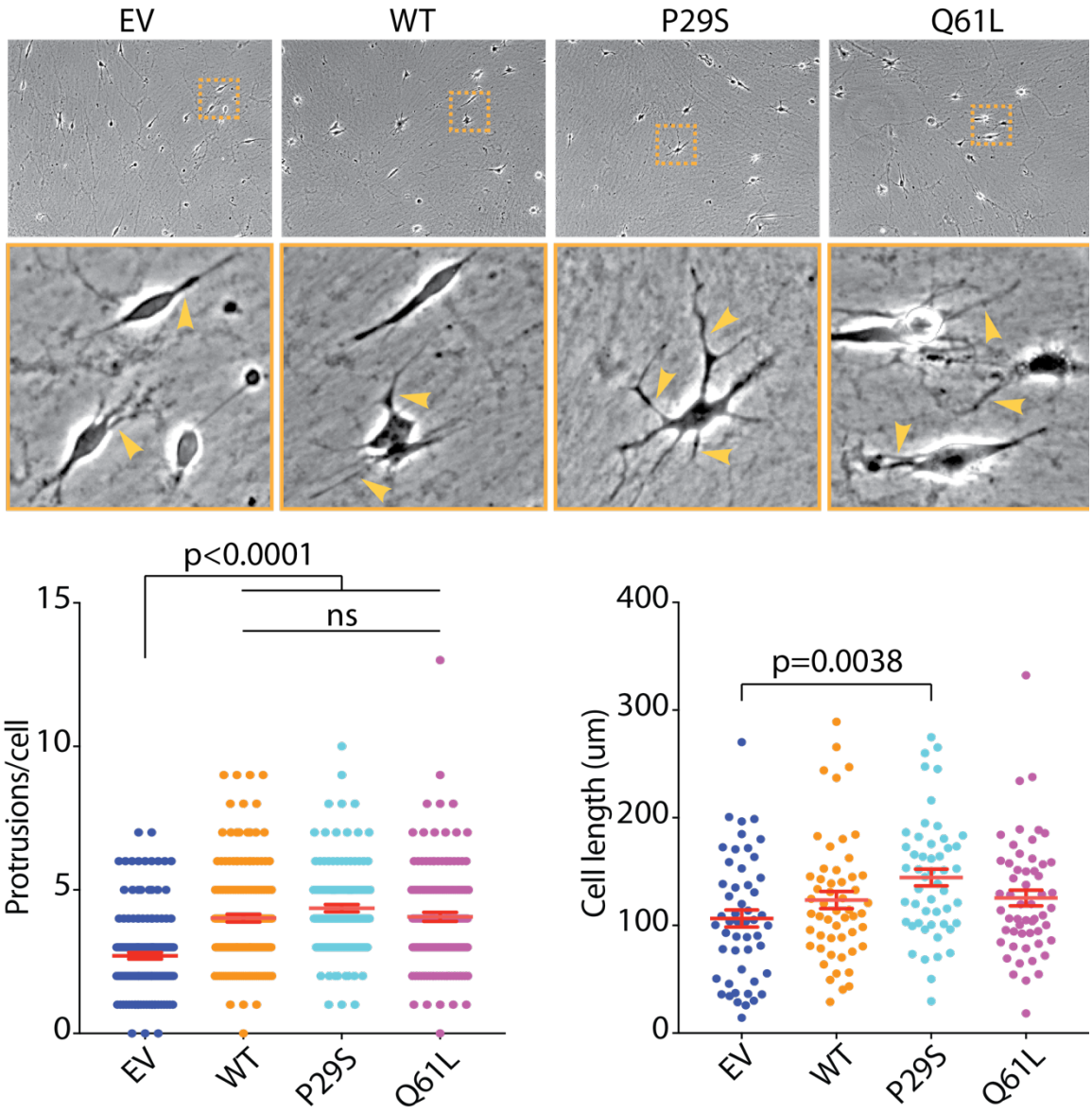

Figure 10.12 Melanocytes expressing RAC1 form more longer protrusions than EV cells

Representative images taking from the time-lapse movie with zoomed images show the differences in the morphology of melanocytes expressing different RAC1 constructs compared to the EV. EV cells form fewer protrusions and are shorter than all three other cells (arrows point at protrusions). Data from 3 independent experiments. Mean ± SEM. ANOVA with multiple comparisons. ns = $p>0.05$.

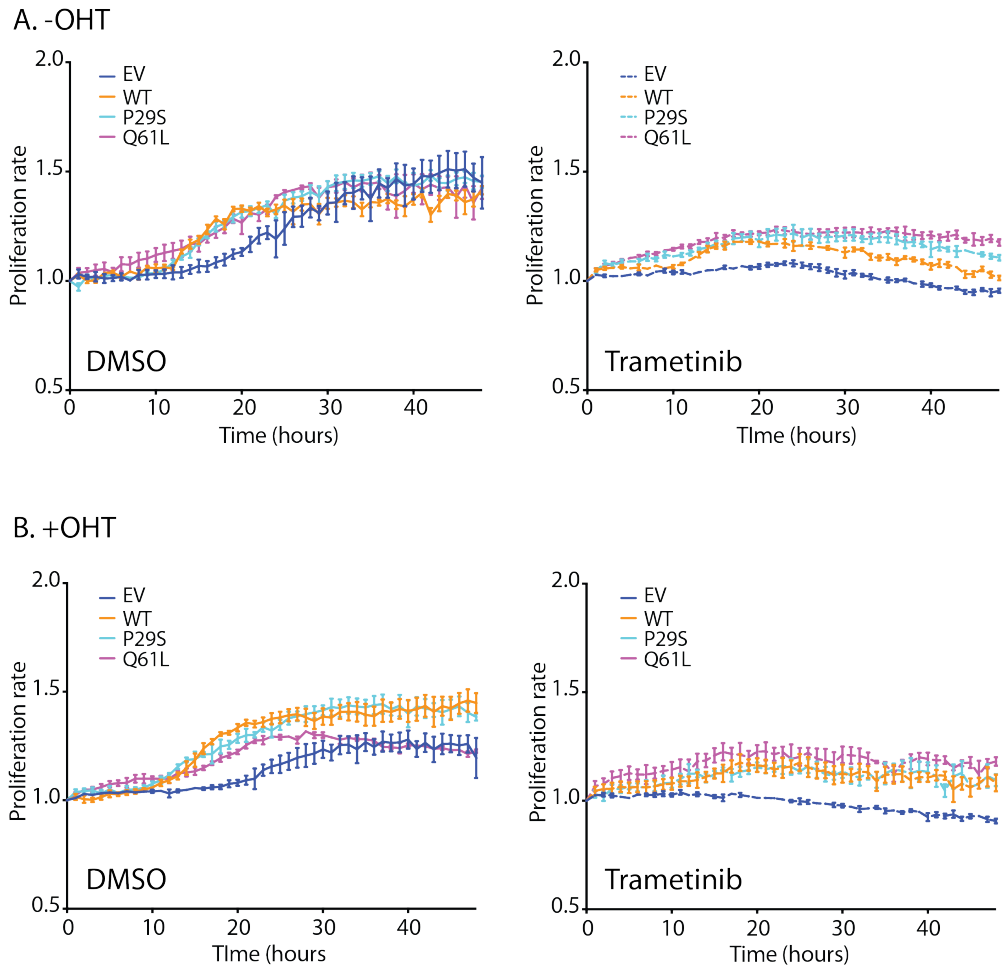

Figure 10.13 Drug response in melanocytes expressing EV or RAC1 constructs

A. -OHT = endogenous RAC1 is present

DMSO treated melanocytes show a slight difference in the proliferation rate (normalised to the original cell number) between melanocytes expressing either WT or mutant RAC1 construct compared to EV cells.

100nM Trametinib treated cells shows the differences in the proliferation rate between the two mutant RAC1 cell lines compared to the EV cells.

B. +OHT = endogenous RAC1 is deleted

DMSO treated melanocytes show a stronger difference between EV and WT and P29S RAC1 cells. Q61L cells show a slight difference at the beginning but quickly plateaued.

100nM Trametinib treated cells now show a strong difference in terms of proliferation between the EV cells and the other three cell lines.

Data from 1 experiment.

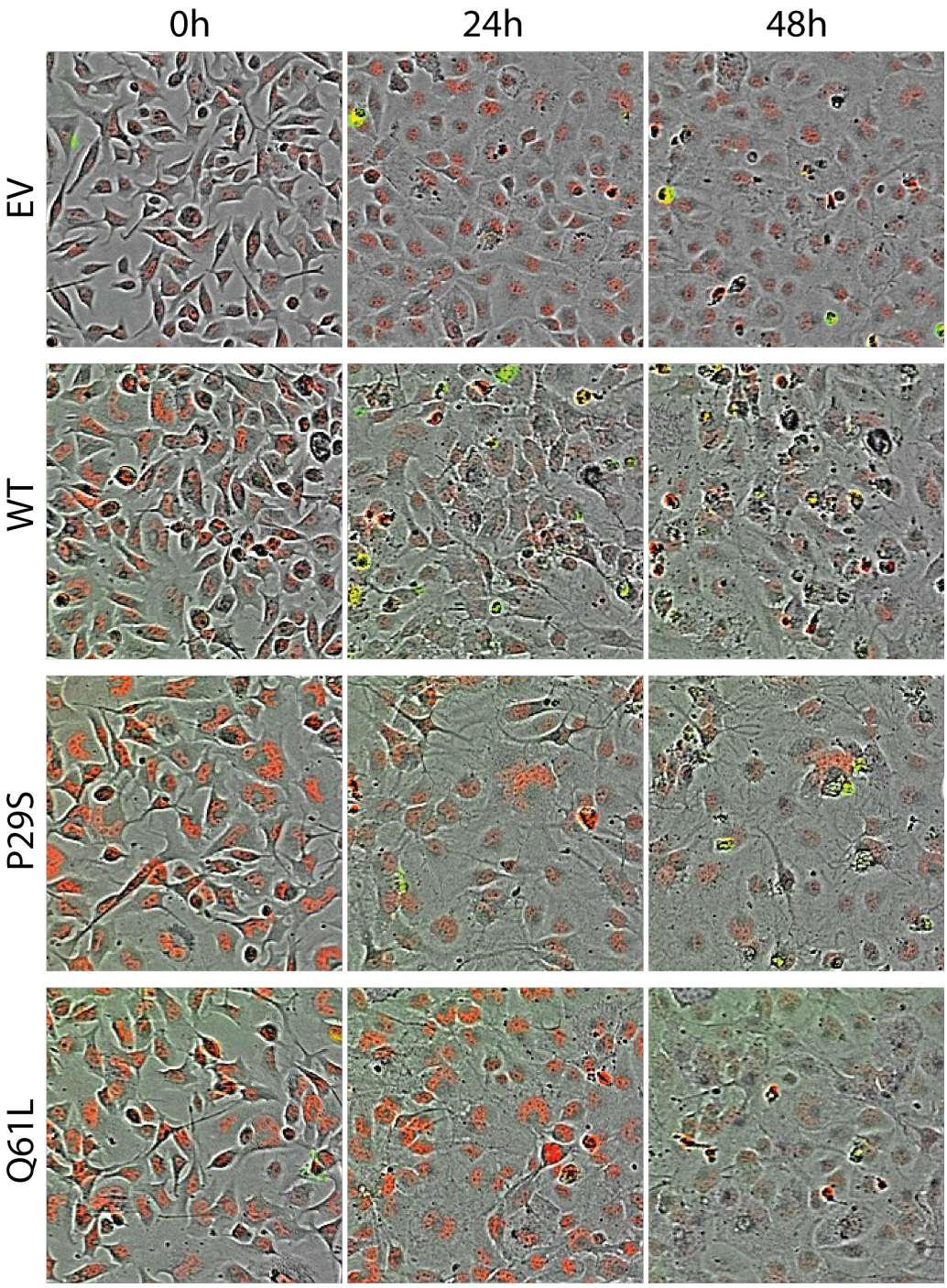

Figure 10.14 Melanocytes (-OHT) morphology after long term exposure to Trametinib

After long term exposure to Trametinib, melanocytes adopt a flat, fried-egg shape irrespective of their RAC1 genotype.

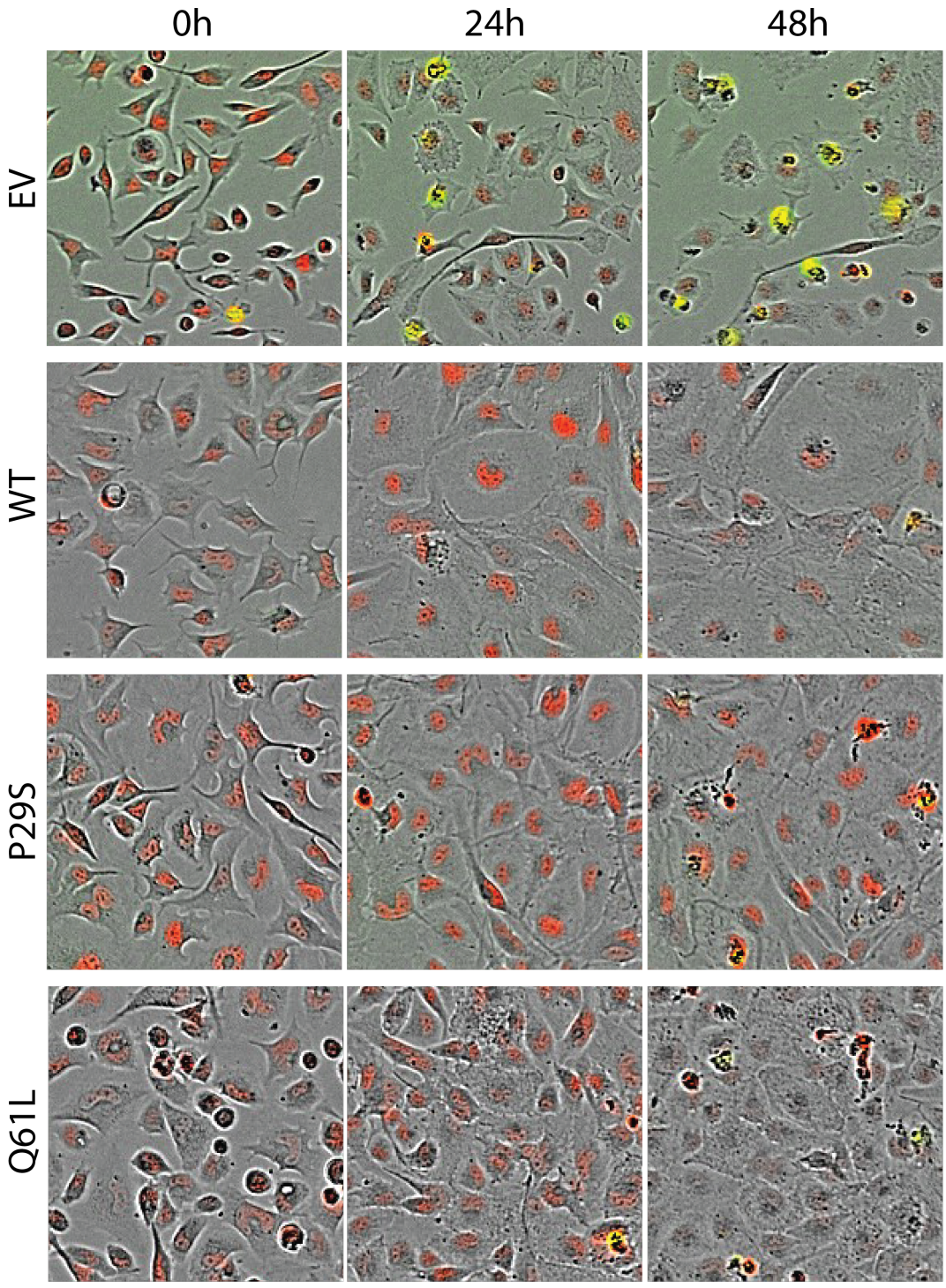

Figure 10.15 Melanocytes lacking endogenous RAC1 (+OHT) also adopt the fried-egg shape morphology after long term exposure to Trametinib

All four cell types adopt the fried-egg shape upon long term exposure to Trametinib. Cells without overexpressing RAC1 and lacking their endogenous RAC1 allele seem to be less effective in forming the large lamellipodia like their counterparts.

10.2.5 RAC1 P29S does not affect tumour growth or lymph node spread in a subcutaneous injection mouse model

Having shown the increased matrix degradation and proliferation of melanocytes expressing active RAC1, we wanted to test for the behaviour of these cells in an *in vivo* model. We utilised a subcutaneous injection mouse model since this is an accepted model for studying tumour growth and uses relatively few mice over a short time period. Melanocytes were prepared in normal growth medium at a concentration of 10,000 cells/ul and injected subcutaneously to the right flank of C57BL/6 mice. We used 8 mice per cell line for a total of 32 mice of the whole cohort. After injection, the cells were left to grow for 1 week before tumours were checked and measured every 2 days until the endpoint (Figure 10.16A). As can be seen, all four cell types are able to form tumours upon injecting into mice (white boxes). Measuring the size of the tumours shows a slight trend in which tumours expressing RAC1 P29S might be slightly bigger at the endpoint compared to the other condition, despite not reaching statistical significance. This would, however, agree with our proliferation data suggesting a slight increase in proliferation of RAC1 P29S cells compared to EV cells at least. Inspecting for lymph node metastasis, however, shows us a surprising observation. Mice injected with EV melanocytes are more frequently (7 out 8 mice) found with lymph node metastasis, both in the inguinal and axillary regions. On the other hand, mice injected with melanocytes with active RAC1 are less frequently found with metastasis, with RAC1 P29S being the least frequent. This, however, would agree with our 3D migration data, where EV melanocytes could be seen migrating faster and more frequent compared to other cell lines. One of the interesting observations we also made is the higher frequency (5 out of 8 mice) in which necrosis was seen in tumours of active RAC1. Mice bearing tumours with constitutively active Rac1 more often displayed ulceration, more severe than with the EV and WT RAC1. This is perhaps a reflection from the increased proliferation of mutant RAC1 cells. Nevertheless, no obvious difference in the time it takes to reach the endpoint between the four conditions is seen, along with no noticeable differences in the percentage of cells in the tumours expressing the proliferative marker Ki67. Our 3D migration data suggest that faster migration may promote lymph node metastasis, but more studies need to be done to see if this is the case.

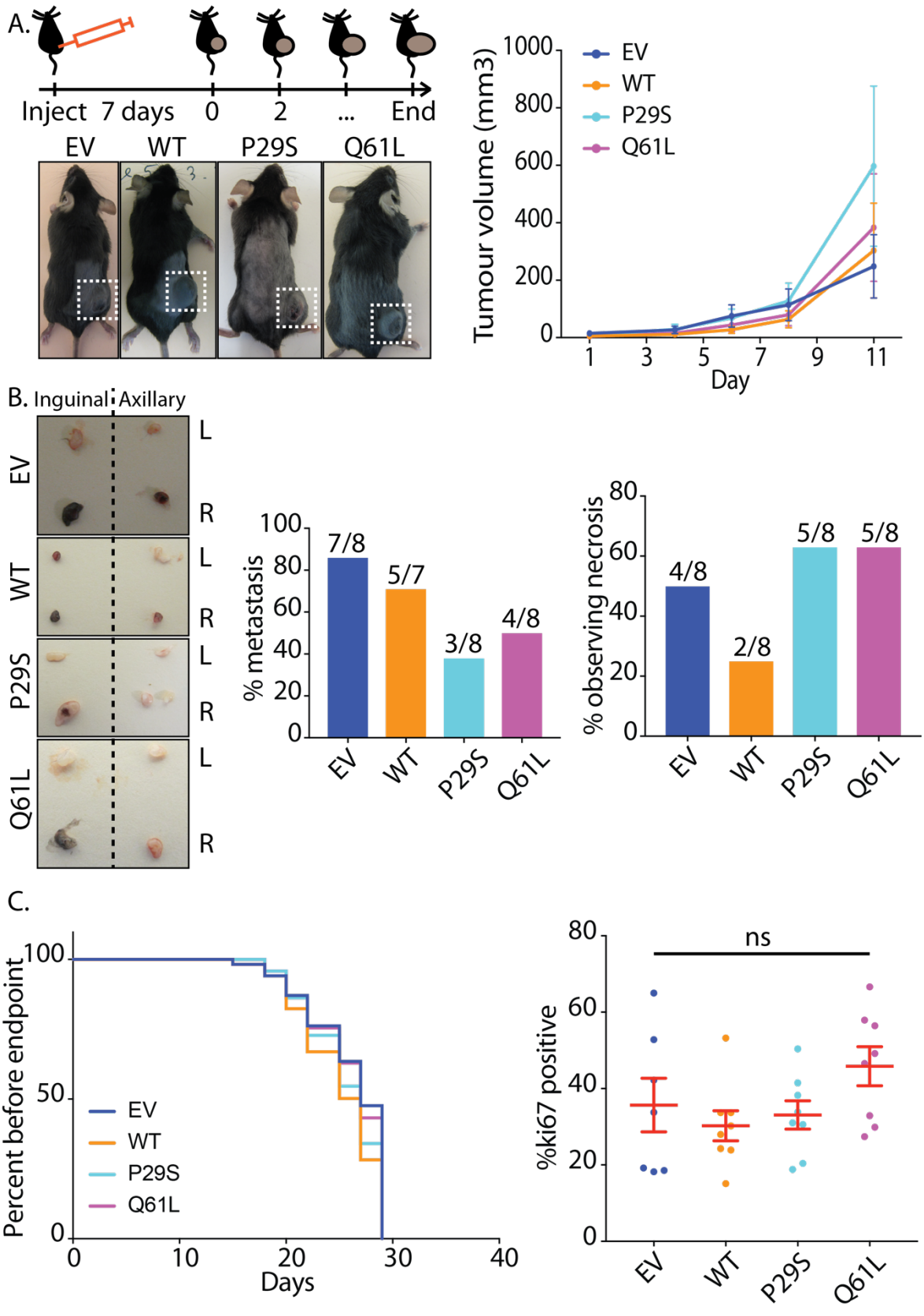

Figure 10.16 Subcutaneous injection model of NRAS transformed melanocytes containing different RAC1 mutants

A. Schematic representation of the subcutaneous model. The endpoint is defined when the tumour reaches 15mm^3 in volume.

Bottom images showing all 4 cell types form visible tumours in C57BL/6 mice upon injection (white boxes). No statistically significant difference in terms of tumour volumes in all 4 types, however, cells containing RAC1 P29S mutant seems to form slightly larger tumours.

B. Both inguinal and axillary lymph nodes were checked for metastasis. Melanocytes containing the EV form the highest number of detectable metastasis compared to the two mutant RAC1 P29S and Q61L (middle graph). However, active mutant RAC1 tend to form more necrotic tumours than the WT and the EV cells.

C. No difference in the percentage of mice before reaching the endpoint is seen between cell types with no significant difference in the percentage of ki67-positive cells in the tumours.

10.3 Discussion

In this chapter, we have explored the potential effects of a new recurrent mutant RAC1 P29S in an NRAS-transformed melanocyte model. We have shown that on a stiff 2D substrate, active RAC1 enhances matrix degradation and migration. However, in 3D CDM, active RAC1-containing melanocytes form multiple protrusions in all directions and thus migrate more slowly than the control. Cells overexpressing RAC1, however, seem to have a proliferative advantage compared to cells that do not have. In human, RAC1 overexpression through gene or chromosome amplification is common across many different types of cancer and is correlated with higher aggressiveness (Bid et al., 2013). RAC1 overexpression might also confer a higher resistant to Trametinib which partly agree with some other reports (Davis et al., 2013, Lionarons et al., 2019, Mohan et al., 2019), but this will require further experiments to make a solid conclusion. In our system, we did not observe any difference between cells overexpressing RAC1 WT and other mutants, while this seemed to be the case in other reports. If time permits, we would like to perform a kill curve experiment where we expose these cells to increasing levels of inhibitor and count the number of cells. We also observe an interesting phenotype where long term exposure to Trametinib leads to increased cell spreading and flattening. A previous report suggests that this phenotype is specific only to A-375 melanoma cells containing RAC1 P29S and not WT nor EV (Mohan et al., 2019). However, our observation seems to disagree with this and suggests this is perhaps a more general RAC1 effect and removing RAC1 seems to reduce the amplitude of this phenotype. It is indeed possible that the differences in the genetic makeup may play a part since our cell lines are NRAS mutant and not BRAF. However, it is also possible that the inhibitor can induce senescence, a state where cells stop proliferating and adopt a spread and flat phenotype. RAC1 suppression by CDK5 was linked to senescence activation (Alexander et al., 2004); but EV melanocytes without the endogenous RAC1 struggled to adopt this spreading phenotype suggest perhaps senescence might not be the main mechanism.

In vivo analysis seems to agree with our *in vitro* data where tumours formed by active RAC1 tend to be larger and more necrotic, perhaps reflecting the faster

growth of these cells. We hypothesize that ulceration might also be the result of increased neo-angiogenesis since secreted metalloproteases such as MMP2 have been linked to increased blood vessel formation in cancer (Rojiani et al., 2010, Webb et al., 2017). Further experiments such as zymography as well as detection of blood vessels in the tumour tissues are needed. Necrosis can also be associated with increased inflammation (Vakkila and Lotze, 2004, Bredholt et al., 2015), it would be interesting to profile the different immune cells that have infiltrated the tumours. The increased growth phenotype also fits nicely with a publication showing that active RAC1 enhances the malignant progression in NRAS-mutant melanoma but not sufficient to drive the tumour formation (Dalton et al., 2013) and that RAC1 P29S-bearing mice form more tumours than WT mice, but not metastasis (Lionarons et al., 2019). It may seem contradictory to our invadopodia data where we showed an increase in the matrix degradation capacity in cells expressing active RAC1. Perhaps in a 2D environment where the substratum surface is stiff glass, this could further promote invadopodia formation in cells with higher RAC1 activity (Parekh and Weaver, 2016, Alexander et al., 2008). However, a softer 3D environment with additional complexities can affect the formation of these invasive protrusion and influence other processes such as growth.

Overall, our data provide the first observation of the effect of active RAC1 in an NRAS-transformed melanocyte model. A quick analysis of the mutual exclusivity between RAC1 and NRAS show a tendency for these two mutations to co-occur (Figure 10.17). In particular, the RAC1 P29S mutant can be found in a significant portion of patient samples along with the NRAS Q61L mutant. Our results support the hypothesis that RAC1 P29S can accelerate the formation of melanoma but not drive metastasis formation *in vivo*.

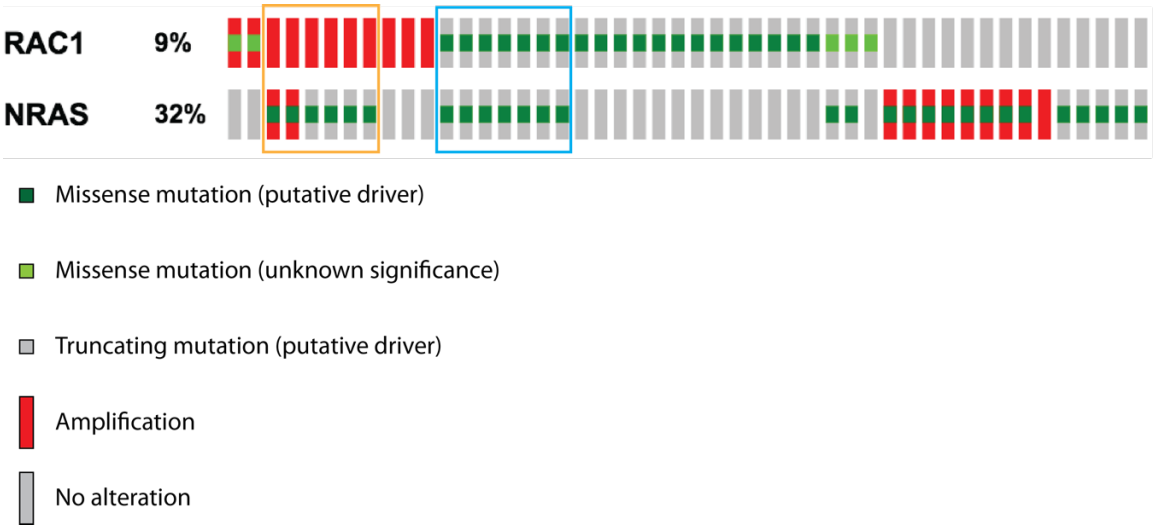

Figure 10.17 Co-occurrence analysis between RAC1 and NRAS mutations in skin cutaneous melanoma

The amplification of RAC1 can be found with the amplification or the mutation NRAS Q61K (orange box), while the mutation RAC1 P29S can be found to co-occur with the mutation NRAS Q61L (cyan box). The overall statistical value for co-occurrence is p = 0.077 and is classified as co-occurrence by cBioportal.

REFERENCES

ABERCROMBIE, M., HEAYSMAN, J. E. & PEGRUM, S. M. 1970. The locomotion of fibroblasts in culture. II. "RRuffling". *Exp Cell Res,* 60**,** 437-44.

ABERCROMBIE, M., HEAYSMAN, J. E. & PEGRUM, S. M. 1971. The locomotion of fibroblasts in culture. IV. Electron microscopy of the leading lamella. *Exp Cell Res,* 67**,** 359-67.

ADAMS, A. E., JOHNSON, D. I., LONGNECKER, R. M., SLOAT, B. F. & PRINGLE, J. R. 1990. CDC42 and CDC43, two additional genes involved in budding and the establishment of cell polarity in the yeast Saccharomyces cerevisiae. *J Cell Biol,* 111**,** 131-42.

AGUIRRE GHISO, J. A., KOVALSKI, K. & OSSOWSKI, L. 1999. Tumor dormancy induced by downregulation of urokinase receptor in human carcinoma involves integrin and MAPK signaling. *J Cell Biol,* 147**,** 89-104.

ALANKO, J., MAI, A., JACQUEMET, G., SCHAUER, K., KAUKONEN, R., SAARI, M., GOUD, B. & IVASKA, J. 2015. Integrin endosomal signalling suppresses anoikis. *Nat Cell Biol,* 17**,** 1412-21.

ALEXANDER, K., YANG, H. S. & HINDS, P. W. 2004. Cellular senescence requires CDK5 repression of Rac1 activity. *Mol Cell Biol,* 24**,** 2808-19.

ALEXANDER, N. R., BRANCH, K. M., PAREKH, A., CLARK, E. S., IWUEKE, I. C., GUELCHER, S. A. & WEAVER, A. M. 2008. Extracellular matrix rigidity promotes invadopodia activity. *Curr Biol,* 18**,** 1295-1299.

ALLEN, W. E., JONES, G. E., POLLARD, J. W. & RIDLEY, A. J. 1997. Rho, Rac and Cdc42 regulate actin organization and cell adhesion in macrophages. *J Cell Sci,* 110 (Pt 6)**,** 707-20.

AMANO, M., FUKATA, Y. & KAIBUCHI, K. 2000. Regulation and functions of Rho-associated kinase. *Exp Cell Res,* 261**,** 44-51.

AMANO, M., NAKAYAMA, M. & KAIBUCHI, K. 2010. Rho-kinase/ROCK: A key regulator of the cytoskeleton and cell polarity. *Cytoskeleton (Hoboken),* 67**,** 545-54.

AMATO, C., THOMASON, P. A., DAVIDSON, A. J., SWAMINATHAN, K., ISMAIL, S., MACHESKY, L. M. & INSALL, R. H. 2019. WASP Restricts Active Rac to Maintain Cells' Front-Rear Polarization. *Curr Biol,* 29**,** 4169-4182 e4.

AMYERE, M., PAYRASTRE, B., KRAUSE, U., VAN DER SMISSEN, P., VEITHEN, A. & COURTOY, P. J. 2000. Constitutive macropinocytosis in oncogene-transformed fibroblasts depends on sequential permanent activation of phosphoinositide 3-kinase and phospholipase C. *Mol Biol Cell,* 11**,** 3453-67.

ANTHIS, N. J., WEGENER, K. L., YE, F., KIM, C., GOULT, B. T., LOWE, E. D., VAKONAKIS, I., BATE, N., CRITCHLEY, D. R., GINSBERG, M. H. & CAMPBELL, I. D. 2009. The structure of an integrin/talin complex reveals the basis of inside-out signal transduction. *EMBO J,* 28**,** 3623-32.

ARAKI, N., EGAMI, Y., WATANABE, Y. & HATAE, T. 2007. Phosphoinositide metabolism during membrane ruffling and macropinosome formation in EGF-stimulated A431 cells. *Exp Cell Res,* 313**,** 1496-507.

ARAKI, N., JOHNSON, M. T. & SWANSON, J. A. 1996. A role for phosphoinositide 3-kinase in the completion of macropinocytosis and phagocytosis by macrophages. *J Cell Biol,* 135**,** 1249-60.

ARIAS-SALGADO, E. G., LIZANO, S., SARKAR, S., BRUGGE, J. S., GINSBERG, M. H. & SHATTIL, S. J. 2003. Src kinase activation by direct interaction with the integrin beta cytoplasmic domain. *Proc Natl Acad Sci U S A,* 100**,** 13298-302.

ARJONEN, A., KAUKONEN, R., MATTILA, E., ROUHI, P., HOGNAS, G., SIHTO, H., MILLER, B. W., MORTON, J. P., BUCHER, E., TAIMEN, P., VIRTAKOIVU, R., CAO, Y., SANSOM, O. J., JOENSUU, H. & IVASKA, J. 2014. Mutant p53-associated myosin-X upregulation promotes breast cancer invasion and metastasis. *J Clin Invest,* 124**,** 1069-82.

ARWERT, E. N., HARNEY, A. S., ENTENBERG, D., WANG, Y., SAHAI, E., POLLARD, J. W. & CONDEELIS, J. S. 2018. A Unidirectional Transition from Migratory to Perivascular Macrophage Is Required for Tumor Cell Intravasation. *Cell Rep,* 23**,** 1239-1248.

ASKARI, J. A., BUCKLEY, P. A., MOULD, A. P. & HUMPHRIES, M. J. 2009. Linking integrin conformation to function. *J Cell Sci,* 122**,** 165-70.

AVIZIENYTE, E., WYKE, A. W., JONES, R. J., MCLEAN, G. W., WESTHOFF, M. A., BRUNTON, V. G. & FRAME, M. C. 2002. Src-induced de-regulation of E-cadherin in colon cancer cells requires integrin signalling. *Nat Cell Biol,* 4**,** 632-8.

AYALA, I., BALDASSARRE, M., CALDIERI, G. & BUCCIONE, R. 2006. Invadopodia: a guided tour. *Eur J Cell Biol,* 85**,** 159-64.

AZEVEDO, C. M. S., MACHADO, R. A., MARTELLI-JUNIOR, H., REIS, S. R. A., PERSUHN, D. C., COLETTA, R. D. & RANGEL, A. 2020. Exploring GRHL3 polymorphisms and SNP-SNP interactions in the risk of non-syndromic oral clefts in the Brazilian population. *Oral Dis,* 26**,** 145-151.

BALLA, A., KIM, Y. J., VARNAI, P., SZENTPETERY, Z., KNIGHT, Z., SHOKAT, K. M. & BALLA, T. 2008. Maintenance of hormone-sensitive phosphoinositide pools in the plasma membrane requires phosphatidylinositol 4-kinase IIIalpha. *Mol Biol Cell,* 19**,** 711-21.

BAR-SAGI, D. & FERAMISCO, J. R. 1986. Induction of membrane ruffling and fluid-phase pinocytosis in quiescent fibroblasts by ras proteins. *Science,* 233**,** 1061-8.

BARBERIS, L., WARY, K. K., FIUCCI, G., LIU, F., HIRSCH, E., BRANCACCIO, M., ALTRUDA, F., TARONE, G. & GIANCOTTI, F. G. 2000. Distinct roles of the adaptor protein Shc and focal adhesion kinase in integrin signaling to ERK. *J Biol Chem,* 275**,** 36532-40.

BARROW-MCGEE, R., KISHI, N., JOFFRE, C., MENARD, L., HERVIEU, A., BAKHOUCHE, B. A., NOVAL, A. J., MAI, A., GUZMAN, C., ROBBEZ-MASSON, L., ITURRIOZ, X., HULIT, J., BRENNAN, C. H., HART, I. R., PARKER, P. J., IVASKA, J. & KERMORGANT, S. 2016. Beta 1-integrin-c-Met cooperation reveals an inside-in survival signalling on autophagy-related endomembranes. *Nat Commun,* 7**,** 11942.

BASS, M. D., SMITH, B. J., PRIGENT, S. A. & CRITCHLEY, D. R. 1999. Talin contains three similar vinculin-binding sites predicted to form an amphipathic helix. *Biochem J,* 341 (Pt 2)**,** 257-63.

BEAR, J. E., SVITKINA, T. M., KRAUSE, M., SCHAFER, D. A., LOUREIRO, J. J., STRASSER, G. A., MALY, I. V., CHAGA, O. Y., COOPER, J. A., BORISY, G. G. & GERTLER, F. B. 2002. Antagonism between Ena/VASP proteins and actin filament capping regulates fibroblast motility. *Cell,* 109**,** 509-21.

BEATY, B. T., SHARMA, V. P., BRAVO-CORDERO, J. J., SIMPSON, M. A., EDDY, R. J., KOLESKE, A. J. & CONDEELIS, J. 2013. beta1 integrin regulates Arg to promote invadopodial maturation and matrix degradation. *Mol Biol Cell,* 24**,** 1661-75, S1-11.

BEAUSEJOUR, M., NOEL, D., THIBODEAU, S., BOUCHARD, V., HARNOIS, C., BEAULIEU, J. F., DEMERS, M. J. & VACHON, P. H. 2012. Integrin/Fak/Src-mediated regulation of cell survival and anoikis in human intestinal epithelial crypt cells: selective engagement and roles of PI3-K isoform complexes. *Apoptosis,* 17**,** 566-78.

BELI, P., MASCHERONI, D., XU, D. & INNOCENTI, M. 2008. WAVE and Arp2/3 jointly inhibit filopodium formation by entering into a complex with mDia2. *Nat Cell Biol,* 10**,** 849-57.

BENINGO, K. A., DEMBO, M., KAVERINA, I., SMALL, J. V. & WANG, Y. L. 2001. Nascent focal adhesions are responsible for the generation of strong propulsive forces in migrating fibroblasts. *J Cell Biol,* 153**,** 881-8.

BERG, J. S. & CHENEY, R. E. 2002. Myosin-X is an unconventional myosin that undergoes intrafilopodial motility. *Nat Cell Biol,* 4**,** 246-50.

BERG, J. S., DERFLER, B. H., PENNISI, C. M., COREY, D. P. & CHENEY, R. E. 2000. Myosin-X, a novel myosin with pleckstrin homology domains, associates with regions of dynamic actin. *J Cell Sci,* 113 Pt 19**,** 3439-51.

BIANCHI-SMIRAGLIA, A., PAESANTE, S. & BAKIN, A. V. 2013. Integrin beta5 contributes to the tumorigenic potential of breast cancer cells through the Src-FAK and MEK-ERK signaling pathways. *Oncogene,* 32**,** 3049-58.

BID, H. K., ROBERTS, R. D., MANCHANDA, P. K. & HOUGHTON, P. J. 2013. RAC1: an emerging therapeutic option for targeting cancer angiogenesis and metastasis. *Mol Cancer Ther,* 12**,** 1925-34.

BIELING, P., HANSEN, S. D., AKIN, O., LI, T. D., HAYDEN, C. C., FLETCHER, D. A. & MULLINS, R. D. 2018. WH2 and proline-rich domains of WASP-family proteins collaborate to accelerate actin filament elongation. *EMBO J,* 37**,** 102-121.

BLANCHOIN, L. & POLLARD, T. D. 1998. Interaction of actin monomers with Acanthamoeba actophorin (ADF/cofilin) and profilin. *J Biol Chem,* 273**,** 25106-11.

BLOOMFIELD, G. & KAY, R. R. 2016. Uses and abuses of macropinocytosis. *J Cell Sci,* 129**,** 2697-705.

BOCZKOWSKA, M., REBOWSKI, G., KAST, D. J. & DOMINGUEZ, R. 2014. Structural analysis of the transitional state of Arp2/3 complex activation by two actin-bound WCAs. *Nat Commun,* 5**,** 3308.

BOHDANOWICZ, M. & GRINSTEIN, S. 2013. Role of phospholipids in endocytosis, phagocytosis, and macropinocytosis. *Physiol Rev,* 93**,** 69-106.

BOKOCH, G. M. & DIEBOLD, B. A. 2002. Current molecular models for NADPH oxidase regulation by Rac GTPase. *Blood,* 100**,** 2692-6.

BOS, J. L., REHMANN, H. & WITTINGHOFER, A. 2007. GEFs and GAPs: critical elements in the control of small G proteins. *Cell,* 129**,** 865-77.

BOUREUX, A., VIGNAL, E., FAURE, S. & FORT, P. 2007. Evolution of the Rho family of ras-like GTPases in eukaryotes. *Mol Biol Evol,* 24**,** 203-16.

BREDHOLT, G., MANNELQVIST, M., STEFANSSON, I. M., BIRKELAND, E., BO, T. H., OYAN, A. M., TROVIK, J., KALLAND, K. H., JONASSEN, I., SALVESEN, H. B., WIK, E. & AKSLEN, L. A. 2015. Tumor necrosis is an important hallmark of aggressive endometrial cancer and associates with hypoxia, angiogenesis and inflammation responses. *Oncotarget,* 6**,** 39676-91.

BRIDGEWATER, R. E., NORMAN, J. C. & CASWELL, P. T. 2012. Integrin trafficking at a glance. *J Cell Sci,* 125**,** 3695-701.

BRYANT, D. M., KERR, M. C., HAMMOND, L. A., JOSEPH, S. R., MOSTOV, K. E., TEASDALE, R. D. & STOW, J. L. 2007. EGF induces macropinocytosis and SNX1-modulated recycling of E-cadherin. *J Cell Sci,* 120**,** 1818-28.

BUCCI, C., LUTCKE, A., STEELE-MORTIMER, O., OLKKONEN, V. M., DUPREE, P., CHIARIELLO, M., BRUNI, C. B., SIMONS, K. & ZERIAL, M. 1995. Co-operative regulation of endocytosis by three Rab5 isoforms. *FEBS Lett,* 366**,** 65-71.

BUCCI, C., WANDINGER-NESS, A., LUTCKE, A., CHIARIELLO, M., BRUNI, C. B. & ZERIAL, M. 1994. Rab5a is a common component of the apical and basolateral endocytic machinery in polarized epithelial cells. *Proc Natl Acad Sci U S A,* 91**,** 5061-5.

BUCKLEY, C. M., GOPALDASS, N., BOSMANI, C., JOHNSTON, S. A., SOLDATI, T., INSALL, R. H. & KING, J. S. 2016. WASH drives early recycling from macropinosomes and phagosomes to maintain surface phagocytic receptors. *Proc Natl Acad Sci U S A,* 113**,** E5906-E5915.

BUCKLEY, C. M. & KING, J. S. 2017. Drinking problems: mechanisms of macropinosome formation and maturation. *FEBS J,* 284**,** 3778-3790.

BUCKLEY, C. M., POTS, H., GUEHO, A., VINES, J. H., MUNN, C. J., PHILLIPS, B. A., GILSBACH, B., TRAYNOR, D., NIKOLAEV, A., SOLDATI, T., PARNELL, A. J., KORTHOLT, A. & KING, J. S. 2020. Coordinated Ras and Rac Activity Shapes Macropinocytic Cups and Enables Phagocytosis of Geometrically Diverse Bacteria. *Curr Biol*.

BUCZYNSKI, G., GROVE, B., NOMURA, A., KLEVE, M., BUSH, J., FIRTEL, R. A. & CARDELLI, J. 1997. Inactivation of two Dictyostelium discoideum genes, DdPIK1 and DdPIK2, encoding proteins related to mammalian phosphatidylinositide 3-kinases, results in defects in endocytosis, lysosome to postlysosome transport, and actin cytoskeleton organization. *J Cell Biol,* 136**,** 1271-86.

BURD, C. & CULLEN, P. J. 2014. Retromer: a master conductor of endosome sorting. *Cold Spring Harb Perspect Biol,* 6.

BYRNE, K. M., MONSEFI, N., DAWSON, J. C., DEGASPERI, A., BUKOWSKI-WILLS, J. C., VOLINSKY, N., DOBRZYNSKI, M., BIRTWISTLE, M. R., TSYGANOV, M. A., KIYATKIN, A., KIDA, K., FINCH, A. J., CARRAGHER, N. O., KOLCH, W., NGUYEN, L. K., VON KRIEGSHEIM, A. & KHOLODENKO, B. N. 2016. Bistability in the Rac1, PAK, and RhoA Signaling Network Drives Actin Cytoskeleton Dynamics and Cell Motility Switches. *Cell Syst,* 2**,** 38-48.

CACCIA, D., MICCICHE, F., CASSINELLI, G., MONDELLINI, P., CASALINI, P. & BONGARZONE, I. 2010. Dasatinib reduces FAK phosphorylation increasing the effects of RPI-1 inhibition in a RET/PTC1-expressing cell line. *Mol Cancer,* 9**,** 278.

CAI, D., CHEN, S. C., PRASAD, M., HE, L., WANG, X., CHOESMEL-CADAMURO, V., SAWYER, J. K., DANUSER, G. & MONTELL, D. J. 2014. Mechanical feedback through E-cadherin promotes direction sensing during collective cell migration. *Cell,* 157**,** 1146-59.

CAMPA, C. C., CIRAOLO, E., GHIGO, A., GERMENA, G. & HIRSCH, E. 2015. Crossroads of PI3K and Rac pathways. *Small GTPases,* 6**,** 71-80.

CANTILE, M., MARRA, L., FRANCO, R., ASCIERTO, P., LIGUORI, G., DE CHIARA, A. & BOTTI, G. 2013. Molecular detection and targeting of EWSR1 fusion transcripts in soft tissue tumors. *Med Oncol,* 30**,** 412.

CANTON, J. 2018. Macropinocytosis: New Insights Into Its Underappreciated Role in Innate Immune Cell Surveillance. *Front Immunol,* 9**,** 2286.

CAREY, S. P., STARCHENKO, A., MCGREGOR, A. L. & REINHART-KING, C. A. 2013. Leading malignant cells initiate collective epithelial cell invasion in a three-dimensional heterotypic tumor spheroid model. *Clin Exp Metastasis,* 30**,** 615-30.

CARLIER, M. F., DUCRUIX, A. & PANTALONI, D. 1999. Signalling to actin: the Cdc42-N-WASP-Arp2/3 connection. *Chem Biol,* 6**,** R235-40.

CARMONA, G., PERERA, U., GILLETT, C., NABA, A., LAW, A. L., SHARMA, V. P., WANG, J., WYCKOFF, J., BALSAMO, M., MOSIS, F., DE PIANO, M., MONYPENNY, J., WOODMAN, N., MCCONNELL, R. E., MOUNEIMNE, G., VAN HEMELRIJCK, M., CAO, Y., CONDEELIS, J., HYNES, R. O., GERTLER, F. B. & KRAUSE, M. 2016. Lamellipodin promotes invasive 3D cancer cell migration via regulated interactions with Ena/VASP and SCAR/WAVE. *Oncogene,* 35**,** 5155-69.

CASE, L. B., ZHANG, X., DITLEV, J. A. & ROSEN, M. K. 2019. Stoichiometry controls activity of phase-separated clusters of actin signaling proteins. *Science,* 363**,** 1093-1097.

CASWELL, P. T., CHAN, M., LINDSAY, A. J., MCCAFFREY, M. W., BOETTIGER, D. & NORMAN, J. C. 2008. Rab-coupling protein coordinates recycling of alpha5beta1 integrin and EGFR1 to promote cell migration in 3D microenvironments. *J Cell Biol,* 183**,** 143-55.

CASWELL, P. T., VADREVU, S. & NORMAN, J. C. 2009. Integrins: masters and slaves of endocytic transport. *Nat Rev Mol Cell Biol,* 10**,** 843-53.

CAVALCANTI-ADAM, E. A., VOLBERG, T., MICOULET, A., KESSLER, H., GEIGER, B. & SPATZ, J. P. 2007. Cell spreading and focal adhesion dynamics are regulated by spacing of integrin ligands. *Biophys J,* 92**,** 2964-74.

CELIA-TERRASSA, T., MECA-CORTES, O., MATEO, F., MARTINEZ DE PAZ, A., RUBIO, N., ARNAL-ESTAPE, A., ELL, B. J., BERMUDO, R., DIAZ, A., GUERRA-REBOLLO, M., LOZANO, J. J., ESTARAS, C., ULLOA, C., ALVAREZ-SIMON, D., MILA, J., VILELLA, R., PACIUCCI, R., MARTINEZ-BALBAS, M., DE HERREROS, A. G., GOMIS, R. R., KANG, Y., BLANCO, J., FERNANDEZ, P. L. & THOMSON, T. M. 2012. Epithelial-mesenchymal transition can suppress major attributes of human epithelial tumor-initiating cells. *J Clin Invest,* 122**,** 1849-68.

CERAMI, E., GAO, J., DOGRUSOZ, U., GROSS, B. E., SUMER, S. O., AKSOY, B. A., JACOBSEN, A., BYRNE, C. J., HEUER, M. L., LARSSON, E., ANTIPIN, Y., REVA, B., GOLDBERG, A. P., SANDER, C. & SCHULTZ, N. 2012. The cBio cancer genomics portal: an open platform for exploring multidimensional cancer genomics data. *Cancer Discov,* 2**,** 401-4.

CHABANON, M., STACHOWIAK, J. C. & RANGAMANI, P. 2017. Systems biology of cellular membranes: a convergence with biophysics. *Wiley Interdiscip Rev Syst Biol Med,* 9.

CHAFFER, C. L. & WEINBERG, R. A. 2011. A perspective on cancer cell metastasis. *Science,* 331**,** 1559-64.

CHALUT, K. J. & PALUCH, E. K. 2016. The Actin Cortex: A Bridge between Cell Shape and Function. *Dev Cell,* 38**,** 571-3.

CHAPMAN, A., FERNANDEZ DEL AMA, L., FERGUSON, J., KAMARASHEV, J., WELLBROCK, C. & HURLSTONE, A. 2014. Heterogeneous tumor subpopulations cooperate to drive invasion. *Cell Rep,* 8**,** 688-95.

CHATTARAGADA, M. S., RIGANTI, C., SASSOE, M., PRINCIPE, M., SANTAMORENA, M. M., ROUX, C., CURCIO, C., EVANGELISTA, A., ALLAVENA, P., SALVIA, R., RUSEV, B., SCARPA, A., CAPPELLO, P. & NOVELLI, F. 2018. FAM49B, a novel regulator of mitochondrial function and integrity that suppresses tumor metastasis. *Oncogene,* 37**,** 697-709.

CHEN, B., CHOU, H. T., BRAUTIGAM, C. A., XING, W., YANG, S., HENRY, L., DOOLITTLE, L. K., WALZ, T. & ROSEN, M. K. 2017. Rac1 GTPase activates the WAVE regulatory complex through two distinct binding sites. *Elife,* 6.

CHEN, C., GUO, Q., SHI, J., JIAO, X., LV, K., LIU, X., JIANG, Y., HUI, X. & SONG, T. 2018. Genetic variants of MGMT, RHPN2, and FAM49A contributed to susceptibility of nonsyndromic orofacial clefts in a Chinese population. *J Oral Pathol Med,* 47**,** 796-801.

CHEN, C. S., ALONSO, J. L., OSTUNI, E., WHITESIDES, G. M. & INGBER, D. E. 2003. Cell shape provides global control of focal adhesion assembly. *Biochem Biophys Res Commun,* 307**,** 355-61.

CHEN, P., CESCON, M. & BONALDO, P. 2013. Collagen VI in cancer and its biological mechanisms. *Trends Mol Med,* 19**,** 410-7.

CHEN, P. I., KONG, C., SU, X. & STAHL, P. D. 2009. Rab5 isoforms differentially regulate the trafficking and degradation of epidermal growth factor receptors. *J Biol Chem,* 284**,** 30328-38.

CHEN, Z., BOREK, D., PADRICK, S. B., GOMEZ, T. S., METLAGEL, Z., ISMAIL, A. M., UMETANI, J., BILLADEAU, D. D., OTWINOWSKI, Z. & ROSEN, M. K. 2010. Structure and control of the actin regulatory WAVE complex. *Nature,* 468**,** 533-8.

CHERTKOVA, A. O., MASTOP, M., POSTMA, M., VAN BOMMEL, N., VAN DER NIET, S., BATENBURG, K. L., JOOSEN, L., GADELLA, T. W. J., OKADA, Y. & GOEDHART, J. 2020. Robust and Bright Genetically Encoded Fluorescent Markers for Highlighting Structures and Compartments in Mammalian Cells. *BioRXIV*.

CHITTY, J. L., FILIPE, E. C., LUCAS, M. C., HERRMANN, D., COX, T. R. & TIMPSON, P. 2018. Recent advances in understanding the complexities of metastasis. *F1000Res,* 7.

CHODNIEWICZ, D. & KLEMKE, R. L. 2004. Regulation of integrin-mediated cellular responses through assembly of a CAS/Crk scaffold. *Biochim Biophys Acta,* 1692**,** 63-76.

CHRISTOFORIDES, C., RAINERO, E., BROWN, K. K., NORMAN, J. C. & TOKER, A. 2012. PKD controls alphavbeta3 integrin recycling and tumor cell invasive migration through its substrate Rabaptin-5. *Dev Cell,* 23**,** 560-72.

CHUGH, P. & PALUCH, E. K. 2018. The actin cortex at a glance. *J Cell Sci,* 131.

CHUMA, M., SAKAMOTO, M., YASUDA, J., FUJII, G., NAKANISHI, K., TSUCHIYA, A., OHTA, T., ASAKA, M. & HIROHASHI, S. 2004. Overexpression of cortactin is involved in motility and metastasis of hepatocellular carcinoma. *J Hepatol,* 41**,** 629-36.

CLARK, E. S., WHIGHAM, A. S., YARBROUGH, W. G. & WEAVER, A. M. 2007. Cortactin is an essential regulator of matrix metalloproteinase secretion and extracellular matrix degradation in invadopodia. *Cancer Res,* 67**,** 4227-35.

CLARK, K., PANKOV, R., TRAVIS, M. A., ASKARI, J. A., MOULD, A. P., CRAIG, S. E., NEWHAM, P., YAMADA, K. M. & HUMPHRIES, M. J. 2005. A specific alpha5beta1-integrin conformation promotes directional integrin translocation and fibronectin matrix formation. *J Cell Sci,* 118**,** 291-300.

COMMISSO, C., DAVIDSON, S. M., SOYDANER-AZELOGLU, R. G., PARKER, S. J., KAMPHORST, J. J., HACKETT, S., GRABOCKA, E., NOFAL, M., DREBIN, J. A., THOMPSON, C. B., RABINOWITZ, J. D., METALLO, C. M., VANDER HEIDEN, M. G. & BAR-SAGI, D. 2013. Macropinocytosis of protein is an amino acid supply route in Ras-transformed cells. *Nature,* 497**,** 633-7.

CONDON, N. D., HEDDLESTON, J. M., CHEW, T. L., LUO, L., MCPHERSON, P. S., IOANNOU, M. S., HODGSON, L., STOW, J. L. & WALL, A. A. 2018. Macropinosome formation by tent pole ruffling in macrophages. *J Cell Biol,* 217**,** 3873-3885.

COOPER, J. & GIANCOTTI, F. G. 2019. Integrin Signaling in Cancer: Mechanotransduction, Stemness, Epithelial Plasticity, and Therapeutic Resistance. *Cancer Cell,* 35**,** 347-367.

CULLEN, P. J. & STEINBERG, F. 2018. To degrade or not to degrade: mechanisms and significance of endocytic recycling. *Nat Rev Mol Cell Biol,* 19**,** 679-696.

DA COSTA, P. E., BATISTA, W. L., MORAES, M. S., STERN, A. & MONTEIRO, H. P. 2018. Src kinase activation by nitric oxide promotes resistance to anoikis in tumour cell lines. *Free Radic Res,* 52**,** 592-604.

DALTON, L. E., KAMARASHEV, J., BARINAGA-REMENTERIA RAMIREZ, I., WHITE, G., MALLIRI, A. & HURLSTONE, A. 2013. Constitutive RAC activation is not sufficient to initiate melanocyte neoplasia but accelerates malignant progression. *J Invest Dermatol,* 133**,** 1572-81.

DANG, I., GORELIK, R., SOUSA-BLIN, C., DERIVERY, E., GUERIN, C., LINKNER, J., NEMETHOVA, M., DUMORTIER, J. G., GIGER, F. A., CHIPYSHEVA, T. A., ERMILOVA, V. D., VACHER, S., CAMPANACCI, V., HERRADA, I., PLANSON, A. G., FETICS, S., HENRIOT, V., DAVID, V., OGUIEVETSKAIA, K., LAKISIC, G., PIERRE, F., STEFFEN, A., BOYREAU, A., PEYRIERAS, N., ROTTNER, K., ZINN-JUSTIN, S., CHERFILS, J., BIECHE, I., ALEXANDROVA, A. Y., DAVID, N. B., SMALL, J. V., FAIX, J., BLANCHOIN, L. & GAUTREAU, A. 2013. Inhibitory signalling to the Arp2/3 complex steers cell migration. *Nature,* 503**,** 281-4.

DANSON, C. M., POCHA, S. M., BLOOMBERG, G. B. & CORY, G. O. 2007. Phosphorylation of WAVE2 by MAP kinases regulates persistent cell migration and polarity. *J Cell Sci,* 120**,** 4144-54.

DAROQUI, M. C., VAZQUEZ, P., BAL DE KIER JOFFE, E., BAKIN, A. V. & PURICELLI, L. I. 2012. TGF-beta autocrine pathway and MAPK signaling promote cell invasiveness and in vivo mammary adenocarcinoma tumor progression. *Oncol Rep,* 28**,** 567-75.

DATTA, S. R., KATSOV, A., HU, L., PETROS, A., FESIK, S. W., YAFFE, M. B. & GREENBERG, M. E. 2000. 14-3-3 proteins and survival kinases cooperate to inactivate BAD by BH3 domain phosphorylation. *Mol Cell,* 6**,** 41-51.

DAVIDSON, A. J. & INSALL, R. H. 2011. Actin-based motility: WAVE regulatory complex structure reopens old SCARs. *Curr Biol,* 21**,** R66-8.

DAVIES, H., BIGNELL, G. R., COX, C., STEPHENS, P., EDKINS, S., CLEGG, S., TEAGUE, J., WOFFENDIN, H., GARNETT, M. J., BOTTOMLEY, W., DAVIS, N., DICKS, E., EWING, R., FLOYD, Y., GRAY, K., HALL, S., HAWES, R., HUGHES, J., KOSMIDOU, V., MENZIES, A., MOULD, C., PARKER, A., STEVENS, C., WATT, S., HOOPER, S., WILSON, R., JAYATILAKE, H., GUSTERSON, B. A., COOPER, C., SHIPLEY, J., HARGRAVE, D., PRITCHARD-JONES, K., MAITLAND, N., CHENEVIX-TRENCH, G., RIGGINS, G. J., BIGNER, D. D., PALMIERI, G., COSSU, A., FLANAGAN, A., NICHOLSON, A., HO, J. W., LEUNG, S. Y., YUEN, S. T., WEBER, B. L., SEIGLER, H. F., DARROW, T. L., PATERSON, H., MARAIS, R., MARSHALL, C. J., WOOSTER, R., STRATTON, M. R. & FUTREAL, P. A. 2002. Mutations of the BRAF gene in human cancer. *Nature,* 417**,** 949-54.

DAVIS, M. J., HA, B. H., HOLMAN, E. C., HALABAN, R., SCHLESSINGER, J. & BOGGON, T. J. 2013. RAC1P29S is a spontaneously activating cancer-associated GTPase. *Proc Natl Acad Sci U S A,* 110**,** 912-7.

DE CARVALHO, T. M., BARRIAS, E. S. & DE SOUZA, W. 2015. Macropinocytosis: a pathway to protozoan infection. *Front Physiol,* 6**,** 106.

DE FRANCESCHI, N., ARJONEN, A., ELKHATIB, N., DENESSIOUK, K., WROBEL, A. G., WILSON, T. A., POUWELS, J., MONTAGNAC, G., OWEN, D. J. & IVASKA, J. 2016. Selective integrin endocytosis is driven by interactions between the integrin alpha-chain and AP2. *Nat Struct Mol Biol,* 23**,** 172-9.

DE HOOP, M. J., HUBER, L. A., STENMARK, H., WILLIAMSON, E., ZERIAL, M., PARTON, R. G. & DOTTI, C. G. 1994. The involvement of the small GTP-binding protein Rab5a in neuronal endocytosis. *Neuron,* 13**,** 11-22.

DE LUCA, M. & BUCCI, C. 2014. A new V-ATPase regulatory mechanism mediated by the Rab interacting lysosomal protein (RILP). *Commun Integr Biol,* 7.

DE, P., ASKE, J. C. & DEY, N. 2019. RAC1 Takes the Lead in Solid Tumors. *Cells,* 8.

DERIVERY, E., SOUSA, C., GAUTIER, J. J., LOMBARD, B., LOEW, D. & GAUTREAU, A. 2009. The Arp2/3 activator WASH controls the fission of endosomes through a large multiprotein complex. *Dev Cell,* 17**,** 712-23.

DERYUGINA, E. I. & QUIGLEY, J. P. 2015. Tumor angiogenesis: MMP-mediated induction of intravasation- and metastasis-sustaining neovasculature. *Matrix Biol,* 44-46**,** 94-112.

DEVITT, B., LIU, W., SALEMI, R., WOLFE, R., KELLY, J., TZEN, C. Y., DOBROVIC, A. & MCARTHUR, G. 2011. Clinical outcome and pathological features associated with NRAS mutation in cutaneous melanoma. *Pigment Cell Melanoma Res,* 24**,** 666-72.

DI SARIO, A., BENDIA, E., SVEGLIATI-BARONI, G., MARZIONI, M., RIDOLFI, F., TROZZI, L., UGILI, L., SACCOMANNO, S., JEZEQUEL, A. M. & BENEDETTI, A. 2002. Rearrangement of the cytoskeletal network induced by platelet-derived growth factor in rat hepatic stellate cells: role of different intracellular signalling pathways. *J Hepatol,* 36**,** 179-90.

DOLAT, L. & SPILIOTIS, E. T. 2016. Septins promote macropinosome maturation and traffic to the lysosome by facilitating membrane fusion. *J Cell Biol,* 214**,** 517-27.

DOSCH, A. R., DAI, X., GAIDARSKI III, A. A., SHI, C., CASTELLANOS, J. A., VANSAUN, M. N., MERCHANT, N. B. & NAGATHIHALLI, N. S. 2019. Src kinase inhibition restores E-cadherin expression in dasatinib-sensitive pancreatic cancer cells. *Oncotarget,* 10**,** 1056-1069.

DOZYNKIEWICZ, M. A., JAMIESON, N. B., MACPHERSON, I., GRINDLAY, J., VAN DEN BERGHE, P. V., VON THUN, A., MORTON, J. P., GOURLEY, C., TIMPSON, P., NIXON, C., MCKAY, C. J., CARTER, R., STRACHAN, D., ANDERSON, K., SANSOM, O. J., CASWELL, P. T. & NORMAN, J. C. 2012. Rab25 and CLIC3 collaborate to promote integrin recycling from late endosomes/lysosomes and drive cancer progression. *Dev Cell,* 22**,** 131-45.

DUTTA, A., LI, J., LU, H., AKECH, J., PRATAP, J., WANG, T., ZERLANKO, B. J., FITZGERALD, T. J., JIANG, Z., BIRBE, R., WIXTED, J., VIOLETTE, S. M., STEIN, J. L., STEIN, G. S., LIAN, J. B. & LANGUINO, L. R. 2014. Integrin alphavbeta6 promotes an osteolytic program in cancer cells by upregulating MMP2. *Cancer Res,* 74**,** 1598-608.

ECHARRI, A. & DEL POZO, M. A. 2015. Caveolae - mechanosensitive membrane invaginations linked to actin filaments. *J Cell Sci,* 128**,** 2747-58.

EDDY, R. J., WEIDMANN, M. D., SHARMA, V. P. & CONDEELIS, J. S. 2017. Tumor Cell Invadopodia: Invasive Protrusions that Orchestrate Metastasis. *Trends Cell Biol,* 27**,** 595-607.

EDEN, S., ROHATGI, R., PODTELEJNIKOV, A. V., MANN, M. & KIRSCHNER, M. W. 2002. Mechanism of regulation of WAVE1-induced actin nucleation by Rac1 and Nck. *Nature,* 418**,** 790-3.

EGAMI, Y., TAGUCHI, T., MAEKAWA, M., ARAI, H. & ARAKI, N. 2014. Small GTPases and phosphoinositides in the regulatory mechanisms of macropinosome formation and maturation. *Front Physiol,* 5**,** 374.

ELLER-BORGES, R., BATISTA, W. L., DA COSTA, P. E., TOKIKAWA, R., CURCIO, M. F., STRUMILLO, S. T., SARTORI, A., MORAES, M. S., DE OLIVEIRA, G. A., TAHA, M. O., FONSECA, F. V., STERN, A. & MONTEIRO, H. P. 2015. Ras, Rac1, and phosphatidylinositol-3-kinase (PI3K) signaling in nitric oxide induced endothelial cell migration. *Nitric Oxide,* 47**,** 40-51.

ELUMALAI, S., KARUNAKARAN, U., LEE, I. K., MOON, J. S. & WON, K. C. 2017. Rac1-NADPH oxidase signaling promotes CD36 activation under glucotoxic conditions in pancreatic beta cells. *Redox Biol,* 11**,** 126-134.

ESKOVA, A., KNAPP, B., MATELSKA, D., REUSING, S., ARJONEN, A., LISAUSKAS, T., PEPPERKOK, R., RUSSELL, R., EILS, R., IVASKA, J., KADERALI, L., ERFLE, H. & STARKUVIENE, V. 2014. An RNAi screen identifies KIF15 as a novel regulator of the endocytic trafficking of integrin. *J Cell Sci,* 127**,** 2433-47.

ETIENNE-MANNEVILLE, S. & HALL, A. 2002. Rho GTPases in cell biology. *Nature,* 420**,** 629-35.

EVANS, I. R., GHAI, P. A., URBANCIC, V., TAN, K. L. & WOOD, W. 2013. SCAR/WAVE-mediated processing of engulfed apoptotic corpses is essential for effective macrophage migration in Drosophila. *Cell Death Differ,* 20**,** 709-20.

FACKLER, O. T. & GROSSE, R. 2008. Cell motility through plasma membrane blebbing. *J Cell Biol,* 181**,** 879-84.

FAFILEK, B., BALEK, L., BOSAKOVA, M. K., VARECHA, M., NITA, A., GREGOR, T., GUDERNOVA, I., KRENOVA, J., GHOSH, S., PISKACEK, M., JONATOVA, L., CERNOHORSKY, N. H., ZIEBA, J. T., KOSTAS, M., HAUGSTEN, E. M., WESCHE, J., ERNEUX, C., TRANTIREK, L., KRAKOW, D. & KREJCI, P. 2018. The inositol phosphatase SHIP2 enables sustained ERK activation downstream of FGF receptors by recruiting Src kinases. *Sci Signal,* 11.

FERRARI, R., MARTIN, G., TAGIT, O., GUICHARD, A., CAMBI, A., VOITURIEZ, R., VASSILOPOULOS, S. & CHAVRIER, P. 2019. MT1-MMP directs force-producing proteolytic contacts that drive tumor cell invasion. *Nat Commun,* 10**,** 4886.

FERREIRA, A. P. A. & BOUCROT, E. 2018. Mechanisms of Carrier Formation during Clathrin-Independent Endocytosis. *Trends Cell Biol,* 28**,** 188-200.

FONSECA, T. B., SANCHEZ-GUERRERO, A., MILOSEVIC, I. & RAIMUNDO, N. 2019. Mitochondrial fission requires DRP1 but not dynamins. *Nature,* 570**,** E34-E42.

FORT, L., BATISTA, J. M., THOMASON, P. A., SPENCE, H. J., WHITELAW, J. A., TWEEDY, L., GREAVES, J., MARTIN, K. J., ANDERSON, K. I., BROWN, P., LILLA, S., NEILSON, M. P., TAFELMEYER, P., ZANIVAN, S., ISMAIL, S., BRYANT, D. M., TOMKINSON, N. C. O.,

CHAMBERLAIN, L. H., MASTICK, G. S., INSALL, R. H. & MACHESKY, L. M. 2018. Fam49/CYRI interacts with Rac1 and locally suppresses protrusions. *Nat Cell Biol,* 20**,** 1159-1171.
FOURRIERE, L., KASRI, A., GAREIL, N., BARDIN, S., BOUSQUET, H., PEREIRA, D., PEREZ, F., GOUD, B., BONCOMPAIN, G. & MISEREY-LENKEI, S. 2019. RAB6 and microtubules restrict protein secretion to focal adhesions. *J Cell Biol,* 218**,** 2215-2231.
FUJII, M., KAWAI, K., EGAMI, Y. & ARAKI, N. 2013. Dissecting the roles of Rac1 activation and deactivation in macropinocytosis using microscopic photo-manipulation. *Sci Rep,* 3**,** 2385.
FUJITA, Y., KRAUSE, G., SCHEFFNER, M., ZECHNER, D., LEDDY, H. E., BEHRENS, J., SOMMER, T. & BIRCHMEIER, W. 2002. Hakai, a c-Cbl-like protein, ubiquitinates and induces endocytosis of the E-cadherin complex. *Nat Cell Biol,* 4**,** 222-31.
GAHMBERG, C. G., FAGERHOLM, S. C., NURMI, S. M., CHAVAKIS, T., MARCHESAN, S. & GRONHOLM, M. 2009. Regulation of integrin activity and signalling. *Biochim Biophys Acta,* 1790**,** 431-44.
GAO, J., AKSOY, B. A., DOGRUSOZ, U., DRESDNER, G., GROSS, B., SUMER, S. O., SUN, Y., JACOBSEN, A., SINHA, R., LARSSON, E., CERAMI, E., SANDER, C. & SCHULTZ, N. 2013. Integrative analysis of complex cancer genomics and clinical profiles using the cBioPortal. *Sci Signal,* 6**,** pl1.
GAY, L. J. & FELDING-HABERMANN, B. 2011. Contribution of platelets to tumour metastasis. *Nat Rev Cancer,* 11**,** 123-34.
GILLI, F., LINDBERG, R. L., VALENTINO, P., MARNETTO, F., MALUCCHI, S., SALA, A., CAPOBIANCO, M., DI SAPIO, A., SPERLI, F., KAPPOS, L., CALOGERO, R. A. & BERTOLOTTO, A. 2010. Learning from nature: pregnancy changes the expression of inflammation-related genes in patients with multiple sclerosis. *PLoS One,* 5**,** e8962.
GILLI, F., NAVONE, N. D., PERGA, S., MARNETTO, F., CALDANO, M., CAPOBIANCO, M., PULIZZI, A., MALUCCHI, S. & BERTOLOTTO, A. 2011. Loss of braking signals during inflammation: a factor affecting the development and disease course of multiple sclerosis. *Arch Neurol,* 68**,** 879-88.
GILMORE, A. P. & BURRIDGE, K. 1996. Regulation of vinculin binding to talin and actin by phosphatidyl-inositol-4-5-bisphosphate. *Nature,* 381**,** 531-5.
GIMENEZ-ANDRES, M., COPIC, A. & ANTONNY, B. 2018. The Many Faces of Amphipathic Helices. *Biomolecules,* 8.
GLIGORIJEVIC, B., WYCKOFF, J., YAMAGUCHI, H., WANG, Y., ROUSSOS, E. T. & CONDEELIS, J. 2012. N-WASP-mediated invadopodium formation is involved in intravasation and lung metastasis of mammary tumors. *J Cell Sci,* 125**,** 724-34.
GOLEY, E. D. & WELCH, M. D. 2006. The ARP2/3 complex: an actin nucleator comes of age. *Nat Rev Mol Cell Biol,* 7**,** 713-26.
GOMEZ, T. S. & BILLADEAU, D. D. 2009. A FAM21-containing WASH complex regulates retromer-dependent sorting. *Dev Cell,* 17**,** 699-711.
GORVEL, J. P., CHAVRIER, P., ZERIAL, M. & GRUENBERG, J. 1991. rab5 controls early endosome fusion in vitro. *Cell,* 64**,** 915-25.
GOTTSCHALK, K. E. 2005. A coiled-coil structure of the alphaIIbbeta3 integrin transmembrane and cytoplasmic domains in its resting state. *Structure,* 13**,** 703-12.
GRACEFFA, P. & DOMINGUEZ, R. 2003. Crystal structure of monomeric actin in the ATP state. Structural basis of nucleotide-dependent actin dynamics. *J Biol Chem,* 278**,** 34172-80.
GRAFINGER, O. R., GORSHTEIN, G., STIRLING, T., BRASHER, M. I. & COPPOLINO, M. G. 2020. beta1 integrin-mediated signaling regulates MT1-MMP phosphorylation to promote tumor cell invasion. *J Cell Sci,* 133.
GU, Z., NOSS, E. H., HSU, V. W. & BRENNER, M. B. 2011. Integrins traffic rapidly via circular dorsal ruffles and macropinocytosis during stimulated cell migration. *J Cell Biol,* 193**,** 61-70.
GUADAMILLAS, M. C., CEREZO, A. & DEL POZO, M. A. 2011. Overcoming anoikis--pathways to anchorage-independent growth in cancer. *J Cell Sci,* 124**,** 3189-97.
GUNNING, P. W., GHOSHDASTIDER, U., WHITAKER, S., POPP, D. & ROBINSON, R. C. 2015. The evolution of compositionally and functionally distinct actin filaments. *J Cell Sci,* 128**,** 2009-19.
GUO, F., DEBIDDA, M., YANG, L., WILLIAMS, D. A. & ZHENG, Y. 2006. Genetic deletion of Rac1 GTPase reveals its critical role in actin stress fiber formation and focal adhesion complex assembly. *J Biol Chem,* 281**,** 18652-9.
GUO, W. & GIANCOTTI, F. G. 2004. Integrin signalling during tumour progression. *Nat Rev Mol Cell Biol,* 5**,** 816-26.
HAEMMERLE, M., TAYLOR, M. L., GUTSCHNER, T., PRADEEP, S., CHO, M. S., SHENG, J., LYONS, Y. M., NAGARAJA, A. S., DOOD, R. L., WEN, Y., MANGALA, L. S., HANSEN, J. M., RUPAIMOOLE, R., GHARPURE, K. M., RODRIGUEZ-AGUAYO, C., YIM, S. Y., LEE, J. S., IVAN, C., HU, W., LOPEZ-BERESTEIN, G., WONG, S. T., KARLAN, B. Y., LEVINE, D. A., LIU, J., AFSHAR-KHARGHAN, V. & SOOD, A. K. 2017. Platelets reduce anoikis and promote metastasis by activating YAP1 signaling. *Nat Commun,* 8**,** 310.
HAGA, R. B. & RIDLEY, A. J. 2016. Rho GTPases: Regulation and roles in cancer cell biology. *Small GTPases,* 7**,** 207-221.
HAGA, Y., MIWA, N., JAHANGEER, S., OKADA, T. & NAKAMURA, S. 2009. CtBP1/BARS is an activator of phospholipase D1 necessary for agonist-induced macropinocytosis. *EMBO J,* 28**,** 1197-207.
HAGEDORN, E. J., KELLEY, L. C., NAEGELI, K. M., WANG, Z., CHI, Q. & SHERWOOD, D. R. 2014. ADF/cofilin promotes invadopodial membrane recycling during cell invasion in vivo. *J Cell Biol,* 204**,** 1209-18.
HALABAN, R. 2015. RAC1 and melanoma. *Clin Ther,* 37**,** 682-5.
HALET, G. 2005. Imaging phosphoinositide dynamics using GFP-tagged protein domains. *Biol Cell,* 97**,** 501-18.
HALET, G. & CARROLL, J. 2007. Rac activity is polarized and regulates meiotic spindle stability and anchoring in mammalian oocytes. *Dev Cell,* 12**,** 309-17.
HALL, D. B.-S. A. A. 2000. Ras and Rho GTPases- A Family Reunion. *Cell,* 103**,** 227-238.
HAMADI, A., BOUALI, M., DONTENWILL, M., STOECKEL, H., TAKEDA, K. & RONDE, P. 2005. Regulation of focal adhesion dynamics and disassembly by phosphorylation of FAK at tyrosine 397. *J Cell Sci,* 118**,** 4415-25.
HAN, J., LIM, C. J., WATANABE, N., SORIANI, A., RATNIKOV, B., CALDERWOOD, D. A., PUZON-MCLAUGHLIN, W., LAFUENTE, E. M., BOUSSIOTIS, V. A., SHATTIL, S. J. & GINSBERG, M. H. 2006. Reconstructing and deconstructing agonist-induced activation of integrin alphaIIbbeta3. *Curr Biol,* 16**,** 1796-806.
HANSEN, C. G., MOROISHI, T. & GUAN, K. L. 2015. YAP and TAZ: a nexus for Hippo signaling and beyond. *Trends Cell Biol,* 25**,** 499-513.
HARMER, S. L. & DEFRANCO, A. L. 1997. Shc contains two Grb2 binding sites needed for efficient formation of complexes with SOS in B lymphocytes. *Mol Cell Biol,* 17**,** 4087-95.
HASEGAWA, J., TOKUDA, E., TENNO, T., TSUJITA, K., SAWAI, H., HIROAKI, H., TAKENAWA, T. & ITOH, T. 2011. SH3YL1 regulates dorsal ruffle formation by a novel phosphoinositide-binding domain. *J Cell Biol,* 193**,** 901-16.
HAUN, F., NEUMANN, S., PEINTNER, L., WIELAND, K., HABICHT, J., SCHWAN, C., OSTEVOLD, K., KOCZOROWSKA, M. M., BINIOSSEK, M., KIST, M., BUSCH, H., BOERRIES, M., DAVIS, R. J., MAURER, U., SCHILLING, O., AKTORIES, K. & BORNER, C. 2018. Identification of a novel anoikis signalling pathway using the fungal virulence factor gliotoxin. *Nat Commun,* 9**,** 3524.
HAZAN, R. B., PHILLIPS, G. R., QIAO, R. F., NORTON, L. & AARONSON, S. A. 2000. Exogenous expression of N-cadherin in breast cancer cells induces cell migration, invasion, and metastasis. *J Cell Biol,* 148**,** 779-90.

HE, S., HUANG, Q., HU, J., LI, L., XIAO, Y., YU, H., HAN, Z., WANG, T., ZHOU, W., WEI, H. & XIAO, J. 2019. EWS-FLI1-mediated tenascin-C expression promotes tumour progression by targeting MALAT1 through integrin alpha5beta1-mediated YAP activation in Ewing sarcoma. *Br J Cancer,* 121**,** 922-933.

HEEKE, S., MOGRABI, B., ALIX-PANABIERES, C. & HOFMAN, P. 2019. Never Travel Alone: The Crosstalk of Circulating Tumor Cells and the Blood Microenvironment. *Cells,* 8.

HELGESON, L. A. & NOLEN, B. J. 2013. Mechanism of synergistic activation of Arp2/3 complex by cortactin and N-WASP. *Elife,* 2**,** e00884.

HETMANSKI, J. H. R., DE BELLY, H., BUSNELLI, I., WARING, T., NAIR, R. V., SOKLEVA, V., DOBRE, O., CAMERON, A., GAUTHIER, N., LAMAZE, C., SWIFT, J., DEL CAMPO, A., STARBORG, T., ZECH, T., GOETZ, J. G., PALUCH, E. K., SCHWARTZ, J. M. & CASWELL, P. T. 2019. Membrane Tension Orchestrates Rear Retraction in Matrix-Directed Cell Migration. *Dev Cell,* 51**,** 460-475 e10.

HIRATA, E., GIROTTI, M. R., VIROS, A., HOOPER, S., SPENCER-DENE, B., MATSUDA, M., LARKIN, J., MARAIS, R. & SAHAI, E. 2015. Intravital imaging reveals how BRAF inhibition generates drug-tolerant microenvironments with high integrin beta1/FAK signaling. *Cancer Cell,* 27**,** 574-88.

HODGE, R. G. & RIDLEY, A. J. 2016. Regulating Rho GTPases and their regulators. *Nat Rev Mol Cell Biol,* 17**,** 496-510.

HOGAN, A., YAKUBCHYK, Y., CHABOT, J., OBAGI, C., DAHER, E., MAEKAWA, K. & GEE, S. H. 2004. The phosphoinositol 3,4-bisphosphate-binding protein TAPP1 interacts with syntrophins and regulates actin cytoskeletal organization. *J Biol Chem,* 279**,** 53717-24.

HONG, W. 2019. SNXs take center stage in endosomal sorting. *Nat Cell Biol,* 21**,** 1175-1177.

HOSHINO, A., COSTA-SILVA, B., SHEN, T. L., RODRIGUES, G., HASHIMOTO, A., TESIC MARK, M., MOLINA, H., KOHSAKA, S., DI GIANNATALE, A., CEDER, S., SINGH, S., WILLIAMS, C., SOPLOP, N., URYU, K., PHARMER, L., KING, T., BOJMAR, L., DAVIES, A. E., ARARSO, Y., ZHANG, T., ZHANG, H., HERNANDEZ, J., WEISS, J. M., DUMONT-COLE, V. D., KRAMER, K., WEXLER, L. H., NARENDRAN, A., SCHWARTZ, G. K., HEALEY, J. H., SANDSTROM, P., LABORI, K. J., KURE, E. H., GRANDGENETT, P. M., HOLLINGSWORTH, M. A., DE SOUSA, M., KAUR, S., JAIN, M., MALLYA, K., BATRA, S. K., JARNAGIN, W. R., BRADY, M. S., FODSTAD, O., MULLER, V., PANTEL, K., MINN, A. J., BISSELL, M. J., GARCIA, B. A., KANG, Y., RAJASEKHAR, V. K., GHAJAR, C. M., MATEI, I., PEINADO, H., BROMBERG, J. & LYDEN, D. 2015. Tumour exosome integrins determine organotropic metastasis. *Nature,* 527**,** 329-35.

HOU, T., TONG, C., KAZOBINKA, G., ZHANG, W., HUANG, X., HUANG, Y. & ZHANG, Y. 2016. Expression of COL6A1 predicts prognosis in cervical cancer patients. *Am J Transl Res,* 8**,** 2838-44.

HUGHES, T. E., ZHANG, H., LOGOTHETIS, D. E. & BERLOT, C. H. 2001. Visualization of a functional Galpha q-green fluorescent protein fusion in living cells. Association with the plasma membrane is disrupted by mutational activation and by elimination of palmitoylation sites, but not be activation mediated by receptors or AlF4. *J Biol Chem,* 276**,** 4227-35.

HUNTER, J. C., MANANDHAR, A., CARRASCO, M. A., GURBANI, D., GONDI, S. & WESTOVER, K. D. 2015. Biochemical and Structural Analysis of Common Cancer-Associated KRAS Mutations. *Mol Cancer Res,* 13**,** 1325-35.

HUTTENLOCHER, A. & HORWITZ, A. R. 2011. Integrins in cell migration. *Cold Spring Harb Perspect Biol,* 3**,** a005074.

HUVENEERS, S. & DANEN, E. H. 2009. Adhesion signaling - crosstalk between integrins, Src and Rho. *J Cell Sci,* 122**,** 1059-69.

IKEDA, Y., KAWAI, K., IKAWA, A., KAWAMOTO, K., EGAMI, Y. & ARAKI, N. 2017. Rac1 switching at the right time and location is essential for Fcgamma receptor-mediated phagosome formation. *J Cell Sci,* 130**,** 2530-2540.

INNOCENTI, M., FRITTOLI, E., PONZANELLI, I., FALCK, J. R., BRACHMANN, S. M., DI FIORE, P. P. & SCITA, G. 2003. Phosphoinositide 3-kinase activates Rac by entering in a complex with Eps8, Abi1, and Sos-1. *J Cell Biol,* 160**,** 17-23.

IVERSEN, L., TU, H. L., LIN, W. C., CHRISTENSEN, S. M., ABEL, S. M., IWIG, J., WU, H. J., GUREASKO, J., RHODES, C., PETIT, R. S., HANSEN, S. D., THILL, P., YU, C. H., STAMOU, D., CHAKRABORTY, A. K., KURIYAN, J. & GROVES, J. T. 2014. Molecular kinetics. Ras activation by SOS: allosteric regulation by altered fluctuation dynamics. *Science,* 345**,** 50-4.

IYENGAR, P., ESPINA, V., WILLIAMS, T. W., LIN, Y., BERRY, D., JELICKS, L. A., LEE, H., TEMPLE, K., GRAVES, R., POLLARD, J., CHOPRA, N., RUSSELL, R. G., SASISEKHARAN, R., TROCK, B. J., LIPPMAN, M., CALVERT, V. S., PETRICOIN, E. F., 3RD, LIOTTA, L., DADACHOVA, E., PESTELL, R. G., LISANTI, M. P., BONALDO, P. & SCHERER, P. E. 2005. Adipocyte-derived collagen VI affects early mammary tumor progression in vivo, demonstrating a critical interaction in the tumor/stroma microenvironment. *J Clin Invest,* 115**,** 1163-76.

JACQUEMET, G., GREEN, D. M., BRIDGEWATER, R. E., VON KRIEGSHEIM, A., HUMPHRIES, M. J., NORMAN, J. C. & CASWELL, P. T. 2013. RCP-driven alpha5beta1 recycling suppresses Rac and promotes RhoA activity via the RacGAP1-IQGAP1 complex. *J Cell Biol,* 202**,** 917-35.

JACQUEMET, G., PAATERO, I., CARISEY, A. F., PADZIK, A., ORANGE, J. S., HAMIDI, H. & IVASKA, J. 2017. FiloQuant reveals increased filopodia density during breast cancer progression. *J Cell Biol,* 216**,** 3387-3403.

JACQUES, C., RENEMA, N., LEZOT, F., ORY, B., WALKLEY, C. R., GRIGORIADIS, A. E. & HEYMANN, D. 2018. Small animal models for the study of bone sarcoma pathogenesis:characteristics, therapeutic interests and limitations. *J Bone Oncol,* 12**,** 7-13.

JERRELL, R. J. & PAREKH, A. 2016. Matrix rigidity differentially regulates invadopodia activity through ROCK1 and ROCK2. *Biomaterials,* 84**,** 119-129.

JOBERTY, G., PETERSEN, C., GAO, L. & MACARA, I. G. 2000. The cell-polarity protein Par6 links Par3 and atypical protein kinase C to Cdc42. *Nat Cell Biol,* 2**,** 531-9.

JOHNSON, D. E., OSTROWSKI, P., JAUMOUILLE, V. & GRINSTEIN, S. 2016. The position of lysosomes within the cell determines their luminal pH. *J Cell Biol,* 212**,** 677-92.

JOHNSON, H. E., KING, S. J., ASOKAN, S. B., ROTTY, J. D., BEAR, J. E. & HAUGH, J. M. 2015. F-actin bundles direct the initiation and orientation of lamellipodia through adhesion-based signaling. *J Cell Biol,* 208**,** 443-55.

JOHNSON, R. P. & CRAIG, S. W. 1995. F-actin binding site masked by the intramolecular association of vinculin head and tail domains. *Nature,* 373**,** 261-4.

JORDAN, S. N. & CANMAN, J. C. 2012. Rho GTPases in animal cell cytokinesis: an occupation by the one percent. *Cytoskeleton (Hoboken),* 69**,** 919-30.

JORDENS, I., FERNANDEZ-BORJA, M., MARSMAN, M., DUSSELJEE, S., JANSSEN, L., CALAFAT, J., JANSSEN, H., WUBBOLTS, R. & NEEFJES, J. 2001. The Rab7 effector protein RILP controls lysosomal transport by inducing the recruitment of dynein-dynactin motors. *Curr Biol,* 11**,** 1680-5.

JOURNET, A., KLEIN, G., BRUGIERE, S., VANDENBROUCK, Y., CHAPEL, A., KIEFFER, S., BRULEY, C., MASSELON, C. & AUBRY, L. 2012. Investigating the macropinocytic proteome of Dictyostelium amoebae by high-resolution mass spectrometry. *Proteomics,* 12**,** 241-5.

JU, J. A., GODET, I., YE, I. C., BYUN, J., JAYATILAKA, H., LEE, S. J., XIANG, L., SAMANTA, D., LEE, M. H., WU, P. H., WIRTZ, D., SEMENZA, G. L. & GILKES, D. M. 2017. Hypoxia Selectively Enhances Integrin alpha5beta1 Receptor Expression in Breast Cancer to Promote Metastasis. *Mol Cancer Res,* 15**,** 723-734.

JUIN, A., SPENCE, H. J., MARTIN, K. J., MCGHEE, E., NEILSON, M., CUTIONGCO, M. F. A., GADEGAARD, N., MACKAY, G., FORT, L., LILLA, S., KALNA, G., THOMASON, P., KOH, Y. W. H., NORMAN, J. C., INSALL, R. H. & MACHESKY, L. M. 2019. N-WASP Control of LPAR1 Trafficking Establishes Response to Self-Generated LPA Gradients to Promote Pancreatic Cancer Cell Metastasis. *Dev Cell,* 51**,** 431-445 e7.

JUNCKER-JENSEN, A., DERYUGINA, E. I., RIMANN, I., ZAJAC, E., KUPRIYANOVA, T. A., ENGELHOLM, L. H. & QUIGLEY, J. P. 2013. Tumor MMP-1 activates endothelial PAR1 to facilitate vascular intravasation and metastatic dissemination. *Cancer Res,* 73**,** 4196-211.

JUNEMANN, A., FILIC, V., WINTERHOFF, M., NORDHOLZ, B., LITSCHKO, C., SCHWELLENBACH, H., STEPHAN, T., WEBER, I. & FAIX, J. 2016. A Diaphanous-related formin links Ras signaling directly to actin assembly in macropinocytosis and phagocytosis. *Proc Natl Acad Sci U S A,* 113**,** E7464-E7473.

KAKSONEN, M. & ROUX, A. 2018. Mechanisms of clathrin-mediated endocytosis. *Nat Rev Mol Cell Biol,* 19**,** 313-326.

KAMURA, S., MATSUMOTO, Y., FUKUSHI, J. I., FUJIWARA, T., IIDA, K., OKADA, Y. & IWAMOTO, Y. 2010. Basic fibroblast growth factor in the bone microenvironment enhances cell motility and invasion of Ewing's sarcoma family of tumours by activating the FGFR1-PI3K-Rac1 pathway. *Br J Cancer,* 103**,** 370-81.

KAUKONEN, R., JACQUEMET, G., HAMIDI, H. & IVASKA, J. 2017. Cell-derived matrices for studying cell proliferation and directional migration in a complex 3D microenvironment. *Nat Protoc,* 12**,** 2376-2390.

KAVRAN, J. M., KLEIN, D. E., LEE, A., FALASCA, M., ISAKOFF, S. J., SKOLNIK, E. Y. & LEMMON, M. A. 1998. Specificity and promiscuity in phosphoinositide binding by pleckstrin homology domains. *J Biol Chem,* 273**,** 30497-508.

KAWAHARA, R., BOLLINGER, J. G., RIVERA, C., RIBEIRO, A. C., BRANDAO, T. B., PAES LEME, A. F. & MACCOSS, M. J. 2016. A targeted proteomic strategy for the measurement of oral cancer candidate biomarkers in human saliva. *Proteomics,* 16**,** 159-73.

KAZAZIAN, K., GO, C., WU, H., BRASHAVITSKAYA, O., XU, R., DENNIS, J. W., GINGRAS, A. C. & SWALLOW, C. J. 2017. Plk4 Promotes Cancer Invasion and Metastasis through Arp2/3 Complex Regulation of the Actin Cytoskeleton. *Cancer Res,* 77**,** 434-447.

KERBER, M. L. & CHENEY, R. E. 2011. Myosin-X: a MyTH-FERM myosin at the tips of filopodia. *J Cell Sci,* 124**,** 3733-41.

KERR, M. C., LINDSAY, M. R., LUETTERFORST, R., HAMILTON, N., SIMPSON, F., PARTON, R. G., GLEESON, P. A. & TEASDALE, R. D. 2006. Visualisation of macropinosome maturation by the recruitment of sorting nexins. *J Cell Sci,* 119**,** 3967-80.

KEUM, E., KIM, Y., KIM, J., KWON, S., LIM, Y., HAN, I. & OH, E. S. 2004. Syndecan-4 regulates localization, activity and stability of protein kinase C-alpha. *Biochem J,* 378**,** 1007-14.

KIM, N. G. & GUMBINER, B. M. 2015. Adhesion to fibronectin regulates Hippo signaling via the FAK-Src-PI3K pathway. *J Cell Biol,* 210**,** 503-15.

KIM, S. M., NGUYEN, T. T., RAVI, A., KUBINIOK, P., FINICLE, B. T., JAYASHANKAR, V., MALACRIDA, L., HOU, J., ROBERTSON, J., GAO, D., CHERNOFF, J., DIGMAN, M. A., POTMA, E. O., TROMBERG, B. J., THIBAULT, P. & EDINGER, A. L. 2018. PTEN Deficiency and AMPK Activation Promote Nutrient Scavenging and Anabolism in Prostate Cancer Cells. *Cancer Discov,* 8**,** 866-883.

KING, J. S. & KAY, R. R. 2019. The origins and evolution of macropinocytosis. *Philos Trans R Soc Lond B Biol Sci,* 374**,** 20180158.

KIRCHHAUSEN, T., OWEN, D. & HARRISON, S. C. 2014. Molecular structure, function, and dynamics of clathrin-mediated membrane traffic. *Cold Spring Harb Perspect Biol,* 6**,** a016725.

KIYATKIN, A., AKSAMITIENE, E., MARKEVICH, N. I., BORISOV, N. M., HOEK, J. B. & KHOLODENKO, B. N. 2006. Scaffolding protein Grb2-associated binder 1 sustains epidermal growth factor-induced mitogenic and survival signaling by multiple positive feedback loops. *J Biol Chem,* 281**,** 19925-38.

KJOLLER, L. & HALL, A. 2001. Rac mediates cytoskeletal rearrangements and increased cell motility induced by urokinase-type plasminogen activator receptor binding to vitronectin. *J Cell Biol,* 152**,** 1145-57.

KOIVUSALO, M., WELCH, C., HAYASHI, H., SCOTT, C. C., KIM, M., ALEXANDER, T., TOURET, N., HAHN, K. M. & GRINSTEIN, S. 2010. Amiloride inhibits macropinocytosis by lowering submembranous pH and preventing Rac1 and Cdc42 signaling. *J Cell Biol,* 188**,** 547-63.

KORONAKIS, V., HUME, P. J., HUMPHREYS, D., LIU, T., HORNING, O., JENSEN, O. N. & MCGHIE, E. J. 2011. WAVE regulatory complex activation by cooperating GTPases Arf and Rac1. *Proc Natl Acad Sci U S A,* 108**,** 14449-54.

KOVAR, D. R. & POLLARD, T. D. 2004. Insertional assembly of actin filament barbed ends in association with formins produces piconewton forces. *Proc Natl Acad Sci U S A,* 101**,** 14725-30.

KOVTUN, O., LENEVA, N., BYKOV, Y. S., ARIOTTI, N., TEASDALE, R. D., SCHAFFER, M., ENGEL, B. D., OWEN, D. J., BRIGGS, J. A. G. & COLLINS, B. M. 2018. Structure of the membrane-assembled retromer coat determined by cryo-electron tomography. *Nature,* 561**,** 561-564.

KRAUTHAMMER, M., KONG, Y., HA, B. H., EVANS, P., BACCHIOCCHI, A., MCCUSKER, J. P., CHENG, E., DAVIS, M. J., GOH, G., CHOI, M., ARIYAN, S., NARAYAN, D., DUTTON-REGESTER, K., CAPATANA, A., HOLMAN, E. C., BOSENBERG, M., SZNOL, M., KLUGER, H. M., BRASH, D. E., STERN, D. F., MATERIN, M. A., LO, R. S., MANE, S., MA, S., KIDD, K. K., HAYWARD, N. K., LIFTON, R. P., SCHLESSINGER, J., BOGGON, T. J. & HALABAN, R. 2012. Exome sequencing identifies recurrent somatic RAC1 mutations in melanoma. *Nat Genet,* 44**,** 1006-14.

KROOK, M. A., NICHOLLS, L. A., SCANNELL, C. A., CHUGH, R., THOMAS, D. G. & LAWLOR, E. R. 2014. Stress-induced CXCR4 promotes migration and invasion of ewing sarcoma. *Mol Cancer Res,* 12**,** 953-64.

KRUGMANN, S., JORDENS, I., GEVAERT, K., DRIESSENS, M., VANDEKERCKHOVE, J. & HALL, A. 2001. Cdc42 induces filopodia by promoting the formation of an IRSp53:Mena complex. *Curr Biol,* 11**,** 1645-55.

KULKARNI, S., AUGOFF, K., RIVERA, L., MCCUE, B., KHOURY, T., GROMAN, A., ZHANG, L., TIAN, L. & SOSSEY-ALAOUI, K. 2012. Increased expression levels of WAVE3 are associated with the progression and metastasis of triple negative breast cancer. *PLoS One,* 7**,** e42895.

LAMORTE, L., RODRIGUES, S., SANGWAN, V., TURNER, C. E. & PARK, M. 2003. Crk associates with a multimolecular Paxillin/GIT2/beta-PIX complex and promotes Rac-dependent relocalization of Paxillin to focal contacts. *Mol Biol Cell,* 14**,** 2818-31.

LAMOUILLE, S., XU, J. & DERYNCK, R. 2014. Molecular mechanisms of epithelial-mesenchymal transition. *Nat Rev Mol Cell Biol,* 15**,** 178-96.

LAROCCA, C., COHEN, J. R., FERNANDO, R. I., HUANG, B., HAMILTON, D. H. & PALENA, C. 2013. An autocrine loop between TGF-beta1 and the transcription factor brachyury controls the transition of human carcinoma cells into a mesenchymal phenotype. *Mol Cancer Ther,* 12**,** 1805-15.

LAUBLI, H. & BORSIG, L. 2010. Selectins promote tumor metastasis. *Semin Cancer Biol,* 20**,** 169-77.

LAW, A. L., VEHLOW, A., KOTINI, M., DODGSON, L., SOONG, D., THEVENEAU, E., BODO, C., TAYLOR, E., NAVARRO, C., PERERA, U., MICHAEL, M., DUNN, G. A., BENNETT, D., MAYOR, R. & KRAUSE, M. 2013. Lamellipodin and the Scar/WAVE complex cooperate to promote cell migration in vivo. *J Cell Biol,* 203**,** 673-89.

LAW, D. A., DEGUZMAN, F. R., HEISER, P., MINISTRI-MADRID, K., KILLEEN, N. & PHILLIPS, D. R. 1999. Integrin cytoplasmic tyrosine motif is required for outside-in alphaIIbbeta3 signalling and platelet function. *Nature,* 401**,** 808-11.

LAWSON, C. D. & RIDLEY, A. J. 2018. Rho GTPase signaling complexes in cell migration and invasion. *J Cell Biol,* 217**,** 447-457.

LEBENSOHN, A. M. & KIRSCHNER, M. W. 2009. Activation of the WAVE complex by coincident signals controls actin assembly. *Mol Cell,* 36**,** 512-24.

LEE, G. Y., KENNY, P. A., LEE, E. H. & BISSELL, M. J. 2007. Three-dimensional culture models of normal and malignant breast epithelial cells. *Nat Methods,* 4**,** 359-65.

LEONE, D. P., SRINIVASAN, K., BRAKEBUSCH, C. & MCCONNELL, S. K. 2010. The rho GTPase Rac1 is required for proliferation and survival of progenitors in the developing forebrain. *Dev Neurobiol,* 70**,** 659-78.

LESLIE, E. J., CARLSON, J. C., SHAFFER, J. R., FEINGOLD, E., WEHBY, G., LAURIE, C. A., JAIN, D., LAURIE, C. C., DOHENY, K. F., MCHENRY, T., RESICK, J., SANCHEZ, C., JACOBS, J., EMANUELE, B., VIEIRA, A. R., NEISWANGER, K., LIDRAL, A. C., VALENCIA-RAMIREZ, L. C., LOPEZ-PALACIO, A. M., VALENCIA, D. R., ARCOS-BURGOS, M., CZEIZEL, A. E., FIELD, L. L., PADILLA, C. D., CUTIONGCO-DE LA PAZ, E. M., DELEYIANNIS, F., CHRISTENSEN, K., MUNGER, R. G., LIE, R. T., WILCOX, A., ROMITTI, P. A., CASTILLA, E. E., MEREB, J. C., POLETTA, F. A., ORIOLI, I. M., CARVALHO, F. M., HECHT, J. T., BLANTON, S. H., BUXO, C. J., BUTALI, A., MOSSEY, P. A., ADEYEMO, W. L., JAMES, O., BRAIMAH, R. O., AREGBESOLA, B. S., ESHETE, M. A., ABATE, F., KORUYUCU, M., SEYMEN, F., MA, L., DE SALAMANCA, J. E., WEINBERG, S. M., MORENO, L., MURRAY, J. C. & MARAZITA, M. L. 2016. A multi-ethnic genome-wide association study identifies novel loci for non-syndromic cleft lip with or without cleft palate on 2p24.2, 17q23 and 19q13. *Hum Mol Genet,* 25**,** 2862-2872.

LESTER, R. D., JO, M., MONTEL, V., TAKIMOTO, S. & GONIAS, S. L. 2007. uPAR induces epithelial-mesenchymal transition in hypoxic breast cancer cells. *J Cell Biol,* 178**,** 425-36.

LEVIN, R., GRINSTEIN, S. & SCHLAM, D. 2015. Phosphoinositides in phagocytosis and macropinocytosis. *Biochim Biophys Acta,* 1851**,** 805-23.

LI, A., DAWSON, J. C., FORERO-VARGAS, M., SPENCE, H. J., YU, X., KONIG, I., ANDERSON, K. & MACHESKY, L. M. 2010. The actin-bundling protein fascin stabilizes actin in invadopodia and potentiates protrusive invasion. *Curr Biol,* 20**,** 339-45.

LI, A., MA, Y., JIN, M., MASON, S., MORT, R. L., BLYTH, K., LARUE, L., SANSOM, O. J. & MACHESKY, L. M. 2012. Activated mutant NRas(Q61K) drives aberrant melanocyte signaling, survival, and invasiveness via a Rac1-dependent mechanism. *J Invest Dermatol,* 132**,** 2610-21.

LI, A., MORTON, J. P., MA, Y., KARIM, S. A., ZHOU, Y., FALLER, W. J., WOODHAM, E. F., MORRIS, H. T., STEVENSON, R. P., JUIN, A., JAMIESON, N. B., MACKAY, C. J., CARTER, C. R., LEUNG, H. Y., YAMASHIRO, S., BLYTH, K., SANSOM, O. J. & MACHESKY, L. M. 2014. Fascin is regulated by slug, promotes progression of pancreatic cancer in mice, and is associated with patient outcomes. *Gastroenterology,* 146**,** 1386-96 e1-17.

LI, H., YANG, L., FU, H., YAN, J., WANG, Y., GUO, H., HAO, X., XU, X., JIN, T. & ZHANG, N. 2013. Association between Galphai2 and ELMO1/Dock180 connects chemokine signalling with Rac activation and metastasis. *Nat Commun,* 4**,** 1706.

LI, L., TANG, Q., NAKAMURA, T., SUH, J. G., OHSHIMA, H. & JUNG, H. S. 2016a. Fine tuning of Rac1 and RhoA alters cuspal shapes by remolding the cellular geometry. *Sci Rep,* 6**,** 37828.

LI, R. A., TRAVER, D., MATTHES, T. & BERTRAND, J. Y. 2016b. Ndrg1b and fam49ab modulate the PTEN pathway to control T-cell lymphopoiesis in the zebrafish. *Blood,* 128**,** 3052-3060.

LI, X., PLACENCIO, V., ITURREGUI, J. M., UWAMARIYA, C., SHARIF-AFSHAR, A. R., KOYAMA, T., HAYWARD, S. W. & BHOWMICK, N. A. 2008. Prostate tumor progression is mediated by a paracrine TGF-beta/Wnt3a signaling axis. *Oncogene,* 27**,** 7118-30.

LI, Y., GONZALEZ, W. G., ANDREEV, A., TANG, W., GANDHI, S., CUNHA, A., PROBER, D., LOIS, C. & BRONNER, M. E. 2020. Macropinocytosis-mediated membrane recycling drives neural crest migration by delivering F-actin to the lamellipodium. *Proc Natl Acad Sci U S A,* 117**,** 27400-27411.

LI, Y., TONDRAVI, M., LIU, J., SMITH, E., HAUDENSCHILD, C. C., KACZMAREK, M. & ZHAN, X. 2001. Cortactin potentiates bone metastasis of breast cancer cells. *Cancer Res,* 61**,** 6906-11.

LI, Y., VIECELI, F. M., GONZALEZ, W. G., LI, A., TANG, W., LOIS, C. & BRONNER, M. E. 2019. In Vivo Quantitative Imaging Provides Insights into Trunk Neural Crest Migration. *Cell Rep,* 26**,** 1489-1500 e3.

LIM, J. P., TEASDALE, R. D. & GLEESON, P. A. 2012. SNX5 is essential for efficient macropinocytosis and antigen processing in primary macrophages. *Biol Open,* 1**,** 904-14.

LIM, J. P., WANG, J. T., KERR, M. C., TEASDALE, R. D. & GLEESON, P. A. 2008a. A role for SNX5 in the regulation of macropinocytosis. *BMC Cell Biol,* 9**,** 58.

LIM, S. T., CHEN, X. L., LIM, Y., HANSON, D. A., VO, T. T., HOWERTON, K., LAROCQUE, N., FISHER, S. J., SCHLAEPFER, D. D. & ILIC, D. 2008b. Nuclear FAK promotes cell proliferation and survival through FERM-enhanced p53 degradation. *Mol Cell,* 29**,** 9-22.

LINDE, N., CASANOVA-ACEBES, M., SOSA, M. S., MORTHA, A., RAHMAN, A., FARIAS, E., HARPER, K., TARDIO, E., REYES TORRES, I., JONES, J., CONDEELIS, J., MERAD, M. & AGUIRRE-GHISO, J. A. 2018. Macrophages orchestrate breast cancer early dissemination and metastasis. *Nat Commun,* 9**,** 21.

LINDSAY, C. R., LAWN, S., CAMPBELL, A. D., FALLER, W. J., RAMBOW, F., MORT, R. L., TIMPSON, P., LI, A., CAMMARERI, P., RIDGWAY, R. A., MORTON, J. P., DOYLE, B., HEGARTY, S., RAFFERTY, M., MURPHY, I. G., MCDERMOTT, E. W., SHEAHAN, K., PEDONE, K., FINN, A. J., GROBEN, P. A., THOMAS, N. E., HAO, H., CARSON, C., NORMAN, J. C., MACHESKY, L. M., GALLAGHER, W. M., JACKSON, I. J., VAN KEMPEN, L., BEERMANN, F., DER, C., LARUE, L., WELCH, H. C., OZANNE, B. W. & SANSOM, O. J. 2011. P-Rex1 is required for efficient melanoblast migration and melanoma metastasis. *Nat Commun,* 2**,** 555.

LIONARONS, D. A., HANCOCK, D. C., RANA, S., EAST, P., MOORE, C., MURILLO, M. M., CARVALHO, J., SPENCER-DENE, B., HERBERT, E., STAMP, G., DAMRY, D., CALADO, D. P., ROSEWELL, I., FRITSCH, R., NEUBIG, R. R., MOLINA-ARCAS, M. & DOWNWARD, J. 2019. RAC1(P29S) Induces a Mesenchymal Phenotypic Switch via Serum Response Factor to Promote Melanoma Development and Therapy Resistance. *Cancer Cell,* 36**,** 68-83 e9.

LIU, D., AGUIRRE GHISO, J., ESTRADA, Y. & OSSOWSKI, L. 2002. EGFR is a transducer of the urokinase receptor initiated signal that is required for in vivo growth of a human carcinoma. *Cancer Cell,* 1**,** 445-57.

LORD, S. J., VELLE, K. B., MULLINS, R. D. & FRITZ-LAYLIN, L. K. 2020. SuperPlots: Communicating reproducibility and variability in cell biology. *J Cell Biol,* 219.

LOZA-COLL, M. A., PERERA, S., SHI, W. & FILMUS, J. 2005. A transient increase in the activity of Src-family kinases induced by cell detachment delays anoikis of intestinal epithelial cells. *Oncogene,* 24**,** 1727-37.

LU, M., MUNGER, J. S., STEADELE, M., BUSALD, C., TELLIER, M. & SCHNAPP, L. M. 2002. Integrin alpha8beta1 mediates adhesion to LAP-TGFbeta1. *J Cell Sci,* 115**,** 4641-8.

LUNDMARK, R., DOHERTY, G. J., VALLIS, Y., PETER, B. J. & MCMAHON, H. T. 2008. Arf family GTP loading is activated by, and generates, positive membrane curvature. *Biochem J,* 414**,** 189-94.

LY, K. T. & CASANOVA, J. E. 2007. Mechanisms of Salmonella entry into host cells. *Cell Microbiol,* 9**,** 2103-11.

M F OLSON, A. A., A HALL 1995. An Essential Role for Rho, Rac, and Cdc42 GTPases in Cell Cycle Progression Through G1. *Science*.

MACDONALD, E., BROWN, L., SELVAIS, A., LIU, H., WARING, T., NEWMAN, D., BITHELL, J., GRIMES, D., URBE, S., CLAGUE, M. J. & ZECH, T. 2018. HRS-WASH axis governs actin-mediated endosomal recycling and cell invasion. *J Cell Biol,* 217**,** 2549-2564.

MACHACEK, M., HODGSON, L., WELCH, C., ELLIOTT, H., PERTZ, O., NALBANT, P., ABELL, A., JOHNSON, G. L., HAHN, K. M. & DANUSER, G. 2009. Coordination of Rho GTPase activities during cell protrusion. *Nature,* 461**,** 99-103.

MACHESKY, L. M., ATKINSON, S. J., AMPE, C., VANDEKERCKHOVE, J. & POLLARD, T. D. 1994. Purification of a cortical complex containing two unconventional actins from Acanthamoeba by affinity chromatography on profilin-agarose. *J Cell Biol,* 127**,** 107-15.

MACHESKY, L. M. & INSALL, R. H. 1998. Scar1 and the related Wiskott-Aldrich syndrome protein, WASP, regulate the actin cytoskeleton through the Arp2/3 complex. *Curr Biol,* 8**,** 1347-56.

MACHESKY, L. M., MULLINS, R. D., HIGGS, H. N., KAISER, D. A., BLANCHOIN, L., MAY, R. C., HALL, M. E. & POLLARD, T. D. 1999. Scar, a WASp-related protein, activates nucleation of actin filaments by the Arp2/3 complex. *Proc Natl Acad Sci U S A,* 96**,** 3739-44.

MACPHERSON, I. R., RAINERO, E., MITCHELL, L. E., VAN DEN BERGHE, P. V., SPEIRS, C., DOZYNKIEWICZ, M. A., CHAUDHARY, S., KALNA, G., EDWARDS, J., TIMPSON, P. & NORMAN, J. C. 2014. CLIC3 controls recycling of late endosomal MT1-MMP and dictates invasion and metastasis in breast cancer. *J Cell Sci,* 127**,** 3893-901.

MADAULE, P. & AXEL, R. 1985. A novel ras-related gene family. *Cell,* 41**,** 31-40.

MADER, C. C., OSER, M., MAGALHAES, M. A., BRAVO-CORDERO, J. J., CONDEELIS, J., KOLESKE, A. J. & GIL-HENN, H. 2011. An EGFR-Src-Arg-cortactin pathway mediates functional maturation of invadopodia and breast cancer cell invasion. *Cancer Res,* 71**,** 1730-41.

MAEKAWA, M., TERASAKA, S., MOCHIZUKI, Y., KAWAI, K., IKEDA, Y., ARAKI, N., SKOLNIK, E. Y., TAGUCHI, T. & ARAI, H. 2014. Sequential breakdown of 3-phosphorylated phosphoinositides is essential for the completion of macropinocytosis. *Proc Natl Acad Sci U S A,* 111**,** E978-87.

MALLIRI, A., VAN DER KAMMEN, R. A., CLARK, K., VAN DER VALK, M., MICHIELS, F. & COLLARD, J. G. 2002. Mice deficient in the Rac activator Tiam1 are resistant to Ras-induced skin tumours. *Nature,* 417**,** 867-71.

MARTINEZ-RAMIREZ, A., RODRIGUEZ-PERALES, S., MELENDEZ, B., MARTINEZ-DELGADO, B., URIOSTE, M., CIGUDOSA, J. C. & BENITEZ, J. 2003. Characterization of the A673 cell line (Ewing tumor) by molecular cytogenetic techniques. *Cancer Genet Cytogenet,* 141**,** 138-42.

MATTILA, P. K. & LAPPALAINEN, P. 2008. Filopodia: molecular architecture and cellular functions. *Nat Rev Mol Cell Biol,* 9**,** 446-54.

MCMAHON, H. T. & BOUCROT, E. 2015. Membrane curvature at a glance. *J Cell Sci,* 128**,** 1065-70.

MD HASHIM, N. F., NICHOLAS, N. S., DART, A. E., KIRIAKIDIS, S., PALEOLOG, E. & WELLS, C. M. 2013. Hypoxia-induced invadopodia formation: a role for beta-PIX. *Open Biol,* 3**,** 120159.

MEHIDI, A., ROSSIER, O., SCHAKS, M., CHAZEAU, A., BINAME, F., REMORINO, A., COPPEY, M., KARATAS, Z., SIBARITA, J. B., ROTTNER, K., MOREAU, V. & GIANNONE, G. 2019. Transient Activations of Rac1 at the Lamellipodium Tip Trigger Membrane Protrusion. *Curr Biol,* 29**,** 2852-2866 e5.

MEHRBOD, M., TRISNO, S. & MOFRAD, M. R. 2013. On the activation of integrin alphaIIbbeta3: outside-in and inside-out pathways. *Biophys J,* 105**,** 1304-15.

MENDOZA, M. C., ER, E. E., ZHANG, W., BALLIF, B. A., ELLIOTT, H. L., DANUSER, G. & BLENIS, J. 2011. ERK-MAPK drives lamellipodia protrusion by activating the WAVE2 regulatory complex. *Mol Cell,* 41**,** 661-71.

MENDOZA, P., ORTIZ, R., DIAZ, J., QUEST, A. F., LEYTON, L., STUPACK, D. & TORRES, V. A. 2013. Rab5 activation promotes focal adhesion disassembly, migration and invasiveness in tumor cells. *J Cell Sci,* 126**,** 3835-47.

MERINO, F., POSPICH, S., FUNK, J., WAGNER, T., KULLMER, F., ARNDT, H. D., BIELING, P. & RAUNSER, S. 2018. Structural transitions of F-actin upon ATP hydrolysis at near-atomic resolution revealed by cryo-EM. *Nat Struct Mol Biol,* 25**,** 528-537.

MERINO-TRIGO, A., KERR, M. C., HOUGHTON, F., LINDBERG, A., MITCHELL, C., TEASDALE, R. D. & GLEESON, P. A. 2004. Sorting nexin 5 is localized to a subdomain of the early endosomes and is recruited to the plasma membrane following EGF stimulation. *J Cell Sci,* 117**,** 6413-24.

METTLEN, M., PLATEK, A., VAN DER SMISSEN, P., CARPENTIER, S., AMYERE, M., LANZETTI, L., DE DIESBACH, P., TYTECA, D. & COURTOY, P. J. 2006. Src triggers circular ruffling and macropinocytosis at the apical surface of polarized MDCK cells. *Traffic,* 7**,** 589-603.

MICHAELSON, D., ABIDI, W., GUARDAVACCARO, D., ZHOU, M., AHEARN, I., PAGANO, M. & PHILIPS, M. R. 2008. Rac1 accumulates in the nucleus during the G2 phase of the cell cycle and promotes cell division. *J Cell Biol,* 181**,** 485-96.

MICHELLE E. MAXSON, H. S., ALLEN VOLCHUK, JOHN H. BRUMELL, SERGIO GRINSTEIN 2020. Rab5 regulates macropinosome closure through recruitment of the inositol 3 5-phosphatases OCRL:Inpp5b and the hydrolysis of PtdIns(4,5)P2. *BioRxiv*.

MIERKE, C. T., FREY, B., FELLNER, M., HERRMANN, M. & FABRY, B. 2011. Integrin alpha5beta1 facilitates cancer cell invasion through enhanced contractile forces. *J Cell Sci,* 124**,** 369-83.

MILLIUS, A., DANDEKAR, S. N., HOUK, A. R. & WEINER, O. D. 2009. Neutrophils establish rapid and robust WAVE complex polarity in an actin-dependent fashion. *Curr Biol,* 19**,** 253-9.

MISHRA, A. K. & LAMBRIGHT, D. G. 2016. Invited review: Small GTPases and their GAPs. *Biopolymers,* 105**,** 431-48.

MITCHELL, C. B. & O'NEILL, G. M. 2016. Cooperative cell invasion: matrix metalloproteinase-mediated incorporation between cells. *Mol Biol Cell,* 27**,** 3284-3292.

MITTAL, M., SIDDIQUI, M. R., TRAN, K., REDDY, S. P. & MALIK, A. B. 2014. Reactive oxygen species in inflammation and tissue injury. *Antioxid Redox Signal,* 20**,** 1126-67.

MIYAMOTO, S., AKIYAMA, S. K. & YAMADA, K. M. 1995. Synergistic roles for receptor occupancy and aggregation in integrin transmembrane function. *Science,* 267**,** 883-5.

MOHAN, A. S., DEAN, K. M., ISOGAI, T., KASITINON, S. Y., MURALI, V. S., ROUDOT, P., GROISMAN, A., REED, D. K., WELF, E. S., HAN, S. J., NOH, J. & DANUSER, G. 2019. Enhanced Dendritic Actin Network Formation in Extended Lamellipodia Drives Proliferation in Growth-Challenged Rac1(P29S) Melanoma Cells. *Dev Cell,* 49**,** 444-460 e9.

MROZIK, K. M., BLASCHUK, O. W., CHEONG, C. M., ZANNETTINO, A. C. W. & VANDYKE, K. 2018. N-cadherin in cancer metastasis, its emerging role in haematological malignancies and potential as a therapeutic target in cancer. *BMC Cancer,* 18**,** 939.

MUELLER, S. C. & CHEN, W. T. 1991. Cellular invasion into matrix beads: localization of beta 1 integrins and fibronectin to the invadopodia. *J Cell Sci,* 99 (Pt 2)**,** 213-25.

MULLER, P. A., CASWELL, P. T., DOYLE, B., IWANICKI, M. P., TAN, E. H., KARIM, S., LUKASHCHUK, N., GILLESPIE, D. A., LUDWIG, R. L., GOSSELIN, P., CROMER, A., BRUGGE, J. S., SANSOM, O. J., NORMAN, J. C. & VOUSDEN, K. H. 2009. Mutant p53 drives invasion by promoting integrin recycling. *Cell,* 139**,** 1327-41.

MUNOZ-COUSELO, E., ADELANTADO, E. Z., ORTIZ, C., GARCIA, J. S. & PEREZ-GARCIA, J. 2017. NRAS-mutant melanoma: current challenges and future prospect. *Onco Targets Ther,* 10**,** 3941-3947.

MYANT, K. B., CAMMARERI, P., MCGHEE, E. J., RIDGWAY, R. A., HUELS, D. J., CORDERO, J. B., SCHWITALLA, S., KALNA, G., OGG, E. L., ATHINEOS, D., TIMPSON, P., VIDAL, M., MURRAY, G. I., GRETEN, F. R., ANDERSON, K. I. & SANSOM, O. J. 2013. ROS production and NF-kappaB activation triggered by RAC1 facilitate WNT-driven intestinal stem cell proliferation and colorectal cancer initiation. *Cell Stem Cell,* 12**,** 761-73.

NAKATSU, F., BASKIN, J. M., CHUNG, J., TANNER, L. B., SHUI, G., LEE, S. Y., PIRRUCCELLO, M., HAO, M., INGOLIA, N. T., WENK, M. R. & DE CAMILLI, P. 2012. PtdIns4P synthesis by PI4KIIIalpha at the plasma membrane and its impact on plasma membrane identity. *J Cell Biol,* 199**,** 1003-16.

NAM, J. M., ONODERA, Y., BISSELL, M. J. & PARK, C. C. 2010. Breast cancer cells in three-dimensional culture display an enhanced radioresponse after coordinate targeting of integrin alpha5beta1 and fibronectin. *Cancer Res,* 70**,** 5238-48.

NARAYANAN, A., LECLAIRE, L. L., 3RD, BARBER, D. L. & JACOBSON, M. P. 2011. Phosphorylation of the Arp2 subunit relieves auto-inhibitory interactions for Arp2/3 complex activation. *PLoS Comput Biol,* 7**,** e1002226.

NAVARRO-LERIDA, I., SANCHEZ-PERALES, S., CALVO, M., RENTERO, C., ZHENG, Y., ENRICH, C. & DEL POZO, M. A. 2012. A palmitoylation switch mechanism regulates Rac1 function and membrane organization. *EMBO J,* 31**,** 534-51.

NGOC, P. C. T., TAN, S. H., TAN, T. K., CHAN, M. M., LI, Z., YEOH, A. E. J., TENEN, D. G. & SANDA, T. 2018. Identification of novel lncRNAs regulated by the TAL1 complex in T-cell acute lymphoblastic leukemia. *Leukemia,* 32**,** 2138-2151.

NISHIMURA, T. & KAIBUCHI, K. 2007. Numb controls integrin endocytosis for directional cell migration with aPKC and PAR-3. *Dev Cell,* 13**,** 15-28.

NISHIMURA, T., YAMAGUCHI, T., KATO, K., YOSHIZAWA, M., NABESHIMA, Y., OHNO, S., HOSHINO, M. & KAIBUCHI, K. 2005. PAR-6-PAR-3 mediates Cdc42-induced Rac activation through the Rac GEFs STEF/Tiam1. *Nat Cell Biol,* 7**,** 270-7.

NIU, S., XIE, H. & MARCANTONIO, E. E. 2003. Integrin-mediated tyrosine phosphorylation of Shc in T cells is regulated by protein kinase C-dependent phosphorylations of Lck. *Mol Biol Cell,* 14**,** 349-60.

NOBES, C. D. & HALL, A. 1995. Rho, rac, and cdc42 GTPases regulate the assembly of multimolecular focal complexes associated with actin stress fibers, lamellipodia, and filopodia. *Cell,* 81**,** 53-62.

NOBES, C. D. & HALL, A. 1999. Rho GTPases control polarity, protrusion, and adhesion during cell movement. *J Cell Biol,* 144**,** 1235-44.

NOLA, S., SEBBAGH, M., MARCHETTO, S., OSMANI, N., NOURRY, C., AUDEBERT, S., NAVARRO, C., RACHEL, R., MONTCOUQUIOL, M., SANS, N., ETIENNE-MANNEVILLE, S., BORG, J. P. & SANTONI, M. J. 2008. Scrib regulates PAK activity during the cell migration process. *Hum Mol Genet,* 17**,** 3552-65.

NOVO, D., HEATH, N., MITCHELL, L., CALIGIURI, G., MACFARLANE, A., REIJMER, D., CHARLTON, L., KNIGHT, J., CALKA, M., MCGHEE, E., DORNIER, E., SUMPTON, D., MASON, S., ECHARD, A., KLINKERT, K., SECKLEHNER, J., KRUISWIJK, F., VOUSDEN, K., MACPHERSON, I. R., BLYTH, K., BAILEY, P., YIN, H., CARLIN, L. M., MORTON, J., ZANIVAN, S. & NORMAN, J. C. 2018. Mutant p53s generate pro-invasive niches by influencing exosome podocalyxin levels. *Nat Commun,* 9**,** 5069.

NOZUMI, M., NAKAGAWA, H., MIKI, H., TAKENAWA, T. & MIYAMOTO, S. 2003. Differential localization of WAVE isoforms in filopodia and lamellipodia of the neuronal growth cone. *J Cell Sci,* 116**,** 239-46.

ORCHARD, S., AMMARI, M., ARANDA, B., BREUZA, L., BRIGANTI, L., BROACKES-CARTER, F., CAMPBELL, N. H., CHAVALI, G., CHEN, C., DEL-TORO, N., DUESBURY, M., DUMOUSSEAU, M., GALEOTA, E., HINZ, U., IANNUCCELLI, M., JAGANNATHAN, S., JIMENEZ, R., KHADAKE, J., LAGREID, A., LICATA, L., LOVERING, R. C., MELDAL, B., MELIDONI, A. N., MILAGROS, M., PELUSO, D., PERFETTO, L., PORRAS, P., RAGHUNATH, A., RICARD-BLUM, S., ROECHERT, B., STUTZ, A., TOGNOLLI, M., VAN ROEY, K., CESARENI, G. & HERMJAKOB, H. 2014. The MIntAct project--IntAct as a common curation platform for 11 molecular interaction databases. *Nucleic Acids Res,* 42**,** D358-63.

OSER, M. & CONDEELIS, J. 2009. The cofilin activity cycle in lamellipodia and invadopodia. *J Cell Biochem,* 108**,** 1252-62.

OUDIN, M. J. & GERTLER, F. B. 2017. Signatures of Breast Cancer Metastasis: aMENAble to Interpretation? *Trends Cancer,* 3**,** 7-9.

OUDIN, M. J., JONAS, O., KOSCIUK, T., BROYE, L. C., GUIDO, B. C., WYCKOFF, J., RIQUELME, D., LAMAR, J. M., ASOKAN, S. B., WHITTAKER, C., MA, D., LANGER, R., CIMA, M. J., WISINSKI, K. B., HYNES, R. O., LAUFFENBURGER, D. A., KEELY, P. J., BEAR, J. E. & GERTLER, F. B. 2016. Tumor Cell-Driven Extracellular Matrix Remodeling Drives Haptotaxis during Metastatic Progression. *Cancer Discov,* 6**,** 516-31.

OUGHTRED, R., STARK, C., BREITKREUTZ, B. J., RUST, J., BOUCHER, L., CHANG, C., KOLAS, N., O'DONNELL, L., LEUNG, G., MCADAM, R., ZHANG, F., DOLMA, S., WILLEMS, A., COULOMBE-HUNTINGTON, J., CHATR-ARYAMONTRI, A., DOLINSKI, K. & TYERS, M. 2019. The BioGRID interaction database: 2019 update. *Nucleic Acids Res,* 47**,** D529-D541.

OWENS, D. W., MCLEAN, G. W., WYKE, A. W., PARASKEVA, C., PARKINSON, E. K., FRAME, M. C. & BRUNTON, V. G. 2000. The catalytic activity of the Src family kinases is required to disrupt cadherin-dependent cell-cell contacts. *Mol Biol Cell,* 11**,** 51-64.

OWUSU-ANSAH, K. G., SONG, G., CHEN, R., EDOO, M. I. A., LI, J., CHEN, B., WU, J., ZHOU, L., XIE, H., JIANG, D. & ZHENG, S. 2019. COL6A1 promotes metastasis and predicts poor prognosis in patients with pancreatic cancer. *Int J Oncol,* 55**,** 391-404.

PACOLD, M. E., SUIRE, S., PERISIC, O., LARA-GONZALEZ, S., DAVIS, C. T., WALKER, E. H., HAWKINS, P. T., STEPHENS, L., ECCLESTON, J. F. & WILLIAMS, R. L. 2000. Crystal structure and functional analysis of Ras binding to its effector phosphoinositide 3-kinase gamma. *Cell,* 103**,** 931-43.

PADRICK, S. B., DOOLITTLE, L. K., BRAUTIGAM, C. A., KING, D. S. & ROSEN, M. K. 2011. Arp2/3 complex is bound and activated by two WASP proteins. *Proc Natl Acad Sci U S A,* 108**,** E472-9.

PALAMIDESSI, A., FRITTOLI, E., DUCANO, N., OFFENHAUSER, N., SIGISMUND, S., KAJIHO, H., PARAZZOLI, D., OLDANI, A., GOBBI, M., SERINI, G., DI FIORE, P. P., SCITA, G. & LANZETTI, L. 2013. The GTPase-activating protein RN-tre controls focal adhesion turnover and cell migration. *Curr Biol,* 23**,** 2355-64.

PALUMBO, J. S., TALMAGE, K. E., MASSARI, J. V., LA JEUNESSE, C. M., FLICK, M. J., KOMBRINCK, K. W., JIROUSKOVA, M. & DEGEN, J. L. 2005. Platelets and fibrin(ogen) increase metastatic potential by impeding natural killer cell-mediated elimination of tumor cells. *Blood,* 105**,** 178-85.

PAPAYANNOPOULOS, V., CO, C., PREHODA, K. E., SNAPPER, S., TAUNTON, J. & LIM, W. A. 2005. A polybasic motif allows N-WASP to act as a sensor of PIP(2) density. *Mol Cell,* 17**,** 181-91.

PAREKH, A. & WEAVER, A. M. 2016. Regulation of invadopodia by mechanical signaling. *Exp Cell Res,* 343**,** 89-95.

PAUL, N. R., ALLEN, J. L., CHAPMAN, A., MORLAN-MAIRAL, M., ZINDY, E., JACQUEMET, G., FERNANDEZ DEL AMA, L., FERIZOVIC, N., GREEN, D. M., HOWE, J. D., EHLER, E., HURLSTONE, A. & CASWELL, P. T. 2015. alpha5beta1 integrin recycling promotes Arp2/3-independent cancer cell invasion via the formin FHOD3. *J Cell Biol,* 210**,** 1013-31.

PECK, J. W., OBERST, M., BOUKER, K. B., BOWDEN, E. & BURBELO, P. D. 2002. The RhoA-binding protein, rhophilin-2, regulates actin cytoskeleton organization. *J Biol Chem,* 277**,** 43924-32.

PELLINEN, T., ARJONEN, A., VUORILUOTO, K., KALLIO, K., FRANSEN, J. A. & IVASKA, J. 2006. Small GTPase Rab21 regulates cell adhesion and controls endosomal traffic of beta1-integrins. *J Cell Biol,* 173**,** 767-80.

PENG, J., WALLAR, B. J., FLANDERS, A., SWIATEK, P. J. & ALBERTS, A. S. 2003. Disruption of the Diaphanous-related formin Drf1 gene encoding mDia1 reveals a role for Drf3 as an effector for Cdc42. *Curr Biol,* 13**,** 534-45.

PERSKVIST, N., ROBERG, K., KULYTE, A. & STENDAHL, O. 2002. Rab5a GTPase regulates fusion between pathogen-containing phagosomes and cytoplasmic organelles in human neutrophils. *J Cell Sci,* 115**,** 1321-30.

PERTZ, O., HODGSON, L., KLEMKE, R. L. & HAHN, K. M. 2006. Spatiotemporal dynamics of RhoA activity in migrating cells. *Nature,* 440**,** 1069-72.

PETIT, V. & LARUE, L. 2016. Any route for melanoblasts to colonize the skin! *Exp Dermatol,* 25**,** 669-73.

PETRIE, R. J., GAVARA, N., CHADWICK, R. S. & YAMADA, K. M. 2012. Nonpolarized signaling reveals two distinct modes of 3D cell migration. *J Cell Biol,* 197**,** 439-55.

PEUROIS, F., PEYROCHE, G. & CHERFILS, J. 2019. Small GTPase peripheral binding to membranes: molecular determinants and supramolecular organization. *Biochem Soc Trans,* 47**,** 13-22.

PFISTERER, K., LEVITT, J., LAWSON, C. D., MARSH, R. J., HEDDLESTON, J. M., WAIT, E., AMEER-BEG, S. M., COX, S. & PARSONS, M. 2020. FMNL2 regulates dynamics of fascin in filopodia. *J Cell Biol,* 219.

PIETILA, M., SAHGAL, P., PEUHU, E., JANTTI, N. Z., PAATERO, I., NARVA, E., AL-AKHRASS, H., LILJA, J., GEORGIADOU, M., ANDERSEN, O. M., PADZIK, A., SIHTO, H., JOENSUU, H., BLOMQVIST, M., SAARINEN, I., BOSTROM, P. J., TAIMEN, P. & IVASKA, J. 2019. SORLA regulates endosomal trafficking and oncogenic fitness of HER2. *Nat Commun,* 10**,** 2340.

PIPATHSOUK, A., BRUNETTI, R. M., TOWN, J. P., BREUER, A., PELLETT, P. A., MARCHUK, K., TRAN, N.-H. T., KRUMMEL, M. F., STAMOU, D. & WEINER, O. D. 2019. WAVE complex self-organization templates lamellipodial formation. *BioRxiv*.

POINCLOUX, R., LIZARRAGA, F. & CHAVRIER, P. 2009. Matrix invasion by tumour cells: a focus on MT1-MMP trafficking to invadopodia. *J Cell Sci,* 122**,** 3015-24.

POLLARD, T. D. 2016. Actin and Actin-Binding Proteins. *Cold Spring Harb Perspect Biol,* 8.

PRIOR, I. A., LEWIS, P. D. & MATTOS, C. 2012. A comprehensive survey of Ras mutations in cancer. *Cancer Res,* 72**,** 2457-67.

RAINERO, E., HOWE, J. D., CASWELL, P. T., JAMIESON, N. B., ANDERSON, K., CRITCHLEY, D. R., MACHESKY, L. & NORMAN, J. C. 2015. Ligand-Occupied Integrin Internalization Links Nutrient Signaling to Invasive Migration. *Cell Rep,* 10**,** 398-413.

RAJADURAI, C. V., HAVRYLOV, S., COELHO, P. P., RATCLIFFE, C. D., ZAOUI, K., HUANG, B. H., MONAST, A., CHUGHTAI, N., SANGWAN, V., GERTLER, F. B., SIEGEL, P. M. & PARK, M. 2016. 5'-Inositol phosphatase SHIP2 recruits Mena to stabilize invadopodia for cancer cell invasion. *J Cell Biol,* 214**,** 719-34.

RAMSAY, A. G., KEPPLER, M. D., JAZAYERI, M., THOMAS, G. J., PARSONS, M., VIOLETTE, S., WEINREB, P., HART, I. R. & MARSHALL, J. F. 2007. HS1-associated protein X-1 regulates carcinoma cell migration and invasion via clathrin-mediated endocytosis of integrin alphavbeta6. *Cancer Res,* 67**,** 5275-84.

RAUHALA, H. E., TEPPO, S., NIEMELA, S. & KALLIONIEMI, A. 2013. Silencing of the ARP2/3 complex disturbs pancreatic cancer cell migration. *Anticancer Res,* 33**,** 45-52.

RAZ, L., ZHANG, Q. G., ZHOU, C. F., HAN, D., GULATI, P., YANG, L. C., YANG, F., WANG, R. M. & BRANN, D. W. 2010. Role of Rac1 GTPase in NADPH oxidase activation and cognitive impairment following cerebral ischemia in the rat. *PLoS One,* 5**,** e12606.

REMORINO, A., DE BECO, S., CAYRAC, F., DI FEDERICO, F., CORNILLEAU, G., GAUTREAU, A., PARRINI, M. C., MASSON, J. B., DAHAN, M. & COPPEY, M. 2017. Gradients of Rac1 Nanoclusters Support Spatial Patterns of Rac1 Signaling. *Cell Rep,* 21**,** 1922-1935.

RIDLEY, A. J. 2001. Rho GTPases and cell migration. *J Cell Sci,* 114**,** 2713-22.

RIDLEY, A. J. & HALL, A. 1992. The small GTP-binding protein rho regulates the assembly of focal adhesions and actin stress fibers in response to growth factors. *Cell,* 70**,** 389-99.

RIDLEY, A. J., PATERSON, H. F., JOHNSTON, C. L., DIEKMANN, D. & HALL, A. 1992. The small GTP-binding protein rac regulates growth factor-induced membrane ruffling. *Cell,* 70**,** 401-10.

RINK, J., GHIGO, E., KALAIDZIDIS, Y. & ZERIAL, M. 2005. Rab conversion as a mechanism of progression from early to late endosomes. *Cell,* 122**,** 735-49.

RITTER, A. T., ASANO, Y., STINCHCOMBE, J. C., DIECKMANN, N. M., CHEN, B. C., GAWDEN-BONE, C., VAN ENGELENBURG, S., LEGANT, W., GAO, L., DAVIDSON, M. W., BETZIG, E., LIPPINCOTT-SCHWARTZ, J. & GRIFFITHS, G. M. 2015. Actin depletion initiates events leading to granule secretion at the immunological synapse. *Immunity,* 42**,** 864-76.

RITTER, B., MURPHY, S., DOKAINISH, H., GIRARD, M., GUDHETI, M. V., KOZLOV, G., HALIN, M., PHILIE, J., JORGENSEN, E. M., GEHRING, K. & MCPHERSON, P. S. 2013. NECAP 1 regulates AP-2 interactions to control vesicle size, number, and cargo during clathrin-mediated endocytosis. *PLoS Biol,* 11**,** e1001670.

ROBERTS, P. J., MITIN, N., KELLER, P. J., CHENETTE, E. J., MADIGAN, J. P., CURRIN, R. O., COX, A. D., WILSON, O., KIRSCHMEIER, P. & DER, C. J. 2008. Rho Family GTPase modification and dependence on CAAX motif-signaled posttranslational modification. *J Biol Chem,* 283**,** 25150-63.

RODRIGUEZ-VICIANA, P., WARNE, P. H., DHAND, R., VANHAESEBROECK, B., GOUT, I., FRY, M. J., WATERFIELD, M. D. & DOWNWARD, J. 1994. Phosphatidylinositol-3-OH kinase as a direct target of Ras. *Nature,* 370**,** 527-32.

ROHATGI, R., HO, H. Y. & KIRSCHNER, M. W. 2000. Mechanism of N-WASP activation by CDC42 and phosphatidylinositol 4, 5-bisphosphate. *J Cell Biol,* 150**,** 1299-310.

ROHATGI, R., MA, L., MIKI, H., LOPEZ, M., KIRCHHAUSEN, T., TAKENAWA, T. & KIRSCHNER, M. W. 1999. The interaction between N-WASP and the Arp2/3 complex links Cdc42-dependent signals to actin assembly. *Cell,* 97**,** 221-31.

ROJIANI, M. V., ALIDINA, J., ESPOSITO, N. & ROJIANI, A. M. 2010. Expression of MMP-2 correlates with increased angiogenesis in CNS metastasis of lung carcinoma. *Int J Clin Exp Pathol,* 3**,** 775-81.

ROLLI, M., FRANSVEA, E., PILCH, J., SAVEN, A. & FELDING-HABERMANN, B. 2003. Activated integrin alphavbeta3 cooperates with metalloproteinase MMP-9 in regulating migration of metastatic breast cancer cells. *Proc Natl Acad Sci U S A,* 100**,** 9482-7.

RUPPER, A., LEE, K., KNECHT, D. & CARDELLI, J. 2001. Sequential activities of phosphoinositide 3-kinase, PKB/Aakt, and Rab7 during macropinosome formation in Dictyostelium. *Mol Biol Cell,* 12**,** 2813-24.

SALTEL, F., MORTIER, E., HYTONEN, V. P., JACQUIER, M. C., ZIMMERMANN, P., VOGEL, V., LIU, W. & WEHRLE-HALLER, B. 2009. New PI(4,5)P2- and membrane proximal integrin-binding motifs in the talin head control beta3-integrin clustering. *J Cell Biol,* 187**,** 715-31.

SANCHEZ-SANCHEZ, B. J., URBANO, J. M., COMBER, K., DRAGU, A., WOOD, W., STRAMER, B. & MARTIN-BERMUDO, M. D. 2017. Drosophila Embryonic Hemocytes Produce Laminins to Strengthen Migratory Response. *Cell Rep,* 21**,** 1461-1470.

SAWADA, K., MITRA, A. K., RADJABI, A. R., BHASKAR, V., KISTNER, E. O., TRETIAKOVA, M., JAGADEESWARAN, S., MONTAG, A., BECKER, A., KENNY, H. A., PETER, M. E., RAMAKRISHNAN, V., YAMADA, S. D. & LENGYEL, E. 2008. Loss of E-cadherin promotes ovarian cancer metastasis via alpha 5-integrin, which is a therapeutic target. *Cancer Res,* 68**,** 2329-39.

SCHAEFER, A., REINHARD, N. R. & HORDIJK, P. L. 2014. Toward understanding RhoGTPase specificity: structure, function and local activation. *Small GTPases,* 5**,** 6.

SCHAKS, M., SINGH, S. P., KAGE, F., THOMASON, P., KLUNEMANN, T., STEFFEN, A., BLANKENFELDT, W., STRADAL, T. E., INSALL, R. H. & ROTTNER, K. 2018. Distinct Interaction Sites of Rac GTPase with WAVE Regulatory Complex Have Non-redundant Functions in Vivo. *Curr Biol,* 28**,** 3674-3684 e6.

SCHEEL, C., EATON, E. N., LI, S. H., CHAFFER, C. L., REINHARDT, F., KAH, K. J., BELL, G., GUO, W., RUBIN, J., RICHARDSON, A. L. & WEINBERG, R. A. 2011. Paracrine and autocrine signals induce and maintain mesenchymal and stem cell states in the breast. *Cell,* 145**,** 926-40.

SCHLAM, D., BAGSHAW, R. D., FREEMAN, S. A., COLLINS, R. F., PAWSON, T., FAIRN, G. D. & GRINSTEIN, S. 2015. Phosphoinositide 3-kinase enables phagocytosis of large particles by terminating actin assembly through Rac/Cdc42 GTPase-activating proteins. *Nat Commun,* 6**,** 8623.

SCIPION, C. P. M., GHOSHDASTIDER, U., FERRER, F. J., YUEN, T. Y., WONGSANTICHON, J. & ROBINSON, R. C. 2018. Structural evidence for the roles of divalent cations in actin polymerization and activation of ATP hydrolysis. *Proc Natl Acad Sci U S A,* 115**,** 10345-10350.

SEAMAN, M. & FREEMAN, C. L. 2014. Analysis of the Retromer complex-WASH complex interaction illuminates new avenues to explore in Parkinson disease. *Commun Integr Biol,* 7**,** e29483.

SEBTI, S. M. & DER, C. J. 2003. Opinion: Searching for the elusive targets of farnesyltransferase inhibitors. *Nat Rev Cancer,* 3**,** 945-51.

SEGUIN, L., DESGROSELLIER, J. S., WEIS, S. M. & CHERESH, D. A. 2015. Integrins and cancer: regulators of cancer stemness, metastasis, and drug resistance. *Trends Cell Biol,* 25**,** 234-40.

SEIBEL, N. M., ELJOUNI, J., NALASKOWSKI, M. M. & HAMPE, W. 2007. Nuclear localization of enhanced green fluorescent protein homomultimers. *Anal Biochem,* 368**,** 95-9.

SENJU, Y., KALIMERI, M., KOSKELA, E. V., SOMERHARJU, P., ZHAO, H., VATTULAINEN, I. & LAPPALAINEN, P. 2017. Mechanistic principles underlying regulation of the actin cytoskeleton by phosphoinositides. *Proc Natl Acad Sci U S A,* 114**,** E8977-E8986.

SHANG, W., JIANG, Y., BOETTCHER, M., DING, K., MOLLENAUER, M., LIU, Z., WEN, X., LIU, C., HAO, P., ZHAO, S., MCMANUS, M. T., WEI, L., WEISS, A. & WANG, H. 2018. Genome-wide CRISPR screen identifies FAM49B as a key regulator of actin dynamics and T cell activation. *Proc Natl Acad Sci U S A,* 115**,** E4051-E4060.

SHARMA, V. P., EDDY, R., ENTENBERG, D., KAI, M., GERTLER, F. B. & CONDEELIS, J. 2013. Tks5 and SHIP2 regulate invadopodium maturation, but not initiation, in breast carcinoma cells. *Curr Biol,* 23**,** 2079-89.

SHEETZ, M. P., FELSENFELD, D., GALBRAITH, C. G. & CHOQUET, D. 1999. Cell migration as a five-step cycle. *Biochem Soc Symp,* 65**,** 233-43.

SHERIDAN, D. L., BERLOT, C. H., ROBERT, A., INGLIS, F. M., JAKOBSDOTTIR, K. B., HOWE, J. R. & HUGHES, T. E. 2002. A new way to rapidly create functional, fluorescent fusion proteins: random insertion of GFP with an in vitro transposition reaction. *BMC Neurosci,* 3**,** 7.

SHI, F. & SOTTILE, J. 2008. Caveolin-1-dependent beta1 integrin endocytosis is a critical regulator of fibronectin turnover. *J Cell Sci,* 121**,** 2360-71.

SHI, Y., BOLLAM, S. R., WHITE, S. M., LAUGHLIN, S. Z., GRAHAM, G. T., WADHWA, M., CHEN, H., NGUYEN, C., VITTE, J., GIOVANNINI, M., TORETSKY, J. & YI, C. 2016. Rac1-Mediated DNA Damage and Inflammation Promote Nf2 Tumorigenesis but Also Limit Cell-Cycle Progression. *Dev Cell,* 39**,** 452-465.

SHIBUE, T., BROOKS, M. W. & WEINBERG, R. A. 2013. An integrin-linked machinery of cytoskeletal regulation that enables experimental tumor initiation and metastatic colonization. *Cancer Cell,* 24**,** 481-98.

SHIRAKIHARA, T., KAWASAKI, T., FUKAGAWA, A., SEMBA, K., SAKAI, R., MIYAZONO, K., MIYAZAWA, K. & SAITOH, M. 2013. Identification of integrin alpha3 as a molecular marker of cells undergoing epithelial-mesenchymal transition and of cancer cells with aggressive phenotypes. *Cancer Sci,* 104**,** 1189-97.

SHISHIDO, S., BONIG, H. & KIM, Y. M. 2014. Role of integrin alpha4 in drug resistance of leukemia. *Front Oncol,* 4**,** 99.

SILVA, J. M., EZHKOVA, E., SILVA, J., HEART, S., CASTILLO, M., CAMPOS, Y., CASTRO, V., BONILLA, F., CORDON-CARDO, C., MUTHUSWAMY, S. K., POWERS, S., FUCHS, E. & HANNON, G. J. 2009. Cyfip1 is a putative invasion suppressor in epithelial cancers. *Cell,* 137**,** 1047-61.

SIMUNOVIC, M., VOTH, G. A., CALLAN-JONES, A. & BASSEREAU, P. 2015. When Physics Takes Over: BAR Proteins and Membrane Curvature. *Trends Cell Biol,* 25**,** 780-792.

SINGH, A., FEDELE, C., LU, H., NEVALAINEN, M. T., KEEN, J. H. & LANGUINO, L. R. 2016. Exosome-mediated Transfer of alphavbeta3 Integrin from Tumorigenic to Nontumorigenic Cells Promotes a Migratory Phenotype. *Mol Cancer Res,* 14**,** 1136-1146.

SINGH, S. B., TANDON, R., KRISHNAMURTHY, G., VIKRAM, R., SHARMA, N., BASU, S. K. & MUKHOPADHYAY, A. 2003. Rab5-mediated endosome-endosome fusion regulates hemoglobin endocytosis in Leishmania donovani. *EMBO J,* 22**,** 5712-22.

SKOBLE, J., AUERBUCH, V., GOLEY, E. D., WELCH, M. D. & PORTNOY, D. A. 2001. Pivotal role of VASP in Arp2/3 complex-mediated actin nucleation, actin branch-formation, and Listeria monocytogenes motility. *J Cell Biol,* 155**,** 89-100.

SMART, E. J., YING, Y. S. & ANDERSON, R. G. 1995. Hormonal regulation of caveolae internalization. *J Cell Biol,* 131**,** 929-38.

SMITH, H. W. & MARSHALL, C. J. 2010. Regulation of cell signalling by uPAR. *Nat Rev Mol Cell Biol,* 11**,** 23-36.

SOKOLOVA, O. S., CHEMERIS, A., GUO, S., ALIOTO, S. L., GANDHI, M., PADRICK, S., PECHNIKOVA, E., DAVID, V., GAUTREAU, A. & GOODE, B. L. 2017. Structural Basis of Arp2/3 Complex Inhibition by GMF, Coronin, and Arpin. *J Mol Biol,* 429**,** 237-248.

SOSSEY-ALAOUI, K., SAFINA, A., LI, X., VAUGHAN, M. M., HICKS, D. G., BAKIN, A. V. & COWELL, J. K. 2007. Down-regulation of WAVE3, a metastasis promoter gene, inhibits invasion and metastasis of breast cancer cells. *Am J Pathol,* 170**,** 2112-21.

SPENCE, H. J., TIMPSON, P., TANG, H. R., INSALL, R. H. & MACHESKY, L. M. 2012. Scar/WAVE3 contributes to motility and plasticity of lamellipodial dynamics but not invasion in three dimensions. *Biochem J,* 448**,** 35-42.

SWANEY, K. F. & LI, R. 2016. Function and regulation of the Arp2/3 complex during cell migration in diverse environments. *Curr Opin Cell Biol,* 42**,** 63-72.

SZKLARCZYK, D., GABLE, A. L., LYON, D., JUNGE, A., WYDER, S., HUERTA-CEPAS, J., SIMONOVIC, M., DONCHEVA, N. T., MORRIS, J. H., BORK, P., JENSEN, L. J. & MERING, C. V. 2019. STRING v11: protein-protein association networks with increased coverage, supporting functional discovery in genome-wide experimental datasets. *Nucleic Acids Res,* 47**,** D607-D613.

TAKAGI, J., ERICKSON, H. P. & SPRINGER, T. A. 2001. C-terminal opening mimics 'inside-out' activation of integrin alpha5beta1. *Nat Struct Biol,* 8**,** 412-6.

TANG, H., LI, A., BI, J., VELTMAN, D. M., ZECH, T., SPENCE, H. J., YU, X., TIMPSON, P., INSALL, R. H., FRAME, M. C. & MACHESKY, L. M. 2013. Loss of Scar/WAVE complex promotes N-WASP- and FAK-dependent invasion. *Curr Biol,* 23**,** 107-17.

TECKCHANDANI, A., MULKEARNS, E. E., RANDOLPH, T. W., TOIDA, N. & COOPER, J. A. 2012. The clathrin adaptor Dab2 recruits EH domain scaffold proteins to regulate integrin beta1 endocytosis. *Mol Biol Cell,* 23**,** 2905-16.

THEVENEAU, E., MARCHANT, L., KURIYAMA, S., GULL, M., MOEPPS, B., PARSONS, M. & MAYOR, R. 2010. Collective chemotaxis requires contact-dependent cell polarity. *Dev Cell,* 19**,** 39-53.

THOMAS, G. J., HART, I. R., SPEIGHT, P. M. & MARSHALL, J. F. 2002. Binding of TGF-beta1 latency-associated peptide (LAP) to alpha(v)beta6 integrin modulates behaviour of squamous carcinoma cells. *Br J Cancer,* 87**,** 859-67.

TI, S. C., JURGENSON, C. T., NOLEN, B. J. & POLLARD, T. D. 2011. Structural and biochemical characterization of two binding sites for nucleation-promoting factor WASp-VCA on Arp2/3 complex. *Proc Natl Acad Sci U S A,* 108**,** E463-71.

TIMPSON, P., MCGHEE, E. J., ERAMI, Z., NOBIS, M., QUINN, J. A., EDWARD, M. & ANDERSON, K. I. 2011. Organotypic collagen I assay: a malleable platform to assess cell behaviour in a 3-dimensional context. *J Vis Exp***,** e3089.

TOKUO, H., MABUCHI, K. & IKEBE, M. 2007. The motor activity of myosin-X promotes actin fiber convergence at the cell periphery to initiate filopodia formation. *J Cell Biol,* 179**,** 229-38.

TOMA-FUKAI, S. & SHIMIZU, T. 2019. Structural Insights into the Regulation Mechanism of Small GTPases by GEFs. *Molecules,* 24.

TSUJI, T., IBARAGI, S., SHIMA, K., HU, M. G., KATSURANO, M., SASAKI, A. & HU, G. F. 2008. Epithelial-mesenchymal transition induced by growth suppressor p12CDK2-AP1 promotes tumor cell local invasion but suppresses distant colony growth. *Cancer Res,* 68**,** 10377-86.

TZIVION, G., DOBSON, M. & RAMAKRISHNAN, G. 2011. FoxO transcription factors; Regulation by AKT and 14-3-3 proteins. *Biochim Biophys Acta,* 1813**,** 1938-45.

UDENWOBELE, D. I., SU, R. C., GOOD, S. V., BALL, T. B., VARMA SHRIVASTAV, S. & SHRIVASTAV, A. 2017. Myristoylation: An Important Protein Modification in the Immune Response. *Front Immunol,* 8**,** 751.

URUNO, T., LIU, J., ZHANG, P., FAN, Y., EGILE, C., LI, R., MUELLER, S. C. & ZHAN, X. 2001. Activation of Arp2/3 complex-mediated actin polymerization by cortactin. *Nat Cell Biol,* 3**,** 259-66.

VADER, P., VAN DER MEEL, R., SYMONS, M. H., FENS, M. H., PIETERS, E., WILSCHUT, K. J., STORM, G., JARZABEK, M., GALLAGHER, W. M., SCHIFFELERS, R. M. & BYRNE, A. T. 2011. Examining the role of Rac1 in tumor angiogenesis and growth: a clinically relevant RNAi-mediated approach. *Angiogenesis,* 14**,** 457-66.

VAKKILA, J. & LOTZE, M. T. 2004. Inflammation and necrosis promote tumour growth. *Nat Rev Immunol,* 4**,** 641-8.

VANDAMME, N. & BERX, G. 2019. From neural crest cells to melanocytes: cellular plasticity during development and beyond. *Cell Mol Life Sci,* 76**,** 1919-1934.

VARNAI, P., BONDEVA, T., TAMAS, P., TOTH, B., BUDAY, L., HUNYADY, L. & BALLA, T. 2005. Selective cellular effects of overexpressed pleckstrin-homology domains that recognize PtdIns(3,4,5)P3 suggest their interaction with protein binding partners. *J Cell Sci,* 118**,** 4879-88.

VASIOUKHIN, V., BAUER, C., YIN, M. & FUCHS, E. 2000. Directed actin polymerization is the driving force for epithelial cell-cell adhesion. *Cell,* 100**,** 209-19.

VELTMAN, D. 2014. Actin dynamics: cell migration takes a new turn with arpin. *Curr Biol,* 24**,** R31-R33.

VELTMAN, D. M., KING, J. S., MACHESKY, L. M. & INSALL, R. H. 2012. SCAR knockouts in Dictyostelium: WASP assumes SCAR's position and upstream regulators in pseudopods. *J Cell Biol,* 198**,** 501-8.

VELTMAN, D. M., LEMIEUX, M. G., KNECHT, D. A. & INSALL, R. H. 2014. PIP(3)-dependent macropinocytosis is incompatible with chemotaxis. *J Cell Biol,* 204**,** 497-505.

VELTMAN, D. M., WILLIAMS, T. D., BLOOMFIELD, G., CHEN, B. C., BETZIG, E., INSALL, R. H. & KAY, R. R. 2016. A plasma membrane template for macropinocytic cups. *Elife,* 5.

VIAL, E., SAHAI, E. & MARSHALL, C. J. 2003. ERK-MAPK signaling coordinately regulates activity of Rac1 and RhoA for tumor cell motility. *Cancer Cell,* 4**,** 67-79.

VICENTE-MANZANARES, M., CHOI, C. K. & HORWITZ, A. R. 2009. Integrins in cell migration--the actin connection. *J Cell Sci,* 122**,** 199-206.

VIGNJEVIC, D., KOJIMA, S., ARATYN, Y., DANCIU, O., SVITKINA, T. & BORISY, G. G. 2006. Role of fascin in filopodial protrusion. *J Cell Biol,* 174**,** 863-75.

VORMOOR, B., KNIZIA, H. K., BATEY, M. A., ALMEIDA, G. S., WILSON, I., DILDEY, P., SHARMA, A., BLAIR, H., HIDE, I. G., HEIDENREICH, O., VORMOOR, J., MAXWELL, R. J. & BACON, C. M. 2014. Development of a preclinical orthotopic xenograft model of ewing sarcoma and other human malignant bone disease using advanced in vivo imaging. *PLoS One,* 9**,** e85128.

VU, H. L., ROSENBAUM, S., PURWIN, T. J., DAVIES, M. A. & APLIN, A. E. 2015. RAC1 P29S regulates PD-L1 expression in melanoma. *Pigment Cell Melanoma Res,* 28**,** 590-8.

WAN, F., WANG, H., SHEN, Y., ZHANG, H., SHI, G., ZHU, Y., DAI, B. & YE, D. 2015. Upregulation of COL6A1 is predictive of poor prognosis in clear cell renal cell carcinoma patients. *Oncotarget,* 6**,** 27378-87.

WANG, J. H. 2012. Pull and push: talin activation for integrin signaling. *Cell Res,* 22**,** 1512-4.

WANG, J. T., KERR, M. C., KARUNARATNE, S., JEANES, A., YAP, A. S. & TEASDALE, R. D. 2010. The SNX-PX-BAR family in macropinocytosis: the regulation of macropinosome formation by SNX-PX-BAR proteins. *PLoS One,* 5**,** e13763.

WANG, W., XU, S., YIN, M. & JIN, Z. G. 2015a. Essential roles of Gab1 tyrosine phosphorylation in growth factor-mediated signaling and angiogenesis. *Int J Cardiol,* 181**,** 180-4.

WANG, Y., ARJONEN, A., POUWELS, J., TA, H., PAUSCH, P., BANGE, G., ENGEL, U., PAN, X., FACKLER, O. T., IVASKA, J. & GROSSE, R. 2015b. Formin-like 2 Promotes beta1-Integrin Trafficking and Invasive Motility Downstream of PKCalpha. *Dev Cell,* 34**,** 475-83.

WARY, K. K., MAINIERO, F., ISAKOFF, S. J., MARCANTONIO, E. E. & GIANCOTTI, F. G. 1996. The adaptor protein Shc couples a class of integrins to the control of cell cycle progression. *Cell,* 87**,** 733-43.

WASSMER, T., ATTAR, N., BUJNY, M. V., OAKLEY, J., TRAER, C. J. & CULLEN, P. J. 2007. A loss-of-function screen reveals SNX5 and SNX6 as potential components of the mammalian retromer. *J Cell Sci,* 120**,** 45-54.

WATSON, I. R., LI, L., CABECEIRAS, P. K., MAHDAVI, M., GUTSCHNER, T., GENOVESE, G., WANG, G., FANG, Z., TEPPER, J. M., STEMKE-HALE, K., TSAI, K. Y., DAVIES, M. A., MILLS, G. B. & CHIN, L. 2014. The RAC1 P29S hotspot mutation in melanoma confers resistance to pharmacological inhibition of RAF. *Cancer Res,* 74**,** 4845-4852.

WEAVER, A. M., KARGINOV, A. V., KINLEY, A. W., WEED, S. A., LI, Y., PARSONS, J. T. & COOPER, J. A. 2001. Cortactin promotes and stabilizes Arp2/3-induced actin filament network formation. *Curr Biol,* 11**,** 370-4.

WEBB, A. H., GAO, B. T., GOLDSMITH, Z. K., IRVINE, A. S., SALEH, N., LEE, R. P., LENDERMON, J. B., BHEEMREDDY, R., ZHANG, Q., BRENNAN, R. C., JOHNSON, D., STEINLE, J. J., WILSON, M. W. & MORALES-TIRADO, V. M. 2017. Inhibition of MMP-2 and MMP-9 decreases cellular migration, and angiogenesis in in vitro models of retinoblastoma. *BMC Cancer,* 17**,** 434.

WEGENER, K. L., PARTRIDGE, A. W., HAN, J., PICKFORD, A. R., LIDDINGTON, R. C., GINSBERG, M. H. & CAMPBELL, I. D. 2007. Structural basis of integrin activation by talin. *Cell,* 128**,** 171-82.

WEI, Y., EBLE, J. A., WANG, Z., KREIDBERG, J. A. & CHAPMAN, H. A. 2001. Urokinase receptors promote beta1 integrin function through interactions with integrin alpha3beta1. *Mol Biol Cell,* 12**,** 2975-86.

WEIDMANN, M. D., SURVE, C. R., EDDY, R. J., CHEN, X., GERTLER, F. B., SHARMA, V. P. & CONDEELIS, J. S. 2016. Mena(INV) dysregulates cortactin phosphorylation to promote invadopodium maturation. *Sci Rep,* 6**,** 36142.

WELCH, H. C., COADWELL, W. J., ELLSON, C. D., FERGUSON, G. J., ANDREWS, S. R., ERDJUMENT-BROMAGE, H., TEMPST, P., HAWKINS, P. T. & STEPHENS, L. R. 2002. P-Rex1, a PtdIns(3,4,5)P3- and Gbetagamma-regulated guanine-nucleotide exchange factor for Rac. *Cell,* 108**,** 809-21.

WELCH, H. C., CONDLIFFE, A. M., MILNE, L. J., FERGUSON, G. J., HILL, K., WEBB, L. M., OKKENHAUG, K., COADWELL, W. J., ANDREWS, S. R., THELEN, M., JONES, G. E., HAWKINS, P. T. & STEPHENS, L. R. 2005. P-Rex1 regulates neutrophil function. *Curr Biol,* 15**,** 1867-73.

WELCH, M. D. & WAY, M. 2013. Arp2/3-mediated actin-based motility: a tail of pathogen abuse. *Cell Host Microbe,* 14**,** 242-55.

WELLIVER, T. P., CHANG, S. L., LINDERMAN, J. J. & SWANSON, J. A. 2011. Ruffles limit diffusion in the plasma membrane during macropinosome formation. *J Cell Sci,* 124**,** 4106-14.

WENNERBERG, K. & DER, C. J. 2004. Rho-family GTPases: it's not only Rac and Rho (and I like it). *J Cell Sci,* 117**,** 1301-12.

WESTHOFF, M. A., SERRELS, B., FINCHAM, V. J., FRAME, M. C. & CARRAGHER, N. O. 2004. SRC-mediated phosphorylation of focal adhesion kinase couples actin and adhesion dynamics to survival signaling. *Mol Cell Biol,* 24**,** 8113-33.

WESTWICK, J. K., LAMBERT, Q. T., CLARK, G. J., SYMONS, M., VAN AELST, L., PESTELL, R. G. & DER, C. J. 1997. Rac regulation of transformation, gene expression, and actin organization by multiple, PAK-independent pathways. *Mol Cell Biol,* 17**,** 1324-35.

WHITE, D. P., CASWELL, P. T. & NORMAN, J. C. 2007. alpha v beta3 and alpha5beta1 integrin recycling pathways dictate downstream Rho kinase signaling to regulate persistent cell migration. *J Cell Biol,* 177**,** 515-25.

WHITFIELD, M. L., GEORGE, L. K., GRANT, G. D. & PEROU, C. M. 2006. Common markers of proliferation. *Nat Rev Cancer,* 6**,** 99-106.

WINKELMAN, J. D., BILANCIA, C. G., PEIFER, M. & KOVAR, D. R. 2014. Ena/VASP Enabled is a highly processive actin polymerase tailored to self-assemble parallel-bundled F-actin networks with Fascin. *Proc Natl Acad Sci U S A,* 111**,** 4121-6.

WISHART, A., PENG, Y., CONNER, S., GUARIN, J., CREWS, R., FATHERREE, J., GREENBERG, A. S. & OUDIN, M. J. 2020. Obesity-driven changes in ECM composition promote local invasion and metastasis of breast tumors.

WISNIEWSKI, J. R., HEIN, M. Y., COX, J. & MANN, M. 2014. A "proteomic ruler" for protein copy number and concentration estimation without spike-in standards. *Mol Cell Proteomics,* 13**,** 3497-506.

WORONIUK, A., PORTER, A., WHITE, G., NEWMAN, D. T., DIAMANTOPOULOU, Z., WARING, T., ROONEY, C., STRATHDEE, D., MARSTON, D. J., HAHN, K. M., SANSOM, O. J., ZECH, T. & MALLIRI, A. 2018. STEF/TIAM2-mediated Rac1 activity at the nuclear envelope regulates the perinuclear actin cap. *Nat Commun,* 9**,** 2124.

WU, C., BAUER, J. S., JULIANO, R. L. & MCDONALD, J. A. 1993. The alpha 5 beta 1 integrin fibronectin receptor, but not the alpha 5 cytoplasmic domain, functions in an early and essential step in fibronectin matrix assembly. *J Biol Chem,* 268**,** 21883-8.

WYCKOFF, J., WANG, W., LIN, E. Y., WANG, Y., PIXLEY, F., STANLEY, E. R., GRAF, T., POLLARD, J. W., SEGALL, J. & CONDEELIS, J. 2004. A paracrine loop between tumor cells and macrophages is required for tumor cell migration in mammary tumors. *Cancer Res,* 64**,** 7022-9.

XIAO, T., TAKAGI, J., COLLER, B. S., WANG, J. H. & SPRINGER, T. A. 2004. Structural basis for allostery in integrins and binding to fibrinogen-mimetic therapeutics. *Nature,* 432**,** 59-67.

XIE, F., LING, L., VAN DAM, H., ZHOU, F. & ZHANG, L. 2018. TGF-beta signaling in cancer metastasis. *Acta Biochim Biophys Sin (Shanghai),* 50**,** 121-132.

XU, X., WANG, Y., CHEN, Z., STERNLICHT, M. D., HIDALGO, M. & STEFFENSEN, B. 2005. Matrix metalloproteinase-2 contributes to cancer cell migration on collagen. *Cancer Res,* 65**,** 130-6.

YAMAGUCHI, H., LORENZ, M., KEMPIAK, S., SARMIENTO, C., CONIGLIO, S., SYMONS, M., SEGALL, J., EDDY, R., MIKI, H., TAKENAWA, T. & CONDEELIS, J. 2005. Molecular mechanisms of invadopodium formation: the role of the N-WASP-Arp2/3 complex pathway and cofilin. *J Cell Biol,* 168**,** 441-52.

YAMAUCHI, J., MIYAMOTO, Y., TANOUE, A., SHOOTER, E. M. & CHAN, J. R. 2005. Ras activation of a Rac1 exchange factor, Tiam1, mediates neurotrophin-3-induced Schwann cell migration. *Proc Natl Acad Sci U S A,* 102**,** 14889-94.

YANG, C., CZECH, L., GERBOTH, S., KOJIMA, S., SCITA, G. & SVITKINA, T. 2007. Novel roles of formin mDia2 in lamellipodia and filopodia formation in motile cells. *PLoS Biol,* 5**,** e317.

YANG, C., PRING, M., WEAR, M. A., HUANG, M., COOPER, J. A., SVITKINA, T. M. & ZIGMOND, S. H. 2005. Mammalian CARMIL inhibits actin filament capping by capping protein. *Dev Cell,* 9**,** 209-21.

YARAR, D., WATERMAN-STORER, C. M. & SCHMID, S. L. 2007. SNX9 couples actin assembly to phosphoinositide signals and is required for membrane remodeling during endocytosis. *Dev Cell,* 13**,** 43-56.

YELLAND, T., LE, A. H., NIKOLAOU, S., INSALL, R., MACHESKY, L. & ISMAIL, S. 2020. Structural Basis of CYRI-B Direct Competition with Scar/WAVE Complex for Rac1. *Structure*.

YOO, S. K., DENG, Q., CAVNAR, P. J., WU, Y. I., HAHN, K. M. & HUTTENLOCHER, A. 2010. Differential regulation of protrusion and polarity by PI3K during neutrophil motility in live zebrafish. *Dev Cell,* 18**,** 226-36.

YOSHIDA, S., HOPPE, A. D., ARAKI, N. & SWANSON, J. A. 2009. Sequential signaling in plasma-membrane domains during macropinosome formation in macrophages. *J Cell Sci,* 122**,** 3250-61.

YOSHIDA, S., PACITTO, R., INOKI, K. & SWANSON, J. 2018. Macropinocytosis, mTORC1 and cellular growth control. *Cell Mol Life Sci,* 75**,** 1227-1239.

YU, X., ZECH, T., MCDONALD, L., GONZALEZ, E. G., LI, A., MACPHERSON, I., SCHWARZ, J. P., SPENCE, H., FUTO, K., TIMPSON, P., NIXON, C., MA, Y., ANTON, I. M., VISEGRADY, B., INSALL, R. H., OIEN, K., BLYTH, K., NORMAN, J. C. & MACHESKY, L. M. 2012. N-WASP coordinates the delivery and F-actin-mediated capture of MT1-MMP at invasive pseudopods. *J Cell Biol,* 199**,** 527-44.

YUKI, K. E., MAREI, H., FISKIN, E., EVA, M. M., GOPAL, A. A., SCHWARTZENTRUBER, J. A., MAJEWSKI, J., CELLIER, M., MANDL, J. N., VIDAL, S. M., MALO, D. & DIKIC, I. 2019. CYRI/FAM49B negatively regulates RAC1-driven cytoskeletal remodelling and protects against bacterial infection. *Nat Microbiol,* 4**,** 1516-1531.

ZAMAN, A., WU, W. & BIVONA, T. G. 2019. Targeting Oncogenic BRAF: Past, Present, and Future. *Cancers (Basel),* 11.

ZECH, T., CALAMINUS, S. D., CASWELL, P., SPENCE, H. J., CARNELL, M., INSALL, R. H., NORMAN, J. & MACHESKY, L. M. 2011. The Arp2/3 activator WASH regulates alpha5beta1-integrin-mediated invasive migration. *J Cell Sci,* 124**,** 3753-9.

ZHANG, Y., DU, P., LI, Y., ZHU, Q., SONG, X., LIU, S., HAO, J., LIU, L., LIU, F., HU, Y., JIANG, L., MA, Q., LU, W. & LIU, Y. 2020. TASP1 Promotes Gallbladder Cancer Cell Proliferation and Metastasis by Up-regulating FAM49B via PI3K/AKT Pathway. *Int J Biol Sci,* 16**,** 739-751.

ZHANG, Z., VUORI, K., REED, J. C. & RUOSLAHTI, E. 1995. The alpha 5 beta 1 integrin supports survival of cells on fibronectin and up-regulates Bcl-2 expression. *Proc Natl Acad Sci U S A,* 92**,** 6161-5.

ZHAO, K., WANG, D., ZHAO, X., WANG, C., GAO, Y., LIU, K., WANG, F., WU, X., WANG, X., SUN, L., ZANG, J. & MEI, Y. 2020. WDR63 inhibits Arp2/3-dependent actin polymerization and mediates the function of p53 in suppressing metastasis. *EMBO Rep,* 21**,** e49269.

ZHENG, J. Q., WAN, J. J. & POO, M. M. 1996. Essential role of filopodia in chemotropic turning of nerve growth cone induced by a glutamate gradient. *J Neurosci,* 16**,** 1140-9.

ZHENG, R., LIANG, J., LU, J., LI, S., ZHANG, G., WANG, X., LIU, M., WANG, W., CHU, H., TAO, G., ZHAO, Q., WANG, M., DU, M., QIANG, F. & ZHANG, Z. 2019. Genome-wide long non-coding RNAs identified a panel of novel plasma biomarkers for gastric cancer diagnosis. *Gastric Cancer,* 22**,** 731-741.